

THE UNIVERSITY *of* ADELAIDE

SURFACE PLASMON RESONANCE SENSING

An optical fibre based SPR platform with scattered light interrogation

by

ELIZAVETA KLANTSATAYA

A thesis submitted for the degree of
Doctor of Philosophy

in the
School of Physical Sciences
Faculty of Sciences

January 2017

Elizaveta Klantsataya: *Surface Plasmon Resonance Sensing,* An optical fibre based SPR platform with scattered light interrogation, © January 2017

SUPERVISORS:
Tanya M. Monro
Heike Ebendorff-Heidepriem
Alexander François

ABSTRACT

This thesis describes the development, fabrication and optimisation of a Surface Plasmon Resonance (SPR) sensing architecture based on optical fibres. Motivated by biosensing applications, SPR was chosen as a simple and sensitive label-free technique that allows real time quantitative measurements of biomolecular interactions.

Unlike conventional fibre SPR probes, this platform utilises a novel interrogation mechanism based on the analysis of scattered radiation facilitated by a rough plasmonic coating. A theoretical study is performed in order to determine the optimal parameters of the sensing configuration, i. e. the metal coating and fibre material. This analysis revealed a trade-off between the sensitivity of these devices, and their resolution. Optical fibres with cores made of lower refractive index materials were found to increase the sensitivity of the sensor, but broaden the SPR spectral signature. This broadening of the linewidth results in an unwanted increase in the sensor resolution, which leads to an undesirable increase in the detection limit. Therefore, experiments were performed to investigate the trade off between the sensitivity and resolution of the sensor to optimise both performance characteristics.

The experimental demonstration and characterisation of a scattering SPR platform based on lead silicate fibres is described. The plasmonic coating with required surface roughness was fabricated using chemical electroless plating. In order to increase the refractive index sensitivity, a fibre SPR sensor with a lower refractive index core made of fused silica was produced. Due to the different surface properties of the silica glass and the lead silicate glass, surface modification with stannous chloride was required to fabricate suitable plasmonic coatings on the fused silica fibres. Characterisation of the new fused silica SPR sensors showed that the sensitivity of the sensing probe was improved, however, the spectral linewidth of the SPR signature was broadened, in agreement with the theoretical modelling. Nevertheless, analysis of the capability of the silica fibre based SPR sensors demonstrated potential for this platform in biological studies.

To improve the resolution without affecting the sensitivity of a sensor, smaller core fibres can be used. However, using conventional small core fibres or fibre tapers is challenging due to their fragility and the requirement for fibre post processing to access the core. To overcome these difficulties, an SPR sensor based on a silica microstructured optical fibre with a core exposed along the entire fibre length was fabricated. Exposed Core Fibres (ECFs) have small cores that are supported by thin struts inside of a larger support structure, providing mechanical robustness to the fibre. The ECF SPR sensing platform doubled the improvement in the spectral linewidth when compared to the large core fused silica fibre sensor, without compromising sensitivity.

Finally, the demonstration of Metal Enhanced Fluorescence (MEF) phenomena is presented. The effect of rough metallic coatings on the enhancement of fluorescence

emission is investigated in planar glass substrates, showing significant improvement in emission when compared to smooth metal films. An optical fibre based MEF platform was demonstrated to illustrate the potential of rough metal coatings on a fibre for surface enhanced optical phenomena.

This work is the first systematic study of a scattering based SPR sensing platform. This architecture addresses existing practical limitations associated with current SPR technologies, including but not limited to bulk design and affordability. Additionally, performance enhancement of the sensing probes is achieved through the use of alternative fibre material and geometry. The demonstrated performance improvements are not class-leading compared to commercial biosensing devices, however, the performance is in agreement with the theoretical analysis which provides a pathway for further improvement. This demonstrated that the scattering based SPR fibre platform is a practical new approach that offers the advantages of high sensitivity and signal to noise ratio, and low resolution, with the capability to improve the detection limit of SPR devices. Most importantly, this novel SPR interrogation approach allows the incorporation of two different sensing techniques, SPR and fluorescence, in the same fibre device, which opens pathways for novel biosensing applications combining the two phenomena.

DECLARATION

I certify that this work contains no material which has been accepted for the award of any other degree or diploma in my name, in any university or other tertiary institution and, to the best of my knowledge and belief, contains no material previously published or written by another person, except where due reference has been made in the text. In addition, I certify that no part of this work will, in the future, be used in a submission in my name, for any other degree or diploma in any university or other tertiary institution without the prior approval of the University of Adelaide and where applicable, any partner institution responsible for the joint-award of this degree.

I give consent to this copy of my thesis, when deposited in the University Library, being made available for loan and photocopying, subject to the provisions of the Copyright Act 1968.

I also give permission for the digital version of my thesis to be made available on the web, via the University's digital research repository, the Library Search and also through web search engines, unless permission has been granted by the University to restrict access for a period of time.

I acknowledge the support I have received for my research through the provision of an Australian Government Research Training Program Scholarship.

Adelaide, Australia, January 2017

Elizaveta Klantsataya,
19 January 2017

PUBLICATIONS

P1. **Elizaveta Klantsataya**, Alexandre François, Agnieszka Zuber, Valeria Torok, Roman Kostecki, and Tanya M. Monro. *Exposed core microstructured optical fiber surface plasmon resonance biosensor*. Proceedings SPIE, 2014.

P2. Alexandre François, Beniamino Sciacca, Agnieszka Zuber, **Elizaveta Klantsataya**, and Tanya M Monro. *Dependence of metal enhanced fluorescence on surface roughness*. In SPIE BiOS. International Society for Optics and Photonics, 2014.

P3. Alexandre François, Beniamino Sciacca, **Elizaveta Klantsataya**, Agnieszka Zuber, Peter Hoffmann, Manuela Klinger-Hoffmann, and Tanya M. Monro. *Surface plasmon scattering: an alternative approach for optical fibers biosensors*. Proceedings SPIE, 2015. (Invited presentation)

P4. Erik P. Schartner, Georgios Tsiminis, Alexandre François, Roman Kostecki, Stephen C. Warren-Smith, Linh Viet Nguyen, Sabrina Heng, Tess Reynolds, **Elizaveta Klantsataya**, Kris J. Rowland, Andrew D. Abell, Heike Ebendorff-Heidepriem, and Tanya M. Monro. *Taming the light in microstructured optical fibers for sensing*. International Journal of Applied Glass Science, 2015. (Invited paper)

P5. **Elizaveta Klantsataya**, Alexandre François, Heike Ebendorff-Heidepriem, Peter Hoffmann, and Tanya M. Monro. *Surface Plasmon scattering in exposed core optical fiber for enhanced resolution refractive index sensing*. Sensors, 2015.

P6. **Elizaveta Klantsataya**, Alexandre François, Heike Ebendorff-Heidepriem, Beniamino Sciacca, Agnieszka Zuber, and Tanya M. Monro. *The effect of surface roughness on metal enhanced fluorescence in planar substrates and optical fibers*. Optical Materials Express, 2016.

P7. William Morrish, Peter West, Nathan Orlando, **Elizaveta Klantsataya**, Kirsty Gardner, Stephen Lane, Raymond Decorby, Alexandre François, and Alkiviathes Meldrum. *Refractometric micro-sensor using a mirrored capillary resonator*. Optics Express, 2016.

P8. **Elizaveta Klantsataya**, Peipei Jia, Heike Ebendorff-Heidepriem, Tanya M. Monro, and Alexandre François. *Plasmonic Fiber Optic Refractometric Sensors: From Conventional Architectures to Recent Design Trends*. Sensors, 2016.

ACKNOWLEDGEMENTS

I would like to express my sincere gratitude to my supervisors, Dr. Alexandre François, Prof. Heike Ebendorff-Heidepriem, and Prof. Tanya M. Monro, for their knowledge contribution, insightful comments, and continuous support during my PhD project. Their guidance has helped me achieve the outcomes of my research and to write this thesis.

Besides my supervisors, I would like to thank my friends and colleagues from The University of Adelaide: Sebastian Ng, Christopher Kalnins, Myles Clark, Agnieszka Zuber, Erik Schartner, Matthew Henderson, Peter Hoffmann, Andre Luiten, Andrew McKinnon, Olivia Towers, Carly Whittaker, Ada Uminska, James Anstie, and Roman Kostecki, for the motivation, stimulating discussions, professional help, and emotional support during my PhD project. I would also like to acknowledge the contribution of Ken Neubauer from Adelaide Microscopy for his expertise and knowledge sharing. In addition, I thank all of my friends, in particular, Elena Gorbunova, Tristan Davies, Tevita Steen, Antonija Mišić, Megan Schartner, and Sharanna Christensen, for their encouragement and support.

This project was made a lot easier with the help of the professional staff of the School of Physical Sciences and the Institute for Photonics and Advanced Sensing. I would also like to express my gratitude to the colleagues from South Australian Research and Development Institute and Institute of Medical and Veterinary Science for their help with the biological aspects of my research during the initial stages of this project.

Last, but not least, I would like to thank my family for their love and encouragement, my Mum, Uncle Sasha, Sergey, Joan, Lawrence, Georgia, Lorraine, Justin, Glenn, Auntie Dot, and Martin. Most of all, I would like to sincerely thank my partner, Seb, for his continuous motivation, infinite patience, and all of his help with my PhD project.

CONTENTS

I INTRODUCTION 1

1 INTRODUCTION TO BIOLOGICAL SENSING 3
- 1.1 Biosensing technologies . . . 3
  - 1.1.1 Bioreceptors . . . 4
  - 1.1.2 Transduction mechanisms . . . 6
  - 1.1.3 Optical biosensors . . . 9
- 1.2 Motivation and project aims . . . 13
  - 1.2.1 Motivation . . . 13
  - 1.2.2 Project aims . . . 15
- 1.3 Thesis structure . . . 16

2 SURFACE PLASMON RESONANCE (SPR) 19
- 2.1 SPR fundamentals . . . 19
- 2.2 Electromagnetic properties of metals . . . 21
- 2.3 Theoretical formalism of surface plasmon polaritons . . . 26
  - 2.3.1 Helmholtz equation . . . 26
  - 2.3.2 TM and TE modes on a single interface . . . 27
  - 2.3.3 Dispersion relation of surface plasmons . . . 28
  - 2.3.4 Characteristics of surface plasmons . . . 32
  - 2.3.5 Surface plasmons in multilayer systems, long range surface plasmons . . . 34
- 2.4 Surface Plasmon Resonance sensors . . . 35
  - 2.4.1 Excitation of surface plasmons . . . 36
  - 2.4.2 Interrogation methods for SPR . . . 40
  - 2.4.3 Principles of biological sensing with SPR . . . 43
  - 2.4.4 Performance characteristics of SPR sensors . . . 46
- 2.5 Review of SPR fibre sensors . . . 48
  - 2.5.1 Classification based on fibre type . . . 49
  - 2.5.2 Classification based on geometry . . . 50
  - 2.5.3 Classification based on type of plasmonic coating . . . 55
  - 2.5.4 Classification based on excitation method . . . 58
  - 2.5.5 Classification based on interrogation method . . . 60
  - 2.5.6 Classification based on application . . . 61
  - 2.5.7 Experimental demonstrations of SPR fibre sensors . . . 63
- 2.6 Summary . . . 65

II DEVELOPMENT OF PLASMONIC FIBRE SENSING ARCHITECTURES 69

3 ANALYTICAL MODELLING OF SPR IN OPTICAL FIBRES 71
- 3.1 Transfer Matrix Method (TMM) . . . 71
  - 3.1.1 TMM formalism . . . 71

3.1.2 Modelling of SPR in prism using TMM . . . 73
3.2 Modelling of SPR fibre sensors with TMM . . . 75
3.2.1 Influence of fibre core material . . . 78
3.2.2 Influence of fibre numerical aperture . . . 83
3.2.3 Influence of fibre core diameter . . . 84
3.2.4 Influence of plasmonic coatings . . . 87
3.3 Summary and scope for improvement . . . 91
4 SCATTERING BASED SPR FIBRE SENSING PLATFORM 93
4.1 Overview of the platform architecture . . . 93
4.1.1 Introduction . . . 93
4.1.2 Experimental setup . . . 94
4.1.3 Performance analysis . . . 95
4.1.4 Discussion . . . 98
4.2 Sensor fabrication . . . 99
4.2.1 Fibre preparation . . . 99
4.2.2 Electroless plating of silver films . . . 99
4.3 Silver coating characterisation . . . 101
4.3.1 Imaging techniques . . . 101
4.3.2 Transmission measurements . . . 103
4.4 Silica surface modification . . . 103
4.4.1 Characterisation of silver films on silica surfaces . . . 104
4.4.2 Silica surface treatments . . . 104
4.4.3 Tin sensitization process optimisation . . . 114
4.5 Silica fibre sensor characterisation . . . 121
4.5.1 Experimental setup . . . 121
4.5.2 Performance characterisation . . . 123
4.5.3 Tapered silica fibre SPR probes . . . 130
4.6 Biosensing applications . . . 132
4.6.1 Surface functionalisation strategy . . . 133
4.6.2 Norovirus (NoV) detection . . . 134
4.6.3 Detection of quantum dots (Qdots) . . . 139
4.7 Summary and scope for improvement . . . 141
5 EXPOSED CORE MICROSTRUCTURED FIBRE (ECF) SPR SENSOR 145
5.1 ECF background . . . 145
5.2 ECF SPR probe fabrication . . . 146
5.3 ECF sensor characterisation . . . 148
5.3.1 Flow cell design . . . 148
5.3.2 Optical setup and experimental procedure . . . 148
5.3.3 Analysis of the results . . . 149
5.4 Multiple SPR peaks in acrylate-coated ECFs . . . 152
5.5 Dependence of resonance on sensing location . . . 156
5.6 Exposed core fibre modification . . . 161
5.7 Summary and potential future work . . . 167
6 METAL ENHANCED FLUORESCENCE (MEF) 169

6.1 Introduction . . . 169
6.2 Distance-dependent enhancement on planar substrates . . . 172
6.2.1 MEF sample fabrication . . . 173
6.2.2 Experimental procedure . . . 174
6.2.3 Results and discussion . . . 176
6.3 Fluorescence enhancement in a fibre based MEF probe . . . 179
6.3.1 MEF fibre sensor fabrication and characterisation . . . 179
6.3.2 Influence of film thickness on fluorescence enhancement . . . 183
6.3.3 AFM study of silver film topography . . . 185
6.3.4 Increasing SPR wavelength with glycerol solutions . . . 188
6.3.5 Dependence of enhancement on sensing region location . . . 189
6.4 Summary and conclusions . . . 190
7 CONCLUSIONS AND RECOMMENDATIONS FOR FUTURE WORK 193
7.1 Summary of the work and conclusions . . . 193
7.2 Recommendations for future work . . . 196

III APPENDIX 199
A APPENDIX A: LIGHT SOURCE SPECTRA 201
B APPENDIX B: STEPS FOR NOV DETECTION 205
C APPENDIX C: SUPPLEMENTARY SPR SPECTRA FOR ECFS 207
D APPENDIX D: PUBLICATIONS 211

BIBLIOGRAPHY 259

LIST OF FIGURES

Figure 1.1 Components of a typical biosensor. 4
Figure 1.2 Schematic representation of antibody-antigen based biosensors. 5
Figure 1.3 Sandwich assay fluorescence technique. 10
Figure 1.4 Fabry Pérot etalon refractometric sensor. 11
Figure 1.5 WGM microresonator. 12
Figure 2.1 Schematic representation of SPR. 20
Figure 2.2 LSPR on a spherical metallic nanoparticles. 21
Figure 2.3 Complex refractive index of three metals, silver, gold and copper, that are commonly used in SPR applications. 23
Figure 2.4 Planar geometry of electromagnetic wave propagating along the interface between two media. 26
Figure 2.5 Dispersion relation of SPPs. 31
Figure 2.6 Magnetic field intensity profile (H_y) showing penetration depths into dielectric and metal at $x = 0$. 32
Figure 2.7 Real part of magnetic field intensity (H_y) showing oscillatory behaviour and decay at the interface ($z = 0$). 33
Figure 2.8 Common SPR supporting structures. 35
Figure 2.9 ATR couplers for optical SPP excitation. 38
Figure 2.10 Total Internal Reflection (TIR) couplers for optical Surface Plasmon Polariton (SPP) excitation. 39
Figure 2.11 Grating coupler for optical SPP excitation. 39
Figure 2.12 Optical excitation of SPPs using high NA microscope objective. 40
Figure 2.13 Angular SPR interrogation. 41
Figure 2.14 Spectral SPR interrogation. 42
Figure 2.15 Conceptual representation of SPR biochemical sensors. 43
Figure 2.16 Schematic design of a SPR biosensor based on Kretschmann configuration. 44
Figure 2.17 SPR sensorgram of binding kinetics. 45
Figure 2.18 Sensitivity of SPR sensors with angular interrogation. 47
Figure 2.19 Classification of SPR fibre sensors. 49
Figure 2.20 Fibre based SPR sensor. 50
Figure 2.21 Schematics of geometry modified optical fibre SPR sensors implemented on a side of an optical fibre. 51
Figure 2.22 Schematics of geometry modified optical fibre tip SPR sensors. 54
Figure 2.23 Cross sections of optical fibre core with common metal coating layouts. 56
Figure 2.24 Schematics of the fibre grating assisted SPR fibre sensors. . . . 59
Figure 3.1 Schematic representation of a stratified medium. 72
Figure 3.2 Prism-based SPR for TMM simulation. 74

Figure 3.3 Reflectance of TM wave in prism SPR. 74
Figure 3.4 Fibre-based SPR for TMM simulation. 75
Figure 3.5 Simulated reflectance of TM wave in F2 fibre SPR with water as an adjacent dielectric ($n = 1.33$). 77
Figure 3.6 Simulated normalised transmitted power in F2 fibre SPR. . . . 78
Figure 3.7 Simulated sensitivity curve for F2 fibre SPR sensor. 79
Figure 3.8 Simulated sensitivity curve for F2 fibre SPR sensor for large range of external RIs. 79
Figure 3.9 Simulated reflectance of TM wave in silica fibre SPR with water as an adjacent dielectric ($n = 1.33$). 80
Figure 3.10 Simulated normalised transmitted power in a silica fibre SPR. 81
Figure 3.11 Simulated sensitivity curve for silica fibre SPR sensor. 81
Figure 3.12 Glass dispersion. 82
Figure 3.13 Sensitivity of SPR sensors with different materials of fibre core. 83
Figure 3.14 Normalised transmitted power for silica fibre sensors with different NAs. 84
Figure 3.15 Sensitivity for silica fibre SPR sensors with different fibre NA. . 85
Figure 3.16 FWHM for silica fibre SPR sensors with different fibre NA. . . . 85
Figure 3.17 Sensitivity of SPR silica fibre sensors with different core diameters. 86
Figure 3.18 FWHM of SPR silica fibre sensors with different core diameters. 87
Figure 3.19 Metal dielectric functions. 88
Figure 3.20 Sensitivity curves for SPR sensors with different metals. 89
Figure 3.21 Normalised transmitted power for a SPR sensor with different Ag film thickness. 90
Figure 3.22 Sensitivity of SPR sensor as a function of Ag film thickness. . . 90
Figure 4.1 A schematic of a scattering based SPR fibre probe. 94
Figure 4.2 Optical setup for F2 fibre SPR sensor characterisation. 95
Figure 4.3 Raw SPR spectra for F2 fibre sensor. 96
Figure 4.4 Processed SPR spectra for F2 fibre sensor. 96
Figure 4.5 Sensitivity curve for F2 fibre sensor. 97
Figure 4.6 A schematic of steps involved in Tollens reaction. 101
Figure 4.7 SEM images of F2 fibre core coated with thin silver film without pre-treatment. 102
Figure 4.8 AFM image of surface topography of a silver film. 102
Figure 4.9 SEM images of silica fibre core coated with thin silver film without pre-treatment. 105
Figure 4.10 SEM images of silica fibre core coated with thick silver film without pre-treatment. 105
Figure 4.11 A schematic of silica surface sensitisation with $SnCl_2$. 108
Figure 4.12 Silver electroless plating on silica ribbons with different surface pre-treatments. 113
Figure 4.13 Thickness of silver films vs. the Tollens deposition time at 26°C, pre-treatment is fresh aqueous $SnCl_2$ solution of 0.5 M. 116

Figure 4.14 Prism setup for SPR characterisation on planar substrates. . . . 116
Figure 4.15 Thickness of silver films vs. the Tollens deposition time at 24°C, pre-treatment is fresh aqueous $SnCl_2$ solution of 0.5 M. 118
Figure 4.16 SPR ratio vs. silver films thickness prepared by Tollens method at 24°C, pre-treatment is a fresh aqueous $SnCl_2$ solution of 0.5 M. 118
Figure 4.17 Thickness of silver films vs. the Tollens deposition time at 24°C for three $SnCl_2$ pre-treatments. 119
Figure 4.18 SPR ratio vs. silver films thickness prepared by Tollens method at 24°C for different $SnCl_2$ pre-treatments. 120
Figure 4.19 Optical setup for silica fibre SPR sensor characterisation. . . . 122
Figure 4.20 Optical setup for SPR fibre sensor characterisation. 122
Figure 4.21 Close up of a cross sectional flow cell. 123
Figure 4.22 Raw SPR spectra for the SiO_2 fibre sensor. 124
Figure 4.23 Processed SPR spectra for SiO_2 fibre sensor. 125
Figure 4.24 Sensitivity curve for SiO_2 fibre sensor. 125
Figure 4.25 Steps of the characterisation experiment for SiO_2 fibre sensor. 126
Figure 4.26 Sensitivity and FWHM for a SiO_2 fibre sensor. 127
Figure 4.27 Scattered SPR spectra for a SiO_2 fibre sensor. 130
Figure 4.28 Transmitted SPR spectra for SiO_2 fibre sensor. 131
Figure 4.29 Raw SPR spectra for SiO_2 fibre sensor of 140 µm core diameter and a taper of 35 µm diameter. 132
Figure 4.30 TEM image of NoV VLPs. 135
Figure 4.31 Surface functionalisation approaches for NoV detection. 137
Figure 4.32 Example of kinetic analysis (sensorgram) for biotin and neutravidin binding. 138
Figure 4.33 Processed SPR spectra for NoV detection with SiO_2 fibre sensor using the Protein A approach. 139
Figure 4.34 Steps of the NoVs detection experiment with a SiO_2 fibre sensor using the Protein A approach. 140
Figure 4.35 Surface functionalisation approaches for the Qdot detection. . 141
Figure 4.36 Processed SPR spectra for Qdot detection with the SiO_2 fibre sensor using Protein A approach. 142
Figure 4.37 Steps of the Qdots detection experiment with the SiO_2 fibre sensor using Protein A approach. 142
Figure 5.1 SEM images of silica fibres' cross sections. 146
Figure 5.2 SEM images of silica ECF coated with silver film. 147
Figure 5.3 Schematic of the new capillary flow cell. 148
Figure 5.4 Optical setup for silica ECF SPR sensor characterisation. 149
Figure 5.5 Raw SPR spectra for the bare ECF sensor. 150
Figure 5.6 Processed SPR spectra for the bare ECF sensor. 150
Figure 5.7 Sensitivity and FWHM for the bare ECF sensor. 151
Figure 5.8 Schematics of cross sections of ECFs with possible coupling conditions. 153

Figure 5.9 Processed SPR spectra for coated ECF sensor with two peaks. . 154
Figure 5.10 Sensitivity curves for coated ECF sensor with two peaks. . . . 154
Figure 5.11 Processed SPR spectra for a coated ECF sensor taken from the core side (two peaks) and the support structure side (one peak).155
Figure 5.12 Sensitivity curves for coated ECF sensor with two spectra collection arrangements. 156
Figure 5.13 Scattered SPR spectra for the 5 spots on the bare ECF sensor with core coupling. 157
Figure 5.14 Scattered SPR spectra for the 5 spots on the bare ECF sensor with support structure coupling. 158
Figure 5.15 Scattered SPR spectra for the 5 spots on the coated ECF sensor with core and support structure coupling (as shown on the inset). 159
Figure 5.16 Scattered SPR spectra for the 5 spots on the coated ECF sensor with support structure coupling (as shown on the inet). 160
Figure 5.17 Number of modes vs core diameter for ECF with air clad and cladding with RI of 1.33. 161
Figure 5.18 Number of modes in a 10 μm ECF vs cladding RI. 162
Figure 5.19 Schematics of pressure filling setup and cross sections of ECFs. 163
Figure 5.20 SEM images of silica ECF filled with polymer. 164
Figure 5.21 Processed SPR spectra for the coated ECF sensor filled with a polymer. 165
Figure 5.22 Processed SPR spectra for bare ECF sensor filled with polymer. 166
Figure 5.23 Sensitivity and FWHM for bare ECF sensor filled with polymer. 166
Figure 6.1 Effect of metal and SPs on fluorescence. 170
Figure 6.2 Schematic of a typical interaction between fluorophore dye and metal nanoparticles. 171
Figure 6.3 Schematic of prism configuration for MEF. 175
Figure 6.4 A typical increase in the angular position of the SPR dip as a function of increasing number of PE layers on a planar substrate. 176
Figure 6.5 Fluorescence emission intensity and SPR signal of a planar substrate. 177
Figure 6.6 Dependence of fluorescence enhancement factor on Polyelectrolyte (PE) spacer thickness for different roughness of silver film in planar substrates. 178
Figure 6.7 Maximum fluorescence enhancement factor vs. surface roughness of silver film in planar substrates. 178
Figure 6.8 Schematic of fibre configuration for MEF. 180
Figure 6.9 Optical setup for MEF fibre sensor characterisation. 180
Figure 6.10 SPR spectra at each step of PE spacer deposition and dye attachment. 181
Figure 6.11 Arrangement of two regions inside one capillary flow cell. . . 182

Figure 6.12 Fluorescence spectra of the organic dye on a 71 nm Ag coated fibre probe. . . . 184
Figure 6.13 Fluorescence spectra of organic dye on a 22 nm Ag coated fibre probe. . . . 184
Figure 6.14 Fluorescence EF vs Ag film thickness. . . . 185
Figure 6.15 Equivalent disk radius of the surface features on a 22 nm-thick Ag film. . . . 186
Figure 6.16 Equivalent disk radius of the surface features on a 71 nm-thick Ag film. . . . 186
Figure 6.17 Fluorescence intensity vs. external RI for fibre probes coated with thick and thin Ag film and corresponding bare regions on F2 fibre. . . . 189
Figure 6.18 Fluorescence spectra of the organic dye on different spots of the fibre probe. . . . 190
Figure A.1 LED spectrum (Thorlabs, MCWHLP1). . . . 201
Figure A.2 Broadband LED spectrum (Thorlabs, MBB1L3). . . . 202
Figure A.3 Halogen light source spectrum (Ocean Optics, HL-2000). . . . 202
Figure A.4 LDLS spectrum (Energetiq Technology, EQ99-XFC-LDLS). . . . 203
Figure C.1 SPR spectra in water for 5 spots on a bare ECF (BOP) sensor. . . . 208
Figure C.2 SPR spectra in water for 5 spots on ECF (BOP) sensor with acrylate coating. . . . 209

LIST OF TABLES

Table 2.1 Free electron densities, relaxation times and plasma frequencies for three noble metals. . . . 25
Table 2.2 Summary of recent experimental demonstrations of SPR fibre sensors. . . . 64
Table 3.1 Performance characteristics of SPR fibre sensors with different core materials. . . . 82
Table 3.2 Performance characteristics of SPR fibre sensors with different plasmonic materials. . . . 88
Table 4.1 Silica surface treatments and their combinations used to analyse the effects on silver adhesion deposited by electroless plating. . . . 111
Table 4.2 Different methods used for optimisation of $SnCl_2$ silica sensitisation. . . . 114
Table 4.3 SPR ratio for planar samples coated with silver films by the Tollens method at 26°C pre-treated with fresh aqueous $SnCl_2$ solution of 0.5 M. The sputtered sample is included for comparison. . . . 117
Table 4.4 Performance comparison of F2 and silica SPR fibre sensors. . . . 128
Table 4.5 Performance comparison of tapered and not tapered silica SPR fibre probes. . . . 132
Table 5.1 Comparison of the performance characteristics of ECF-based silica SPR sensors. . . . 151
Table 6.1 Properties of silver films fabricated by different methods. Thickness of the silver films was estimated through transmission measurements. Atomic Force Microscopy (AFM) was used to determine silver film roughness and verify film thickness. . . . 174
Table 6.2 Grain distribution analysis of chemically deposited silver films. 187
Table B.1 Typical steps for Norovirus (NoV) detection experiment using protein A – antibody approach. . . . 205

ACRONYMS

AFM Atomic Force Microscopy

APTES (3-Aminopropyl) triethoxysilane

ATR Attenuated Total Reflection

BOP Beginning of Pull

CVD Chemical Vapour Deposition

DL Detection Limit

DNA Deoxyribo- Nucleic Acid

ECF Exposed Core Fibre

EDC (1-Ethyl-3-(3-Dimethylaminopropyl)-Carbodiimide)

EF Enhancement Factor

ELISA Enzyme-Linked Immunosorbent Assay

FBG Fibre Bragg Grating

FOM Figure of Merit

FRET Förster resonance energy transfer

FWHM Full Width at Half Maximum

GI Graded Index

HBGA Histo-Blood Group Antigen

HeC Hetero-core

HeNe Helium Neon

HoC Hollow-core

Ig Immunoglobulin

IMI Insulator-Metal-Insulator

IR Infrared

ITO Indium Tin Oxide

LED Light Emitting Diode

LDLS Laser Driven Light Source

LPF Long Pass Filter

LPFG Long Period Fibre Grating

LRSP Long Range Surface Plasmon

LRSPR Long Range Surface Plasmon Resonance

LSP Localised Surface Plasmon

LSPR Localised Surface Plasmon Resonance

MEF Metal Enhanced Fluorescence

MIM Metal-Insulator-Metal

MOF Microstructured Optical Fibre

MMF Multi Mode Fibre

NA Numerical Aperture

NHS N-Hydroxysuccinimide

NoV Norovirus

NP Nanoparticle

PAH Poly(Allylamine Hydrochloride)

PBS Phosphate-Buffered Saline

PCF Photonic Crystal Fibre

PCR Polymerase Chain Reaction

PE Polyelectrolyte

pH Potential Hydrogen

PSS Poly(Sodium 4-Styrenesulfonate)

PMF Polarization Maintaining Fibre

PVD Physical Vapour Deposition

Qdot Quantum Dot

RI Refractive Index

RIU Refractive Index Units

RMS Root Mean Square

RNA Ribonucleic Acid

SARDI South Australian Research and Development Institute

SEM Scanning Electron Microscopy

SERS Surface Enhanced Raman Scattering

SNR Signal to Noise Ratio

SMF Single Mode Fibre

SP Surface Plasmon

SPM Scanning Probe Microscopy

SPP Surface Plasmon Polariton

SPR Surface Plasmon Resonance

SPW Surface Plasmon Wave

SRSP Short Range Surface Plasmon

TEM Transmission Electron Microscopy

TFBG Tillted Fibre Bragg Grating

TIR Total Internal Reflection

TE Transverse Electric

TEM Transmission Electron Microscopy

TFBG Tilted Fibre Bragg Grating

TM Transverse Magnetic

TMM Transfer Matrix Method

UV Ultraviolet

VLP Virus Like Particle

WGM Whispering Gallery Mode

Part I

INTRODUCTION

In Part I an introduction and relevant theoretical background for this research is provided. The field of biosensing is introduced in Chapter 1. Motivation for this research, the project aims and thesis structure are presented at the end of the chapter. Chapter 2 gives an introduction to Surface Plasmon Resonance (SPR) and the history of its discovery, describes the fundamental concepts and theoretical formalism of surface plasmons based on Maxwell's equations, and outlines principles of SPR based sensing. A classification scheme and literature review of optical fibre based SPR sensors are provided at the end of the chapter.

1

INTRODUCTION TO BIOLOGICAL SENSING

Biological sensing plays a significant role in science and modern technology allowing the study of interactions between biomolecules and the detection of biological species. Biosensors are widely used in a broad range of applications, such as medical diagnostics, drug design, life science research, and food safety. Various biosensing platforms have been developed including electrochemical, calorimetric, magnetic, and optical, to name a few [1]. Regardless of the mechanism that underpins each biosensor, all sensing devices aim to achieve a low detection limit, specificity to targets, fast detection, simplicity of fabrication, and low cost.

Due to the wide range of sensor designs and potential applications, biosensor development builds on a variety of research fields including biology, chemistry, physics, engineering, and computer science. The transdisiplinary approach used in biosensing research is very attractive as it is rich with untapped opportunity, and was the main motivator for pursuing work in the area of biological sensing. However, it requires an appreciation of the many challenges that cross the border between disciplines and are addressed in this thesis. This chapter provides a background on biosensing technologies. Particular attention is given to optical sensing techniques and their use in biological applications. The motivation and aims of this research as well as the structure of the thesis are presented at the end of the chapter.

1.1 BIOSENSING TECHNOLOGIES

A sensor is a device that can convert a property of an analyte, the properties of biomolecules in the case of biosensors, into a detectable response [2]. The main components of a biosensor are biorecognition elements (or bioreceptors) that directly interact with the analyte and allow the recognition of specific biomolecules of interest, and transducers that transform this interaction into a physical or chemical response (Figure 1.1). Both, transducers and biorecognition elements play an important part in determining the sensitivity of the biosensor [2].

As the interaction between biological and physiochemical components of a biosensor occur at nanoscale distances, they need to be placed in close proximity of each other. In order to achieve this, the surface of the transducer is functionalised. Typically, this involves immobilisation of the bioreceptors on the surface of the transducer [3]. Using these mechanisms, biosensors are capable of determining the presence or concentration of certain biological species in the analyte. Moreover, label-free biosensing platforms allow the study of binding kinetics and the determination of association and dissociation constants, which are of critical importance for biological research [4].

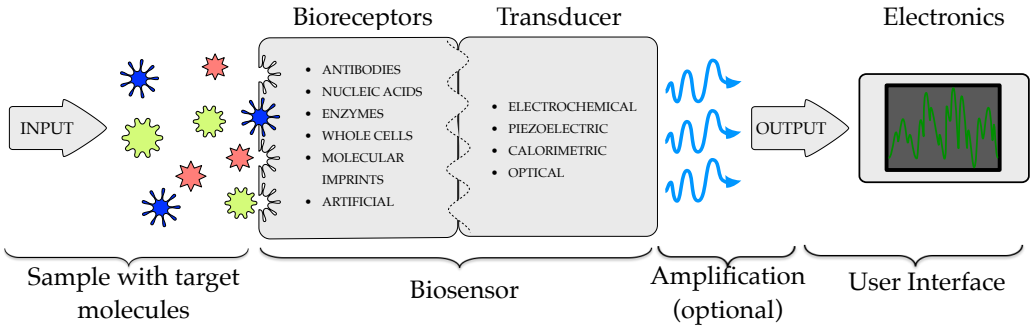


Figure 1.1: Components of a typical biosensor: the bioreceptor recognizes the analyte on a molecular level, while the transducer converts molecular recognition into a measurable signal.

Traditionally, biosensors are categorised based on the biorecognition principle and the transduction mechanisms they employ. The following section reviews a range of biosensors based on these two classification schemes.

1.1.1 *Bioreceptors*

Bioreceptors are biomolecular species or living biological systems that use a biochemical mechanism for target recognition. The choice of bioreceptor molecules is dictated by their specificity to the target in the analyte [5]. The most common forms of biomolecular interactions that biorecognition elements utilise are: nucleic acid interactions, antibody-antigen interactions, enzymatic interactions, cellular interactions, and interactions using synthetic materials [1].

NUCLEIC ACID BIORECEPTORS Nucleic acid based biosensors rely on the conversion of base-pair recognition events into measurable signals. The complementary pairing of base pairs (adenine-thymine and cytosine-guanosine in Deoxyribo- Nucleic Acid (DNA)-based sensors for example) forms a basis for the recognition principle in nucleic acid-based biosensors. If the sequence of a target nucleic acid, such as a viral DNA or Ribonucleic Acid (RNA), is known, the complementary strand can be synthesised [1]. Various forms of transduction have been used with nucleic acid-based bioreceptors. The most common DNA sensors use fluorescent labels, as well as molecular beacons, although electrochemical detection, surface plasmon resonance, and surface-enhanced Raman scattering equivalents have also been demonstrated [1, 6]. The main disadvantage of these sensors, however, is the temperature sensitivity of the nucleic acid interactions. Many nucleic acids undergo denaturation at increased temperatures, and therefore, strict temperature control is required.

ANTIBODY-ANTIGEN BIORECEPTORS An antibody is a complex biological molecule that can specifically bind to certain structures such as antigens. Antibodies are produced by a host in response to the invasion of foreign molecules, such as viruses [7]. These unique binding capabilities make antibodies useful for biosensing

applications where antigens that are present in an analyte can specifically bind to immobilised antibodies.

For biosensors that involve antibodies as bioreceptors, the performance can be drastically improved by using a specific orientation of the antibodies with respect to the sensor surface rather than a random orientation. This is a result of the structure of antibodies that commonly has a Y-shaped layout with two identical antigen binding sites at the tip of each arm. A typical antibody consists of four polypeptide chains, two identical light chains, and two identical heavy chains. Two binding sites are formed by N-terminal regions of light and heavy chains, as shown in Figure 1.2 [7].

Antibody-antigen interactions are among the most commonly used biorecognition methods. Antibodies can be raised specifically to target virus particles, other antibodies, proteins or biomolecules. High affinity binding can be achieved using antibody bioreceptors [8]. The major advantage of antibody based biosensors is that less rigorous purification of the sample is required. Moreover, the potential for fast in-field measurements make these immunosensors a preferable technique in comparison with traditional immunoassays. Various transduction mechanisms were successfully used with antibody bioreceptors including but not limited to optical, acoustic, and electrochemical techniques [5, 9].

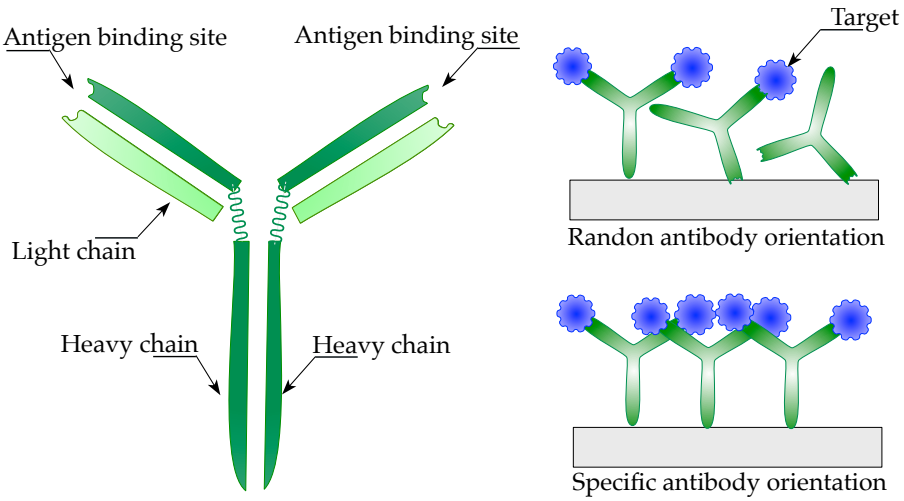


Figure 1.2: Schematic representation of antibody-antigen based biosensors.

ENZYMATIC BIORECEPTORS Enzymatic interaction is another popular biorecognition element. Enzymes are chosen as bioreceptors based on their catalytic activity as well as their specific binding to desired molecules. A wide variety of measurable reaction products, such as heat, light, protons and electrons, result from the catalytic processes making enzymes a very attractive choice for biosensing applications. The generated product usually determines the transduction mechanism of enzymatic biosensor [1]. Even though enzymes provide attractive catalytic properties and specific binding capabilities, many factors can potentially affect an enzyme-based biosensor performance. Enzymes are very sensitive to temperature and Potential Hy-

drogen (pH) factor and their catalytic activity can easily be altered. The type of immobilisation and thickness of the enzyme layer can also negatively influence the biosensor performance [5, 6].

CELLULAR BIORECEPTORS Whole cells and cellular structures have been successfully used as bioreceptors. The whole cell or organism, or just a particular cellular component might be capable of specifically binding to certain target species. Biosensors based on cellular interactions generally feature a low detection limit. Whole cells have many biochemical pathways and are therefore sensitive to various biochemical stimuli. Cell-based biosensors use the direct measurement of physiological function and changes induced by viruses and toxins, therefore there is a potential of using whole cells for previously unknown pathogens. Typically, cells and microbial organism based sensors are much cheaper to produce in comparison with antibody and nucleic acid-based biosensors. However, the major drawback of using cellular bioreceptors is that the same cellular response can be produced by different agents. This makes it difficult to classify the type of the agent based only on the functional activity of the cells [10].

SYNTHETIC BIORECEPTORS Synthetic, or biomimetic, bioreceptors are a promising tool that has emerged as an alternative to natural biorecognition elements. An artificial bioreceptor is fabricated to mimic the binding capabilities of antibodies, enzymes, nucleic acids, etc. Several techniques fall into biomimetic bioreceptor category. Among them are artificial membranes [10], molecular imprinting, and genetically engineered molecules, such as aptamers [6, 8]. Even though, this technique promises various advantages including versatility of target molecules and high affinities, fabrication of these materials is complex [1].

Various kinds of biorecognition elements have been successfully used in biosensing applications. The choice of bioreceptors significantly affects biosensor performance. As such, specificity and binding strength are greatly influenced by the capabilities of the bioreceptors. In addition, the surface functionalisation technique is influenced by bioreceptor choice. Specific binding is provided by antibody-antigen interaction, antibody orientation on the sensor surface, and availability of various antibodies, making this type of bioreceptors a preferential choice for the application of the sensors developed in the current work.

1.1.2 *Transduction mechanisms*

In addition to the bioreception principle, biosensors can be classified by the physical or chemical transduction mechanism they employ. Traditionally, transducers are divided into the following categories: electrochemical, electrical, piezoelectric, calorimetric, magnetic, and optical.

ELECTRICAL AND ELECTROCHEMICAL TRANSDUCERS Electrochemical sensors are based on the principle that a chemical reaction between immobilised molecules

and an analyte produces or consumes electrons or ions which changes the electrical properties of the solution. Depending on the key measurable electrical property, electrochemical biosensors can be further classified onto amperometric, potentiometric, impedance, and ion-sensitive biosensors [9].

Amperometric biosensors typically rely on the quantification of biochemicals based on their enzyme-catalyzed electro-oxidation or electroreduction. This is among the most widely used type of electrochemical sensor [8]. Potentiometric biosensors are based on the measurements of potential generated across an ion sensitive membrane that separates two electric solutions when no current is applied. They can be easily mass fabricated and are commercially available in a variety of forms [6]. Impedance biosensors measure changes in conductance or resistance of the solution which results from biochemical reactions that produce electrons or ions. Conductance measurements, however, often have relatively low sensitivity. Ion-sensitive biosensors use field-effect transistors to measure ion concentration in the solution. When the ion concentration in the solution changes due to a biochemical reaction, the current through the transistor changes accordingly.

The majority of electrochemical biosensors are relatively inexpensive, robust, sensitive and suitable for mass production. However, there are several problems associated with electrochemical techniques, such as high sensitivity to pH change and non-specific binding of molecules which leads to an increase in false positive results. Modern options include the use of nanofabrication to create miniaturized and highly sensitive devices based on nanowires, i. e. silicon nano-wires, carbon nanotubes, conducting polymer nanowires, metallic nanowires, etc. However, non trivial design and difficulties in the fabrication and assembly make these biosensors very challenging to produce [11].

PIEZOELECTRIC TRANSDUCERS Piezoelectric biosensors employ another means of physical transduction. These sensors are made of dielectric materials that exhibit piezoelectric properties, such as quartz or tourmaline. Quartz crystal microbalances are an example of a piezoelectric mass sensitive technique. These crystals deform or vibrate under the influence of an electric field. The frequency of this oscillation is dependent on the frequency of the applied electric field as well as the mass of the crystal. As the mass changes due to the binding of molecules, the vibrational frequency changes. The amount of molecules bound to the surface of the crystal can then be determined through the resulting change in resonant frequency.

Surface acoustic wave technology also takes advantage of the piezoelectric effect. Using input and output transducers on the surface of a piezoelectric crystal, these devices generate and detect acoustic waves. The acoustic energy is strongly confined at the surface, therefore making the wave very sensitive to changes in the mass, viscosity and conductivity of the surface. Such sensors have been applied in chemical and biological sensing including bacteria, proteins and virus particles detection. They have shown high sensitivity, down to picograms/cm^3, and high specificity [12].

Microcantilevers are another type of mass sensitive biosensor. These sensors transduce adsorption of biomolecules on a microcantilever surface into a mechanical response, either the cantilever bending or a change in its vibrational frequency. Even though it is intrinsically a mechanical mass-based transduction principle, cantilevers often utilise the piezoelectric effect, as the microcantilever's oscillation is usually mediated by a piezoactuator. Such sensors can also be equipped with integrated piezoresistors for measuring cantilever bending [13, 14].

In literature, piezoelectric transducers are classified based on the underlying principle of transduction such as mass-sensitive transducers (quartz crystal microbalance, microcantilever), and acoustic transducers (surface acoustic wave, membrane based) [1, 9, 10].

CALORIMETRIC TRANSDUCERS Many biological reactions are exothermic meaning that they release energy. This is the foundation principle of calorimetric, or thermometric, biosensors. Calorimetric biosensors have the capability to measure the reaction rate and define the concentration of an analyte [15]. The temperature changes are usually determined by thermistors, that are devices for which the resistance varies with temperature. Thermometric biosensors allow label free measurements and do not require the use of complex instruments. Another advantage of calorimetric biosensors is that they are independent of the optical properties of the sample. However, the requirements for strict temperature control makes these transducers difficult to deploy [6].

MAGNETIC TRANSDUCERS Magnetic transducers are promising candidates for biosensing applications. These transducers are based on magnetic labels which are detected using magneto-resistive sensor chips. The target analyte is labelled with magnetic beads and the sensor's surface is functionalised appropriately to ensure binding specificity to the target molecules such that they form a sandwich of sensor-target-bead. A variety of suitable magnetic beads for biosensing applications are commercially available today, which makes the technology easy to deploy [16].

OPTICAL TRANSDUCERS Optical biosensors detect changes in the optical properties of a sample in order to determine the presence and/or concentration of a species of interest. The measurable optical properties often include light amplitude, phase, polarisation, photon energy, or decay time of emitted signal [1]. Optical transducers have received considerable attention in biological sensing due to their sensitivity, relative simplicity, and low detection limits. Optical transducers offer a wide range of subclasses based on the fundamental optical phenomena that underpins the transduction mechanism such as reflection, refraction, absorption, dispersion, fluorescence, chemiluminescence, and surface plasmon resonance. In addition, optical biosensors are often classified based on materials and detection methods used in the transducer (waveguide biosensors, fibre optic based sensors, reflectance spectroscopy biosensors, etc.) [17]. There are several major advantages that optical transducers provide to biosensing in comparison to other transducing techniques. In

particular, these include high sensitivity, low detection limits, as well as simplicity of implementation. More importantly, some optical biosensors offer label-free detection that is of interest to most biosensing applications. Due to these advantages of the optical transduction mechanisms, the next section focuses on the currently available optical biosensing technologies.

1.1.3 *Optical biosensors*

The interaction of light with matter provides a basis for a range of observable optical phenomena that can be used to derive information about the system under study. These interactions can result in the absorption of light, scattering, emission of radiation, or change of refractive index. The interaction of light with biological molecules is the basic principle behind optical biosensors. The most commonly used optical biosensors are based on absorption, fluorescence, Raman scattering, and/or refractometry.

ABSORPTION SPECTROSCOPY Absorption spectroscopy relies on the absorption of light at a particular wavelength by biomolecules, a process in which the energy of a photon is taken up by electrons or atoms in matter. Light is passes through the sample and optical techniques are subsequently used to analyse the attenuated light. By characterising the transmitted spectrum, the presence and concentration of biomolecules may be determined. Depending on the energy of absorbed photons, Ultraviolet (UV), visible, or Infrared (IR) absorption spectroscopy methods are used. This technique allows to create simple sensing devices for determination of the concentration of a substance, kinetic measurements of certain chemical reactions, and identification of materials. However, the major limitation of all absorption based optical transducers is that not all molecules have distinctive absorption pattens from which they can be identified. Therefore, the method cannot be applied to all biological species, or molecular recognition labels with specific absorption properties are need to provide specificity [18].

FLUORESCENCE SENSORS Fluorescence is an underlying optical phenomenon that is commonly used in biosensors. Fluorescence occurs when a fluorescent atom absorbs a photon of high energy which excites an electron into one of the many higher energy vibrational states. This causes fluorescent molecules to emit photons of lower energy in response to the absorption of light from an external source. This emitted radiation can be detected and the intensity of light indicates the concentration of the fluorescent molecules. Therefore, if target molecules are bound to the fluorescent label, their concentration can be quantified. There are various fluorescent methods that exist today. One example is a sandwich assay of fluorescent labelled antibodies that specifically bind to a target that is attached to primary bioreceptors (Figure 1.3).

Fluorescent optical transduction is one of the most popular techniques in biosensing due to its very high sensitivity. However, a limited number of reactions pro-

duce fluorescent products or intermediates, therefore, molecules need to be labelled with fluorescent particles. Furthermore, fluorescent quenching is often a problem where a fluorophore collides with another molecule which results in a return to its ground state without photon emission. The intrinsic background fluorescence of other molecules in a sample can also limit the sensitivity of such biosensors. The main limitation of the technology, however, is photo-bleaching of organic dye labels, or irregular blinking of quantum dots (random switching between bright and dark states) if these are used to tag molecules [19].

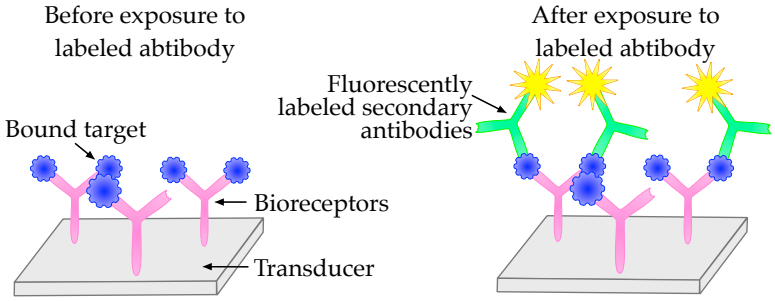


Figure 1.3: Schematic representation of sandwich assay fluorescence technique. After exposure to labelled secondary antibodies, fluorescent signal can be detected.

RAMAN SPECTROSCOPY Raman spectroscopy is a powerful analytical technique that has been widely used in biosensing. It is especially useful in cellular based biosensors as it allows efficient monitoring of cell metabolism and biochemical changes related to cell death [20, 21]. The underlying phenomenon behind the technique is Raman scattering which is the inelastic scattering of photons (photons undergo change in their energy after the impact) that interact with vibrating molecules in a sample. The vibrational energy of the molecules is transferred to or received by the photons, thus, the energy change corresponds to the vibrational energy of molecules in the sample. In this manner, proteins, RNA, DNA and other biological elements can be identified. Therefore, the Raman spectrum is a fingerprint of the biochemical composition of a sample [22]. Although the Raman technique is highly efficient for small chemical compounds, large macromolecules, such as proteins or viruses, result in very complex Raman spectra due to the large number of possible vibrational states. In addition, Raman spectrum is often related to conformation of molecules, which is very difficult to establish [21].

Biosensors based on Surface Enhanced Raman Scattering (SERS) make use of Raman scattering that is enhanced by molecules adsorbed on rough metallic surfaces. The enhancement factor can be such that a single virus particle can be detected. SERS has been successfully utilised to detect viral proteins, nucleic acids, and other biological targets. High levels of sensitivity, narrow peaks characterization, and the absence of any dyes susceptible to photo-bleaching are among advantages of the Raman scattering technique when compared with traditional fluorescent tags assays. The major disadvantages, however, are a relatively small signal to noise ratio, and the fact that the spectra of complex samples are often hard to interpret [23].

REFRACTOMETRIC SENSORS The index of refraction, n, is the ratio of the speed of light in a vacuum, c, to the speed of light in the medium, v: $n = c/v$. As a fundamental physical property of a substance, the Refractive Index (RI) can be used for measuring the concentration of a solute in a solvent, and quantitatively monitoring changes in its chemical composition. The presence of biological molecules varies the RI of the analyte making refractometry a useful tool for biosensing applications. This offers label-free detection, an attractive alternative to fluorescent labels that eliminates issues with photo-bleaching and significantly reduces ongoing costs.

Refractometric sensors can rely on refraction, reflection, or changes in phase, but are often based on interference effects and resonance phenomena. Microcavity-based sensors underpinned by optical resonances are a promising technology for biosensing applications. These sensors include but are not limited to Fabry-Pérot-type strait cavity resonators, Bragg gratings, as well as circular cavities that produce Whispering Gallery Mode (WGM) resonances. The Fabry-Pérot resonator is generally comprised of two parallel reflecting surfaces separated by a certain distance, as shown in Figure 1.4. The reflection and transmission spectra of the cavity can be described as the wavelength-dependent intensity modulation of the input light spectrum, caused by the optical phase difference between reflected or transmitted beams. When a perturbation of refractive index is introduced to the cavity, the optical path difference changes resulting in the wavelength shift of the interference spectrum [24].

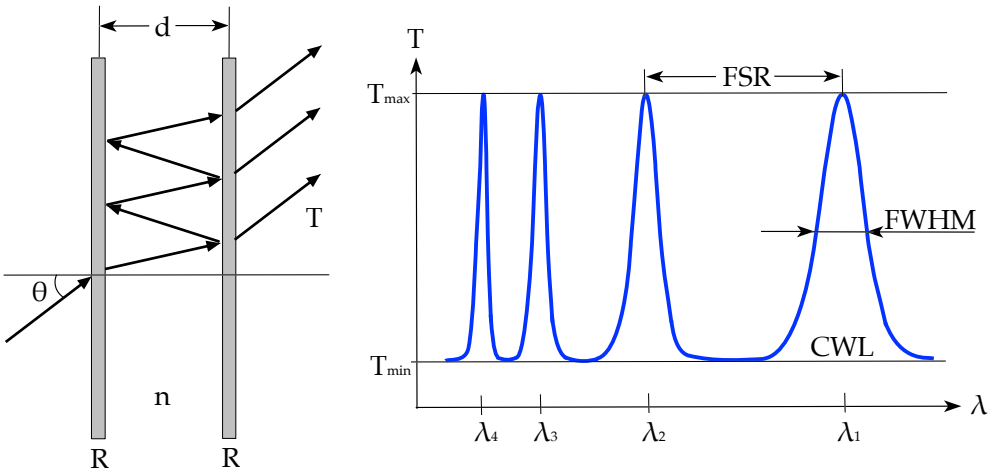


Figure 1.4: Schematic representation of a Fabry Pérot etalon refractometric sensor and its transmission spectrum. Two mirrors of reflectivity R are separated by the distance d. FSR is the Free Spectral Range, FWHM is the Full Width at Half Maximum, and CWL is the Central Wavelength are parameters defined by the cavity arrangement and refractive index between the mirrors, n. Adapted from [25].

Bragg gratings are structures formed by periodic variations in the effective refractive index, that reflect particular wavelengths of light and transmit the others. Due to the strain and temperature dependence of the grating period and its refractive index, the wavelength of the reflected component of light changes as function of temperature and/or strain. Therefore, Bragg grating sensors display high sensitivity to strain, temperature, and vibrations. Etched fibre Bragg gratings inscribed in

an optical fibre have also been used for detecting refractive index shifts and have been applied to biological sensing [26].

WGM sensing devices borrow their name from the famous Whispering Gallery of St. Paul's Cathedral. These sound waves travel along the curved walls so that whispering on one side of the dome can be heard at the opposite side. The same principle underpins WGM biosensors where light waves are trapped inside a microsphere, or a resonator of some other circular shape, and travel along curved paths around its circumference by TIR. The WGM can achieve very low losses providing that the refractive index contrast at the resonator interface is high, the radius of the curvature exceeds several wavelengths, and the intrinsic scattering and surface roughness of the resonator are small [27]. If a particle is attached to the resonator, the resonant condition changes and the resulting shift in the resonant frequency can be measured [28]. A schematic representation of a WGM microresonator ring is illustrated in Figure 1.5.

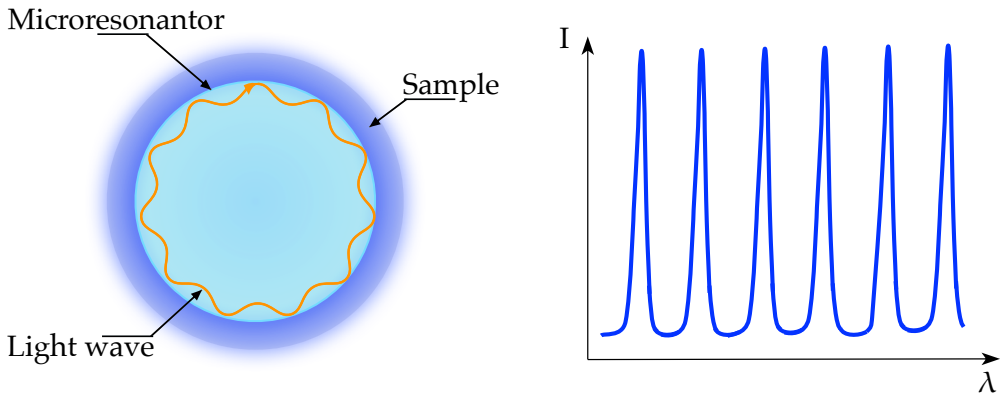


Figure 1.5: Schematic representation of a WGM microresonator ring. Surface mode of the light wave circulates along the surface of microresonator and interacts repeatedly with analyte molecules attached to the surface of the resonator.

Several biosensors have been developed based on resonant optical cavities as this technique provides the reasonably high sensitivity of a few hundreds of nm/RIU. WGM sensors can even be used to get information about the orientation of adsorbed molecules [27] and, using some enhancement techniques such as introducing noble metal nanoparticles, can even be used for a single molecule detection [29, 30]. Despite the potential for low detection limits, high data acquisition speed, and quality factor of WGM biosensors their disadvantages include difficulties in the preparation and calibration of microresonators, challenging microfluidics integration, low reproducibility, and susceptibility to laser intensity fluctuations [31].

SPR devices are based on resonances of electron gas in metals induced by an optical wave. SPR is a phenomenon that occurs on the boundary between a metal and a dielectric. When a light wave is incident on the surface of a metal and its propagation constant matches that of the free electrons oscillating on the surface, light wave couples to the electron oscillations resulting in absorption of the light. By monitoring the angular or spectral position of the SPR absorption feature, it is possible to identify very small changes in the refractive index of the adjacent dielectric [32]. Sim-

ilarly to the previously discussed refractometric sensors, detection specificity in SPR biosensors is provided by surface functionalisation. SPR biosensors have been used for detection of various targets including proteins, virus particles, allergens, and bacteria, and are not limited to molecules that exhibit strong absorption bands. Among advantages of SPR biosensing probes are the relative simplicity, versatility, and low cost. In addition, fast response time, high sensitivity and low detection limit are attributed to SPR biosensors. The possibility of further performance enhancement through probe design made this technology an attractive optical technique for the development of a compact biosensing probe. Therefore, the SPR phenomenon and SPR-based biosensing technologies are more thoroughly discussed in Chapter 2.

The detection of biological targets has been performed with all of the types of biosensors discussed above. Each of these techniques have advantages and limitations that are intrinsic to the physical principle that underpins it or the methods and instruments that are used for the fabrication of the biosensors. All transducers are potentially able to produce quantitative results depending on the technology used. Sensitivity and detection limit vary dramatically from one platform to another and also depend on the chosen bioreceptors, microfluidics and many other factors. Exceptional sensitivity and very low detection limits are often attributed to SPR and WGM biosensors respectively [33, 34]. It is important to remember, however, that even for applications where ultra high sensitivity is a paramount goal, there are often limits imposed by both, the optical detection system and the transport of the analyte in the microfluidic system [35].

1.2 MOTIVATION AND PROJECT AIMS

1.2.1 *Motivation*

Biological sensing plays a crucial role in the analysis of interactions between molecules, determining fundamental properties of these interactions, studying the role of compounds for a range of processes, as well as discovering new biological species and new interaction mechanisms. In addition, biosensing is irreplaceable for health sciences in the diagnosis of medical conditions and early prevention of diseases, development of novel clinical diagnostic techniques for rapid and reliable medical testing, and discovery of new biomarkers for medical conditions.

Various biosensing technologies exists today including well established commercial techniques and thousands of research-stage biosensors based on different underlying physical principles suitable for the target application. Despite the variety of available biosensors, all sensing devices aim to achieve high sensitivity, low detection limit, high specificity to target molecules, simplicity of fabrication, and low cost. Due to the difficulty of detecting the intrinsic physical properties of biomolecules, such as their size, mass, or electrical characteristics, biosensors traditionally employ a means of labelling the targeted species. Labels must be easily detected and act as an indirect indication of presence of the molecules they have been attached to. Fluorescent dyes [36–38], quantum dots [19, 39], radioactive labels [40], or magnetic beads

[16, 41] are among the most commonly used labelling techniques. Even though high performance can be achieved with these label based approaches, several practical difficulties, for example the degradation of labels with time and light exposure, exist. As a result, label-free biosensing has become extremely popular due to its simplicity and ability to directly measure physical properties of biomolecules [42].

Label-free techniques do not require any labels to be subsequently attached to the target analyte. Instead, they are based upon translating the intrinsic properties of a sample (such as refractive index, scattering, absorption for optical sensors) into a quantifiable signal that is proportional to the number of target biomolecules that are present. As such, most label-free technologies are optical biosensors that work by transmitting light through the sensor and detecting changes that occur in transmitted or reflected light after interaction with the analyte. One of the most widely used class of label-free optical biosensors are refractometric sensors that measures small changes in the refractive index of a sample induced by the presence of biomolecules. All optical biosensors share the advantages of high sensitivity and low detection limits that are generally attributed to these techniques. For that reason, there is a high demand for the development of label-free biosensing probes.

SPR is an example of a label-free biosensing technology that has attracted significant interest in the past three decades. Commercial SPR instruments are commonly used tools that allow real time detection of biological targets and kinetic studies of biomolecular interactions [43]. However, all commercial SPR instruments are very large and expensive, with significant ongoing costs required for consumables. Due to the performance scalability of this technology and the relative ease of implementation, SPR sensors have been the focus of a significant body of research over the past few decades. However, there is still a significant scope for the development of SPR sensing platforms with improved capabilities in terms of the performance characteristics, reliability, applicability, and cost effectiveness. Therefore, this project focuses on the development of a compact SPR architecture based on an optical fibre that, in addition to the aforementioned capabilities and inherent control over the guided light properties, has the advantages of a small size that opens up opportunities for in-vivo applications, with potential for remote and multiplexed sensing.

In addition to the questions related to the applicability and performance scalability of the SPR platforms, the research presented in this thesis addresses some practical challenges associated with fabrication of the optical fibre based SPR probes. The common fabrication techniques rely on complex metal deposition procedures, such as physical vapour deposition, as well as the processing of optical fibres such as tapering, side-polishing, etc. A key method presented in this thesis relies on the simple chemical silver deposition technique and avoids fibre processing, providing advantages of low production cost, and ease of fabrication without involvement of expensive equipment. The SPR configuration relies on collection of scattered light mediated through plasmon excitation on a rough metal surface, the method developed by François *et al.* [44]. The current work is focused on the implementation of plasmon scattering based SPR probes in optical fibres, characterisation of the performance parameters of the sensing probes and their advancement through modi-

fication of the platform architecture, as well as testing the potential applicability of the SPR scattering based fibre probes for the detection of biological targets.

Finally, as applications of SPR sensors range from biological [45] and chemical sensing [46] to spectroscopy and thin film characterisation [47–49], plasmonics presents a prolific avenue for development of universally applicable sensing platforms with great potential in different areas of science, providing additional motivation to the project. In addition, the ability to combine SPR with other physical phenomena in order to enhance emissive processes, such as fluorescence or Raman scattering, thereby improve sensing capability of the device, opens up further opportunities. In this respect, combining SPR with fluorescence in a single device for fluorescent signal amplification is explored in the current study.

1.2.2 *Project aims*

This project aims to develop an SPR biosensing platform that will have high performance, reliability, low cost, and applicability to biosensing. The major objectives of this research are to perform a systematic study of the scattering based SPR architecture, analyse its performance characteristics, identify avenues for improvements in the configuration, and implement them. In a broader perspective, the research is aimed at advancing the current knowledge of light-matter interactions and tailor them to sensing applications.

The multidisciplinary nature of biosensing research requires a broad understanding of the physical concepts that underpin the sensing system under development, as well as an appreciation of the biological aspects of the project. Therefore, the research is conceptually divided into three areas: 1) theoretical modelling of SPR in optical fibres; 2) the development of a biosensing platform with improved performance characteristics; and 3) the demonstration of applicability of the SPR system to biological sensing.

Those broad aims of the research lead to the identification of the following specific project objectives:

- Perform a critical review of the state-of-the-art in optical fibre SPR sensors to identify opportunities in existing technologies and select the initial SPR architecture.
- Implement an initial platform design and assess performance of the sensing probes.
- Construct a general theoretical model for the analysis of SPR in optical fibres in order to identify the relationship between configuration parameters and SPR sensing performance characteristics.
- Using this model, optimise sensor configuration parameters, such as optical fibre glass and geometry, plasmonic coating, interrogation mechanisms, and determine the performance trade-offs.

- Develop capabilities for improved sensor fabrication techniques, probe characterisation, and data analysis.
- Examine the performance of the improved sensing probes as biosensors.
- Explore the feasibility of integration of the SPR architecture with fluorescence for improved sensing capabilities.

Even though SPR is a mature technology, there is an opportunity to address the unique challenges of sensor design through tailoring the interaction of free electrons in metals and electromagnetic radiation that underpins SPR phenomenon. It is envisaged that the platform will be applicable to a wide range of applications including biological and chemical sensing, providing suitable conversion from the measurable quantity into refractive index is found. Last but not least, the techniques developed in the project, such as metal coating fabrication, surface functionalisation, and characterisation of the sensing probes, are readily adaptable, and can be used for development of different plasmonic devices, including SERS sensors, which can contribute to the field of optical fibre sensing.

1.3 THESIS STRUCTURE

This thesis is comprised of three parts that contain seven chapters and are organised as follows:

PART I Part I ("Introduction") presents background information relevant to the project and includes two chapters. The current chapter, Chapter 1, provides a general background on biosensing technologies, describes different bioreception techniques and transducing mechanisms. It also includes the motivation, project aims, and outlines the structure of the thesis.

Chapter 2 gives a detailed description on the physics underpinning SPR, the principles of biological sensing with SPR, and presents a critical literature review on plasmonic sensors based on optical fibres. The material presented in Section 2.5 of this chapter was published in the review paper, **P8**.

PART II Part II ("Development of plasmonic fibre sensing architectures") is dedicated to the experimental and theoretical work that has been performed during the project. This part is comprised of five chapters that are organised as follows.

Chapter 3 describes the theoretical modelling of SPR based on a Transfer Matrix Method (TMM). The performance of an optical fibre based SPR configuration is analysed for a set of variable parameters, such as fibre core material, fibre Numerical Aperture (NA), core diameter, metal, and metal film thickness. The results of the modelling are summarised at the end of the chapter.

Chapter 4 describes experimental work dedicated to the development of a scattering based platform architecture that utilises Multi Mode Fibres (MMFs) with large core sizes. Sensor fabrication procedure, including fibre preparation, silver coat-

ing deposition process, and experimental procedures for sensor characterisation are presented in detail. Modification of the silica surface required for chemical deposition of silver film onto the fibre is described. Performance of SPR fibre sensors based on high RI (lead silicate) and low RI (fused silica) fibres is compared. Application examples including NoV detection, and the detection of NoV surrogates (Quantum Dots (Qdots)) are presented at the end of the chapter.

Chapter 5 presents the experimental demonstration of a scattering based SPR platform implemented in microstructured Exposed Core Fibre (ECF). The sensor fabrication procedure, probe characterisation are described, and performance of the ECF-based SPR sensors is compared to the large core MMFs from Chapter 4. Sections of the work presented in this chapter have been reported in publications **P1** and **P5**.

Chapter 6 provides a description of the experimental work dedicated to development of a Metal Enhanced Fluorescence (MEF) sensor. Background on MEF phenomena and a correspondingliterature review is given at the beginning of the chapter. An experimental study on the influence of metal surface roughness on the enhancement of fluorescent emission is described. The analysis of the optimal distance between fluorescent molecules and the metal surface is given. The fluorescence enhancement factor is then estimated for silver films of different thickness. The work described in this chapter has been reported in publications **P2** and **P6**.

Chapter 7 is the final chapter that summarises work presented in this thesis, provides conclusion and potential future directions for the work.

PART III Part III includes appendices that contain supplementary materials referenced in the thesis and peer-reviewed journal articles, **P5** and **P6**.

2

SURFACE PLASMON RESONANCE (SPR)

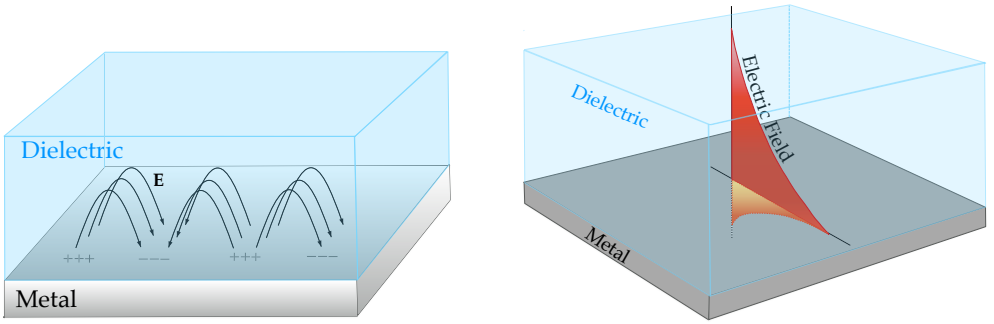
The field of plasmonics incorporates the study of interactions between electromagnetic waves and free electrons in metals. The first recorded observations of wavelength specific interactions of light with noble metals dates back to the Roman Empire where metal particles were used to colour glasses [50]. The enhanced resonant light-matter interaction that is attributed to plasmonics is responsible for a wide range of applications that spans from sensing, to spectroscopy and beyond. Recent developments in metamaterials and nanofabrication advances make plasmonics one of the most dynamic research fields.

2.1 SPR FUNDAMENTALS

From the perspective of classical theory, Surface Plasmons (SPs) are longitudinal charge density oscillations that can exist on the interface of two media with dielectric constants of opposite signs like a metal (real part of the dielectric constant < 0) and a dielectric (dielectric constant > 0). The presence of free electrons at the interface is essential for generating these oscillations. In practice this almost always implies that one medium is metal where free electrons are abundant. A schematic representation of such oscillations is shown in Figure 2.1a. In addition to propagating electron density fluctuations, surface plasmons can be viewed as electromagnetic waves that are strongly bound to the interface. A Surface Plasmon Wave (SPW) is a Transverse Magnetic (TM)-polarized wave with magnetic vector perpendicular to its direction of propagation and parallel to the plane of interface. The field vectors of the SPW reach their maxima at the interface and decay exponentially into both media. Typically, more than 90% of the field is concentrated in the dielectric, as shown in Figure 2.1b [51]. Due to this nature of SPWs, SPR is a powerful tool for studying the properties of these interfaces.

SPs can be understood using tools from a range of sub-disciplines, such as optics, electromagnetism, solid state and condensed matter physics, and are described by classical and quantum theories. This interlinked nature of the phenomenon contributed to the discovery of SPs throughout the 20th century in a variety of different contexts.

A mathematical description of surface waves at radio frequencies propagating along a cylindrical conducting wire with small surface resistivity was firstly proposed by A. Sommerfeld in 1899 [52]. At the beginning of the twentieth century R. Wood described an anomalous diffraction pattern from a metal backed diffraction grating in the visible domain [53, 54]. Although he speculated about the interaction between light, metal and the grating, an appropriate description of the phenomenon was not given. Plasma oscillations, i. e. oscillations of the electron density



(a) Plasma oscillations on a boundary between metal and dielectric media.

(b) Electric field profile on the metal-dielectric interface.

Figure 2.1: Schematic representation of SPR.

in conducting media, were first described in 1952 by D. Bohm and D. Pines [55]. They analysed the behaviour of electrons in a dense electron gas and pointed out that long range Coulomb interactions result in collective electron density fluctuations similar to charge oscillations in ionised gases (Langmuir waves) described earlier by L. Tonks and I. Langmuir [56], thereby explaining the energy losses of fast electrons in the metal films studied by G. Ruthemann and W. Lang in 1948 [57].

The existence of surface plasmons in metal films was first predicted in 1957 by R. Ritchie [58] who studied the diffraction of an electron beam by thin metallic foils. Optical excitation of Sommerfield waves by means of Attenuated Total Reflection (ATR) in a glass prism was demonstrated in 1968 by E. Kretschmann [59] and A. Otto [60]. Thereafter, a unified description of the phenomena as Surface Plasmon Polaritons (SPPs) was established and applied to the characterisation of thin films [61, 62], as well as biological and chemical sensing [63–66].

A SPP can be viewed as a quantum phenomenon that results from the coupling of a photon with a SP. In solid state physics, a plasmon is a quantum of plasma oscillation and is considered a quasi particle as it arises from the quantisation of a collective oscillation. A plasmon can couple with a photon creating another quasi particle called a plasma polariton. The plasma oscillations can also be described as an instability in the dielectric function of a free electron gas that oscillates at plasma frequency ω_p [67]. The plasma frequency can be recognised as a natural frequency of oscillation of conductive electron gas in the fixed positive background of the ion cores in the metal lattice. The quanta of this oscillation is a volume (or bulk) plasmon. Volume plasmons propagate through the volume for frequencies $\omega > \omega_p$. Volume plasmons do not couple to transverse electromagnetic waves and can only be excited by particle interactions [68]. Surface plasmon polaritons, on the other hand, are excitations that result from the coupling of the electromagnetic fields to oscillations of the conductor's electron plasma. Those oscillations exist for a range of frequencies between 0 and $\omega_{sp} < \omega_p$, and propagate at the interface between a dielectric and a conductor, evanescently confined in the perpendicular direction.

In addition to propagating SPPs on flat surfaces, non-propagating excitations of conductive electrons coupled to electromagnetic radiation, so called Localised

Surface Plasmons (LSPs), exist in metallic nanostructures. A LSP results from the confinement of a SP to a nanoparticle or nanostructure providing that the nanoparticle dimensions are smaller than the wavelength of light that excites SP. LSPs manifest themselves as a strong enhancement of the electromagnetic field near the nanoparticle which falls exponentially with distance. A schematic representation of Localised Surface Plasmon Resonance (LSPR) effect is presented on figure 2.2 where the electron cloud of metallic nanoparticles illuminated by light displaces relative to the position of the nuclei [69]. LSPR occurs when the frequency of incident photons is resonant with the collective oscillation of the conductive electrons in the metal nanoparticles. In addition to the strong enhancement of the local electromagnetic fields, LSPR exhibits wavelength-sensitive absorption with very high extinction coefficients and strong light scattering [69, 70].

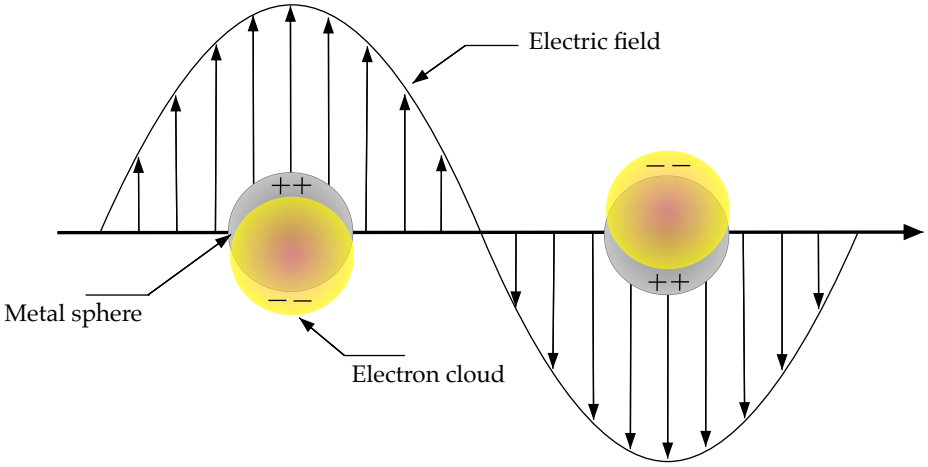


Figure 2.2: LSPR on a spherical metallic nanoparticles. Under the influence of the electric field of a light wave the conductive electron charge cloud displaces relative to the nuclei.

2.2 ELECTROMAGNETIC PROPERTIES OF METALS

Even though SPPs are a quantum phenomenon, the interaction of metal with electromagnetic radiation can be described in a classical framework through Maxwell's equations [68], and this is the approach that will be used here. Maxwell's equations connect macroscopic electromagnetic fields (electric field $\mathbf{E}$, dielectric displacement $\mathbf{D}$, magnetic field $\mathbf{H}$ and magnetic induction $\mathbf{B}$) with external charge density ρ and current density $\mathbf{J}$ [68]:

$$\nabla \cdot \mathbf{D} = \rho \tag{2.1}$$

$$\nabla \cdot \mathbf{B} = 0 \tag{2.2}$$

$$\nabla \times \mathbf{E} = -\partial \mathbf{B}/\partial t \tag{2.3}$$

$$\nabla \times \mathbf{H} = \mathbf{J} + \partial \mathbf{D}/\partial t. \tag{2.4}$$

For a linear isotropic non-magnetic media, **D** and **B** become:

$$\mathbf{D} = \epsilon_0 \epsilon \mathbf{E} \tag{2.5}$$

$$\mathbf{B} = \mu_0 \mathbf{H}, \tag{2.6}$$

where ϵ_0 and μ_0 are the electric permittivity and magnetic permeability of vacuum, respectively, and $\epsilon = \epsilon(\omega)$ is a frequency dependant dielectric constant that is in general a complex function: $\epsilon(\omega) = \epsilon(\omega)' + i\epsilon(\omega)'$ with ω being angular frequency of oscillation. The dielectric function is connected to complex refractive index via $\tilde{n}(\omega) = n(\omega) + \iota\kappa(\omega) = \sqrt{\epsilon(\omega)}$ [51]. Therefore, one can obtain the following expressions:

$$\epsilon' = n^2 - \kappa^2 \tag{2.7}$$

$$\epsilon'' = 2n\kappa \tag{2.8}$$

$$n = \sqrt{\frac{\sqrt{\epsilon'^2 + \epsilon''^2} + \epsilon'}{2}} \tag{2.9}$$

$$\kappa = \sqrt{\frac{\sqrt{\epsilon'^2 + \epsilon''^2} - \epsilon'}{2}}. \tag{2.10}$$

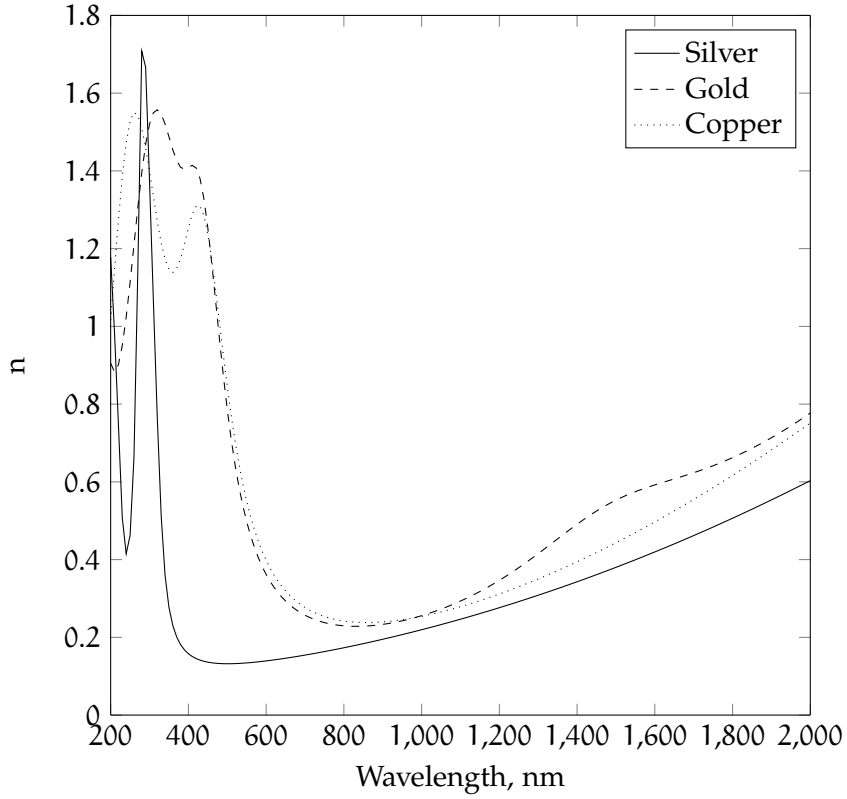
The real part of the complex refractive index $n(\omega)$ determines the dispersive properties of the medium, while the imaginary part $\kappa(\omega)$, called the extinction coefficient, describes losses due to absorption and scattering. The extinction coefficient κ is connected to the attenuation coefficient α from Beer's law that describes the exponential decay of radiation along the x direction through a medium [68]: $I(x) = I_0 e^{-\alpha x}$ as:

$$\alpha(\omega) = \frac{2\omega}{c}\kappa(\omega), \tag{2.11}$$

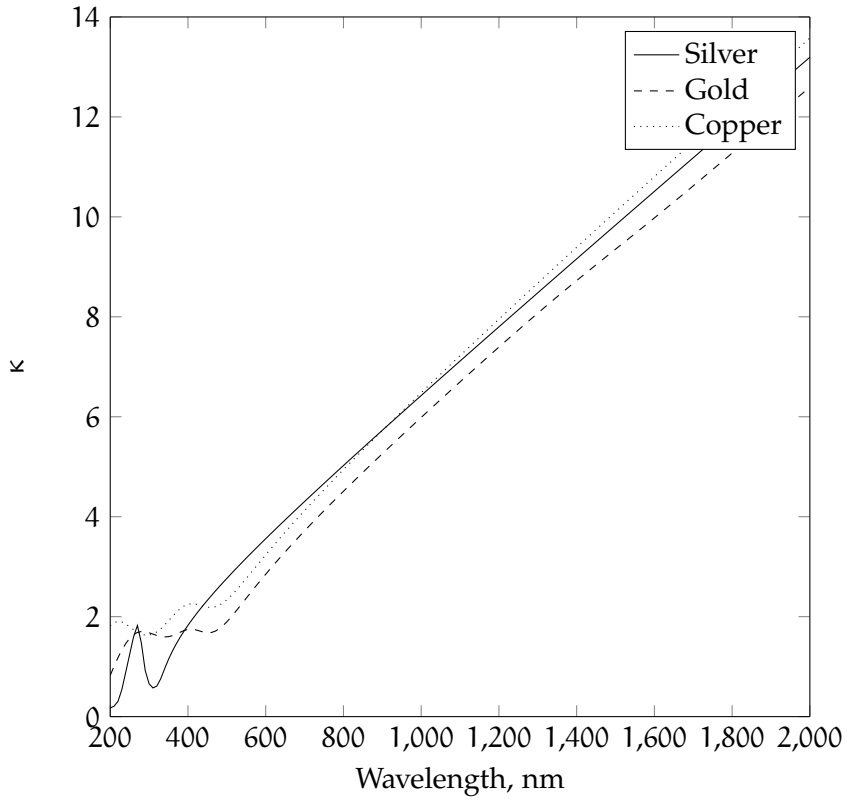
with $c = 1/\sqrt{\epsilon_0 \mu_0}$ being the speed of light in vacuum. Figure 2.3a and Figure 2.3b show the real and imaginary parts of the complex refractive index for three noble metals, silver, gold and copper, that are commonly used in SPR applications.

In terms of their optical properties, metals can be described as plasma over a large range of frequencies. In this approximation, electron gas of density N is assumed to freely propagate through the relatively stationery background of positive nuclei. In the presence of a time varying electromagnetic field $\mathbf{E}(t) = \mathbf{E}_0 e^{-\iota\omega t}$, electrons start to oscillate and are damped through collisions with a characteristic rate $\gamma = 1/\tau$, where τ is a relaxation time of free electron gas and is an order of $\approx 10^{-14}$s at room temperature. The equation of motion of free electrons can be written as [67]:

$$m\frac{d^2\mathbf{x}}{dt^2} + m\gamma\frac{d\mathbf{x}}{dt} = -e\mathbf{E}(t). \tag{2.12}$$



(a) Real part of complex refractive index.



(b) Imaginary part of complex refractive index.

Figure 2.3: Complex refractive index of three metals, silver, gold and copper, that are commonly used in SPR applications.

Considering the harmonic time dependence of the electron oscillation in the periodic electromagnetic field, one can obtain a solution to the Equation 2.12:

$$\mathbf{x}(t) = \frac{e}{m(\omega^2 + \imath\gamma\omega)}\mathbf{E}(t). \tag{2.13}$$

If electrons in plasma are displaced from a positively charged background of ions, electric fields are built up in such a direction as to restore the electric neutrality of plasma by pulling electrons back to their original positions. As electrons have inertia, they will overshoot and oscillate around their equilibrium position with characteristic frequency, known as plasma frequency. Electrons that are displaced relative to the positive background generate a polarisation proportional to their displacement: $\mathbf{P} = -Ne\mathbf{x}$ with N being the free electron density. Considering that dielectric displacement (Equation 2.5) can be written as $\mathbf{D} = \epsilon_0\mathbf{E} + \mathbf{P}$, we obtain the following relation:

$$\mathbf{D} = \left(\epsilon_0 - \frac{Ne^2}{m(\omega^2 + \imath\gamma\omega)}\right)\mathbf{E}. \tag{2.14}$$

If now we introduce plasma frequency $\omega_p = \sqrt{\frac{Ne^2}{m\epsilon_0}}$ [68], Equation 2.14 becomes:

$$\mathbf{D} = \epsilon_0\left(1 - \frac{\omega_p^2}{\omega^2 + \imath\gamma\omega)}\right)\mathbf{E}. \tag{2.15}$$

Comparing Equation 2.15 with Equation 2.5, dielectric function of metal can be written as:

$$\epsilon(\omega) = \left(1 - \frac{\omega_p^2}{\omega^2 + \imath\gamma\omega}\right). \tag{2.16}$$

Equation 2.16 describes the complex dielectric function of free electron gas, which classical analogue is known as the Drude model [68]. If we substitute the electron collision frequency γ with the relaxation time τ through $\tau = 1/\gamma$, the real and imaginary components of the complex dielectric function can be written as:

$$\epsilon(\omega)' = 1 - \frac{\omega_p^2\tau^2}{1 + \omega^2\tau^2}; \qquad \epsilon(\omega)'' = \frac{\omega_p^2\tau}{\omega(1 + \omega^2\tau^2)}. \tag{2.17}$$

It is insightful to analyse the complex permittivity for different frequency regimes with respect to the collision frequency γ. For high frequencies ($\omega >> \gamma$), the product $\omega\tau >> 1$, the permittivity of the material is mostly real and can be approximated as:

$$\epsilon(\omega) = 1 - \frac{\omega_p^2}{\omega^2}. \tag{2.18}$$

At this frequency regime, there is negligible damping and metals can be considered as undamped electron plasma. It should be noted, however, that the behaviour of noble metals in this frequency regime is modified by the presence of interband transitions. For frequencies $\omega > \omega_p$, the electric permittivity is positive and metals essentially behave as dielectrics. For frequencies $\tau \leqslant \omega \leqslant \omega_p$, ϵ' is negative and the complex refractive index $\tilde{n} = \sqrt{\epsilon}$ becomes mostly imaginary leading to a reflection coefficient $R \approx 1$, meaning that the metals are highly reflective in this frequency region.

For very low frequencies, where $\omega\tau << 1$, the real and imaginary part of the complex permittivity have comparable magnitude and metals are mainly absorbing with an absorption coefficient α:

$$\alpha = \sqrt{\frac{2\omega_p^2 \tau \omega}{c^2}}, \tag{2.19}$$

which is related to the absorption coefficient α in Beer's law: $I(z) = I_0 e^{-\alpha z}$. This implies that for very low frequencies the electromagnetic field inside the metal falls off exponentially as $e^{-z/\delta}$, with a characteristic skin depth $\delta = 2/\alpha$.

From this simple analysis of the optical response of metals at different frequencies, it is clear that plasma frequency can be considered as a frequency at which metals start becoming transparent to electromagnetic radiation. For most metals ω_p lies in the ultraviolet part of the spectrum which explains why metals are reflective at visible wavelengths. Table 2.1 shows examples of plasma frequency values and the corresponding wavelengths for three noble metals.

Table 2.1: Free electron densities N and relaxation times τ with corresponding plasma frequencies ω_p and wavelengths λ for three noble metals at room temperature in vacuum [71].

Metal	N, $\times 10^{22}$ cm^{-3}	τ, fs	ω_p, $\times 10^{16}$ 1/s	λ, nm
Silver	5.86	40	1.365	138
Gold	5.90	30	1.370	138
Copper	8.47	27	1.643	115

It is important to point out that the Drude model is only adequate to describe optical properties of metals for photon energies below the threshold of interband transitions. The alkali metals like lithium, sodium and potassium, have almost Drude-like response. However, for noble metals the transitions between electronic bands become significant for visible frequencies. Nevertheless, the advantage of the Drude model is its simplicity and its ability to be modified to incorporate for the interband transitions making it an adequate description of the optical response of the noble metals for most practical purposes [68].

2.3 THEORETICAL FORMALISM OF SURFACE PLASMON POLARITONS

It is informative to investigate the possibility of electromagnetic excitations that propagate along an interface between two media. It will be assumed that the complex permittivity ϵ only varies in one spatial dimension z: $\epsilon = \epsilon(z)$ and the boundary between two media coincides with $z = 0$. The direction of propagation of the electromagnetic wave is along the x-axes as illustrated in the Figure 2.4. SPPs are electromagnetic waves that propagate along the interface between a dielectric and a conductor, and are strongly confined to the interface. SPPs are described by their dispersion relation, spatial electromagnetic field profile and field confinement.

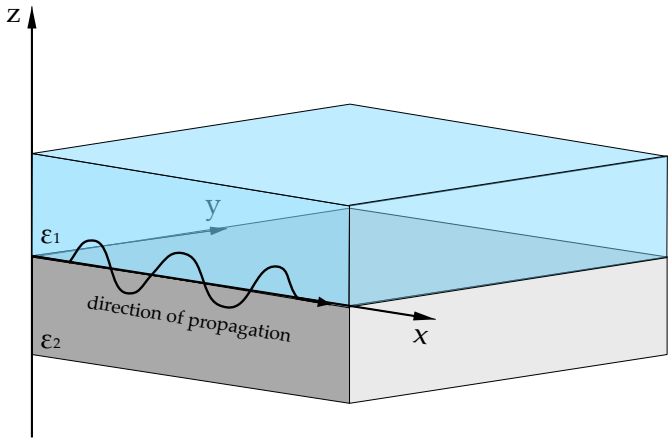


Figure 2.4: Planar geometry of electromagnetic wave propagating in the x-direction along the interface between two media with electric permittivities ϵ_1 and ϵ_2.

2.3.1 *Helmholtz equation*

Recalling Maxwell's equations from Section 2.2, and considering non magnetic media without external charge and current densities, the equations 2.3 and 2.4, can be rewritten as [68]:

$$\nabla \times \nabla \times \mathbf{E} = -\mu_0 \frac{\partial^2 \mathbf{D}}{\partial t^2}, \tag{2.20}$$

Applying vector identities $\nabla \times \nabla \times \mathbf{E} \equiv \nabla(\nabla \cdot \mathbf{E}) - \nabla^2 \mathbf{E}$, yields

$$\nabla(\nabla \cdot \mathbf{E}) - \nabla^2 \mathbf{E} = -\mu_0 \epsilon_0 \epsilon \frac{\partial^2 \mathbf{E}}{\partial t^2}. \tag{2.21}$$

Considering that in the absence of external stimuli $\nabla \cdot \mathbf{D} = \nabla(\epsilon \epsilon_0 \mathbf{E}) = 0$ and applying vector identity $\nabla \cdot (\epsilon \mathbf{E}) \equiv \mathbf{E} \cdot \nabla \epsilon + \epsilon \nabla \cdot \mathbf{E}$, the equation becomes:

$$\nabla^2 \mathbf{E} = \nabla(-\frac{1}{\epsilon} \mathbf{E} \cdot \nabla \epsilon) + \mu_0 \epsilon_0 \epsilon \frac{\partial^2 \mathbf{E}}{\partial t^2}. \tag{2.22}$$

Assuming that the permittivity does not vary significantly with distance on the order of the optical wavelength, one can write the simplified equation in the form:

$$\nabla^2\mathbf{E} - \frac{\epsilon}{c^2}\frac{\partial^2\mathbf{E}}{\partial t^2} = 0. \tag{2.23}$$

If we assume a harmonic time dependence of the electric field: $\mathbf{E}(\mathbf{r}, t) = \mathbf{E(r)}e^{-i\omega t}$, and denote $k_0 = \omega/c$, the Equation 2.23 becomes:

$$\nabla^2\mathbf{E} + k_0^2\epsilon\mathbf{E} = 0, \tag{2.24}$$

which is known as Helmholtz equation and is a central equation of the electromagnetic wave theory [68]. k_0 in the Equation 2.24 is the wave vector of a wave propagating in a vacuum.

2.3.2 *TM and TE modes on a single interface*

Taking into account the propagation geometry of the wave travelling in the x- direction along the interface between two media, as illustrated in Figure 2.4, and assuming that electric permittivity only varies in z-direction, the propagating wave can be written in the form: $\mathbf{E}(\mathbf{r}) = \mathbf{E}(z)e^{i(\beta x - \omega t)}$, where complex parameter $\beta = k_x$ is the component of the wave vector in the direction of propagation and is known as the propagation constant of the travelling wave [4]. Inserting the expression for propagating wave into the Equation 2.24 yields

$$\frac{\partial^2\mathbf{E}(z)}{\partial z^2} + (k_0^2\epsilon - \beta^2)\mathbf{E}(z) = 0. \tag{2.25}$$

Equation 2.25, as well as the similar expression for the magnetic field $\mathbf{H}$, are used for the analysis of the guided electromagnetic modes in the optical waveguides.

In order to obtain the dispersion relation of the waves propagating along the surface and investigate the spatial field profiles, we will use Maxwell's curl equations, Equation 2.3 and Equation 2.4, to determine the components of the electromagnetic fields $\mathbf{E}$ and $\mathbf{H}$. As we assumed that the propagating wave varies harmonically with time, $\frac{\partial}{\partial t} \rightarrow -i\omega$. For the wave travelling in x-direction without spatial change in the y-direction, $\frac{\partial}{\partial x}$ and $\frac{\partial}{\partial y}$ in Equation 2.3 and Equation 2.4 can be substituted to $i\beta$ and 0 respectively. Therefore, the curl equations, Equations 2.3 and 2.4, can be written as system of equations for the electromagnetic fields' components [72]:

$$\begin{cases} \frac{\partial E_y}{\partial z} = -i\omega\mu_0 H_x \\ i\beta E_y = i\omega\mu_0 H_z \\ \frac{\partial H_x}{\partial z} - i\beta H_z = -i\omega\epsilon_0\epsilon E_y \end{cases} \tag{2.26}$$

$$\begin{cases} \frac{\partial H_y}{\partial z} = i\omega\epsilon_0\epsilon E_x \\ i\beta H_y = -i\omega\epsilon_0\epsilon E_z \\ \frac{\partial E_x}{\partial z} - i\beta E_z = i\omega\mu_0 H_y \end{cases} \tag{2.27}$$

The first set of equations, Equation 2.26, correspond to the Transverse Electric (TE) modes where $E_x = 0$ and $H_x \neq 0$ and all of the components of the electric field **E** are transverse to the direction of propagation. For the TE wave the only non zero components are E_y, H_x, and H_z. Taking a partial derivative $\frac{\partial}{\partial z}$ of the first equation in Equation 2.26 and making some rearrangements, the system of equations 2.26 and 2.27 reduces to

$$\text{TE} \begin{cases} \frac{d^2E_y}{dz^2} + (k_0^2\epsilon - \beta^2)E_y = 0 \\ H_x = i\frac{1}{\omega\mu_0}\frac{dE_y}{dz} \\ H_z = \frac{\beta}{\omega\mu_0}E_y \\ E_x = 0 \\ E_z = 0 \\ H_y = 0. \end{cases} \tag{2.28}$$

An analogous set of equations can be derived for the case of TM modes where all of the magnetic field components are perpendicular to the x-direction:

$$\text{TM} \begin{cases} \frac{d^2H_y}{dz^2} + (k_0^2\epsilon - \beta^2)H_y = 0 \\ E_x = -i\frac{1}{\omega\epsilon_0\epsilon}\frac{dH_y}{dz} \\ E_z = -\frac{\beta}{\omega\epsilon_0\epsilon}H_y \\ H_x = 0 \\ H_z = 0 \\ E_y = 0. \end{cases} \tag{2.29}$$

2.3.3 *Dispersion relation of surface plasmons*

Lets assume that the interface between two media depicted on Figure 2.4 is formed by a non absorbing half space ($z > 0$) with positive real permittivity ϵ_1, like that of a dielectric, and a conducting half space ($z < 0$) with complex permittivity ϵ_2 where real part of the permittivity $\epsilon_2' < 0$ (metal). Looking for solutions that describe a wave that propagates along x-axes and exponentially decays further from the interface along z-axes, the field distribution that satisfy these conditions can be

expressed as $H_y(z) = Ae^{i\beta x}e^{-k_z z}$. Here, A is an amplitude coefficient, $e^{i\beta x}$ is a propagation term, and $e^{-k_z z}$ is the term reflecting exponential decay in the direction perpendicular to the interface. k_z is the component of the wave vector perpendicular to the interface with absolute reciprocal value $|1/k_z|$ defining the evanescent decay length.

For the TM solutions the non-zero field components from equations 2.29 can be written as [51]:

$$\begin{cases} H_y(z) = A_1 e^{i\beta x}e^{-k_{z1}z} \\ E_x(z) = i\frac{1}{\omega\epsilon_0\epsilon_1}A_1 k_{z1} e^{i\beta x}e^{-k_{z1}z} \qquad \text{(for } z > 0\text{)}, \\ E_z(z) = -\frac{\beta}{\omega\epsilon_0\epsilon_1}A_1 e^{i\beta x}e^{-k_{z1}z}, \end{cases} \tag{2.30}$$

and

$$\begin{cases} H_y(z) = A_2 e^{i\beta x}e^{k_{z2}z} \\ E_x(z) = -i\frac{1}{\omega\epsilon_0\epsilon_2}A_2 k_{z2} e^{i\beta x}e^{k_{z2}z} \qquad \text{(for } z < 0\text{)}. \\ E_z(z) = -\frac{\beta}{\omega\epsilon_0\epsilon_2}A_2 e^{i\beta x}e^{k_{z2}z}. \end{cases} \tag{2.31}$$

The boundary conditions imply that the tangential electric and magnetic field components should be continuous at the interface ($z = 0$). For the TM modes this means that H_y and E_x should be continuous:

$$\begin{cases} H_y^{(z>0)} = H_y^{(z<0)} \\ E_x^{(z<0)} = E_x^{(z<0)}, \end{cases} \tag{2.32}$$

or, from the equations 2.30 and 2.31

$$\begin{cases} A_1 e^{-k_{z1}z} = A_2 e^{k_{z2}z} \\ i\frac{1}{\omega\epsilon_0\epsilon_1}A_1 k_{z1} e^{-k_{z1}z} = -i\frac{1}{\omega\epsilon_0\epsilon_2}A_2 k_{z2} e^{k_{z2}z}. \end{cases} \tag{2.33}$$

At the boundary between metal and dielectric ($z = 0$), the Equation 2.33 can be written as:

$$A_1 = A_2 \tag{2.34}$$

$$\frac{k_{z1}}{k_{z2}} = -\frac{\epsilon_1}{\epsilon_2}.. \tag{2.35}$$

The Equation 2.35 implies that for the surface wave to be confined to the interface, the real parts of the k_{z1} and k_{z2} need to be positive, which in turn means that the real parts of the complex permittivities of the two media must have opposite signs [4]. This condition is satisfied for a metal and dielectric in the visible and

longer wavelengths (below the plasma frequency) where metals have negative real part of their complex permittivity as discussed in Section 2.2.

Recalling that the wave number $k = \frac{\omega}{v} = \frac{\tilde{n}\omega}{c} = \tilde{n}k_0$, where v is a phase velocity of the travelling wave in a medium, and $\tilde{n} = \sqrt{\epsilon}$ is a complex refractive index, we can derive the relation for the magnitude of the wave vector $k^2 = k_x^2 + k_z^2 = \tilde{n}^2 k_0$ [68]. Remembering that the component of the wave vector in the direction of propagation $k_x = \beta$, we obtain:

$$k_z^2 = k_0^2 \epsilon - \beta^2. \tag{2.36}$$

Inserting this relation for k_z in both media into Equation 2.35, one can write the expression for the complex propagation constant of SPPs on the interface between two media:

$$\beta = k_0 \sqrt{\frac{\epsilon_1 \epsilon_2}{\epsilon_1 + \epsilon_2}}. \tag{2.37}$$

Equation 2.37 is known as the dispersion relation of SPPs [68].

Considering that for the dielectric the permittivity is real: $\epsilon_1 = \epsilon_1'$, and for the metal, it is complex: $\epsilon_2 = \epsilon_2' + i\epsilon_2''$, and assuming that the imaginary part of the permittivity of metal is smaller than the absolute value of its real part: $\epsilon_2'' < |\epsilon_2'|$, it is possible to write the expressions for the real and imaginary parts of the complex propagation constant of the SPPs $\beta = \beta' + i\beta''$ as:

$$\beta' = k_0 \Big(\frac{\epsilon_1 \epsilon_2'}{\epsilon_1 + \epsilon_2'} \Big)^{1/2} \tag{2.38}$$

$$\beta'' = k_0 \Big(\frac{\epsilon_1 \epsilon_2'}{\epsilon_1 + \epsilon_2'} \Big)^{3/2} \frac{\epsilon_2''}{2\epsilon_2'^2}. \tag{2.39}$$

Figure 2.5 shows the plots of the dispersion relation of the SPPs (Equation 2.37) supported by the interface between air and a Drude metal (black curves), and the interface between a glass and a Drude metal (blue curves). The dielectric function of air is taken as 1, glass is 2.25 (refractive index of 1.5), and for metal the dielectric function is estimated using Equation 2.18 with plasma frequency $\omega_p = 1.365 \times 10^{16}\ s^{-1}$, like that of silver, and the dumping is assumed to be negligible. The straight lines on the plot are light lines $\beta_0 = k_0\sqrt{\epsilon_1}$ for air and glass, which is where light would follow given free propagation in a dielectric medium. Real and imaginary parts of the propagation constant of SPPs are shown (solid and dashed curves respectively).

It can be seen from the Figure 2.5 that there is a transparency regime, where $\omega > \omega_p$. Here, radiation into the metal occurs resulting in a collective oscillation of free electron gas inside the metal called bulk or volume plasmons. Below this region, there is a regime where only the imaginary part of the propagation constant

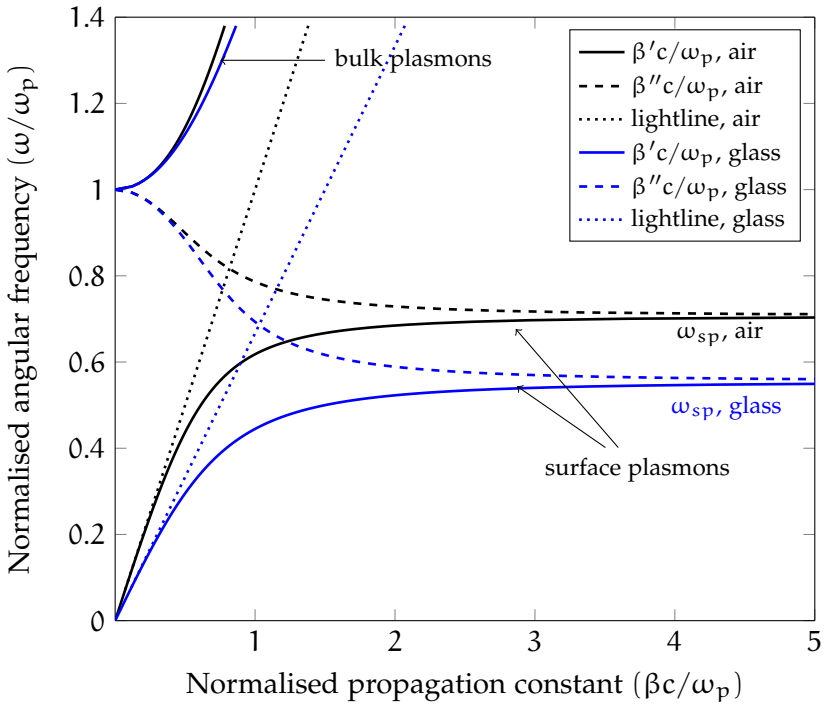


Figure 2.5: Dispersion relation of SPPs propagating at the interface between a Drude metal and air (black curves), and a Drude metal and a glass with refractive index of 1.5 (blue curves).

exists and therefore, no propagation is allowed. Below this frequency region, the propagation constant approaches characteristic frequency ω_{sp} [51]:

$$\omega_{sp} = \frac{\omega_p}{\sqrt{1+\epsilon_1}}, \tag{2.40}$$

known as the surface plasmon frequency. Propagation constant $\beta \to \infty$ as $\omega \to \omega_{sp}$ and, therefore, the group velocity of the wave $v_g = d\omega/d\beta \to 0$. For small frequencies, corresponding to mid-infrared and infrared, the propagation constant approaches lightline β_0 meaning that the SPW become less confined as the frequency decreases. It can also be seen from the plot on Figure 2.5 that the propagation constant of the surface modes (where $\omega < \omega_{sp}$) is always lower that the lightline corresponding to the dielectric. This indicates that SPPs cannot be transformed into light and therefore are called non-radiative. The opposite is also true, the SPPs cannot be excited by simply irradiating the interface with light. Specific methods are needed to increase the propagation constant of incident light to match the propagation constant of surface plasmons which will be discussed in Section 2.4.1.

For completeness, let us consider the TE solutions to the equations 2.28. The boundary conditions for the continuity of the tangential field components at the interface in case of TE modes imply that $E_{y1} = E_{y2}$ and $H_{x1} = H_{x2}$. After similar manipulations that has been done for the case of TM modes, we obtain the conditions for the TE waves at the interface:

$$\begin{cases} A_1 = A_2 \\ -A_1 k_{z1} = A_2 k_{z2}, \end{cases} \tag{2.41}$$

or

$$A_1(k_{z1} + k_{z2}) = 0. \tag{2.42}$$

Considering that the confinement to the interface requires $\mathrm{Re}(k_{z1})$ and $\mathrm{Re}(k_{z2})$ to be positive as discussed earlier, the condition Equation 2.42 can only be fulfilled when the amplitudes of the wave are zero: $A_1 = A_2 = 0$. This conveys the important fact that SPPs only exist for the TM polarisation.

2.3.4 *Characteristics of surface plasmons*

In addition to their dispersion relation, SPs are described by the electromagnetic field distribution at the interface that supports them. Figures 2.6 and 2.7 show the distribution of magnetic field component H_y for a TM wave on a boundary between silver and water illustrating exponential decay of the field away from the interface (z-direction) (Figure 2.6) and as the wave propagates (x-direction) (Figure 2.7) from Equation 2.30 and Equation 2.31.

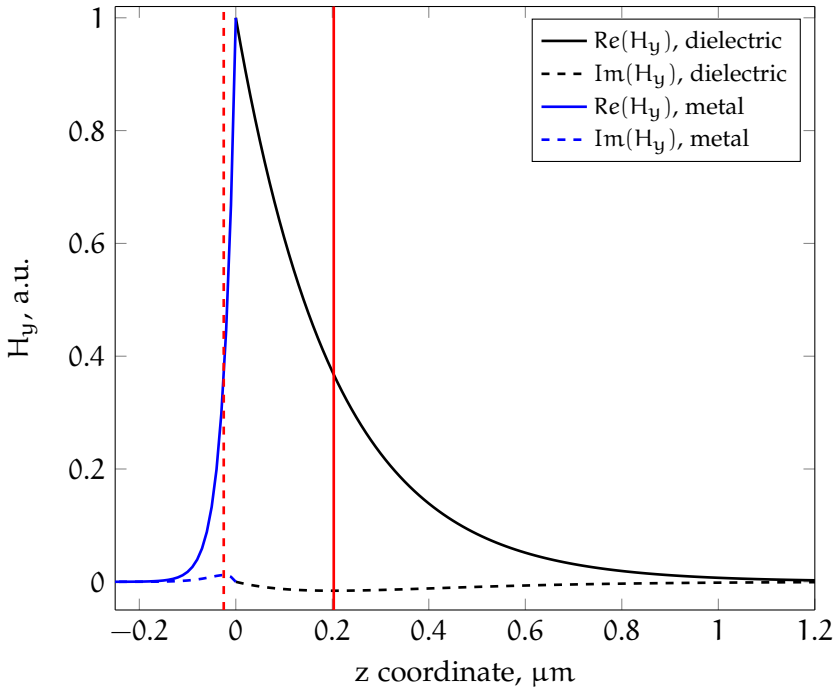


Figure 2.6: Distribution of magnetic field (H_y) of an SP at the interface of silver ($\epsilon_2 = -14.44 + i\ 1.09$ [73]) and non-dispersive medium ($n_1 = 1.33$) at $\lambda = 632$ nm. Magnetic field intensity profile shows penetration depths into dielectric (solid red line) and metal (dashed red line), of 203 nm and 25 nm respectively, at $x = 0$.

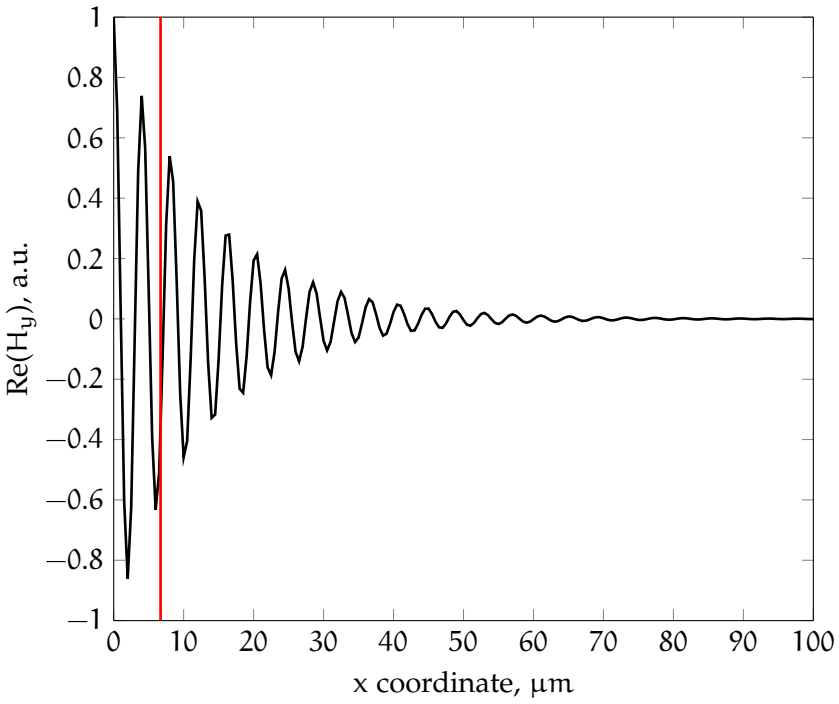


Figure 2.7: Real part of magnetic field intensity (H_y) showing oscillatory behaviour and decay at the interface ($z = 0$). Propagation length of the SP is 6.7 μm (vertical red line) at the interface of silver ($\epsilon_2 = -14.44 + i\ 1.09$ [73]) and nondispersive medium ($n_1 = 1.33$) at $\lambda = 632$ nm.

Two important characteristics of the SPs are the penetration depths into the metal and dielectric, and the propagation length along the interface. Evanescent decay into the media (called penetration depth) quantifies the confinement of the wave to the surface and is defined as the distance where the magnitude of the electromagnetic fields drops to $1/e$:

$$\hat{z} = \frac{1}{|k_{zj}|}, \tag{2.43}$$

where $j = 1$ or 2 for dielectric or metal respectively. The larger the penetration depth, the weaker the confinement of the SP wave to the interface. The penetration depth of the field into a dielectric is higher than into a metal with typical values of an order of hundreds of nanometers for dielectrics and around $20 - 30$ nm for metals in the visible range.

The surface plasmon decay in x-direction can be quantified from imaginary part of propagation constant as the field in that direction decays as $e^{-2\beta'' x}$. The propagation length L may be obtained as:

$$L = \frac{1}{2\beta''}. \tag{2.44}$$

Typical values for the propagation length of SPPs are between a few micrometers up to hundreds of micrometers in the visible regime depending on the metal and dielectric that support the interface.

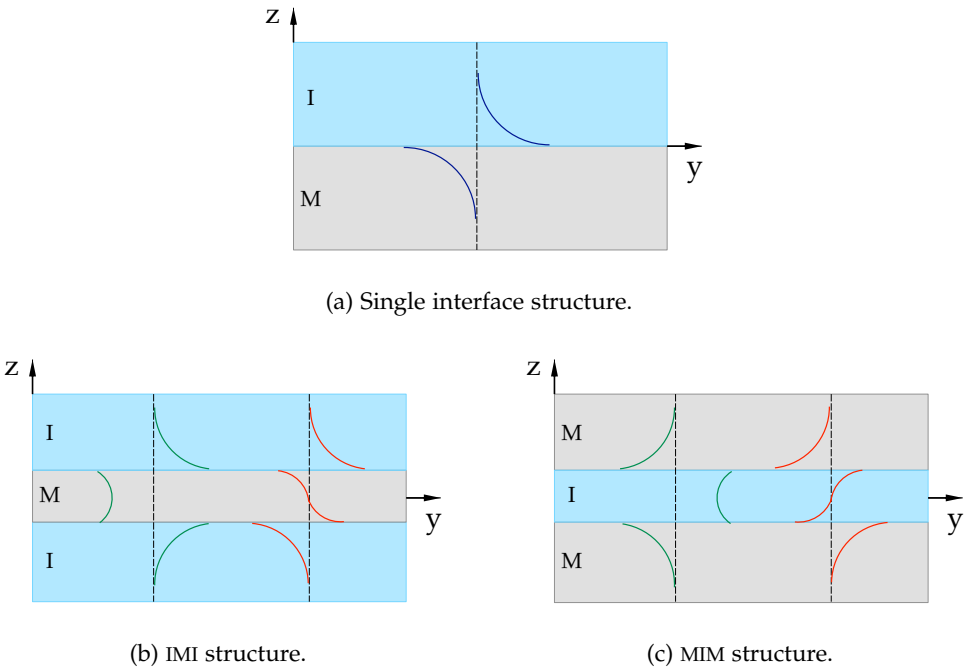
As it is evident from the dispersion relation of the surface plasmons (Figure 2.5), both penetration depth $\hat{z}$ and propagation length L are frequency dependant. As the frequency approaches surface plasmon frequency ω_{sp}, the propagation constant β increases leading to large values of k_z which results in a strong confinement to the surface on one hand, but short propagation distances on the other hand due to the increased damping. This trade-off between energy confinement to the surface (localisation) and the propagation length of the SPPs is typical to plasmonics and dictates that the materials and a range of wavelengths used strongly depend on a particular application.

2.3.5 *Surface plasmons in multilayer systems, long range surface plasmons*

In general, SPPs can be supported by structures consisting of multiple layers of metals and dielectrics. The simplest and by far the most common configuration of a multilayer system is a three layer structure that consists of a metal film sandwiched between two semi-infinite dielectrics. This structure is often abbreviated as Insulator-Metal-Insulator (IMI). In this configuration both metal-dielectric interfaces can support SPs. If the metal film is thin enough, SPs propagating at the opposite sides of the film couple, giving rise to two separate electromagnetic modes, symmetric and antisymmetric surface plasmons. The designation for symmetric and antisymmetric modes is given depending on the symmetry of the magnetic field intensity distribution with respect to the interface [74]. Given that attenuation of the symmetric modes is from 2 to 3 times lower than SPPs supported by a single interface [74], the symmetric modes are named Long Range Surface Plasmons (LRSPs) and antisymmetric modes Short Range Surface Plasmons (SRSPs). The mathematical formalism for the description of surface plasmons in a three layer system is similar to that presented for the single interface. Here, we will focus on a brief description of the interesting properties of plasmons on such structures.

Figure 2.8 shows three main SPR configurations where the double interfaces shown in Figure 2.8b and Figure 2.8c can support both, LRSPs and SRSPs, and a single interface (Figure 2.8a) supporting SPPs is shown for comparison. It is obvious that the existence of coupled modes in IMI structures depends on the thickness of the metal film. When the metal film is much thicker than the penetration depth of the surface plasmons, each metal-dielectric boundary supports two separate SPPs at each interface. However, as the metal thickness decreases, the two SPPs can start interacting which results in coupled electromagnetic surface modes (LRSPs and SRSPs).

It is interesting to note how the propagation constant of symmetric and antisymmetric modes depends on the thickness of the metal film in the IMI configuration. As the thickness of the metal film decreases, the propagation constant of the surface modes supported by a single interface branches into symmetric and antisymmetric counterparts. Both, the real and imaginary parts of the propagation constant of the symmetric mode decrease with the decreasing metal thickness meaning that the effective refractive index and mode attenuation are reduced leading to less energy confinement, therefore larger penetration depth into dielectric, and longer propaga-



(a) Single interface structure.

(b) IMI structure.

(c) MIM structure.

Figure 2.8: Common SPR supporting structures. Electric field component $Re(E_y)$ is shown schematically: in blue for a single interface structure, in green (symmetric), and red (antisymmetric) for IMI and MIM structures. The propagation is assumed to be in the x-direction perpendicular to the page. Adopted from Fig.B1 [75].

tion length. On the other hand, the real and imaginary parts of the antisymmetric mode increase with the reduced film thickness resulting in a strong confinement of the mode to the interface and short propagation distance [68]. For an asymmetric IMI structure where a metal film is surrounded by two dielectrics with different permittivities, the symmetric mode ceases to exist after a certain thickness as the film thickness decreases, a phenomenon known as mode cut-off [4].

MIM structures, similar to those depicted on Figure 2.8c, can support long range plasmons and have been widely studied due to their unique properties [76–79]. In particular, as the penetration depth in metal is much smaller than that into dielectric (usually an order of $20-30$ nm in the visible range), having a thin dielectric slab sandwiched between two metal layers allows to achieve very high localisation of the electromagnetic field, typically around 10% of the wavelength of light, without the expense of the propagation distance [78]. These structures are promising candidates for simultaneous use with conventional electronic devices and plasmonic interconnects where sub-wavelength field confinement is required.

2.4 SURFACE PLASMON RESONANCE SENSORS

The application areas of plasmonics are versatile due to the unique properties associated with SPs. The strong confinement of the electromagnetic field and relatively long propagation lengths of the plasmons allow the exploitation of the extraordinary light transmission and production of plasmonic waveguides and antennas with sub-wavelength light confinement. This provides an opportunity to reduce

photonic devices to sub-wavelength dimensions. In addition, SPs are known to enhance emissive processes, such as SERS and MEF, as well as non-linear effects. Since SP characteristics are highly dependent upon the properties of materials that support them, SPs found a niche in spectroscopy and sensing.

This sensitivity to the changes in the interface underpins the use of SPR in refractometric sensors that can detect very small changes in the refractive index of the dielectric adjacent to the metal surface. It was discussed in Section 1.1 that refractive index changes can be used in biological and chemical sensors to detect binding of molecules. The concept of optical sensors based on excitation and detection of SPs is often referred to as SPR sensors. The versatility of SPR based sensors can not be overestimated. Hundreds of research papers on SPR based sensing technologies have been published during the last few decades. Several commercially produced SPR biosensors, such as Biacore (GE Healthcare), Reichert (Reichert Technologies), SPR2/4 (Sierra Sensors), IBIS-MX96 (IBIS Technologies), and others, are available today. Interest in this technique continues to grow due to the benefits it provides. SPR sensors can be used for a wide variety of biological targets including proteins, virus particles, allergens, bacteria, and many others. This section will present the fundamental principles of SPR based biochemical sensors including excitation and interrogation methods that are used to inflict and detect the resonance, SPR performance characteristics, and current trends in SPR sensing configurations.

2.4.1 *Excitation of surface plasmons*

There are two main methods that have been employed to excite SPs, bombardment with charged particles, usually electrons, and by using photons. Originally, SPs were described by Ritchie in [58] who theoretically studied the loss spectra of low energy electron beams diffracted by thin metal films and predicted an additional loss at lower energy of $\hbar\omega_p/\sqrt{2}$ corresponding to the surface excitations, in addition to the volume plasmon losses at $\hbar\omega_p$. Even though surface plasmon excitation in early experiments was achieved by electron beams incident to metal surfaces, most of the later SPR studies are related to excitation of surface plasmons by photons and, therefore, attention will be focused on optical excitation methods.

As discussed in Section 2.3.3, surface plasmons are confined to the interface between a metal and a dielectric due to the fact that the the propagation constant of SPs β is greater than propagation constant of the wave in dielectric. This leads to the fact that the dispersion curve of the surface plasmons lies to the right of the light line of the dielectric (Figure 2.5). This necessitates the requirement to match the propagation constant of incident light with that of surface plasmons, thereby satisfying the resonant condition. This can typically be achieved by angular modulation or spectral modulation accomplished by various means such as ATR method, grating coupler and others, which are discussed in this section.

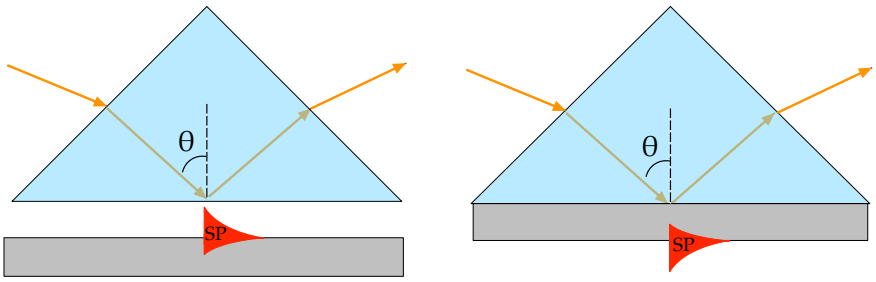
Total Internal Reflection based configurations

To overcome the difficulties with excitation of SPPs by electron beams, Otto [60], Kretschmann and Raether [59] proposed ways of optical SPR excitation by means of Total Internal Reflection (TIR) using a glass prism. TIR is an optical phenomenon which occurs when a propagating light wave is incident on the interface between two dielectrics with different refractive indices n_1 and n_2 from a dielectric of higher refractive index (n_1). If the incidence angle (measured with respect to the normal at the interface boundary) is larger than a critical angle $\theta_c = \arcsin(\frac{n_2}{n_1})$, no light is transmitted and the wave gets totally reflected from the interface with evanescent wave extending beyond the boundary into the second dielectric medium.

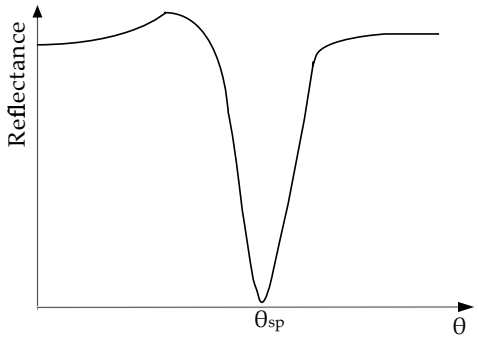
PRISM BASED EXCITATION Two TIR methods are commonly used for SPR excitation. The Otto configuration employs a glass block, often a glass prism, in close proximity to a metal surface, as shown in Figure 2.9a. Monochromatic light is incident to a facet of the prism which faces the metal surface at an angle larger than the critical angle so that the light is totally reflected. Due to the TIR the evanescent wave penetrates through the boundary and interacts with the electron oscillations on the metal surface thereby triggering the plasmons' propagation. The Kretschmann configuration, on the other hand, consists of a glass prism onto which a thin metal film is directly deposited, as illustrated in Figure 2.9b. The evanescent wave penetrates through the metal and SPs are excited on the opposite side of the metal film. In both cases the angle of incidence of the light beam is varied to adjust the propagation constant of the incident light and match it with that of surface plasmons in a resonant manner. When the component of the wave vector of the incident light parallel to the interface k_x is equal to the propagation constant of surface plasmons β, the energy of the excitation light is transferred to the SPs which is seen as a sharp dip in the reflected spectrum (Figure 2.9c). As an alternative to the monochromatic light, a broadband beam at a fixed angle can also be used to excite SPPs in prism based configurations.

In order to achieve sufficient excitation in Otto configuration, the metal surface needs to be in a very close proximity to the prism facet, usually a few tens of nanometres. This requires that both metal and prism surfaces have to be perfectly flat and positioned parallel to each other. This imposes experimental limitations and as a result, Otto configuration is only preferable when direct contact with the surface is not desirable and is mostly used for surface quality studies [68]. Due to the simplicity of implementation, Kretschmann setup gained popularity in refractometric sensing platforms based on SPR and is currently used in commercial SPR sensing instruments.

EXCITATION WITH DIELECTRIC WAVEGUIDE A more general SPR configuration based on TIR excitation method is a dielectric waveguide. An optical waveguide is a structure that guides electromagnetic waves by means of TIR. Excitation of SPs occurs where evanescent wave couples to the metal deposited on the waveguide, in



(a) Otto configuration. (b) Kretschmann configuration.



(c) Dip in the reflectance corresponding to SPR.

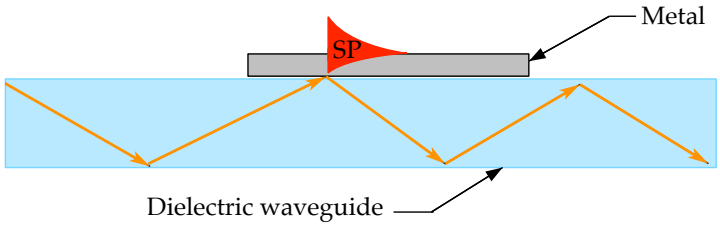
Figure 2.9: ATR couplers for optical SPP excitation. Dip in the reflection is associated with SPR excitation.

a similar fashion as in Kretschmann configuration, at points of reflection, as shown in Figure 2.10a. Optical fibres are a special case of a dielectric waveguide with cylindrical geometry where metal film is generally deposited on a side of the fibre core as illustrated in Figure 2.10b.

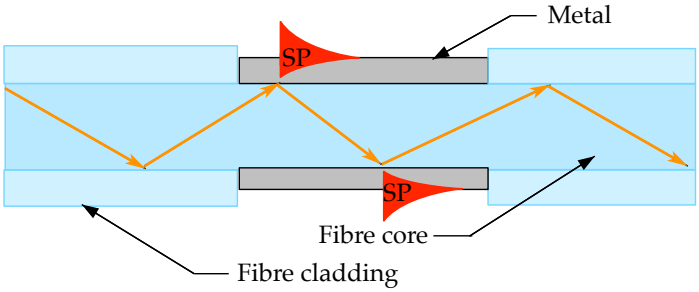
Although prism based SPR sensors provide excellent sensitivity, most recent developments have been concentrated on SPR sensors based on waveguides, in particular, optical fibres. These configurations offer a number of advantages in comparison with traditionally used prism based couplers. They provide the highest level of miniaturisation, mechanical flexibility, and offer the possibility of remote sensing.

Grating coupler

The mismatch between the in-plane wave vector of the incident light and the propagation constant of the SPs can be overcome by using a periodically patterned metal surfaces, such as one-dimensional or two-dimensional gratings or grooves (Figure 2.11). When monochromatic light with a wave vector k is incident to the grating at an angle θ, it couples into modes with wave vectors $k\sin\theta \pm m\frac{2\pi}{d}$ [4], where d is the slit spacing or lattice constant of the grating, and m is the mode order. By adjusting the angle of incidence, grating constant, and the wavelength of incident light, higher order reflections from the grating can satisfy the resonant condition and excite SPs. As the grating can be constructed from inexpensive plastics, it is suitable for mass production, making this excitation approach an attractive technique used in SPR sensors. However, this method is less commonly used than the TIR excita-



(a) Planar waveguide coupler.



(b) Optical fibre coupler.

Figure 2.10: TIR couplers for optical SPP excitation.

tion because in grating based SPR sensors the light is incident through the dielectric sample, and therefore, the sample and the flow cell need to be optically transparent [80, 81].

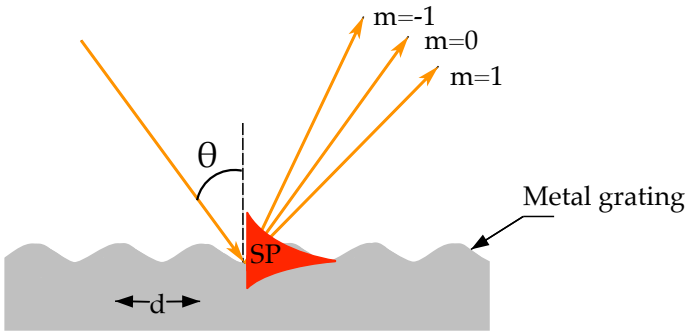


Figure 2.11: Grating coupler for optical SPP excitation.

Excitation using microscope objectives and near-field radiation

An alternative method of SPR excitation is a highly focused optical beam produced by microscope objectives with high NA. This is a far-field method that relies on the detection of the intrinsic lossy modes associated with plasmon propagation in thin films presented by Bouhelier and Wiederrecht in 2005 [82]. A schematic of the setup is shown in Figure 2.12. For excitation, coherent white light is incident on a glass slide coated with a metal film after passing through a high NA microscope objective. The angle of incidence of the beam and the angular spread can be controlled through adjustment of the beam position with respect to the optical axis of the objective. As in the Kretschmann configuration, the SPs are excited on the opposite

side of the metal film with the field decaying exponentially into dielectric and metal. As the field penetrates through the metal film to the opposite interface between the metal and the glass, it couples into the radiative leaky wave propagating in the glass. As the incident beam is highly focused, the excitation area is significantly smaller than the lateral spread of the SPs, and therefore, the leakage radiation can be detected. This method allows to simultaneously excite and observe SPs with broad spectral distribution, and directly determine their propagation lengths.

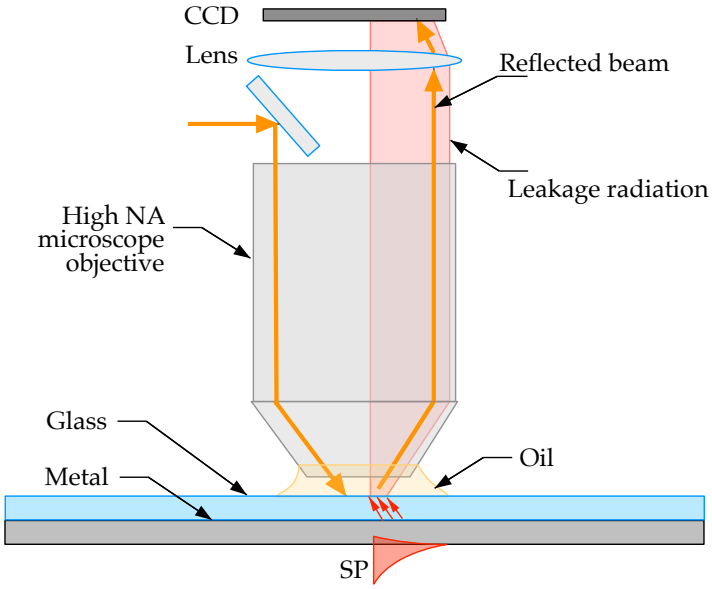


Figure 2.12: Optical excitation of SPPs using high Numerical Aperture (NA) microscope objective. The SPPs are observed trough leakage radiation. Adapted from [82].

Near-field techniques allow for the local excitation of SPs over areas that are much smaller than the wavelength of the excitation light source and therefore, can produce a point source of SPPs. A typical near field optical setup consists of a small probe, for example a tapered optical fibre tip, and an aperture that is smaller than the wavelength of light. Having the small aperture size ensures that the light from the tip will have wave vector components that can be matched with propagation constant of SPs. Plasmons propagating from the illuminated spot can be imaged by collecting the leakage radiation with specific mirror arrangements or microscope objectives [83]. Using this local excitation, it is possible to study the effects of surface topography on propagation of SPPs, as well as excitation and analysis of localised SP modes on individual metal particles and surface defects.

2.4.2 *Interrogation methods for SPR*

Once SPs are excited, variations of the optical properties of the adjacent dielectric, i. e. its refractive index, can be detected. Various detection approaches are possible such as the measurement of intensity near resonance, measurement of resonant momentum of the optical wave (that includes angular and wavelength interrogation), measurement of changes in phase [84–86] or polarisation [87] associated with the

resonance, as well as direct SPR imaging. The choice of interrogation techniques is dictated by materials and methods used to excite the surface plasmons (i.e. prism or optical fibre coupling), as well as the required performance characteristics (angular and spectral interrogation offer better signal to noise ratio, etc.) [88].

Indirect SPP detection

The most commonly used SPR probing methods are angular and wavelength interrogation, as well as intensity measurements [88]. The SPR resonant condition depends upon the angle of incidence as well as on the wavelength of the incident light. Consequently, the position of the SPR feature in the analysed spectrum can be measured by varying the angle of incidence at a fixed wavelength (Figure 2.13), or finding a resonant wavelength at a fixed angle (Figure 2.14). These approaches are common in TIR excitation methods where the light reflected from the metal coating is analysed with respect to the modulated parameter (angle of incidence or wavelength). Intensity interrogation is essentially similar to the spectral methods where the resonant condition is assessed through measuring intensity of a monochromatic light at a fixed angle of incidence which is indicative of the extent of the spectral overlap between resonant wavelength of SPs and excitation wavelength. The approaches based on angular and spectral interrogation are the most prevalent owing to the simplicity of optical setup and relatively high Signal to Noise Ratio (SNR).

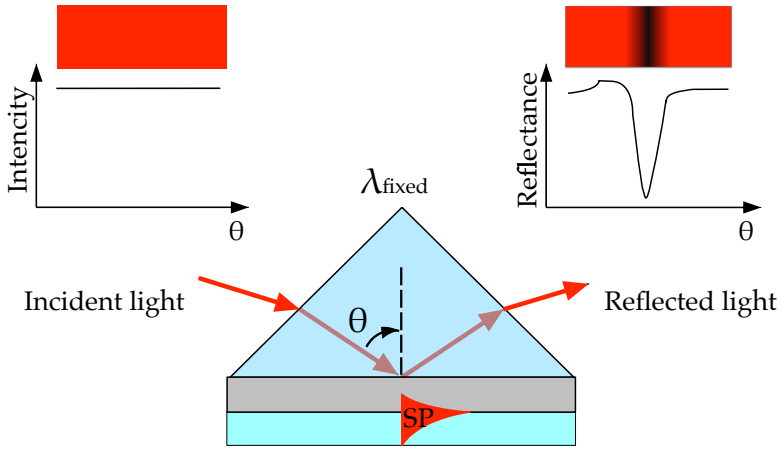


Figure 2.13: SPR detection using angular interrogation technique. By varying angle of incidence of monochromatic light, θ, SPR condition can be satisfied.

Direct imaging of SPPs

Instead of inferring the existence of the SPs through measurements of optical properties of the light wave that have undergone interaction with the plasmons, a direct visualisation of SPPs is possible. Imaging of SPs allows the determination of their properties, such as the amount of confinement to the surface and propagation length, thereby enabling design of state-of-the-art plasmonic devices. The most widely used approaches for SPR imaging are near-field microscopy, leakage radiation microscopy, fluorescent imaging, and scattered light based imaging.

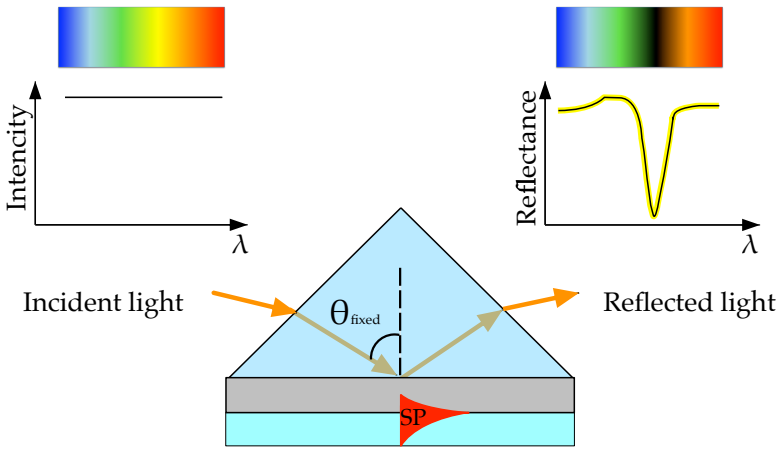


Figure 2.14: SPR detection using spectral interrogation technique. Using broadband light incident on the metal surface at a fixed angle θ, SPR is detected as a dip in the reflected spectrum at a resonant wavelength.

Near-field microscopy is the only SPR imaging technique with a sub-wavelength resolution. A near-field microscope probe is brought within the vicinity of a flat metal surface, such that it is immersed into the tail of the evanescent field of SPPs. Excitation of the SPs can be performed by the tip itself (as described in Section 2.4.1), or more commonly, via a Kretschmann prism setup. The intensity of the near-field collected above the metal surface enables direct visualisation of propagating SPPs.

Leakage radiation microscopy is an SPR imaging technique that relies on the fact that propagating SPs on a thin metal film are not completely evanescent and a significant portion of their energy is lost into a supporting substrate [89]. There are two types of losses responsible for the short lengths of propagation of SPs, intrinsic losses in metal and radiative losses into a substrate named leakage radiation. The intrinsic losses in metal do not depend on the thickness of the metal film. However, the radiative losses decrease with increasing film thickness and are almost negligible once the film thickness reaches more than 70 nm. The propagation length of the SPs decreases as the metal film thickness is reduced due to the increased leakage radiation. For thin metal films, leakage radiation can be responsible for a significant proportion of the energy loss of the propagating plasmons, and therefore, it can be detected using high NA microscope objective (as discussed in Section 2.4.1). Leakage radiation provides information about the intensity of the electromagnetic field associated with SPs and their wavevectors which can be visualized in the image and Fourier planes. The advantage of the technique is its simplicity, however, the necessity to use thin metal films to increase the available signal implies that it it is achieved at the expense of reduced propagating lengths [50].

An SPR associated field can be used to excite emitters such as fluorescent labels or quantum dots placed in the close proximity to the metal surface. If the SP resonant wavelength lies within the spectral range of the absorption of the emitter, fluorescent label can be excited by plasmons' evanescent field and the emission intensity is proportional to the local field surrounding the fluorophore. This technique allows for mapping of propagating plasmons through observation of the fluorescent radi-

ation. Although these techniques are simple and do not require complex equipment, quantitative measurements of the fluorescent molecules might be difficult due to the bleaching effects [90].

Propagating SPs can be mapped by collecting light that is lost due to scattering from metal surface features. Scattering at local imperfections allows for adjustment of the wavevector of SPPs so that it can couple into radiation thus emitting photons. The scattered light intensity maps the propagation of the plasmons on surfaces with random or periodic irregularities, such as metal gratings or even rough metal surfaces. However, the scattering is dramatically reduced for smooth surfaces, with surface roughness of an order of a few nanometers [91], making the techniques inapplicable for films with smooth surface quality.

2.4.3 *Principles of biological sensing with SPR*

As discussed in Section 2.1 and Section 2.3, the SPR condition strongly depends upon the materials that constitute the interface. Any change to the interface, for example a change in the refractive index of the adjacent dielectric, alters the propagation constant of SPs resulting in a shift of the SPR coupling conditions, whether it is the incidence angle or wavelength. The SPR sensors are essentially refractometric devices that detect changes in the bulk or surface refractive index of the adjacent dielectric that is often referred to as sample or analyte. A common classification of SPR sensors is based on which characteristic of the light wave is interrogated. Figure 2.15 illustrates the concept of SPR sensing devices and shows the typical classification of SPR sensors.

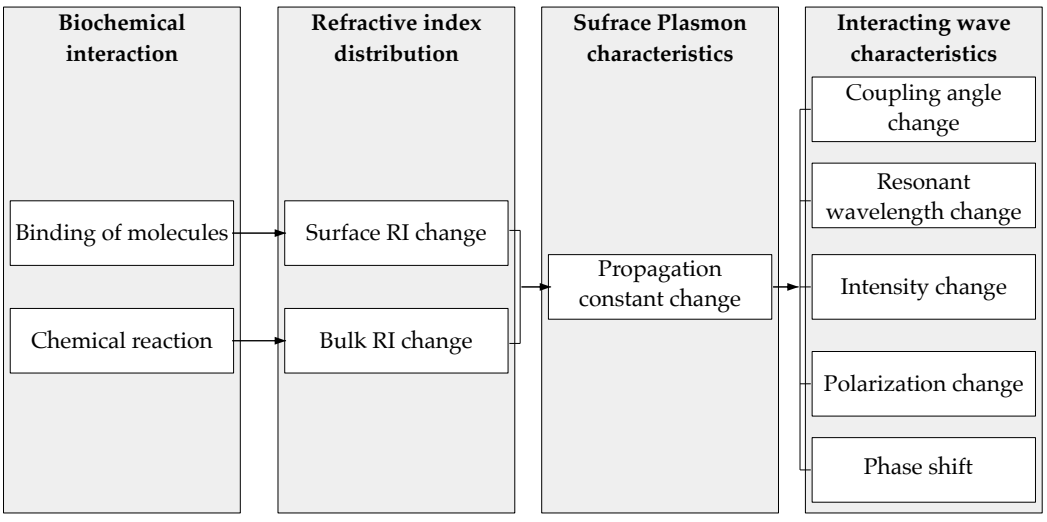


Figure 2.15: Conceptual representation of SPR biochemical sensors. Adapted from [4].

SPR sensors can detect either bulk or surface RI changes. Configurations that allow stronger confinement of the SP field to the interface are used for the detection of RI changes that occur in the close proximity of the metal surface. As an example, bimolecular interactions typically occur within nanometres from the metal film

where biorecognition elements, such as antibodies, are immobilized onto the metal surface. On the other hand, chemical and gas SPR sensors detect bulk RI changes that occur further away from the metal surface, and therefore, architectures with larger penetration depths of the plasmons, i. e. Long Range Surface Plasmon Resonance (LRSPR), are beneficial.

To be useful as a biosensing technology, SPR sensors have to provide specificity and quantitative analysis of biomolecular interactions. As the change in the RI can potentially be caused by attachment of any molecules that are present in the sample, affinity assay techniques are often used in SPR biosensors in order to ensure specificity. Through the use of surface preparation, also called functional coatings, specificity, desired coverage density and specific orientation of molecules can be achieved. Figure 2.16 shows a typical SPR affinity biosensor based on the Kretschmann configuration. Due to its simplicity, it is used in most biosensing configurations based on SPR and is an underlying technology in most commercially available SPR biosensors including Biocore (GE Healthcare) [92].

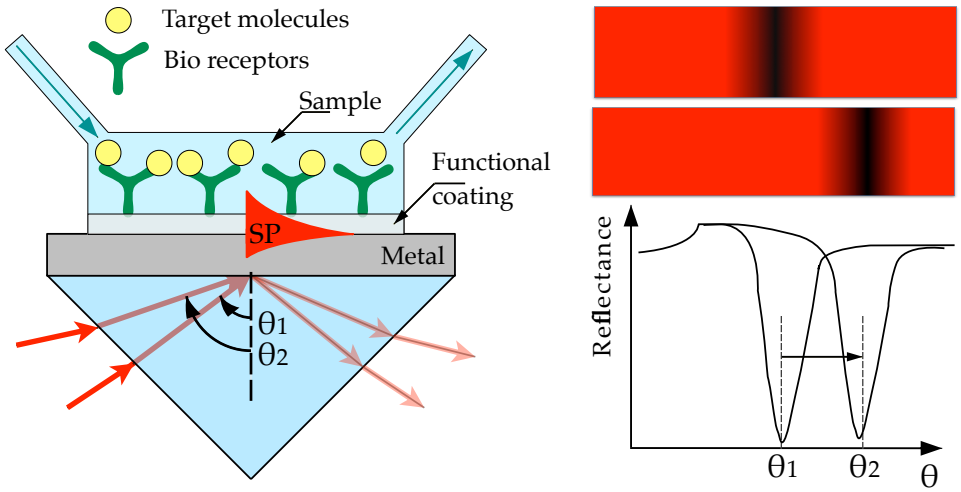


Figure 2.16: Schematic design of a SPR biosensor based on Kretschmann configuration. Bioreceptors are attached to the functional coating on the metal film. Target molecules in a sample flow through the flow cell and get captured by bioreceptors causing a shift in the angular position of the resonance ($\Delta\theta = \theta_2 - \theta_1$).

In SPR biosensors biorecognition elements, i. e. antibodies, are immobilised to the metal surface, typically through attachment to a functional coating. The latter consists of surface preparation with chemical and/or biological molecules to which biorecognition elements, also called ligands, can be attached. A typical surface chemistry consists of hydrogel surfaces with accessible carboxyl groups for linkage with biotin or other molecules, depending on a coupling protocol. Biotin and streptavidin have the strongest binding constant and therefore, streptavidin or its alternatives are used to produce the next mono-layer on the biotin coated surface. Antibodies that are functionalised with biotin are then immobilised onto the streptavidin surface. Non-specific binding sites of the functional coating are blocked with other proteins, such as bovine serum albumin or casein. The surface is rinsed with buffer solution between each step to remove unbound molecules.

After the functional coating is attached to the sensor surface, target molecules that are specific to the antibodies are captured causing a RI change which in turn results in a change in the propagation constant of the SP. The resonant condition can be matched by changing the modulated parameter, such as angle of incidence, wavelength, etc., and is quantitatively measured by means of optical apparatus. As the amount of change in the propagation constant of SPs is proportional to the amount of change in the refractive index, or the concentration of captured molecules, quantitative measurements are possible with SPR biosensing techniques.

In addition to specificity and quantitative measurements, SPR biosensors allow the study of real time interaction kinetics between biomolecules and the determination of the parameters associated with this interaction. Interaction kinetics are comprised of three distinct stages, association, steady state, and dissociation. In the association stage the amount of binding sites on receptor molecules available to the target molecules is greater, which causes an increase of the SPR response with time. Eventually, when the surface reaches saturation, meaning that the all binding sites are occupied by the target molecules, the interaction enters steady state. Dissociation takes place when the bonds between ligand and target molecules break apart, which causes a decrease of the SPR response with time. A typical plot of the temporal SPR response is called a sensorgram and is presented in Figure 2.17. These 3 stages contain information about the interaction between molecules in terms of how fast association and dissociation happens and how strong the interaction is, and parameters associated with it, i. e. association and dissociation constants, can be quantified.

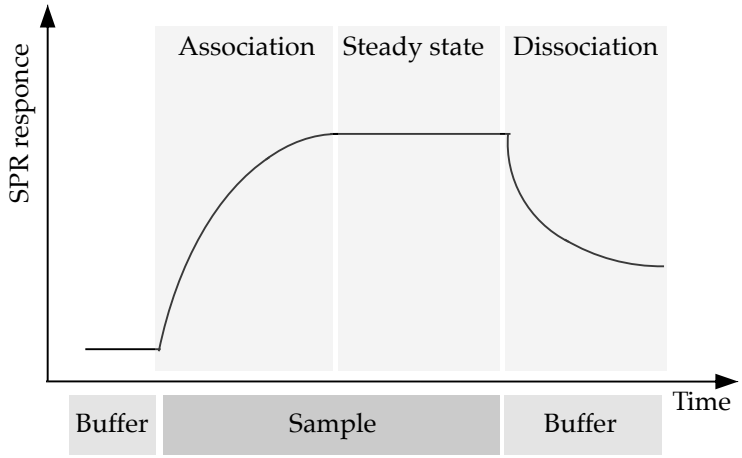


Figure 2.17: Sensorgram showing 3 stages of molecular interaction for determining parameters of binding kinetic with SPR sensors.

The sensorgram allows to track the association and dissociation of molecular complexes over the entire course of the interaction. These real time quantitative measurements are invaluable for molecular interaction analysis in areas of biological and medical research, drug discovery, and clinical studies.

2.4.4 *Performance characteristics of SPR sensors*

For SPR excitation by means of TIR in a prism or a waveguide, the resonance condition is matched when the wavevector of the incident light in the plane of the surface (k_x) matches the wavevector of the SPW in the metal film (k_{sp}), as was derived from Maxwell's equations in Section 2.3. The wavevectors of the incident light and the SPW are expressed as [4]:

$$k_x = \frac{2\pi}{\lambda} n_p \sin\theta \tag{2.45}$$

$$k_{sp} = \frac{2\pi}{\lambda} \sqrt{\frac{\epsilon_m \epsilon_d}{\epsilon_m + \epsilon_d}}, \tag{2.46}$$

where n_p is the refractive index of prism or a waveguide, and ϵ_d and ϵ_m are dielectric constants of adjacent dielectric and metal respectively, and λ denotes the wavelength of incident light. Resonance is satisfied when $k_x = k_{sp}$, which can be achieved by varying either the incident angle, θ, in case of angular interrogation, or the wavelength of incident light, λ, in case of spectral modulation.

The main characteristics that describe performance of an SPR sensor are sensitivity, resolution, detection limit, and dynamic range. Sensitivity of an SPR sensor is defined as the change in the monitored parameter (such as wavelength or angle of incidence) with respect to a change in the parameter that caused the response (refractive index). For angular interrogation based sensors sensitivity can be written as [4]:

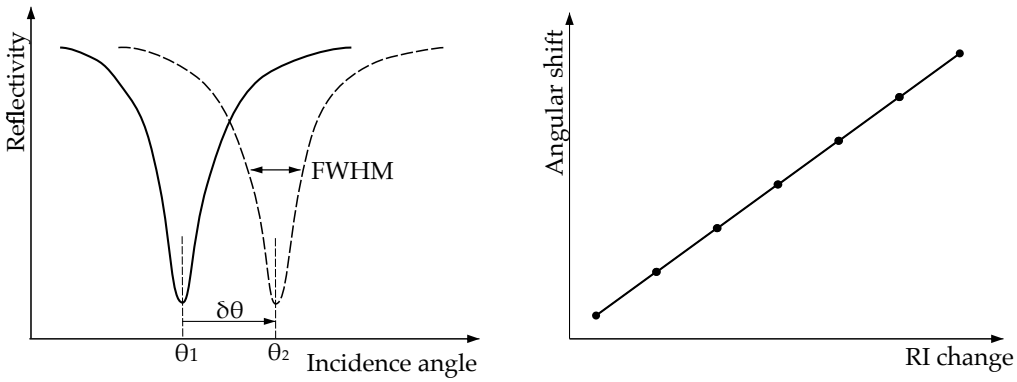
$$S_\theta = \frac{\delta\theta}{\delta n} \tag{2.47}$$

Similarly, for a wavelength interrogation SPR sensor sensitivity is defined as the change in the resonant wavelength with respect to the change in the refractive index:

$$S_\lambda = \frac{\delta\lambda}{\delta n} \tag{2.48}$$

Figure 2.18 illustrates that the RI sensitivity is determined by measuring shift in the angular position for a known change in sample's RI [93].

Sensitivity of SPR sensors based on wavelength interrogation and intensity measurement has been found to increase with increasing resonant wavelength. This phenomena is due to material dispersion and was extensively investigated by Homola [94]. For SPR systems with wavelength modulation, an increase in the refractive index of a prism or a waveguide shifts the resonant condition towards longer wavelengths, as follows from the Equation 2.45, and gives rise to the sensitivity of the sensor [94]. The choice of metal significantly affects the sensitivity of SPR sensors. As such, silver offers higher sensitivity in comparison with gold films. Alternative metals, alloys and multilayer systems have also been used to increase sensitivity of SPR sensors [95, 96]. Other factors, such as thickness of the metallic layer and type of excitation used, also influence sensitivity to a smaller extent [94].



(a) Shift in the resonant position.

(b) Sensitivity curve.

Figure 2.18: Sensitivity of SPR sensors with angular interrogation as a shift in the angular resonance position with a change in the sample's RI. Slope of the sensitivity curve gives sensitivity value.

Another important SPR performance characteristic is the sensor's resolution. The resolution (R), defined as the smallest shift in the monitored parameter (i. e. resonant wavelength) detectable by a sensing platform, depends on the optical setup and on the linewidth of the SPR signature. Resonance curves with narrower linewidths filter spectral noise more efficiently. This leads to lower spectral deviation from the actual position of an SPR feature allowing for very slight spectral shifts to be resolved [93, 97]. Resolution primarily depends on the system configuration such as geometry, materials, interrogation and excitation methods, as well as instrumentation and data processing techniques. Resolution can be calculated as an average of the noise contribution from three sources [93]:

$$R = 3\sigma = 3\sqrt{\sigma_{ampl}^2 + \sigma_{spectral}^2 + \sigma_{thermal}^2}, \tag{2.49}$$

where σ_{ampl} is noise contribution from the signal amplitude, $\sigma_{spectral}$ - spectral noise factor, and $\sigma_{thermal}$ - thermal noise. According to the results presented in [93], numerical simulations predict linear dependency of the standard deviation of the resulting spectral variation σ on the Full Width at Half Maximum (FWHM) of the response ($\Delta\lambda_{0.5}$), and exponential relationship with SNR:

$$\sigma \approx \frac{\Delta\lambda_{0.5}}{4.5(SNR)^{0.25}}. \tag{2.50}$$

Sensitivity and resolution determine one critical performance characteristic – the Detection Limit (DL). In SPR sensing, the DL is defined as the smallest change of the refractive index that can be measured [4, 93] and is determined as:

$$DL = \frac{R}{S}. \tag{2.51}$$

Therefore, to improve a sensor's DL, one would have to increase the sensitivity of the sensor, and/or reduce the resolution by either minimizing FWHM of SPR response or/and increasing SNR.

As the sensor resolution is inversely proportional to the linewidth of the SPR feature in the analysed signal, it is often convenient to define a Figure of Merit (FOM) as a ratio between sensitivity and FWHM ($\Delta\lambda_{0.5}$):

$$\text{FOM} = \frac{S}{\Delta\lambda_{0.5}}. \tag{2.52}$$

Considering that the resolution is often difficult to estimate, this FOM indicates that it is easier to measure the exact location of a narrow resonance feature rather than a broad one, and also allows comparison with non SPR platforms.

The dynamic range of an SPR sensor is the range of values of the parameter to be determined (refractive index) that can be measured by the sensor. Typically, the dynamic range of angular interrogation-based and wavelength interrogation-based sensors is determined by the detection system's operating range (spectral analyser in the case of wavelength interrogation) but is often limited by the optical properties of the materials that constitute the sensor with typical detectable RI values ranging from 1 to 1.5, suitable for gas and aqueous solution sensing [88].

For indirect SPR sensors, such as affinity biosensors, when the change in the RI near the sensor surface is an intermediate parameter and the parameter to be determined is the concentration of bound molecules, the performance characteristics depend not only upon intrinsic characteristics described above. The performance of SPR affinity biosensors is also determined by the molecular weight of the target molecules, surface preparation, interaction between biorecognition elements and the target, surface coverage density, and many other characteristics. These are generally difficult to predict analytically and, therefore, benchmark performance characteristics for such sensors are determined empirically.

2.5 REVIEW OF SPR FIBRE SENSORS

SPR is a mature technology that has significantly evolved over the past few decades. Many enhancement mechanisms and novel SPR sensing approaches have been developed. Optical fibres have extended the waveguide excitation approach further allowing for miniaturisation of biosensors. This brought the ability to use these devices in previously inaccessible locations, including in-vivo diagnostic of medical conditions [98]. This section presents an overview of fibre optic based SPR sensing configurations, main classifications of fibre SPR sensors, performance comparison, and current trends in advancing fibre based SPR sensing architectures.

Traditional optical fibres are designed to guide light inside the fibre with as little loss as possible. Therefore, the construction of conventional optical fibres prevents guided modes from escaping into the surroundings, typically through the use of cladding. For that reason, the geometry of the fibres needs to be modified in order to allow the guided fibre modes to interact with the metal coatings or particles and excite plasmonic resonances. Owing to the flexibility of the optical fibre design and their availability, recent advances in nano fabrication techniques, and the relative

simplicity of fabrication of plasmonic materials, thousands of fibre SPR configurations have been proposed. Even though there are multiple excellent review articles on fibre based SPR sensors which have been published recently [99–102], it is often difficult to categorise the SPR fibre probes. In order to systematically present pros and cons of different fibre SPR probe types, various classification schemes for the fibre SPR sensors are proposed in this thesis. The classification schemes are based on different characteristics such as fibre type, fibre geometry, type of metal coating, excitation and interrogation methods, as well as sensor' application, as summarised in Figure 2.19. This classification of SPR fibre sensors was published in the review paper **P8**.

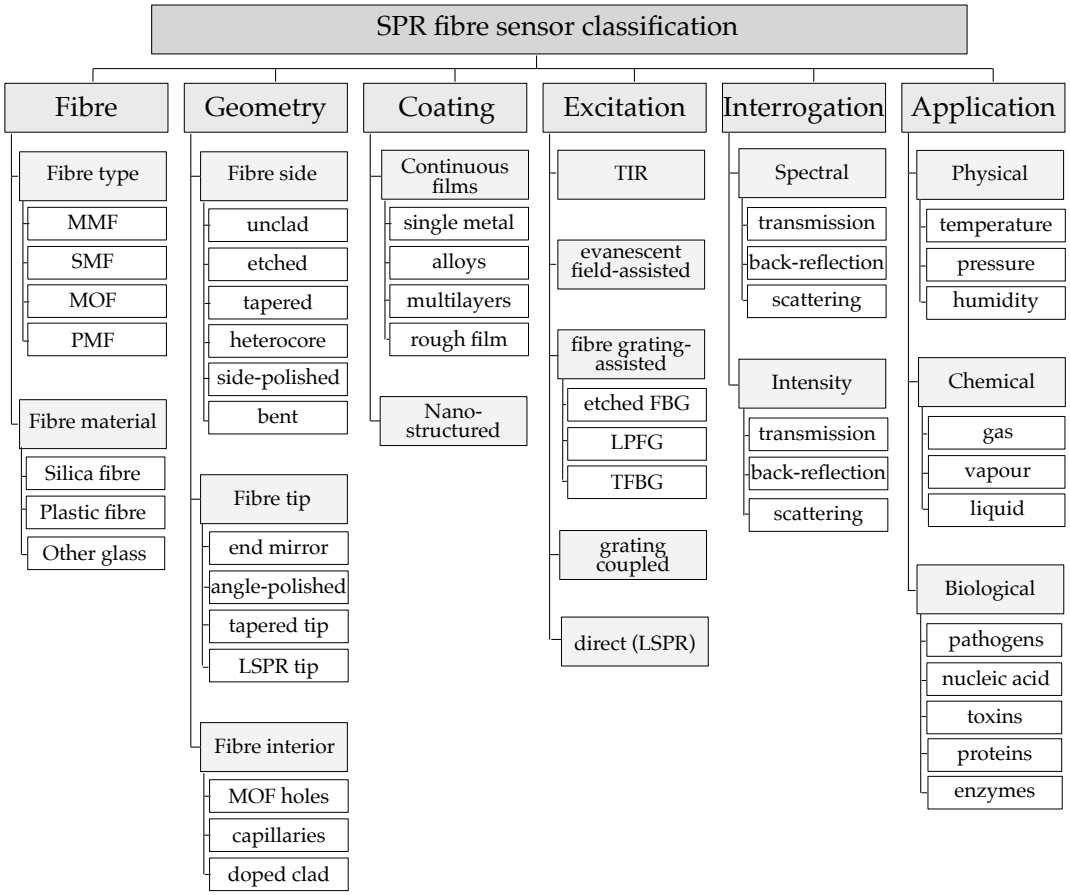


Figure 2.19: Classification of SPR fibre sensors.

2.5.1 *Classification based on fibre type*

SPR sensors' properties depend upon optical fibre type and fibre materials used to fabricate the probes. According to the type of an optical fibre, the plasmonic sensors can be categorised as Multi Mode Fibre (MMF)-, Single Mode Fibre (SMF)-, Microstructured Optical Fibre (MOF)-, and Polarization Maintaining Fibre (PMF)-based SPR sensors. Large core MMFs, with core diameters much bigger than the wavelength of guided light, obey the same set of physical principles as prism based couplers and can be approximated by the laws of geometrical optics [96, 103, 104].

Early fibre optic SPR sensors were mainly constructed from MMFs where the cladding has been removed from a section of the fibres to expose the core for metal deposition. Transmitted light is traditionally collected at the end of the fibre. The SPPs' excitation wavelength appears as a dark region in the transmitted spectra (Figure 2.20).

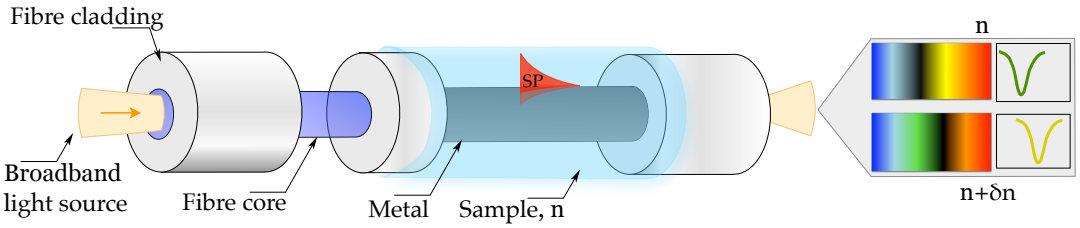


Figure 2.20: Fibre based SPR sensor. Change in the refractive index of the sample δn causes change in the resonant condition which is seen as a shift of the resonant wavelength (dip in the transmitted spectra).

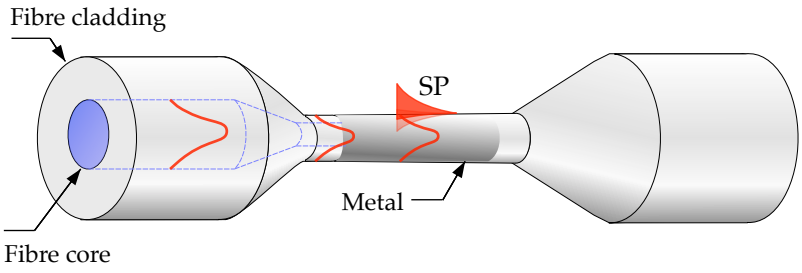
However, due to the large number of modes that propagate inside a multi-mode fibre, the SPR spectral feature broadens increasing minimum resolvable sensor resolution. One of the approaches used to overcome this broadening is the use of SMFs or MOFs where a large external structure supports a small guiding core. With the recent advances in fabrication technologies of MOFs, various exotic MOF SPR-based designs have been explored. These include speciality MOFs with metallized air holes [105], suspended core MOF sensors [106], D-shaped hollow core MOF fibres [107], Photonic Crystal Fibres (PCFs) [108], and more exotic configurations based on speciality fibres such as ECF [109] that are presented as a part of the current work (Chapter 5). Using these speciality fibre allows to control properties of the guided light and achieve increase interaction between electromagnetic radiation, SPs, and a dielectric sample for improved sensing performance.

2.5.2 *Classification based on geometry*

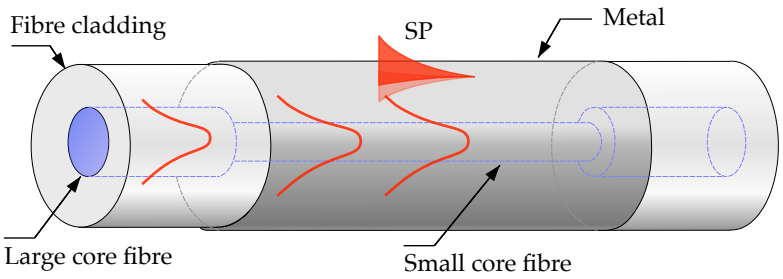
In order to allow fabrication of the sensing region in optical fibres, the fibre geometry needs to be modified to allow interaction of the guided modes with the plasmonic coating. Geometry modified fibre optic sensors have been demonstrated as early as 1993 [110]. Based on a modified geometry, the fibre SPR sensors can be classified as fibre-side SPR sensors, fibre-tip SPR sensors, as well as fibre-interior SPR sensors. A variety of sensing probes are produced on the side of an optical fibre where fabrication methods range from unclad or etched optical fibres, tapered fibres and hetero-core structures, to side polished fibres, and bent fibre probes. Performance of the fibre-side SPR sensors depends on the fibre type, materials, fabrication methods, and geometry. Figure 2.21 schematically shows the geometry-modified optical fibre SPR sensors implemented on a side of an optical fibre.

Unclad, etched and tapered fibre SPR probes

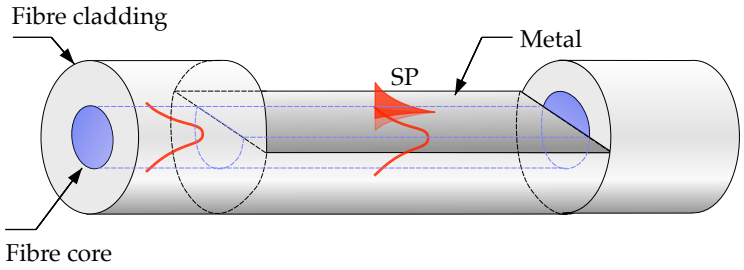
To allow for interaction of the guided light with the metal coating, the plasmonic materials have to be deposited on the fibre core. For large core MMFs where the



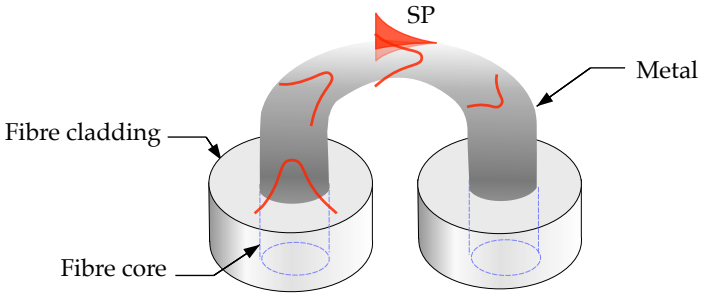
(a) Tapered fibre SPR probe.



(b) Hetero-core structure.



(c) D-shaped SPR probe.



(d) U-shaped SPR probe.

Figure 2.21: Schematics of geometry modified optical fibre SPR sensors implemented on a side of an optical fibre.

cladding typically consists of a soft polymer layer, the core can be easily exposed by stripping off the polymer layer. However, if the cladding is made of glass, like in double clad or graded index MMFs, etching must be performed to access the fibre core region. Alternatively, the fibre can be stretched over a short region along its length by heating the section of the fibre with a filament in a controlled manner such that the fibre glass becomes soft, and then gently pulling the fibre along its axis to elongate that section. In the stretched region the fibre can be made so thin that the evanescent field escapes through the cladding and interacts with the surroundings. The tapered region is then coated with a metal film for SPR sensing (Figure 2.21a). These structures also provide the benefit of having small cores that results in narrow SPR features and therefore, increased resolution. The RI sensitivity for tapered probes reaches up to 12000 nm/RIU [111], however, the fragility of the tapered probes make them impractical for many applications.

Hetero-core fibre structure

To overcome the issue with the fragility of the tapered fibre designs, other SPR fibre configurations, called hetero-core structures, have been proposed [112–115]. This configuration consists of splicing two different kinds of fibres with mismatched core sizes, typically an SMF fibre region is spliced between two MMF fibres (Figure 2.21b). The mismatch between the cores causes the guiding modes to couple into the cladding of the SMF fibre where plasmonic interaction can occur providing the region is coated with metal.

Side polished (D-shaped) SPR probes

If the fibre cladding is made of glass, like in double-clad or gradient index fibres, and is not easily removable, side polishing can be used to expose a portion of the fibre core, as illustrated in Figure 2.21c. Typically, the fibre is enclosed inside a resin block at a slight curve and a portion of the fibre, together with the resin, is polished off [76, 116–118]. An alternative approach to side polishing is to fabricate a grove along the fibre with a femtosecond laser to expose the core for metal deposition. Feasibility of MOFs as D-shaped SPR probes have also been theoretically studied [107]. Sensitivity of side polished structures vary depending on a fibre core materials with up to 3300 nm/RIU being reported for a silica SMF-based side polished SPR sensor [116]. Sensitivity and detection limit are also affected by fibre type, polishing depth, as well as plasmonic coating.

Bent (U-shaped) SPR fibre sensors

The easiest and most non-intrusive way of extracting light propagating in the fibre core, is by bending the fibre to introduce losses. When the fibre is bent beyond a critical radius, the core modes can couple into the cladding, and therefore, if the bent region is coated with metal, a portion of this radiation can excite SPR. Bent fibre probes, also called U-shaped fibres, are usually fabricated from unclad large core MMFs by heating the glass and forming a permanent U-shaped bend

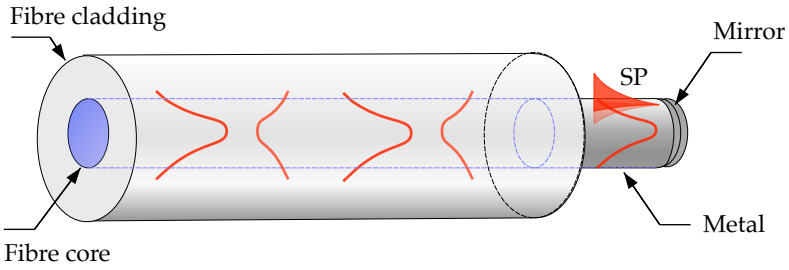
as shown on Figure 2.21d. Even though simple flexing of the fibre can have the same effect, it would be hard to achieve the required level of reproducibility due to high tensile strength in the glass at the outer side of the bend. Sensitivity of the bent SPR sensors increases as the bend radius decreases, with theoretical values of up to 70000 nm/RIU achieved for a bend radius of 1 cm, reducing by an order of magnitude for a bend radius of 2 cm [119]. With precise temperature controlled techniques it is possible to fabricate U-shaped SPR probes with desired bend radii down to 0.5 mm. For the same light launching conditions, sensitivity values of the U-shaped fibre sensors are typically several times more than for tapered probes, and around 25 times higher than for a straight sensing region implemented on the same fibre [119]. One of the attractive benefits of the U-shaped SPR probes is that it can be used as a point sensor or a dip sensor.

End face mirror SPR fibre probe

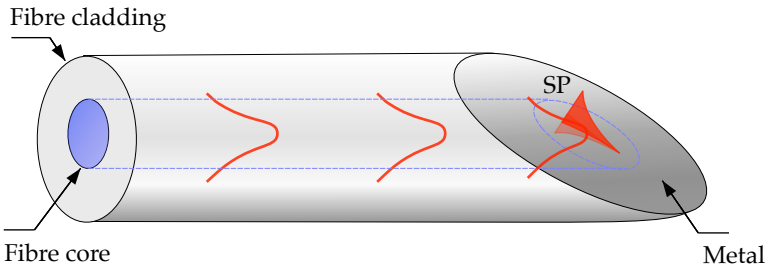
All of the above geometry modified fibre SPR sensors are implemented on the side of an optical fibre, however, many applications require point of contact probes. As the sensing regions on the side-of-fibre SPR devices are typically located in the middle of the fibre and often require microfluidic integration, it is difficult to construct these sensors as contact probes. So called dip SPR fibre sensors are implemented on (or near) the tip of an optical fibre allowing to use these devices in previously inaccessible locations and in situ applications. The simplest implementation of a fibre tip SPR sensor is creating a sensing region on a side of the fibre near a cleaved fibre end coated with metallic mirror (Figure 2.22a). This configuration is essentially the same as the unclad fibre sensor described above and is usually fabricated using MMF. The interrogation of SPR is performed through analysing light back reflected from the mirror on the fibre end facet [110, 120, 121].

Angle-polished and tip-tapered SPR sensors

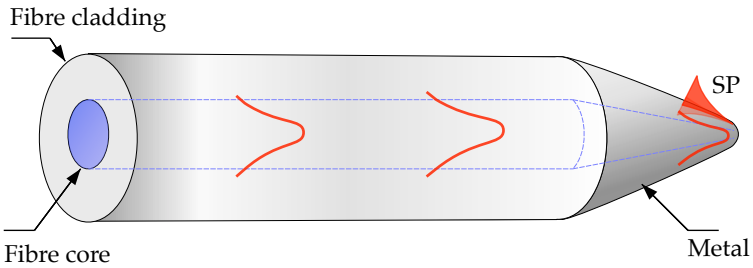
Instead of creating a sensing region on a side of the fibre near the fibre tip, a sensing region can be created on the end of the fibre minimising contact with the sample. However, as the angles of incidence of light propagating inside the fibre with the cleaved fibre end face are typically very small (near normal incidence), additional preparation of the fibre tip is required to match the SP resonance condition. One technique is to polish the fibre end at an angle thereby modifying the incidence angle range onto the fibre end (Figure 2.22b). This method allows the use of a monochromatic light source by adjusting the polished angle such that the wavelength of the monochromatic light and the incident angle pair satisfy the condition for SPs excitation. The first fibre optic sensor with angle polished fibre tip was proposed as early as 1993 [122]. After that, several advances have been made [121, 123–125] including one fibre tip with multiple angles to acquire sensitivity to both, gas and liquid phases [126]. Recently, an interesting design of an angle polished fibre tip SPR sensor that utilises a speciality fibre with twin cores with a sensitivity of 5213 nm/RIU has been demonstrated [127]. An alternative approach to the flat fibre tip that allows



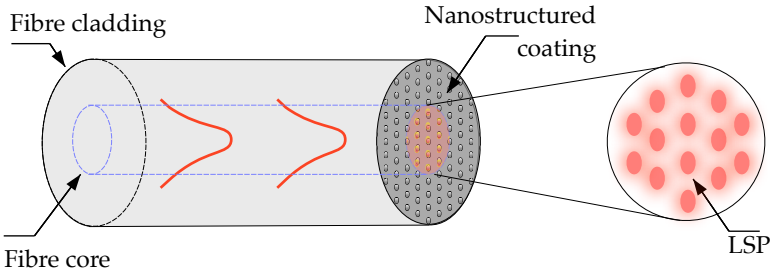
(a) Flat fibre tip SPR probe with end mirror.



(b) Angle polished flat fibre tip SPR sensor.



(c) Tapered tip SPR probe.



(d) LSPR fibre tip probe.

Figure 2.22: Schematics of geometry modified optical fibre SPR sensors implemented on a tip of an optical fibre. These probes allow the usage of the devices as dip sensors or contact probes.

matching of the SPR coupling condition at the end facet of the fibre is to modify the fibre by tapering its tail. The same techniques that are used for tapering the middle section of the fibre are employed, but the fibre is cleaved within the tapered region. The surface of the taper is then coated with plasmonic coating (Figure 2.22c) [128].

Fibre end face LSPR sensors

Another important subset of fibre tip SPR sensors are LSPR based probes implemented on the square cleaved fibre facets using nano-patterned plasmonic films, metal nanoparticle coatings, or periodically structured fibre tip surfaces (Figure 2.22d). The guided light is directly exposed to the nanostructure causing a localised plasmonic response. With the recent advances in nano fabrication technologies, a variety of nano-structured surface have been used to pattern the fibre tip. These include coating the fibre end with metal nanoparticle arrays [129, 130], and two-dimensional nanostructures [131], nano-hole array [132, 133], using PCFs with holes at the tip [134], or machining the metal coated fibre tip with sub-micron periodicity using focus ion beam [135]. As the LSPR can occur at normal incidence, angle polishing or tapering the fibre tip is not required.

Interior of the fibre SPR sensors

Instead of implementing the sensing region on the exterior of an optical fibre, plasmonic materials can be deposited on the inside of a fibre. This requires either using special MOFs with air holes or micro-capillaries. Not only does the utilization of MOFs provides the advantageous guiding properties, but also it allows to use the same fibres as microfluidic channels for samples. MOFs with a variety of air cavity shapes coated with metal particles or films have been reported. These include but are not limited to circular air holes and crescent-shape holes [105], triangular shaped holes [106], and inner cavities of PCFs [136]. Recently, hollow core fibre SPR sensors, implemented using silver coating deposited inside capillaries, have been reported [137–139]. In addition to coating air cavities inside optical fibres, interior fibre SPR sensors can be implemented in the bulk of the glass fibre cladding by doping the cladding material during the fibre preform fabrication stage with plasmonic nanoparticle dopants [140]. This avoids the additional fabrication steps when depositing materials inside the air cavities but requires manufacturing of speciality optical fibres and restricts the usage of these fibres to SPR applications.

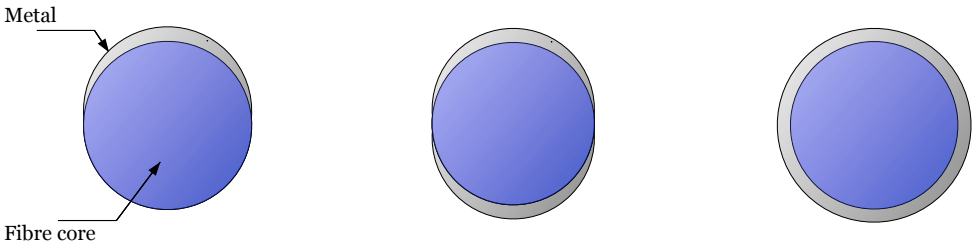
2.5.3 *Classification based on type of plasmonic coating*

Continuous metal films

SPR fibre sensors can be classified based on the type of plasmonic coating. The most common coating is fabricated by physical deposition techniques, such as thermal vacuum evaporation or magnetic sputtering, which results in smooth continuous films that are optimal for SPs propagation. Typical materials that are used for smooth con-

tinuous films are silver (Ag), gold (Au), aluminium (Al), and copper (Cu) [96]. The performance of these sensors, such as sensitivity, resolution, and dynamic range, depend on the choice of metal for the plasmonic coating. Silver generally provides higher sensitivity [88], but due to the chemical stability of gold, it is more commonly used for the majority of sensing applications. Recently, more exotic materials such as Indium Tin Oxide (ITO) and graphene have been used in fibre optic SPR sensors [108, 141, 142].

Due to the nature of physical deposition techniques that are commonly used for fabrication of plasmonic films, where metal vapour or sputter is deposited directionally, the resulting coatings on the side of cylindrical optical fibres are typically not even in thickness. Figure 2.23 shows possible metal film layouts on a side of an optical fibre that can be produced by different deposition methods. Having metal coatings with varying thickness, such as single- or double-sided coatings shown on Figure 2.23a and Figure 2.23b respectively, can result in multiple resonances [143] and an increase in the sensor's dynamic range [144, 145]. However, the layout of the plasmonic coating influences sensor performance by, for example, broadening the SPR feature for single- or double-sided coatings and with stronger SPR signals typically obtained with double-sided (Figure 2.23b) and cylindrical (Figure 2.23c) coatings.



(a) One sided coating. (b) Double sided coating. (c) Cyllindrical coating.

Figure 2.23: Cross sections of optical fibre core with common metal coating layouts. (a) and (b) layouts are typically produced by thermal evaporation or sputtering techniques, and (c) by chemical deposition.

The thickness of continuous metal films influences the SPR sensor performance, with optimal thickness values ranging from $20 - 80$ nm depending on sensor configuration [4, 102]. In addition to the thickness, an important parameter that defines the sensing characteristics is film roughness. Smooth metal films are traditionally used for most SPR configurations due to the higher propagation length of the SPs and, therefore, better performance. Smooth high quality metal films with precise thickness control are typically fabricated by a thermal vacuum evaporation technique, or magnetic sputtering. However, using rough metal coatings provides some advantages, in particular, the ability to use the scattered light interrogation method instead of transmission measurements, such as those used in conventional fibre optic SPR sensors with smooth coatings. The SPR sensing architectures described in the current dissertation rely on rough metal coatings produced by a chemical deposition technique and will be described in detail in Chapter 4.

Layered coatings

Instead of using a single metal as a SP supporting material, alloys consisting of multiple metals can be designed to provide desired performance. Smooth plasmonic coatings can also be stacked with dielectric or metallic layers to produce structures that modify SPR sensor characteristics. Bimetallic coatings consisting of silver and gold have been used to increase sensor performance as well as to protect the silver from oxidizing [104, 146]. Dielectric layers, i. e. silica, magnesium fluoride, fluorinated polymers, deposited between metal films have been used to improve sensing performances [145, 147, 148], tune the resonant wavelength [149], generate LRSPR [138, 150], and as protective coatings [103].

Nano-structured coatings and nanoparticles

In addition to continuous metal films, nano-structured plasmonic coatings and nanoparticle films have been used to produce LSPR fibre optic sensors. LSPs are charge density oscillations that are confined to metallic nanostructures. Numerous LSPR-supporting metallic structures have been used including but not limited to metal particles of various shapes and sizes, metal nanoshells, nanorods, nanodisks, nanorings, periodically arranged nanostructures, and arrays of holes in metallic films. Various methods to prepare materials for LSPR exist today. Some commonly used techniques to produce nanoparticles are chemical synthesis, nanolithography techniques, vacuum evaporation, laser ablation, and electrodeposition. Chemical synthesis allows the production of high concentration colloidal nanoparticles in various sizes and shapes with tunable optical properties that are subsequently attached to a fibre substrate. Nanoparticles can be immobilised to the fibre surface using self assembly [129, 151, 152], assembly using polyelectrolytes [153, 154], electron beam lithography [130, 155, 156], photodeposition methods [157], or dip coating using silanes [158, 159].

Amongst the less common techniques of nanoparticle preparation used for fabrication of LSPR sensors is vacuum evaporation that allows the production of very thin metallic nano islands. Ultra thin, less than 10 nm, gold films with nanoislands prepared by this technique have properties similar to those of nanoparticles produced by chemical synthesis. Laser ablation typically utilises pulsed lasers with controlled pulse duration and energy and involves treating metallic plates immersed in aqueous solution of $NaCl$ or surfactants. The result is the formation of metallic nanoparticles and composite alloy particles (like Ag-Au) in a solution that can subsequently be attached to a fibre substrate. Laser beams have also been deployed to transform spherical metallic nanospheres to nanorods, nanodisks, and nanoprisms [160]. Electrodeposition is a very attractive technique due to the high degree of control that can be achieved [69]. Although the sensitivity of SPPs propagating on planar surfaces is much larger (four orders of magnitude) than that of LSPR based sensors, the latter poses advantages such as lower cost, no need for temperature control, high spacial resolution, and better small particle sensitivity [70].

2.5.4 *Classification based on excitation method*

TIR and evanescent field assisted SPR sensors

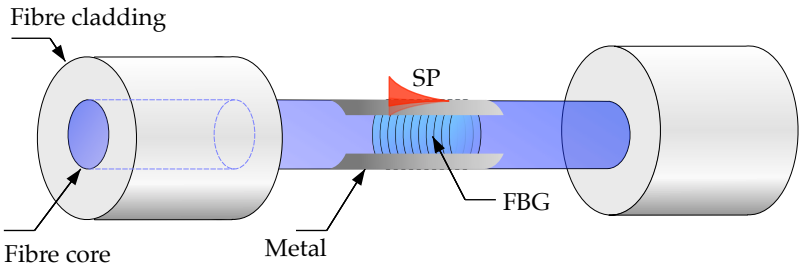
Most of the approaches of SPR excitation described in Section 2.4.1 can be implemented in fibre. The most common method is TIR excitation where a proportion of the evanescent field that penetrates through the interface on ordinary total reflection can excite SPs. Most of the geometry modified fibre SPR sensors, i. e. based on unclad or angle polished fibres, employ this approach. An additional increase of the evanescent field can be achieved by introducing inhomogeneities in the fibre such as tapering the fibre core, hetero-core structures, bent fibres, side polished fibres, and MOF. These SPR fibre sensors can be unified as evanescent-field-assisted sensors, as similar structures but without plasmonic coatings are used in so-called evanescent wave fibre sensors [161].

Fibre grating-assisted and grating-coupled SPR sensors

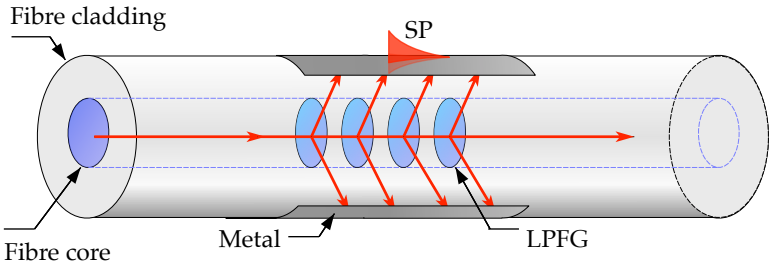
Due to mechanical strength and availability of fibre gratings, remarkable progress has been made in order to achieve SPR excitation through the use of Fibre Bragg Gratings (FBGs), Long Period Fibre Gratings (LPFGs), and Tilted Fibre Bragg Gratings (TFBGs). A fibre grating is a periodic structure in the refractive index of the fibre core which generates a wavelength specific dielectric mirror. Instead of modifying the fibre geometry to access core-guided light, photo-inscribed fibre gratings can be used to diffract a proportion of light from the core into the cladding where it can interact with a plasmonic coating deposited on the outer surface of the cladding. This overcomes the major limitation of geometry modified SPR fibre sensors, their mechanical strength. The ability to preserve the mechanical integrity of the fibre make it possible to use grating assisted SPR sensing devises in previously not accessible ways.

The technique of inscribing gratings into a fibre is reliant on the fact that some glasses, i. e. germanium doped silica, are photo sensitive, and therefore, a high intensity UV laser can be used to change the RI of the core with the desired periodicity [162]. Traditional short period sub-wavelength fibre gratings, also known as FBGs, act as a wavelength sensitive mirrors that reflects light at a certain wavelengths and transmits the other wavelengths as shown in Figure 2.24a. Although the FBGs are very sensitive to the strain and temperature changes, the core-guided light does not out couple into the cladding making the FBG insensitive to the environment outside the cladding. FBGs can be used in SPR sensors by etching a portion of the cladding [163].

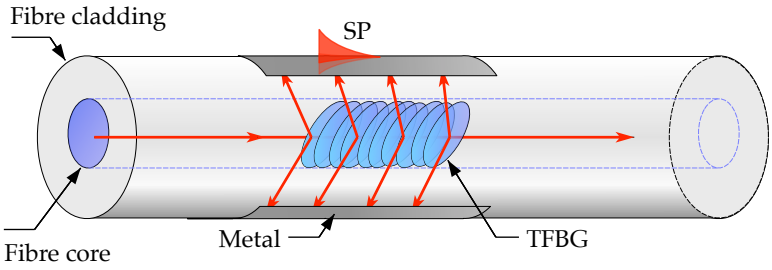
LPFGs have a long RI modulation period, typically three orders or magnitude higher than that of a FBG. LPFGs wavelength-selectively couples core-guided light into the cladding modes which are then attenuated in the cladding structure. This results in multiple attenuation bands in the transmitted spectra which are sensitive to the period of the LPFG, its length, and the conditions of the surrounding environment, such as strain, bend radius, temperature, and external RI [162]. Due



(a) Etched FBG SPR sensor.



(b) LPFG SPR sensor.



(c) TFBG SPR sensor.

Figure 2.24: Schematics of the fibre grating assisted SPR fibre sensors. FBG is generally needs to be etched to access the core, while LPFG and TFBG allow out-coupling of the propagating core modes into the cladding modes where SPs are excited on the outer surface of the cladding.

to the much longer period of the LPFG, typically an order of 50 to 500 μm, they are easier to fabricate than the short period FBGs. What makes it useful for the SPR fibre sensors is that LPFG couples forward propagating core modes into forward propagating cladding modes, as illustrated in Figure 2.24b. If a plasmonic coating is deposited on the fibre cladding surface, the cladding modes can couple to SPs. A few configurations of LPFG-assisted SPR and LSPR fibre sensors have been reported in [164–167]. Recently, LPFGs have been proposed to be used in a WGM-coupled SPR fibre sensor implemented by bending a fibre in a loop in order to avoid a small bent curvature radius [168–170].

Another attractive approach of the grating-assisted SPR excitation in optical fibres is by using TFBG. A TFBG is essentially a short period grating (like FBG) with the periodic RI modulations tilted at a slight angle with respect to the normal of the fibre axis (Figure 2.24c). In addition to self-coupling with backward propagating core modes like in a straight FBG, the forward propagating core mode couples with many backward propagating cladding modes. This results in a comb-like transmitted spectrum with multiple narrow-band cladding resonances on the shorter wavelengths part of the spectrum from the Bragg resonance feature. Pioneering research work on the TFBG-assisted SPR fibre sensors has been done recently with multiple sensor configurations developed [171–175]. One of the most important features of the TFBG-assisted SPR sensors is the presence of Bragg resonance that can be used as a reference control for compensation of temperature and power fluctuations [100].

It is important to differentiate between grating-assisted and grating-coupled SPR fibre sensors. As described above, in the grating assisted sensors, the fibre grating inscribed in the core is used to out-couple guided light into the cladding where it interacts with metal coating thereby excites SPs. In grating-coupled SPR configurations, metal grating is used as a coupler to adjust propagation constant of light incident to the metal [176]. An alternative to the metal grating, periodic corrugations can be fabricated on the fibre surface or fibre tip where metal is deposited over the dielectric grating [177].

2.5.5 *Classification based on interrogation method*

Spectral Interrogation

Most SPR interrogation methods described in Section 2.4.2 can be used with optical fibres. However, as the range of angles the light rays propagate inside optical fibres is limited by the fibre's NA, spectral interrogation is the most commonly employed technique. A traditional approach is to analyse broadband light transmitted through the fibre after it undergoes reflection from the sensing region, which is essentially analogous to the reflectance measurements performed in prism based SPR configurations [112, 114, 140, 178, 179]. An alternative approach to transmission measurements is back reflection measurements, where the light propagating inside the fibre reflects back from the mirror deposited on the fibre tip [127, 144, 166]. This

methods also relies on wavelength interrogation and is commonly used in dip SPR sensors, like the one illustrated in Figure 2.22a. The back reflection method is not limited to dip sensors and can be used in any fibre-side SPR sensors. The advantage of the back reflection technique is that analysed light undergoes interaction with sensing region twice, however, splitting optics need to be used at the front end of the fibre. A choice between transmission or back reflection measurements is typically dictated by the envisaged application.

A novel spectral interrogation technique for SPR in optical fibres has been demonstrated by François *et al.* [44], where excitation of surface plasmons was observed by monitoring scattering of the plasmonic wave by a rough surface. When a metallic surface has periodic or random corrugations, light that couples to SPs undergoes elastic scattering resulting in radiation of photons into free space. In this configuration SPs can be detected by collecting this scattered radiation in the far field by a microscope objective above the sensing region. The current work is based on the scattering based SPR fibre platform and aimed at advancing the architecture, and therefore, will be discussed in detail in the relevant chapters (Chapter 4 and Chapter 5). Among the advantages of the scattering based spectral interrogation are the low reliance on the quality of the metal coating and therefore low fabrication cost. Moreover, it allows the use of multiple sensing regions along the length of one fibre for self referencing and multiplexed sensing.

Intensity interrogation

The intensity interrogation technique can also be used in fibre based configurations. A monochromatic light source can be used to excite SPs providing that the wavelength of excitation is chosen such that the combination of wavelength and angles of incidence satisfy SP resonant condition. SPR is observed indirectly through analysing the intensity of the collected light, either transmitted, back reflected or scattered, where the intensity indicates the amount of spectral overlap between SP resonance spectrum and the excitation wavelength. A compact smart phone based fibre SPR device that uses the intensity interrogation method with performance exceeding commercial SPR apparatus has been reported [180]. The advantage of this technique is its simplicity, however, careful selection of the excitation wavelength, and the SPR resonant wavelength, which is determined by materials that constitute the sensor as well as RI of the sensed medium, is required for successful application.

2.5.6 *Classification based on application*

Due to their versatility, SPR based fibre sensors have been used in a large variety of applications including biochemical research studies, medical diagnostics, and environmental monitoring, to name a few. Intrinsically, an SPR sensor is a refractometer that produces a response to a change in the RI of the sensed medium. Therefore, additional elements, i. e. surface functionalisation or physical modifications to sensor configuration, need to be incorporated in the architecture in order to generate RI

change in response to the parameter to be determined (external stimuli). Therefore, the vast range of applications for SPR fibre sensing platforms can be categorised fundamentally on the basis of the external stimuli as physical, chemical, or biological.

Physical SPR fibre sensors

Being physical sensing devices that measure fundamental optical property, the RI, SPR sensors have been used for the detection of other physical quantities, such as temperature, pressure, and humidity. As the SPR resonant condition is, in general, not highly sensitive to these quantities, specially designed functional coatings that translate changes in these physical parameters into changes in the RI need to be used. Due to small refractive index changes with temperature (thermo-optic coefficients) of fibre core and plasmonic coating materials [181, 182], temperature SPR fibre sensors typically using dielectric materials with a high-value thermo-optic coefficients that are adjacent to the plasmonic coating [183–186].

SPR fibre sensors have been used for pressure detection where an elastic polymer which refractive index depends on applied pressure was used [187]. A theoretical design of an SPR fibre probe for pressure sensing has been proposed in [188] with a U-shaped SPR probe enclosed in a silicon rubber block. When pressure is applied to the block, the bend radius of fibre probe changes, which results in the change of the resonant condition.

Similarly, SPR humidity sensors rely on functional materials where RI is dependent on the number of water molecules it adsorbs. Typically, humidity sensitive polymeric over-layers in the proximity of a plasmonic coating are used [141, 189]. Changes in humidity near the polymeric layer trigger variations of the coating thickness as well as its RI, causing a shift in SPR condition. SPR dew sensors can detect temperature and humidity gradients in adjacent environment by detecting changes of thickness of water layers forming on the sensing surface [190].

Chemical SPR fibre sensors

A large category of SPR sensing applications is the detection of chemicals in liquid, vapour or gas phases. Chemical sensing covers a broad range of sub-applications such as science, environmental monitoring, food safety, mining, agriculture, drug discovery, and medical diagnostics. Chemical SPR sensors can be of any type described above. The presence of the chemicals of interest is determined by either designing a functional coating that is capable of binding the desired chemicals, or the direct detection of the RI changes caused by the presence of the sensed target chemical in a sample. For example, a pyrrole/chitosan composite coating was used to bind heavy metal ions onto Ag-ITO plasmonic coating for the detection of water contamination [191]. Hydrogen peroxide SPR fibre sensor based on Ag film coated with Ag nanoparticle-doped polyvinyl alcohol nanocomposite have been reported [192]. Other methods rely on dependence of the dielectric's RI on the concentration of the target chemicals, such as for a water salinity sensor [193]. pH fibre optic LSPR sensors have also been reported [194, 195]. Glucose or sucrose concen-

tration measurements are usually performed for SPR sensor characterisation as the RI of the solutions is known. Gas sensing with SPR typically relies on metals (palladium, silver) or semiconducting metal oxide over-layers (ITO, tin dioxide, nickel oxide, zinc oxide, titanium dioxide) that change their electric permittivity when exposed to the gas environment, i. e. ammonia sensor [196], chlorine gas sensor [197], hydrogen SPR sensor [142, 149, 198], and hydrogen sulphate gas sensor [199], to name a few.

Biological SPR fibre sensors

By far the biggest application domains for SPR fibre sensors are biological and medical studies. This popularity is due to the fact that the SPR technique provides some important advantages for the detection of biological targets in comparison to competitive methods. These advantages include elimination of labels (such as fluorescent molecules that are susceptible to bleaching), high sensitivity, a low detection limit, low volume of samples required, quantitative real time measurements, and possibility of in-vivo and in-situ applications. Detection of the presence and interaction of biological molecules together with chemical sensing make SPR biosensors an irreplaceable technology for biological, medical and pharmaceutical research, and clinical diagnostics.

For an SPR response to occur in a biosensor, the sensing surface must be functionalised with bioreceptors which are designed to interact specifically with the analyte and produce the measurable change in the RI. While the type of biomolecules can vary widely, the SPR biosensors can be classified by the type of the interaction involved as antibody-antigen, enzymatic, protein, and nucleic acid interactions which rely on well established biological detection techniques for functionalisation of the SPR sensor surface. SPR fibre based sensors have been applied to the detection of pathogens, such as viruses [44, 179] or bacteria [200], biomarkers of medical conditions [201–203], study of DNA and DNA-protein interactions [204, 205], and detection of bio-hazardous compounds [206]. However, even with its high sensitivity SPR sensors can only be successfully applied for detection of molecules with high molecular weights or relatively large concentrations of the target in the sample. Moreover, the inherent drawback of the SPR technique lies in the intervening of the results by non-specific binding. Therefore, there is a significant scope for the development of SPR fibre optic sensing platforms with improved performance characteristics. This can be achieved through refining surface chemistry and designing smart sensing architectures with improved capabilities, and combining SPR with other phenomena such as fluorescence, Förster resonance energy transfer (FRET), SERS, and WGM [207].

2.5.7 *Experimental demonstrations of SPR fibre sensors*

It is difficult to compare the performance of SPR sensing devices as they not only depend on the RI sensitivity but also on sensitivity of functional materials to the

change in the parameter to be determined, such as the change of RI with molecular concentration, temperature, or pressure. Also, even RI sensitivity is highly dependent on a particular sensor configuration, the materials of the fibre core, plasmonic coating, type and size of the fibre, as well as geometrical modifications. For these reasons, it is impractical to compare performance characteristics within one category, and therefore, Table 2.2 presents a summary of recent experimental demonstrations of SPR fibre sensors with their performance characteristics and the description of major aspects of their configurations.

Table 2.2: Summary of recent experimental demonstrations of SPR fibre sensors.

Fibre type / Geometry Coating	Excitation Interrogation	RI, RIU λ range, nm	S_λ, nm/RIU FWHM, nm	Ref.
SMF / tapered Al/InN bi-layer, assym.	evan.-field assisted TIR spectral, transmission	1.41-1.429 800-1300	11800 ca. 50-70	[111]
MMF GI - SMF / HeC Ag film	evan.-field assisted TIR spectral, transmission	1.333-1.398 500-900	1500-2100 ca. 150-200	[113]
MMF GI, SMF / bent HeC Au/Cr bi-layer, sym.	evan.-field assisted TIR intensity, transmission	1.333-1.412 500-800	n/a ca. 75-100	[115]
MMF GI, SMF / HeC Au/Ta_2O_5 bi-layer, sym.	evan.-field assisted TIR intensity, transmission	1.333-1.398 1000-1300	n/a n/a	[114]
SMF / side-polished $Cr/Au/Ta_2O_5$, assym.	TIR spec. & inten., trans.	1.329-1.342 700-900	3100-3300 ca. 50	[116] [117]
MMF / side-polished $Au/ZnS\text{-}SiO_2/Au$, assym.	evan.-field ass. TIR spectral, trans. (LSPR)	1.332-1.380 500-1000	2200 ca. 40-70	[76]
MMF GI / side-polished Au film	evan.-field assisted TIR spectral, transmission	1.30-1.39 500-900	1570 ca. 130-140	[118]
SMF / angle-polished tip Ag film	TIR spectral, side reflection	1.331-1.331 450-700	7650 ca. 150-200	[124]
MMF / angle-polished tip Au film	TIR spectral, back-reflect.	1.000-1.337 500-900	ca. 2650 ca. 100-150	[126]
MMF / angle-polished tip Au/Cr bi-layer	TIR spectral, back-reflect.	1.000-1.400 500-800	n/a ca. 100	[125]
MMF / fibre tip end mirror Au film, symmetric	TIR, dual colour intensity, back reflect.	1.333-1.362 612 and 680	n/a n/a	[121]
MMF / fibre tip end mirror Au film, symmetric	TIR spectral, back-reflect.	1.333-1.3469 500-700	1557 ca. 80	[120]
SMF twin core/ang. tip & mirr. Au film	TIR spectral, back-reflect.	1.333-1.371 600-1000	5213 ca. 100	[127]
SMF, SiO_2 / fibre tip LSPR Au film cross apertures	direct (LSPR) spectral, back-reflect.	1.0-1.4 1200-1600	755 ca. 200	[132]
n/a / fibre tip LSPR 2-D Au/dielec. nanopattern	direct (LSPR) spectral, back-reflect.	1.333-1.378 1300-1400	125 ca. 60	[131]
MMF / fibre tip LSPR Au NPs, non periodic	direct (LSPR) intensity, back-reflect.	1.33-1.38 500-700	n/a ca. 100	[129]
SMF / fibre tip LSPR Au nanoparticles, periodic	direct (LSPR) spectral, transmission	1.329-1.377 600-800	196 ca. 70	[130]
MMF / fibre tip LSPR Au nanohole array, periodic	direct (LSPR) spec., trans.&back-refl.	1.333-1.368 600-900	265-595 ca. 50-70	[133]
MMF / flat & taper. tip LSPR Au nanoholes, periodic	direct (LSPR) spectral, transmission	1.33-1.376 400-600	533 ca. 80	[135]
HoC, fluor. plastic/interior Ag film	TIR, from sample spectral, transmission	1.42-1.69 400-800	1000 ca. 200	[137]
HoC / interior cavity Ag/dielectric	TIR, from sample, LRSPR spectral, transmission	1.522-1.581 500-800	2000-6600 50-250	[138]
Speciality fibre / interior Au NPs dopped glass clad	TIR spectral, transmission	1.418-1.448 350-450	178-945 50-200	[140]

Table 2.2 (continued): Summary of recent experimental demonstrations of SPR fibre sensors.

Fibre type / Geometry Coating	Excitation Interrogation	RI, RIU λ range, nm	S_λ, nm/RIU FWHM, nm	Ref.
SMF / tapered Au film, assymetric	evan.-field assisted TIR spectral, transmission	1.434-1.458 700-1300	ca. 25000 ca. 150	[143]
MMF / fibre tip end mirror Au film, assymetric	TIR spectral, back-refl.	1.333 to 1.363 550-750	1433 ca. 150	[144]
MMF / unclad fibre side Ag/Al bi-layer, symmetric	TIR intensity, trans.	1.333-1.365 633	n/a n/a	[145]
SMF / fibre side Cr/Au film	LPFG-assisted spectral, transmission	1.33-1.36 1550-1600	n/a n/a	[165]
SMF / fibre tip end mirror Au film	LPFG-assisted intensity, back-refl.	1.000-1.379 660	n/a n/a	[166]
SMF / bent into loop Pt/Pd film and Ag film	ev.-field ass. TIR, WGM intensity, transmission	ca. 1.000 1500-1600	n/a n/a	[168]
SMF / fibre side Ag film, assymetric	TFBG-assisted spectral, transmission	1.31-1.42 1500-1600	550-673 5	[171, 172] [174]
SMF / side-polished Ag film	TIR spectral, transmission	1.32 to 1.40 500-800	1523-4365 40-90	[208]
MMF, unclad fibre side Ag rough film, symmetric	TIR spectral, scattering	1.33-1.47 500-800	500-700 100-120	[44, 201] [202]
MOF, SiO_2 capillary/unclad Au film	TIR intensity, transmission	1.328-1.363 590	n/a n/a	[180]
MMF / unclad & tip mirror Ag rough film, symmetric	TIR spec, trans. & back-refl.	1.348-1.375 600-800	ca. 250 ca. 200	[186]
MMF / unclad side ITO film, symmetric	TIR spectral, transmission	ca. 1.000 900-1500	n/a n/a	[141]

Although, a considerable range of SPR fibre sensing configurations has been proposed and demonstrated, there is a significant scope for the development of improved SPR systems suitable for a range of applications. The aspects of development that need to be addressed include but are not limited to engineering miniature sensing probes, improving microfluidic systems, the usability of the sensors, low cost manufacturing techniques, as well as improved sensing performance, such as sensitivity and detection limit.

2.6 SUMMARY

The unique optical properties of metals provide the basis to a diverse set of plasmonic phenomena due to the interaction of light and free electrons. The dispersive characteristics of metals can be described via their complex dielectric function, or RI. The strong frequency dependence of the light-matter interaction is the fundamental physical principle that underpins many applications of plasmonics.

Propagating SPs, as longitudinal electron density oscillations, can be firmly described through classical electromagnetic theory. The solutions to Maxwell's equations predict the existence of TM waves that are strongly bound to the interface between a metal and a dielectric. The electromagnetic field intensity associated with resonance of SPs, reaches a maximum at the interface and exponentially decays into metal and dielectric. The enhanced electromagnetic field associated with SPs, their confined nature, and the strong dependency on the properties of the supporting interface make SPR an indispensable tool for a large range of applications includ-

ing plasmonic waveguides and nano-antennas, enhancement of emissive processes, spectroscopy, and RI sensing.

SPR occurs when the propagation constant of incident radiation is equal to the propagation constant of SPs. Directly following from their dispersion relation, SPs cannot be excited with light incident directly from air. Several methods are commonly used to enhance the propagation constant of incident light. These include TIR excitation in a prism or dielectric waveguide, through a grating, excitation using a high NA microscope objective, or near-field excitation. SPR manifests itself as a resonant transfer of energy from incoming radiation to the SPs which is observed as minima in the reflected light. The most conventional techniques used for SPR interrogation are angular or spectral modulation, where either the angle of incidence or the wavelength of the excitation light is varied in order to satisfy the resonant condition.

Owing to the strong dependency of the resonant condition on the optical properties of the interface, any change in the vicinity of the metal surface causes a shift in the SPR condition. This forms the basis for using the SPR phenomenon as a refractometric sensing technique where small changes in the RI of a dielectric adjacent to a metal surface can be accurately measured. Refractometry can be further applied to biological, chemical, or physical sensing where the sensed event can be converted into a change in the RI. For example, the binding of biomolecules to the sensor surface causes local changes in the RI which can be efficiently detected through a shift in the SPR response.

The intrinsic performance of SPR sensors depends upon the properties of the materials constituting the sensor, especially metal and its thickness, as well as the dielectric from which SPs are excited. Sensitivity, resolution, detection limit, and dynamic range are the major performance characteristics that depend upon the material properties, sensor configuration, as well as optical setup. SPR sensors may also be characterised on the basis of the parameter of interest, such as the presence or concentration of molecules, which in turn are determined by a range of parameters, such as the sensor surface preparation, experimental procedure, or an intrinsic RI change that can be caused by the sensed event.

Optical fibres present an attractive alternative method of SPR excitation to traditional prism based SPR configurations. This is due to their flexibility, small size, availability of fibre design options, and low cost. Because of these features, optical fibres became a pre-eminent technology in SPR sensing. As the construction of conventional optical fibres prevents the interaction between the guided modes and external environment, optical fibres used for SPR sensors are designed or modified in various ways to promote this interaction.

Numerous SPR sensing architectures have been developed over the last decade with the goal of improving sensitivity and other performance characteristics. Classification schemes based on the fibre type, modified geometry, plasmonic coating, excitation and interrogation methods, as well as application, have been presented in this chapter. The experimental demonstrations of SPR fibre sensors that have been reviewed in the current chapter display this diversity and expose the large number of parameters that affect sensing performance. Even though a substantial range of SPR based fibre sensors have been proposed and demonstrated, there is a consid-

erable scope for the further development of advanced sensing architectures with improved performance.

In order to design an SPR sensing platform, whether it is generic or tailored to a particular application, it is important to understand how the sensing architecture influences intrinsic sensor performances. Furthermore, the platform design need to address engineering and usability aspects such as robustness, reproducibility, cost of fabrication and ongoing expense, and ease of use. Optical fibre based SPR sensors offer a range of additional advantages such as miniaturisation, versatility, applicability for remote and in-vivo sensing. Optimising sensitivity, resolution, and detection limit through the choice of materials and sensing configurations, will help to develop novel SPR fibre sensing architectures with improved performance. The next part of this thesis is dedicated to the optical fibre based plasmonic architectures developed throughout this project, where the first chapter presents the theoretical modelling performed to determine the relationship between the performance characteristics and the parameters of the fibre sensing configuration.

Part II

DEVELOPMENT OF PLASMONIC FIBRE SENSING ARCHITECTURES

Part II of this thesis describes the development of optical fibre based plasmonic sensors. Chapter 3 is dedicated to modelling SPR in optical fibres in order to illustrate the effect of different fibre sensor parameters on sensing performance. These modeling outcomes are compared to the experimental results for the relevant fibre SPR sensors described in Chapter 4 and Chapter 5. The remaining chapters (from Chapter 4 to Chapter 6) describe the experimental work undertaken. The development, fabrication and optimisation of a fibre SPR platform that utilises scattering is described in Chapter 4. The development and fabrication of a new, more sensitive, silica fibre SPR sensor is presented, including silica surface modification, a silver electroless plating technique, sensor characterisation and optimisation. The main application domain for these SPR sensors is biomedical diagnostics and chemical sensing, and therefore, application examples using the silica fibre SPR sensing platform including Quantum Dots (Qdots), and Norovirus (NoV) detection are presented. An advanced SPR architecture built upon an enhanced resolution Exposed Core Fibre (ECF) SPR sensor, its development, characterisation and performance comparison are described in Chapter 5. Chapter 6 is dedicated to the study of plasmonic enhancement of the fluorescence (Metal Enhanced Fluorescence (MEF)), in planar substrates and optical fibres. The final chapter, Chapter 7, summarises the presented work and suggests directions for potential future research.

3

ANALYTICAL MODELLING OF SPR IN OPTICAL FIBRES

Performance defining parameters for SPR fibre sensors need to be identified in order to find project directions leading towards improved SPR fibre sensing platforms. In this chapter the results of theoretical modelling are presented that studied the influence of fibre and plasmonic materials and geometrical parameters on the performance of SPR fibre probes.

3.1 TRANSFER MATRIX METHOD (TMM)

TIR excitation of SPs either in a prism configuration, or in an optical waveguide, can be described through the Fresnel reflection equations. In its simplest form, an SPR configuration consists of at least three materials: glass, metal, and adjacent dielectric. In a general form, reflection and transmission of propagating electromagnetic radiation through a stratified medium consisting of multiple layers needs to be considered.

3.1.1 *TMM formalism*

The TMM was first proposed by Abelés in [209] and later generalised for absorbing media by Hansen [210]. This method is based on the fact that according to Maxwell's equations, there are simple boundary conditions for the electromagnetic field that need to be satisfied as the propagating radiation passes across an interface from one material to another. The TMM is indispensable in determining reflectivity, transmission, and absorption of light for a stack of parallel materials with an arbitrary number of layers. If the field at the beginning of the interface is known, the field at the end of the interface can be determined through a matrix operation. Multiple layers of a stratified media can then be represented as the product of individual layer matrices.

Let us consider a stratified medium consisting of a stack of N homogeneous isotropic layers with otherwise arbitrary optical parameters each of thickness d_j and refractive index $\tilde{n}_j$, separated by $N-1$ interface planes and confined between semi-infinite first and last phases, as shown in Figure 3.1. For each layer j between discontinuity planes $z_{j-1} < z < z_j$, as well as for the final phase $z > z_{N-1}$ there is a characteristic matrix M_j that describes wave propagation in the phase. Tangential electromagnetic field components at the first boundary $z = z_1 = 0$, U_1 and V_1, are related to those at the final boundary $z = z_{N-1}$, U_{N-1} and V_{N-1} as [210]:

$$\begin{bmatrix} U_1 \\ V_1 \end{bmatrix} = M_2 \cdot M_3 \cdots M_{N-1} \begin{bmatrix} U_{N-1} \\ V_{N-1} \end{bmatrix} = M \begin{bmatrix} U_{N-1} \\ V_{N-1} \end{bmatrix}, \tag{3.1}$$

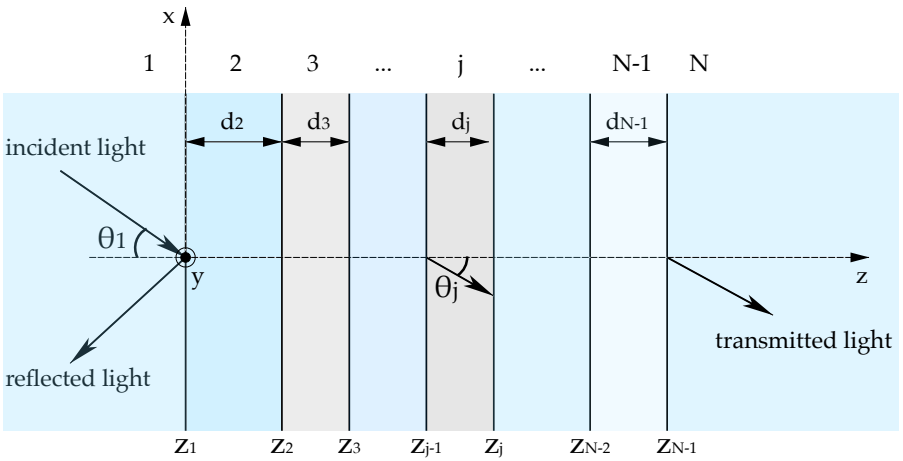


Figure 3.1: Schematic representation of a stratified medium consisting of multiple arbitrary layers each with individual thickness d_j and (in general complex) refractive index $\tilde{n}_j$. Adapted from [210].

where M is a characteristic matrix of the stratified space given as a product of matrices of individual layers:

$$M = \begin{bmatrix} m_{11} & m_{12} \\ m_{21} & m_{22} \end{bmatrix} = \prod_{j=2}^{N-1} M_j. \tag{3.2}$$

For TE polarisation the tangential field components at a boundary j are given as $U_j = E_y^t + E_y^r$ and $V_j = H_x^t + H_x^r$, where superscripts t and r denote transmitted and reflected waves respectively. For TM polarisation $U_j = H_y^t + H_y^r$ and $V_j = E_x^t + E_x^r$. It is convenient to define $\xi_j \equiv \tilde{n}_j \cos\theta_j = (\tilde{n}_j^2 - n_1^2 \sin^2\theta_1)^{1/2}$, and $\beta_j \equiv \frac{2\pi}{\lambda} d_j \xi_j$. Characteristic matrix for j-th layer M_j considering TE polarisation can then be written as:

$$M_j = \begin{bmatrix} \cos\beta_j & -i\sin\beta_j/p_j \\ -ip_j \sin\beta_j & \cos\beta_j \end{bmatrix}, \qquad \text{TE polarisation} \tag{3.3}$$

where $p_j = (\epsilon_j/\mu_j)^{1/2} \cos\theta_j$. For TM polarisation, a similar characteristic matrix can be written:

$$M_j = \begin{bmatrix} \cos\beta_j & -i\sin\beta_j/q_j \\ -iq_j \sin\beta_j & \cos\beta_j \end{bmatrix}, \qquad \text{TM polarisation} \tag{3.4}$$

where $q_j = (\mu_j/\epsilon_j)^{1/2} \cos\theta_j = \xi_j/\epsilon_j$.

Then, reflection and transmission coefficients of the stack of layers, r and t, can be derived from Equation 3.1 [210]:

$$r^{TE} = \frac{E^r_{y1}}{E^t_{y1}} = \frac{(m_{11} + m_{12}p_N)p_1 - (m_{21} + m_{22}p_N)}{(m_{11} + m_{12}p_N)p_1 + (m_{21} + m_{22}p_N)} \tag{3.5}$$

$$r^{TM} = \frac{H^r_{y1}}{H^t_{y1}} = \frac{(m_{11} + m_{12}q_N)q_1 - (m_{21} + m_{22}q_N)}{(m_{11} + m_{12}q_N)q_1 + (m_{21} + m_{22}q_N)} \tag{3.6}$$

$$t^{TE}_E = \frac{E^t_{yN}}{E^t_{y1}} = \frac{2p_1}{(m_{11} + m_{12}p_N)p_1 + (m_{21} + m_{22}p_N)} \tag{3.7}$$

$$t^{TM}_H = \frac{H^t_{yN}}{H^t_{y1}} = \frac{2q_1}{(m_{11} + m_{12}q_N)q_1 + (m_{21} + m_{22}q_N)} \tag{3.8}$$

$$t^{TM}_E = \frac{\mu_N}{\mu_1}\frac{n_1}{\tilde{n}_N} t^{TM}_H. \tag{3.9}$$

From these equations reflectance R and transmittance T with corresponding phase change ϕ can be determined:

$$R^{TE} = |r^{TE}|^2, \qquad \phi^{TE}_r = \arg r^{TE} \tag{3.10}$$

$$T^{TE} = \frac{\mu_1 Re(\tilde{n}_N cos\theta_N)}{\mu_N n_1 cos\theta_1}|t^{TE}_E|^2, \qquad \phi^{TE}_t = \arg t^{TE}_E \tag{3.11}$$

$$R^{TM} = |r^{TM}|^2, \qquad \phi^{TM}_r = \arg r^{TM} \tag{3.12}$$

$$T^{TM} = \frac{\mu_N Re(\tilde{n}_N cos\theta_N/\tilde{n}^2_N)}{\mu_1 n_1 cos\theta_1/n^2_1}|t^{TE}_H|^2, \qquad \phi^{TM}_t = \arg t^{TM}_E \tag{3.13}$$

3.1.2 *Modelling of SPR in prism using TMM*

TMM has been extensively used for simulating light reflection and transmission for various applications such as spectroscopy, ellipsometry, design of anti-reflection coatings and dielectric mirrors. The method proved to be useful in modelling of SPR response in prism based configurations as well as large core multi-mode optical fibres [96, 103, 150, 184, 211]. A model has been developed in Matlab to implement the TMM for modelling SPR response in a prism and a MMF in order to evaluate the performance achieved with various configurations.

Let us consider the simplest case of three layer SPR system consisting of a glass prism with RI n_1, metal layer of thickness $d_2 < \lambda$ and a complex RI $\tilde{n}_2$, and a dielectric medium of semi-infinite thickness with RI n_3, as shown in Figure 3.2.

Based on Equation 3.6 and Equation 3.12 reflectivity R can be plotted as a function of incident angle θ. Figure 3.3 shows an example of reflectivity curves for a TM wave incident on a 50 nm-thick Ag surface from a BK7 glass prism adjacent to three different dielectric layers: air ($n_3 = 1.00$), water ($n_3 = 1.33$), and 50% glycerol ($n_3 = 1.40$). The wavelength of light was fixed at 633 nm.

As the refractive index of the external dielectric increases, resonance occurs at larger incident angles and the minima in the reflectivity curves shift right, as evident from Figure 3.3. Sensitivity of the prism-based SPR sensor in this example can be estimated as $S_\theta = \Delta\theta/\Delta\lambda$ and is around 120 deg./RIU. It is important to note that as the adjacent dielectric RI gets closer to the prism RI, the reflectance curves broaden resulting in larger values of FWHM, and therefore, the FOM.

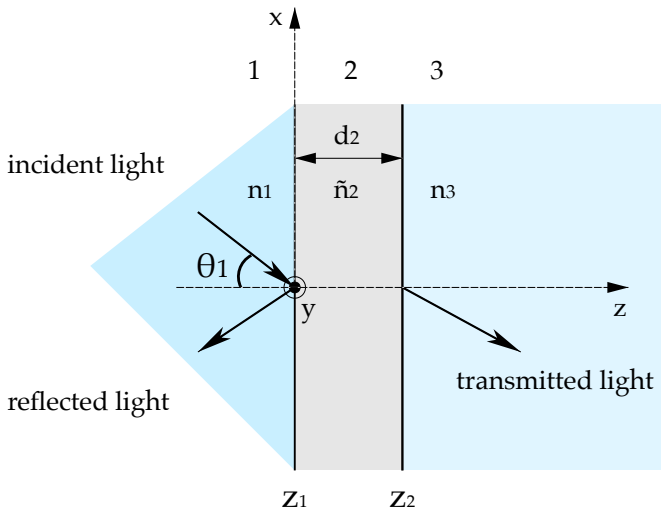


Figure 3.2: Schematic representation of a prism-based SPR for TMM simulation.

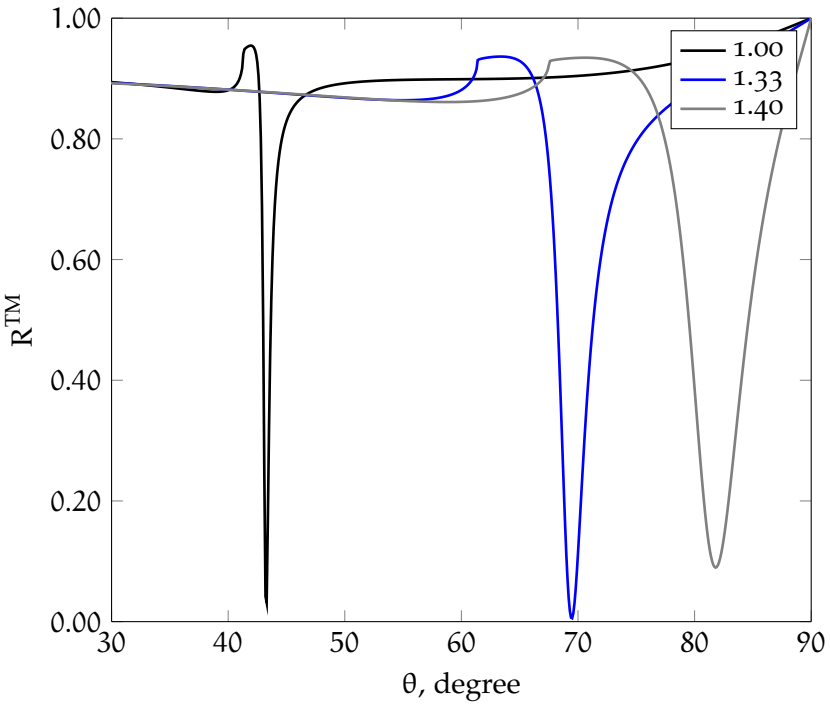


Figure 3.3: Reflectance of TM wave incident on Ag surface of 50 nm ($\tilde{n}_2 = 0.1446 + i3.810$) from BK7 glass prism ($n_1 = 1.515$) for three adjacent dielectric layers: air ($n_3 = 1.00$), water ($n_3 = 1.33$), and 50% glycerol ($n_3 = 1.40$). Analytical modelling is performed in Matlab.

3.2 MODELLING OF SPR FIBRE SENSORS WITH TMM

Let us now consider a fibre geometry, as illustrated in Figure 3.4. A glass fibre core of RI n_1 is coated with a lower RI cladding $n_{clad} < n_1$ to ensure TIR and therefore light guiding. A part of the fibre cladding of length L is removed and a metal film with complex RI $\tilde{n}_2$ of thickness t uniformly covers the fibre core. The structure is suspended in an external dielectric (sensed medium) of RI n_3. In the fibre example, we consider a polychromatic light source in order to satisfy the resonant condition as the range of angles the light rays propagate inside the fibre θ is limited ($0 \leqslant \theta \leqslant \theta_{cr}$, where $\theta_{cr} = n_{clad}/n_1$).

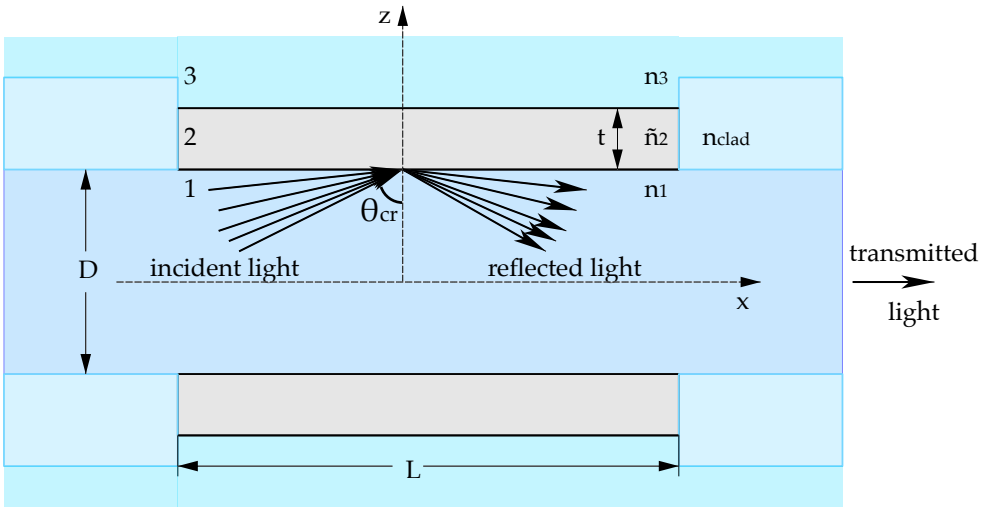


Figure 3.4: Schematic representation of an optical fibre-based SPR for TMM simulation consisting of a fibre core (1) with diameter D, coated with a cladding. A sensing region of length L is a metal layer (2) of thickness t. The structure is submersed in semi-infinite external dielectric layer (3). The designations for refractive indices of all layers are shown.

The variation of the refractive index of the fibre core material with wavelength, also known as dispersion, is modelled using Sellmeier's equation [212]:

$$n_1(\lambda) = \sqrt{1 + \frac{A_1\lambda^2}{\lambda^2 - B_1} + \frac{A_2\lambda^2}{\lambda^2 - B_2} + \frac{A_3\lambda^2}{\lambda^2 - B_3}} \tag{3.14}$$

with A_1, A_2, A_3, B_1, B_2 and B_3 being the Sellmeier coefficients which are different for different glasses.

The frequency-dependent complex permittivity of metal $\epsilon_2 = \tilde{n}^2$ is described by the Lorentz-Drude model that considers K damped harmonic oscillators to describe the small resonances occurring in the metal's frequency response that is expressed in the following form:

$$\epsilon_2(\omega) = \epsilon_\infty + \sum_{k=0}^{K} \frac{f_k \omega_p^2}{\omega_k - \omega^2 + i\Gamma_k\omega_k}, \tag{3.15}$$

where ϵ_∞ is dielectric constant at infinite frequency, f_k, ω_k and Γ_k are strength, resonant frequency, and damping frequency of k-th oscillator, and ω_p is the plasma frequency for the metal [213].

In the sensed dielectric medium the resonant condition is achieved when the propagation constant of the light incident on the interface between metal and dielectric at an angle θ matches the propagation constant of the surface plasmons and is expressed as [4]:

$$\frac{2\pi}{\lambda} n_1 \sin\theta = Re(\beta_{sp}), \tag{3.16}$$

where the left part of the equation correspond to the propagation constant of light and the right part, to the propagation constant of SPPs with

$$\beta_{sp} = \frac{2\pi}{\lambda}\sqrt{\frac{\epsilon_2 n_3^2}{\epsilon_2 + n_3^2}}. \tag{3.17}$$

Reflectance, R, found using Equation 3.12 is plotted in Figure 3.5. The fibre core material used to simulate the curves is lead silicate glass (F2) and has a refractive index of 1.616 at 633 nm. Fibre dispersion estimated using Sellmeier equation was taken into account in the calculation. The fibre cladding was assumed to be made of non-dispersive polymer with a RI fixed at 1.520. A silver film of 50 nm was used as the metal layer. The fibre core diameter is 160 nm and the sensing region length is 1 cm. These starting parameters were chosen as the F2 fibre coated with silver film has been previously used in a SPR fibre-based sensing configuration demonstrated by our group [44, 201, 202]. Water with RI of 1.33 was used as an external dielectric medium.

As can be seen from Figure 3.5, the resonance condition depends on both, the wavelength of the incident light as well as incidence angle, resulting in a spread of reflectance curves over the range of wavelengths. This is also clear from the resonant condition (Equation 3.16) where for larger wavelengths, the incident angle has to be smaller in order to match the propagation constant of SPRs for the silver-water interface. To accommodate all of the angles of incidence that satisfy the resonance, the angular power distribution of rays guided in the fibre has to be considered. The angular power distribution of guided rays is given as [214]:

$$dP \propto \frac{n_1^2 \sin\theta\cos\theta}{(1 - n_1^2\cos\theta^2)^2} d\theta. \tag{3.18}$$

In order to calculate the effective transmitted power, the reflectance R for a single incidence needs to be raised to the power of the number of reflections that each ray undergoes with the sensing surface interface which can be estimated as:

$$N_{ref}(\theta) = \frac{L}{D\tan\theta}. \tag{3.19}$$

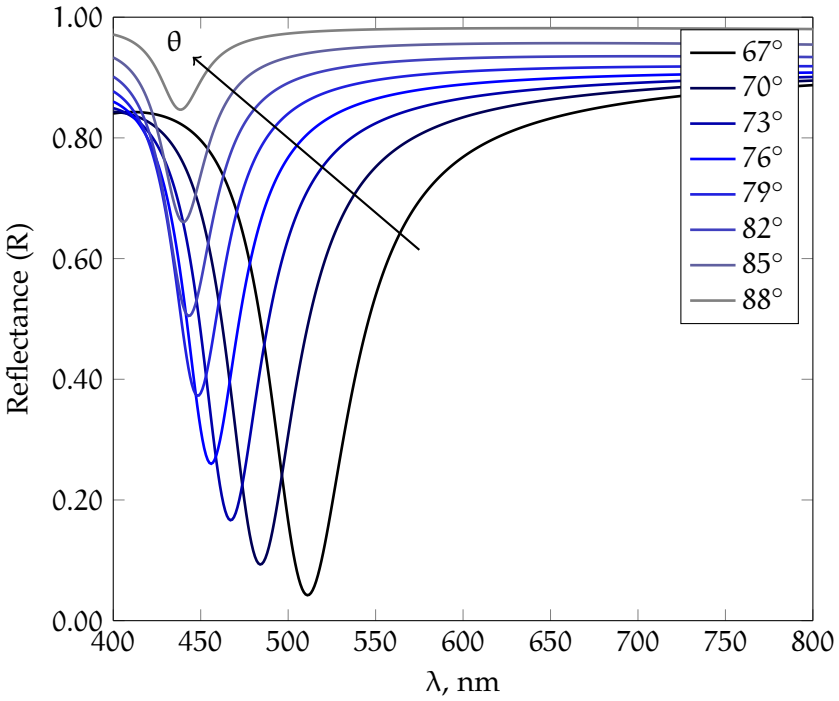


Figure 3.5: Simulated reflectance curves for a range of increasing angles propagating inside a lead silicate fibre (F2) (θ, shown in legend). Consecutive curves increase by 3°. The fibre is side-coated with 50 nm Ag film of 1 cm length. Fibre core diameter is 160 μm. Analytical modelling is performed in Matlab.

Then, the normalised transmitted power through an optical fibre for TM polarised light is given as:

$$P_{trans} = \frac{\int_{\theta_{cr}}^{\pi/2} R^{N_{ref}} (n_1^2 \sin\theta \cos\theta / (1 - n_1^2 \cos\theta^2)^2) d\theta}{\int_{\theta_{cr}}^{\pi/2} (n_1^2 \sin\theta \cos\theta / (1 - n_1^2 \cos\theta^2)^2) d\theta}. \tag{3.20}$$

Figure 3.6 shows the normalised transmitted power as a function of wavelength, $P_{trans}(\lambda)$, that is obtained by integrated reflectance R from Figure 3.5 over the range of angles that propagate inside the fibre. As can be seen from the Figure 3.6, the consideration of different angles that simultaneously matches the resonant condition at different wavelengths that is intrinsic in a fibre based configuration causes the broadening of SPR response which results in an increase in FWHM to up to around 100 nm.

Sensitivity of the F2 fibre based sensor can now be estimated as a wavelength shift per change in the refractive index of the external medium and the sensitivity curve is plotted in Figure 3.7. For a small range of RIs of an external medium, the sensitivity curve behaves linearly and the sensitivity value is given as the slope of the curve. For the fibre considered, the estimated sensitivity is 868 nm/RIU, which is broadly consistent with the reported experimental data [44]. It is interesting to note that the sensitivity curve is not linear when a large range of external RIs are considered. As illustrated in Figure 3.8, sensitivity rapidly increases for the larger values of sensed medium RI. This can be explained by the fact that when the difference between RIs of fibre core and adjacent dielectric decreases, the confinement of

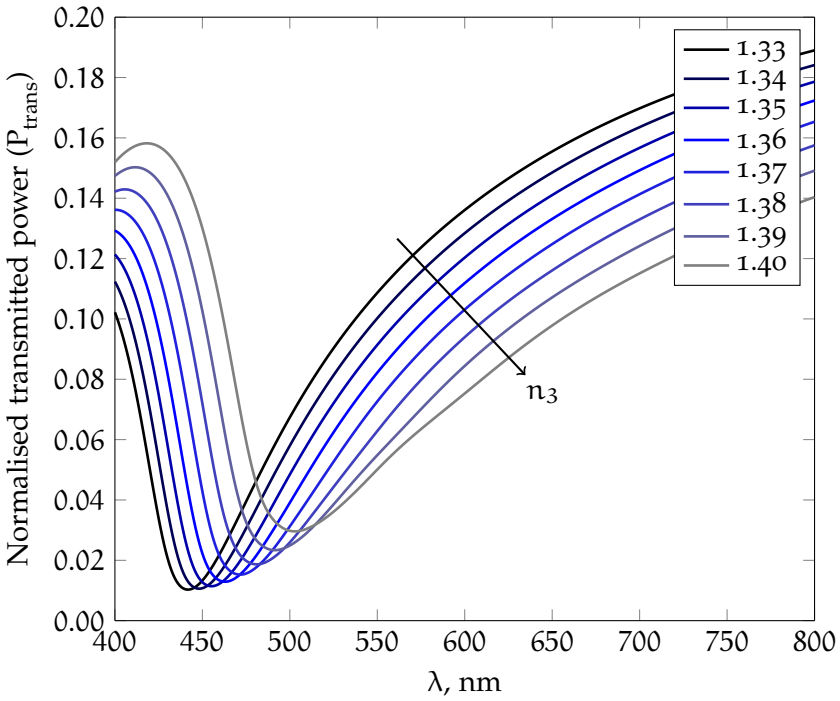


Figure 3.6: Simulated normalised transmitted power through a lead silicate (F2) fibre integrated over all angles of incidence on a 50 nm Ag film for a varying RI of the adjacent dielectric (n_3, shown in legend). Length of the coated region is 1 cm). Fibre core diameter is 160 µm. Analytical modelling is performed in Matlab.

the light wave decreases causing the evanescent wave to penetrate deeper into the dielectric medium resulting in an increase in the sensitivity value. Therefore, it is common in literature, to estimate the sensitivity within a small range of RIs as well as specify the range of the RIs where the sensitivity value is valid. As the majority of the fibre based SPR sensors are used for biosensing applications where the range of the RI is small and is close to aqueous environment, we will focus on estimating the performance parameters in this RI range, between 1.33 and 1.40.

3.2.1 *Influence of fibre core material*

Instead of F2 glass, let us consider a silica optical fibre of the same diameter of 160 µm. The RI of fused silica is around 1.457 at 633 nm. The cladding is considered to be made of a low refractive index polymer of RI, n_{clad}, of 1.375. These fibre parameters have been chosen due to the abundant availability of such fibre for further experimental validation. Figures 3.9 and 3.10 show the simulated reflectance curves for a range of incident angles and normalised transmitted power integrated over a range of available angles respectively using water as an external dielectric medium. It is apparent that for the silica glass, the reflectance curves spread across the wavelength range. Considering the resonant condition of SPs represented by Equation 3.16, similarly to the previous fibre, for small angles, the wavelength needs to be large to satisfy the resonant condition. In addition, as the n_1 for silica glass is smaller than that for previously considered F2 fibre, the wavelength for smaller angles is larger than that for F2 fibre which results in a larger spectral spread of

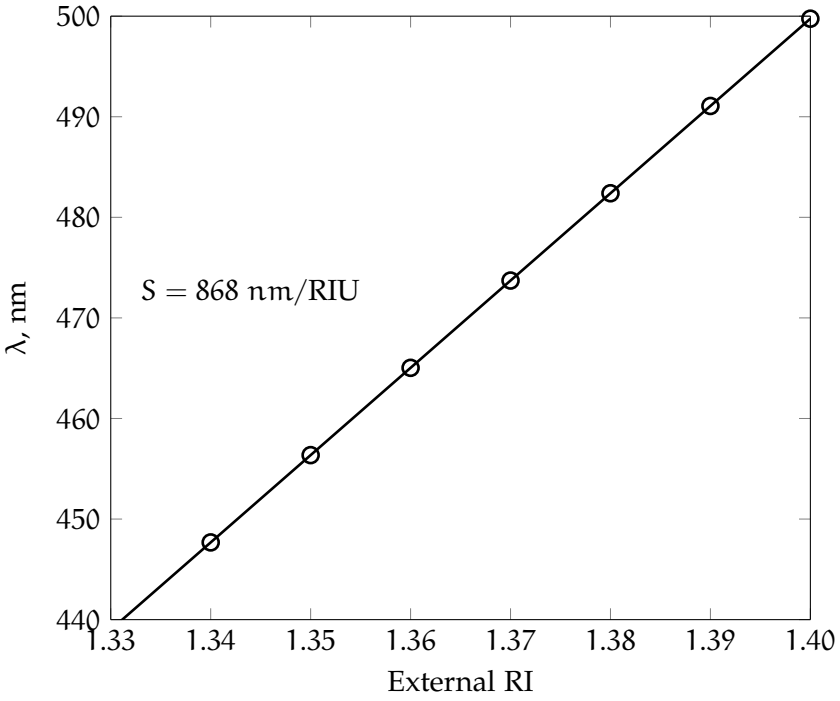


Figure 3.7: Simulated sensitivity curve for a lead silicate (F2) fibre SPR sensor, side-coated with 50 nm Ag film of 1 cm length. Fibre core diameter is 160 μm. Slope of the curve gives the sensitivity value. Analysis is performed in Matlab using the described analytical model.

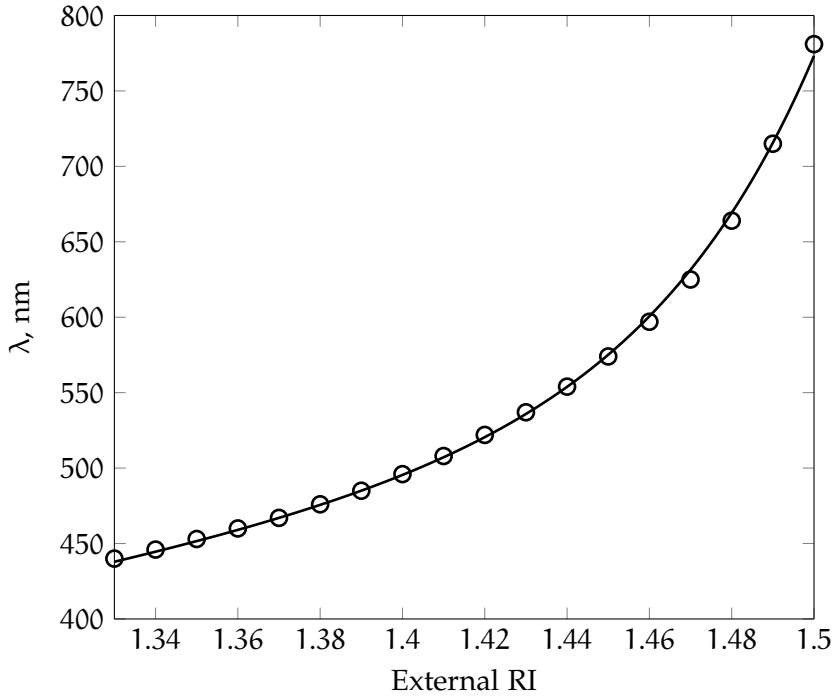


Figure 3.8: Simulated sensitivity curve for a lead silicate (F2) fibre SPR sensor, side-coated with 50 nm Ag film of 1 cm length for an expanded range of external RIs. The fibre core diameter is 160 μm. When the difference between the external RI and the RI of core material decreases, sensitivity rapidly increases. Analysis is performed in Matlab using the described analytical model.

reflectance curves for silica (Figure 3.9) when compared to F2 glass (Figure 3.5). This in turn is responsible for the broadening of the resonant features in the transmitted power spectra (Figure 3.10) in comparison to those for F2 glass (Figure 3.6).

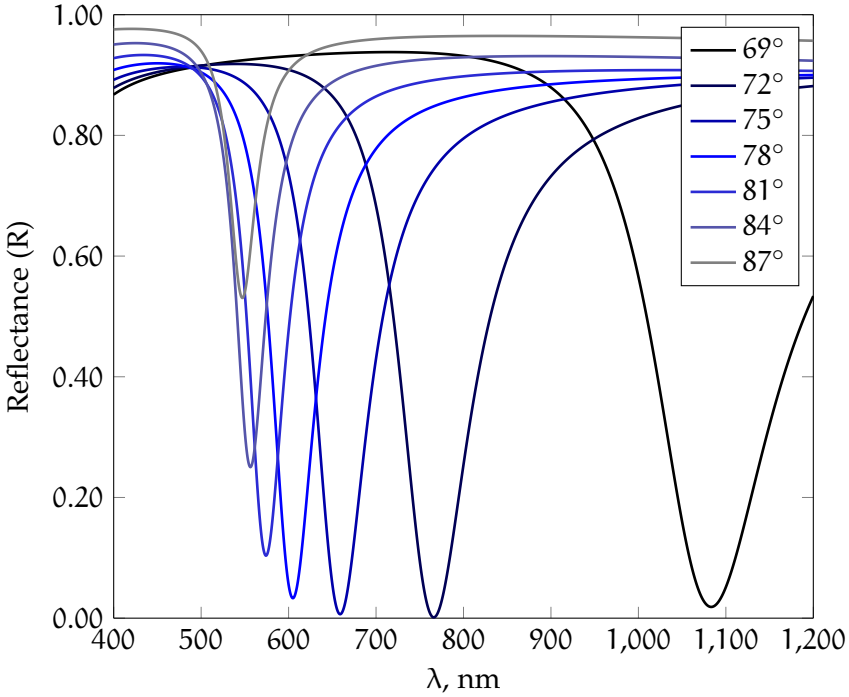


Figure 3.9: Simulated reflectance curves for a range of angles propagating inside a silica fibre, θ, (shown in legend). The fibre is side-coated with 50 nm Ag film of 1 cm length. Fibre core diameter is 160 μm. Analytical modelling is performed in Matlab.

Figure 3.11 shows the sensitivity curve obtained from the shift of the resonant dip in the normalised transmitted power estimated in the range of external medium RI values between 1.33 and 1.35. The resulting sensitivity value of 3470 nm/RIU was estimated from the slope of the linear sensitivity curve, which is much larger than 868 nm/RIU achieved for F2 glass.

In order to investigate the influence of the fibre core material, in particular its RI, a range of glasses have been explored. Figure 3.12 shows the dispersion relations for five different glasses, fused silica (SiO_2), lead silicate glass (F2), dense flint (SF57), bismuth oxide glass (Bi), and tellurite glass (Te) used to simulate fibre core material [37, 215, 216].

In order to eliminate the influence of the NA of the fibre and investigate the solo influence of the fibre core material on SPR, the value of NA was fixed at 0.482 which corresponds to the NA of silica fibre at 633 nm used in the previous simulation example. Therefore, the RIs of the fibre claddings were calculated as $n_{clad} = \sqrt{n_1^2 - NA^2}$ that follows from the definition of the fibre NA. Considering the fibre diameter to be 160 μm and the silver coating of thickness 50 nm as in the previous examples, the sensitivity versus RI of glass is plotted in Figure 3.13. The relation clearly displays that the sensitivity of the fibre SPR sensor depends on the RI of the core and is much larger for cores made of lower RI glass. The resonance is shifted towards

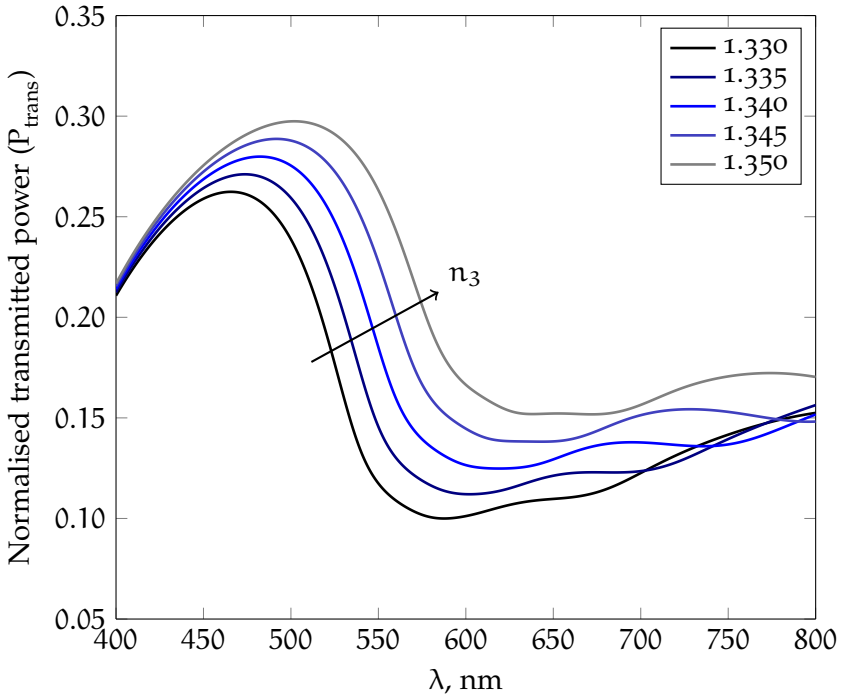


Figure 3.10: Simulated normalised transmitted power through a silica fibre side-coated with 50 nm Ag film for varying RI of adjacent dielectric (n_3, shown in legend). Length of the coated region is 1 cm. Fibre core diameter is 160 µm. Analytical modelling is performed in Matlab.

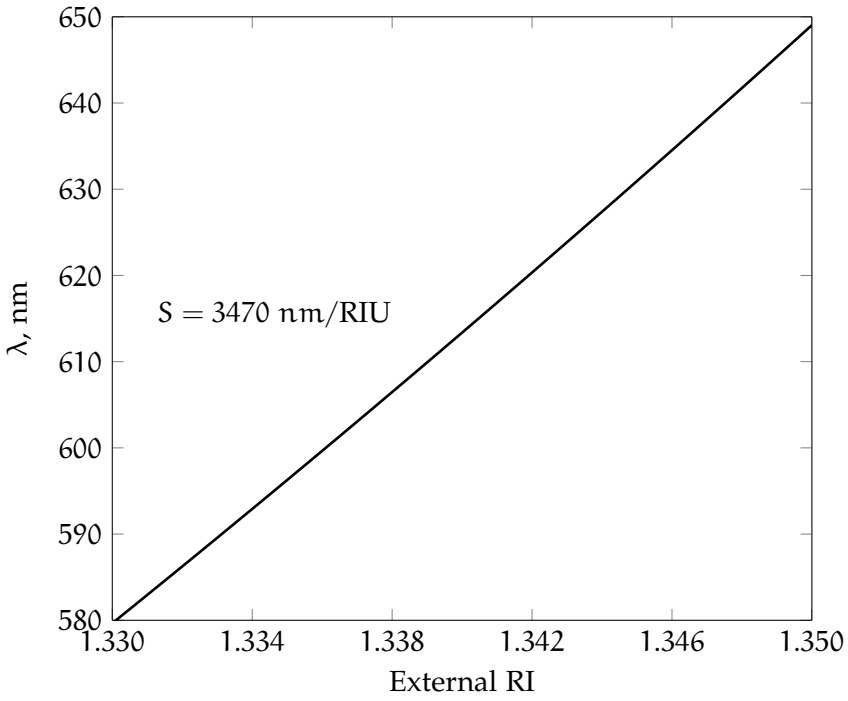


Figure 3.11: Simulated sensitivity curve for a silica fibre SPR sensor side-coated with 50 nm Ag film of 1 cm length. Fibre core diameter is 160 µm. Slope of the curve gives the sensitivity value. Analysis is performed in Matlab using the described analytical model.

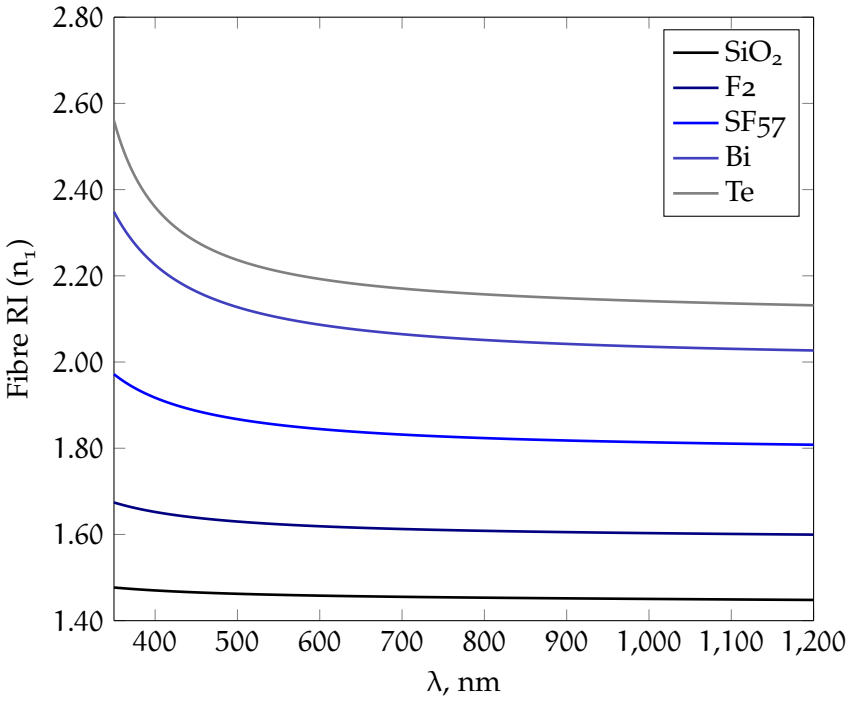


Figure 3.12: Dispersion of glasses used to simulate material of fibre core: fused silica (SiO_2), lead silicate (F2), dense flint (SF57), bismuth oxide glass (Bi), and tellurite glass (Te).

longer wavelength where SPR sensitivity is known to be larger. This phenomena is due to the material dispersion and was elaborated by Homola [94].

Table 3.1: Performance characteristics of SPR fibre sensors with different core materials side-coated with 50 nm Ag film of 1 cm length. Fibre core diameter is 160 µm. NA of the fibre is kept constant at 0.482.

Core material	Core RI†	S††, nm/RIU	FWHM, nm	FOM, RIU^{-1}	$\lambda^{1.00}$‡, nm	$\lambda^{1.33}$‡, nm
SiO_2	1.457	3470	200	17.3	360	580
F2	1.616	868	100	8.7	353	440
SF57	1.839	240	60	4.0	350	400
Bi	2.078	200	40	5.0	345	385
Te	2.184	160	30	5.3	340	383

† RIs of core glasses are estimated at 633 nm.
†† Sensitivity is calculated for a range of external RIs between 1.33 and 1.35, typical for biosensing applications.
‡ $\lambda^{1.00}$ and $\lambda^{1.33}$ are SPR resonant wavelengths in air and water, respectively.

Table 3.1 summarises the performance parameters obtained by simulating the SPR response in optical fibres with cores made of different glasses. The SP resonant wavelength is dependent on the RI of the core material and shifts toward longer wavelengths as the core RI decreases. Intricately higher sensitivities are attributed to fibre sensors with lower RI cores even though the NA of the fibres are kept the

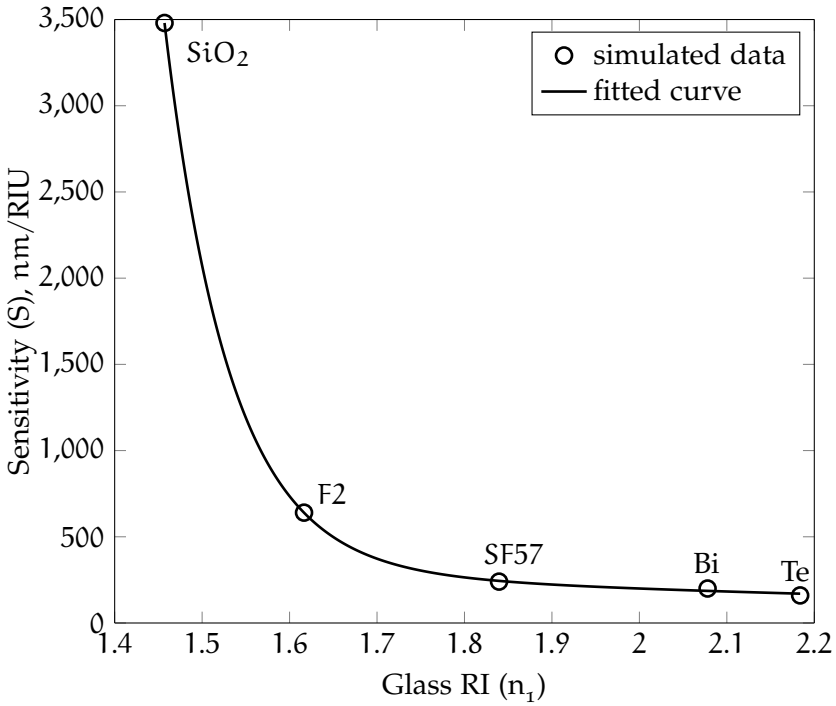


Figure 3.13: Sensitivity of SPR sensors with different materials of fibre core: fused silica (SiO_2), lead silicate (F2), dense flint (SF57), bismuth oxide glass (Bi), and tellurite glass (Te). NAs of the fibres were kept constant at 0.482. Fibre core diameter is 160 μm. Analysis is performed in Matlab using the described analytical model.

same and therefore the range of propagating angles or fibre modes is not changed. Even though the sensitivity of the sensors with lower core RIs is larger, the FWHM of the spectral SPR response is much broader. As it has been discussed above, the larger spectral spread of the individual resonances contributed from reflections of the guided light propagated at different angles toward the overall response causes the broadening of the resonance features that results in the degradation of sensor resolution. This trade off between sensitivity and spectral width of the SPR response as well as lower operating range achieved with lower RI core fibre sensors are important considerations that need to be addressed in development of SPR based fibre sensing platforms.

3.2.2 *Influence of fibre numerical aperture*

In the previous analysis of the effect of the fibre core material on the SPR response, the NA of the fibre was fixed in order to eliminate its influence. Here, we use fused silica core fibre of a constant diameter of 160 μm and study the effect of varying the NA of the fibre on the performance of the sensor. Figure 3.14 shows the normalised transmitted power for silica based fibres with different NAs coated with Ag film of 50 nm thickness and 1 cm length. The increase in the NA results in a broadening of the SPR feature which is caused by the larger number of propagating angles and therefore larger spectral spread that different propagating angles contribute to the integrated response. The resonant wavelength changes slightly towards red

for fibres with higher NA when sharper angles, that satisfy resonance condition at longer wavelengths, are allowed to propagate inside the fibre.

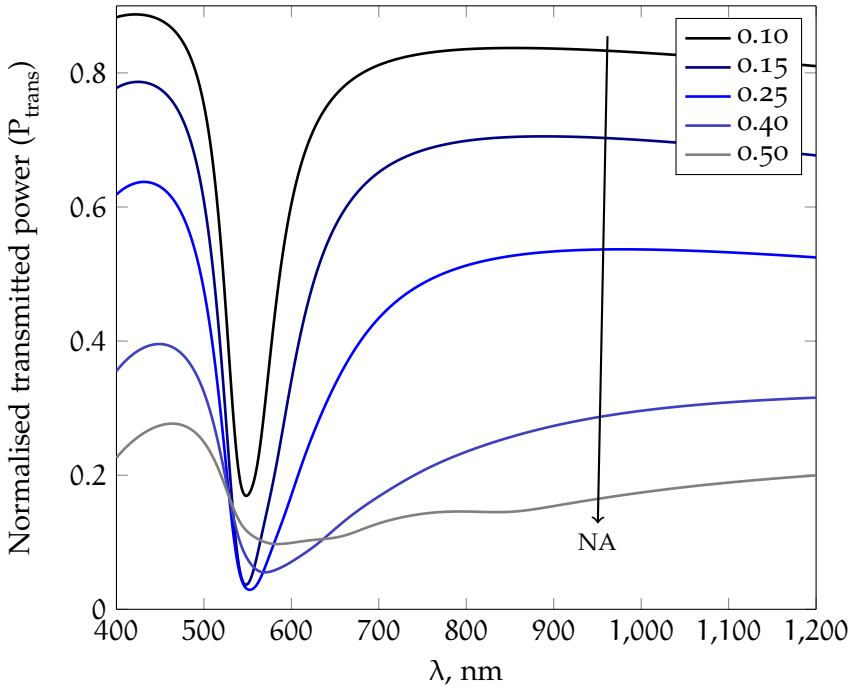


Figure 3.14: Normalised transmitted power for SPR sensors based on silica fibres with different NAs (shown in legend). Fibre core diameter is 160 μm. Ag coating thickness is 50 nm.RI of external dielectric is 1.33. Analytical modelling is performed in Matlab.

Sensitivity of fibre sensors increases with higher fibre NAs, as shown in the Figure 3.15. This behaviour, however, is not supported by the fact that fibres with higher NA guide light more strongly and less evanescent field is available to excite surface plasmons. As the core RI decreases, the confinement of the guided modes decreases resulting in stronger interaction between guided light and external environment. This consideration would lead to a potential increase in the sensitivity for fibres with smaller NA, although it is not supported by the modelling results. This dependency, however, might be explained from wave optics perspective where fibres with larger NAs support more guided modes, or equivalently, using a geometrical optics formalism, a larger range of propagating angles, and therefore, there are more reflections that the guided light undergoes with the sensing surface. On the other hand, this larger range of propagating angles results in the increase of the FWHM of the SPR response, as it is illustrated in the Figure 3.16. As with fibre core material, the sensitivity and spectral linewidth are two competing performance characteristics when the influence of the NA of the fibre is considered.

3.2.3 *Influence of fibre core diameter*

To investigate the effect that core diameter has on the SPR sensor performance, we consider a silica fibre with a fixed NA of 0.482 coated with a 50 nm thick silver film of 1 cm length. The rules of geometrical optics can only be applied to fibres with

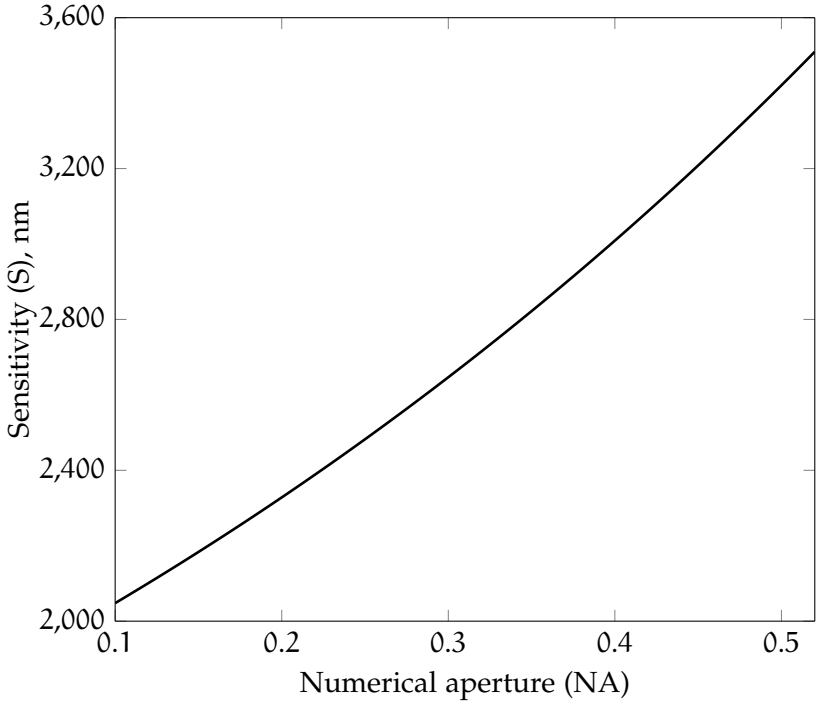


Figure 3.15: Sensitivity for silica fibre SPR sensors as a function of fibre NA. Fibre core diameter is 160 µm. Ag coating thickness is 50 nm.RI of external dielectric is 1.33. Analysis is performed in Matlab using the described analytical model.

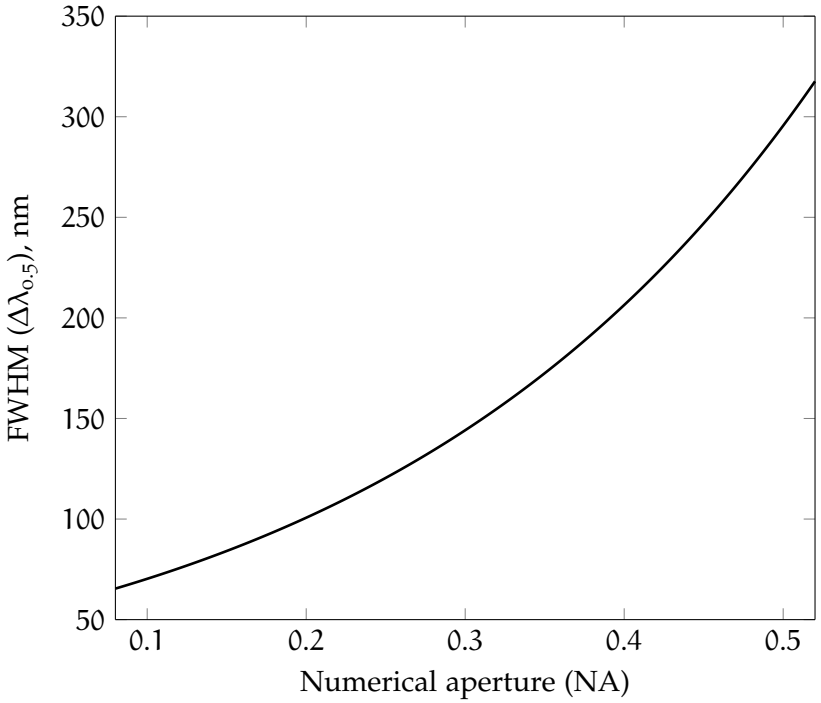


Figure 3.16: FWHM for silica fibre SPR sensors as a function of fibre NA. Fibre core diameter is 160 µm. Ag coating thickness is 50 nm.RI of external dielectric is 1.33. Analysis is performed in Matlab using the described analytical model.

large core diameters, more than 100 μm. Therefore, fibre core diameter was varied from 100 to 1000 μm, as optical fibres with core sizes within this range are readily available. Figures 3.17 and 3.18 present the sensitivity and FWHM respectively as functions of fibre core diameter.

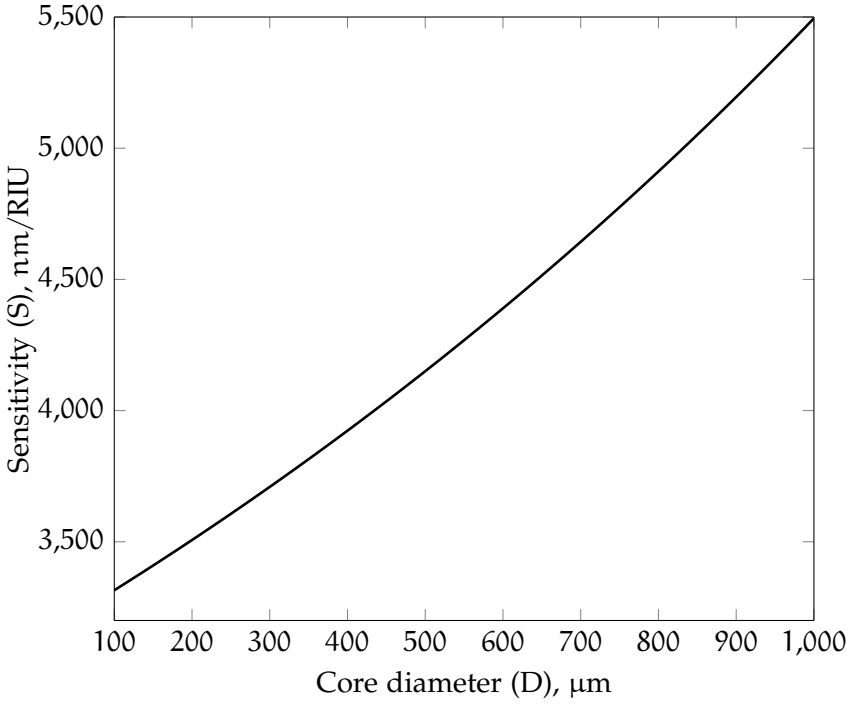


Figure 3.17: Sensitivity of SPR silica fibre sensors with different core diameters. Analysis is performed in Matlab using the described analytical model.

Both, sensitivity and spectral width, rise with increase in the fibre core diameter. In a MMF, the number of guided modes M these be approximated by [217]:

$$M \approx \frac{V^2}{2}, \tag{3.21}$$

where V is the fibre V-number given by $V = \frac{D\pi}{\lambda} NA$. Therefore, for fibres with large cores, the number of supported modes is larger. This can explain the increase in the sensitivity as more fibre modes interact with SPs. This in turn results in the broadening of the spectral width of the SPR feature leading to a decrease in the resolution. As with the previous studies of performance influencing parameters, fibre core diameter affects SPR performance characteristics resulting in a trade off between the sensitivity and FWHM of SPR fibre sensors. Nevertheless, even for small core fibres, sensitivity does not drop significantly and is larger than 3000 nm/RIU. On the other hand, SPR curves with twice as narrow FWHMs are attributed to the fibre with the smallest core diameter (100 μm) when compared to the largest core fibre in the study (1000 μm). This is likely to be of a more significant advantage in real applications, even considering the sacrifice in the sensitivity. Moreover, it was previously reported that fibres with very small core diameters, down to a few micron that support only a few modes, can provide large sensitivity values [111, 116, 208]. This can be attributed to an increased interaction between the fundamental mode and any lower order modes with the plasmonic coating that results in the

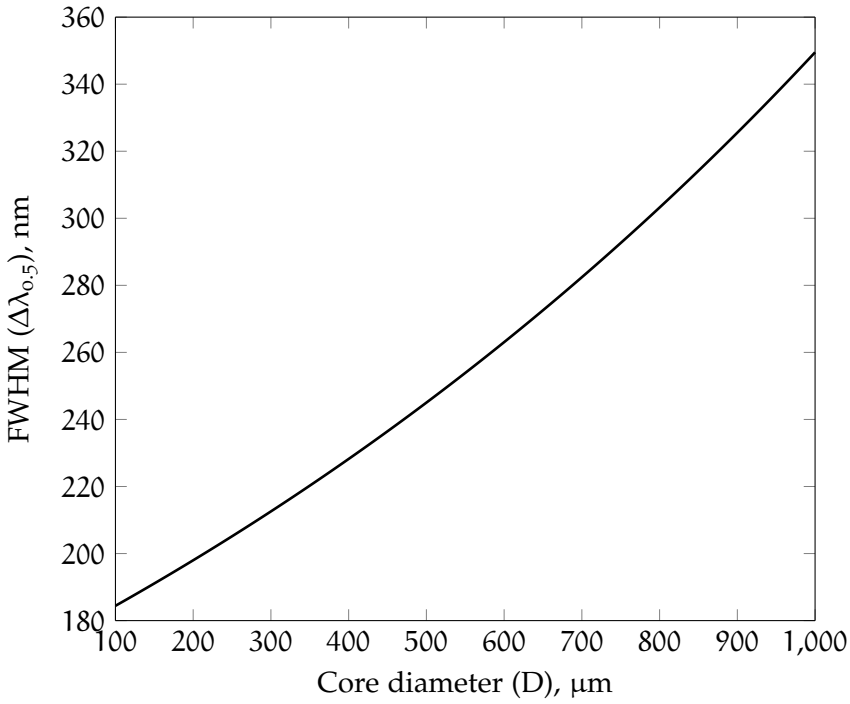


Figure 3.18: Spectral linewidth (FWHM) of SPR silica fibre sensors with different core diameters. Analysis is performed in Matlab using the described analytical model.

increased sensitivity values. Small core fibres, however, cannot be modelled using the TMM, and a numerical or analytical simulation suitable for small core fibres is required to analyse this behaviour. Nevertheless, the analysis shows the trend that using small core diameter of the fibre allows to achieve reduction in the spectral linewidth of the SPR response, thereby reducing resolution of the device.

3.2.4 *Influence of plasmonic coatings*

After analysing how optical fibre parameters, such as fibre core material, core size, and fibre NA, influence the performance of the SPR sensor, let us consider how metal coatings affect the sensor functionality. Here, we will consider three metals, silver (Ag), gold (Au), and copper (Cu), which are commonly used in SPR sensors. These metals are freely available, and allow coatings that can be fabricated by a number of simple techniques, such as Physical Vapour Deposition (PVD) (thermal evaporation, magnetic sputtering) [218], or chemical deposition (Chemical Vapour Deposition (CVD) [219], electroless plating [220], electrodeposition [221]). Optical properties of metals are taken from Rakić *et al.* [73] and complex dielectric functions are plotted in Figure 3.19.

Fused silica core fibre of 160 μm diameter with a fixed NA of 0.482 was considered in the simulation. The thickness of the metal coatings is 50 nm and the length of the sensing region is 1 cm. The resulting sensitivity curves for all three metals are presented in Figure 3.20. In the small RI range close to the aqueous environment, sensitivity of the silver coating is the largest. Sensitivities of gold and copper are comparable and almost 2.5 times smaller than that of silver. Silver has been previously reported to provide the highest sensitivity which is due to the

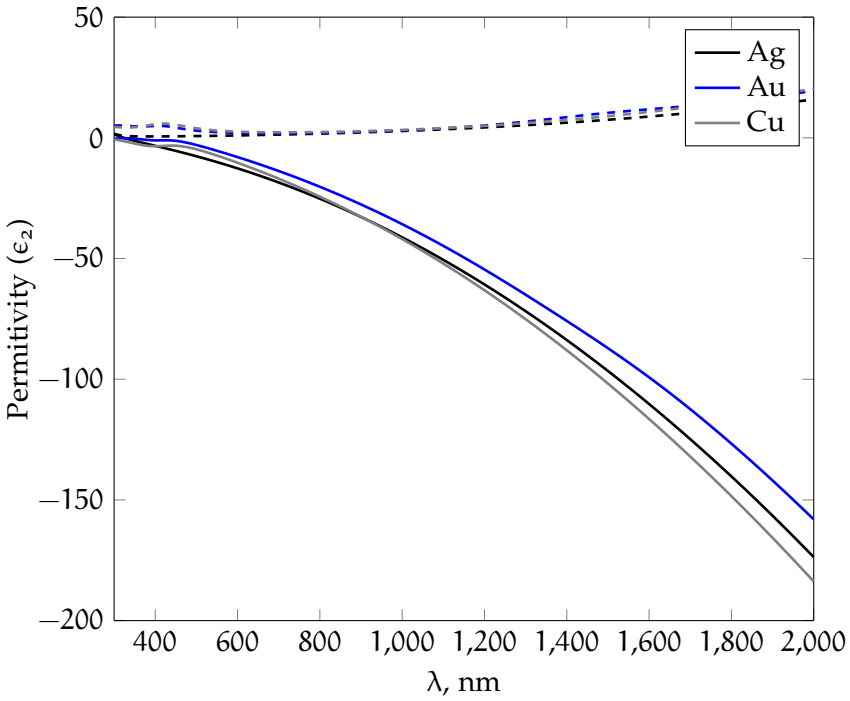


Figure 3.19: The dielectric function of three metals used for SPR simulation. Real parts of dielectric functions (ϵ'') are shown in solid line and imaginary parts (ϵ') are shown in dashed lines. Plotted in Matlab using complex dielectric functions from [73].

higher penetration depth of the evanescent field into metal and dielectric, as well as the longer propagation lengths on silver films in comparison to gold [88]. The resonance wavelength for Ag in water is the lowest and Au has the longest SPR wavelength at 1.33. Spectral width did not change significantly for sensors with different metals in the investigated parameter range. Table 3.2 provides a brief summary of the major parameters attributed to performance of SPR sensors with Ag, Au, and Cu coatings.

Table 3.2: Performance characteristics of SPR fibre sensors with different plasmonic materials side-coated with 50 nm Ag, Au, or Cu film of 1 cm length. The fibre core diameter is 160 µm. NA of the fibre is kept constant at 0.482.

Metal film	S†, nm/RIU	FWHM, nm	FOM, RIU^{-1}	$\lambda^{1.00}$‡, nm	$\lambda^{1.33}$‡, nm
Ag	3470	200	17.3	360	580
Au	1480	200	7.3	420	630
Cu	1400	200	7.0	435	600

† Sensitivity is calculated for a range of external RIs between 1.33 and 1.35, typical for biosensing applications.
‡ $\lambda^{1.00}$ and $\lambda^{1.33}$ are SPR resonant wavelengths in air and water respectively.

As silver has shown the best sensitivity performance, we will analyse the influence of the Ag coating thickness on the SPR fibre sensor. Again, a silica fibre of 160 µm coated with silver films of 1 cm length have been used to simulate the response of the sensor with coatings of different thickness. Transmitted power curves

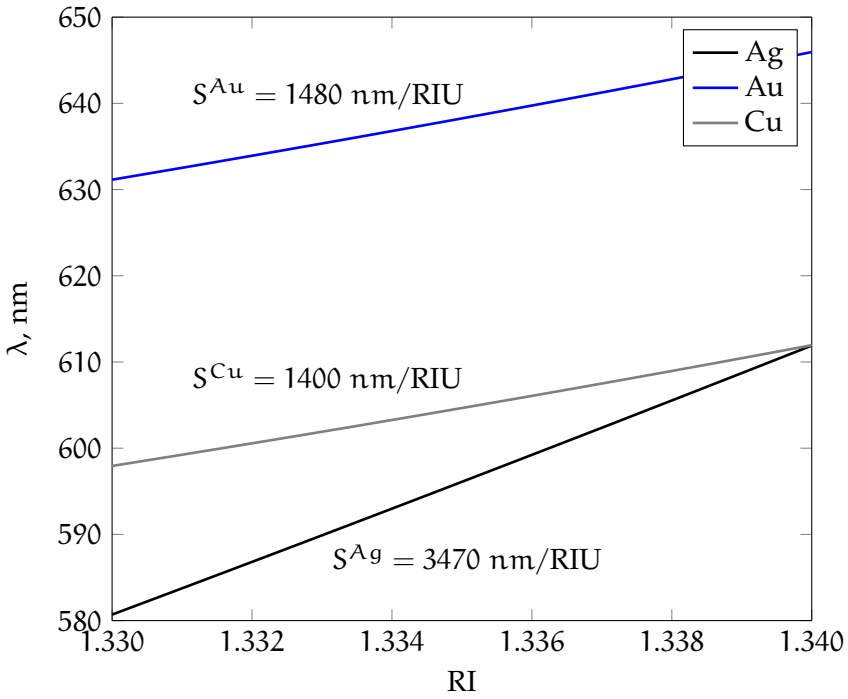


Figure 3.20: Sensitivity curves for SPR sensors with three different metals deposited on the side of a silica fibre. Thickness of the metal films is 50 nm. Length of the sensing region is 1 cm. The fibre core diameter is 160 µm. Analysis is performed in Matlab using the described analytical model.

for water normalised to their maxima are presented in Figure 3.21, showing that the resonant wavelength and linewidth of the response depend on the metal film thickness. Figure 3.22 shows the results of the simulation for sensitivity.

The SPR response exists in the range of thicknesses between approximately 20 and 90 nm. The optimal thickness for maximum sensitivity is around 50 nm as presented in Figure 3.22. The linewidth of the SPR feature was found to be optimal for film thicknesses close to 50 nm. Above the optimum thickness the dip in reflected light becomes shallower, below the optimum thickness the dip becomes broader. Considering that the penetration depth of SPs on a silver-water interface is around 25 nm, a thinner metal thickness results in the perturbation of the effective propagation constant of the SP from the side of the film interfacing with fibre core, or increased leakage radiation into the core, which results in a broadening of SPR response. SPPs excited through TIR are inherently leaky waves, whose energy is lost not only due to the intrinsic absorption inside the metal, but also due to leakage of radiation into the prism. It is believed that the minimum in the intensity of the reflected light is due to destructive interference between this leakage radiation and the reflected part of the excitation light [68]. When the metal film thickness is optimum, the amount of damping due to the leakage radiation is equal to the absorption losses; the destructive interference is maximised, providing nearly zero reflected beam intensity, so that the leakage radiation is suppressed and not detected. On the other hand, if the film thickness is too large, radiation damping due to intrinsic absorption into the metal is increased resulting in less light being available to couple to SPs leading to

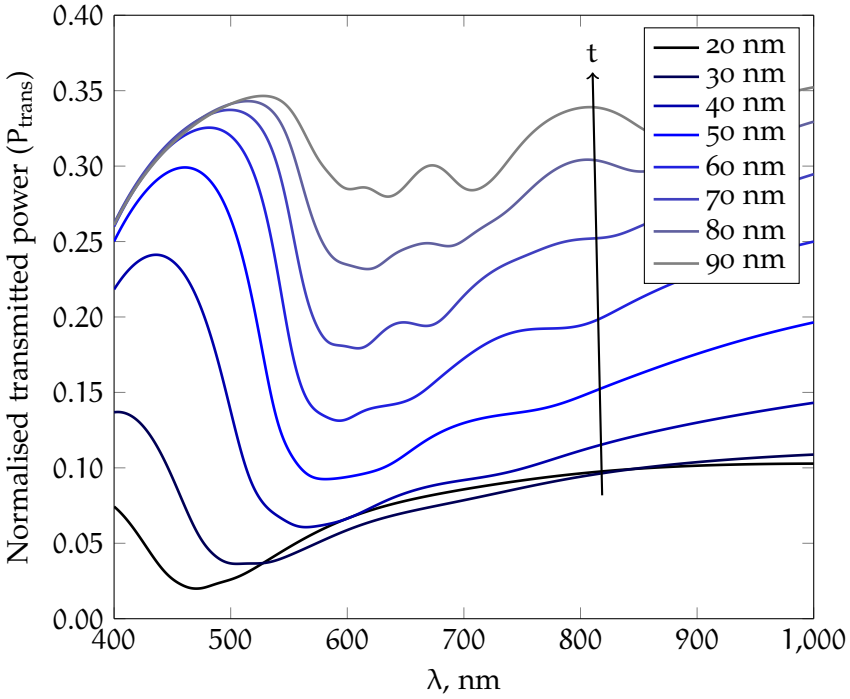


Figure 3.21: Normalised transmitted power for a silica fibre SPR sensor with varying thickness of the Ag film coating (t, shown in legend). The fibre core diameter is 160 µm. Sensing region length is 1 cm. External dielectric medium is assumed to be water (RI = 1.33.) Analytical modelling is performed in Matlab.

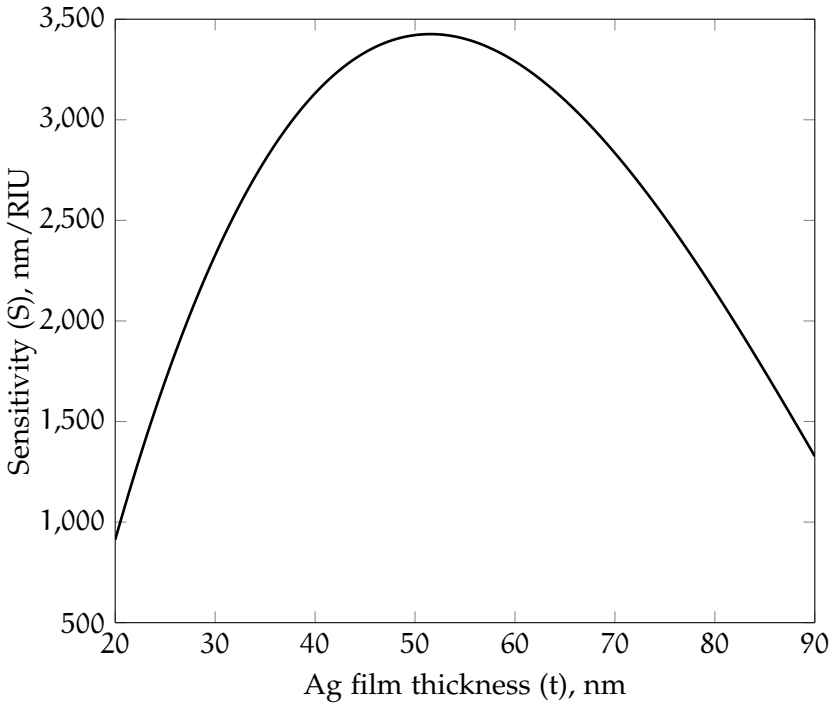


Figure 3.22: Sensitivity of silica fibre SPR sensor as a function of Ag film coating. Fibre core diameter is 160 µm. Sensing region length is 1 cm. Analysis is performed in Matlab using the described analytical model.

shallower reflectance curves. Although different metals can have different optimal thicknesses, it generally lies within $40 - 50$ nm range [4, 32]. Even though higher SPR performance is attributed to silver, gold remains the predominant plasmonic metal due to its resistance to oxidation.

3.3 SUMMARY AND SCOPE FOR IMPROVEMENT

It is essential to understand the dependency of sensor performance characteristics on the configuration design. In order to build this understanding, the behaviour of a simple SPR fibre sensor has been modelled using TMM. The effect of various parameters, e. g. fibre core material, core size, fibre NA, metal and film thickness, have been investigated. Silver coatings showed the best performance compared to gold or copper films with an optimal thickness of around 50 nm. The intrinsic RI sensitivity and spectral width were determined to be highly dependent on the fibre core material with higher sensitivity values, but broader SPR curves (therefore, higher resolution), attributed to core materials with lower RIs. Fibre NA and core size also impose competition on the sensitivity and resolution of the fibre sensor. Even though the modelling cannot take into account all aspects of the studied configuration, e. g. fibre mode distribution, or change in the incident light spectrum after interaction with the sensing region, the simulation provides an important understanding how various parameters affect sensor response.

Owing to this trade-off between performance characteristics (i. e. sensitivity vs. FWHM) that is often present when optimising sensor performance, it is necessary to understand the importance that every parameter has in view of a particular application. More importantly, it is crucial to identify configurations that improve certain performance characteristics without affecting the others, such as using alternative plasmonic coatings, different fibre designs, like MOFs, or novel interrogation techniques. The simulated SPR fibre design implemented on the side of an optical fibre presents a versatile yet simple architecture that is suitable for the development of sensor systems with improved performance.

According to the modelling results, the optimal SPR fibre design uses a low RI optical fibre, such as fused silica or fluorine doped glass, with a silver coating of around 50 nm thickness to maximise the sensitivity of the sensor. The broadening of the SPR response that arises from using low RI fibre can be overcome with low NA fibres with small cores. This allows minimisation of the number of guided modes responsible for SPR excitation. The work presented in the current thesis attempts to address these trade-offs that arise from changes in the materials of the SPR fibre sensors through adapting rough plasmonic coatings on low RI fused silica fibres, and exploiting the scattering of radiation by plasmonic waves due to the significant surface roughness. Furthermore, with recent advances in the fabrication of MOFs it has become possible to gain a high level of control over sensor characteristics without changing materials, as well as create more robust sensors with exceptional sensitivity. In the next chapters, it is explored how low RI fibre and a modification of MOF geometry, in particular an ECF, improve SPR sensor performance. The outcomes

of the modelling presented in this chapter are compared to the experimental results in Chapter 4 and Chapter 5.

4

SCATTERING BASED SPR FIBRE SENSING PLATFORM

SPR interrogation in optical fibres is traditionally performed by analysing transmitted light, as was discussed in Chapter 2. A novel technique has been demonstrated by François *et al.* [44] where the excitation of surface plasmons was observed by monitoring the scattering of plasmonic waves by a rough metal surface. The majority of the work presented in the current thesis is built upon the scattering based SPR platform originally presented in [44] with the goal of advancing the performance characteristics of the fibre sensing probe. The current chapter describes the demonstration of the basic scattering SPR architecture that utilises a lead silicate optical fibre, and presents a study on the sensitivity improvement through the use ofachieved with optical fibres of lower RI. Section 4.1 introduces the platform architecture and its advantages over traditional transmission based fibre SPR configurations, and describes the characterisation of the sensing probes that was performed to assess SPR performance. Section 4.2.2 describes a chemical electroless plating technique for fabrication of rough silver films on optical fibres that is suitable for scattering based SPR interrogation. The remaining sections focus on the development of a fused silica fibre SPR probe including the silica surface modification, sensor characterisation, as well as the application of the platform for the detection of biological species.

4.1 OVERVIEW OF THE PLATFORM ARCHITECTURE

4.1.1 *Introduction*

SPR fibre sensors offer a compact and cost effective alternative to prism based configurations. Due to these advantages, a vast range of fibre SPR probe designs have been proposed and demonstrated over the last decade, as was discussed in Chapter 2. In the majority of the fibre SPR sensors the excitation of SPs is inferred through an absorption feature in the transmitted light (Figure 4.1). Although this method has proven to be robust, there are several issues associated with the transmission measurement approach. Firstly, the SNR of the transmitted signal is generally low which complicates data processing and limits sensor resolution. Secondly, temperature control and the collection of reference measurements are generally required for transmission measurements. Most importantly, to achieve good SNR and dip absorption feature, precise control over the quality of the metal film, in particular coating thickness and surface quality (i. e. roughness), is required. To fabricate metal coatings with the desired surface quality, physical deposition techniques, such as magnetic sputtering, or thermal evaporation [218], are required.

The properties of SPs supported by rough metal surfaces were studied more than 40 years ago by Kretschmann and Raether [51, 222]. The SPs on a rough surface undergo elastic scattering due to the spatial variation in the dielectric function of

the interface. This results in localization of SP and increased electromagnetic field near the rough surface, as well as radiation of electromagnetic energy into free space [223]. This radiation due to the scattering of SPs has the same propagation constant as the SPs. Providing the resonant wavelength lays in the visible part of the spectrum, this scattered light can be directly seen with naked eyes or imaged with a standard camera. This SP scattered radiation is collected above the sensing region and analysed with a spectrometer.

This phenomenon was exploited by François *et al.* [44] where scattered radiation was collected directly above the sensing region and analysed with a compact spectrometer. This interrogation method offers a range of advantages in comparison to traditional transmission measurements such as lower reliance on the surface quality of the metal coating, as well as film thickness, higher SNR, and ability to perform traditional transmission measurements together with scattered light interrogation for improved reliability. In addition to the above, multiple sensing regions can be created along one fibre probe for self-referencing or multiplexed sensing [202]. Last, but not least, the method allows the combination of SPR measurements with other sensing phenomena, such as fluorescence on a single device for enhanced functionality.

4.1.2 *Experimental setup*

SPR sensors were fabricated on the side of an in-house made MMF with a core diameter of 160 µm made of lead silicate (F2) glass. A small section of the acrylate coating was stripped off to exposed the glass core and a 50 nm silver film was deposited using a chemical electroless plating technique. A detailed description of the fibre fabrication is provided in Section 4.2. A schematic representation of a scattering based SPR probe is shown in Figure 4.1.

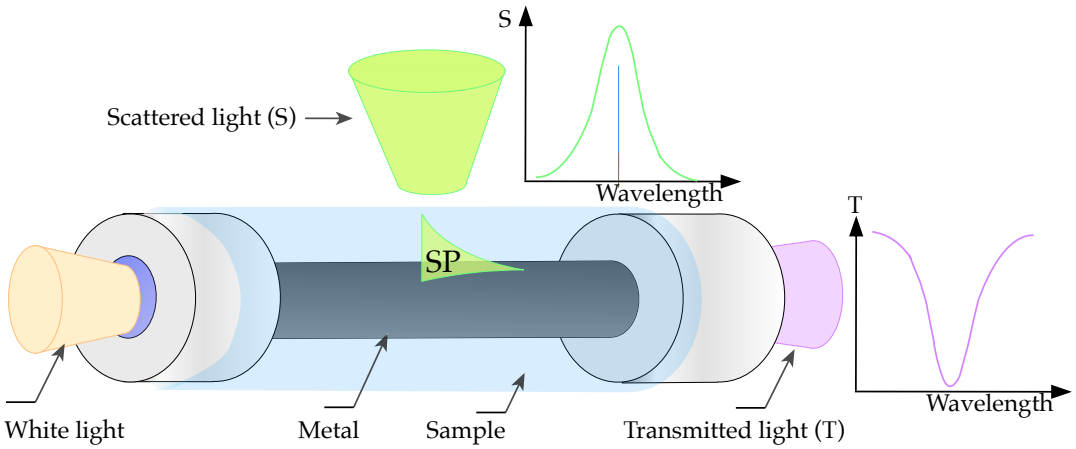


Figure 4.1: A schematic of a scattering based SPR fibre probe. Instead of measuring the transmitted light spectrum (T), SPR is inferred through analysis of the scattered light (S).

The sensing region was enclosed inside a cross sectional flow cell with an inlet and outlet for the liquid. The flow cell contains a transparent window to allow

scattered light collection. A schematic of the optical setup used to perform SPR measurements is illustrated in Figure 4.2. A broadband Light Emitting Diode (LED) in the visible range (Thorlabs, MCWHLP1) was used as a light source. The beam was coupled into the SPR fibre probe using a microscope objective with a NA greater than that of the fibre. Scattered light was collected using an assembly consisting of a microscope objective, a converging lens, and a fibre patch cable (Ocean Optics), and analysed with a compact spectrometer (Ocean Optics, QE65000, spectral range $200 - 1100$ nm, resolution 1 nm).

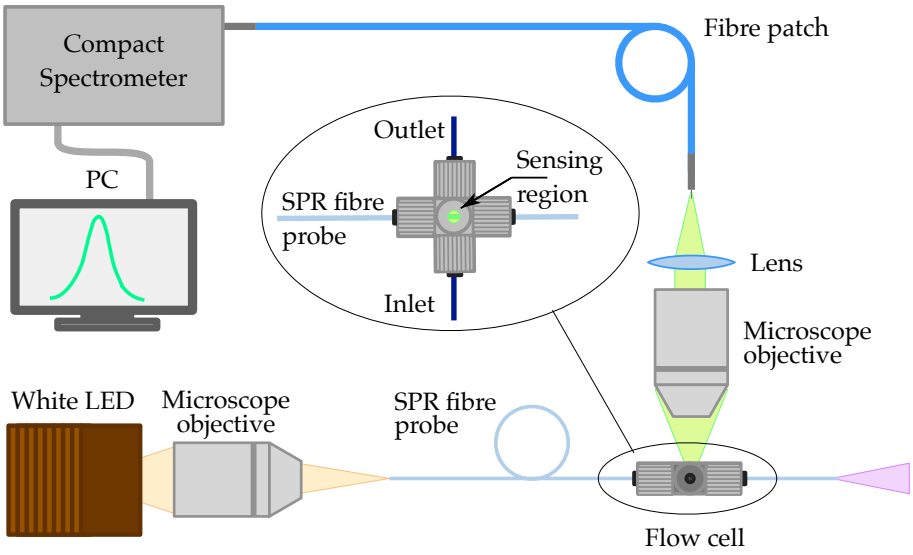


Figure 4.2: Schematic of the optical setup for F2 fibre SPR sensor characterisation. Top view of the cross sectional flow cell with window for light collection is shown in the inset.

4.1.3 *Performance analysis*

The performance of the SPR sensors was analysed by measuring shifts of the resonance wavelength caused by known changes in the external dielectric RI (aqueous solutions of glycerol with varying concentration). Spectra were recorded using SpectraSuite software provided by the spectrometer manufacturer. A Matlab program was written to assist data analysis of the collected spectra. An example of a raw spectral data obtained from the sensing region is presented in Figure 4.3. The increase in the intensity of the subsequent peaks is caused by the emission characteristics of the LED (Figure A.1 in Appendix A). Spectra were further processed by subtracting the background, normalising, and smoothing with local regression using a weighted linear least squares and a second degree polynomial model. The processed spectra and plot of the resonance wavelength as a function of glycerol solution RI are shown on Figure 4.4 and Figure 4.5, respectively.

The sensitivity of the sensors was estimated in a small range of RIs close to the aqueous environment which generally occurs in biosensing applications. For small RI changes, the relation between resonant wavelength and RI can be approximated as linear and the sensitivity value is given as the slope of the curve. Based on 11

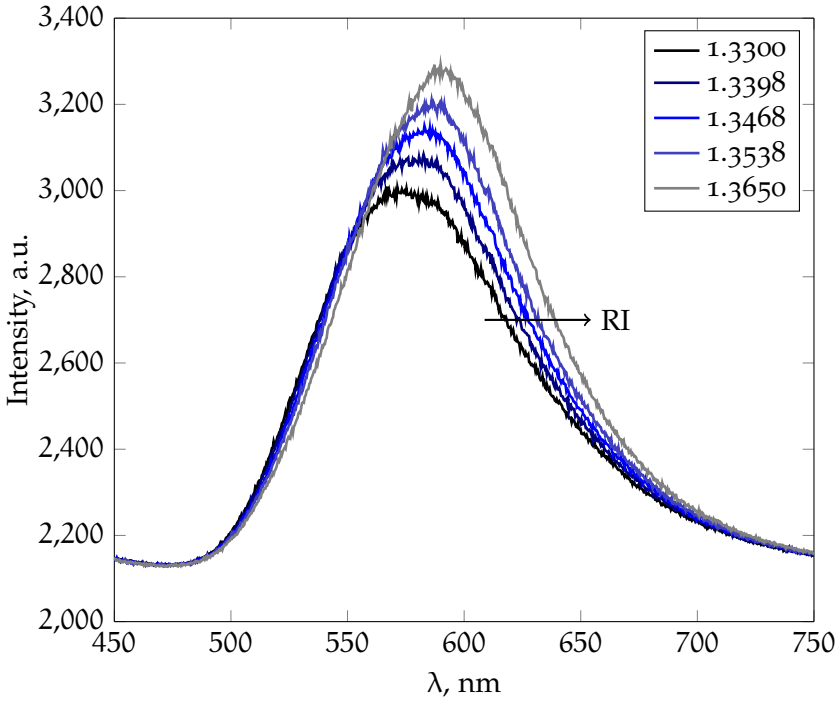


Figure 4.3: Raw SPR spectra for F2 fibre sensor collected at varying RI of external dielectric (aqueous solutions of glycerol).

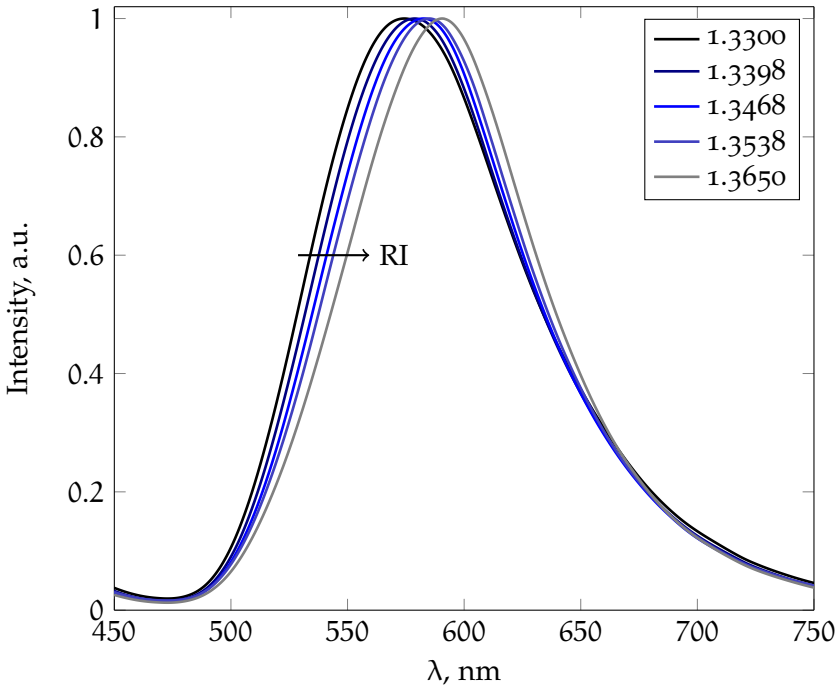


Figure 4.4: Processed SPR spectra (normalised and filtered) for F2 fibre sensor collected at varying RI of external dielectric (aqueous solutions of glycerol).

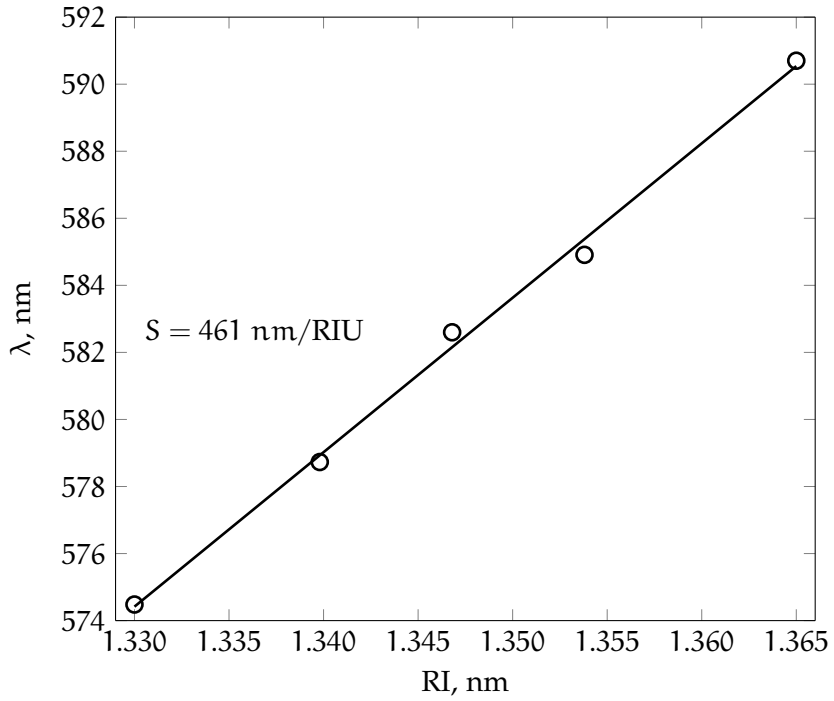


Figure 4.5: Sensitivity curve for F2 fibre sensor characterised using aqueous solutions of glycerol. Coefficient of determination $R^2 = 0.9968$.

samples prepared at various times throughout the project, the average sensitivity value for the F2 fibre based SPR sensors was estimated to be 485 $\pm$ 78 nm/RIU and the FWHM of the SPR curves was found to be 112 $\pm$ 14 nm, where the uncertainties are estimated as the standard deviation. These results are in partial agreement with theoretically predicted values for the sensitivity and FWHM of 868 nm/RIU, and 100 nm respectively, as was presented in Chapter 3. The overestimation of the theoretical sensitivity value is likely due to the estimation of the dielectric constant of the metal coating and the assumption of low surface roughness. Average resonant wavelength of F2 fibre SPR probes was found to be 559 $\pm$ 13 nm which significantly differs from the theoretically predicted value of 440 nm. The wave vector of a SP propagating on an irregular surface is greater than that of an equally energetic SP on a smooth surface [224], which should result in shortening of the resonant wavelength [225]. However, the roughness parameters, such as size of the surface features, can significantly affect the results by introducing hot spots with localised resonances. Moreover, the dielectric function of the rough metal itself has a spatial perturbation resulting in a change of the plasmon wavevector [225]. Therefore, the difference of the experimental results with the simulated values for the spectral position of the resonance is most likely due to the presence of significant surface roughness in the metallic coating (experimental results presented in Chapter 6), and a difference in the dielectric function of the thin metal film and that of the bulk metal used in the simulation.

4.1.4 *Discussion*

A scattering based SPR sensing platform allows the creation of powerful devices that open up possibilities for multiplexing, distributed sensing, and the combination of SPR with other detection techniques, such as fluorescence, which are not possible with traditional transmission based SPR fibre sensors. In contrast to conventional SPR fibre sensors where high quality smooth metal surfaces with precise thickness control is required, scattering based sensing architecture benefits from the presence of surface roughness. This allows the fabrication of sensors on demand using simple chemical method without engaging expensive equipment, such as a sputterer or a thermal evaporator. Lower reliance on the thickness of the metal coating also provides additional flexibility and simplifies sensor fabrication.

The possibility of analysing scattered light from multiple sensing regions on one fibre probe opens up a range of opportunities. First of all, one of the sensing regions can be used as a real time reference for correcting temperature fluctuations or light coupling variations that can potentially occur during the experiment and influence sensor performance, i. e. linewidth, height, and position of the peak. Moreover, multiple sensing regions can be used to detect different refractive indices simultaneously in one device. This is especially useful for biological or chemical sensing applications where multiple targets may need to be detected. Multiplexed sensing on the F2 fibre based scattering SPR platform has previously been used for simultaneous detection of two gastric cancer biomarkers in a single optical fibre probe [202]. As optical fibre probes can be of arbitrary length, multiple sensing regions can potentially be used for distributed SPR sensing. However, due to the fact that SPR is a lossy mechanism, issues such as the light loss in the previous regions, as well as the cross-talk artefacts mentioned in [202] where a change of RI around the first sensing region affects the spectra in the next region, need to be carefully considered.

As far as the performance characteristics are concerned, the SNR of the scattering based measurements is higher than that of transmission measurements, up to 33 db in comparison to 14 db, respectively [44]. SNR of optical signal is of importance as spectral response with higher SNR allows to determine the position of the resonant feature more accurately, which in turn influences sensor resolution [93]. Sensitivity and FWHM of the scattering based fibre probes is in agreement with the analytical simulations presented in Chapter 3 within the experimental uncertainties, as discussed in the previous section. Although, sensitivity of the F2 fibre based SPR sensor is comparable with most of the reported SPR fibre probes presented in Section 2.5, there is still significant scope for improvement in sensitivity, as well as the FWHM, or the resolution. As predicted by theoretical modelling, sensitivity of the sensor can be improved by lowering the RI of glass core. Fused silica has a refractive index of around 1.457 at 633 nm which is the smallest RI of low cost glass materials that are readily available. Fused silica fibres can be commercially purchased in various forms and specialised fused silica fibres with desired parameters can be easily fabricated. Theoretical improvement in the sensitivity of fused silica fibre sensors can potentially be up to 5 times, as predicted by the theoretical calculations (Chapter 3). Therefore, fused silica was chosen as a material to be used as the fibre core in order to improve sensitivity of the scattering based SPR fibre sensor. The subsequent sec-

tions describe the general sensor fabrication procedure and coating characterisation techniques, as well as silica surface modification work that was required in order to produce silver coatings on the silica fibres suitable for SPR sensing. In addition, demonstration of the silica fibre sensor in biosensing applications is presented at the end of the chapter.

4.2 SENSOR FABRICATION

4.2.1 *Fibre preparation*

The fibre sensing region was fabricated on the side of a bare core lead silicate (F2) MMF of 160 μm diameter coated with an acrylate cladding. The RIs of the fibre core and acrylate cladding are 1.62 and 1.52 at 633 nm respectively. To fabricate the sensing region, a portion of the cladding was stripped off to expose a section of the glass core which was then coated with a thin silver film of approximately 50 nm thickness using chemical deposition which is described in detail below. Fibre samples were cleaned prior to metal deposition by sonicating the striped regions in a detergent (Deacon90) for 30 min, and subsequently sonicating in de-ionised water for at least 30 min to ensure thorough rinsing. The cleaning of the fibre samples prior to deposition of the plasmonic film allows to remove any organic material from the surface of the samples. This reduces the contamination of the plating solution as well as promotes better adhesion of the silver coating to the surface of the substrate. The fibre samples were then dried in air prior silver deposition.

4.2.2 *Electroless plating of silver films*

Electroless plating is an auto-catalytic plating method that does not involve the use of external electrical power, as opposed to galvanic electrochemical plating techniques. Chemical electroless plating of silver, also knows as the Tollens reaction or the silver mirror reaction, has been known for a long time and is normally used to make silver mirrors as well as test for the presence of aldehydes. While a number of methods can be employed to fabricate silver films on optical fibres, i. e. thermal vapour deposition, sputtering, or electrodeposition, electroless plating method offers a simple, and inexpensive way of fabricating thin silver coatings on glass fibre substrates [226]. Furthermore, using a chemical method it is possible to fabricate symmetrical coatings with even thickness around the cylindrical fibre core, which is beneficial for fibre-side SPR sensors but is more challenging to achieve with physical deposition methods. Most importantly, the chemical electroless plating allows to produce silver films with significant surface roughness that plays a key role in scattering of the electromagnetic radiation by SPs, transforming an initial drawback into an advantage.

Electroless plating is a redox reaction that chemically reduces silver ions into elemental silver and consists of adding a solution of silver ammonia to a reducing agent, usually a sugar, such as glucose, in order to produce silver particles which can be subsequently attached to a glass substrate. The initial protocol for the reac-

tion was taken from [227] and the reaction conditions, such as time and temperature, have been optimised for the fabrication of suitable SPR coatings. The preparation of the reagents starts with transformation of a silver nitrate in an aqueous solution (0.24 mol/L of $AgNO_3$) into silver oxide using potassium hydroxide (0.25 mol/L of KOH) according to the chemical reaction:

$$2AgNO_3 + 2KOH \rightarrow Ag_2O(s) + 2KNO_3 + H_2O. \tag{4.1}$$

40 μL of KOH is added to 20 mL of the $AgNO_3$ solution. The silver oxide formation results in a brown precipitate in an initially transparent silver nitrate solution. In order to control the temperature of the solution, the reaction is performed in a water bath at 23°C. Ammonia (3 mol/L of NH_3) is then added drop by drop in order to dissolve the silver oxide and produce a transparent silver ammonium complex ($Ag(NH_3)2NO_3$) according to the reaction:

$$Ag_2O(s) + 4NH_3 + 2KNO_3 + H_2O(l) \rightarrow 2(Ag(NH_3)_2)NO_3 + 2KOH. \tag{4.2}$$

It is important not to exceed the amount of ammonia added to the solution as this will interfere with the plating process, and therefore, small drops of ammonia are added at a slow rate, just enough to dissolve the brown precipitate particles remaining in the solution. During this process the reagent is mixed using a magnetic stirrer. Once the silver ammonia complex becomes colourless, the reducing agent is added to the solution. The reducing agent consists of a 1 : 2 mixture of methanol and glucose (1.9 mol/L) solution. Once the reducing agent is added to the silver ammonia solution, a metallic silver coating is produced following the reaction:

$$CH_2OH(CHOH)_4CHO + 2(Ag(NH_3)_2)^+ + 3OH^- \rightarrow \\ 2Ag(s) + CH_2OH(CHOH)_4CO_2^- + 4NH_3 + 2H_2O. \tag{4.3}$$

As the reaction starts immediately after mixing the reducing agent with the reagent, the solution has to be quickly poured onto the glass substrates. The deposition time was measured after the fibres are immersed into the solution, which differs from the reaction time (after adding the glucose) by a few seconds. The reaction and deposition rates depend on the solution temperature, therefore, the time of the reaction and temperature need to be carefully monitored in order to achieve the desired coating thickness. To produce silver film thickness of around 50 nm on F2 glass substrates, the reaction temperature was optimised at 24°C with a corresponding deposition time of 8 min. A schematic of the steps of the chemical electroless plating process is illustrated in Figure 4.6.

Without surface treatment, silver particles do not get deposited on the acrylate fibre coating, presumably due to the higher hydrophobicity of the acrylate in comparison to glass. Therefore, the silver film is visible only on the exposed glass core of the fibre sample immediately after being submerged in the reagent; thin silver films appear grey, then reflective as the coating becomes thicker. During the course of the reaction the initially light grey solution becomes opaque and acquires a brown tint.

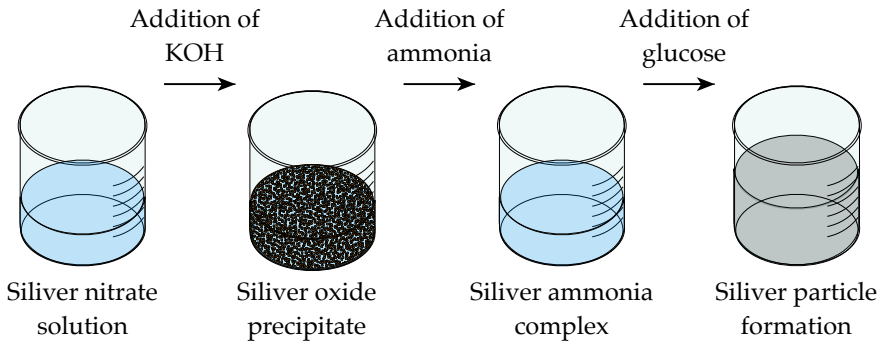


Figure 4.6: A schematic of steps involved in the Tollens reaction (chemical electroless plating of silver) used for fabrication of thin silver films on optical fibre core. After the glucose is added into the silver ammonia complex, the solution is poured onto the fibres to start the deposition process.

After the reaction time has passed, methanol is added to the solution to stop the deposition, and the fibre samples are taken out of the solution, rinsed with methanol, deionised water, then dried. The fabricated sensors were stored in a desiccator under low vacuum to prevent oxidation and prolong their shelf life.

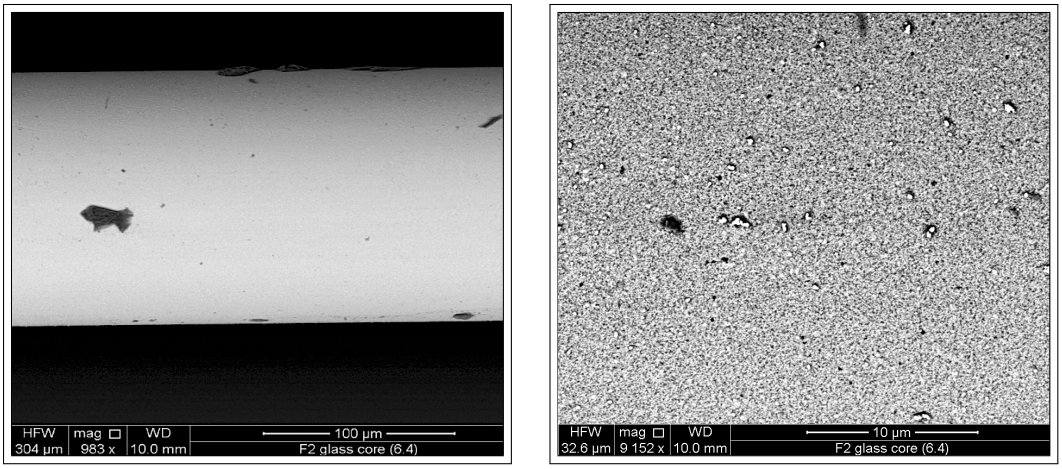
4.3 SILVER COATING CHARACTERISATION

Silver films were characterised in a number of ways. Quantitative measurements of the silver film thickness were performed using imaging techniques, such as Scanning Electron Microscopy (SEM) and Atomic Force Microscopy (AFM), as well as transmission measurements, as described below. Surface topography of the fabricated silver coatings, in particular surface roughness parameters, were studied using the AFM technique. The analysis of the coating thickness and topography of the surface is necessary for characterisation of the parameters that affect SPR performance. Qualitative analysis of the suitability of the coatings for SPR sensing has been performed by visual inspection of scattered light spectrum and the characterisation of SPR performance.

4.3.1 *Imaging techniques*

Two common techniques for the characterisation of surfaces at nanometer scale are SEM and AFM. Two SEM instruments have been used: Quanta 450 FEG (FEI) and XL30 (Philips). SEM was used to image and analyse the surface topography utilising either secondary electrons or backscattered electrons, and to characterise and determine samples' elemental composition with x-ray analysis (Quanta 450 instrument). An example of SEM images of silver films fabricated on F2 fibre is shown in Figure 4.7.

Atomic force microscopy is a high resolution Scanning Probe Microscopy (SPM) technique that is used to measure and analyse surface topography and morphology at the nanoscale. An AFM instrument consists of a cantilever with a sharp tip which is raster-scanned with respect to a sample surface. By measuring the reaction of the probe to the atomic forces that the sample imposes on it, it is possible to form an

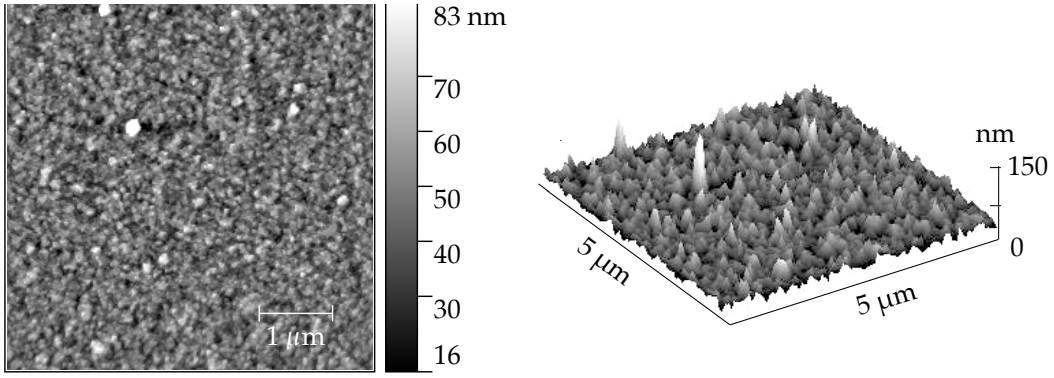


(a) A side view of the fibre. Magnification 983×. Scale bar 100 µm.

(b) A close up of the coating. Magnification 9152×. Scale bar 10 µm.

Figure 4.7: SEM images of lead silicate (F2) fibre core coated with silver film of around 50 nm by a chemical deposition technique.

image of the topography of the sample. The collected data provides information on the height of surface features, which allows both, 2- and 3- dimensional imaging of a sample surface. The AFM instrument (NT-MDT, Ntegra Solaris) was primarily used to study the surface roughness parameters of the silver surfaces as well as measuring the thickness of the silver films. An example of an AFM image of the silver coating deposited by a chemical technique is shown in Figure 4.8.



(a) 2D AFM image of a silver film.

(b) 3D view of the same AFM image.

Figure 4.8: AFM image of surface topography of a silver film of 56 nm fabricated by a chemical deposition technique.

Analysis of the SEM images was performed with Fiji, an open-source platform for scientific image analysis [228]. The software allows the processing of SEM and other digital microscopy images, and features capabilities for particle analysis, distance measurements, and many other practical tools. AFM images were analysed using the manufacturer's software (NT-MDT, Nova SPM Software), as well as Gwyddion, an open source data visualization and analysis package for SPM [229]. Gwyddion is a powerful software package that includes statistical characterisation of images, levelling, data filtering, and grain distribution analysis.

4.3.2 *Transmission measurements*

The thickness of thin silver films can be measured optically through the transmission of light that passes through the film. As these measurements are not practical to perform on optical fibres, planar glass substrates were prepared simultaneously with optical fibre samples in the same coating process. By measuring the transmitted power of Helium Neon (HeNe) laser light ($\lambda = 633$ nm) passing through a silver coated glass slide (I), as well as the power of light passing through a non-coated sample (I_0), the coating thickness (t) can be estimated using the Beer-Lambert law: $I = I_0 e^{-t\alpha}$, where $\alpha = 756310\ cm^{-1}$ is the absorption coefficient of silver at 633 nm [230]. Due to the surface roughness of the metal films which introduces scattering losses, as well as the reflection from the surfaces, the amount of light detected in transmission is reduced, this might result in overestimates of the film thickness. To evaluate the scale of these effects, the metal film thickness for several samples was verified using AFM at the edge of the coatings. The AFM estimated values of thickness were found to lie within the uncertainty ranges of the values calculated using transmission measurements, which indicates that the transmission method could be used as a simple and fast alternative for measuring the metal film thickness. It has also been previously determined in [15] that the transmission measurements can be used to characterise silver coating thickness by performing those measurements on films with known thickness in the range of 20 to 80 nm measured by quartz crystal microbalance with a coefficient of determination $R^2 = 0.9986$. This indicates that the transmission measurement is a valid method for estimating the thickness of the silver films and was used as a routine thickness analysis technique where determination of coating thickness was required.

4.4 SILICA SURFACE MODIFICATION

As discussed in Section 4.1.4, the sensitivity of the scattering based SPR platform could be improved through the use of an optical fibre with the core made of a lower RI glass, such as fused silica. A bare core fused silica MMF was drawn in-house from a commercially purchased F300 silica rod (Heraeus Quarzglas GmbH & Co.KG) with a RI of 1.456 at 633 nm. The fibre core with diameter of 140 µm was coated with a fluorine doped acrylate polymer (Luvantix, Efiron PC-373) with a RI of 1.375 at 852 nm, according to the manufacturer's specification [231].

Similarly to the F2 fibre, a small 1 cm-long section of the acrylate coating was stripped off from the fibre to expose the glass core for silver film deposition. The silica fibre was cleaned by sonicating in detergent, then water, prior silver deposition. Silver films were deposited on the silica fibre samples by the Tollens method following the same protocol as for F2 fibres, as described in Section 4.2.2. F2 fibre samples were used as a positive control for the coating procedure.

4.4.1 *Characterisation of silver films on silica surfaces*

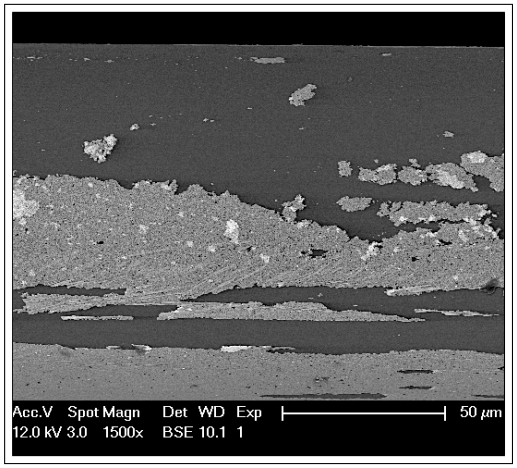
The fabricated silica sensors were tested using the SPR setup, as shown in Figure 4.2, where the LED was changed to a supercontinuum white light source (NKT Photonics A/S, KOHERAS SuperK Compact). The light source was changed due to the expected red shift in the resonance wavelength of the silica sensor in comparison to F2 (of approximately 140 nm from the results of theoretical modelling presented in Table 3.1 in Chapter 3), where the white light LED (Thorlabs, MCWHLP1) used for SPR excitation in the F2 fibres was no longer suitable (spectrum shown in Figure A.1.)

The tests were performed with the same conditions as for F2 fibre probes, however, no SPR signals were detected from the silica fibre samples, even though positive controls performed as expected. It was observed that the silver coatings on the silica fibre samples appeared thinner than of corresponding F2 samples, and therefore, it was assumed that silver deposition rate depended on the substrate material and was lower for silica than for lead silicate glass. Consequently, different times of the silver deposition on silica samples (from 4 to 16 min) were analysed in order to determine the optimal time that would result in the desired silver film thickness of around 50 nm. However, none of the silica samples showed SPR signals when tested. Moreover, silver coatings on the silica samples prepared with longer reaction times appeared to have less adhesion than the thin coatings and were observed to peel off when the sensors were submerged into liquid samples. In order to investigate this issue, a SEM analysis of the silver coatings fabricated on the silica fibres was performed to assess the quality of the silica fibres and silver surfaces, and to compare them with those of F2 fibre samples.

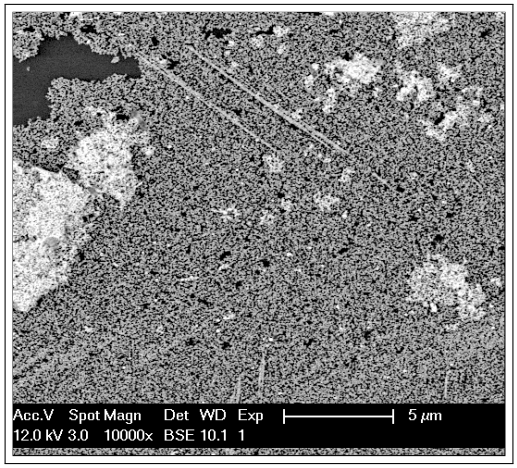
Figures 4.9 and 4.10 show the SEM images of silver films fabricated on silica fibres using the chemical electroless plating method with 6 and 11 min reaction time respectively. The same deposition protocol as was used for F2 fibres was followed and no pre-treatment was performed on those silica fibre samples. It is clear that the deposited silver is not homogeneous on the silica fibre surface when compared to the F2 fibre that has an even silver coating, as shown in Figure 4.7. As was predicted from the visual observation of the coatings on silica fibres, the thinner films are discontinuous and form silver islands with total coverage of less than 50 % of the fibre surface, whereas the thicker films (Figure 4.10) begin peeling from the silica fibre surface. Study of the surface of the F2 and silica fibres did not reveal any significant differences in the quality of the surfaces. It was hypothesised that this behaviour of the silver films on silica surfaces resulted from low adhesion of the silver to the silica. Therefore, a study of surface treatments was undertaken in order to modify the silica surface to be suitable for silver adhesion.

4.4.2 *Silica surface treatments*

Several methods have been reported for the modification of the surface chemistry of silica. These methods include but are not limited to optical treatment with UV radiation [232, 233], thermal treatment [233], mechanical surface roughening [234],

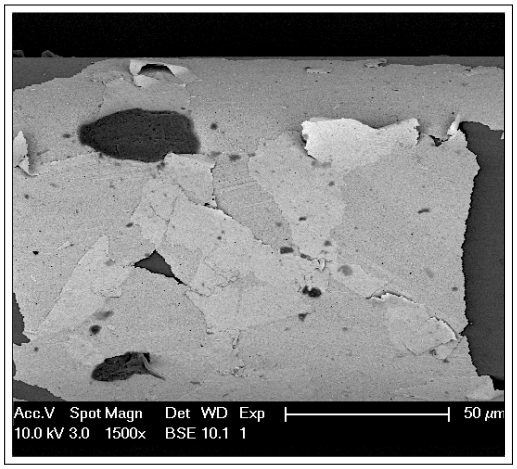


(a) A side view of the fibre. Magnification 1500×. Scale bar 50 µm.

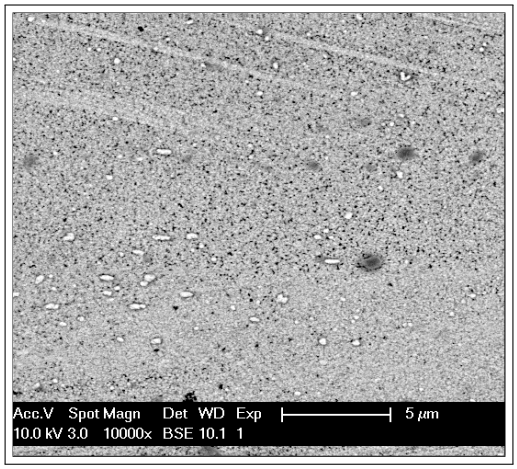


(b) A close-up of the coating. Magnification 10000×. Scale bar 5 µm.

Figure 4.9: SEM images of silica fibre core coated with thin silver film without pre-treatment. Tollens reaction time is 6 min.



(a) A side view of the fibre. Magnification 1500×. Scale bar 50 µm.



(b) A close-up of the coating. Magnification 10000×. Scale bar 5 µm.

Figure 4.10: SEM images of silica fibre core coated with thick silver film without pre-treatment. Tollens reaction time is 11 min.

chemical etching [234], ultrasonic-assisted metal deposition [235], carbon layer adhesion promoters [236], and various chemical procedures of glass cleaning and grafting of different functional groups to the surface [236].

Adhesion of various species onto the silica surface depends on the surface chemistry, in particular net surface charge, acidity, and hydrophilic/hydrophobic properties. On silica surfaces the air humidity forms polar OH-bonds. Such substrates with surface hydroxyl groups are hydrophilic (i. e. good adhesion of water), with hydroxyl groups dominating the chemical interactions, such as monolayer adhesion and bonding, at the silica surface [237]. Hydrophilic surfaces are believed to be beneficial for electroless plating of metals as hydrophobic materials generally result in non-uniform thin film formation and poor adhesion [238]. The study of the surface chemistry of lead silicate and silica fibres showed that silica fibre had less OH-bonds when compared to F2 fibre which is a result of higher drawing temperature required for fabrication of silica fibres [239]. This explains the poor adhesion of silver onto the silica fibre during chemical plating process.

To promote the adhesion between two materials, such as silica glass and metal, the substrate surface can be roughened prior coating process to increase the effective surface area. Chemical etching and mechanical grinding have previously been shown to promote metal adhesion on the silica surface [234, 237]. It is difficult to routinely perform controllable mechanical grinding on a cylindrical surface of an optical fibre, therefore, this method was not used for silica fibre surface treatment. An alternative method to mechanical grinding, is chemical etching that is commonly performed with acids. Nitric acid is used to clean glass surfaces from organic and non-organic compounds and remove metallic residues on the surface. Hydrofluoric acid is used to produce abrasive sponge-like glass surfaces. Hydrofluoric acid etching also promotes formation of silanol groups ($Si-OH$) on the silica surface thereby increasing hydrophilic properties of the surface [240]. However, the hydrofluoric acid is not only corrosive, but is also a highly toxic agent that readily penetrates the skin, causing destruction of deep tissue layers, including bone. As the etching process had to be routinely performed, the safely concerns involved with the hydrofluoric acid etching would significantly increase the cost and time required for sensor fabrication.

Piranha solution etching

Another chemical etchant that is widely used to clean glass surfaces is Piranha solution. Piranha solution is a mixture of sulphuric acid (H_2SO_4) and hydrogen peroxide (H_2O_2) that is a strong oxidizing agent that removes most organic compounds and heavy metal contaminants from an etched surface, and hydroxylates it with OH groups and SiO^- species [232, 241]. Various recipes for the etching solution have been reported. The most common are the acid Piranha consisting of a mixture of concentrated sulphuric acid with hydrogen peroxide, and base piranha, a mixture of ammonium hydroxide (NH_4OH) with hydrogen peroxide. Cleaning off organic compounds with Piranha solution is very effective due to the mechanism of the cleaning that consists of two different processes: dehydration and oxidation, which occur at different rates. The faster process is the dehydration of organic molecules

by sulphuric acid which manifests itself as carbonisation. Dehydration of hydrogen peroxide results in the formation of atomic oxygen that is extremely reactive and oxidises the remaining carbon into CO_2. Moreover, Piranha solution adds protons to non-bridging oxygen atoms to increase the quantity of $Si-OH$ groups present on the surface promoting hydrophillicity of the substrate. It was also reported that the percentage of silanol groups on Piranha-washed silica and untreated F2 glass substrates was the same [239], which suggests that the Piranha treatment of silica surfaces should result in similar hydrophobicity to lead silicate glass. Even though, Piranha solution is highly corrosive and has a possibility to explode, if handled with care following the precautions, it can be safely used as a routine silica fibre cleaning method.

The following protocol was used to clean silica samples with Piranha solution. A $7:3$ mixture of concentrated sulphuric acid with 30% hydrogen peroxide was used. As the acid Piranha reaction is self-starting and is exothermic, the solution heats up significantly, up to $100°C$. Peroxide was added to the acid slowly to avoid heat shock and breakage of the glass container. As the Piranha solution reacts violently with organic compounds, samples were thoroughly cleaned with acetone, methanol, and de-ionised water, then dried, to remove most of the organic materials from the sample surfaces. For the fibres coated with acrylate cladding, the coating was removed prior Piranha treatment. A fresh etching solution was used immediately after preparation and the silica fibre samples were immersed into the solution for about $30\ min$, then rinsed with de-ionised water and dried with nitrogen gas.

Silanization with APTES

(3-Aminopropyl) triethoxysilane (APTES) is an aminosilane that is used for functionalisation of surfaces with alkoxysilane molecules, a process known as silanization. APTES is used to prepare positively charged surfaces and has also been reported to be helpful in the attachment of silver nanoparticles to silica substrates, which is believed to be due to the strong interaction between nitrogen atoms and the silver nanoparticles' surface [242–244]. Silanization with APTES was chosen as one of the silica surface preparation methods. Glass surfaces contain hydroxyl groups which displace the alkoxy groups on the silane forming a covalent $Si-O-Si$ bond. Silanization of glass increases hydrophobicity of the surface [245]. Piranha solution can be used to increase the density of OH groups on the silica surface prior to silanization. APTES is terminated with amine groups (NH_2), and has proven to be important for biological applications due to formation of electrostatic interactions with biomolecules [246].

Silica surface modification was accomplished by liquid phase deposition of APTES silane in an organic solvent, toluene. Toluene is required to regulate the degree of polymerization of amino-silanes at the surface and in the solution itself. A 5% APTES solution (Sigma-Aldrich) was diluted in a 95% toluene solution (Sigma-Aldrich), w/w. Cleaned silica samples (generic cleaning with acetone, methanol, and water, as well as Piranha cleaning) were immersed into silane solution and incubated for 3 hours inside a desiccator in the dark. Then, the samples were rinsed in toluene, dried, and hydrolysed in de-ionised water. After hydroxylation, silica samples were

dried with nitrogen, then placed inside a desiccator and left to dry overnight in the dark at room temperature.

Polyelectrolyte assisted synthesis of silver

Self-assembled polyelectrolyte multilayers are fabricated by sequential deposition of positively and negatively charged polyelectrolytes. These multilayers have previously been reported to be used as a template for the nucleation and growth of silver nanoparticles [247–249]. This approach is based on electrostatic interactions of the polymeric chains and the immobilization of silver nanoparticles into thin films. Poly(Allylamine Hydrochloride) (PAH) films at low pH contain free carboxylic acid groups (COOH) that during the film assembly do not bind electrostatically to the positively charged groups of PAH chains. It is believed that these free acid groups in the polyelectrolyte multilayer film are responsible for binding silver nanoparticles which are produced in the reagent solution. Pre-cleaned silica samples were coated with positively charged PAH by immersion in a PAH solution (2 mg/mL in 1 M NaCl aqueous solution). The samples were left in the PAH solution for 30 min, rinsed with de-ionised water, then dried prior electroless silver plating process.

Sensitizing with tin(II) chloride

Another method of silica surface preparation for electroless plating that has been widely used in silver mirror manufacturing is a traditional chemical conditioning of glass with sensitizing agents that typically contain tin ions, like tin(II) chloride ($SnCl_2$, or stannous chloride), and tin(IV) chloride ($SnCl_4$, or stannic chloride). Sn^{2+} ions from $SnCl_2$ were reported to be more effective at binding silver to the silica surfaces [250]. While the exact mechanism of the sensitisation process is still debated in literature, it is believed that tin ions adsorbed on the substrate surface create nucleation sites to which silver particles may be deposited [234]. This process is depicted in the Figure 4.11.

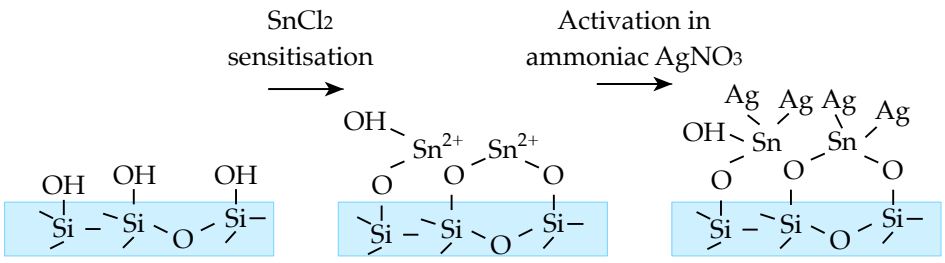


Figure 4.11: A schematic of silica surface sensitisation with $SnCl_2$ and silver attachment to tin ions. Adopted from [238].

Solubility of the metallic silver in glasses can be increased by the presence of metallophillic ions, such as Pb^{2+} and Sn^{2+} that provide the bridge between non-polarizable $Si-O-Si$ bonds and polarizable metallic silver [251]. A similar mechanism might contribute to the process of glass surface sensitization that improves adhesion of Ag atoms to the glass surface. Considering this, the presence of Pb^{2+} ions in F2 glass can provide an explanation of the superior adhesion properties of

silver to lead silicate glass and provide justification for using other metallophillic ions, Sn^{2+}, on silica surfaces.

Another mechanism that can potentially influence silver film formation on $SnCl_2$-treated surfaces is the contribution of Sn^{2+} ions towards the reduction of silver ions into metallic silver. In addition to the attachment of the metallic silver reduced by the glucose solution to the tin(II) ions bound to the glass substrate, Sn^{2+} ions contribute to the reduction of Ag^{+} ions from the solution itself according to the reaction:

$$Sn^{2+}(aq) + 2Ag^{+}(aq) \rightarrow Sn^{4+}(aq) + 2Ag^{0}(s). \tag{4.4}$$

After $SnCl_2$ sensitization, the Ag^{+} ions are reduced to Ag^{0} following a redox reaction mechanism and, after attachment to the Sn^{2+} ions on the surface, form nucleation sites on the glass for consecutive silver deposition. The electroless plating can then occur on these formed nucleation sites [238]. The role of tin(II) chloride as a reducing agent for silver can be compared to the "purple of Cassius" where gold from $AuCl_3$ is reduced to metallic gold through the redox reaction with stannous chloride in solution [252]:

$$2AuCl_3(aq) + 3SnCl_2(aq) \rightarrow 2Au(s) + 3SnCl_4(aq), \tag{4.5}$$

forming finely dispersed metallic Au adsorbed onto an insoluble form of hydrous stannic oxide:

$$SnCl_4(aq) + 4H_2O(l) \rightarrow Sn(OH)_4(s) + 4HCl(aq). \tag{4.6}$$

Stannous chloride can be dissolved in less than its own mass of water without apparent decomposition, however, in highly diluted aqueous solutions it undergoes hydrolysis with a formation of an insoluble basic salt according to the equation:

$$SnCl_2(aq) + H_2O(l) \leftrightarrow Sn(OH)Cl(s) + HCl(aq). \tag{4.7}$$

Therefore, to prevent the decomposition of the $SnCl_2$ solution into two phases, it must be dissolved in hydrochloric acid, typically of the same or greater molarity as the $SnCl_2$ [253]. Moreover, solutions of tin(II) chloride undergo chemical oxidation in air resulting in the formation of stannic chloride:

$$6SnCl_2(aq) + O_2(g) + 2H_2O(l) \rightarrow 2SnCl_4(aq) + 4Sn(OH)Cl(s). \tag{4.8}$$

It was reported that in the tin(II) chloride sensitisation reaction, two processes contribute to Sn^{2+} deposition on the substrate. The first process is the formation of basic salt colloids in the solution due to the chemical oxidation of Sn^{2+} ions into Sn^{4+} ions in air, as well as hydrolysis in water. The second process is the precipitation of tin species from the liquid layer adhering to the glass substrate. The

latter results from a rapid change in pH on the surface of the substrate during the water rinsing step [254]. Based on the described mechanism, the effectiveness of the sensitisation process can be affected by the solution's pH value, concentration of tin(II) chloride, as well as solution ageing. During ageing colloids are formed in the solution and oxidation processes result in some of the Sn^{2+} ions being converted to Sn^{4+}. It was speculated that aged Sn^{4+} ions form a colloidal dispersion that adsorbs to the substrate and entraps some Sn^{2+} ions [250]. Overall, ageing $SnCl_2$ was found to improve the sensitization process by converting the hydrophobic surface to a more hydrophilic one [238]. In addition, ageing of the $SnCl_2$, as well as decreasing the solution pH, were reported to affect the nucleation particles size and density of tin-ion species on the surface of the substrate. However, concentration of $SnCl_2$ was reported to have lesser effect on the process of sensitization. Moreover, the result of the pre-treatment was found to be independent on sensitization time after 5 min [238].

Various recipes for preparation of tin(II) chloride sensitising solutions have been reported. The following procedure was followed for the initial pre-treatment of silica samples. A 0.5 M aqueous solution of tin(II) chloride dihydrate (Chem-Supply, $SnCl_2 \cdot 2H_2O$) was used as a sensitiser. Cleaned silica samples (acetone, methanol, water), and piranha cleaned samples were soaked in the freshly prepared sensitising solution for 5 min. As $SnCl_2$ is not completely soluble in water and results in formation of white precipitate that deposits on the substrate, the solution was agitated during the sensitising process to prevent deposition of non-soluble precipitate on the silica samples. After 5 minutes the substrates were thoroughly rinsed in de-ionised water, then dried in air at room temperature prior to the electroless plating of silver.

In summary, the following methods described above were chosen for silica surface pre-treatment with subsequent silver mirror coatings –

- Piranha solution cleaning to remove organic residues from the silica surfaces as well as to add OH groups to the surface;
- Silanisation with APTES to add amino- groups to the surface of silica; the method was used with and without prior Piranha cleaning;
- Polyelectrolyte coating (PAH) to increase surface charge; the method was used with and without prior Piranha cleaning; and
- Sensitising the silica surface with tin(II) chloride to create nucleation sites for silver particles (chemical conditioning); the method was used with and without prior Piranha cleaning.

Results verification and testing

A range of different samples have been pre-treated with various methods as well as combinations of them, as shown in Table 4.1. Samples include silica fibres and silica ribbons, as well as F2 fibre samples for positive control. A silica ribbon is essentially a flat optical fibre drawn from a rectangular silica rod. It was convenient to use flat surfaces, in addition to the traditional cylindrical optical fibres, for simplification of

subsequent testing by various methods, such as visual inspection, mechanical adhesion test, or imaging techniques, which are easier to perform in planar geometry. In contrast with conventional planar glass slides, silica ribbon fibres allow coupling of light for SPR analysis of the silver coating in a similar manner to cylindrical fibre samples. Two types of fused silica ribbon were available, a small silica ribbon, of size similar to the optical fibres, and a large silica ribbon, around 2 mm wide, that was cut from the beginning of the ribbon fibre draw. Short sections, around 10 cm-long, of the ribbon fibres were prepared, together with several silica and F2 fibres. As the silica ribbon fibre did not have polymer coatings on them, no additional preparation was required. Optical fibres were prepared by exposing 1 cm-long sections of the cores by removing the acrylate fibre claddings with a carbon blade. All samples were cleaned with acetone, methanol, and de-ionised water, then dried prior to the surface pre-treatments.

Table 4.1: Silica surface treatments and their combinations used to analyse the effects on silver adhesion deposited by electroless plating.

Sample	Silica surface treatments				
	Piranha	APTES	PAH	$SnCl_2$	None
1	✓				
2		✓			
3			✓		
4				✓	
5					✓
6	✓	✓			
7	✓		✓		
8	✓			✓	

The quality of the formed silver films was tested after the deposition to assess whether a certain approach of silica surface pre-treatment gave any improvement to the metal adhesion. An ideal adhesion test should be quantitative to some extent, reproducible, not very time consuming, easily adaptable to routine testing, relatively simple to perform, valid over a range of sample sizes, whether those are slides, ribbons, or fibres. The following methods were used to assess the silver adhesion and overall quality of the film, i. e. surface roughness and thickness. As the first two methods are non destructive, it was possible to perform all the methods in order, if desired –

- Visual observation of the kinetics of formation of the silver films including qualitative estimated of rate of film formation, density of the film during formation, time required to form a film of the desired thickness, and homogeneity of the coating.
- An SPR measurement was used as an ultimate test of the silver coating quality as it gave information about the suitability of the deposited films for the desired application.

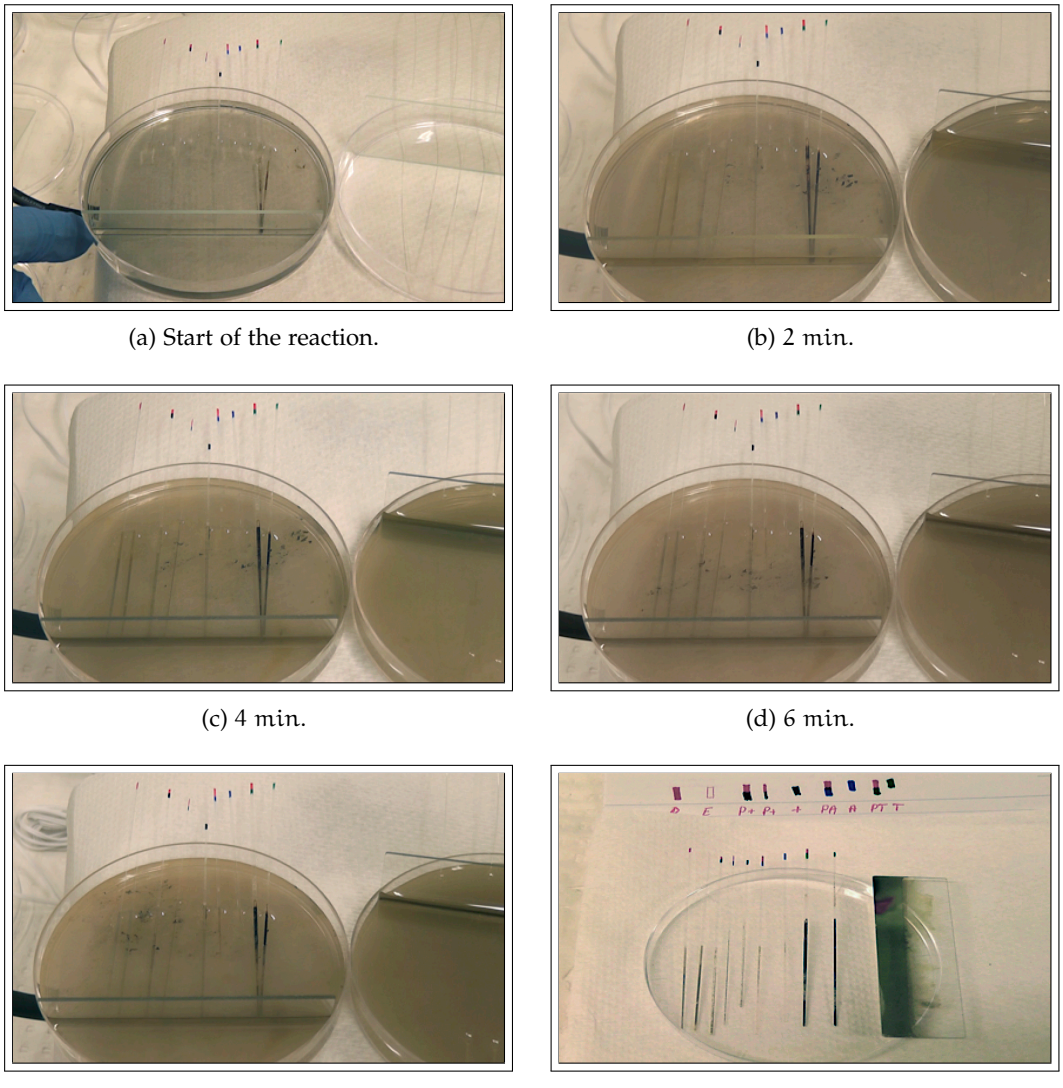
- Mechanical methods that use some means of removing silver film from the substrate were applied to estimate the adhesion when the coating visually appeared to have the desired thickness but no SPR signal was observed.
- Imaging techniques were used when required to analysed the morphology of the formed films (SEM), as well as the surface topography (AFM).

All samples, including optical fibres and fibre ribbons, were coated with silver using the Tollens method described in Section 4.2.2. Visual observation of electroless plating kinetics was performed to qualitatively estimate the effect of the different silica surface pre-treatments. The information derived from it led to a better understanding of the silver film deposition process and the film structure. The coating formation on samples with different pre-treatments was recorded and images of the samples in the Tollens solution at different times during the reaction are presented in Figure 4.12.

From the visual assessment of the samples it was clear that silver deposits at different rates for samples with different pre-treatments. Piranha cleaned samples appeared identical to samples without any pre-treatment. This was against the expectation that this type of treatment should increase the number of OH species on the surface and thereby improve silver adhesion. Moreover, cleaning with Piranha solution did not lead to a significant difference on the samples that were subsequently treated with PAH and APTES in comparison to those generically cleaned and treated. Less silver was deposited on silica ribbons treated with PAH. APTES silanised samples prevented silver from depositing almost completely. This may be due to increased hydrophobicity of the silica surface that resulted from APTES treatment.

By far the thickest coating and the fastest silver deposition rates were observed on samples sensitised with tin(II) chloride. However, the coating did not appear homogeneous with black sections on the otherwise reflective silver coated surface, indicating that tin nucleation sites were not evenly distributed or the surface was contaminated. The presence of white residues on these treated samples prior to silver coating suggests that chloride precipitate was left on the surface after pre-treatment. Black residue and loose silver agglomerates were found floating in the Tollens solution near the tin treated samples. This is likely to be the result of the presence of loose $SnCl_2$ particles that were detached from the silica surface due to insufficient rinsing or overly high concentration of $SnCl_2$ in the sensitising solution. This was supported by the fact that the tin sensitised samples appear to have white islands on the surface before contact with the Tollens reagent solution.

All samples have also been tested in the SPR setup and, as expected, non-tin-treated coatings were too thin for an optimal SPR film thickness. Tin-treated samples appeared too thick and no SPR signal was observed. Silver film adhesion was qualitatively estimated by scratching the surface of the samples when coating is wetted with isopropanol. Piranha cleaned samples appeared to have stronger coatings on average. Adhesion of the tin treated samples without Piranha pre-cleaning appeared slightly weaker, however, it was significantly stronger than non-treated samples. Even though, the aforementioned testing procedures did not quantify the properties of the silver films, they gave a clear qualitative assessment of which pre-treatment



(a) Start of the reaction.

(b) 2 min.

(c) 4 min.

(d) 6 min.

(e) 8 min.

(f) After reaction is completed.

Figure 4.12: Silver electroless plating on silica ribbons with different surface pre-treatments shown at different times during the deposition. Samples from left to right: Piranha cleaned, not treated, Piranha+PAH, Piranha+PAH, PAH, Piranha+APTES, APTES, Piranha+$SnCl_2$, and $SnCl_2$.

methods could be explored further in order to produce silver coatings on silica suitable for SPR sensing. Overall, it has been concluded that the most promising approach for silica surface pre-treatment was sensitisation with $SnCl_2$. General cleaning process for samples with acetone, methanol, and water was chosen to reduce the complexity of sample preparation, as Piranha cleaning did not show any significant improvement on the silver coatings of the tin sensitised samples.

4.4.3 *Tin sensitization process optimisation*

The tin(II) chloride sensitisation of silica surfaces prior to the electroless plating of silver showed that this pre-treatment method results in an improvement of silver adhesion and promotes silver particles growth on the silica substrates. This is believed to be due to tin ions adsorbed on the surface that create nucleation sites for the silver particles. As discussed earlier, the density and size of these nucleation sites depend on the $SnCl_2$ concentration, pH, as well as sensitiser ageing. It was reported that adding hydrochloric acid (HCl) or aged stannic chloride ($SnCl_4$) into the aqueous tin(II) chloride solution to adjust its pH, changes the hydrophillicity of the surface, results in the increase of the density of the nucleation sites, and decreases size of the nucleates [238]. Various recipes for stannous chloride ($SnCl_2$) sensitisers exists, and therefore, several different methods for tin treatment listed in Table 4.2 have been studied.

Table 4.2: Different methods used for optimisation of $SnCl_2$ silica sensitisation prior silver electroless plating.

Recipe	$SnCl_2$ concentration, M	Solvent	Ageing†	Drying‡
1	0.5	H_2O	minutes	dry
2	0.25	H_2O	minutes	dry
3	0.05	H_2O	minutes	dry
4	0.5	H_2O	minutes	wet
5	0.5	H_2O +2% 1M HCl	minutes	dry
6	0.5	H_2O	$\approx$ 5 hours	dry
7	0.5	0.1 M HCl	minutes	dry
8	0.1	0.1 M HCl	minutes	dry
9	0.1	0.1 M HCl	$\approx$ 5 hours	dry
10	0.1	0.1 M HCl	$\approx$ 5 hours	dry
11	0.1	H_2O	$\approx$ 20 hours	dry
12	0.1	0.1 M HCl	$\approx$ 20 hours	dry
13	0.1	0.1 M HCl	$\approx$ 50 hours	dry

† Ageing was performed in the dark at room temperature inside a 'toxic chemical' cabinet in a full sealed glass container to minimise the amount of air inside the container.

‡ Samples were either dried after the rinsing step, or kept moist in de-ionised water prior to silver plating.

Silica fibre samples were used to test the SPR response on fibres pre-treated by different methods of stannous chloride sensitisation. Freshly prepared aqueous solutions of $SnCl_2$ were initially used. It was found that the concentration of $SnCl_2$ did not have a significant effect on the performance of the SPR silica fibre sensors and the majority of the prepared probes had strong scattered SPR signal at around 680 nm. As predicted by theoretical modelling, sensitivity of the silica fibre based SPR probes is significantly higher than that achieved with F2 fibre based probes that were previously used in the platform. Sensitivity values of up to 2500 nm/RIU have been achieved for some probes. This has demonstrated that the tin pre-treatment can be an effective method of modifying silica surfaces for chemical deposition of silver for plasmonic applications. The sensor characterisation will be described in detail in Section 4.5.

High variability between the sensors pre-treated with aqueous stannous chloride sensitiser was noticed; many samples had black residues on the surface and the sensitivity of the SPR probes varied dramatically, from 1000 nm/RIU up to 2500 nm/RIU with the majority of sensors exhibiting sensitivity of around 1000 nm/RIU. To investigate the reasons behind the low reproducibility, planar soda-lime microscope glass slides (Deckgläser, Cover Glasses 22x22) were prepared using various tin-treatments with subsequent silver plating. The use of planar substrates instead of ribbon fibres allowed the estimation of the silver film thickness through transmission measurements described in Section 4.3.2. This, in turn, allowed the optimisation of the Tollens reaction parameters for achieving the optimal thickness, as the varying silver film thickness was assumed to be a result of the pre-treatment and a cause of the low reproducibility of the sensors' performance.

Planar glass slides were first pre-treated with a fresh aqueous tin(II) chloride solution of 0.5 M and subsequently coated with silver by the chemical method in order to investigate the reasons behind the low reproducibility of the silver coating quality. The result of transmission measurements of the thickness of the films is presented in Figure 4.13. The deposition rate of the coating can be estimated from the slope of the linear fit and is around 5.4 nm/min which is larger than 4.5 nm/min previously determined on glass slides without pre-treatment [15]. It is important to note that the film thickness as a function of deposition time can only be approximated as linear within a small range of times. As the intercept of the linear fit does not pass through the origin, at the beginning of the reaction the film formation rate is larger, and it slows down with time. It is obvious from the Figure 4.13 that, even though the film thickness follows a linear trend in the range of times between 6 and 15 minutes, the faster deposition rate at the beginning of the reaction results in the formation of thicker films even for shorter reaction times of $6-7$ minutes than was used for F2 fibres. It is hypothesised that sensitisation of glass samples before silver coating speeds up the formation of the silver films, especially at the initial stages of the deposition due to binding of silver to Sn^{2+} on the surface of the substrates.

In order to analyse the effect of the thicker films on the quality of SPR response, silver coated glass slides were tested in the Kretschmann setup, shown in Figure 4.14. A right angle BK7 prism was positioned on a rotational stage and a silver coated glass slide was attached to the prism facet using index matching liquid. A linearly polarised HeNe laser was used as the excitation source.

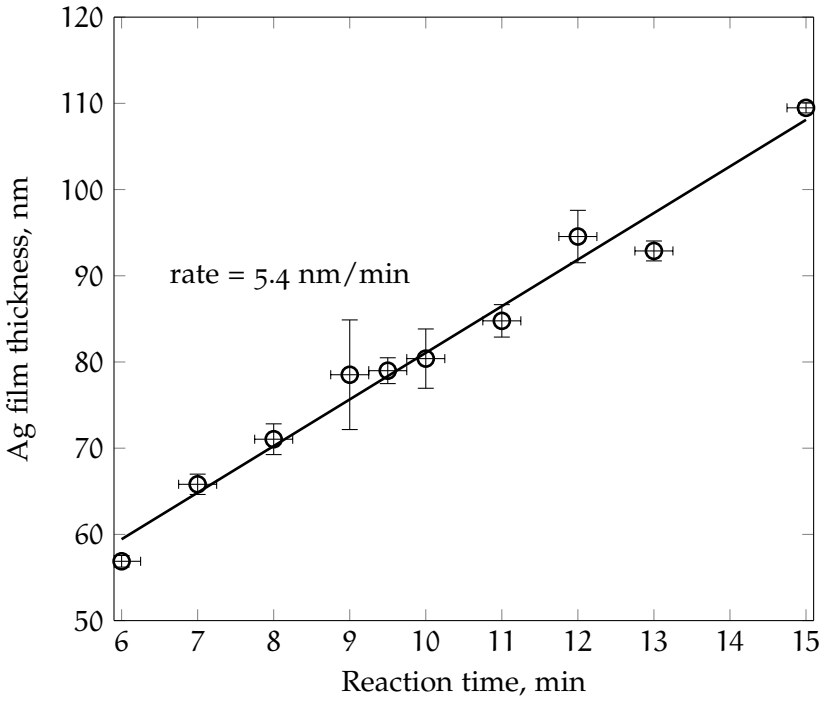


Figure 4.13: Thickness of silver films as a function of the Tollens deposition time at 26°C on planar substrates pre-treated with fresh aqueous $SnCl_2$ solution of 0.5 M. Each data point represents one glass slide, error bars are determined from 5 points on each samples. Slope of the linear fit gives a deposition rate of 5.4 nm/min. Coefficient of determination $R^2 = 0.9766$. Coating thickness is larger than optimal 50 nm even for shorter deposition times than was used with F2 fibres.

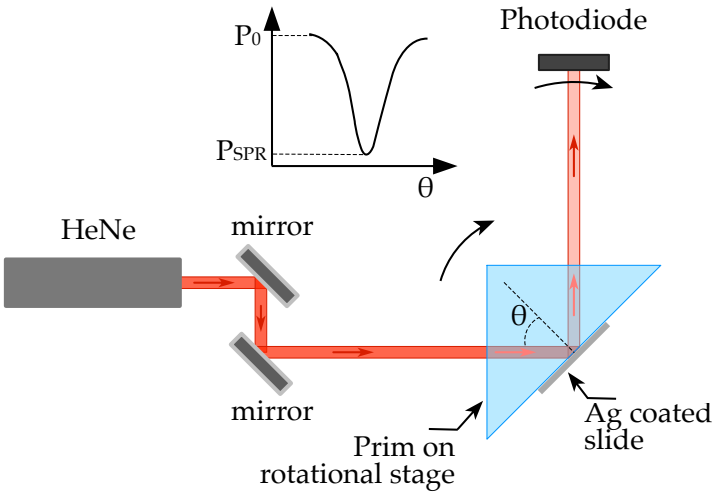


Figure 4.14: Schematic of the prism (Kretschmann) setup for SPR characterisation on planar substrates used to test silver coating quality.

SPR ratio is a measure of the magnitude of the dip of the reflected light and was calculated as a ratio of the minimum reflected power, P_{SPR}, and the maximum reflected power, P_0, as shown on the Figure 4.14. A good quality SPR ratio is low, with a significant drop of the reflected power at the resonance. However, the SPR ratios of the prepared films were too high, from 0.78 to 0.96, as summarised in the Table 4.3. For comparison, SPR ratios for thin silver coating prepared by sputtering

technique was estimated to be lower than 0.23. This is expected to be due to the increased thickness of the coatings, as well as presence of sensitiser residue left on the films after pre-treatment. Even though the RI sensitivity of the glass slides was not tested in the prism setup, the SPR ratio gave an estimation of the suitability of the silver coatings for SPR.

Table 4.3: SPR ratio for planar samples coated with silver films by the Tollens method at 26°C pre-treated with fresh aqueous $SnCl_2$ solution of 0.5 M. The sputtered sample is included for comparison.

Thickness, nm	Tollens time, min	SPR ratio
57	6	0.78
66	7	0.88
71	8	0.87
79	9	0.96
80	10	0.75
25	Sputtered	0.23

The analysis of the silver films indicated that thinner coatings needed to be prepared. The rate of the deposition of the silver during the reaction can be controlled by reaction time and temperature, therefore, both of the parameters were adjusted to produce thinner coatings. Figure 4.15 shows the results of the testing of the film thickness performed through transmission measurements on glass slides with silver coatings fabricated at 24°C with the same tin treatment (fresh aqueous $SnCl_2$ solution of 0.5 M).

The produced coatings were thinner as expected; lowering the temperature of the Tollens reaction resulted in lower deposition rate estimated at 4 nm/min. However, a large scatter of the measured thickness values versus reaction time was observed. This was likely to be due to the pre-treatment of samples with the tin sensitiser which resulted in uneven coverage of the nucleation tin ions on the surface as well as residues of the undissolved tin(II) chloride after rinsing, and therefore, inhomogeneous silver deposition. The SPR ratio analysed for these samples as a function of film thickness resulted in a large scatter of values, as presented on Figure 4.16.

These results indicate that the pre-treatment of the glass with stannous chloride indeed improved adhesion of the silver particles to the glass surface, as well as accelerated the deposition rate of the electroless plating. Reducing the deposition time or lowering the temperature during the coating process resulted in the desired reduction of the deposition rate and thinner coatings. However, slower deposition results in lower reproducibility of the film thickness. This is predicted to be a result of an uneven distribution of the tin ions on the surface after pre-treatment which was not as apparent for fast deposition rates, and/or due to deposition of insoluble $Sn(OH)_4$ particles, or attachment of undissolved $SnCl_2$ particles that contaminated the surface. The visual observation of the silver coating on the glass substrates also

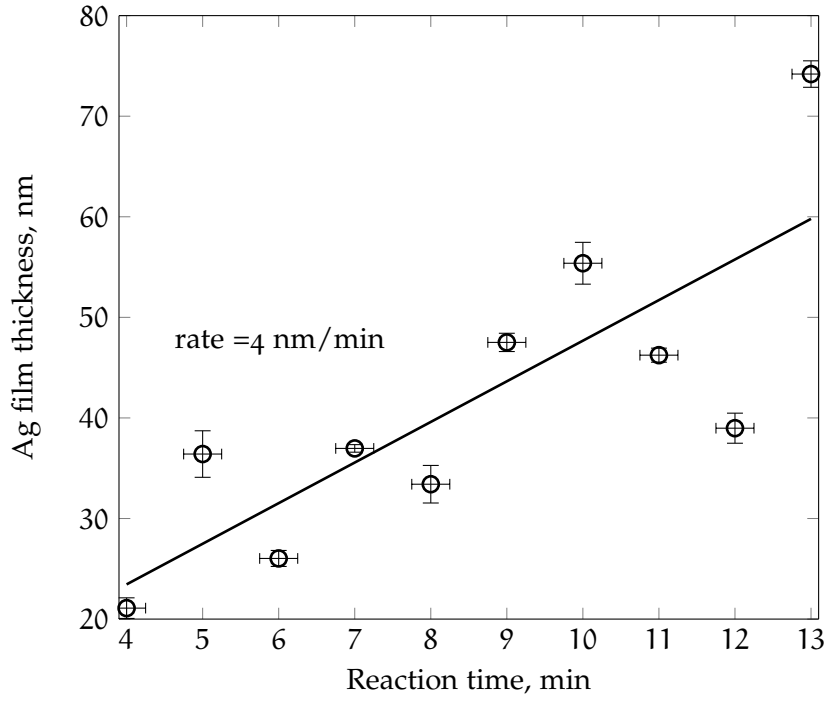


Figure 4.15: Thickness of silver films as a function of the Tollens deposition time at 24°C on planar substrates pre-treated with a fresh aqueous $SnCl_2$ solution of 0.5 M. Slope of the linear fit gives the deposition rate of 4 nm/min. Coefficient of determination of $R^2 = 0.6425$ shows poor linearity.

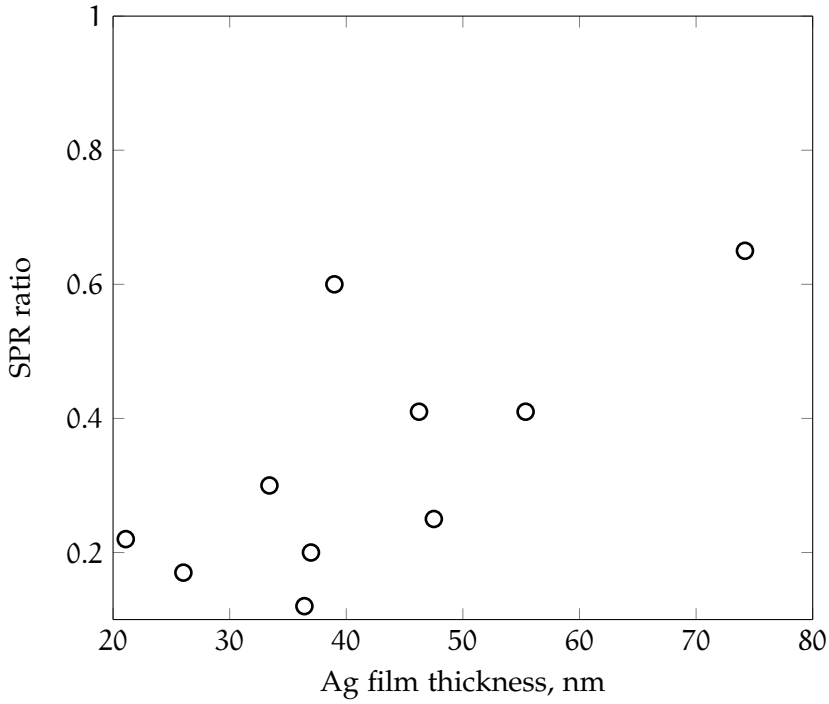


Figure 4.16: SPR ratio vs. silver films thickness prepared by Tollens method at 24°C on planar substrates pre-treated with a fresh aqueous $SnCl_2$ solution of 0.5 M. Large scatter of the data values indicates significant variation in the quality of the silver coating.

indicated the presence of residues on the surface and uneven reflectivity. Therefore, a study of different tin sensitising protocols wa undertaken.

Due to the partial insolubility of the $SnCl_2$ in water, the sensitiser was agitated during pre-treatment in order to avoid excessive deposition of the precipitate from the liquid phase onto the substrates. As was mentioned above, stannous chloride can be dissolved in HCl. Therefore, other protocols (also listed in Table 4.2) for preparation of the tin sensitising solutions were evaluated, including the use of HCl and solution ageing. The temperature of the reaction was kept at 24°C to achieve slower deposition rates.

Figure 4.17 shows silver film thickness as a function of Tollens reaction time for three different pre-treatments: aged 0.1 M solution of $SnCl_2$ in 0.1 M of hydrochloric acid; aged 0.1 M aqueous solution of $SnCl_2$; and fresh 0.1 M aqueous solution of $SnCl_2$ with the addition of 2% of hydrochloric acid (37%). The former two sensitisers were aged for approximately 20 hours in the dark at room temperature in full glass air tight containers, reducing the amount of air inside the container, and therefore, minimising oxidation. Figure 4.18 shows the measured SPR ratios as a function of silver film thickness for slides prepared with the three tin sensitising protocols.

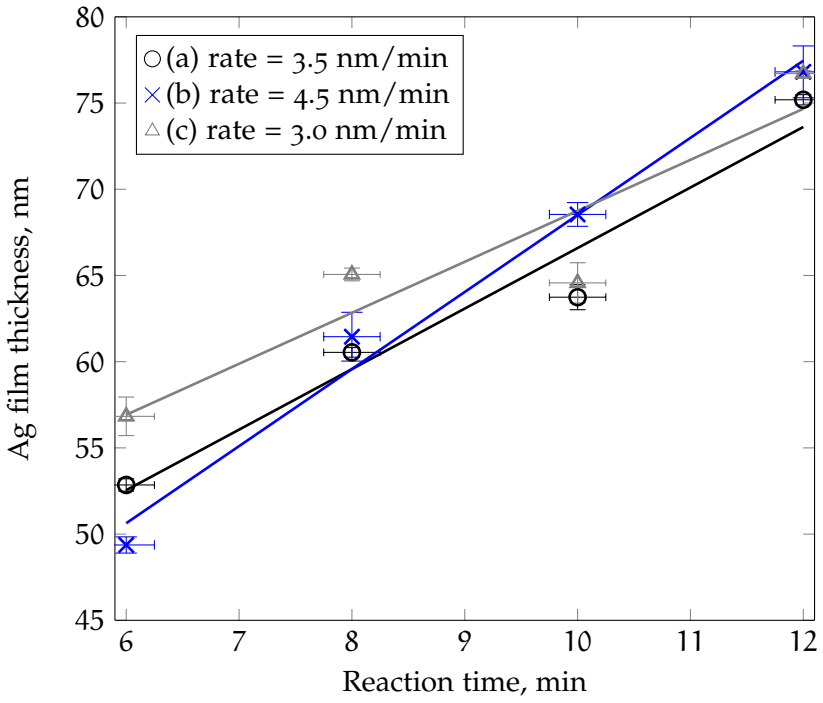


Figure 4.17: Thickness of silver films as a function of the Tollens deposition time at 24°C on planar substrates pre-treated with one of the three solutions of stannous chloride: (a) 20 h aged 0.1 M $SnCl_2$ in 0.1 M HCl; (b) 20 h aged 0.1 M aqueous $SnCl_2$; and (c) fresh aqueous 0.1 M $SnCl_2$ with 2%HCl. Slopes of the linear fits give the deposition rates as shown in legend with R^2 values for (a), (b), and (c) of 0.9549, 0.9863, and 0.868 respectively.

The deposition rates for the reaction at 24°C decreased, as expected, and the silver film thickness deposited in 6 minutes was estimated to be neat the optimum thickness of 50 nm. Analysis of the SPR ratios shows that the optimal film thickness of approximately 50 nm has the smallest SPR ratio, which corresponds to the

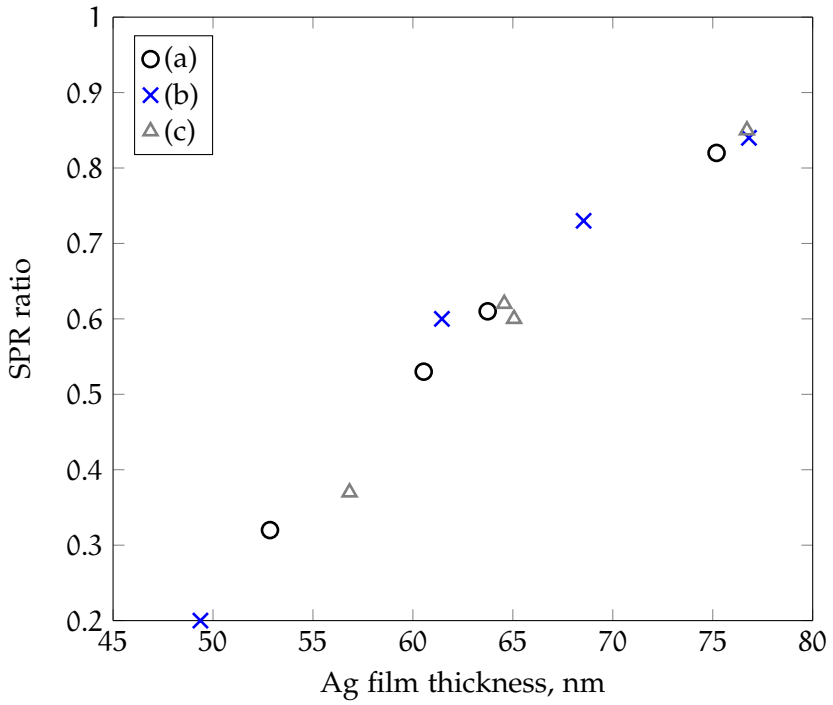


Figure 4.18: SPR ratio vs. silver films thickness prepared by Tollens method at 24°C on planar substrates pre-treated with three pre-treatments of stannous chloride: (a) 20 h aged 0.1M $SnCl_2$ in 0.1M HCl; (b) 20 h aged 0.1M aqueous $SnCl_2$; and (c) fresh aqueous 0.1M $SnCl_2$ with 2% of 1M HCl.

largest magnitude of the SPR response, and SPR ratios indeed increased with the silver film thickness. Other tin sensitiser recipes shown in Table 4.2 were studied and the results indicated that concentration of $SnCl_2$ between 0.1 M and 0.5 M or sensitisation time after 5 minutes did not have a significant effect on the resulting quality of the coatings. However, solution ageing and the addition of hydrochloric acid resulted in greater solubility of the solid stannous chloride which eliminated the necessity of agitating the solution during sensitisation and greatly reduced the presence of salt residues on the treated surfaces. When using this acidic aged sensitizing solution tin nucleation sites deposited on the substrates more homogeneously in comparison to fresh sensitising solutions, which had a significant effect on the quality of the plated silver films. The optimal ageing time was found to be between $10-30$ hours with longer times resulting in higher oxidation of the sensitiser. The three pre-treatment methods presented in Figure 4.17 and Figure 4.18 performed similarly with higher reproducibility achieved with 0.1 M $SnCl_2$ solution in 0.1 M hydrochloric acid aged for about 24 hours. Therefore, the subsequent silica surface treatment was performed using this method with the adjusted electroless plating time of 6 minutes.

4.5 SILICA FIBRE SENSOR CHARACTERISATION

4.5.1 *Experimental setup*

Once the fabrication procedure of the silver coating was optimised, the SPR silica fibre sensors were characterised. Performance characterisation of the silica fibre probes was performed using a similar optical setup as was used to characterise F2 fibres, however, the white LED light source (MCWHLP1) that was used with F2 fibres was not suitable due to the insufficient overlap between the light source spectrum and the SPR resonant wavelength of silica fibre sensors. The resonant wavelength of the silica SPR sensors was around 684 nm where the white LED had a significant drop in intensity in this range (Figure A.1 in Appendix A). Various white light sources with improved spectral overlap have been explored. These include a broadband LED source (Thorlabs, MBB1L3, Figure A.2), a halogen light source (Ocean Optics, HL-2000, Figure A.3), a Laser Driven Light Source (LDLS) (Energetiq Technology, EQ99-XFC-LDLS, Figure A.4), and a supercontinuum white light source (NKT Photonics, Koheras SuperK Compact, REF). It was found that the halogen light source HL-2000 and the broadband LED source did not provide sufficient optical power for the low SNR scattered light measurements.

The LDLS as well as the supercontinuum source have a relatively flat spectrum over the range of wavelengths of interest between 600 and 800 nm (Figure A.4), and provided equally good results for SPR excitation in silica fibre sensors. The supercontinuum white light source (Koheras SuperK Compact) was used for the duration of the project as it provided higher coupling efficiency in comparison with the highly divergent LED. A schematic of the optical setup used for characterisation of SPR silica fibre sensors is presented in Figure 4.19. Light from the fibre-coupled supercontinuum source was reflected from two mirrors to facilitate alignment into the SPR probe. A photograph of the setup is shown in Figure 4.20. A cross sectional flow cell with an inlet and an outlet for the sample flow and a sensing region inside was positioned underneath the scattered light collection apparatus as shown in Figure 4.21.

In addition to the choice of the light source for SPR excitation, a modification of optical setup and coupling optimisation was studied. In particular, it was predicted that coupling of light into the fibre probe may effect the sensor performance. Two coupling conditions have been tested: the maximisation of power of the transmitted light through the fibre probe, and the maximisation of the intensity of the scattered light. The former was achieved by measuring the power of the transmitted light at the end of the fibre with a power meter, and the latter, by maximising the intensity of the peak of the collected scattered light analysed by the compact spectrometer. Even though the two methods did not provide the same coupling conditions, the SPR performance was not affected by either of the two coupling methods. Therefore, to simplify the apparatus, coupling was optimised by maximising the intensity of the scattered signal with the spectrometer.

In addition to these coupling configurations, coupling of light into a SPR fibre probe through a SMF (Corning, SMF28) was tested. It was predicted that if fewer guided modes would propagate in the fibre, less modes would satisfy the SPR res-

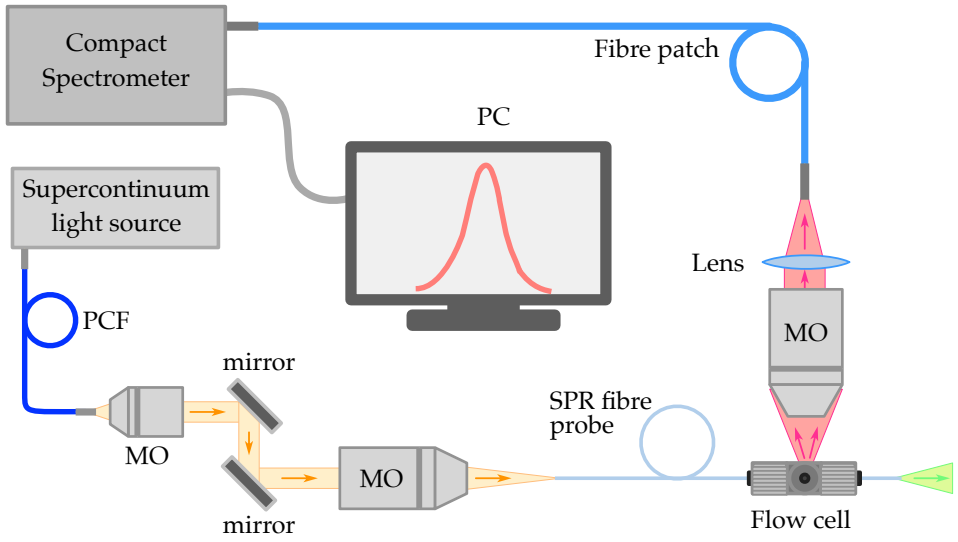


Figure 4.19: Schematic of the optical setup for silica fibre SPR sensor characterisation. MO - microscope objective, PCF - photonic crystal fibre.

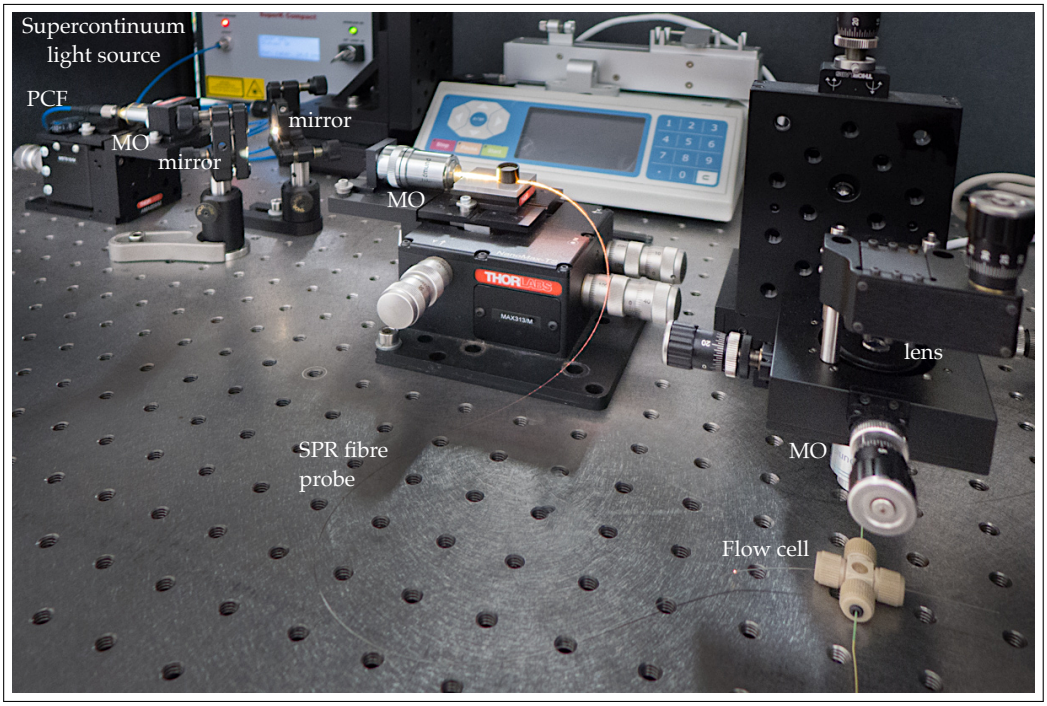


Figure 4.20: Optical setup for SPR fibre sensor characterisation. From left to right: a beam from a fibre-coupled supercontinuum white light source is reflected from two mirrors and is coupled to a SPR fibre probe with $\times 40$ microscope objective. Sensing region of the SPR fibre probe is enclosed in a cross-sectional flow cell with a transparent window from where scattered radiation is collected using a collection apparatus consisting of a $\times 20$ microscope objective, converging lens and a patch fibre (not visible on the photo) which is connected to a compact spectrometer (not on the photo).

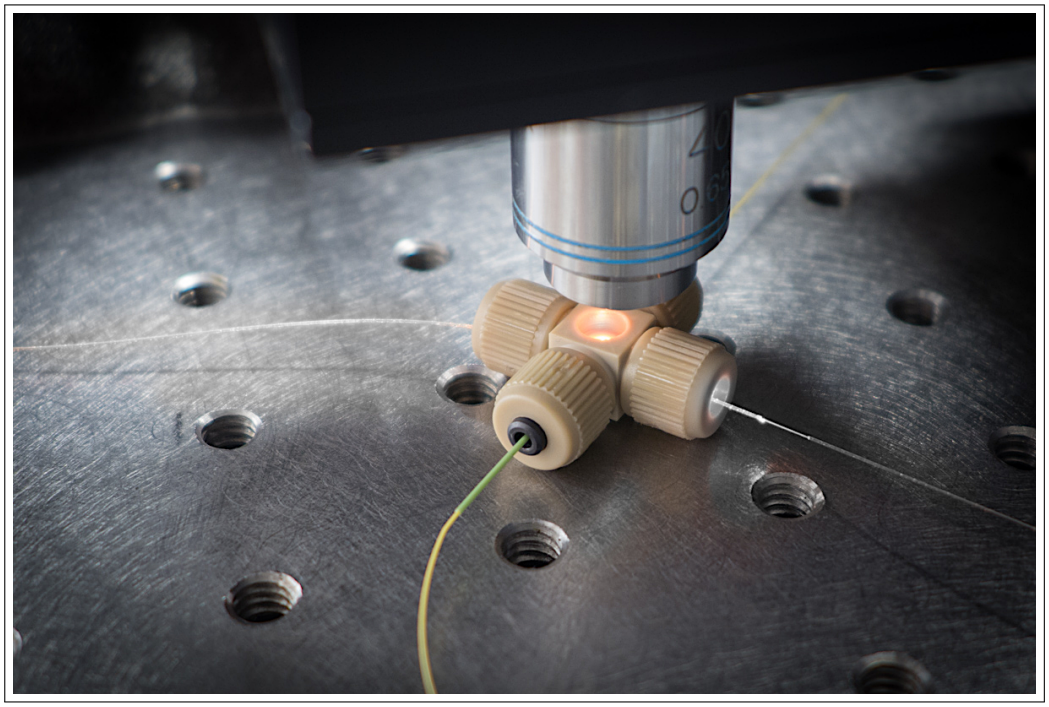


Figure 4.21: Close up of a cross sectional flow cell with SPR fibre probe (left to right), an inlet (bottom) and outlet (top).

onant condition and the linewidth of the SPR response would be reduced. Even thought SMF28 does not operate in the single mode regime in the visible part of the spectrum, it supports significantly fewer modes than the highly MMF used for SPR probes. A piece of SMF28 of around 1 meter long was inserted between the coupling microscope objective and the SPR silica fibre probe. The light was coupled into the SMF28, then butt-coupled into the SPR fibre probe. The SPR sensor performance was characterised in the new setup, however, no significant difference was found when compared to the direct coupling of light into the SPR fibre probe. This is likely to be due to the length of the SPR fibre probe as well as bending which results in coupling of the propagating modes inside a highly MMF with higher order modes producing essentially the same output independent of the mode input coupling. In addition, the amount of scattered light has been reduced due to the mismatch in the NA of the butt-coupled fibres. Therefore, to minimise the complexity of the optical setup, direct coupling into the SPR fibre probe was used.

4.5.2 *Performance characterisation*

Experimental procedure

To characterise the silica fibre SPR probes, a serial dilution of glycerol in water was used as the external dielectric medium. A procedure similar to that used for the F2 fibre sensors was employed to determine the sensitivity of the new sensors from the wavelength shifts caused by a known change in the glycerol solution's RI. An example of the raw scattered spectra obtained from a silica based SPR sensor is shown in Figure 4.22 with the supercontinuum light source used for plasmon excitation.

The raw spectral data appears noisy due to variations in the intensity of the light source which can be compensated by averaging multiple readings on the spectrometer and applying smoothing at the data processing stage. Figure 4.23 shows the same spectra after background removal, normalisation, and local regression smoothing. The sensitivity curve for the sensor, resonant wavelength shift as a function of glycerol solutions' RI, is presented in Figure 4.24. Sensitivity curve for the sensor, resonant wavelength shift as a function of glycerol solution RI is presented in Figure 4.24.

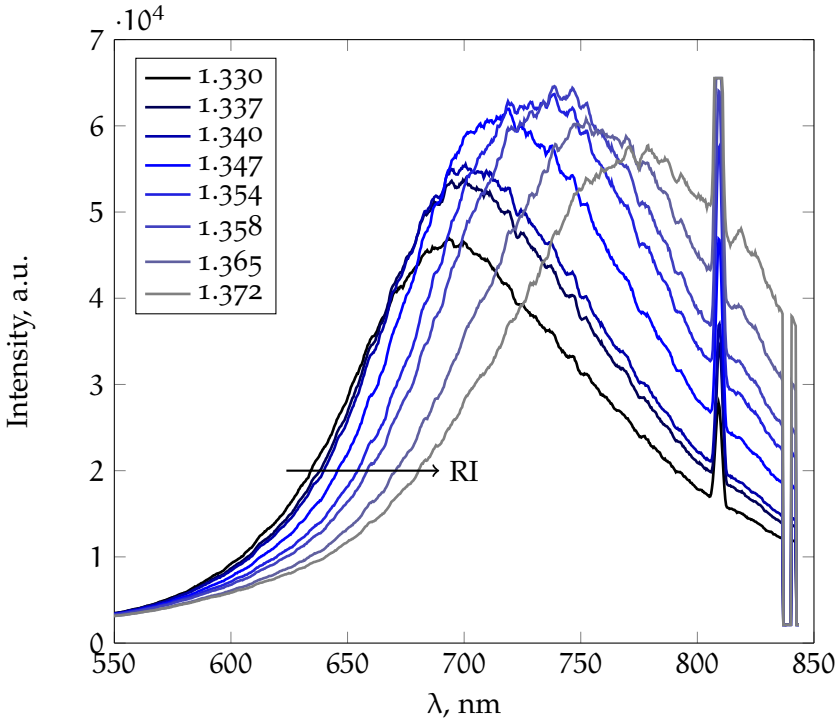


Figure 4.22: Raw SPR spectra for the SiO_2 fibre sensor collected at varying RI of the external dielectric (aqueous solutions of glycerol). Excitation using Koheras SuperK Compact supercontinuum light source. The peak around 800 nm is the pump source for the supercontinuum source and is not related to SPR.

Scattered spectra were recorded for each sample's RI and for the intermediate water rinsing steps to ensure thorough removal of the previous sample and facilitate the analysis of experimental errors, as described below. Figure 4.25 shows experimental steps for characterisation of the silica fibre SPR sensor performance. Here, each subsequent glycerol concentration is followed by a water rinsing step. The deviations of the resonant wavelength of each water rinsing step from the initial value for water was used to estimate the experimental errors. This drift is likely caused by changes in alignment of the sensing region under the collection apparatus as the SPR spectrum is highly sensitive to location along the sensing region, as well as coupling light into the fibre.

To consider both performance identifying parameters, sensitivity and FWHM, a FOM was evaluated. It was defined as the ratio between the sensitivity of a sensor and the average FWHM of SPR response curves (FOM= $S_\lambda/\Delta\lambda_{0.5}$). To compare the different light sources and coupling conditions, the height of each SPR peak was measured with a constant integration time. Often in literature, another perform-

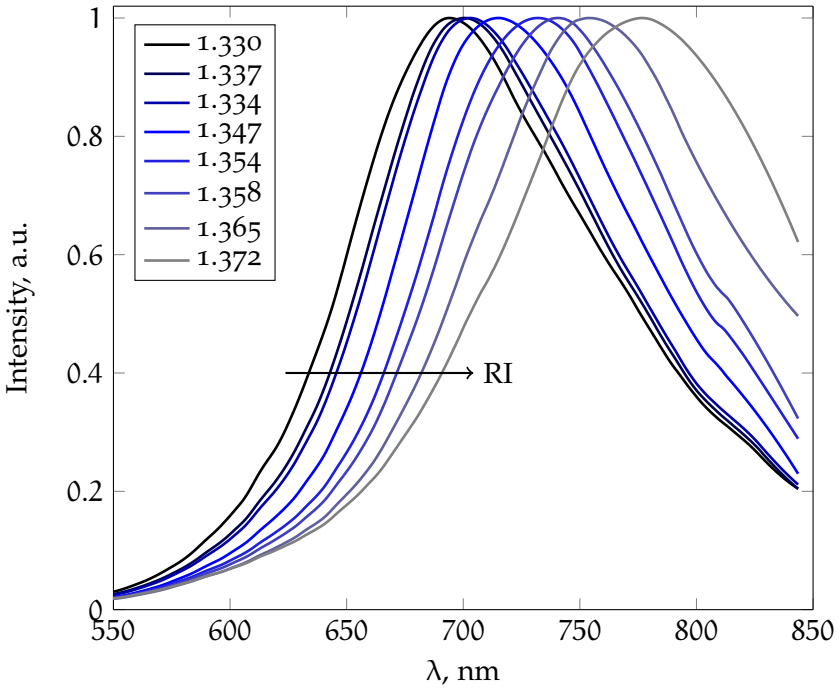


Figure 4.23: Processed SPR spectra (normalised and filtered) for SiO_2 fibre sensor collected at varying RI of external dielectric (aqueous solutions of glycerol). Techniques used to process the raw spectral data are described in subsection "Data analysis" below.

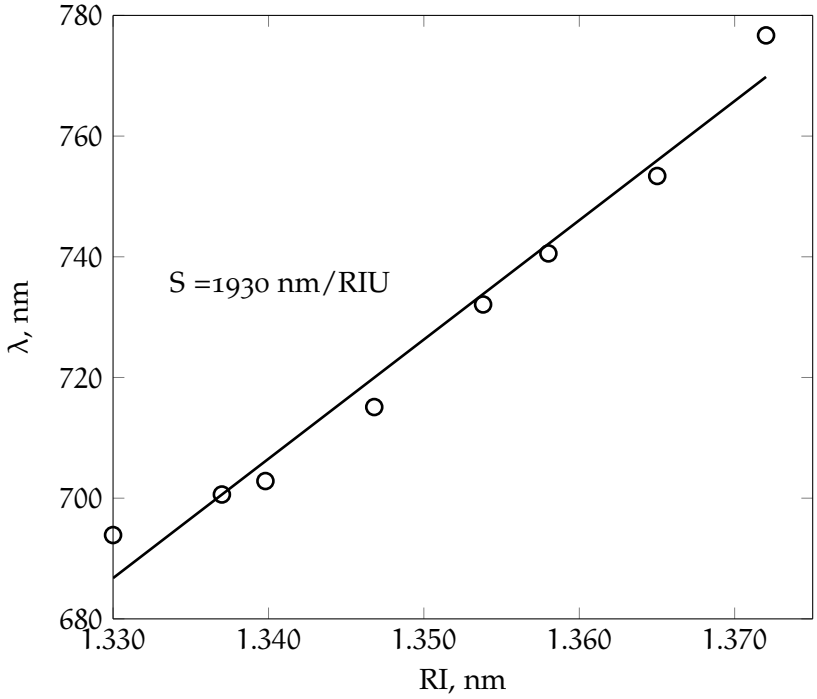


Figure 4.24: Sensitivity curve for SiO_2 fibre sensor characterised using aqueous solutions of glycerol.

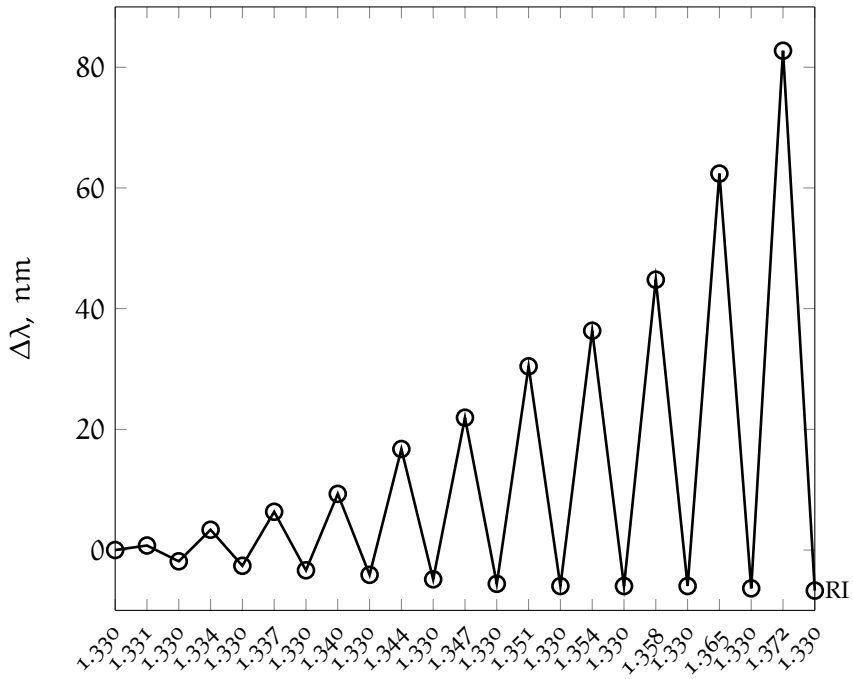


Figure 4.25: Steps of the characterisation experiment for SiO_2 fibre sensor: cumulative wavelength shift at each RI of external dielectric (aqueous solutions of glycerol) with intermediate water rinsing steps.

ance parameter, quality factor (Qfactor) is considered, which is defined as the ratio between the height of the spectral feature, and its FWHM. SNR for each sensor was calculated as the mean of the squared signal amplitude divided by the mean of the squared noise amplitude for each data point averaged over all SPR peaks for each sample's RI. The sensitivity and FWHM of the silica sensor, with uncertainty estimates and other performance parameters, are presented in Figure 4.26, corresponding to the spectra presented in Figure 4.22 and Figure 4.23 .

Data analysis

Analysis of all spectral data was performed in Matlab. Similarly to the F2 fibres, a typical analysis of the spectral data for the silica SPR sensor characterisation consisted of subtracting the background, normalisation, and smoothing with local regression using weighted linear least squares and a second degree polynomial model. Positions of the maxima were then found which correspond to the resonant wavelength for each RI of the external dielectric. Another method of data processing was fitting the spectral data with a Gaussian function and determining the maximum of the fit to find the value of the resonant wavelength. The wavelength shift with respect to the change in the RI of the external dielectric was then plotted and the slope of the linear fit of the curve was considered as the sensor's sensitivity value. The FWHM was found from the Gaussian fit for each peak as $2\sqrt{-2\ln(0.5)}\sigma$, σ being the square root of the variance. The mean of values for every RI of the sample was taken as the FWHM for a sensor. Local regression and Gaussian fit provided same sensitivity values within uncertainty estimates. Gaussian fitting was preferable when determining the FWHM of a sensor as it allowed finding the FWHM

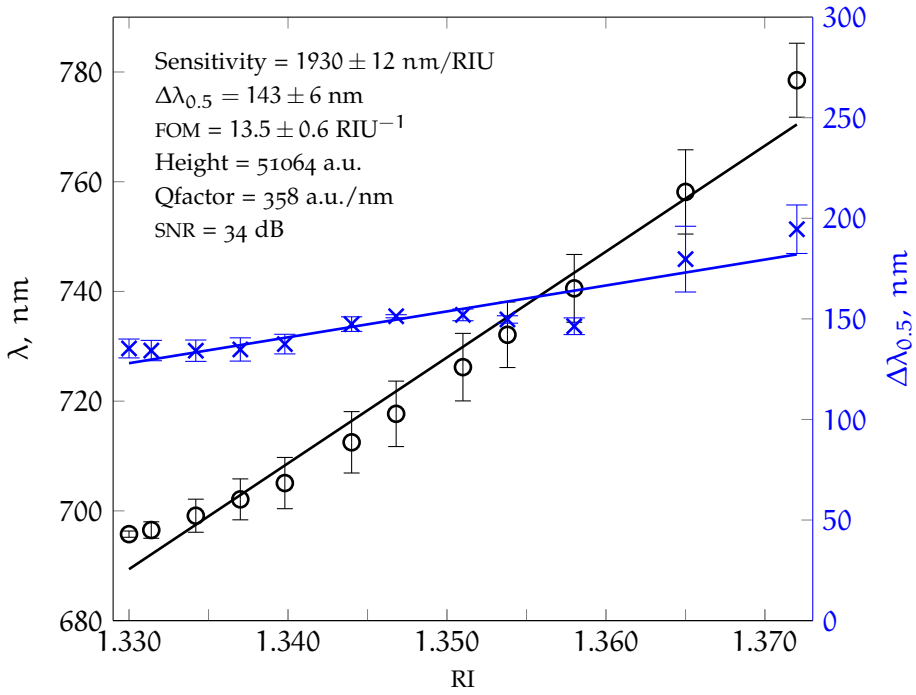


Figure 4.26: Sensitivity (black circles) and FWHM (blue crosses) for a SiO_2 fibre sensor characterised using aqueous solutions of glycerol. Experimental and fitting errors are shown as error bars. Maximum absolute uncertainty in RI of glycerol solutions is 0.001.

through the fit parameters. Another data processing method that was explored to analyse the sensitivity was cross-correlation. This method measures similarity of two spectral features as a function of the lag between them. This method, however, was found to slightly underestimate spectral shifts, relative to the other described methods, as shapes of the subsequent peaks in the series of data was not completely identical.

To determine the errors in the resonant wavelength shift and the FWHM, the experimental errors and data processing uncertainties were added. Water rinsing steps were used to estimate experimental errors. In particular, the sum of deviations of the position of a peak at rising steps before and after each glycerol concentration from the original step for water was considered an experimental uncertainty. Those errors mainly come from a change in coupling conditions due to a stage drift or a fibre movement, and a change in the alignment of the sensing region under the collection setup during the experiment. Errors in the refractive indices of the prepared glycerol solutions were calculated as a sum of the uncertainties in the solution RI due to thermal fluctuations, spectral dispersion, and preparation of the serial dilutions of glycerol.

To estimate the data processing errors for Gaussian fitting of the experimental data, a threshold parameter, that is a fraction from the maximum height of a peak where data for the fit has been taken from, was used. Errors in the fit for a peak wavelength and FWHM were estimated as the scatter of the values (standard deviations) of the three different fits: a broad fit that considers larger number of points around the maxima, a narrow fit with less number of points, and a fit between

those two at which all of the parameters (S_λ, FWHM, height, and FOM) were evaluated. Overall, experimental and data processing errors for sensitivity and FWHM did not exceed 4.2% and were typically around 3.5%.

Performance comparison of silica and F2 SPR fibre probes

Performance of the silica fibre based SPR sensors was compared to the lead silicate based probes. In agreement with theoretical modelling, the sensitivity of sensors based on silica fibre was increased compared to the F2 fibres. The experimental increase in the sensitivity was a factor of 3.8, which is comparable to the sensitivity improvement of 4.0-fold predicted by theoretical modelling. The FWHM of the silica sensors, however, was also increased, by approximately 50 nm (or 44%) compared to the F2 fibre. This increase was also expected and is a known trade off when lower refractive index glasses are used for SPR excitation.

The height of the peaks and, therefore, quality factors, are performance characteristics that are less relevant for characterisation of the intrinsic sensor performances as they are mostly dependent on the light source and integration time of the spectrometer. The SNR depends on the platform configuration, the light source, as well as the collection apparatus, and was found to be around 34 dB for both, the silica and lead silicate SPR sensors.

A summary of major performance characteristics for the silica and F2 fibre sensors based on the experimental studies and theoretical modelling are presented in Table 4.4. The values of sensitivity and FWHM are mean values obtained from analysing $11-20$ sensors prepared throughout the project with uncertainties shown as standard deviations.

Table 4.4: Performance comparison of lead silicate (F2) and fused silica (F300) SPR fibre sensors; experimental results and theoretically predicted data.

Fibre	Experimental				Theoretical			
	S_λ, nm/RIU	$\Delta\lambda_{0.5}$, nm	FOM, RIU^{-1}	λ_{res}, nm	S_λ, nm/RIU	$\Delta\lambda_{0.5}$, nm	FOM, RIU^{-1}	λ_{res}, nm
F2	485±78	112±14	4.3±1.2	559±13	868	100	8.7	440
F300	1827±218	161±24	11.3±3.0	684±15	3470	200	17.3	580

Comparison of the experimental results for the two fibres with the theoretical modelling, suggests that the sensitivity and FWHM for both sensors as well as the resonant wavelength are not matched with the theoretically predicted values within the conservative uncertainty estimates. The observed resonant wavelength is around 100 nm longer than that predicted by theoretical modelling. These discrepancies can be attributed to the assumptions that the modelling was based on, such as the perfect smoothness of the silver film, or the idealised dielectric function of silver, for example.

It has previously been demonstrated that in the presence of surface roughness, SPs are attenuated by two main processes: radiation into free space, and scattering into other SPP states; the former is believed to be responsible for increasing the spectral width of the resonant curve, and the latter leads to a resonant curve shift [255].

Previous experiments have also demonstrated that the effective dielectric functions of rough metal films and SP wavevectors change tremendously under the influence of an increase in the roughness amplitude [256]. This was verified by testing a silica fibre samples with silver coatings fabricated by the sputtering technique. The sensitivity of the sputtered fibre probe was found to be similar to silica fibre sensors with chemically deposited silver film. The FWHM, however, was smaller, 85 nm, and the resonant wavelength was matched with the theoretically predicted value of 580 nm in water.

In addition to the presence of surface roughness, the metal film prepared by chemical deposition could have a different dielectric function to that of silver modelled by the Lorentz-Drude model. Furthermore, thin silver films have a different dielectric function than bulk metals, this was not taken into account in the theoretical modelling. Moreover, it is difficult to take into account the oxidation of silver films that is inevitable during the experiments and will be discussed in the following section. These considerations may explain the discrepancies between the experimental and theoretical values of the performance characteristics for the studied SPR sensor. Nevertheless, silica outperformed F2 fibre SPR sensor in terms of sensitivity. Larger spectral width, and the red-shift of the resonance wavelength also qualitatively follow the predictions. Moreover, FOM of the silica SPR sensors exceeded that of F2 sensors by the factor of 2.6 which is close to the theoretically estimated improvement.

Sensor degradation test

To evaluate the effect of silver film oxidation on the performance of the sensors, sensor degradation tests have been performed. Fibre sensors were typically prepared in batches of $8-10$ in order to minimise the required time for fabrication per sensor. It was observed that the storage of the sensors in air quickly resulted in oxidation of the silver film, typically in the order of two days depending on the environmental conditions of the room, leading to drastic degradation of the performance. To prolong the sensors' shelf life, they were stored inside a vacuum desiccator with silica gel, minimising moisture and oxygen concentration inside the container. In these conditions, the sensors showed a reasonably good shelf life, typically up to several weeks with performance degradation estimated down to 10%.

The degradation of the silver coating was estimated in an aqueous environment to which the sensors are typically exposed during routine biosensing applications. The testing was performed by flushing a Phosphate-Buffered Saline (PBS) solution through a flow cell with the sensor at a rate of 10 $\mu L/min$, and measuring the sensitivity with glycerol solutions at various times. The degradation of the sensor's sensitivity was found to drop down to 15% of original sensitivity within 2.5 hours of the experiment, which was considered to be time required for a detection of simple biomolecules, including the required surface functionalisation steps. This decrease in the sensor performance is acceptable for a demonstration of the sensing platform, but could be improved with the use of protective anti-oxidation coating, such as MF_2, on top of the silver film, if commercial applications are required. It is important to note that the characterised sensor sensitivity is an intrinsic performance

of the bare sensor, and surface functionalisation required for a particular application will affect the performance parameters resulting in a decrease in the effective surface sensitivity.

Scattering vs. transmission measurements

Finally, the scattered light based measurements of the SPR silica fibre sensor were compared to the conventional transmission measurement techniques. Figure 4.27 shows SPR scattered spectra collected above the sensing region fabricated on a silica MMF for different RIs of external dielectric. Transmission spectra from the same fibre is presented in Figure 4.28.

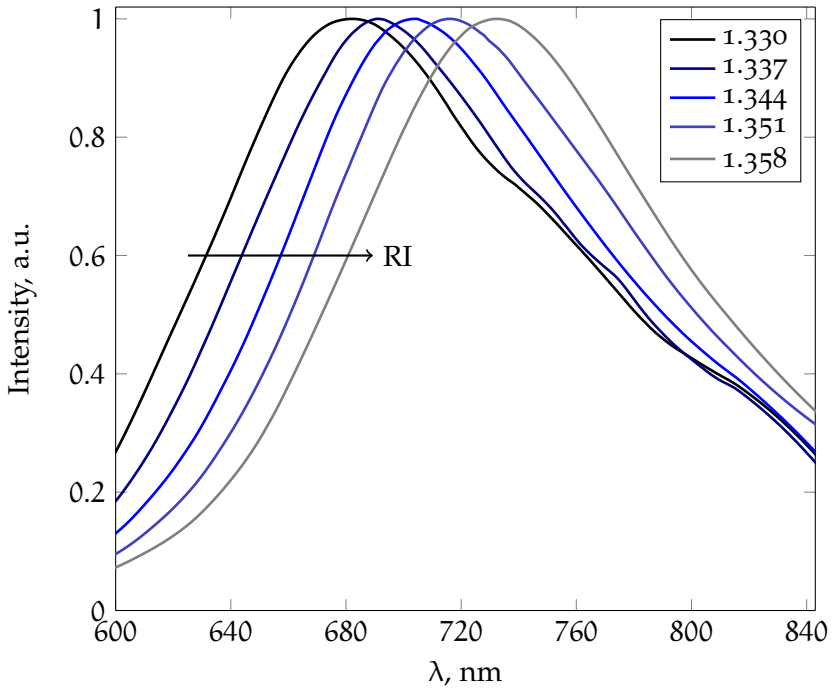


Figure 4.27: Scattered SPR spectra (normalised and filtered) for a SiO_2 fibre sensor collected at varying RI of external dielectric (aqueous solutions of glycerol).

It is clear from the comparison of the two methods that the position of the resonance can be determined using both of interrogation techniques. However, the scattered spectra have a much smaller linewidth in comparison to the transmitted spectra, where the absorption valley broadens significantly as the sample RI increases. This illustrates the major advantage of the scattering based SPR architecture, as more precise measurements of the wavelength shift could be obtained providing better spectral resolution of the sensing platform.

4.5.3 *Tapered silica fibre SPR probes*

The improved sensitivity of the silica based fibre sensors showed that the new probes have a high potential for applications where small RI changes need to be detected. However, the increased spectral linewidth of the SPR response can restrict the resolution, and therefore, the detection limit of the device. SPR sensors based on SMFs or few-mode fibres typically have a narrower response, which is believed

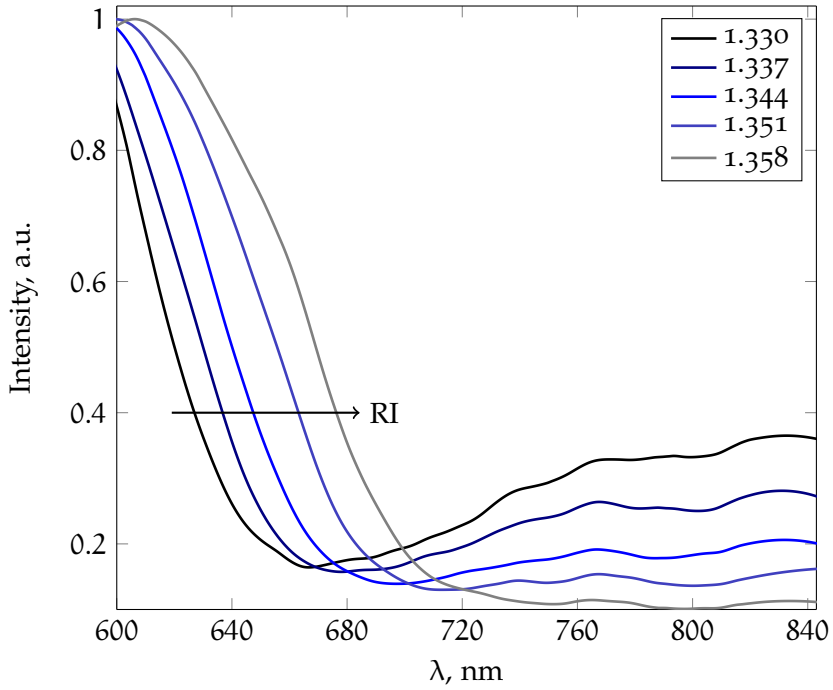


Figure 4.28: Transmitted SPR spectra (normalised and filtered) for SiO_2 fibre sensor collected at varying RI of external dielectric (aqueous solutions of glycerol). Data for the same sample as in Figure 4.27 is presented.

to be due to smaller number of modes that excite SPs [124]. Therefore, it was predicted that using fibres with smaller cores will provide an advantage in terms of the reduced spectral linewidth. In order to investigate this further, silica fibres were tapered with a range of taper waist diameters. Tapering was performed using a glass processing platform (Vytran, GPX300 Series). Samples of 100, 70, and 35 µm taper waist diameters and 5 mm taper waist lengths were prepared from 140 µm fused silica fibre. Uniform tapered waists of the probes were then coated with silver by a chemical deposition technique.

Tapered SPR probes were characterised and their performance compared with standard 140 µm-core fibre sensors. The result of the performance comparison is presented in Table 4.5. However, no improvement in the linewidth was observed in the range of the core diameters studied. This is assumed to be due to the smallest taper of 35 µm diameter still being a highly multi-mode fibre with thousands of guided modes that satisfy the resonant condition, which results in a broader spectral response, similar to that achieved with not tapered fibre sensors. An effort was made to fabricate smaller waist diameter tapers, however, it was found to be impractical due to drastic fragility of the probes when exposed to the Tollens coating conditions, which resulted in a very low yield of successful samples.

The differences between large core fibre samples and tapered probes were the reduced height of the spectral feature and reduced SNR. An example of the raw spectra for not tapered and 35 µm tapered probes is shown in Figure 4.29. This lower intensity of the scattered signal and the presence of spikes in the spectra can be attributed to the smaller surface area over which the scattered signal is integrated. The small increase in the SNR should not significantly affect the data processing,

Table 4.5: Performance comparison of tapered (100, 70, and 35 μm taper waist diameters), and not tapered (140 μm core diameter) silica SPR fibre probes.

Performance	Taper diameter, μm			
characteristic	140	100	70	35
Sensitivity, nm/RIU	1827 ± 218	1468 ± 135	1558 ± 323	1619 ± 179
FWHM, nm	161 ± 24	145 ± 9	145 ± 5	160 ± 14

however, might became an issue when even smaller core fibres are used. The prepared tapered fibres did not show notable improvement in the sensor performance, which is believed to be due to the large taper waist diameters. SPR sensors based on SMFs, small tapers and MOFs with small cores, down to 10 μm, were reported to have narrower SPR response [116, 257]. Therefore, using smaller core fibres is a promising approach if the fragility issues can be overcome.

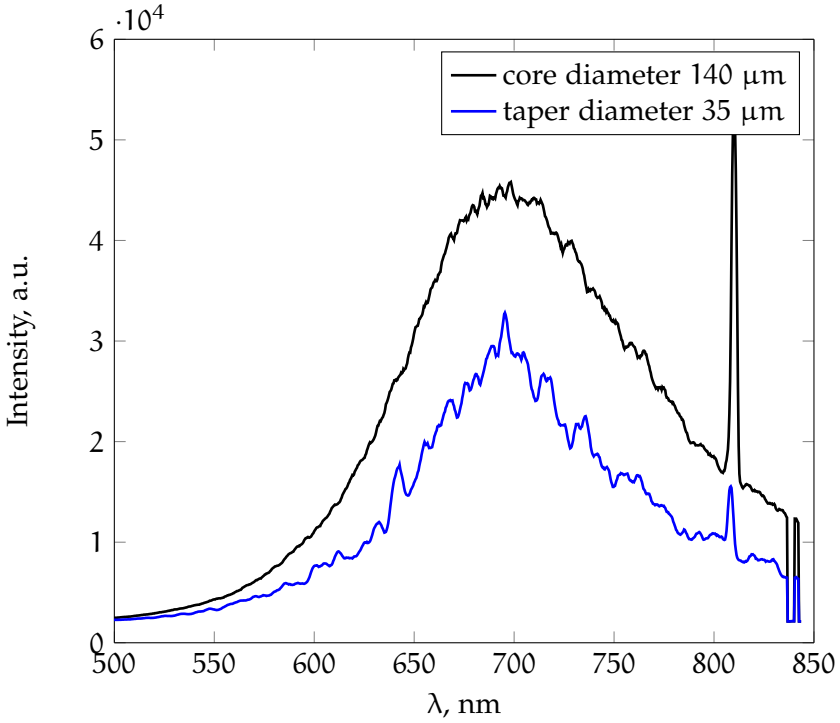


Figure 4.29: Raw SPR spectra for SiO_2 fibre sensors: a fibre probe of 140 μm core diameter (black) and a tapered fibre of 35 μm taper waist diameter (blue). Excitation of SPR using Supercontinuum light source. Integration time of the spectrometer is 100 msec for both samples.

4.6 BIOSENSING APPLICATIONS

The primary purpose of the developed sensing platform is for biological applications, hence, it is important to test the capabilities of the improved SPR sensing probe based on silica fibre for the detection of biological targets.

Biosensing is a promising tool for healthcare and food safety that offers significant advantages in comparison with traditional detection and diagnostic techniques. Conventional analytical methods such as cell culture [258], microscopy [259, 260],

immunoassay based methods [261], and various Polymerase Chain Reaction (PCR) techniques [262], have been successfully used in pathogen detection for several decades. However, most of these methods require significant time (sometimes up to several days) for diagnosis to be made. Furthermore, such laboratory based methods are often labour intensive which makes them unsuitable for rapid in-field detection. Moreover, special skills are required for performing detection with traditional analytical techniques and there is often a need for large quantities of samples and bioreceptors resulting in additional costs.

SPR biosensing offers a range of significant benefits in comparison to traditionally used methods for pathogen detection (PCR and Enzyme-Linked Immunosorbent Assay (ELISA)), as well as with other biosensing techniques, such as fluorescence, and electrochemical biosensors. Those advantages are a lower volume of biological materials (sample and bioreceptors) required, rapid testing, miniaturisation, absence of labels, low detection limit, and ease of fabrication and use. Kretschmann SPR configuration has successfully been used as a commercial biosensing tool, however due the bulky prism design and reliance on high quality gold coated sensors, the commercial instruments are large and consumables are expensive. Capability of the developed SPR fibre sensing platform for biosensing applications was studied with the detection of Norovirus (NoV) chosen as a primary focus.

4.6.1 *Surface functionalisation strategy*

In order to prepare the sensor surface for capturing biological molecules, it needs to be functionalised with bioreceptors. Surface functionalisation is an important aspect in biosensing that influences the performance of the biosensor. A poor functionalisation of the surface results in a low surface density of bioreceptors or random orientation of the bioreceptor molecules that leads to their low bio- functionality and reduced surface coverage of the captured target molecules, and poor binding affinity. Another important consideration is non-specific binding of the target species to the surface of the sensor which can be prevented by a choice of surface functionalisation techniques.

The two major mechanisms of sensor surface functionalisation is covalent binding and physical adsorption [263]. Covalent binding implies the utilisation of chemical groups to create a covalent bond between the sensor surface and immobilised molecules. Hydroxyl groups (OH) on the surface of oxides, such as silica, some polymers and metals, are commonly used to create covalent bonds. Typical binding chemistries for OH group bonding include phosphonates, carboxylates, amines, and silanes [263]. Other common chemistries include carboxymethylated dextran and thiol reactions [264]. Thiols can be adsorbed from solution onto gold or silver surfaces forming oriented self-assembled monolayer films. The sensor surface with thiol groups can then bind a ligand which is modified to have active disulphide groups. Due to the nature of the covalent binding surface functionalisation strategy, the technique is highly dependent on the intrinsic surface chemistry of the sensing platform.

An alternative approach to covalent bonding is physical adsorption, a technique that does not rely on the surface chemistry of the sensor surface, and therefore, can be used on any surface. One common method of physical adsorption is attachment of charged polymers in solutions, called Polyelectrolytes (PEs) [265]. The surface of the sensor can be prepared by layer-by-layer adsorption of positively and negatively charged PE layers, Poly(Allylamine Hydrochloride) (PAH) and Poly(Sodium 4-Styrenesulfonate) (PSS) respectively. Attachment of PE layers provides reactive groups that can subsequently be utilised to immobilise antibodies in a standard immunoassay [44]. Unlike covalent binding surface functionalisation strategies, the PE multilayer technique relies only on the electrostatic forces and can be deposited on any surface. In addition, the technique allows for a simple and reproducible surface functionalisation process without involving the plasma activation or acid cleaning that are often required for covalent binding methods. For these reasons, the PE surface functionalisation technique was chosen for the sensor surface preparation and further attachment of bioreceptor molecules onto the SPR fibre probe.

Streptavidin and neutravidin are large proteins from the avidin family that have an extraordinarily high affinity for biotin, a molecule known as vitamin B7 or vitamin H. The binding of streptavidin or neutravidin to biotin is one of the strongest non-covalent interactions known in nature [266], and therefore, streptavidin-biotin complex is highly resistant to organic solvents, detergents, enzymes, and harsh temperatures and pH factors. For these reasons, streptavidin-biotin or neutravidin-biotin interaction is extensively used in molecular biology [266]. Biotin can be immobilised to the reactive amino groups of PEs on the sensor surface with subsequent attachment of neutravidin. Specific biotinylated antibodies can then be immobilised onto the neutravidin layer. This approach allows a particular antibody orientation on the surface, favourable for the capture of target molecules [267].

Non-specific binding is a common concern for label free sensing technologies. Casein has been successfully used to limit non-specific binding in complex biological samples [261]. The blocking solution can be applied after antibody attachment to passivate any exposed sites that can cause binding of non-target molecules from the solution.

4.6.2 *Norovirus (NoV) detection*

NoV is a human pathogen that contaminates oysters and other shellfish, and is the most common cause of viral gastroenteritis in humans with adverse symptoms. The importance of early detection of NoV infection cannot be overestimated due to its high infectivity, generic but severe symptoms associated with virus invasion, and unavailability of immunisation [268]. More importantly, sensitivity of the detection of NoV has to be high due to the very low dose (estimated to be 18 infectious particles) needed to cause the infection [2]. In addition, it is difficult to grow NoV in cell culture which makes it very hard to study and detect [269].

NoVs are single stranded RNA, non-enveloped viruses with high genome diversity. Current laboratory methods for NoV detection include PCR and ELISA. However, no custom built fibre SPR biosensor tailored specifically for NoV has been developed to

the extent of our knowledge. Commercial SPR instruments (Biacore, GE Healthcare) have been employed to study NoVs [270–272]. However, a reported detection limit of approximately $10^6 - 10^7$ viral particles [272] is not low enough for detection of an infectious dose ($10 - 100$ particles).

The biological part of the project was carried out using the capabilities of the South Australian Research and Development Institute (SARDI). Biological materials required for the research, such as proteins, antibodies, and Virus Like Particles (VLPs), were provided by the collaborators. SARDI also provided expertise for the development of the biorecognition principles. In order to avoid potential contamination, NoV VLPs were used instead of infectious viral samples. VLPs are essentially non-infectious (empty) protein capsids which have been shown to be morphologically and antigenically similar to native NoV virions. NoV VLPs have been sensitised by SARDI for the project. A Transmission Electron Microscopy (TEM) image of grown NoV VLPs obtained with FEI Tecnai G2 Spirit instrument is shown in Figure 4.30.

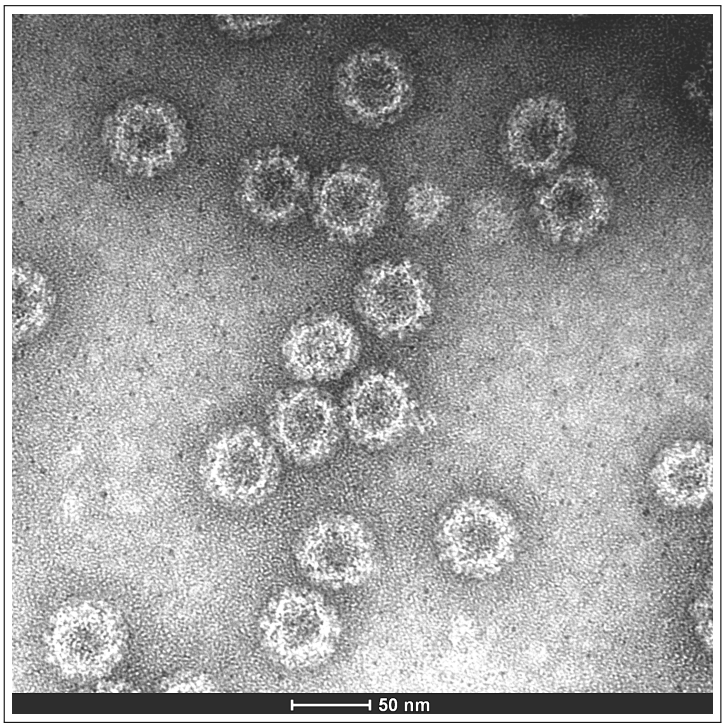


Figure 4.30: TEM image of NoV VLPs taken with FEI Tecnai G2 Spirit instrument. Scale bar is 50 nm. Samples prepared by negative staining with uranyl acetate.

Bio-reception strategies

It is known that the NoV genome undergoes frequent change, and therefore, no universal serological test exists for the detection of all known NoV strains. This is due to the large variability within the amino acid sequences of the virus. For that reason, specific antibodies that are raised for a particular NoV genotype need to be used. Polyclonal antibodies have the advantage over monoclonal antibodies that they are relatively quick and inexpensive to produce and are generally less specific in that they are capable of recognising multiple binding sites on NoV capsid. Polyclonal antibodies raised in rabbits against the VLP of a NoV GII.3 and GII.4 genotypes were

used as bioreceptors for VLPs GII.3 and GII.4, respectively, in this project. As no biotinylated antibodies were available at the time, biotinylated Protein A, known to bind the NoV specific antibodies was used as an intermediate receptor.

Human susceptibility to NoV infections is determined by Histo-Blood Group Antigens (HBGAs) [270, 273]. Therefore, binding of NoV to HBGA carbohydrates can be utilised in a sensor format for capturing VLPs.

Two main methods were used for designing the bio-reception part of the sensing system for NoV detection. Those methods were –

- A specific approach using NoV antibodies with sensor format: biotin → neutravidin → biotinylated Protein A → polyclonal antibody (sera) → casein block → NoV VLPs, where biotinylated Protein A is used as an intermediate layer to replace the antibody biotinylation; and
- A general approach using HBGA: biotin → neutravidin → biotinylated antigen HBGA B → polyclonal antibody (sera) → casein block → NoV VLPs.

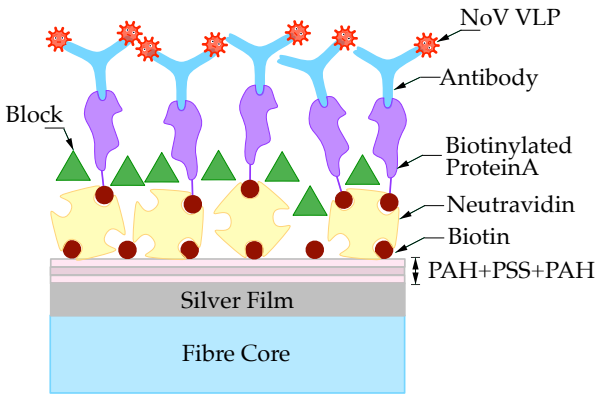
Both approaches involve attaching a biotin layer to polyelectrolytes on the sensor surface, then immobilising a monolayer of neutravidin onto the biotin. In the specific approach, biotinylated Protein A is bound to the neutravidin which, in turn, captures the NoV specific antibody, or, for the general approach, biotinylated HBGA B is attached to the neutravidin layer. After NoV receptors, either antibodies or antigen, are immobilised to the sensor surface, blocking is performed to prevent non-specific binding, and NoV VLPs are captured by the bioreceptor. The Protein A surface functionalisation approach is schematically presented in Figure 4.31a and the general antigen approach is shown is Figure 4.31b.

Sensor preparation for immunoassay

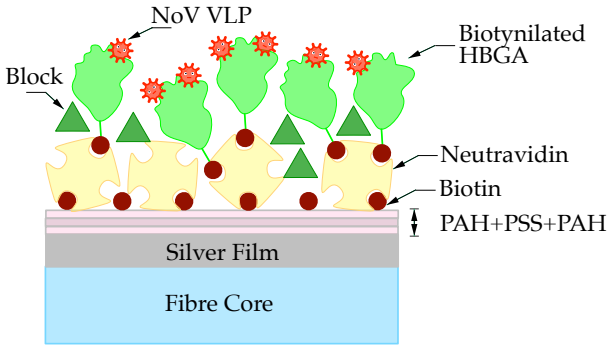
The surface preparation of the fibre SPR sensors starts with layer-by-layer adsorption of PE layers, PAH and PSS. PE solutions of 2 mg/mL were prepared in 1M of aqueous sodium chloride. Silver coated fibre samples were immersed in each PE solution for $20 - 30$ min, starting from PAH, and rinsed in deionized water between each step.

Fibre sensing probes were then enclosed in a flow cell and rinsed with PBS solution. Biotin was attached to the PE functionalised surface using amine coupling via reactive esters, (1-Ethyl-3-(3-Dimethylaminopropyl)-Carbodiimide) (EDC) (75 g/l) and NHS (11.5 g/l) (GE Healthcare). Powdered biotin (Thermo Scientific) was used to prepare 1 mg/mL solution, which was then mixed with EDC and N-Hydroxysuccinimide (NHS) in the ratio of 2 : 1 : 1 respectively prior immobilisation. Neutravidin (Thermo Scientific) (100 $\mu g/mL$) was used to form a monolayer on biotin-functionalised sensor surface.

Biotinylated Protein A (200 nM) was attached to the neutravidin layer with subsequent immobilisation of polyclonal antibodies (2 μM), specific to NoVs VLP GII.3 or GII.4. In the general approach with antigen binding, biotinylated HBGA B (200 nM) was immobilised to the neutravidin coated surface instead of Protein A-antibodies. Protein A, polyclonal antibodies, HBGA, and VLPs were supplied by the collaborators (SARDI). After immobilisation of NoV receptors, the surface was blocked with a casein blocking solution (Candor Bioscience) diluted 1 : 10 in PBS to prevent non



(a) Protein A.



(b) HBGA.

Figure 4.31: Schematic representation of surface functionalisation approaches for NoV detection.

specific binding. After the surface of the sensor was blocked, NoV VLPs with concentrations of 10^3, then 10^6 VLPs per mL were injected.

Experimental procedure

Binding kinetics were collected for every immobilisation step in order to ensure surface saturation. In particular, the wavelength shift was measured every few seconds. The injection of a sample at every step was performed until the sensor surface was saturated with the biomolecules which could be monitored by observing a straight line, i. e. no wavelength shift over time, on the binding kinetic sensorgrams. An example of the kinetic analysis for a biotin-neutravidin binding is shown in Figure 4.32.

From the measurement of the resonant wavelength shift, it was possible to conclude whether a particular bio-reagent attached to the sensor surface, where the magnitude of the spectral shift is proportional to the molecular weight of the bio-reagent. As such, biotin, being a small molecule, typically resulted in a spectral shift of $2-4$ nm, whereas the attachment of large neutravidin molecules caused a shift of around 10 nm. The surface saturation is achieved when no spectral shift is observed over time.

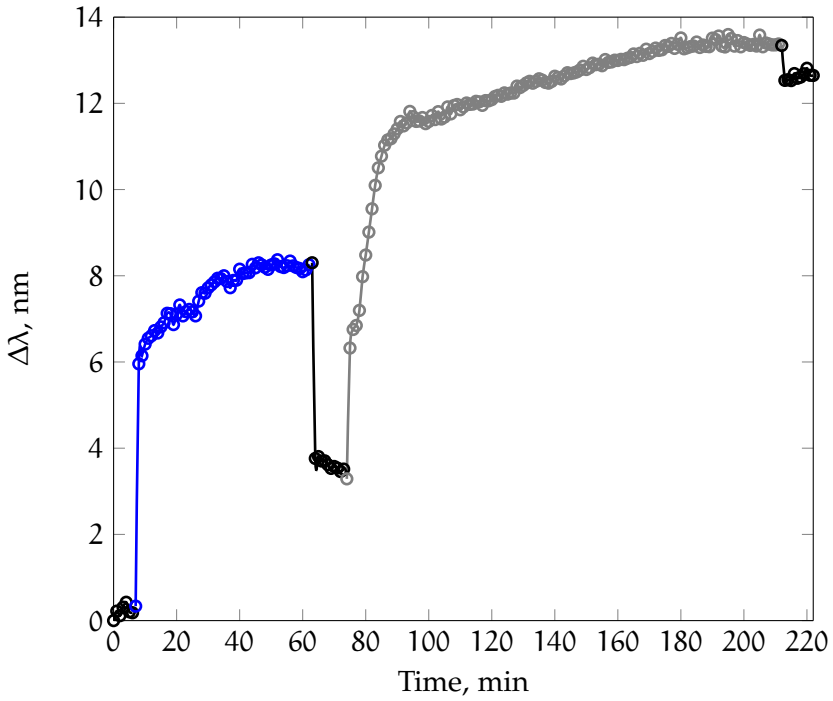


Figure 4.32: Example of kinetic analysis (sensorgram) for biotin and neutravidin binding on a functional coating of PE layers adsorbed onto a silica fibre SPR sensor. Initial PBS rinsing (black) followed by biotin (1 µg/mL) binding (blue), subsequent PBS rinsing (black), followed by neutravidin (41 µg/mL) immobilisation (grey), with final PBS rinse (black).

Injection of the samples was performed using a programmable syringe infusion pump (NanoJet, Chemyx) at a controlled flow rate. Bio-reagents were typically injected at a slow rate of 5 µL/min to ensure proper binding, where the intermediate rinsing steps with PBS were accomplished at a higher rate of 100 µL/min and larger volumes to remove any unbound material. Table B.1 in Appendix B lists the steps and approximate flow rates and volumes for Protein A experiments. Similar steps were used for the HBGA functionalisation approach where steps 6 (Protein A) and 8 (sera) were substituted by HBGA attachment.

Results and discussion

A typical result for the NoV detection experiment is presented in Figure 4.33 showing scattered light spectra collected from the sensing region. The data points in Figure 4.34 present the measure of the cumulative wavelength shift at the end of each step of the experiment.

Although a large number of experiments have been performed and intermediate problems with the non-viability of some reagents were rectified, the results for the detection of NoV VLPs were not conclusive for either, Protein A – antibody or HBGA, bio-functionalisation approaches. It is apparent from the example of the spectral shifts presented in Figure 4.34 that the experiments were not conclusive at the last step, VLP attachment. Therefore, it was hypothesised that either polyclonal sera does not capture the NoV VLPs, or VLP samples are not viable. To determine the viability of the polyclonal sera, as well as estimate the capability of the sensing platform for

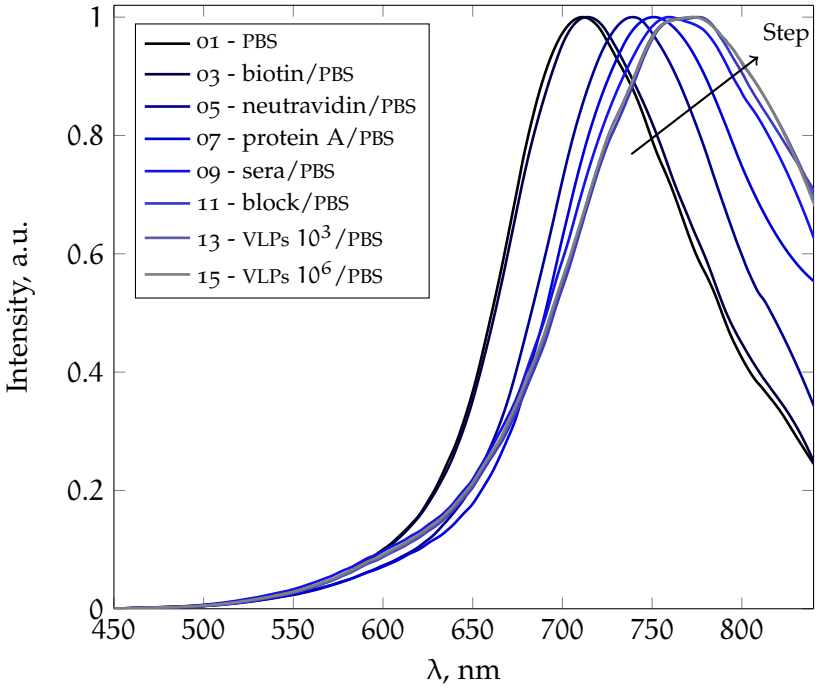


Figure 4.33: Processed SPR spectra for detection of NoV with SiO_2 fibre sensor using the Protein A surface functionalisation strategy. Presented curves are taken for PBS rinsing steps after each step of surface functionalisation as indicated in the legend. Processing of spectral data is performed using techniques described in subsection 'Data analysis'.

biosensing applications, a new sensor format have been proposed. This included the same functionalisation protocol as NoV detection using Protein A – antibody approach, except NoV VLPs were substituted with Qdots functionalised with antigens that are specific to NoV antibodies, as described in the Section 4.6.3.

4.6.3 *Detection of quantum dots (Qdots)*

In order to investigate potential issues with the Protein A bio-functionalisation strategy and ensure the viability of the sensing platform for biological applications, experiments with Qdots using the Protein A approach, as well as using antibody cross linking on the sensor surface, have been conducted. The choice of Qdots as a NoV substitute was dictated by the availability of the Qdot probes with the same binding affinity as NoV (conjugated with antigens specific to NoV antibodies). Therefore, the surface functionalisation for the Protein A experiment was identical to NoV detection where Immunoglobulin (Ig)-conjugated Qdots (Thermo Scientific, Qdots 705 goat F(ab)2 anti-rabbit IgG conjugate) was used instead of NoV VLPs at the last step,as shown in Figure 4.35a. The sensor format for the antibody cross linking approach was: polyelectrolyte layers → NoV antibody (sera) amino-coupled to the PE layers with EDC and NHS → block → Qdot conjugate, as presented in Figure 4.35b. In both experiments two concentrations of Qdots, 10 nM and 100 nM, have been used.

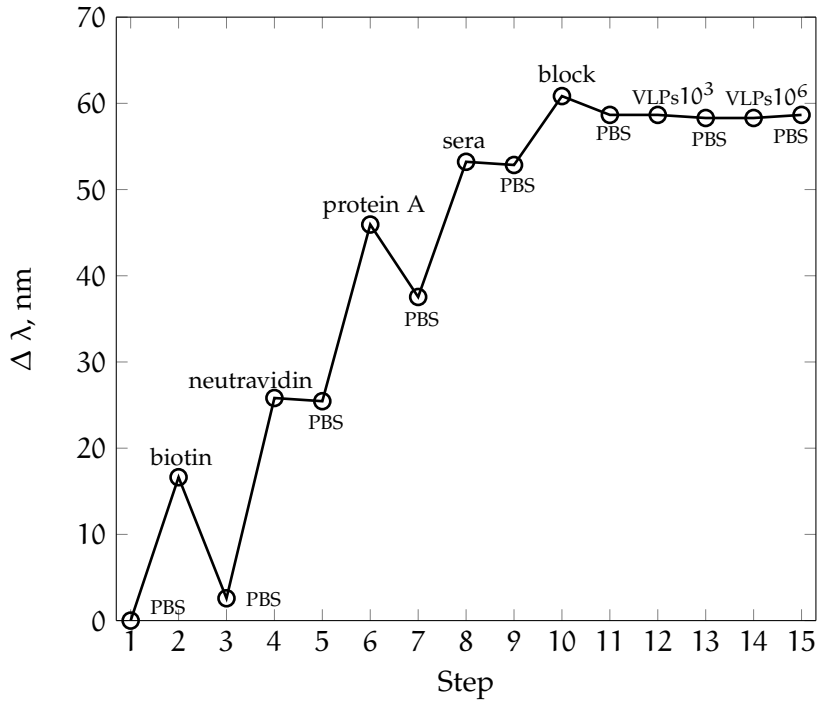
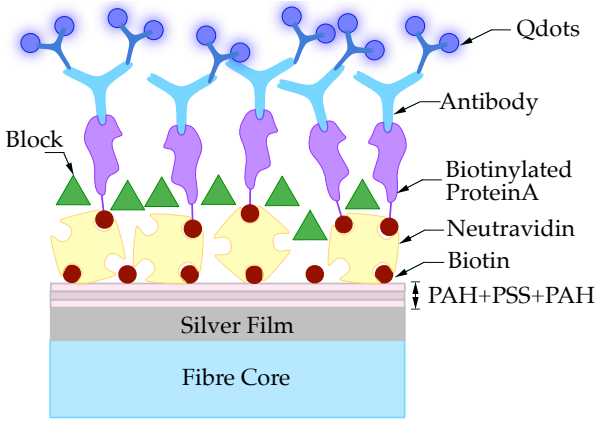


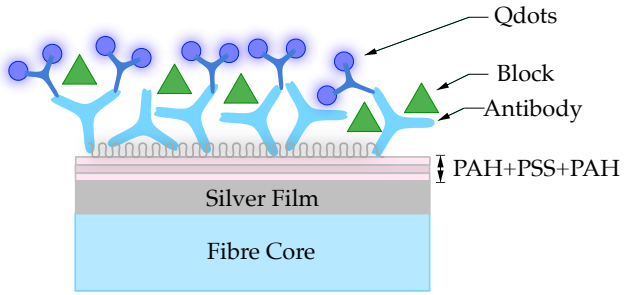
Figure 4.34: Steps of the NoVs detection experiment with a SiO_2 fibre sensor using the Protein A approach: cumulative wavelength shift at each step of surface functionalisation with intermediate PBS rinsing steps. The decrease in the resonant wavelength during rinsing steps indicates the removal of unbound molecules from the bulk solution.

Scattered SPR spectra collected at each step of the experiment with the Protein A approach is presented in Figure 4.36; the cumulative wavelength shifts at each step of the bio-functionalisation are presented in Figure 4.37.

From the results of the experiment, it can be concluded that Ig-conjugated Qdots were successfully captured by the polyclonal antibodies, causing SPR shifts of around 10 nm and 16 nm for 10 nM and 100 nM concentrations respectively. Negative control experiments, one without polyclonal antibodies and one without Protein A, were performed in order to eliminate the possibility of non-specific binding of the conjugated Qdots to the sensor surface. Negative controls show that no non-specific binding occurs and no Qdots were attached without presence of either sera or Protein A. It can be concluded that polyclonal sera used in the experiments for NoV detection is viable but might not bind the VLPs supplied, or VLP themselves are not able to attach to the antibodies. Assuming that the RI of the VLPs is around 1.4, as for typical proteins [274], and the RI of the Qdots is around 2.64 [275], one can expect a larger shift caused by the attachment of a monolayer of higher RI Qdots. However, considering the smaller size of the Qdots ($10 - 15$ nm) in comparison to the size of the VLP ($38 - 50$ nm), the fraction of volume where the evanescent field overlaps with the VLPs monolayer is larger, resulting in an increased effective RI. Even though the quantitative estimation of the effective RI caused by the binding of Qdot vs. VLPs is difficult, the detection of Qdots is indicative of the successful applicability of the SPR sensing platform for biological applications.



(a) The Protein A approach.



(b) The cross-linking approach.

Figure 4.35: Schematic representation of the surface functionalisation approaches for Qdot detection. In both cases, Qdots are conjugated with the secondary antibodies that are specific to the primary NoV antibodies (sera). Cross-linking causes random orientation of the antibodies on the sensor surface.

4.7 SUMMARY AND SCOPE FOR IMPROVEMENT

In this chapter, a scattering based SPR platform that utilises optical fibres has been described. The development of a silica surface functionalisation technique using sensitisation with stannous chloride allowed the fabrication of thin silver films on low RI silica fibres using chemical electroless plating. Characterisation of the silica fibre SPR probes was performed and compared to F2 fibre sensors. The lower RI of silica compared to the F2 glass allowed theprovided an increase in sensitivity of the SPR probe by almost a factor of 4.

Increasing the refractive index sensitivity by using lower RI fibre came at the cost of a reduction in the resolution from an increased spectral linewidth of the SPR response. For every label free sensing technology, the best performance is achieved by maximising both, sensor sensitivity and resolution, which eventually drives the detection limit. Therefore, we investigated pathways to improve silica sensor linewidth by using fibre tapers. This study showed that to achieve any significant improvement in the spectral linewidth of the SPR response curves, the taper waist diameters have to be smaller than 35 nm, which proved to be challenging due to the extreme fragility of the tapered samples.

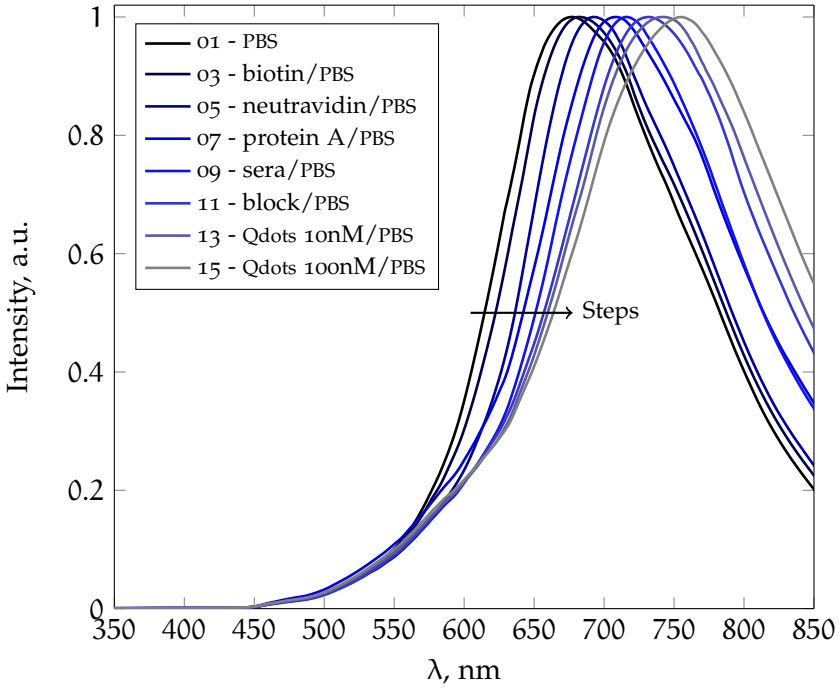


Figure 4.36: Processed SPR spectra for detection of Qdots with the SiO_2 fibre sensor using the Protein A surface functionalisation strategy. Presented curves are taken for the PBS rinsing steps after each step of surface functionalisation, as indicated in the legend.

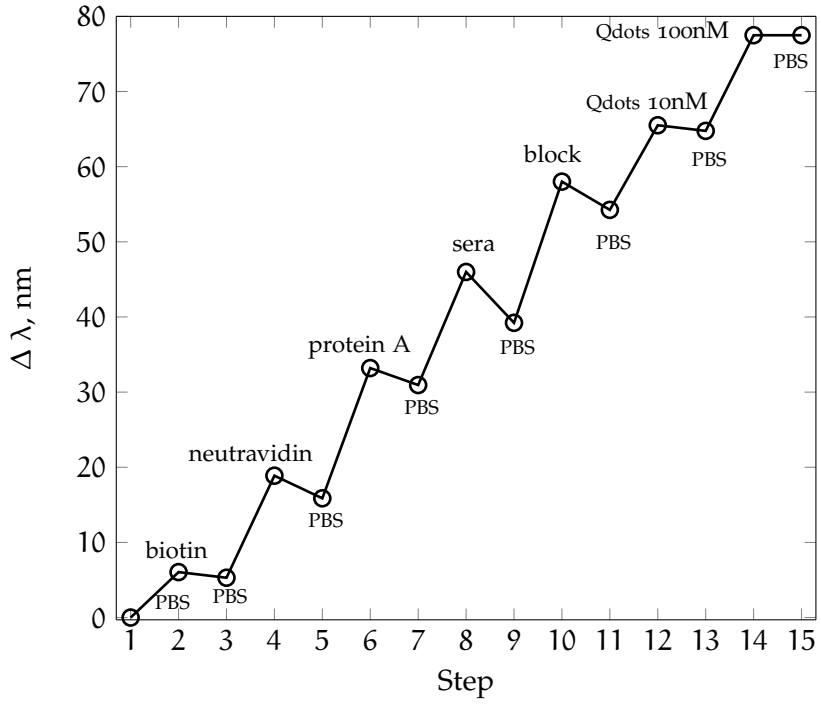


Figure 4.37: Steps of the Qdots detection experiment with the SiO_2 fibre sensor using the Protein A approach: cumulative wavelength shift at each step of the surface functionalisation with intermediate PBS rinsing steps.

It was proposed that the linewidth of the SPR signature could be reduced by designing the fibre itself to limit the number of optical modes propagating in the fibre. Therefore, silica MOFs with small cores were investigated to increase the sensors' resolution. The new sensing probe design, fabrication, and characterisation of the SPR sensors based on a small core MOF are presented in the following chapter.

Finally, the silica fibre based SPR platform has been tested for a biosensing application, NoV detection. Although it was not possible to derive a definite conclusion about the detection of NoV from the results of the experiments, using bio-target surrogates (functionalised Qdots) instead of the NoV VLPs, allowed the successful detection of small concentrations of targets with the same bio-functionalisation approach. This application example indicated that the developed SPR platform is suitable for biological applications. However, while the intrinsic refractive index sensing performance of the sensor is important, the interface between the physical platform and its surrounding biological environment is crucial to ensure that the sensor can be used in real life applications.

5

EXPOSED CORE MICROSTRUCTURED FIBRE (ECF) SPR SENSOR

Increasing the sensitivity of an SPR probe by lowering the refractive index of a waveguide is a straight forward approach for improving performance. However, this results in the increase of the linewidth of the SPR signature that in turn increases the resolution and detection limit of the device. As presented in the previous chapters, the use of fused silica fibres in the scattering based SPR sensing platform allowed an increase in the sensitivity by almost a factor of 4 when compared to a higher RI F2 fibres. This improvement, however, was accompanied by an undesired doubling of the FWHM of the SPR response. As discussed in Chapter 2, the spectral linewidth primarily depends on the geometry of an SPR system and materials that constitute the sensor. To overcome the trade off between the sensitivity and linewidth brought by the choice of fibre core material, the geometry of an SPR device can be modified to narrow the linewidth without significantly affecting sensitivity. In particular, reducing the size of the fibre core should allow an improvement in the FWHM through the reduction of the number of guided modes capable to excite SPs. However, the main challenge associated with the use of small core fibres is their fragility which makes it challenging to implement in an SPR architecture.

MOFs allow the construction of a small core surrounded by air holes which is supported inside a larger structure, typically made of the same material as the guiding core. With abundant flexibility of the cross sectional fibre design, it is possible to achieve a broad range of physical and optical properties with MOFs that are favourable for sensing. In addition to tailored design and adjustable optical properties, MOFs are well suited for sensing applications due to the presence of longitudinal air holes that can be used as microfluidic channels for samples [105]. MOFs can be designed to increase the overlap between the guided light and the sample located in the fibre holes thereby improving fibre sensing capabilities [276].

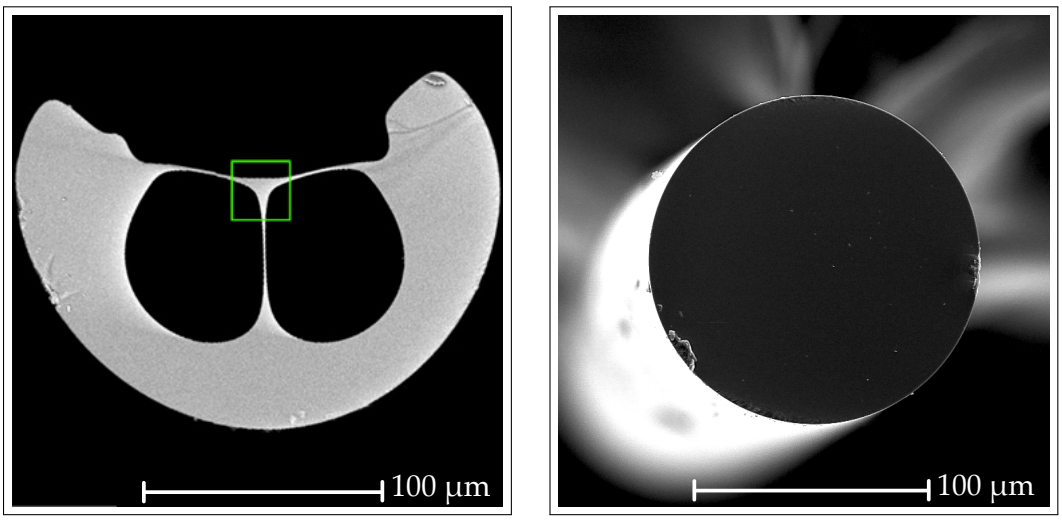
A number of SPR sensor designs based on MOFs have been proposed [105–107]. The fabrication of plasmonic coatings inside MOFs has been reported [139, 227, 277], however, it remains experimentally challenging to create finite-length SPR sensing regions inside the air holes and integrate microfluidics for liquid phase RI sensing applications. Here, we describe the development of an SPR sensor based on a specialised MOF designed specifically for sensing applications [278, 279]. The particular MOF, called Exposed Core Fibre (ECF), has one side of the core exposed to the surrounding environment along the whole fibre length allowing for simple deposition of the plasmonic coating as well as convenient liquid phase sensing.

5.1 ECF BACKGROUND

The idea of modifying a MOF to expose the core was first proposed Y. Hoo *et al.* [280]. Since then, several experimental demonstrations creating a short opening

in MOFs to expose the core using focused ion beam and femtosecond laser micromachining have been presented. F. Cox *et al.* [281] showed that long length openings in MOFs can be created at the preform fabrication stage by drilling a slot into the support structure of a polymer MOF preform. A fabrication of ECF in lead silicate glass with a slot in the support structure using extrusion and caning was first reported by S. Warren-Smith *et al.* in [279], followed by silica ECF demonstrated by R. Kostecki *et al.* [278].

In this work, fused silica ECF was used as the basis for the SPR sensing probes. The fibres were made in-house from F300 silica preforms (Heraeus Quarzglas GmbH) [278]. The ECF has a relatively small core of 10 µm diameter supported by thin struts within a 200 µm support structure. The ECF is essentially a modified suspended core fibre with an asymmetric geometry where one side of the core is exposed along the whole fibre length as shown in Figure 5.1a. A cross section of the large core silica fibre used for the SPR sensors presented in the previous chapter is shown for comparison is Figure 5.1b.



(a) ECF cross section. Triangular core is shown in green rectangle.

(b) Unstructured MMF core cross section.

Figure 5.1: SEM images of silica fibres' cross sections: ECF of effective core diameter of 10 µm (outlined in green) with support structure of approximately 200 µm, and unstructured MMF of 140 µm diameter.

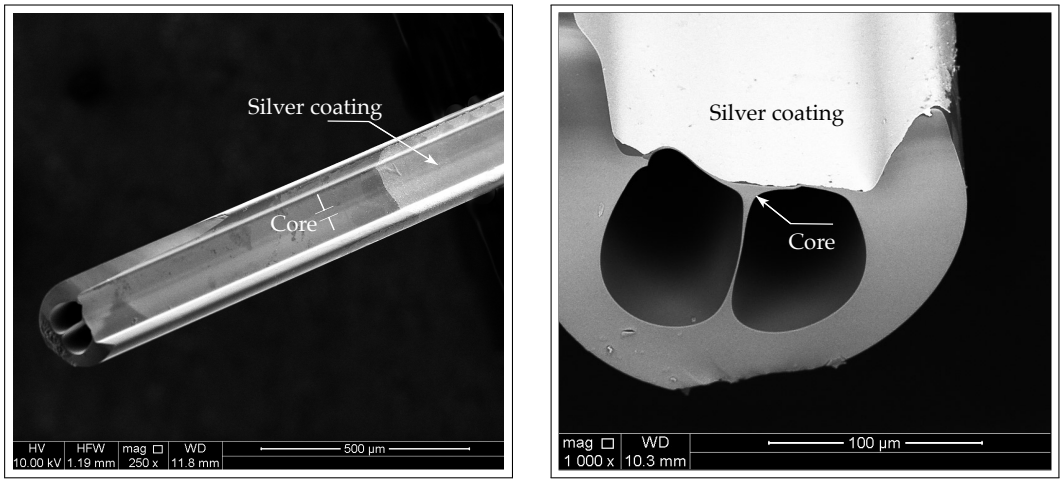
5.2 ECF SPR PROBE FABRICATION

As the core of the ECF is open to the external environment on one side, the silver coating can be deposited directly onto the fibre core without the need to fill the fibre air holes. The chemical electroless plating technique described in Section 4.2.2 was used to fabricate the silver coatings on the ECF. However, the absence of a polymer coating on the bare ECF resulted in the migration of the liquid solutions, tin sensitiser and Tollens reagent, along the ECF's groove by capillary forces. This resulted in an uneven silver coating at the edges of the silver film and longer than desired sensing regions. Attempts to remove the excess silver coating were made by

dissolving the silver with nitric acid. However, the liquid nitric acid moved along the fibre groove by capillary motion, destroying the silver on the sensing region.

Due to these initial difficulties with wet chemistry for the silver film fabrication on the bare ECFs, thermal evaporation of silver was performed. Silver was thermally evaporated under vacuum at 2×10^{-4} Pa using a thermal evaporator (JEOL, JEE 420). The evaporation source (fine silver grounds, Peter W Beck Pty. Ltd.) was evaporated from a tungsten crucible at a low current of 28 Amps. This resulted in silver surfaces of higher roughness suitable for scattering SPR platform. Sensors produced with thermally evaporated silver films were used for initial concept demonstration of ECF SPR sensor and the work was reported in [282]. However, the thermally deposited silver films, though evaporated at a low current, had significantly smaller roughness than chemically produced coatings. For the optimum performance in the scattering based SPR platform, as well as for the fair comparison with the large core silica MMF sensors, chemical deposition technique was desirable.

To account for this, the Tollens coating procedure was modified to accommodate the new geometry of ECFs. In particular, instead of using a large Petri dish where the fibres were immersed in the Tollens solution for coating, plastic lids perforated with small holes on the opposite walls of each lid were prepared. The plastic that the lids were made of is hydrophobic, therefore, the small size of the openings in the lids' walls acted as a seal and prevented liquid solutions to move along the groove of the bare ECF. This modified Tollens deposition method allowed the preparation of plasmonic coatings with the desired length, determined by the diameter of the lids, and was used to fabricate functional SPR sensors on the bare ECFs. The resulted silver coatings were fabricated around the entire ECF's circumference, as shown in Figure 5.2. As the light is guided in the core of the bare ECF, the SPs are only excited in the exposed part on top of the fibre core.



(a) ECF groove with silver coating. Magnification 250×. Scale bar is 500 µm.

(b) Close up of a cleave through the silver film. Magnification 2000×. Scale bar is 50 µm

Figure 5.2: SEM images (backscattered electron mode) of silica ECF coated with silver film. Silver appears as white region on the images.

5.3 ECF SENSOR CHARACTERISATION

5.3.1 *Flow cell design*

Due to the asymmetry of the ECF, it proved difficult to position the exposed core part of the fibre inside the cross sectional flow cell such that it faced the transparent window for scattered light collection. Moreover, the presence of the small grove along the fibre length meant that it might be more difficult to remove the residues of the samples during the rinsing steps considering that the flow in the cross sectional flow cell is directed across the fibre. Therefore, a new flow cell was designed to accommodate these concerns.

The new flow cell was constructed from a disposable glass micro capillary pipette tube (Kimbel, Fisher Scientific), cut into sections of $3-4$ cm length. The design of the new flow cell is presented in the Figure 5.3. The ECF with the silver coated region was placed inside the capillary together with polymer sleeves that served as the inlet and outlet for the liquid samples. The ends of the tube were then sealed with a UV-curable polymer, which was cured with UV light irradiation (Rolence Enterprise, Q-LUX UV). A low RI polymer (MY Polymers, MY-133-V2000) was used to seal the capillary ends when the bare ECF was used. This minimised the loss of the guided light at the seals as the polymer of RI of 1.33 was lower than the RI of silica.

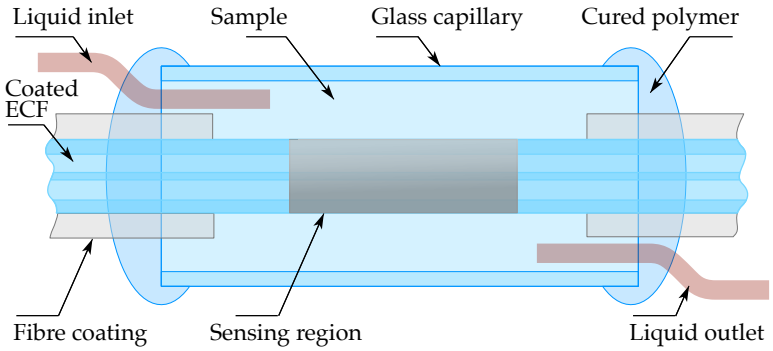


Figure 5.3: Schematic of the new flow cell constructed from a glass capillary tube used for the characterisation of ECF SPR sensors. For coated ECFs ends of the capillary were sealed with a UV curable optical adhesive (Norland, NA 68) with a RI of 1.54. For bare ECFs a low RI UV curable polymer (MY Polymers, MY-133-V2000) was used instead.

5.3.2 *Optical setup and experimental procedure*

The optical setup used to excite SPs in ECF based sensors was analogous to the optical setup used for the large core silica SPR sensors with additional microscope objective used at the end of the ECF to ensure coupling into the core of the fibre rather than the support structure. The modified setup is presented in Figure 5.4. With the large core MMF it was not critical to chose the magnification of the coupling objectives. With the small core ECF, however, optimal coupling into the core required the use

of an objective with × 20 magnification. A projected image of the fibre facet onto the screen was formed using × 10 microscope objective. Coupling was adjusted by maximising the light transmitted through the core of the ECF and eliminating the light guided in the support structure.

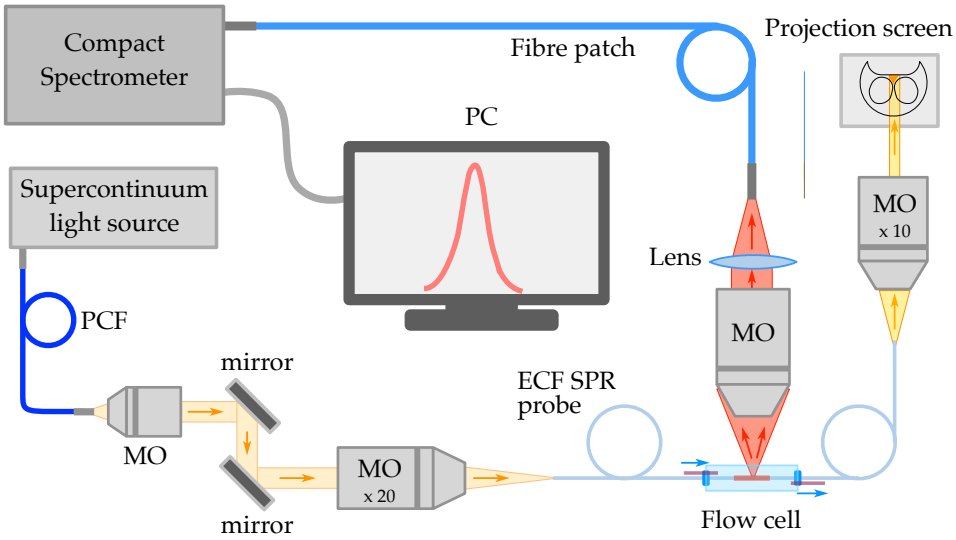


Figure 5.4: Schematic of the optical setup for silica ECF SPR sensor characterisation. MO - microscope objective, PCF - photonic crystal fibre. Coupling conditions were monitored by observation of the projected image on the screen formed by light transmitted through the fibre.

The ECF based sensors were characterised using a serial dilution of glycerol in water, following the procedure described in detail in Section 4.5. An example of the SPR scattered spectra collected from the silver coated core of a bare ECF is presented in Figure 5.5 and Figure 5.6. The data analysis technique described in Section 4.5 was used to process the scattered SPR spectra collected from the sensing region.

5.3.3 *Analysis of the results*

The resulted sensitivity curve and FWHM for the bare ECF SPR sensor is shown in Figure 5.7. The analysis of the performance suggests that average sensitivity of the ECF SPR sensors is similar to that achieved with the large core MMF silica sensors, and is estimated to be 1779 ± 108 nm/RIU based on ten sensors. As expected, the FWHM of the SPR response curve is twice as small as that of the large core silica SPR sensor, averaged at 77 ± 12 nm. This improvement of the spectral linewidth should lead to an improved sensor resolution, and detection limit of the platform, as well as a doubling of the FOM. Moreover, the errors estimated for the ECF sensor performance were smaller than for the MMF probes, indicating less variability between values for different samples in the data sets. Summary of the performance characteristics of the ECF based SPR sensors and comparison with the unstructured large core silica and lead silica fibres is presented in Table 5.1.

Further analysis of the experimental performance of the ECF sensors suggests that a drawback of using the smaller core ECF sensor is a lower SNR, 27 dB in comparison to 34 dB, estimated for the large core MMF sensors. Even though the standard

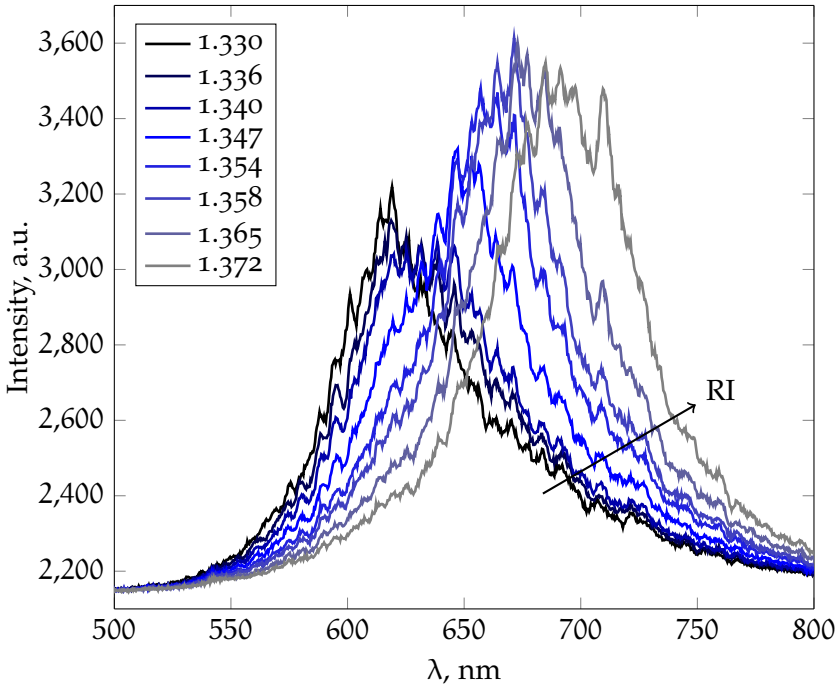


Figure 5.5: Raw SPR spectra for the silica bare ECF sensor collected at varying RI of the external dielectric (aqueous solutions of glycerol). Excitation using Koheras SuperK Compact supercontinuum light source.

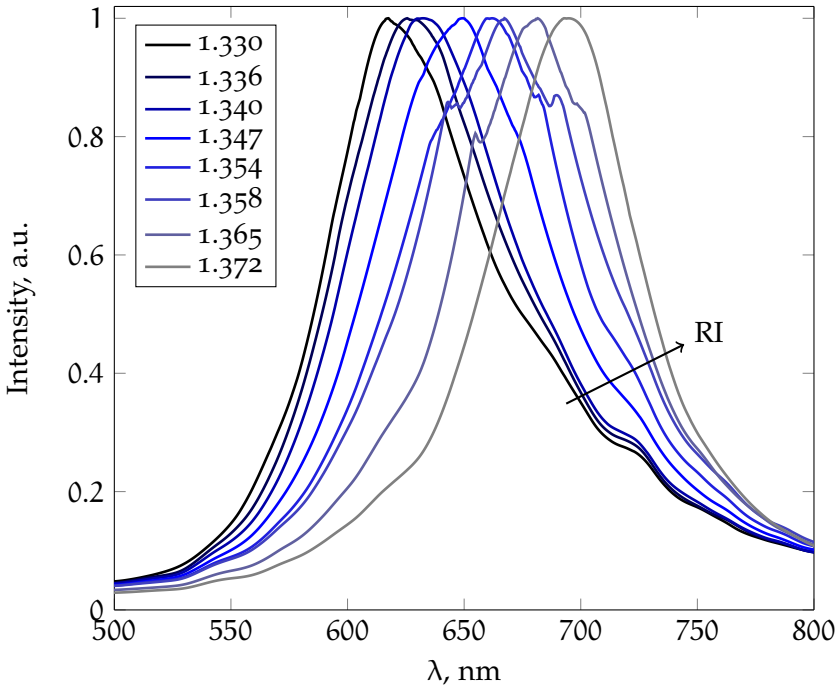


Figure 5.6: Processed SPR spectra (normalised and filtered) for the bare ECF sensor collected at varying RI of the external dielectric (aqueous solutions of glycerol). The data analysis techniques described in Section 4.5 'Data analysis' were used to process the spectra.

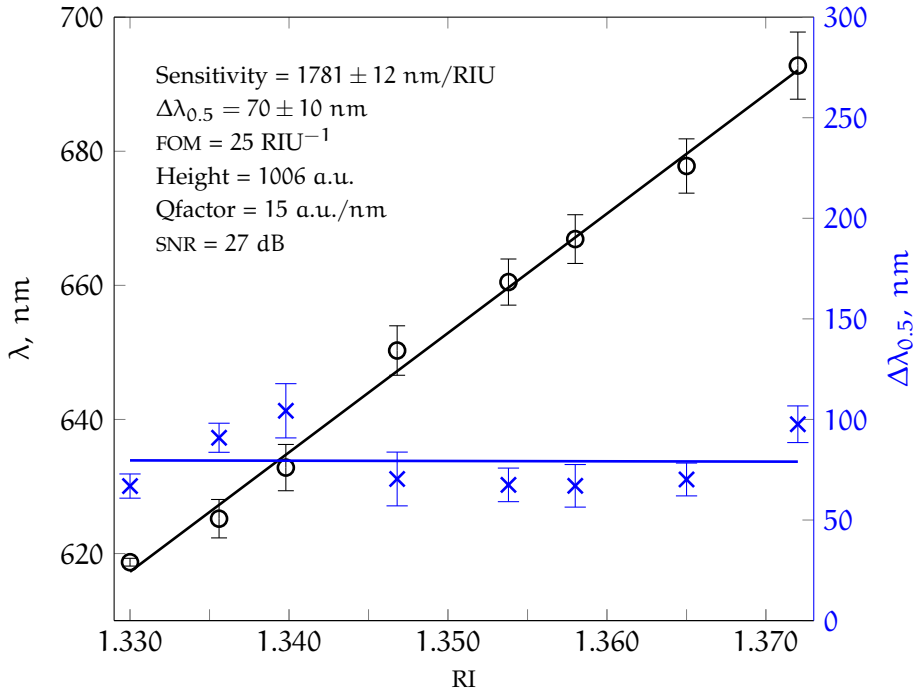


Figure 5.7: Sensitivity (black circles) and FWHM (blue crosses) for the bare ECF sensor characterised using aqueous solutions of glycerol. Experimental and fitting errors are shown as error bars. Maximum absolute uncertainty in RI of glycerol solutions is 0.001.

Table 5.1: Comparison of performance characteristics of ECF-based silica SPR sensors with MMF-based sensing probes in the scattering based platform.

Characteristic	Large core MMF, lead silicate (F2)	Large core MMF, silica (F300)	Small core ECF silica (F300)
Sensitivity, nm/RIU	485 ± 78	1827 ± 218	1789 ± 108
FWHM, nm	112 ± 14	161 ± 24	77 ± 12
FOM, RIU^{-1}	4 ± 1	11 ± 3	23 ± 5
λ_{res}, nm	559 ± 13	684 ± 15	607 ± 8
Height, a.u.‡	n/a †	$\sim 10^4$	$\sim 10^3$
Qfactor, a.u./nm‡	n/a †	$\sim 10^2$	$\sim 10^1$
SNR, dB	34	34	27

† Height and Qfactor depend on the light source and therefore are not comparable to silica fibre sensors.

‡ Estimated at the same spectrometer integration time of 100 msec.

deviations for the ECF probes were smaller, the increased spectral noise can potentially cause a larger uncertainty when determining the position of maxima in the spectral response leading to a deterioration of the sensor resolution. Therefore, sensor resolution may or may not be improved by a smaller spectral linewidth of the SPR response, depending on the contribution of the reduced SNR towards sensor resolution. The contribution of SNR can be estimated recalling the numerically simulated expression ($R \approx \frac{\Delta\lambda_{0.5}}{4.5\ SNR^{0.25}}$), presented in [93], the resolution for the large

core silica sensors and the ECF sensors can be estimated as 5.11 nm and 4.69 nm respectively. This results in the detection limit of 0.003 RIU for the large core silica sensor and 0.002 RIU for the ECF sensor leading to an improvement factor of around 1.4 for the ECF sensor. However, the experimental contribution of SNR toward resolution might be different from the numerically predicted dependency. Particularly, the curve fitting for data analysis is influenced by both parameters, linewidth and SNR. The average fitting error in determining the spectral position of the peaks for the large core silica MMF sensor was estimated to be 2.47 nm, and only 1.21 nm for the ECF sensor, which approaches the spectral resolution of the spectrometer. While the calculated values for the resolution and the detection limit are rough estimates, the analysis shows that the reduced linewidth of the smaller core SPR sensors improves the resolution and the detection limit, even in the presence of increased noise level. The latter can be alleviated by a use of a light source with reduced intensity noise.

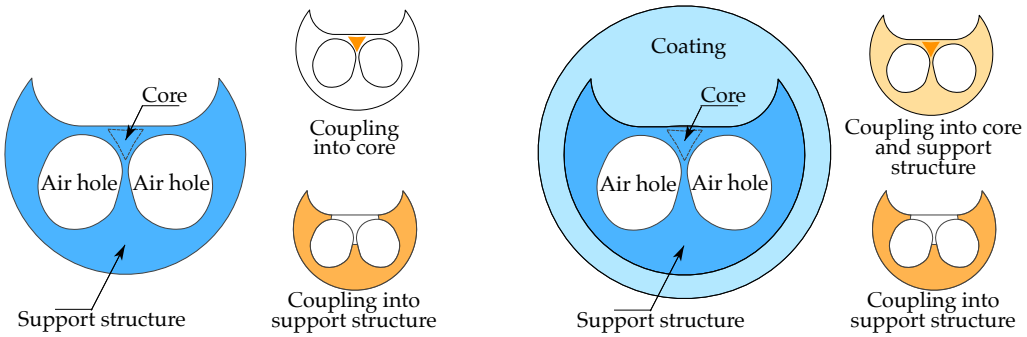
The experimentally demonstrated results for the performance of ECF SPR sensor were compared to a theoretically predicted modelling based on numerical simulation of SPR in ECFs reported concurrently in [283, 284]. The predicted sensitivity of a silver coated SPR sensor based on an ECF of similar geometry and the core size of 12 μm is in the range of $2000 - 4000$ nm/RIU for the range of samples' RIs between $1.33 - 1.37$, and the FWHM of SPR response is around 50 nm [284]. The slightly lower performance of our experimentally demonstrated ECF sensor is likely attributed to a different dielectric function of the silver coating produced by chemical electroless plating and the surface roughness of the silver film. Nevertheless, the experimental values obtained for the ECF SPR sensors and the overall trend when decreasing the core size are, in general, in agreement with the predicted results. The demonstration of the SPR sensor based on the bare ECF and its comparison with the large core silica MMF sensor was reported in [109].

5.4 MULTIPLE SPR PEAKS IN ACRYLATE-COATED ECFS

In addition to the bare ECF, another type of ECF, an acrylate-coated ECF was available for testing. With the coated ECF, the support structure and the exposed core were overlaid with a polymer of RI of 1.375. The chemical electroless plating technique was used to fabricate 50 nm a silver coating on the acrylate-coated ECFs. For the coated ECF, it was possible to deposit silver film following the same wet chemistry procedure used for the large core silica MMF sensor presented in Chapter 4. A 1 cm-long section of the acrylate coating was removed from the coated ECF with a scalpel blade to expose a section of the fibre core, then coated with silver using the same process as for large core silica fibres. The sensing regions were then enclosed in a microfluidic flow cell. For the acrylate-coated ECF sensors the exposed section of the fibre with the silver coating was shorter than the flow cell length. Therefore, it was possible to use a higher RI polymer (Norland, NA 68), instead of the low RI polymer, due to its lower cost.

In the coated ECF, the higher RI of the acrylate cladding, relative to air in the bare ECF, resulted in coupling of the guided light into the support structure. Therefore, it was not possible to achieve light guidance exclusively in the core and some

proportion of light was always guided in the support structure. The schematics of cross sections of the bare and coated ECFs with the possible coupling conditions are shown in Figure 5.8. For that reason, the analysis of the sensor performance from the previous section is based on the study of SPR in the bare ECF for the fair comparison of the influence of the core size on the performance characteristics. However, an interesting behaviour was noticed when analysing SPR in acrylate-coated ECF, which will be presented in the current section.



(a) Bare ECF with possible coupling into the core, or support structure.

(b) Coated ECF with possible coupling into the core and support structure, or support structure.

Figure 5.8: Schematics of cross sections of ECFs with possible coupling conditions maximised into core or support structure.

Simultaneous coupling into the core and the support structure of the coated ECF SPR probe resulted in the appearance of two peaks in the scattered SPR spectra, as shown in Figure 5.9. The two peaks appear at different wavelengths once the sensor was immersed in water, the first peak at around $590-600$ nm, and the second peak at around $690-700$ nm, both moving towards longer wavelengths with increasing RI of the external dielectric medium. Multiple coated ECF SPR sensors with simultaneous coupling have been analysed and all showed the presence of these two peaks. The sensitivity of both peaks was found to be similar, as shown in the sensitivity curves in Figure 5.10, and comparable to the sensitivity values obtained with MMF silica sensor and bare ECF with core-only coupling. The overlap of the two peaks on the spectra at different wavelengths form a dip at around $620-630$ nm which also shifts towards longer wavelengths as the sample RI increases. The difference between the sensitivity of the dip and the two SPR maxima is not statistically significant. The sensitivity curve for the dip between two SPR peaks in the scattered SPR spectra is also shown in the Figure 5.10. The FWHM of the shorter wavelength peak was found to be approximately 75 nm, and $100-120$ nm for the longer wavelength peak.

From the analysis of the resonant wavelength and spectral linewidth for the coated ECF, bare ECF and large core silica SPR sensors, it was predicted that the twin peaks in the scattered spectra occur due to excitation of SPs in the fibre core and also the support structure. To further investigate the origins of the twin peaks, scattered light from the support structure needed to be isolated from the core SPR scattering. In order to achieve this, spectra were first collected from the exposed core side of

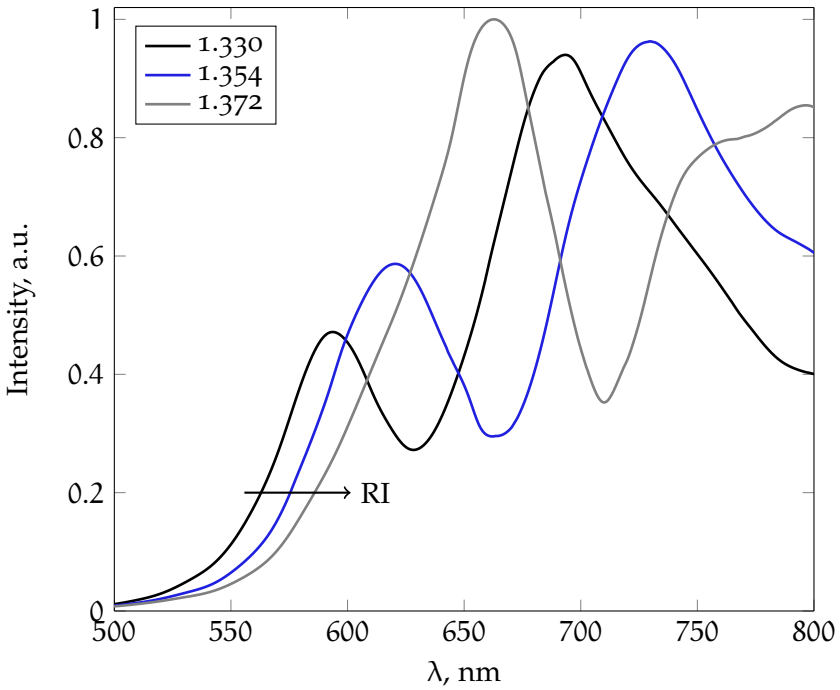


Figure 5.9: Processed SPR spectra (normalised to local maxima and filtered) for acrylate-coated ECF sensor collected at varying RI of external dielectric (aqueous solutions of glycerol). Two SPR peaks are present.

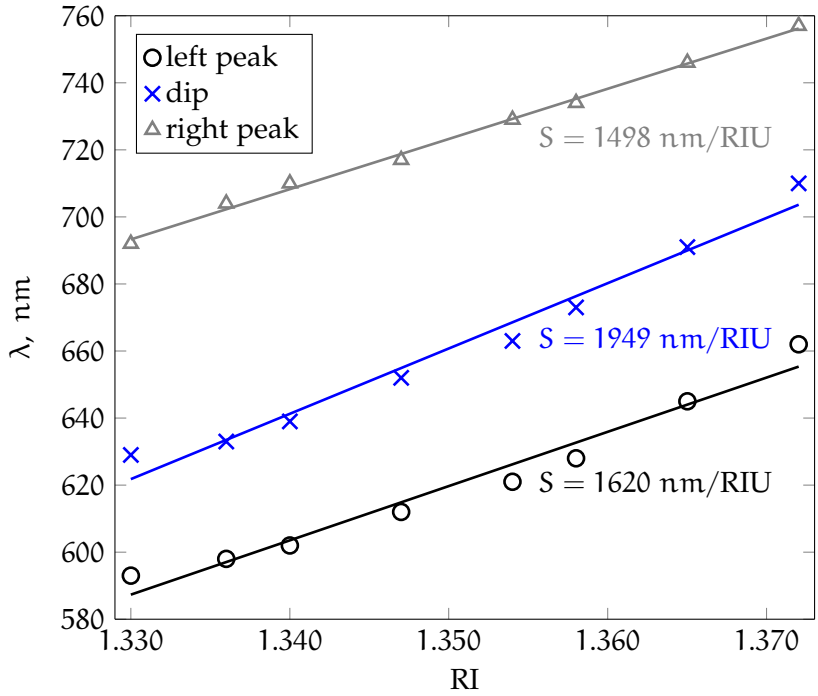


Figure 5.10: Sensitivity curves for acrylate-coated ECF sensor characterised using aqueous solutions of glycerol for the two peaks and the dip.

the sensing region gathering scattered light from the core and the support structure, then the flow cell was rotated 180 degrees and, without changing the coupling conditions, the scattered light was collected from the support structure only. The result of the experiment is shown in Figure 5.11 where scattered light collection is specified in the insets. Two peaks are present for the core-side collection and only one peak is present for collection of scattered light from the support structure. The position of the peaks indicate the overlap between the support structure SPR and longer wavelength peak appearing for the core-support structure coupling.

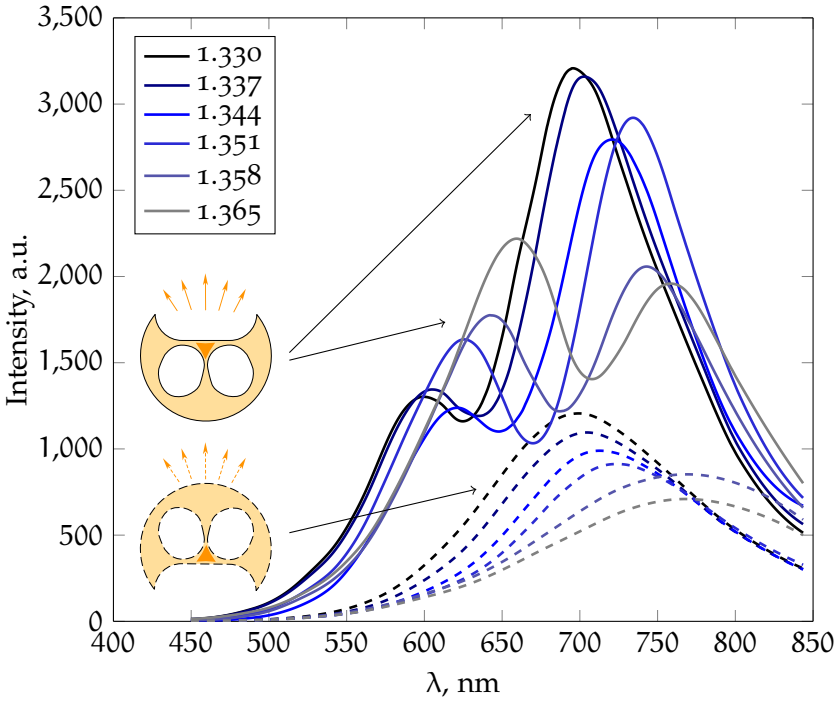


Figure 5.11: Processed SPR spectra (smoothed, relative heights preserved) for an acrylate-coated ECF sensor collected at varying RI of the external dielectric (aqueous solutions of glycerol). Two SPR peaks are present in the scattered spectra collected from the core side (solid lines), one peak is present in scattered spectra collected from the support structure on the opposite side of the core (dashed lines). Scattered light collection is shown on the insets.

Sensitivity curves for the two SPR peaks for core-side collection, dip between the two peaks, and the single peak in the scattered light collected from the support structure are presented in Figure 5.12. It is apparent that the resonant wavelengths for the longer wavelength peak in the double-peak spectra matches the resonant wavelengths for the support structure, which agrees with initial prediction of the origins of the double peaks in the SPR spectra for core-support structure coupling. Sensitivity values for all of the features in SPR spectra presented in Figure 5.12 agree with sensitivity achieved in silica fibre based sensors within their uncertainty estimates.

The presence of two resonant peaks in the scattered SPR spectra collected from the acrylate-coated ECF is an artefact that results from the guiding properties of the fibre which couples light into the support structure. Nonetheless, it results in an interesting double resonance effect within one fibre structure. It is informative that

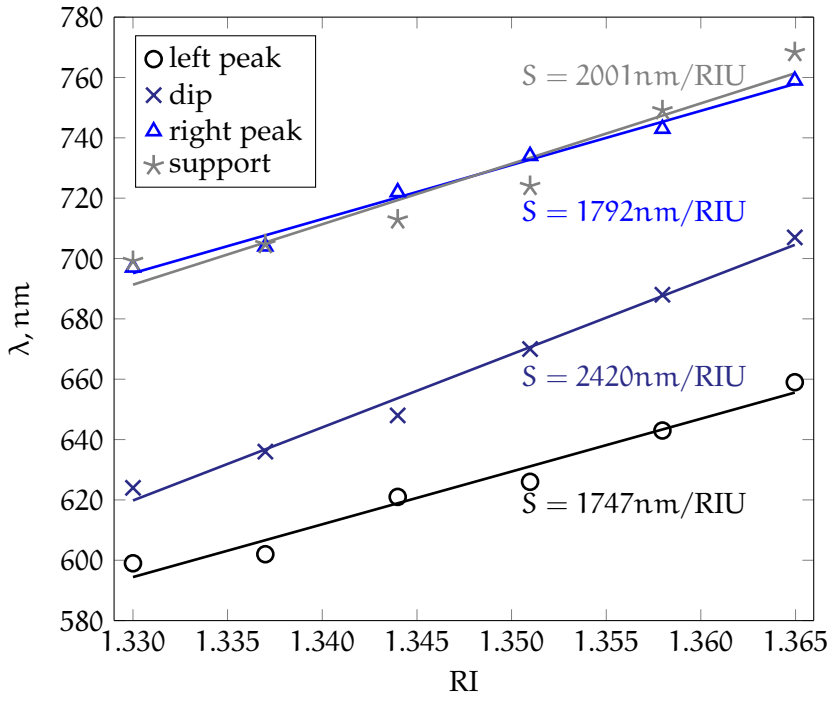


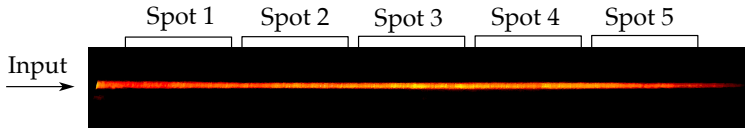
Figure 5.12: Sensitivity curves for acrylate-coated ECF sensor characterised using aqueous solutions of glycerol (spectra from Figure 5.11) for two arrangements of scattered light collection: collection from core (two peaks and a dip), and collection from support structure (single peak).

the spectral separation between the two SPR peaks causes three traceable SPR features to occur. All of those three signatures, two peaks and a dip between them, are sensitive to the change in the external dielectric's RI, and therefore, can be separately tracked for the improved reliability of the sensing platform. Furthermore, the spectral separation of the SPR features in one fibre probe could potentially be useful in designing multiplexed sensing devices with spectrally independent sensing regions, facilitated by a design of microfluidic channels or metal coatings that overlap the different fibre structures at distributed locations along the fibre. Those observations further support that the structural parameters of the fibre have a strong influence on the resonant position and the linewidth of the SPR feature. Sensitivity, however, seems to depend more on the properties of materials, i. e. fibre glass, where design of the fibre and the spatial dimensions of the waveguide do not have significant influence on the sensitivity value.

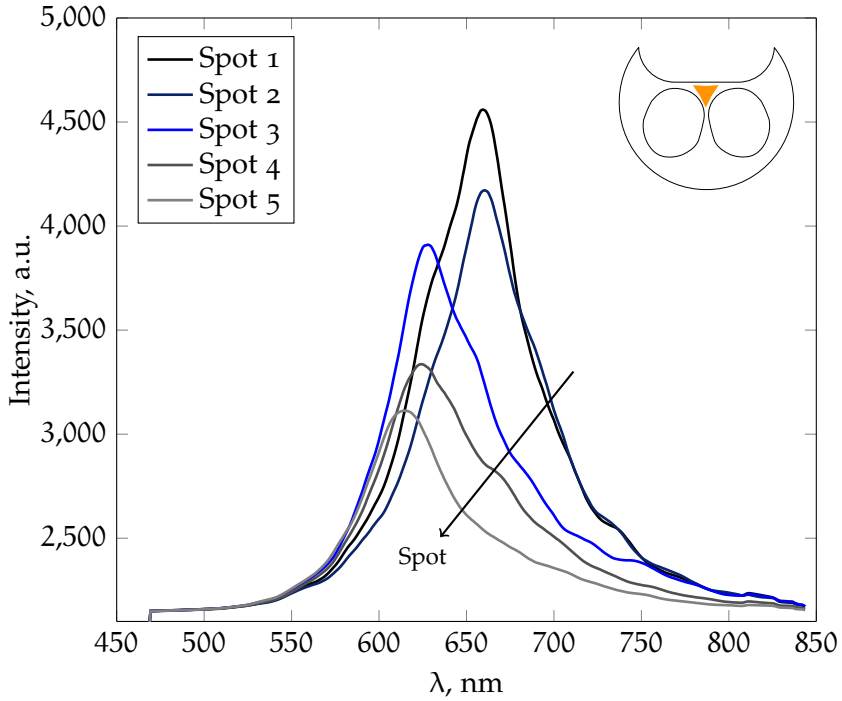
5.5 DEPENDENCE OF RESONANCE ON SENSING LOCATION

In addition to the coupling and the guiding in ECFs, the SPR wavelength is affected by the spectral characteristics of the excitation light, which in turn is influenced by the interaction with the metal coating. SPR is a lossy process that causes attenuation of electromagnetic radiation near the resonance frequency. Therefore, interaction with the metal film changes the spectral properties of the guided light in the fibre. As a result, the observed wavelength of the SPR peak in the scattered signal collected from a particular spot on the sensing region is affected by the losses that occur in the fibre

prior to that location. This concept is demonstrated by comparing spectra taken from five equidistant positions along a sensing region, as depicted in Figure 5.13a. Figure 5.13b presents scattered spectra for a bare ECF SPR sensor collected from these 5 locations (spots) on the sensing region of 15 mm length with the same outer dielectric medium, water. As longer wavelengths are scattered at the beginning of the sensing region, the SPR peak shifts towards shorter wavelengths.



(a) Photograph of the sensing region showing multiple spots in the bare ECF with core coupling.

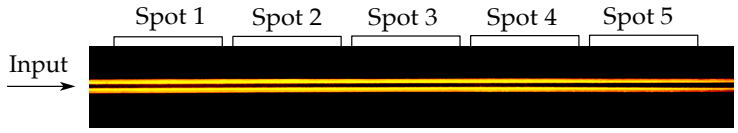


(b) Scattered spectra collected from the 5 locations.

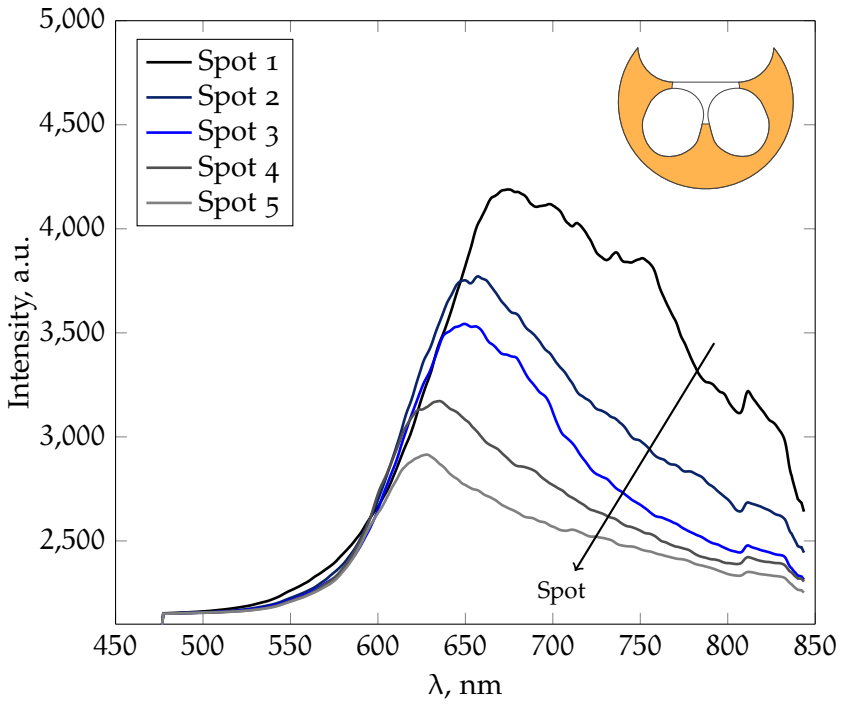
Figure 5.13: Scattered SPR spectra for the 5 locations (spots) on the silica bare ECF sensor with core coupling (as shown on the inset). Supercontinuum light source is coupled from the left in (a). Silver coating is 55 nm. Spectra are taken in water (RI=1.33).

This is also noticeable when light is launched into the support structure rather than the small core Figure 5.14. Sensor spot positions from which the spectra were taken are depicted in Figure 5.14a. The 200 µm diameter support structure is sufficiently large that it could be considered as a highly multi-mode fibre. The FWHM is larger at the first location on the sensing region reaching around 180 nm, then reducing down to 150 nm along the length of the sensing region (Figure 5.14b). The broadening of the peak at the beginning of the sensing region for the support structure coupling might be attributed to the larger scattering area that introduces more scattered background unrelated to SPR at the boundary of the coated region. This effect is not noticeable for the small core sensor (core coupling condition) where FWHM does not noticeable vary with the position on the sensing region

(Figure 5.13b). Photos of each location on the sensing region with corresponding spectra for bare ECF sensor can be found in Figure C.1.



(a) Photograph of the sensing region showing multiple spots in the bare ECF with support structure coupling.

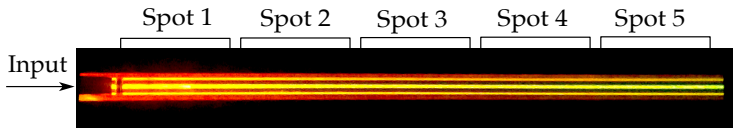


(b) Scattered spectra collected from the 5 locations.

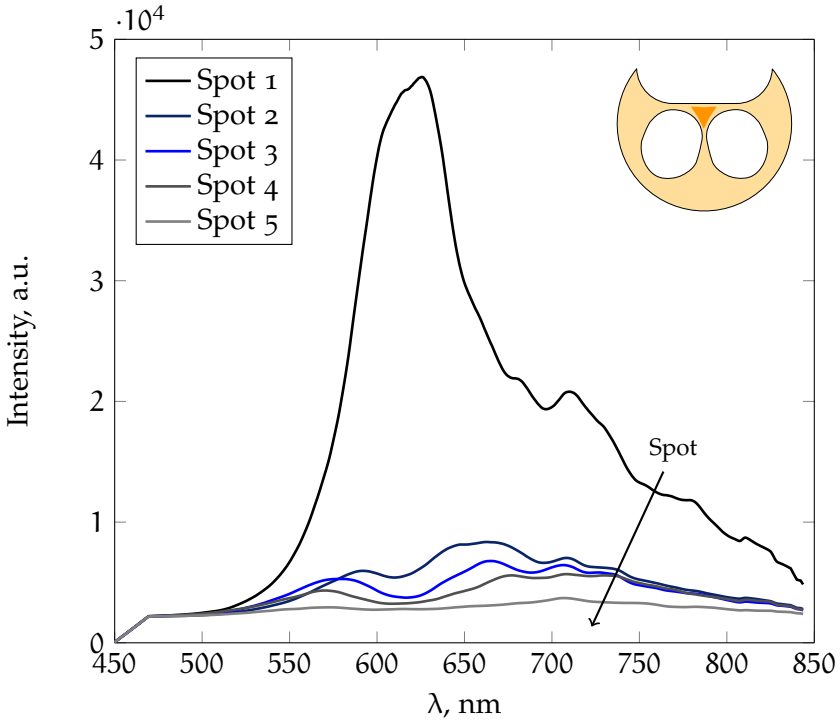
Figure 5.14: Scattered SPR spectra for the 5 locations (spots) on the silica bare ECF sensor with support structure coupling (as shown on the inset). Supercontinuum light source is coupled from the left in (a). Silver coating is 55 nm. Spectra are taken in water (RI=1.33).

The dependence of the resonance position on the location on the sensing region is also evident for the coated ECF with simultaneous coupling into the core and the support structure, as illustrated in Figure 5.15b. As noticeable from the photograph of the sensing region in Figure 5.15a, core, support structure, and the edges of the support structure have SPR excitation at different colours. At the beginning of the sensing region (spot 1) the smaller structures, fibre core and edges of the support structure, scatter yellow, which correspond to the peak at around 610 nm. The larger support structure scatters light at longer wavelengths (red) which corresponds two the smaller peak at around 700 nm. At the further locations on the sensing region, both of the peaks blue-shift due to the loss of the guided light caused by interaction with the metal film at prior locations. Photos of each spot on the sensing region with corresponding spectra for coated ECF sensor can be found in Figure C.2.

When the light is guided in the support structure of the coated ECF only, a broad single SPR peak occurs at around 700 nm, as shown in Figure 5.16b. The peaks move towards shorter wavelengths for the further locations on the sensing region. As the



(a) Photograph of the sensing region showing multiple spots in the coated ECF with core coupling.

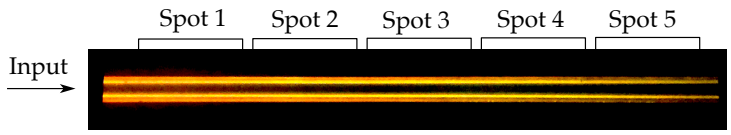


(b) Scattered spectra collected from the 5 locations.

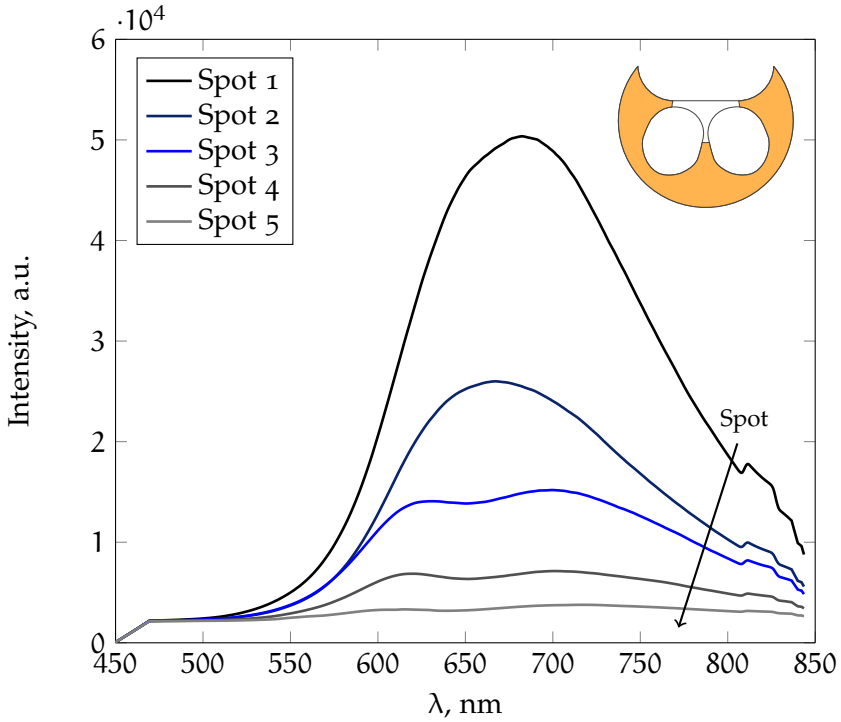
Figure 5.15: Scattered SPR spectra for the 5 locations (spots) on the silica acrylate-coated ECF (BOP) sensor with core coupling. Supercontinuum light source is coupled from the left in (a). Silver coating is 47 nm. Spectra are taken in water (RI=1.33).

guided light is attenuated through coupling into SPR modes at the support structure, two peaks start appearing at around the centre of the sensing region (spot 3). This also becomes apparent on the image of the scattered light from the sensing region, Figure 5.16a. At the beginning of the region, the strong SPR scattering from the support structure dominates, resulting in a broad single peak at longer wavelengths. As the light attenuates by coupling to SPs, the distinction between colours of the large support structure and the small edges become apparent causing the split in the SPR spectra into the two peaks.

The analysis shows that SPR spectral position is indeed influenced by the dimensions of the structure as well as spectral properties of the excitation light. Even though the sensitivity of the fibre sensor is not significantly affected by the spatial dimensions of the waveguide, linewidth of the SPR response is determined by the size of the SPR supporting substrate. The observed resonant wavelength is the result of the convolution of different resonance peaks, each caused by a specific resonance condition satisfied by a given mode-wavelength combination. The number of modes contributing to the resonance could be one of the potential reasons for the broadening of SPR peaks in larger waveguide structures. It has been noticed that



(a) Photograph of the sensing region showing multiple spots in the coated ECF with support structure coupling.



(b) Scattered spectra collected from the 5 locations.

Figure 5.16: Scattered SPR spectra for the 5 locations (spots) on the silica acrylate-coated ECF (BOP) sensor with support structure coupling. Supercontinuum light source is coupled from the left in (a). Silver coating is 47 nm. Spectra are taken in water (RI=1.33).

in a highly multi-mode fibre with thousands of modes, such as in the large core unstructured silica fibre, the coupling conditions do not have a strong effect on the observed SPR wavelength. However, for the smaller core fibres, such as the ECF, we noticed a stronger dependency of the scattered peak wavelength on the properties of the guided light, which in turn is influenced by coupling. It is reasonable to assume that the presence of the double SPR features in the acrylate-coated ECF sensors, which were not observed in the bare ECF-based probes, may be caused by the asymmetry of the RI profile between the air-clad core and the acrylate-clad support structure. Moreover, the increase in the resonant wavelength for a larger size waveguide structure is not in disagreement with the theoretical calculations reported in Chapter 3, which predicted an increase in the resonant wavelength of the SPs for sharper incidence angles to the metal interface (Figure 3.9). Considering that the sharper propagating angles correspond to higher order guided modes, which is a valid assumption for large waveguides, an increase in the SPR wavelength, as well as broadening of the SPR signature, should be expected for larger waveguides, such as the support structure of ECF.

5.6 EXPOSED CORE FIBRE MODIFICATION

A potential method of further improving the spectral linewidth of the SPR response is the use of an ECF with an even smaller core. Figure 5.17 shows how the number of modes in a step-index fibre, air clad and with cladding of RI of 1.33, is influenced by the core diameter. A reduction of the fibre core diameter from 10 µm down to 2 µm results in reduction of the number of modes supported by the fibre, from almost a thousand down to $30-40$. Smaller core ECFs would present an attractive option for potential improvement in the SPR sensor linewidth, providing that challenges with the fibre fragility and coupling could be overcome.

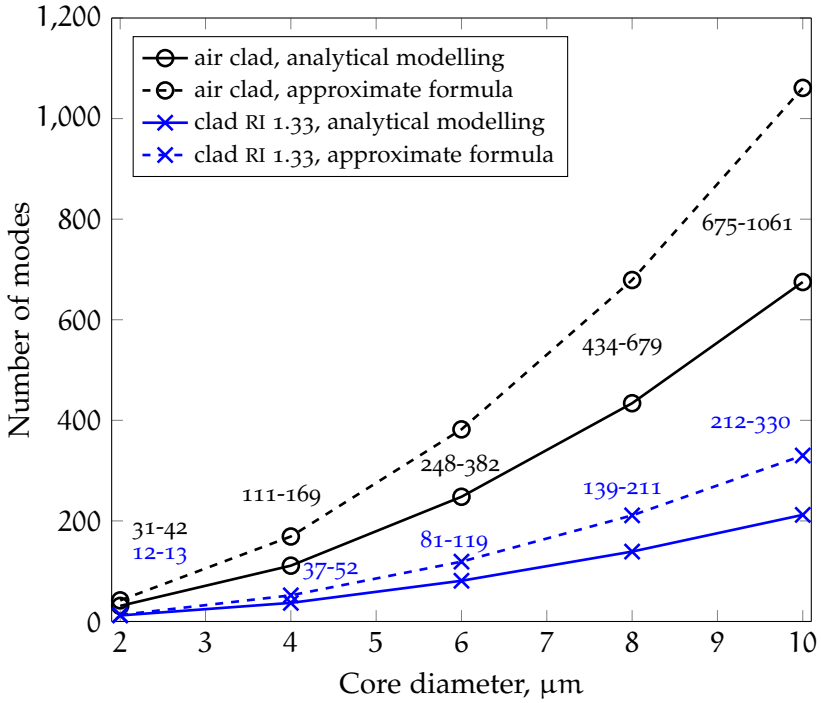


Figure 5.17: Number of modes as a function of core diameter for a step index fibre with air-cladding (black circles) and polymer cladding of RI of 1.33 (blue crosses). Calculation of number of modes using analytical modelling with Maxwell's equations (solid lines), and approximate formula for estimation of number of modes in MMF (dashed lines). The data point labels show the values for the number of modes.

In order to further reduce the number of modes without decreasing the fibre core size, the NA of the fibre can be reduced. We explored the possibility of filling the air holes of the ECF with a dielectric material of RI lower than silica, to preserve the guiding capability of the fibre, but higher than air, in order to provide smaller index contrast and reduce the number of modes propagating in the fibre. Figure 5.18 shows the number of modes in an optical fibre with core diameter of 10 µm as a function of cladding RI.

The approximation of the number of modes in the ECF with a step index fibre of the same core size could be a reasonable estimate for demonstrative purposes. The number of modes in Figure 5.18 and Figure 5.17 was calculated using two methods,

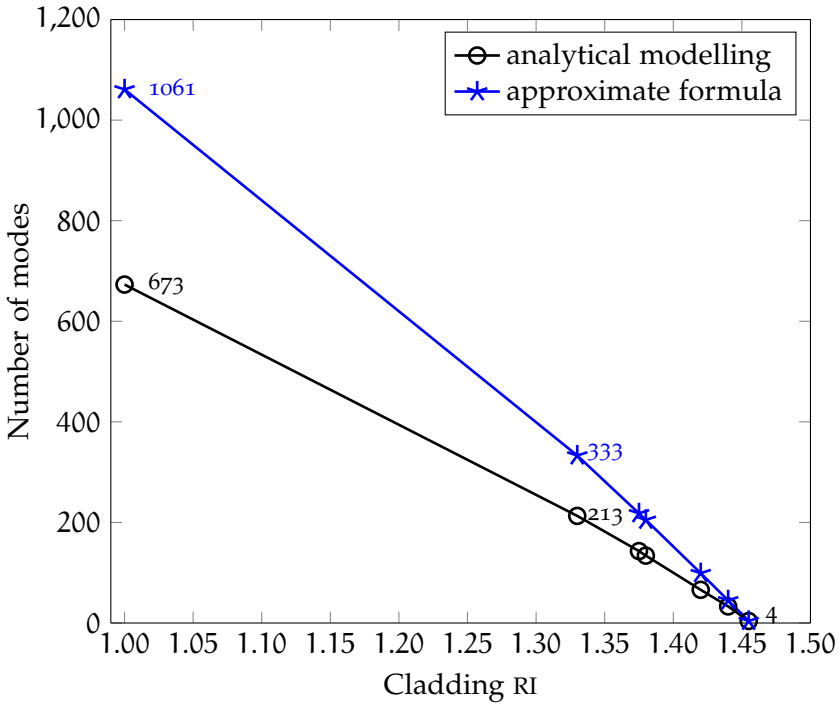


Figure 5.18: Number of modes in a 10 µm ECF as a function of cladding RI estimated at 650 nm using analytical modelling with Maxwell's equations (black circles) and approximate formula for MMFs (blue crosses). RIs of commercially available polymers are chosen as values of cladding RIs.

analytical modelling based on Maxwell's equations, and an approximate formula for MMF:

$$M \approx \frac{V^2}{2}, \tag{5.1}$$

where V is the V-number of a waveguide, a dimensionless parameter that depends on the fibre core diameter (d) and fibre NA, and is defined as

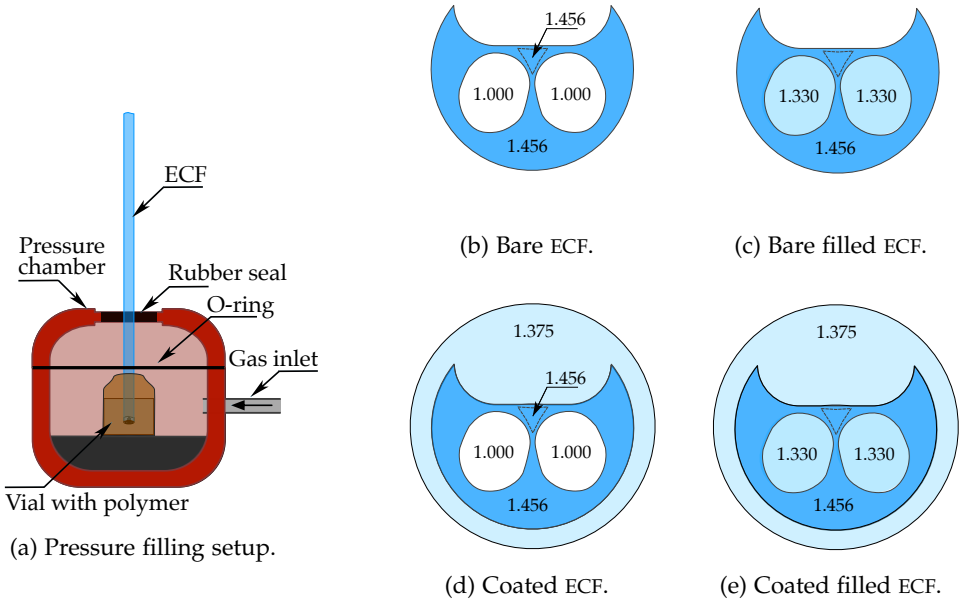
$$V = \frac{\pi}{\lambda} d\ NA. \tag{5.2}$$

The approximate formula is valid for only large V-numbers and may overestimate the number of modes in fibres with small V-numbers. Analytical modelling, however, is applicable for small V-numbers and could be used for fibres with just a few guided modes. A Mat Lab model that analytically solves Maxwell's equations was used to find solutions (propagation constants) for all fibre modes of a step-index optical fibre with specified parameters (fibre diameter, wavelengths, and RIs of the core and cladding), and calculates the number of existing solutions [285]. The analytical model performs better for fibres with fewer modes and may underestimate the number of existing modes for a highly MMF. Therefore, estimating the number of modes in a step-index MMF with a relatively small core using both methods, gives upper and lower boundaries for the actual number of supported modes.

Regardless of the method for estimating the number of modes, changing the cladding RI of the silica fibre from air to 1.33 gives a relative reduction to the number

of modes by 30%, as is clear from the Figure 5.18. Increasing the RI of the cladding to 1.45 would result in the almost single mode regime with only a few guided modes supported by the fibre. Even though the step-index approximation considers symmetric RI profile of the fibre, filling the ECF would result in an asymmetric RI profile, reducing the index contrast between air channels and the silica core would discriminate against higher order modes.

An initial attempt was made to fill the ECF's air channels with pure glycerol (RI of 1.47). However, this was not possible to contain the liquid glycerol inside the air channels as the solution was moving inside the fibre holes and escaping through the fibre ends. As a result, it was not possible to preserve consistent coupling into the filled ECF. To eliminate the issue of containing liquid solutions inside the fibre air holes, a low RI UV curable polymer, typically employed as optical fibre claddings and optical adhesives, was used as an alternative to the liquid solutions. Therefore, the air channels of the bare and the coated ECFs were filled with a polymer of RI of 1.33 (My Polymers, MY-133-2000V). The filling was performed using an in-house built pressure setup which is schematically shown in Figure 5.19a.



(a) Pressure filling setup.

(b) Bare ECF.

(c) Bare filled ECF.

(d) Coated ECF.

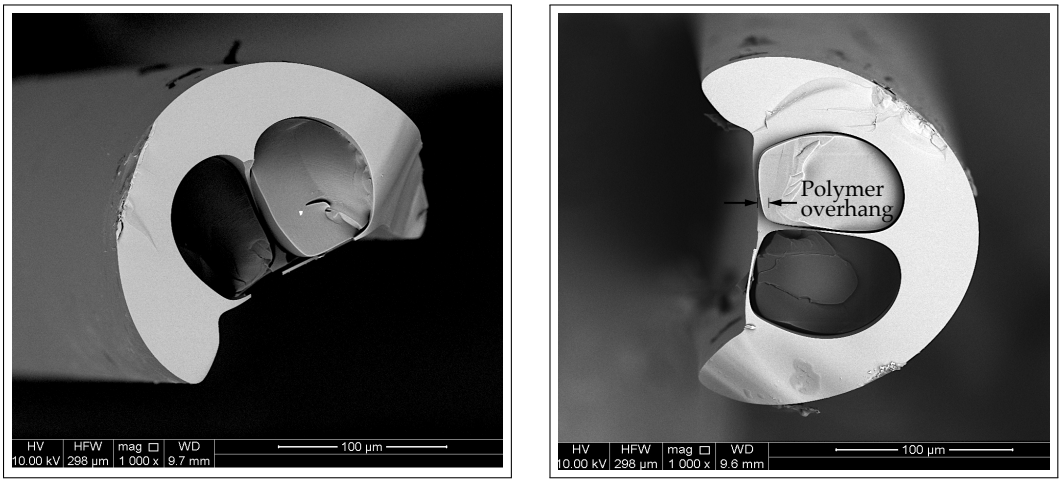
(e) Coated filled ECF.

Figure 5.19: Schematics of (a) pressure filling setup used to fill ECFs with a low RI UV curable polymer; and (b-e) cross sections and nomenclature of ECFs used to fabricate SPR sensors with RIs of the materials shown.

One end of the ECF was submersed into the vial filled with the liquid polymer. The vial was placed inside the pressure chamber. The other end of the fibre was passed through a rubber seal in the chamber lid. Argon was supplied at 200 psi to pressurise the chamber. The pressure gradient between the fibre ends forced the liquid polymer up the fibre, filling the air channels. The chamber was pressurised for around $8-10$ hours depending on the length of the ECF with approximate filling rate of $5-6$ cm/hour. After the fibre samples were completely filled, they were removed from the pressure filling apparatus and the polymer inside the channels

was cured with UV light exposure. The resulting cross sections of the fibres with RIs are shown in the Figure 5.19c and Figure 5.19e.

Despite the relative simplicity of filling the fibre holes with the polymer, cleaving of the filled fibres proved to be challenging. Cleaving of glass ECFs is typically performed manually using "scribe-and-brake" method [286]. Two polymer strands inside the ECF's channels stayed intact after performing a break of the ECF during the cleaving procedure. The polymer strands needed to be cut often resulting in overhangs of the polymer above the fibre facet, or breakage of the fibre core. Figure 5.20 shows SEM images of the filled ECF cleaves with a broken core and polymer overhangs.



(a) Cleave of ECF with brocken core.

(b) Cleave of ECF with polymer overhang.

Figure 5.20: SEM images of silica ECF filled with a UV cured low RI polymer (MY Polymers, MY-133-V2000).

An attempt of removing the polymer strands with the flame of a butane lighter prior to fibre cleaving was made. However, a controlled temperature flame gun was not available at the time and the procedure typically resulted in breakage of the silica struts after the polymer was burned. It is difficult to conclude if this was a result of polymer expansion when heated or an excessive temperature gradient resulting in fracturing. These difficulties with cleaving the filled ECFs could potentially be avoided by not filling the whole section of the fibre with the polymer. Nevertheless, some decent cleaves were achieved and performance of the SPR sensors based on filled bare and coated ECFs were analysed. SPR scattered spectra for the coated filled ECF SPR sensor and bare ECF SPR sensor are presented in Figure 5.21 and Figure 5.22, respectively.

Spectra presented in Figure 5.21 were collected from the same sample that were shown in Figure 5.9 after the characterised sensor was filled with the polymer. As before the filling, two peaks are present in the scattered spectra. The sensitivity of the first peak, that was previously determined to correspond to the core SPR excitation, and the dip of the filled ECF sensor was estimated to be 1716 nm/RIU and 2212 nm/RIU, respectively. Those sensitivity values are consistent with the results for the unfilled coated ECF sensor within experimental uncertainties (Figure 5.10). The second peaks at longer wavelength, that are believed to be a result of the ex-

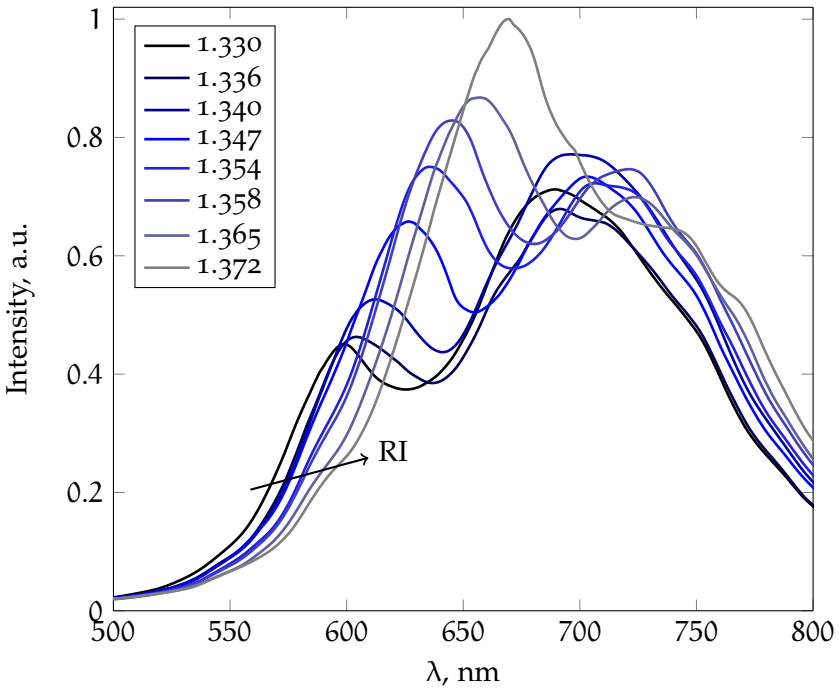


Figure 5.21: Processed SPR spectra (normalised to local maxima and filtered) for the acrylate-coated ECF sensor filled with MY-133 polymer (same sample as in Figure 5.9). Sensitivity of the shorter wavelength peak is 1716 nm/RIU, sensitivity of the dip is 2212 nm/RIU. The support structure mode is suppressed (smaller peak at longer wavelengths when compared with spectra before filling the air holes, Figure 5.9) and has a lower sensitivity of 749 nm/RIU.

citation of SPs in the fibre support structure, appear smaller than before the sensor was filled with polymer, and have half the sensitivity, just 749 nm/RIU in comparison to 1498 nm/RIU before the fibre was filled. The cause of this suppression of the second SPR response in the filled coated ECF is not clear and could potentially be due to the change in the guided modes, coupling conditions, or location on the sensing region from where the scattered spectra were collected. As far as linewidth of the SPR response is concerned, no significant change was detected between filled and not filled coated ECF.

Normalised scattered SPR spectra in a bare ECF filled with the polymer is shown in Figure 5.23. Sensitivity curve, FWHM, and other performance parameters for the sensor is presented in Figure 5.23. It is clear from the results that no significant change was present with most of the performance parameters. The FWHM of the SPR response was higher than average for the unfilled bare ECF SPR sensors, around 100 nm in comparison to 77 nm, however, this change might not be statistically significant due to the small number of filled ECF samples was analysed. SNR for the filled bare ECF sensor was smaller than that for the air clad ECF sensor, which is most likely a result of more challenging coupling.

Despite the expected three times reduction in the number of modes in the filled ECF in comparison to the air clad ECF, no noticeable improvement in either sensitivity or FWHM was observed. There are a few possible reasons of this lack of enhancement in the sensor performance. In the best case scenario the number of modes in the ECF of 10 µm core diameter could be reduced from approximately 670

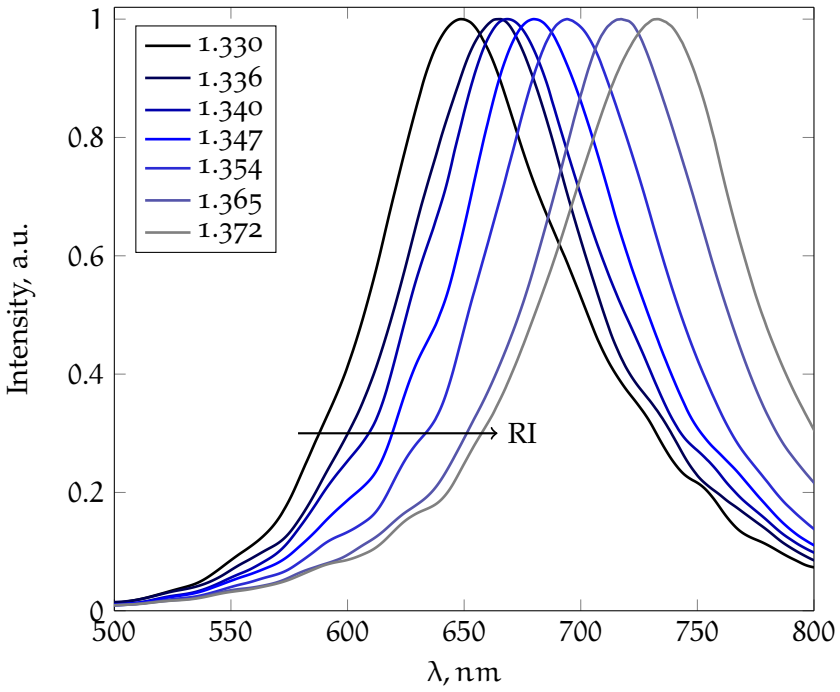


Figure 5.22: Processed SPR spectra (normalised and filtered) for bare ECF sensor filled with MY-133 polymer.

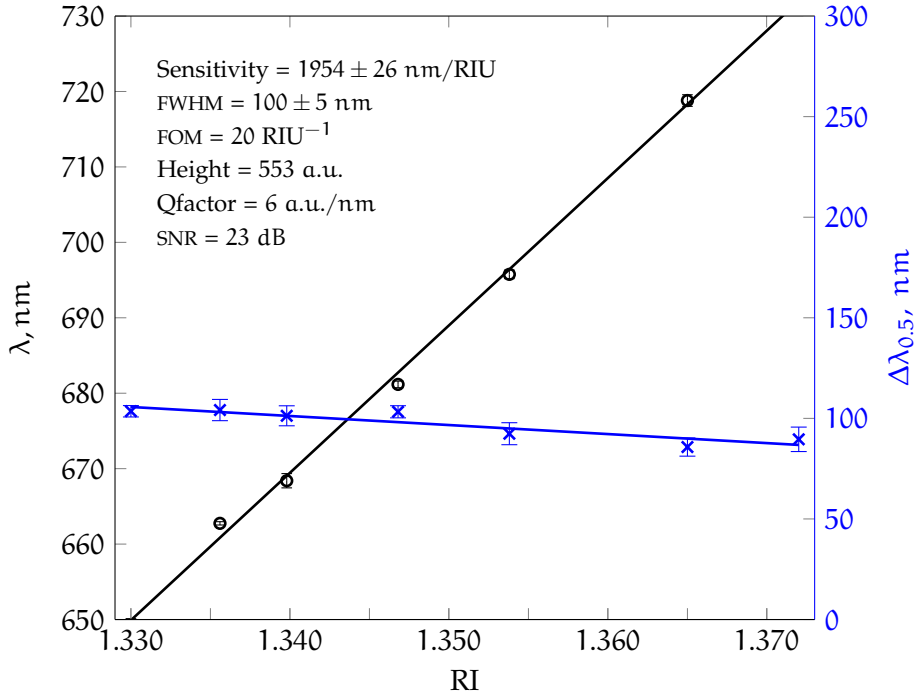


Figure 5.23: Sensitivity (black circles) and FWHM (blue crosses) for bare ECF sensor filled with MY-133 polymer characterised using aqueous solutions of glycerol. Fitting errors are shown as error bars. Maximum absolute uncertainty in RI of glycerol solutions is 0.001.

down to 210 modes by changing the cladding RI from 1.00 to 1.33 (Figure 5.18). The observed double improvement in the FWHM in ECF sensor in comparison to the large core silica sensor resulted from the change in the core size from 140 µm down to

10 μm. In terms of the number of modes, the large core step index fibre presented in Chapter 4 has around two orders of magnitude more modes than the air clad ECF. Even though the number of modes in the filled fibre was decreased, the reduction is likely to be insufficient to cause a noticeable difference in the spectral linewidth of SPR response. Moreover, the design of the ECF allows the filling of the two air holes inside the fibre when the exposed side of the core still has air cladding. This results in an asymmetric RI contrast between core and cladding that will influence the number of modes and their structure. A numerical analysis is needed to evaluate the expected SPR response in this case. It is also possible to use higher RI polymer to fill the fibre holes. Reducing the index contrast between silica core and polymer holes down to 0.001 could bring the 10 μm core-ECF to a nearly single mode regime. However, in addition to the above considerations, there are some practical difficulties related to cleaving the fibres once filled with the polymer.

5.7 SUMMARY AND POTENTIAL FUTURE WORK

The sensitivity and resolution of SPR sensors, both have critical importance for sensing applications. After demonstration of the silica fibre based SPR sensors with improved sensitivity, the increased linewidth of the SPR response, and therefore degraded resolution, needed to be addressed. It was predicted that the reduction in the number of guided modes propagating in the fibre would decrease the number of modes whose propagation constants match that of SPs. As a result, the spectral linewidth of the scattered SPR response could be reduced, enabling higher resolution in determining the wavelength shift. However, due to the inherent fragility of the small core fibres and fibre tapers, using these sensors in real applications presented a significant challenge. In this chapter, the development of an SPR sensor based on the MOF with modified geometry of the exposed core was presented. The major advantage of the ECF is that the plasmon film can be deposited directly on the exposed section of the fibre core without additional fibre processing or coating of the air holes inside the fibre, as it is typically done with MOF-based SPR sensors.

The silver coating fabrication process on the ECF using chemical electroless plating is similar to the large core silica fibres. This allowed the production of metal coatings with high surface roughness, required for the enhanced scattering of the SPs, and the use of the ECF-based probe in our SPR architecture. The large support structure of the ECF allowed simple handling of the fibres with the small core of 10 μm diameter.

SPR sensing probes were characterised and compared to the large, 140 μm-diameter core MMF-based lead silicate and silica fibre sensors. Refractive index sensitivity of the new ECF probe was found to be comparable with the large core silica based sensors, 1789 ± 108 nm/RIU. The experimentally demonstrated FWHM of the SPR sensor based on the small core ECF was 77 ± 12 nm, which is halved in comparison to the large core silica SPR sensor, and a factor of 1.5 improvement in comparison to the higher RI lead silicate fibre SPR probe.

The analysis of the behaviour of the SPR response in ECF based sensors suggests that there is a strong dependence of the width of the spectral SPR feature on the structural dimensions of the optical fibre. Structures with smaller dimensions, such

as the ECF core or edges of the support structure, have SPR response at shorter wavelengths than larger features, such as the support structure itself, or the large core fibre probes. While the spectral width of the SPR signature is narrower for the small structural features, the RI sensitivity was found to be independent on the spatial dimensions of the waveguide. These properties could be utilised for designing SPR sensing probes with multiple spectrally independent sensing regions in the same device.

Further improvements in the spectral width of the SPR response can be achieved through the reduction of the core size of the ECF. An attempt to taper the ECF diameter proved to be challenging and resulted in breakage of the tapered probes' cores. This damage occurred even at a small tapering ratio of 2, which was likely a result of the strut damage. The fabrication of ECFs with smaller cores of around $1-3$ μm were recently reported [287], which opens potential avenues for further improvement in the linewidth of the SPR signature.

An interesting alternative to reducing the number of modes propagating in the ECF without changing its core size is through modifying the fibre NA. Preliminary experiments were performed to successfully fill the ECF's air channels with low RI UV-curable polymer for 5 fibre samples. Even though no significant performance improvement was detected, the experiments demonstrated a proof of concept for this fabrication technique. It is envisaged that the use of higher RI polymers for smaller index contrast between the core and cladding, as well as adjustments in the cleaving procedure, could be an interesting direction for future experiments.

The ECF sensors with the spectral interrogation of the scattered plasmonic wave provided some advantages in comparison to conventional transmission-based MMF SPR sensors, such as a small linewidth, a reduced SNR, and a lower dependency of the sensor performance on the coating thickness. Combined with the high sensitivity of the silica core, the ECF-based SPR sensing architecture is promising for applications such as biological or chemical sensing where improved resolution and high sensitivity are required.

6

METAL ENHANCED FLUORESCENCE (MEF)

6.1 INTRODUCTION

Fluorescence analysis is one of the principal techniques in biochemical sensing and medical diagnostics studies due its high sensitivity, simplicity, and availability of fluorophores [288]. However, there is a drive to further improve detection limits as the detectability of fluorophores is limited by quantum yield, photostability and an onset of autofluorescence. In the last decade MEF, also referred to as plasmon enhanced fluorescence, has attracted significant attention as an emerging tool in fluorescent spectroscopy.

The spectroscopic properties of fluorophores can be varied by changing the free-space condition, i. e. modifying the photonic mode density near the fluorophore. This can be accomplished by placing the fluorophore molecule near a conducting particle or surface. To understand the effect of metals on fluorescence, it is important to define the quantum yield of a fluorophore and its fluorescence lifetime. Figure 6.1a shows a Jablonski diagram for conventional fluorescence and modifications due to the presence of metal.

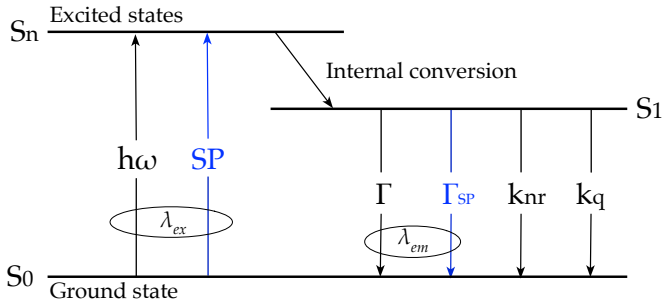
In classical fluorescence, a fluorophore molecule results in an excited state upon absorption of a photon at λ_{ex}. The fluorophore then can return to its ground state via the radiation of a photon of lower energy, or longer wavelength λ_{em} at a constant rate Γ, or through non radiative decay, k_{nr}, or through some other non-radiating processes, such as quenching, k_q. Quantum yield, Q_0, is a measure of the competition between radiative processes, e. g. emission of the photon, and all non-radiative processes and can be estimated as:

$$Q_0 = \frac{\Gamma}{\Gamma + k_{nr} + k_q}. \tag{6.1}$$

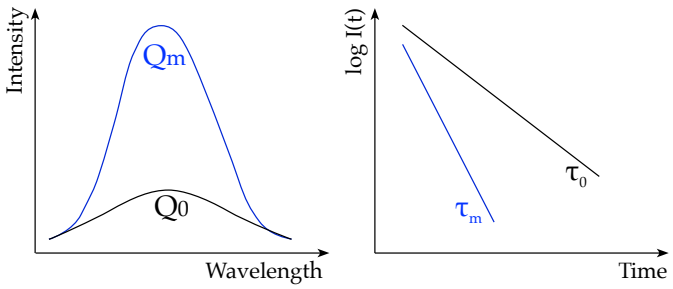
The fluorescence lifetime, or decay time, is the mean time that the fluorophore remains in the excited state and is given by:

$$\tau_0 = \frac{1}{\Gamma + k_{nr} + k_q}. \tag{6.2}$$

It is of interest that Γ is essentially a constant for a specific fluorophore molecule and is determined by its extinction coefficient. Therefore, changes in fluorescence intensities and lifetimes are mainly due to changes in non-radiative decay rates, k_{nr} and k_q and are strongly influenced by the environment surrounding the fluorophore, such as RI, phase, and temperature [289]. Metals, however, provide unique opportunities of changing the radiative decay rate through modifications in the rate of excitation and emission. Strongly confined electromagnetic fields associated with LSPs and propagating SPs can interact with the fluorophore at its excitation and



(a) Jablonski diagram.



(b) Increased quantum yield and decreased lifetime.

Figure 6.1: Effect of metal and SPs on fluorescence. Adapted from [289]. Modified Jablonski diagram shows SP mediated transitions between the fluorophore ground state and higher excited states. Classical Jablonski diagram is shown in black and modifications due to presence of metal is shown in grey.

emission wavelengths, altering the respective transitions between ground state and excited states, as shown in Figure 6.1a. For a fluorophore near metal, the quantum yield and lifetime can be written as:

$$Q_m = \frac{\Gamma + \Gamma_m}{\Gamma + \Gamma_m + k_{nr} + k_q}, \tag{6.3}$$

and

$$\tau_m = \frac{1}{\Gamma + \Gamma_m + k_{nr} + k_q}. \tag{6.4}$$

Therefore, in addition to the enhancement of the excitation by electromagnetic field associated with SPs, the quantum yield and fluorescence lifetime is improved by altering the radiative decay rate, Γ. Decreased fluorophore lifetimes are typically an undesired effect in the absence of metals and are associated with lower quantum yields and lower intensities. However, in the presence of fluorophore-metal interactions the decreased lifetimes can be beneficial and result in a higher photon flux from the excited state to the ground state and increased photostability, thereby improving fluorophore detectability [289, 290].

Nanostructured metal films or nanoparticles that exhibit localised surface plasmon resonances have been extensively studied for MEF [291–297]. The strong elec-

tromagnetic field associated with localised plasmons on metal particles can resonantly interact with fluorophore molecules causing high amplification of the fluorescence emission intensities. The enhancement factors depend on the type, shape, size, and separation between nanoparticles ranging from 10 up to 10^6 reported for some configurations [298]. Plasmonic enhancement of fluorescence has been achieved on inhomogeneous metal structures. In particular, enhancement factors of 6-, 17-, and 50-fold were reported for metal nanoparticles attached to glass substrates [299], electrochemically grown metal fractals [300], and metal colloids [301], respectively. MEF has also bee demonstrated for metal nanoparticles conjugated with fluorophores. For example, 40-fold fluorescence emission enhancement was shown on gold nanorods with a single fluorophore molecule attached to the end of the nanorod. Homogeneous metal structures provide advantage of having a periodic or defined structure where the enhancement effects can be mapped out and utilised to improve plasmonic enhancement. An enhancement of fluorescence of up to a 117-fold was recently shown on a structure by isolating a dye molecule in the 23 nm spacing between two 100 nm gold nanoparticles [302]. A remarkable 1340-fold fluorescence enhancement was shown for a single molecule in a gold bowtie nano-antenna with a 10 nm spacing [303].

An important factor for efficient enhancement is the match between the excitation wavelength of the fluorophore and the resonant wavelength of the SPs. In addition to the spectral properties of the metal itself, MEF is highly dependent on the distance between the fluorophore and the metal. The optimal distance depends on the fluorophore, metal, and surrounding environment, and is between $8-20$ nm [289, 292, 304, 305]. Figure 6.2 shows a conventional schematic of fluorophore molecules located at the optimal distance from metal nanoparticles.

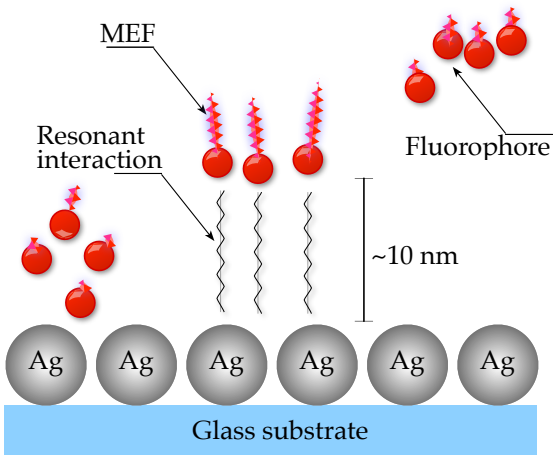


Figure 6.2: Schematic of a typical resonant interaction between fluorophore dye molecules and SPs on metal nanoparticles (Ag) causing enhancement of fluorescent emission at the optimal distance.

Although impressive fluorescence enhancement factors of up to 10^6 [306] were achieved with metal nanoparticles and nanostructures, it remains experimentally difficult to produce large nanostructured surfaces with consistent surface density and reproducible MEF properties [298]. Lower enhancement factors, typically an order of 2, are attributed to continuous smooth metal films [307]. Therefore, in order

to bridge the gap between metal nanostructures and continuous films, there has been some interest in study of rough metal surfaces. As discussed in Chapter 4, the SPs on a rough surface undergo elastic scattering due to the spatial fluctuation in the dielectric function of the metal-dielectric interface. This fluctuation results in localisation and increased density of optical states as well as amplified electromagnetic field amplitude near the rough surface in comparison to that supported by a smooth film [223]. The continuous metal films that have previously been reported to be suitable for MEF were achieved by thermally annealing silver films [293], by slow thermal evaporation of silver [308], or fabrication of very thin particulate metal films [309].

In most MEF experiments metal particles or nanostructured metal surfaces are attached to planar substrates. In those experiments the fluorophore and localized SPs are excited by light incident to the surface. Propagating SPs in planar metal films could only be generated by light that is passed through a higher refractive index dielectric, such as a glass prism, due to the mismatch of propagation constants of light and SPs at the air-metal interface, as was discussed in detail in Chapter 2. Therefore, the Kretschmann configuration is the method of choice for most experimental demonstrations of MEF [294, 310]. Although this approach offers high resolution and simple experimental realization, it is somewhat cumbersome, expensive and is not applicable for remote sensing. Fibre based MEF sensors, on the other hand, offer the advantages of low cost, simple microfluidics integration, and the potential for multiplexing. Although some fibre-based MEF configurations were proposed [307, 311], MEF fibre based architectures remain an interesting and a little-explored topic for the development of improved fibre optic sensing probes.

The SPR fibre configuration presented in Chapter 4 and Chapter 5 is a promising platform for development of MEF fibre based sensors. The scattering of light at the resonance frequency mediated by the rough silver coating results in a strong electromagnetic field amplification near the metal surface that could be used to achieve fluorescent enhancement. In order to explore this, we investigated the effect of surface roughness of continuous thin silver films on fluorescence enhancement in regard to their potential applications for MEF fibre-based sensors. This chapter presents a study on the effect of surface roughness on fluorescence enhancement in planar substrates where plasmons are excited in the Kretschmann configuration, as well as the development of MEF-based sensor fabricated on the side of a MOF. The initial work was performed by François *et al.* and presented in a conference paper [312]. An advanced study on the fibre based configuration was performed by the author, is described in this chapter and published in a peer reviewed journal [313].

6.2 DISTANCE-DEPENDENT ENHANCEMENT ON PLANAR SUBSTRATES

In order to investigate the dependency of fluorescent intensity on the roughness of silver coatings as well as to determine an optimal distance between the fluorophore and the metal film, experimental studies in planar geometry were performed. The planar substrates allow for simplified analysis of the topography of the surfaces,

as well as the silver film thickness, which in the case of cylindrical fibre would require much more complex study techniques. Cover slips (Deckgläser, Cover Glasses 22x22) were chosen as the substrate onto which thin silver films of around 50 nm thickness were deposited. To provide a range of silver film roughnesses, two methods have been used to deposit Ag thin films onto the glass slides, thermal vacuum evaporation and chemical electroless plating. The distance between the fluorophore and the metal film was varied through layer-by-layer deposition of a polyelectrolyte multilayer spacer, as described in Chapter 4.

6.2.1 *MEF sample fabrication*

Preparation of the planar substrates started with thorough cleaning by sonication in acetone for 30 minutes then rinsing with ethanol and deionised water. All samples were dried prior metal coating. Two deposition techniques were used to fabricate the silver films on the prepared glass slides: thermal evaporation, and chemical deposition described in the Section 4.2.2. Thermal evaporation is a physical vapour deposition technique that involves heating a source material inside a vacuum chamber until its atoms acquire enough energy to escape the surface and travel through the chamber adhering to a substrate. The pressure inside the chamber must be sufficiently low to make the mean free pass, a distance the atom can travel before it collides with another particle, longer than the distance between the evaporation source and the substrate.

Thermal vacuum evaporation was performed in house using a thermal evaporator (JEOL, JEE 420) with a tungsten crucible under 2×10^{-4} Pa. No thickness control of the deposited films was available with the evaporator, and therefore, the instrument was calibrated to allow fabrication of silver coatings with the desired thickness. In particular, the thickness of deposited silver films depends on the internal pressure, current applied to the source, weight of the evaporation source, positioning of the substrate inside the chamber, and time of the substrate exposure to the vapour. All of these conditions were adjusted to fabricate silver films of around 50 nm, the optimal thickness for SPR excitation.

The thickness of the fabricated silver films on glass substrates has been determined through transmission measurements, as was described in Section 4.3.2. Topography of the metal coatings was studied using AFM technique (NT-MDT, Ntegra Solaris). Silver film thickness for several samples was also verified through AFM by measuring the surface profile at the edge of the coatings. The surface roughness values presented in the current thesis are Root Mean Square (RMS) roughness, R_q, and were estimated using scanning probe microscopy data analysis software provided by the manufacturer of the instrument (NT-MDT, Nova SPM Software), as well as an open source software package (Gwyddion) [229].

Slowly evaporated silver films are known to have higher surface roughness, a behaviour that is unique to silver. When evaporated at a low rate, silver films form aggregates that tend to grow more in height, i. e. become thicker before joining together. This is opposite to the rapidly formed films for which the aggregates remain thin and grow out over the substrate [314]. Therefore, the deposition rate

Table 6.1: Properties of silver films fabricated by different methods. Thickness of the silver films was estimated through transmission measurements. AFM was used to determine silver film roughness and verify film thickness.

Deposition method	Thickness, nm	Rate, nm/s	Roughness, nm
Thermal evaporation, 28 Amps	46.50±1.50	0.32	4.13±0.38
Thermal evaporation, 30 Amps	51.42±3.36	0.73	2.83±0.66
Thermal evaporation, 36 Amps	50.69±0.51	2.29	2.46±0.14
Thermal evaporation, 40 Amps	49.77±0.13	3.52	1.69±0.22
Chemical electroless plating	53.00±5.00	0.11	7.92±0.55

was altered by changing the evaporation current from 28 to 40 $Amps$ to produce coating with a range of surface roughnesses, while the exposure time was adjusted accordingly to provide the desired thickness of 50 nm. This range of evaporation currents allowed to obtain a varying degree of silver film roughness, from 1.7 to 4.1 nm, measured by AFM, as listed in Table 6.1. The demonstrated results are supportive of the reported behaviour where lower deposition rate caused the formation of rougher surfaces. Lower evaporation currents, below 28 $Amps$ resulted in poor reproducibility of the silver coating properties, and therefore, were not used. The chemical electroless plating technique was also used to fabricated samples with high surface roughness of around 8 nm, above the range achievable with the thermal deposition method.

6.2.2 *Experimental procedure*

Surface functionalisation

In order to find the optimal separation, the distance between silver film and fluorophore was finely tuned through layer-by-layer adsorption of positively and negatively charged PE layers, PAH and PSS [265]. The solutions of 2 mg/mL were prepared in 1M of aqueous $NaCl$. The silver coated glass slides were immersed in each PE solution for approximately 15 minutes and thoroughly rinsed in deionized water between each subsequent step. To determine the size of the spacer where maximum fluorescence enhancement occurs, samples with an odd number of PE layers, ranging from 1 to 21 with positively charged PAH as a first and the last layer, were prepared to vary the gap between the metal film and the fluorophore.

PE layer formation using layer-by-layer technique has been extensively studied in literature including distance tuning for MEF [292, 315]. It has been reported that PE layers follow uniform growth with the number of deposited layers [315]. Even though the formation of the first PAH/PSS bi-layer can be different for substrates with different surface charge, it has been shown that a small amount of PAH on a surface is sufficient to facilitate the subsequent adsorption of PSS, thereby allowing multilayer thin film formation [316]. Moreover, the PE layer formation follows a linear increase after the deposition of four polyelectrolyte layers [316]. Therefore, it is reasonable to expect that after the deposition of multiple layers, the assumption

of uniform thickness and density of the polyelectrolyte holds for the silver coated and bare glass substrates.

An organic dye functionalised with carboxyl groups (Sigma Aldrich, 4-(2- Carboxyphenyl)-7- diethylamino- 2-(7-diethylamino- 2-oxochroman- 3-yl)- chromylium perchlorate), further referred to as 'the organic dye', was covalently attached to the last PAH layer using amine coupling reagents, EDC and NHS. The organic dye is comparable to Cyanine 5 (Cy5) with maximum absorption (λ_{ex}) at 654 nm and peak emission wavelength (λ_{em}) at around 694 nm. A concentration of 10.9 mg of the organic dye in 10 mL of water and 5 mL of methanol was used in the experiments.

Experimental setup

A Kretschmann prism setup with a linearly polarised HeNe laser source was used for characterisation of surface plasmon fluorescent enhancement in planar substrates. PE-functionalised glass slide samples were mounted on a facet of a BK7 prism using index matching oil (RI 1.51 at 25°C), as schematically shown in Figure 6.3. The prism was positioned on a computer-controlled rotational stage to allow precise control over a range of incident angles onto the metal film. The minimum in the reflected spectrum which corresponded to the excitation of SPs at a particular angle was monitored with a power meter on the opposite side of the prism. The fluorescent signal was collected from the fluorophore coated glass slide surface and analysed with a compact spectrometer (Ocean Optics, QE 65000).

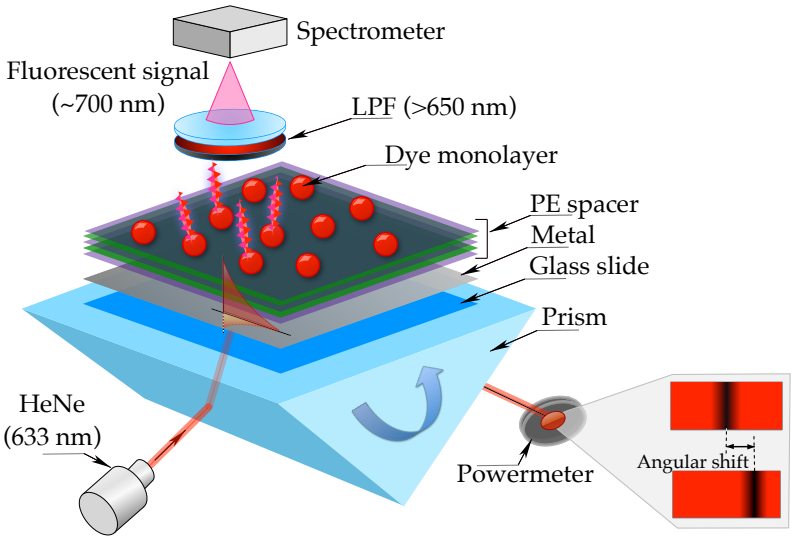


Figure 6.3: Schematic of a prism configuration used for the characterisation of MEF on planar substrates. The optical setup is identical to the Kretschmann configuration shown in Figure 4.14. The fluorescent signal is collected from the facet of the prism and laser background was filtered out through a Long Pass Filter (LPF). Measurements were performed in air.

To characterise the enhancement of fluorescence on the glass slides, fluorescent signal intensity and reflectivity of the laser light, that corresponds to SPR response, were analysed at varying incidence angles for samples with different silver coating roughness and an increasing number of PE layers, from 1 to 21.

6.2.3 *Results and discussion*

A typical SPR response on planar substrates is presented in Figure 6.4 where angular shifts of the minima of the reflected spectra correspond to adsorption of each subsequent PE layer. The maximum in the fluorescent signal intensity coincides with the minimum in the reflected spectra associated with SPR excitation, as shown in Figure 6.5.

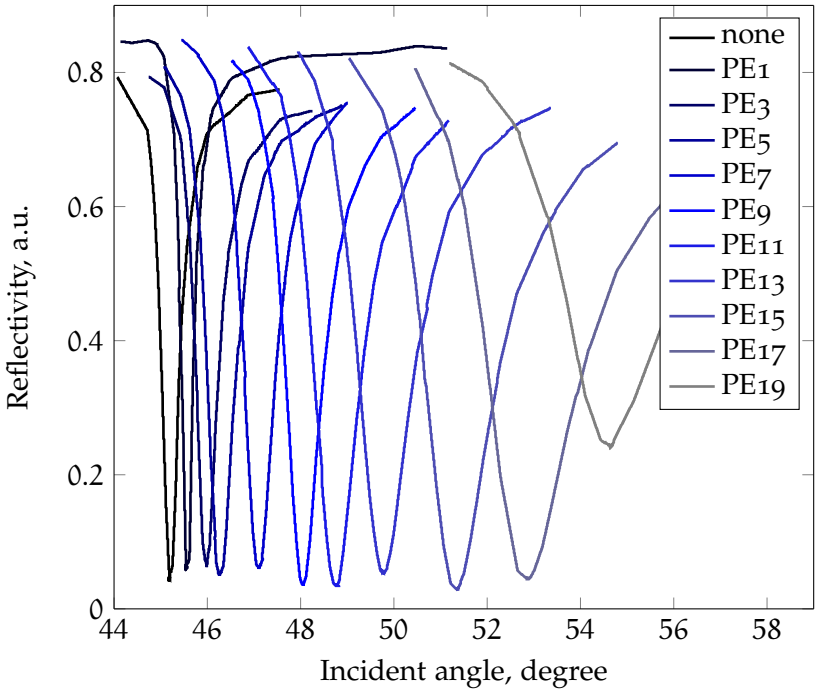


Figure 6.4: A typical increase in the angular position of the dip in the reflected spectra corresponding to SPR as a function of increasing number of PE layers on a planar substrate.

The fluorescence enhancement factor (EF) is defined as the ratio of maxima of fluorescent intensities of silver-coated and uncoated glass slides, after immobilization of the fluorescent dye on the PE-functionalised surface:

$$EF = \frac{I_{coated}}{I_{uncoated}}. \tag{6.5}$$

It was found that for all samples where silver coatings were produced by thermal evaporation, the maximum fluorescence enhancement occurred after the deposition of 7 PE layers, which corresponds to $\approx 12 \pm 0.8$ nm, as shown in Figure 6.6. The thickness of the PE spacer was determined from the SPR angular response using multilayer TMM described in Chapter 3 and is shown as the top horizontal axis in the Figure 6.6. The RIs of glass and PE coating was assumed to be 1.54 and 1.47 respectively [27], and the complex dielectric function of silver was estimated using the Lorentz-Drude model [73]. This value is broadly consistent with the previously reported thickness of individual PE layers of ≈ 1.5 nm [27, 265]. For the slides with silver films deposited by the chemical method the SPR shift was larger than for the samples with thermally evaporated coatings. This is likely attributed to the different

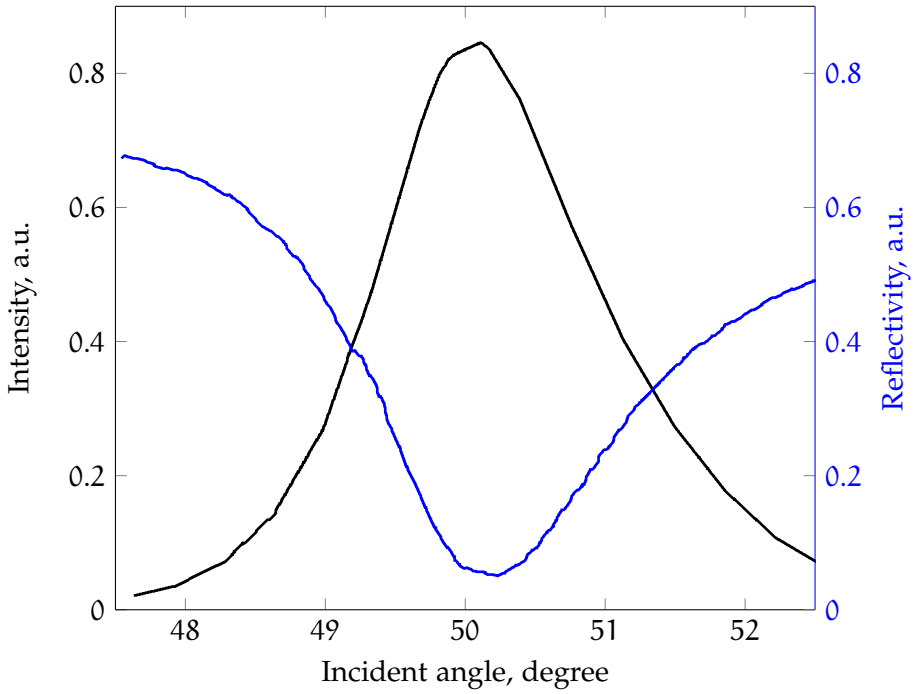


Figure 6.5: Fluorescence emission intensity of the dye (black) and SPR signal (reflectivity) (blue) of a planar substrate. A sample with thermally evaporated coating was used as an example.

dielectric function of silver deposited by the chemical technique rather than the difference of thickness of the PE spacer, or stronger interaction of SP field with the environment due to the roughness of the silver surface. This is supported by the fact that the maximum fluorescence enhancement factor for chemically coated slides was observed after the deposition of 7 PE layers.

This analysis revealed a strong dependence of the fluorescence enhancement factor in planar substrates on the thickness of the PE spacer, as well as silver film roughness, as evident from Figure 6.6. The distance-dependent behaviour of the fluorescence enhancement is attributed to the fundamental nature of interaction between the fluorophore and the metal surface. Given the evanescent character of the SP field, one can expect that the fluorophore has to be placed as close as possible to the metal surface to maximise the possibility of excitation. However, it was predicted theoretically [305], and then proved experimentally numerous times, that the fluorophore-metal interaction has a rather complex behaviour. There are three distance regions that are of importance. At close distances of $5-7$ nm Förster energy transfer occurs between the fluorophore molecule as a donor and the metal as acceptor system which results in dissipation of the fluorescence emission into the metal, hence, reduced fluorescence intensity. For intermediate separation between the fluorophore and the metal, which is between $8-20$ nm depending on the particular configuration, SP modes excite the fluorophore with a proportion of the fluorescence light is coupled back to the metal exciting lower energy SP states. For larger separation, no efficient coupling between the excited fluorophore and the plasmonic mode can occur and conventional fluorescence emission occurs [305]. The separation of around 12 nm, found to be optimal for this configuration, is

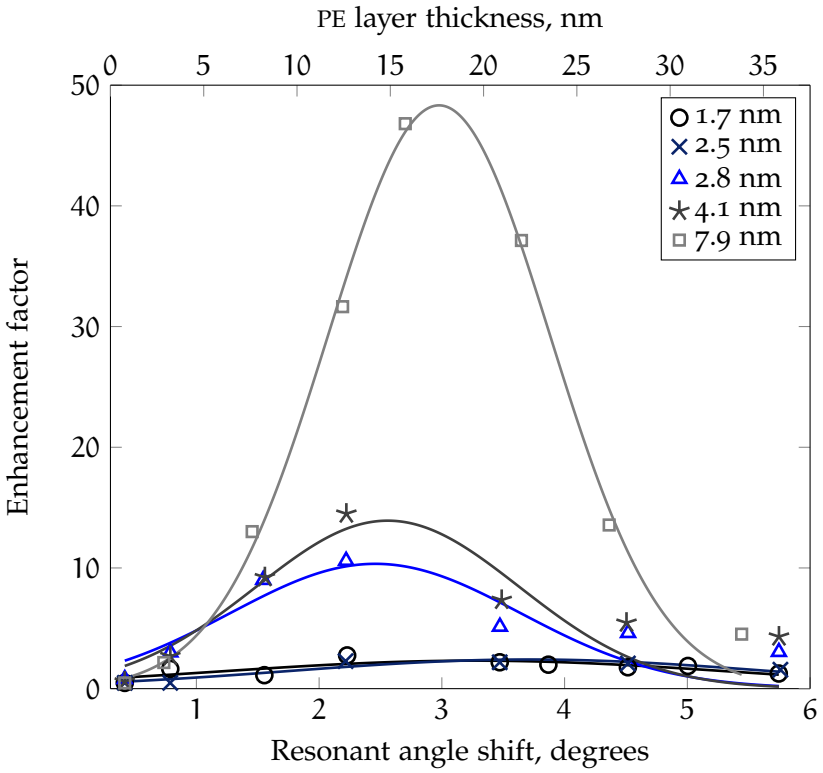


Figure 6.6: Dependence of fluorescence enhancement factor of the organic dye on planar substrates coated with silver coating of different surface roughness (shown in legend) as a function of PE spacer thickness and resonant angle.

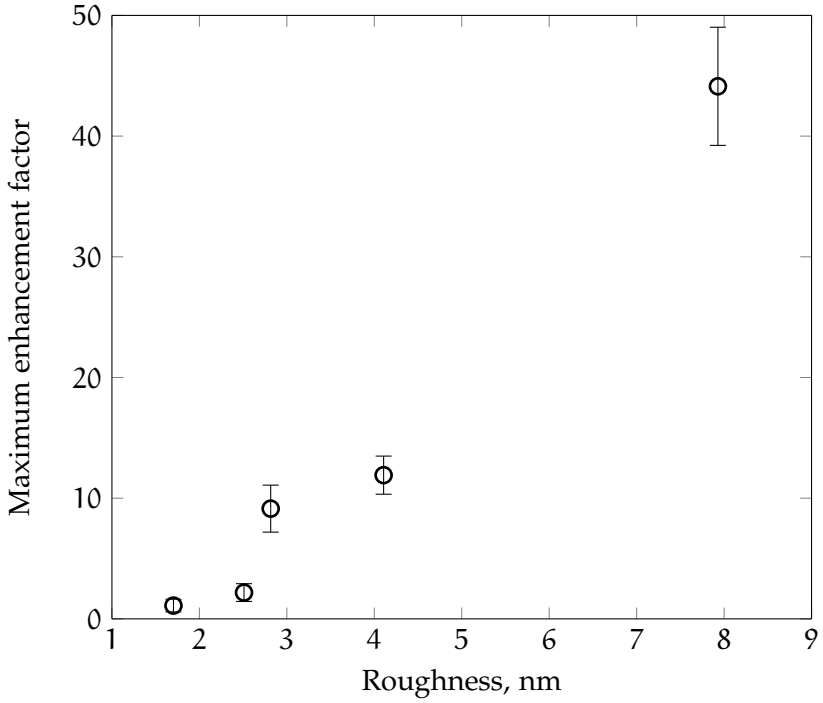


Figure 6.7: Maximum fluorescence enhancement factor of the organic dye as a function of surface roughness (RMS roughness) of silver films on planar substrates.

within the range of previously reported values for the optimal distance between the fluorescent molecules and the silver film.

Expectedly, the fluorescence enhancement increases as the surface roughness of the Ag film increases (Figure 6.7), ranging from a factor of 3 for low surface roughness of 1.7 nm up to a factor of 47 for the roughness of 8 nm. The field intensity of the SPs supported on a rough film is larger than the field supported on a smooth film. This concept was first suggested by Kretschmann [59] and then further explored in relation to the enhancement of fluorescence on rough surfaces by other authors [223, 317]. The observation of much larger fluorescence enhancement on the rough silver coating in comparison to smooth films indicates that the chemically deposited silver coatings are promising candidates for MEF and the fibre based platform developed for SPR provides a good basis for development of a MEF fibre based probe.

6.3 FLUORESCENCE ENHANCEMENT IN A FIBRE BASED MEF PROBE

Once the suitability of the chemically deposited silver coating and the optimal spacer thickness were determined for the planar geometry, the enhancement of fluorescent emission was investigated on the side of an optical fibre, the configuration analogous to the SPR platform presented in the Chapter 4. Lead silicate (F2) fibre was chosen for the experiments as the silica fibre SPR wavelength ($\approx$ 685 nm prior any surface functionalisation) lies far from the HeNe excitation source of 633 nm.

6.3.1 *MEF fibre sensor fabrication and characterisation*

The F2 fibre SPR probes were prepared using the same procedure as described in Section 4.2. After deposition of a 50 nm silver coating was complete, the fibre samples were enclosed in a capillary flow cell (Figure 5.3) and aPE spacer was deposited layer-by-layer with intermediate rinsing performed between each subsequent coating. A monolayer of fluorescent labels was then attached to the last PAH layer. The resulting fibre MEF probe is schematically shown in Figure 6.8.

The experimental procedure for the characterisation of the fibre MEF probes was as follows. First, the HeNe source was coupled into the fibre, transmitted power was measured at the opposite end of the fibre, and the coupling was optimised to maximise the transmitted power. The laser source was then switched off, the power meter removed, and the LED light was coupled from the other fibre end to maximise the scattered light intensity. SPR scattered spectra were then collected and analysed at each step of the fibre functionalisation process, including attachment of PE layers and immobilisation of fluorescent molecules onto the fibre probe surface. The optical setup for SPR characterisation is analogous to that for F2 fibre (Figure 4.2) with a white LED source (Thorlabs, MCWHLP1) used to excited plasmons. Collection of the plasmon scattered spectra was performed using a microscope objective, a converging lens, and a patch fibre cable, connected to a compact spectrometer (Ocean Optics, QE65000). The characterisation apparatus for the fluorescence enhancement

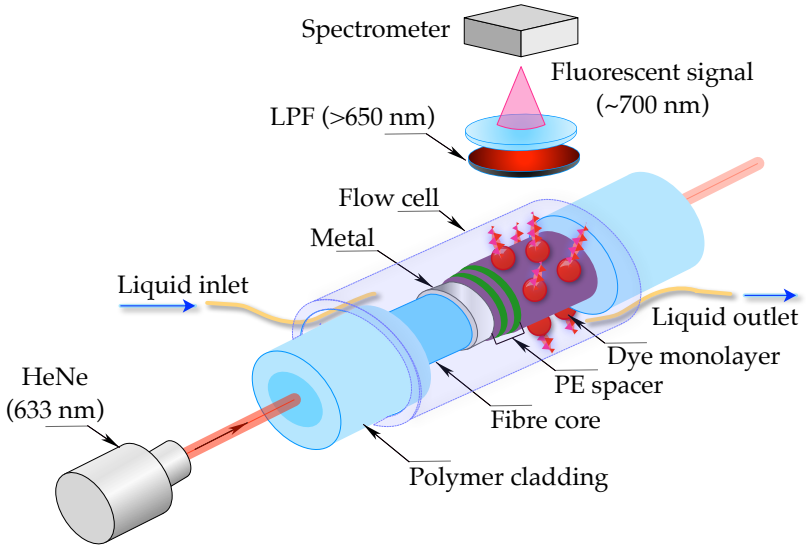


Figure 6.8: Schematic of a fibre based configuration used for characterisation of MEF in optical fibres.

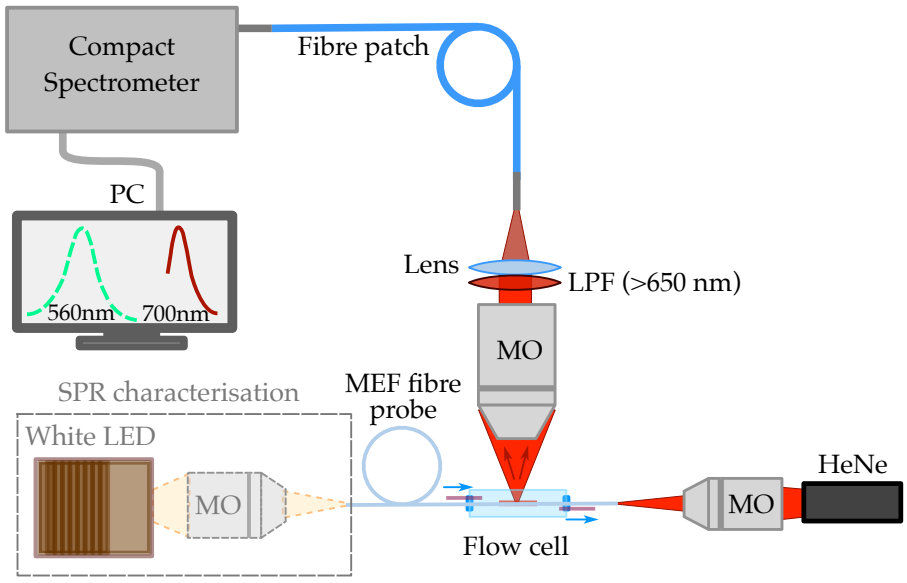


Figure 6.9: Optical setup for MEF fibre sensor characterisation. A metal coated fibre probe is functionalised with a PE spacer and SPR response is analysed after each step of the functionalisation process using the LED setup (shown in dashed lines). For fluorescence analysis, the LED is off, the HeNe laser is coupled into the opposite end of the fibre probe, and LPF is used to block scattered radiation from the laser source.

studies consisted of a linearly polarised HeNe laser source (Thorlabs, HRP050-1, 5mW) coupled into the opposite end of the fibre from the LED, and the same collection apparatus as for SPR with a Long Pass Filter (LPF) (Thorlabs, FELH0650) inserted between the microscope objective and the converging lens to filter out the excitation source background radiation at 633 nm. The combined SPR-fluorescence characterisation setup is shown in Figure 6.9. Either the LED or the HeNe source was used in the Figure 6.9 depending on the stage of the experiment.

The experiments with MEF fibre based probes were performed using the same organic dye used in the planar configuration. A typical SPR scattered spectra at each step of the Ag-coated fibre functionalisation process is shown in Figure 6.10. However, this initial demonstration did not result in enhancement factors larger than 2.3 [312]. It was postulated that the reason for the much smaller enhancement of fluorescence in the fibre is due to insufficient overlap between the SPR wavelength after functionalisation is complete (around 580 nm) and the excitation of the dye at 633 nm, as shown in the Figure 6.10 in dashed black and red lines respectively. In the Kretschmann geometry, the SPR condition is satisfied for the excitation wavelength by varying the angle of incidence of the laser light onto the metal surface. However, the range of angles that are allowed to propagate in an optical fibre is limited by its NA. This results in a mismatch between the fluorophore excitation wavelength and the maximum SPR peak with less than 40% of the intensity of the scattered SPR available to contribute to excitation of fluorescence.

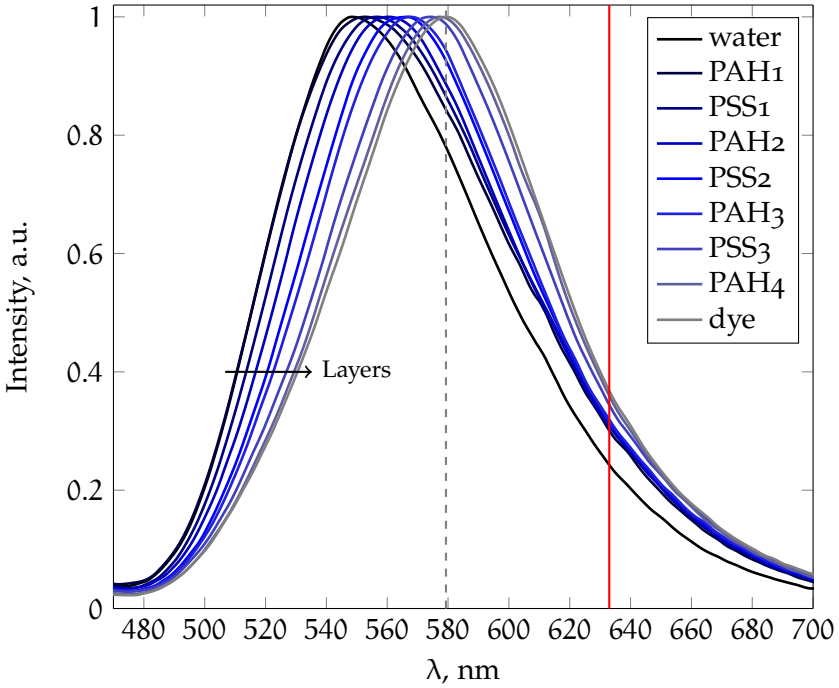


Figure 6.10: SPR scattered spectra at each step of PE spacer deposition and dye attachment. Vertical lines mark the SPR resonant wavelength after dye attachment at 580 nm (dashed) and the excitation wavelength of the laser source at 633 nm (red).

To investigate the reasons behind the lack of fluorescence enhancement, several additional experiments have been undertaken. The dependence of fluorescence intensity on the transmitted power was studied in order to evaluate if it had a linear

trend. The laser light was coupled into the fibre and the coupling was adjusted to maximise the transmitted power. The distance between the fibre tip and the coupling microscope objective then was varied to gradually reduce the amount of light coupled into the fibre. The fluorescence intensity as a function of transmitted power showed a linear trend.

In this experiment the coupling of the laser light into the fibre was varied only through the distance between the fibre tip and the coupling objective along the fibre axis. However, it was noticed that when the alignment of the fibre core and the microscope objective was offset, the transmitted light forms a doughnut shaped projected pattern. In this case, the transmitted power is lower than that for the Gaussian shaped pattern, but the fluorescence intensity was found to be higher. This demonstrated that fluorescence spectra depends on coupling conditions.

This observation indicated that the linear dependence of the fluorescence intensity on the transmitted power only holds under certain conditions where the coupling results in the majority of the optical power residing in a particular fibre mode. Higher order radial modes, such as LP_{11}, LP_{21}, have stronger intensity near the boundary of the fibre core and air, and more evanescent field available to excite the fluorophore in comparison to Gaussian-like modes, such as LP_{01} and LP_{02}. As the fibre is highly multi-mode, it is difficult to ensure the same coupling conditions between the experiments. As the resulting fluorescence intensity is very sensitive to the propagating fibre modes, it was important to preserve the same coupling conditions for the coated and bare fibre samples for comparability of the results. Therefore, a new arrangement of MEF probes on the side of a fibre was proposed.

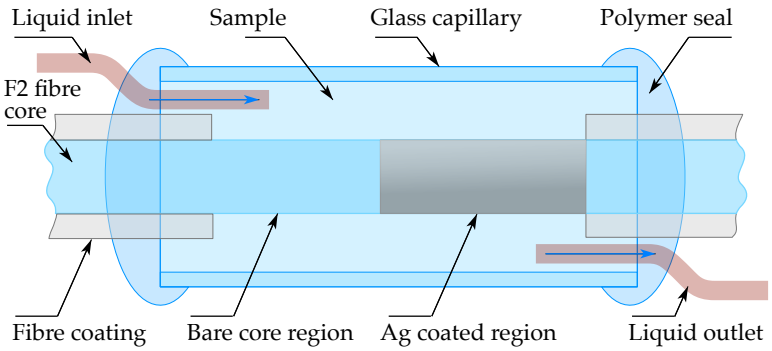


Figure 6.11: Arrangement of two regions on F2 fibre probe (Ag coated and bare core regions) inside one capillary flow cell used to eliminate inconsistency with coupling of excitation light into the fibre.

New fibre probes were designed such that two regions, metal coated and a bare core region, were positioned next to each other on one fibre sample. After the silver coating was deposited on the side of a fibre sample, a portion of the fibre acrylate cladding, next to the Ag-coated region, was removed exposing the fibre core. The dual sensing region was then enclosed inside a capillary flow cell, as shown in Figure 6.11. This eliminated any difference in the coupling conditions between the two regions, while ensuring both parts of the MEF probe undergo the same surface functionalisation procedure enabling direct comparison of the results.

The results of the initial experiments of fluorescence enhancement in optical fibre was reproduced with the maximum fluorescent enhancement factor of 2.4. As discussed earlier, this is likely attributed to the mismatch between the SPR resonant condition represented by an angle-wavelength pair to the excitation wavelength of the fluorophore at 633 nm. Considering the nature of the fluorophore excitation by the evanescent field of the guided fibre modes, as well as the additional SP field in the case of the metal coating, it was predicted that the efficiency of the excitation should depend on the position on the sensing region as well as thickness of the metal film. It is believed that MEF is related to the ability of SPs to scatter light on rough surfaces, and therefore, more efficient scattering should be favourable for fluorescent enhancement [291, 305, 308]. The scattering component is related to the topography of the metal coating as well as thickness of the film, and therefore, a study of the fluorescence enhancement on fibre probes with different film thickness was undertaken.

6.3.2 *Influence of film thickness on fluorescence enhancement*

Fibre probes with silver films of 71, 56, 35, and 22 nm thickness and 7 PE layers were prepared. All samples were fabricated using chemical electroless plating with varying reaction time keeping the deposition rate constant to allow fabrication of films of different thickness without significantly affecting the surface structure. The characterisation of fluorescence on each fibre probe revealed that, as predicted, the emission depended on the silver film thickness. In particular, fluorescence is quenched on thick films ($\sim$ 70 nm) and is enhanced on thinner coatings ($\leqslant$ 56 nm) with larger enhancement factors attributed to thinner films. Figure 6.12 and Figure 6.13 shows the organic dye emission spectra for the 71 nm and 22 nm silver films with the corresponding bare core regions, respectively.

The fluorescence enhancement factor as a function of silver film thickness is presented in Figure 6.14. It can be seen from the plot that the enhancement factor is reduced with increasing coating thickness, where Enhancement Factors (EFs) below 1 indicate a reduction in fluorescent emission intensity. Fluorescence EF of up to 15-fold was achieved for the fibre samples with the thinnest film of 22 nm. Even though the optimal film thickness for propagating SPs excitation is around 50 nm, the fluorescence was enhanced more efficiently on the thinner silver coating where SPR signal was too weak to be measured in the current optical apparatus.

The extinction properties of metals depend on both, the absorption and scattering components, where absorption contributes to fluorophore quenching while scattering is responsible for enhancement [305]. As the metal film becomes thicker, the intrinsic absorption losses in metal increase leading to a smaller proportion of the evanescent field of the guided modes as well as lower SP field available to excited the fluorophore. In addition to the intrinsic losses in metal, the scattering efficiency and localised SPs depend on the coating thickness, resulting in the change of the fluorescence emission. In Mie theory, small metal particles are expected to quench fluorescence while the larger ones should contribute to the enhancement. This is due to the fact that the scattering component dominates over absorption for metal

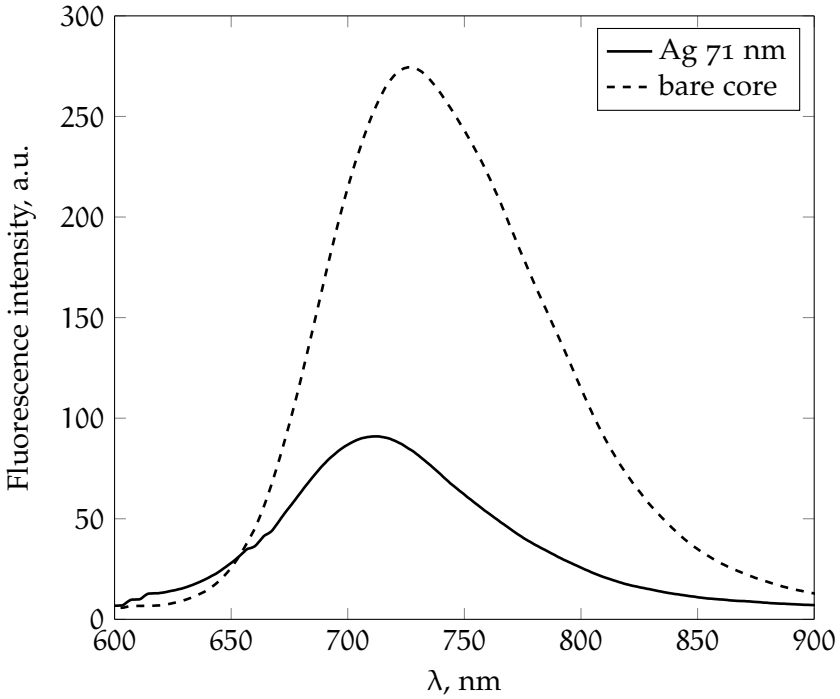


Figure 6.12: Fluorescence spectra of the organic dye on a 71 nm Ag film deposited on a side of the F2 fibre and bare core region of the fibre probe. 7 PE layers were used as a spacer.

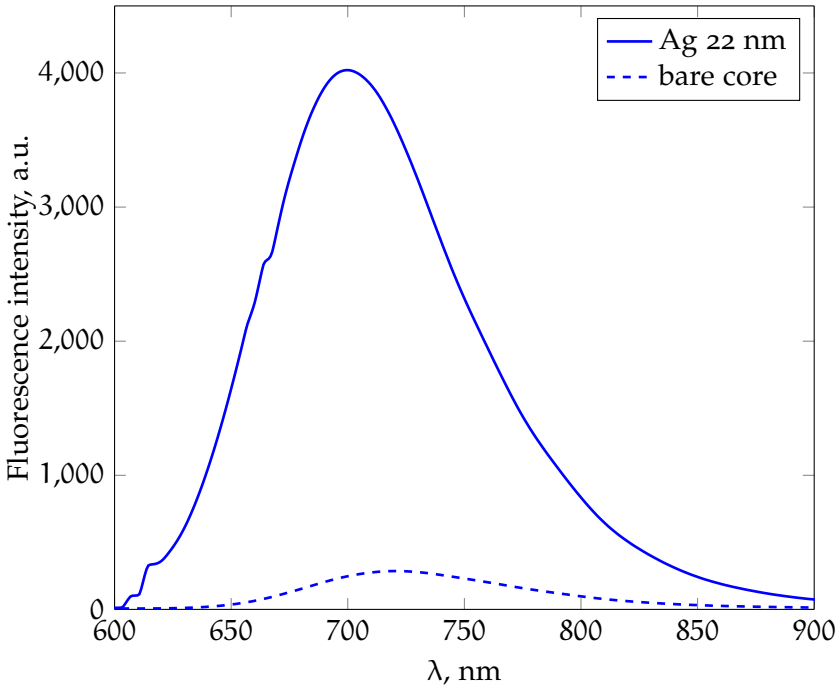


Figure 6.13: Fluorescence spectra of the organic dye on a 22 nm Ag film deposited on a side of the F2 fibre and bare core region of the fibre probe. 7 PE layers were used as a spacer.

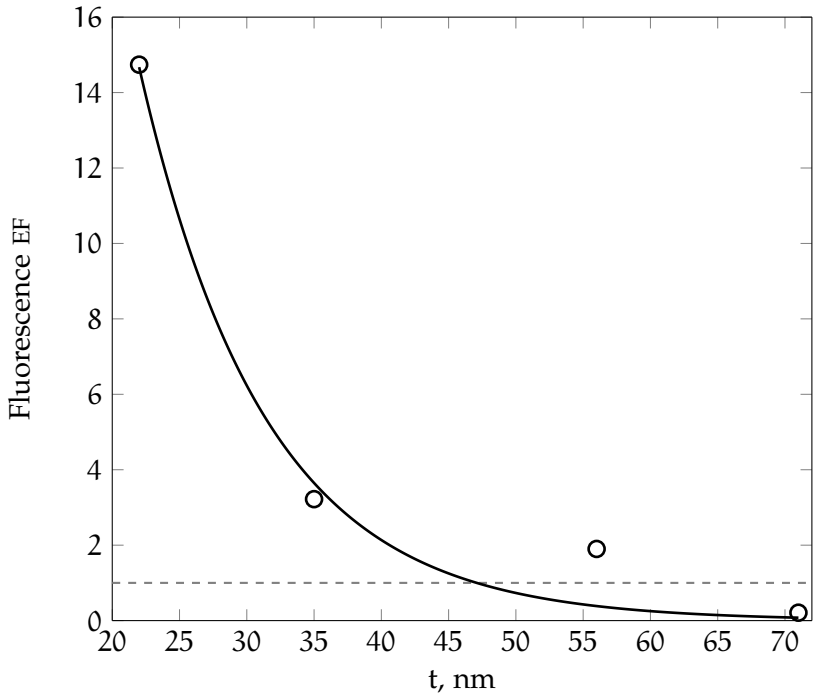


Figure 6.14: Fluorescence EF as a function of Ag film thickness deposited on a side of the F2 fibre probe. Fluorescence EF > 1 (above horizontal dashed line) indicates fluorescence intensity enhancement, < 1 - reduction of fluorescence intensity.

particles with larger size [318]. It is reasonable to expect that the size of surface features on a metal film deposited under the same conditions should increase with increasing film thickness, resulting in stronger scattering cross sections [308, 309]. Therefore, a study of silver film topology was undertaken in order to determine the characteristics of the coating surface for different thicknesses.

6.3.3 *AFM study of silver film topography*

To investigate the particle composition on the surface of silver films of different thickness, grain analysis was performed on AFM images. Planar glass slides with silver films of different thickness coated simultaneously with the corresponding fibre samples were used to simplify the imaging of the coating surface. Thickness of the coating was determined through transmission measurements, and verified by studying the surface profile at the edge of the coatings across a scratch with an AFM instrument (NT-MDT, Ntegra Solaris). The topography study was performed on 5×5 μm sections of the coating and analysed using scanning probe microscopy data visualization and analysis software (Gwyddion). Figures 6.15 and 6.16 show the distribution of equivalent disk radius, the radius of a disk with the same projected area as the grain, for thin (22 nm) and thick (71 nm) silver coatings, and the corresponding AFM images.

A summary of the grain distribution analysis showing the statistics of the grain composition is presented in Table 6.2. The analysis suggests that the mean grain size increases with the thickness of the metal film but not significantly, from 50 nm to 76 nm for 22 and 71 nm films respectively. Size distribution of the particles on the

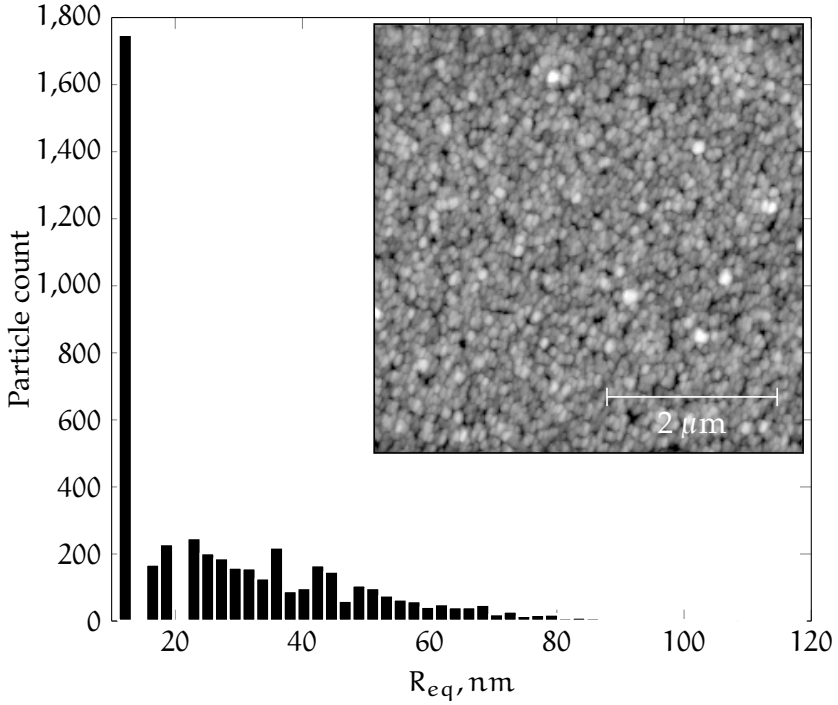


Figure 6.15: Equivalent disk radius of the surface features on a 22 nm-thick Ag film. An AFM image of the 5×5 μm section used in the particle distribution analysis is shown on the inset.

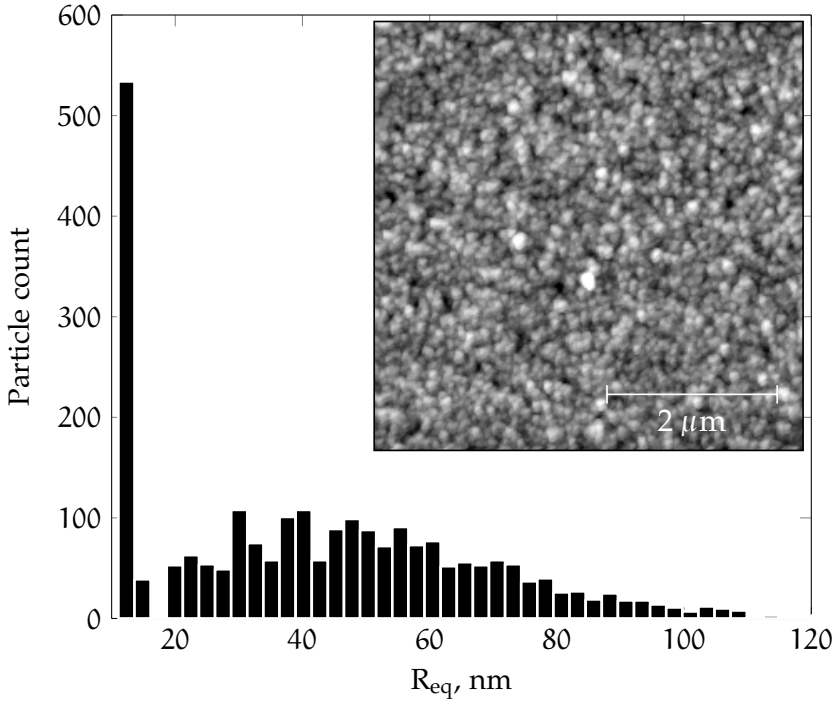


Figure 6.16: Equivalent disk radius of the surface features on a 71 nm-thick Ag film. An AFM image of the 5×5 μm section used in the particle distribution analysis is shown on the inset.

surface of 22 nm film revealed that around 35% of the particle population consists of small grains of around 10 nm radius (large peaks in histogram in Figure 6.15). For the 71 nm film, small gains contribute to 22% of the particle population (Figure 6.16). Analysis of the surface roughness of films of various thickness did not reveal dependence on the film thickness with average value of 9.4 ± 1.1 nm, where error represents the standard deviation.

Table 6.2: Summary of grain distribution analysis of chemically deposited silver films performed by AFM on 5×5 μm sections of planar substrates.

Parameter	Sample				
Thickness, nm	22.4 ± 2.2	34.9 ± 2.9	56.3 ± 3.4	64.5 ± 3.2	71.1 ± 2.5
Number of grains	4815	4284	3783	2909	2447
Total proj. area (abs.), μm^2	17.5	17.8	18.3	19.1	19
Total proj. area (rel.), %	69.56	70.62	72.58	75.72	75.51
Mean grain area, $\times 10^{-15}$ m^2	3.6	4.2	4.8	6.6	7.8
Mean grain size, nm	50	54	58	65	76
$R_q^{\dagger}$, nm	8.8±0.6	9.1±1.7	11.0± 2.2	10.3 ±1.4	9.4±0.1
$\lambda_q^{\ddagger}$, μm	0.17±0.01	0.16±0.01	0.16±0.02	0.22±0.02	0.18±0.01

† R_q is RMS roughness.

‡ λ_q is RMS wavelength of the profile.

Surface scattering depends not only on the amplitude parameters of the roughness, such as RMS roughness, but also on the spatial parameters given by the autocorrelation function and power spectrum density function. Autocorrelation functions for thin and thick films have been analysed and the autocorrelation lengths for both samples were found to be similar, around 130 nm. No significant dependence on the film thickness was found for the spatial roughness parameter, RMS wavelength of the profile from Table 6.2. In case of a system with multiple layers, multilayer roughness influences surface scattering. Cross-correlation between different surface profiles can provide more information on the scattering surface topography. The influence of the silver film roughness on the enhancement of fluorescence was examined under the assumption that the PE layer formation is similar for rough and smooth films and, after the deposition of multiple layers, is not dependent on a substrate, that has been previously reported in [316].

It can be concluded that the size distribution of the metal particles on a surface varies insignificantly, and the amplitude and spatial roughness parameters remain analogous for the thin and thick films. However, the film thickness plays an important role in the presence of considerable surface roughness. For the thin films of 22 nm thickness the relative roughness is around half of the film thickness with the valleys between surface features reaching down to a few nanometres depth. These thin films can be considered particulate consisting of a mixture of nanoparticles of various sizes which can contribute to the localisation of the SPs. On the other hand, thick silver films with the relative surface roughness of around $1/10^{th}$ of the film thickness become continuous with propagating plasmons on the rough metal surface that scatter light at the resonance wavelength into free space [44, 319]. For those thick films the intrinsic absorption in metal dominates over scattering, even

though the later is augmented by the surface roughness, resulting in fluorophore quenching.

Properties of propagating SP depend on metal film thickness with the optimal performance usually expected on 50 nm-thick smooth films. The maximum performance of SPR on rough silver coatings in terms of its refractive index sensitivity in a fibre based configuration was achieved for coatings of $55 - 65$ nm. As the silver film becomes thinner, the sensitivity of the propagating SPs to refractive index decreases, however, the fluorescence is more efficiently enhanced. This might indicate that localised plasmons, that are known for higher fluorescence enhancement [296], become prevalent in the thinner particulate films. However, the distinction between localised SPs and scattered SPs on a rough surface is not trivial. In addition to the localised surface modes on individual particles, the near-field interaction between nanoparticles located at nanometre proximity is known to give rise to new plasmonic modes with a stronger field intensity, confined in the gap between the particles. This interaction creates plasmonic "hot spots" that might be a contributing factor to the strong surface enhancement effects observed on metal nanoparticles dimers and arrays [302, 320].

6.3.4 *Increasing SPR wavelength with glycerol solutions*

Deposition of the PE spacer increases the SPR resonant wavelength resulting in around $580 - 590$ nm for 7 PE layers after the functionalisation process is completed. As was mentioned earlier, this results in less than 40% overlap between the SPR scattered spectra at its maximum and the excitation wavelength of the laser at 633 nm, as shown in Figure 6.10. Therefore, in order to match the SPR resonant wavelength and fluorophore excitation wavelength, more PE layers could be deposited. It was hypothesised that there are two competing processes occurring: spectral matching of the SPR resonant wavelength after surface preparation with excitation of the fluorophore at 633 nm, and optimal distance between the fluorophore and the metal surface. Therefore, it was proposed to introduce glycerol solutions ranging from 30% to 100% after attachment of the fluorescent dye in order to increase the RI of the outer dielectric, thereby shifting the SPR resonance towards longer wavelengths, minimising the gap between the SPR maximum and the excitation laser wavelengths.

Figure 6.17 presents the dependence of the fluorescence intensity for silver coated and bare fibre regions as a function of RI of the external dielectric. Thick and thin silver coatings are shown for comparison. For the bare regions of the fibre samples fluorescence intensity increases with the increased RI of the solution. At these regions the fluorophore is excited by light scattered from the fibre surface as well as by the evanescent field of the guided modes. As the external RI increases, the index contrast between the fibre core and outer environment decreases resulting in reduced confinement of the fibre modes and increased loss at the interface core/external dielectric. Scattering would also increase for higher RIs considering the inverse proportionality between the RIs of water or glycerol and wavelength in the visible range [321, 322] under Rayleigh approximation.

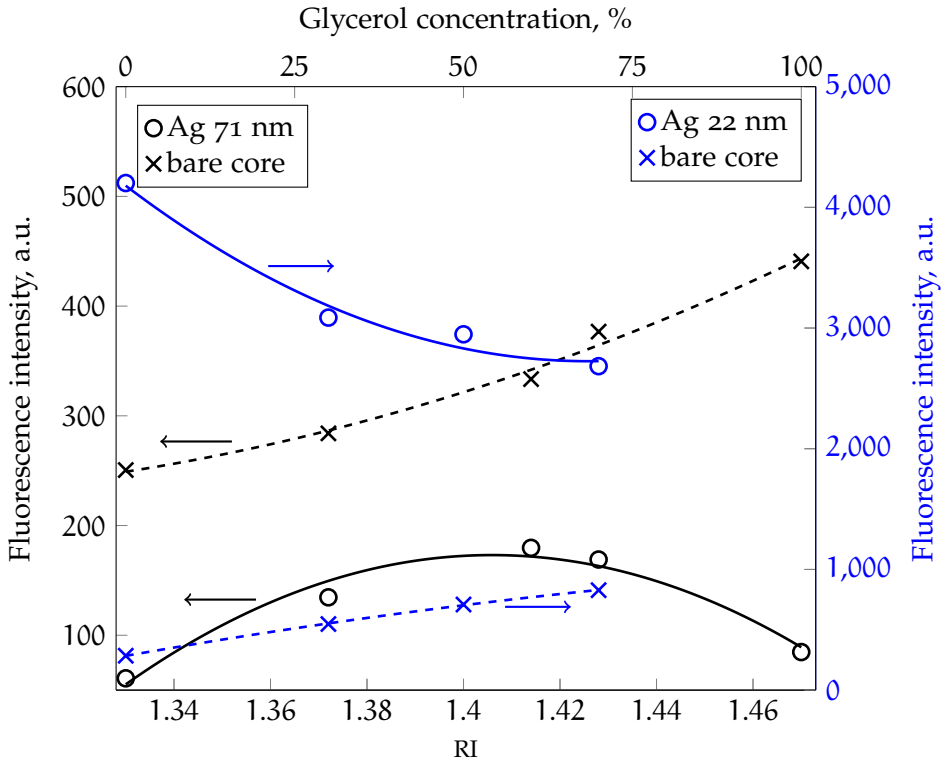


Figure 6.17: Fluorescence intensity as a function of the external RI (glycerol solutions) for the F2 MEF fibre probes: black – coated with a thick (71 nm) and blue – thin (22 nm) Ag films and the corresponding bare regions on the fibre (shown in dashed lines).

However, for the 71 nm-thick silver film, the fluorescence intensity reaches a maximum at the RI of around 1.4, which corresponds to the SPR wavelength of 635 nm. This supports the expectation that the maximum overlap between the SPR scattered spectra and the excitation source results in the maximum enhancement of the fluorescent signal.

For the thin silver film of 22 nm thickness the fluorescence intensity decreases with increasing RI. It is assumed that at this thickness the film can no longer be considered continuous as the relative roughness increases significantly. For a particulate film localised effects dominate. The resonant wavelength of the localised SPR depends on the size, shape and spacing between the particles, as well as the dielectric function of the metal itself, and it is hard to predict without performing LSPR measurements. Furthermore, the sensitivity of LSPR sensors is typically smaller than that for propagating plasmons [69], and therefore, it is likely that even in pure glycerol the wavelength does not reach the excitation wavelength of 633 nm. Considering the range of RIs of the external dielectric, the enhancement of fluorescent emission was found to be at maximum in water.

6.3.5 *Dependence of enhancement on sensing region location*

Finally, a simple study was performed to investigate the enhancement of fluorescent signal at different positions along the fibre probe, relative to the propagation direction of the guided excitation light. Fluorescence emission spectra of the organic dye

collected at the bare core region, and two locations on a silver coated fibre probe is shown on the Figure 6.18.

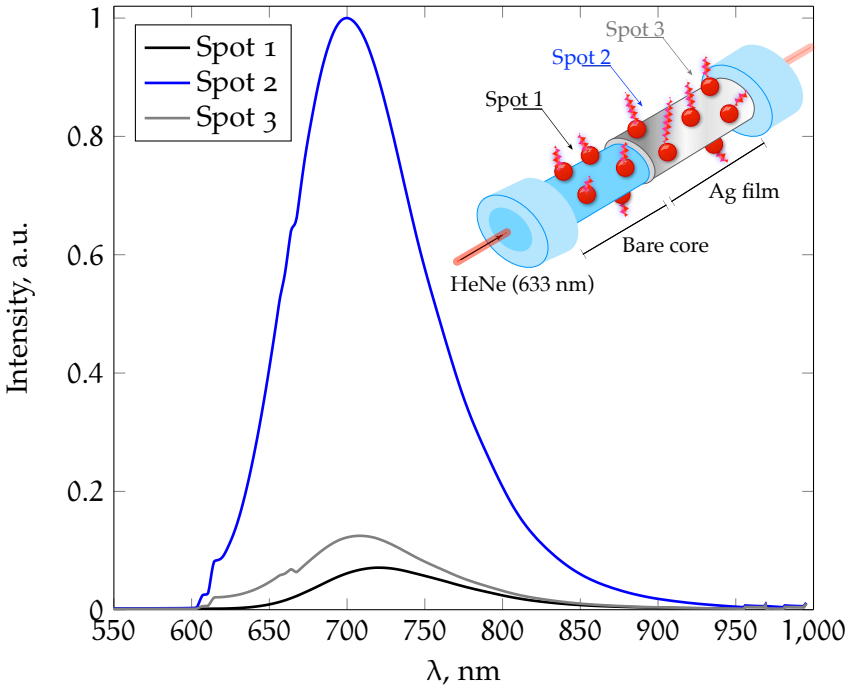


Figure 6.18: Fluorescence spectra of the organic dye at different locations (spots) on the F2 fibre probe: the bare core (spot 1), the location closest to the excitation (spot 2), and the location further from the excitation light (spot 3). The locations on the sensing region are shown on the inset. Silver film thickness is 22 nm.

It was found that fluorescent intensity on the silver coated region, and therefore the enhancement factor, strongly depended upon the location on the sensor. In particular, higher intensity was achieved for locations on the silver film positioned closer to the end of the fibre where excitation laser is coupled. Here, the excitation light interacts more strongly with the metal coating resulting in stronger scattering intensity, either SPR mediated or non-SPR related scattering. At the further spots the intrinsic losses in the metal causes the intensity of scattering to reduce. More importantly, the energy of the incident light dissipates quickly through coupling to plasmonic modes and strong scattering enhanced by the roughness of the metal surface. A similar effect was observed on silver coated fibres with different film thickness, although for thicker films ($\geqslant$ 35 nm) fluorescent emission was only enhanced at short distances from the start of the metal coated region and quenched further away. This illustrates that in a fibre based configuration where the interaction of propagating light and SPs occurs along a reasonable length of the sensing region, there is a significant difference between fluorescence enhancement factors that could be achieved at distinct locations along the metal film length.

6.4 SUMMARY AND CONCLUSIONS

In this MEF study, the influence of surface roughness of silver films on the enhancement of emission of fluorophore molecules located at around 10-nanometre proxim-

ity of the metal surface was investigated. The optimal distance of the fluorophore from the metal film for the maximum enhancement of fluorescent emission was adjusted by fine tuning the thickness of a multilayer PE spacer and was found to be around 12 nm which agrees with previous studies [289, 292, 304, 305]. The maximum fluorescent enhancement factor of up to 47 was achieved on planar glass substrates coated with silver films of high surface roughness of around 8 nm fabricated by the chemical deposition technique. While this enhancement factor appears to be moderate in comparison to those achieved with nanostructured metal films, it demonstrates that the simple chemical method could be readily used for fabrication of low cost alternative plasmonic coatings suitable for enhancing fluorescent intensity.

The same silver coating fabrication technique and surface functionalisation methods were used to produce MEF sensors on the side of an optical fibre. The fluorescence emission intensity was found to be strongly dependent on the silver film thickness with the maximum fluorescent enhancement factor of 15-fold observed on a 22 nm silver film. The surface topology of silver films of different thickness was studied using AFM showing that the structure of the surface is indeed rough and is comprised of an ensemble of nanoparticles of different size averaging at $50-60$ nm grain diameter. The analysis of the results suggests that the surface roughness plays a significant role in fluorescent enhancement especially for thinner films where the relative roughness with respect to the film thickness is more pronounced and the coating can be considerate particulate-like.

It is also possible to conclude that scattering is directly related to the enhancement of fluorescence near the metal films, however, it is difficult to differentiate between scattering cause by plasmons and scattering that is not related to SPR. Considering the analysis of the fluorescence response in the presence of the external dielectrics with different RI, it is possible to conclude that propagating plasmons play a role in the enhancement process. While the physics that underpins MEF in a configuration that involves metal surfaces with random roughness interacting with fibre modes is complex, it is believed that the mechanism behind enhancement of fluorescence intensity is through the increase of electromagnetic field strength, and therefore fluorophore absorption, mediated by SP excitations.

There is significant scope for improvement in the proposed MEF architecture, which would include analysis of a broader range of silver film thickness, as well as a study of the properties of LSPR, in order to fully understand the complex behaviour of the system and explore the possible enhancement achieved in the fibre based platform. The fluorophore has to be carefully chosen to achieve maximum overlap between SPR and fluorophore absorption spectra. Considering this, using fluorescent labels with broad absorption, such as Qdots, might be a more suitable option in fibre based MEF sensors. The MEF fibre sensor could find potential applications in biological sensing, medical research, or analytical chemistry where the enhancement of fluorescence signal could bring significant advantages. The fabrication and analysis procedures are easily adaptable and cost effective making the fibre-based MEF configuration a competitive candidate for compact fluorescent spectroscopy.

7

CONCLUSIONS AND RECOMMENDATIONS FOR FUTURE WORK

7.1 SUMMARY OF THE WORK AND CONCLUSIONS

Motivated by biosensing applications and the high demand for label-free sensing techniques, the present research focuses on developing a biosensing architecture based on SPR technology, covering aspects of the platform design, theoretical parametric studies, and performance characterisation of the sensing probes. The development of a novel scattering-based SPR fibre sensing architecture is described in this thesis. This platform relies on the presence of significant surface roughness of the plasmonic coating which induces scattering of the surface plasmon-coupled light from the surface features, turning an intrinsically non-radiative process into a radiative one. This allows the SPR signal to be collected from the scattered light emission, enabling a different an alternativecollection mechanism than that used in traditional SPR fibre sensors. This configuration provides some significant advantages in comparison to conventional fibre-based SPR transmission measurements, such as higher SNR of the SPR response, the ability to fabricate multiple sensing regions along one fibre, as well as the combination of SPR sensing with other detection techniques, such as fluorescence analysis. In addition, the much lower reliance on quality and thickness of the metal coating allows the use of a simple and inexpensive chemical silver deposition method that does not require specialised instrumentation and allows simultaneous production of a large number of sensors.

The initial scattering based platform was built using high index lead silicate MMF. Theoretical modelling showed that reducing the refractive index of the fibre core or reducing the number of fibre modes through the use of fibres with smaller NA, could provide improvement in the sensitivity of the fibre probe and resolution of the sensor, respectively. These modifications were implemented in the scattering-based platform resulting in the demonstration of silica MMF and silica ECF SPR probes, showing the expected improvement in the performance. The improvement in the sensor sensitivity was 3.8 times, while the linewidth of the SPR feature was reduced by a factor of two. The silica MMF SPR probe was then tested in a biosensing application. Finally, the suitability of the rough plasmonic coating was explored for the application of MEF, the enhancement of fluorescence emission by molecules located at a nanometre-scale distance from the metal coating. The roughness of the metal film was found to be a significant contributing factor in enhancing the fluorescent radiation. An optical fibre based MEF probe was experimentally demonstrated providing promising avenues for the further development of miniaturised MEF sensors.

The theoretical background for this work was combined in Part I of the thesis. Chapter 1 introduced the general principles of biological sensing, as the main application domain that motivated the current work. The major parts of the biosensor, including bioreceptors and transducers, were discussed. SPR and other label-free

optical transducing mechanisms that rely on resonance phenomena were compared. SPR was identified as one of the most promising label-free optical biosensing techniques with exceptionally high sensitivity, versatility, and ease of implementation. A detailed description of the SPR phenomenon was presented in Chapter 2. An introduction to the physics of the surface plasmons was given with theoretical formalism described by Maxwell's equations. The principles of biological sensing with SPR was provided with performance characteristics as well as an explanation of various excitation and interrogation mechanisms. Finally, a review of the state-of-the-art for optical fibre-based SPR sensors was given within classification schemes based on different foundations. The SPR platform based on the interrogation of scattered light was recognised as a promising approach due to its advantages of simplicity, and cost effectiveness, among many others.a range of advantages including it's simplicity and potential for low cost mass production.

Part II of the thesis incorporated the theoretical and experimental work undertaken to fulfil the goals of the project. Chapter 3 presented a parametric study of the SPR fibre sensor performance that was conducted using the Transfer Matrix Method (TMM) for multi-layered systems. This theoretical investigation analysed the influence of fibre and metal coating parameters on the performance characteristics of the fibre sensing probes. This study revealed a trade-off between the performance parameters that affect the detection limit, which are sensitivity and resolution. In particular, using fibre with a low RI core increases the sensitivity, however, broadens the SPR response curves, thereby degrading sensor resolution. The modelling also showed that a decrease in the linewidth of the SPR spectral feature can be achieved by reducing the fibre NA or the core size, which is thought to be attributed to the smaller number of fibre modes that can satisfy the resonant condition and couple to the plasmons. Even though modelling of SPR in small core fibres that support a few guided modes was not performed, it was clear that the sharper SPR response is attributed to the smaller core fibres, continuing the trend predicted with modelling of large core fibres. Although the modelling did not take into account some aspects of real platform configurations that could influence performance characteristics, such as roughness of the metal coating, or variations in the dielectric function of a thin metal film compared to a bulk metal, the study provided guidance for the project directions towards improvement of the performance of the scattering based SPR fibre architecture and is applicable to all of the currently available fibre based SPR sensors.

The remainder of the thesis focuses on the experimental work dedicated to the implementation of a scattering-based SPR fibre optic configuration and advancing the platform architecture through the improvement ofenhancing the major performance characteristics, sensitivity and linewidth of the platform. Chapter 4 describes the implementation of the scattering based SPR platform using in-house fabricated lead silicate (F2) MMF, explains the process of silver coating fabrication using a chemical electroless plating technique, and details characterisation of the sensing probes. The first performance improvement was the use of a fibre with a core made of a material with lower RI. Fused silica was chosen due to its low RI, high availability, and robustness. A fused silica (F300) MMF was produced in-house to verify the change in performance. Unfortunately, the same silver film deposition technique

that was used to fabricate the plasmonic coatings on F2 fibres could not be readily adapted for silica fibres. A study was performed to determine the reasons for poor coating quality and adhesion, as well as investigating various silica surface modification techniques, such as Piranha etching, silanisation, and tinning. Experimental analysis of the several silica surface modification techniques revealed that the most effective method of silica surface treatment prior to chemical silver deposition was tin(II) chloride sensitisation. The parameters of the pre-treatment protocol and subsequent silver deposition reaction were optimised to allow fabrication of silver films suitable for SPR sensing. The silica MMF-based SPR probes were characterised and compared to F2 SPR sensors, as well as modelling predictions. The expected sensitivity improvement for the silica fibre based sensors was achieved in comparison to F2 fibre probes. Lastly, the suitability of the silica MMF SPR probes for biosensing applications was evaluated with the detection of Norovirus (NoV). Sensor surface functionalisation was performed using a bio-affinity assay technique with PE layer assembly as an interface between the metal coating and the biological constituent of the sensor. Antibodies were chosen as a bioreceptor due to their specificity and ability to achieve the desired orientation on the surface, providing maximum surface coverage of captured target molecules. As the NoV capture result was inconclusive, an assessment of the surface bio-functionalisation was performed using NoV surrogates, Qdots functionalised with NoV antigens. The success of these experiments indicated that the likely reason for not binding of the NoV particles to the bioreceptors was non-viability of the target probes. The results demonstrated the feasibility of biological sensing using the scattering based SPR platform utilising silica MMF, although no further work was performed specifically on NoV due to the lack of availability of reliable samples.

The remainder of this thesis focused on further improving the platform, as well as finding novel applications for the scattering based SPR architecture. Even though the sensitivity of the silica MMF based sensors was improved in comparison to F2 fibre probes, the linewidth of the SPR response was increased, demonstrating the predicted performance trade-off between sensitivity and resolution. As indicated by the theoretical studies, the spectral linewidth of the SPR response can be reduced by limiting the number of modes propagating in the optical fibre. Therefore, the next step was to verify that the use of a small core fibre resulted in an improvement of the linewidth of the SPR response. Chapter 5 provides a description of the development of the scattering based SPR platform based on silica MOF with an exposed core. Using a microstructured fibre is rationalised by the mechanical robustness of the fibre with a small core that allows ease of handling. Exposed Core Fibre (ECF) provides unrestricted access to the core along the fibre length. This allows the deposition of plasmonic coatings without additional fibre processing, or coating the interior of the fibre holes, as it is done in MOF SPR sensors. ECF SPR probe fabrication and characterisation were described and a performance comparison revealed an improvement in the spectral linewidth in comparison to the large-core silica MMF. In addition, some interesting observations were made in relation to ECF sensors, such as the presence of multiple peaks in the scattered spectra, as well as a dependence of the resonance wavelength on the position along the sensing region. An effort was made to further reduce the NA of the ECF by filing the fibre air holes with

a low RI polymer. Although no significant improvement in the spectral linewidth was achieved with the filled fibres, the feasibility of the polymer filling technique was demonstrated. It is also reasonable to assume that polymers with RIs closer to silica could be used to provide the desired improvement. Nevertheless, the ECF SPR sensitising probe showed twice as narrow SPR features than the silica fibre in the same scattering based configuration, which highlights the potential of using ECFs for improved resolution SPR sensing.

In Chapter 6 the suitability of the rough silver coating for enhancement of fluorescent emission was investigated. Metal particles and nanostructures are commonly used for Metal Enhanced Fluorescence (MEF), however, complex fabrication procedures are required to produce them. The influence of the surface roughness of the silver film was analysed on the planar substrates using a Kretschmann prism setup, showing that silver coatings of higher roughness provide increased enhancement factors. The fluorescence enhancement was also studied as a function of distance between the metal film and the fluorophore that was finely tuned through layer-by-layer adsorption of a PE spacer, showing the existence of an optimal separation distance, in agreement with previous studies. The scattering based SPR fibre platform was expanded to accommodate MEF analysis. The analysis of the fluorescence emission was performed in the fibre configuration showing the dependence of the enhancement on the silver coating thickness and the position on the sensing probe. The enhancement factors achieved with the fibre configuration were modest in comparison to the planar substrates. This was attributed to the mismatch between the SPR wavelength in the fibre based configuration and the peak absorption of the fluorophore, while the SPR condition in the prism configuration can be precisely matched by varying the incident angle of the excitation light. This accentuates that the careful selection of the fluorescent dye is required for fibre based MEF probes. This study shows that the amplification of fluorescence emission can be achieved with high enhancement factors, in both, planar substrates and optical fibres, but more importantly, using a rough silver coating fabricated with a simple chemical deposition technique.

7.2 RECOMMENDATIONS FOR FUTURE WORK

The scattering based SPR sensing platform has been demonstrated to be a practical and highly adaptable refractive index sensing platform with the potential to be used in biological applications. However, the results of biosensing experiments highlighted some limitations that resulted from the bio-functionalisation approach that was adopted, the plasmonic coating, and the platform configuration itself. First of all, the bio-functionalisation approach used in the experiments for NoV detection relied on the preparation of the functional coating layer-by-layer in order to achieve antibody immobilisation for capture of the target molecules. This procedure takes considerable time, often resulting in the necessity to leave the sensor overnight during functionalisation. Not only can this result in contamination of the sensor surface by precipitates from the sample solution, but also introduces significant challenges caused by the viability of biological probes at the temperature of the experiment,

parasitic drift of the optical micro-stage that leads to movement of the sensor under the collection apparatus, as well as degradation of the plasmonic coating in the liquid environment. These effects are negligible within the few hours of the experimental procedure, and therefore, a reduction in the number of steps required for bio-functionalisation of the sensor surface could significantly improve the results. The use of an anti-oxidation coating on top of the plasmonic film, such as magnesium fluoride or thin silica film, could significantly improve the sensors' longevity without requiring specific storage conditions. This would also allow to avoid film oxidation and the associated change in the dielectric constant of the coating with time, significantly improving the reproducibility of the experiments.

Even though the rough silver coating is essential for the functionality of the scattering based SPR platform, the presence of the roughness results in an intrinsic broadening of the SPR spectral feature, when compared to a smooth metal film. This is detrimental to the sensor's resolution, and therefore, the linewidth of the SPR response is an essential parameter in the scattering based SPR architecture. Moreover, when using a lower RI waveguide in order to improve the sensitivity of the sensor, attention should be taken to the inherent trade-off between the sensitivity and spectral linewidth of the SPR response. The use of smaller core ECF was demonstrated to be an efficient way to reduce the linewidth of the SPR spectral feature. This could be explored further by using even smaller core ECF that has recently become available [287]. An alternative way of reducing the number of modes in a fibre is to reduce its NA. Filling the inner holes of the ECF with a UV-curable polymer showed the feasibility of the fabrication technique and is a potential way of limiting the spectral linewidth of the SPR, provided that a sufficiently low NA aperture is achieved.

The MEF experiments have shown that rough silver coatings and the scattering based SPR fibre platform can be successfully used to enhance fluorescence emission. The factor for improvement, however, is the fluorophore selection due to the prerequisite of the spectral overlap of the fluorophore absorption and the SPR resonant wavelength. The design of the fibre configuration itself could be adjusted in order to facilitate this spectral overlap through customising the SPR wavelength by using a fibre with a different core material or size, or modifying the plasmonic coating. Ultimately, enhancement of the fluorescence by rough metal coatings could find potential applications in high throughput spectroscopy and plasmonic lasers development. In addition, rough metal coatings have shown potential in the surface enhanced techniques, including the well known Surface Enhanced Raman Scattering (SERS) [323]. The silver coating fabrication technique and the sensing platform presented in this work could be easily adapted to create promising fibre optic SERS sensing devices.

The demand for inexpensive, simple, and portable devices drives the current research in the area of biological sensing with SPR. However, future avenues for plasmonic research span beyond conventional biosensing applications. The ability of surface plasmons to confine electromagnetic radiation into sub-wavelengths dimensions beyond the diffraction limit of light opens vast opportunities for development of nanoscale light amplification, plasmonic circuits, ultra high resolution colour printing with plasmons, imaging, and many other areas where research is still in it infancy.

Part III

APPENDIX

APPENDIX A: LIGHT SOURCE SPECTRA

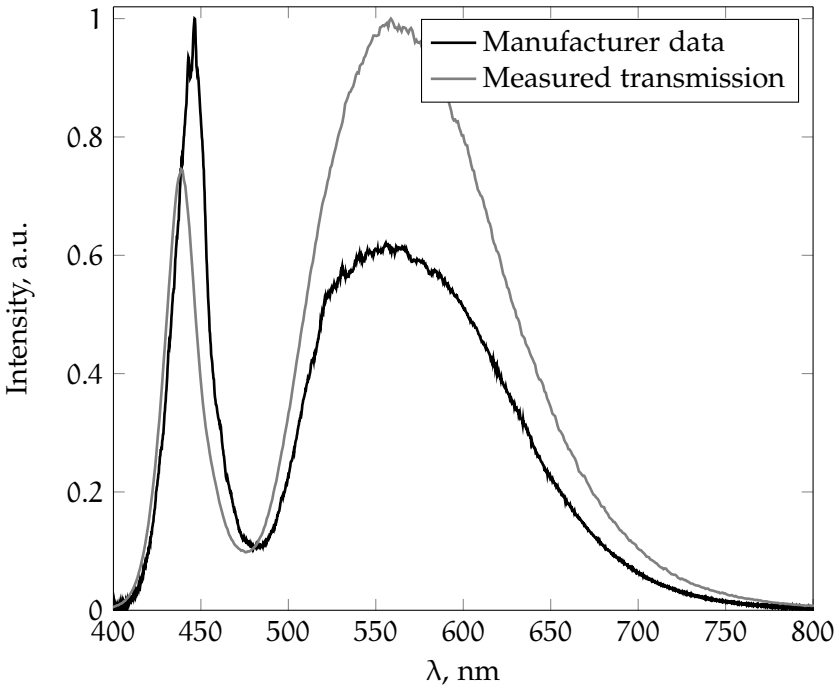


Figure A.1: LED spectrum (MCWHLP1) obtained from the manufacturer (Thorlabs) - black curve; and spectrum transmitted through a lead silicate fibre (F2) without sensing region.

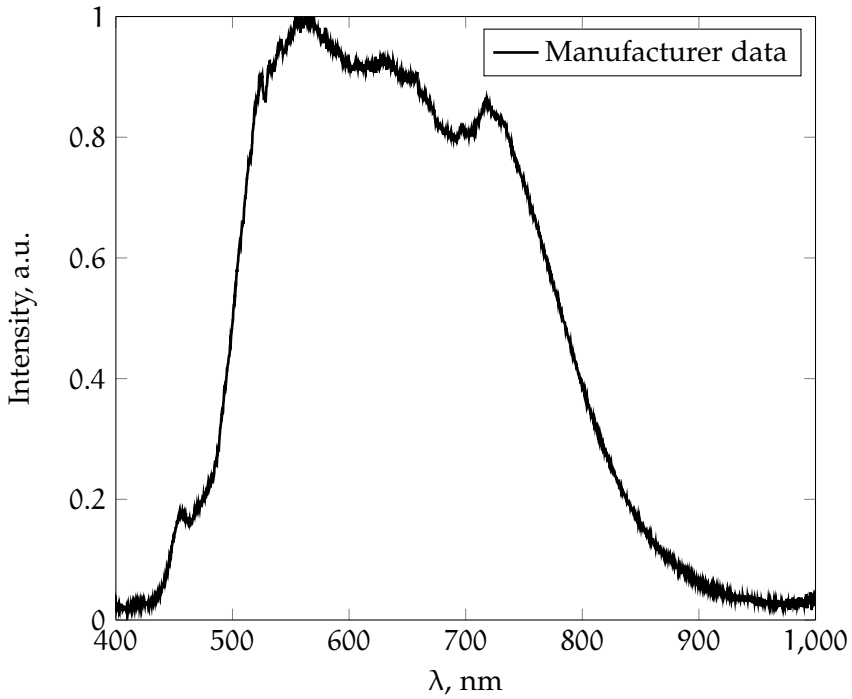


Figure A.2: Broadband LED spectrum (MBB1L3) obtained from the manufacturer (Thorlabs).

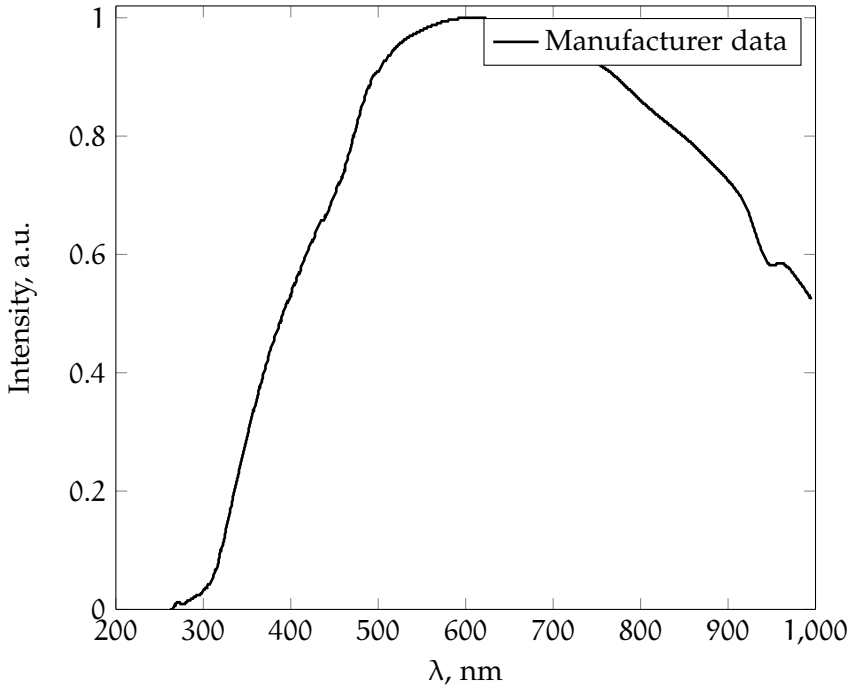


Figure A.3: Halogen light source spectrum (Ocean Optics, HL-2000). Data reconstructed from manufacturer's bitmap plot with Data Thief software.

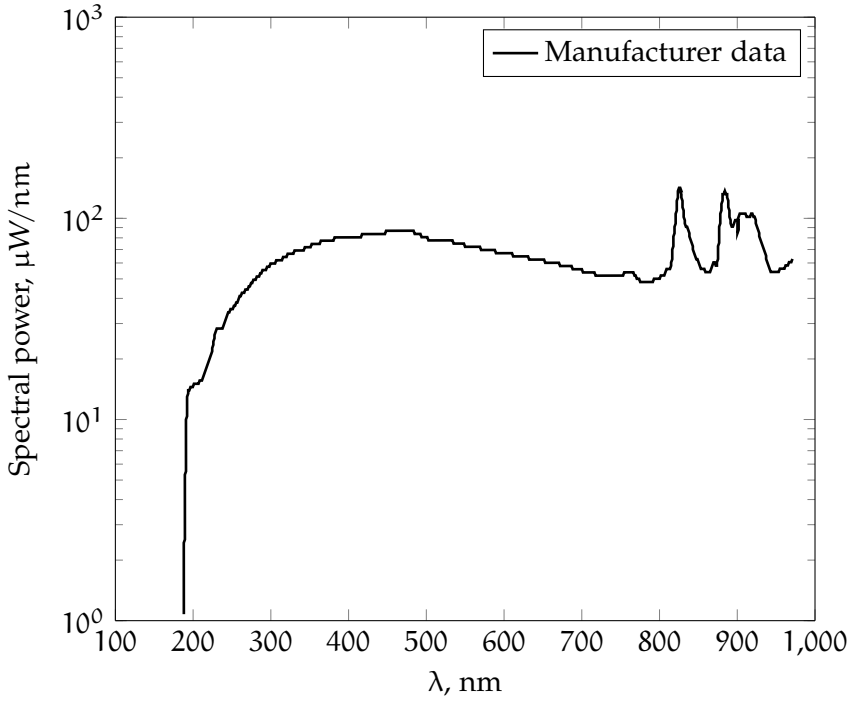


Figure A.4: Lase Driven Light Source (LDLS) spectrum (Energetiq Technology, EQ99-XFC-LDLS). Data reconstructed from manufacturer's bitmap plot with Data Thief software.

B

APPENDIX B: STEPS FOR NOV DETECTION

Table B.1: Typical steps for NoV detection experiment using protein A – antibody approach.

Step	Bioreagent	Volume, µL	Flow rate, µL/min
-	PAH	arbitrary	soaked, 30 min
-	PSS	arbitrary	soaked, 20 min
-	PAH	arbitrary	soaked, 20 min
1	PBS	800	100
2	Biotin	250	5
3	PBS	800	100
4	Neutravidin	250	5
5	PBS	800	100
6	Protein A	800	50 µL/hour††
7	PBS	800	100
8	Sera	450	5
9	PBS	800	100
10	Block	450	5
11	PBS	1600	100
12	VLPs 10^3 †	300	5
13	PBS	800	100
14	VLPs 10^6 ‡	300	5
15	PBS	800	100

† Concentration of VLP is 10^3 particles/mL.
‡ Concentration of VLP is 10^6 particles/mL.
†† This step was typically performed overnight due to long time required to perform the experiment.

C

APPENDIX C: SUPPLEMENTARY SPR SPECTRA FOR ECFS

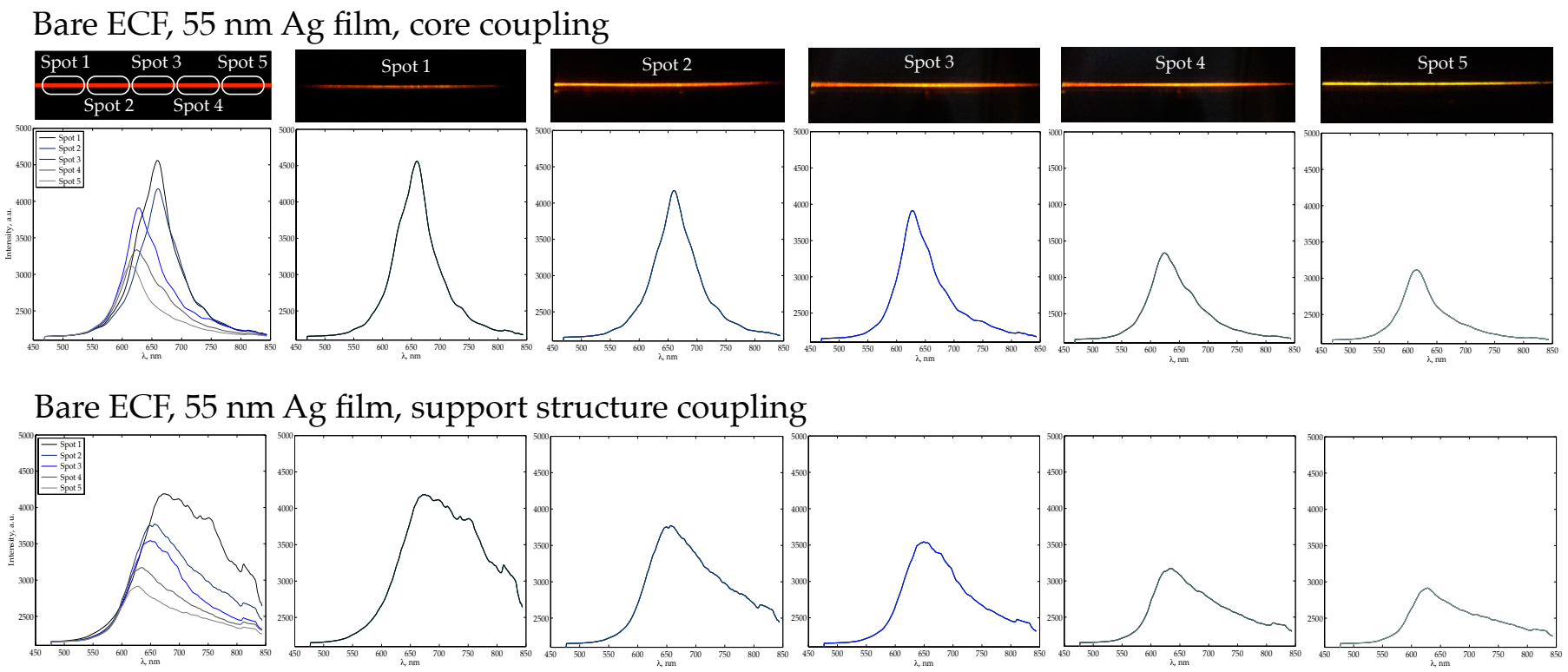
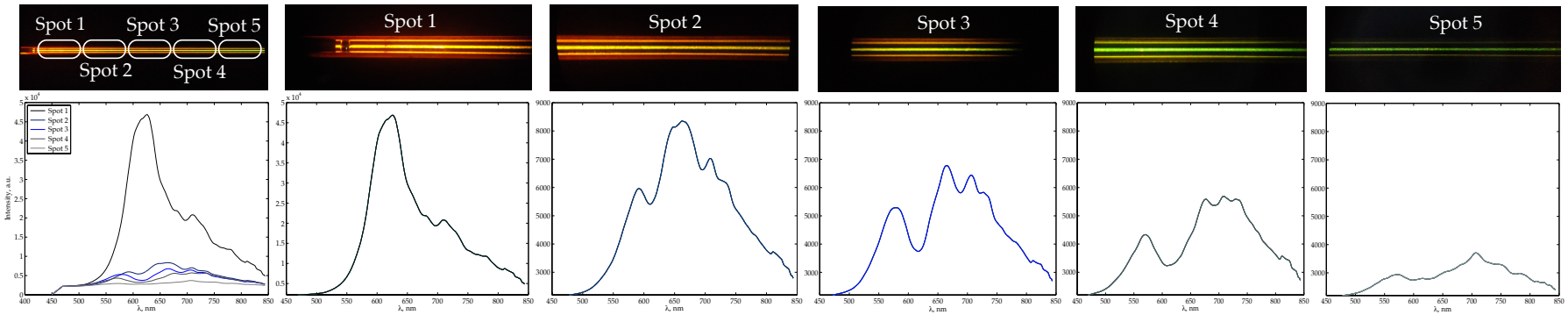


Figure C.1: SPR spectra in water for 5 spots on a bare ECF (BOP) sensor. Top: Core coupling, Bottom: support structure coupling.

Coated ECF, 47 nm Ag film, core coupling



Coated ECF, 47 nm Ag film, support structure coupling

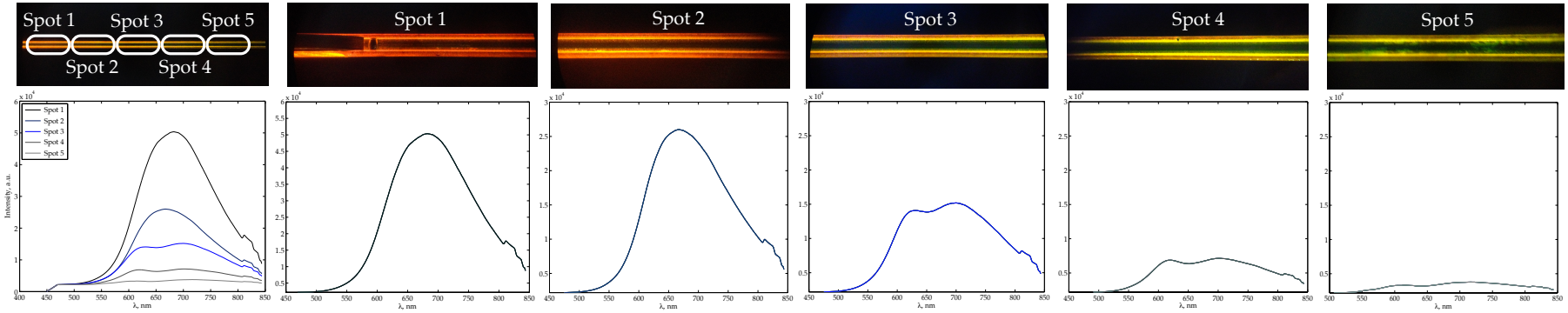


Figure C.2: SPR spectra in water for 5 spots on ECF (BOP) sensor with acrylate coating. Top: Core coupling, Bottom: support structure coupling.

D

APPENDIX D: PUBLICATIONS

Sensors **2015**, *15*, 25090-25102; doi:10.3390/s151025090

OPEN ACCESS
sensors
ISSN 1424-8220
www.mdpi.com/journal/sensors

Article

Surface Plasmon Scattering in Exposed Core Optical Fiber for Enhanced Resolution Refractive Index Sensing

Elizaveta Klantsataya [1,*], Alexandre François [1,2,4], Heike Ebendorff-Heidepriem [1,2], Peter Hoffmann [1,3] and Tanya M. Monro [1,2,4]

[1] Institute for Photonics and Advanced Sensing, The University of Adelaide, Adelaide, SA 5005, Australia; E-Mails: alexandre.francois@adelaide.edu.au (A.F.); heike.ebendorff@adelaide.edu.au (H.E.-H.); peter.hoffmann@adelaide.edu.au (P.H.); tanya.monro@adelaide.edu.au (T.M.M.)

[2] ARC Centre of Excellence for Nanoscale BioPhotonics (CNBP), The University of Adelaide, Adelaide, SA 5005, Australia

[3] Adelaide Proteomics Centre, The University of Adelaide, Adelaide, SA 5005, Australia

[4] University of South Australia, Adelaide, SA 5001, Australia

* Author to whom correspondence should be addressed; E-Mail: elizaveta.klantsataya@adelaide.edu.au; Tel.: +61-8-8313-0589.

Academic Editor: Vittorio M.N. Passaro

Received: 28 August 2015 / Accepted: 24 September 2015 / Published: 29 September 2015

Abstract: Refractometric sensors based on optical excitation of surface plasmons on the side of an optical fiber is an established sensing architecture that has enabled laboratory demonstrations of cost effective portable devices for biological and chemical applications. Here we report a Surface Plasmon Resonance (SPR) configuration realized in an Exposed Core Microstructured Optical Fiber (ECF) capable of optimizing both sensitivity and resolution. To the best of our knowledge, this is the first demonstration of fabrication of a rough metal coating suitable for spectral interrogation of scattered plasmonic wave using chemical electroless plating technique on a 10 μm diameter exposed core of the ECF. Performance of the sensor in terms of its refractive index sensitivity and full width at half maximum (*FWHM*) of SPR response is compared to that achieved with an unstructured bare core fiber with 140 μm core diameter. The experimental improvement in *FWHM*, and therefore the detection limit, is found to be a factor of two (75 nm for ECF in comparison to 150 nm for the large core fiber). Refractive index sensitivity of 1800 nm/*RIU* was achieved for both fibers in the sensing range of aqueous environment (1.33–1.37) suitable for biosensing applications.

Keywords: microstructured optical fiber; surface plasmon resonance; surface plasmon scattering; plasmonics; biosensing

1. Introduction

The widespread use of refractometric sensing devices based on SPR phenomenon can be attributed to its high sensitivity, immediate response, and simplicity of implementation [1]. Being a label-free transduction mechanism that determines changes of refractive index through a resonant wavelength shift, SPR allows for real time quantitative measurements that enable the detection of specific biomolecules for biomedical diagnostic applications [2,3] as well as the characterization of binding constants (association and dissociation constants) for biomolecular interactions studies [4].

Surface Plasmon Resonance (SPR) refers to the collective oscillation of free electrons at a metal-dielectric interface stimulated by incident light. For the resonant condition to occur, the propagation constant of the incident light has to match the propagation constant of the surface plasmons. This can be accomplished using a glass prism, and this approach is known as the Kretschmann SPR configuration [5]. While this method remains the gold standard for commercial SPR systems, they are bulky, expensive and not suitable for some applications such as remote sensing. To overcome these limitations, waveguides and optical fiber based SPR sensors have been developed, with the fiber/waveguide fulfilling the role of the prism for coupling the incident light with the plasmons [6]. Using optical fibers also enables development of alternative strategies for either exciting the plasmons or improving sensing performance. Some examples include bent fibers [7], tilted fiber Bragg grating SPR sensors [8], tapered probes [9,10], and many other more exotic architectures [11–18].

The sensitivity of refractive index sensors ($S_\lambda = \delta\lambda/\delta n$) is often used solely to characterize their performance. This ignores the sensor's resolution, which is critical to the performance of the device. The resolution (R), defined as the smallest wavelength shift detectable by a sensing platform, depends on the optical setup and on the linewidth of the SPR signature. Resonance curves with narrower linewidths filter spectral noise more efficiently. This leads to lower spectral deviation from the actual position of an SPR peak making a very slight spectral shift to be resolvable [19,20]. Although a more comprehensive expression for the resolution of an SPR sensor can be found elsewhere [5,19], for the purposes of this paper it is sufficient to state that R of a sensor is directly proportional to the full width at half maximum ($FWHM$) of its SPR response. However, there is a trade off between sharper response curves and lower signal to noise ratio (SNR).

Sensitivity and resolution determine one critical performance characteristic—the detection limit (DL). The DL of an SPR sensor ($DL = R/S_\lambda$) is the smallest change of the refractive index that could be measured. Therefore, to improve the sensor's DL, one would have to increase the sensitivity of the sensor, or reduce the resolution by either minimizing $FWHM$ of SPR response or/and increasing SNR.

Sensitivity of an SPR sensor is highly dependent on the material of the fiber core and metal that supports surface plasmons. Higher sensitivity is generally attributed to lower refractive index fiber sensors. Using low refractive index glass results in shifting of the resonance towards longer wavelengths and an increase in the sensitivity but also causes broadening of SPR response leading to deterioration

of the sensor resolution [21]. Silver is also known to provide better sensitivity in comparison to gold and other plasmonic metals due to its high SPR ratio (ratio between the absolute values of the real and imaginary parts of the dielectric constant) [22,23]. To overcome the trade-off between resolution and sensitivity, alternative fiber designs and sensing architectures have been explored. For example, reducing the fiber core diameter decreases the number of modes whose propagation constants match the propagation constant of surface plasmons. As a result, the linewidth of the SPR signal is reduced, enabling improved resolution in determination of the wavelength shift [24]. However, due to additional fiber processing requirements and the inherent fragility of nanowires or tapered fibers, using those sensors in a real application presents a significant challenge.

The SPR fiber sensor presented here relies on surface plasmon scattering for analyzing the SPR signal, the architecture previously described in [25–27]. The scattering is induced by high surface roughness of the silver coating deposited using an electroless plating method described in Section 2.2. While SPR scattering in optical fibers presents some advantages when compared with standard transmission measurements [25,26], using a rough metallic coating results in an increase of the SPR signal's linewidth [28,29], which is detrimental to the overall sensor performance. This disadvantage can be alleviated by using a fiber with smaller core to enhance sensor resolution.

In this paper, we report an experimental demonstration of an SPR sensor based on silica Microstructured Optical Fiber with a core exposed along the fiber length (ECF). The relatively small core of 10 µm diameter is supported by an outer silica structure providing robustness to the fiber. The performance of the ECF SPR sensor is compared with a larger ($\varnothing$ = 140 µm) multimode unstructured silica bare core fiber. As the presented fiber sensor architecture relies on surface plasmon scattering, further improvement in sensor resolution is provided by improved SNR. We also discuss other advantages and limitations of the scattering based SPR platform in relation to usage of small core fibers.

2. Experimental Section

2.1. Exposed Core Optical Fiber

To analyze the influence of the fiber core diameter on SPR sensor performance, two different fibers, both made in-house out of F300 silica preform (Heraeus Quarzglas GmbH & Co.KG, RI of 1.457 at 633 nm, Kleinostheim, Germany), have been used to fabricate the sensors. One fiber is an ECF with a 10 µm core supported by thin struts within a 200 µm support structure [30]. The ECF is a modified suspended core fibre with an asymmetric geometry where one side of the core is exposed along the whole fibre length as shown in Figure 1a. Due to the specific ECF geometry, no additional fibre processing, such as side polishing or tapering, is required to access the core to allow for metal deposition. Another fiber is a bare core fiber with a core diameter of 140 µm as shown in Figure 1b for comparison.

The estimated number of modes in a silica fiber of 10 µm core diameter and air cladding is 670, compared to the 140 µm bare core fiber with cladding RI of 1.375, which supports over 42,000 modes. The calculation of the number of modes is performed for a wavelength of 650 nm using numerical simulation for an unstructured air-clad fiber. Even though the simulation assumes a circular fiber core

while the ECF core is analogous to a triangular cross section of suspended core fibers [31], this simple calculation is sufficient for estimating the number of modes that could be supported by ECFs.

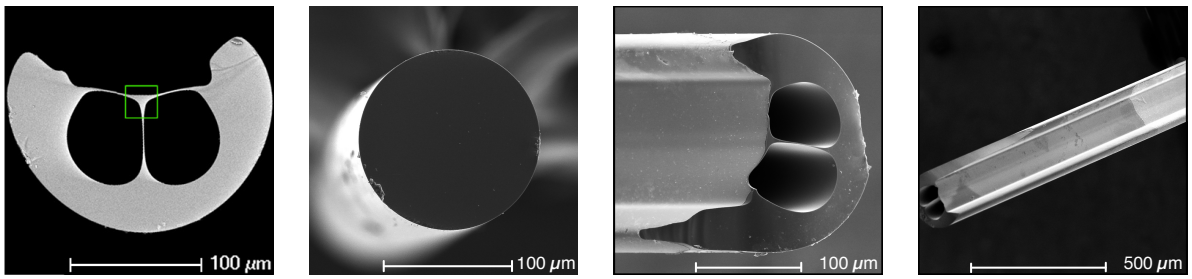


Figure 1. Scanning Electron Microscopy (SEM) images of optical fibers used for Surface Plasmon Resonance (SPR) sensor fabrication. (**a**) Exposed core fibre (ECF) cross section. Green rectangle shows the triangular core; (**b**) Bare core fiber cross section (shown for comparison); (**c**,**d**) Silver film fabricated on ECF (appears as lighter regions). The film fabricated around the outer fibre surface and the flat region where the core is located.

2.2. Sensor Fabrication

A thin silver film of approximately 50 nm thickness was deposited on a 1 cm-long section around each fiber sample using an electroless plating method. As the ECF's core is exposed to an external environment, the sensor fabrication procedure is essentially the same for both, bare core and ECF sensors. A silver film fabricated on ECF is shown in Figure 1c,d.

First, the fiber samples were thoroughly cleaned with methanol and deionized water followed by washing in a detergent (Decon90), rinsing in deionized water, and finally dried. After the cleaning process, the fiber surfaces were sensitized to promote silver film adhesion with 0.1 M of stannous chloride solution ($SnCl_2$) in 0.1 M aqueous solution of hydrochloric acid (HCl). The fiber samples were soaked in the sensitizer for 5 min then rinsed with deionized water. The mechanism behind the sensitization process involves precipitation of soluble tin ions from the liquid layer adhering to the dielectric substrate during water rinsing due to rapid pH increase [32]. This pre-treatment step is required to chemically modify the silica surface prior electroless plating of silver on the silica substrate. It is speculated that tin ions absorbed on a glass surface act as nucleation sites onto which silver may be deposited [33].

The electroless plating process, also known as Tollens silver mirror reaction, is described in [34] and consists of the deposition of a thin film via precipitation of metallic silver from ammoniacal silver nitrate solution in the presence of a reducing agent. Tollens reaction parameters were adjusted to produce silver coatings of around 50 nm on fibres and glass slides. The coating thickness was characterized using Atomic Force Microscopy (AFM). In addition, the thickness characterization on glass slides was performed through transmission measurements using HeNe laser (λ = 633 nm). Calculation of the thickness of the films was carried out using Beer-Lambert law: $I = I_0 e^{-t\alpha}$, where I and I_0 are incident and transmitted power respectively, t—film thickness, and α = 756,310 cm^{-1}—absorption coefficient of silver at 633 nm [35]. The results for the silver film thickness acquired with the transmission

measurements agree with those obtained using microscopy and, therefore, further thickness control of every sensor batch was estimated by measuring thickness of the silver coatings on glass slides prepared together with the fiber samples.

Even though the ECF has a small core held up by thin struts, the support structure of 200 µm diameter provides sufficient mechanical strength. There is no specific handling required to produce SPR sensors using ECF and the silver coating and fibre preparation procedures are similar to those used with large bare core sensors. The fabrication yield of the ECF SPR sensors is comparable to bare core SPR sensors: up to 10–15 fibres can be simultaneously coated in one chemical deposition reaction regardless of the fibre type.

2.3. Experimental Setup

To perform SPR characterization of the prepared fiber probe, the sensing region was enclosed in a flow cell that was constructed from a glass capillary tube allowing to flow liquid samples along the exposed core of the fiber sensor. Having one side of the ECF core exposed to the environment allows to perform sensing without filling the air holes which significantly simplifies the sensing apparatus. A schematic of a cross section of the flow cell with enclosed ECF SPR sensor is presented in Figure 2a. Plastic tubings were inserted for the liquid inlet and an outlet at two opposite ends of the tube. The flow cell was sealed using a low refractive index curable adhesive (MY-133-V2000, My Polymers Ltd., Nes Ziona, Israel). Serial dilutions of glycerol in deionized water (from 0% to 30%) with refractive indices ranging from 1.330 to 1.372 were used as liquid dielectric samples for RI measurements. The small range of the refractive indices close to aqueous environment used in the experiments was chosen to simulate refractive index changes that often occur in biosensing applications.

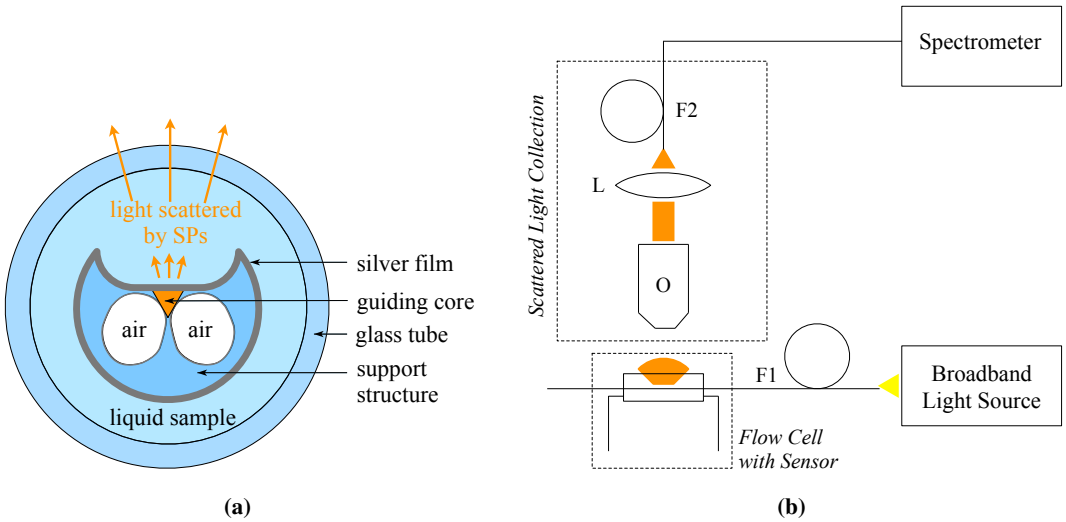


Figure 2. (**a**) Cross section of a flow cell with enclosed ECF SPR sensor (not to scale) where Surface Plasmons (SPs) are excited on the exposed part of the fibre core; and (**b**) Optical setup for SPR sensors characterization. F1—optical fiber with a sensing region enclosed in a flow cell, F2—optical fiber Ocean Optics with 200 µm core diameter, L—converging lens, O—microscope objective ×20, Numerical Aperture 0.4. Broadband light used to excited SPR is shown in yellow. Light scattered by the plasmons is shown in orange.

The setup used for SPR sensor characterization is schematically shown in Figure 2b. A supercontinuum light source (KOHERAS SuperK Compact, NKT Photonics A/S, Birkerød, Danmark) was coupled into the fiber (F1) with the sensing region enclosed in the flow cell. The scattered light collection apparatus consisted of an objective (O), a converging lens (L), and an optical patch cord cable (F2) to transfer the collected light to an Ocean Optics compact spectrometer (QE 65000) for analysis. Light transmitted through the optical fiber was projected onto a screen to ensure coupling into the core as opposed to the support structure in the case of ECF based sensors.

2.4. Data Analysis

Scattered spectra were recorded for every sample's RI and for intermediate water rinsing steps to ensure thorough removal of a previous sample. The spectral position of a peak in the scattered signal was found by fitting collected data with a Gaussian function. The wavelength shift with respect to the change in the RI of the sample surrounding the sensing region was plotted and the slope of the linear fit of the curve was considered to be the sensor's sensitivity value. $FWHM$ was found from the Gaussian fit for each peak as $2\sqrt{-2\ln(0.5)}\sigma$, σ being square root of the variance, and the mean of values for every sample was taken as a $FWHM$ for a sensor. Full width at ninetieth of the maxima ($FWNM$ or $\Delta\lambda_{0.9}$) was evaluated as $2\sqrt{-2\ln(0.9)}\sigma$. To consider both performance identifying parameters, a Figure of Merit (FOM) was defined as the ratio between the sensitivity of a sensor and the average $FWHM$ of SPR response curves ($FOM = S_\lambda/\Delta\lambda_{0.5}$). $Height$ of a peak was measured as maximum intensity in arbitrary units ($a.u.$) keeping integration time of the spectrometer constant. SNR for each sensor was calculated as the mean of the squared signal amplitude divided by the mean of the squared noise amplitude for each data point averaged over all SPR peaks for each RI.

Errors in resonant wavelength shift and $FWHM$ were calculated by combining experimental uncertainties and fitting errors. Water rinsing steps were used to estimate experimental errors. In particular, the sum of deviations of the position of a peak at rising steps before and after each glycerol concentration from the original step for water was considered an experimental uncertainty. Those errors mainly come from a change in coupling conditions due to a stage drift or a fiber movement, and a change in the alignment of the sensing region under the collection setup during the experiment. Errors in refractive indices of the prepared glycerol solutions were calculated as a sum of uncertainties in the solution RI due to thermal fluctuations, spectral dispersion, and preparation of the serial dilutions of glycerol.

To estimate fitting errors of the experimental data, a threshold parameter, that is a fraction from the maximum height of a peak where data for the fit has been taken from, was used. Errors in the fit for a peak wavelength and $FWHM$ were estimated as scatter of the values (standard deviations) of the three different fits: broad fit that considers larger number of points around the maxima, narrow fit with less number of points, and a fit between those two at which all of the parameters (S_λ, $FWHM$, $FWNM$, $Height$, and FOM) were evaluated.

3. Results and Discussion

Bare core fiber SPR sensors of 140 μm core diameter were compared to sensors fabricated using a ECF of 10 μm core prepared following the same procedure. Experimentally obtained spectra for the

bare core fiber sensor exposed to the different refractive index solutions are presented in Figure 3a. Resonant wavelength with respect to the refractive index of the sample (sensitivity curve) and *FWHM* of the scattered signal are shown in Figure 3c. The slope of the sensitivity curve yields the sensitivity of 1823 ± 58 nm/*RIU* while the mean value of the *FWHM* is calculated to be 149 ± 8 nm for the sensor. The small secondary peak at around 820 nm in the Figure 3a is scattered light from the light source pump and is not related to the SPR signal. The results of the experiments that were conducted using an ECF are presented in Figure 3b,d. Sensitivity of the ECF SPR sensor is 1753 ± 27 nm/*RIU* and the mean value of the *FWHM* is 75 ± 10 nm. Spectra presented in Figure 3a,b are scattered light intensities normalized to their maxima with moving average function applied to smooth data fluctuations. The values for sensitivity, *FWHM*, and other performance parameters are evaluated from Gaussian fits as described in Section 2.4.

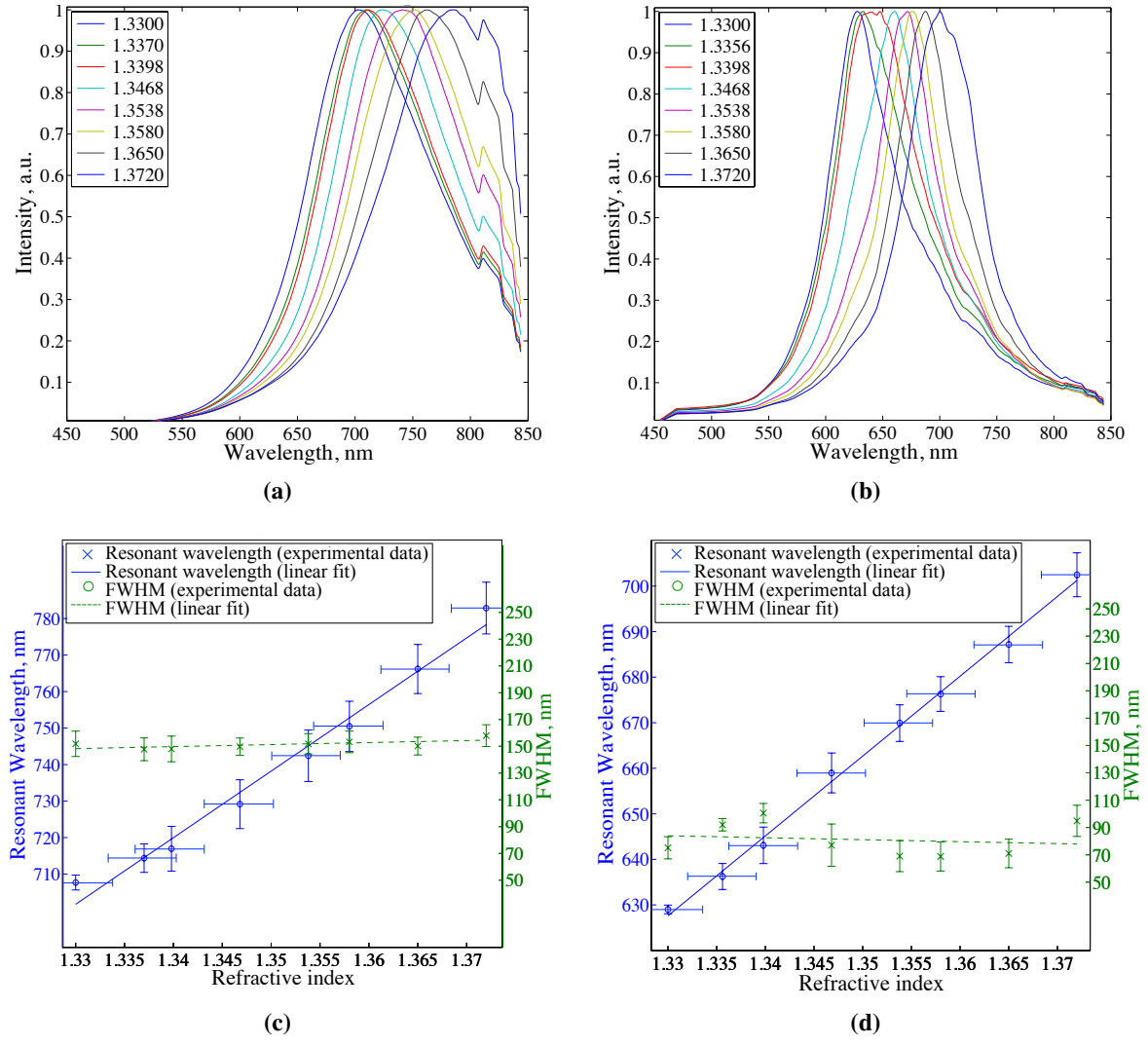


Figure 3. Normalized scattered spectra for (**a**) bare core fiber SPR sensor and (**b**) exposed core fibre (ECF) SPR sensor. Legends show the values of glycerol solutions' refractive indices used in the experiment. Sensitivity curves and full width at half maximum (*FWHM*) for (**c**) bare core SPR sensor and (**d**) ECF SPR sensor. Bare core sensor: core diameter 140 µm, silver film thickness 57 nm. ECF sensor: core diameter 10 µm, silver film thickness 55 nm.

Table 1 summarizes the performance characteristics of the two types of sensors, bare core SPR sensor and ECF SPR sensor. The sensitivities of both devices are the same within their uncertainty ranges. As far as the linewidth is concerned, ECF SPR sensor manifests twice as narrower scattered peaks than the bare core SPR sensor which is expressed in the variable $FWHM$ and $FWNM$. This makes smaller wavelength shifts of the plasmonic resonance resolvable leading to an improvement in ECF sensor resolution and detection limit, and an increase in FOM by at least a factor of two. For the comparative analysis multiple ECF and bare core SPR sensors have been prepared and characterized and the performance parameters have shown sufficient reproducibility.

Table 1. SPR performance characteristics of the bare core fibre sensor and the exposed core fibre (ECF) sensor.

Performance/Parameters	**Bare Core Sensor**	**ECF Sensor**
Core diameter ($\varnothing$), μm	140	10
Silver film thickness (t), nm	57	55
Peak wavelength (λ_{res}), nm for RI 1.33	708 ± 2	629 ± 1
Sensitivity (S_λ), nm/*RIU*	1823 ± 58	1753 ± 27
FWHM ($\Delta\lambda_{0.5}$), nm	149 ± 8	75 ± 10
FWNM ($\Delta\lambda_{0.9}$), nm	58	29
$Height$, $a.u.$	51,539	997
SNR, *dB*	33	27
FOM, RIU^{-1}	12 ± 1	23 ± 3

The experimentally demonstrated results for the ECF SPR sensor presented here are, in general, in agreement with previously reported theoretical work based on numerical simulation of SPR in ECFs [36,37]. The predicted sensitivity of a silver coated SPR sensor based on an ECF of similar geometry is 2000–4000 nm/*RIU* for the range of samples' RIs between 1.33–1.37, and the $FWHM$ of SPR response is around 50 nm [37]. Despite the slightly lower performance of our experimentally demonstrated ECF sensor, which is likely to be attributed to a different dielectric function of the silver coating produced by chemical electroless plating and the roughness of the film, the experimental values obtained for the ECF SPR sensor support the results previously predicted by the modelling.

Further analysis of experimental data suggests that a drawback of using the small core ECF sensor is its lower SNR of 460 in comparison to SNR of 2050 estimated for the bare core fibre sensor. An increased noise causes an increased uncertainty in determining an extremum in the spectral response leading to a deterioration of the sensor resolution. Therefore, depending on the contribution of the reduced SNR towards resolution, narrower linewidth of the SPR response might or might not result in an improvement of the sensor resolution. Considering the numerically simulated expression presented in [19] ($R = 3\sigma \approx 3(\Delta\lambda/(4.5\,SNR^{1/4}))$, where $\Delta\lambda$ is $FWNM$), we estimated the resolution for the bare core and ECF sensors as 5.75 nm and 4.17 nm respectively. This would give the detection limit of 0.0032 RIU for the bare core sensor and 0.0023 RIU for the ECF leading to the improvement factor of 1.4 for the ECF sensor. On the other hand, the experimental contribution of the SNR might differ from the numerically predicted dependency. Specifically, curve fitting for data analysis is influenced by

both parameters, linewidth and SNR. The average fitting error in determining the spectral position of the peaks for the bare core sensor was estimated to be 2.47 nm, while this for the ECF sensor is only 1.21 nm which approaches the spectral resolution of the spectrometer. While the calculated values for the resolution and the detection limit are somewhat speculative, the analysis shows the trend that the reduced linewidth of smaller core SPR sensors tend to improve the resolution and the detection limit, even in the presence of increased noise level. The latter could be potentially alleviated by the choice of light source used to excite SPR.

Based on the results of the described experiments one may conclude that the structural parameters of the fiber have a strong influence on the sensor performance as well as on the scattered peak position. The observed wavelength is the result of the convolution of different resonance peaks each caused by a specific resonance condition satisfied by a given mode-wavelength combination. The number of modes contributing to the resonance could be one of the potential reasons for broadening of SPR peaks. It has been noticed that in a highly multimode fiber with thousands of modes, such as the bare core fiber used in the experiments, the coupling conditions do not have a strong effect on the observed SPR wavelength. However, for the smaller core multimode fiber, such as the ECF used here, we registered a stronger dependency of the scattered peak wavelength on the properties of the guided light, which in turn is influenced by coupling. Thus, in order to achieve coupling consistency between different fiber sensors, we aimed at maximizing intensity of the signal scattered from the sensing region.

In addition to the coupling efficiency, properties of the guided light are affected by interaction with the metal coating itself. SPR is a lossy process that causes attenuation of electromagnetic radiation near the resonance frequency. After the guided light undergoes an interaction with the metal film, its spectral properties change. As a result, the observed wavelength of the peak in the scattered signal from a particular spot on the sensing region shifts depending on the losses that occurred in the fiber prior to that spot. This concept is demonstrated by comparing spectra taken from five equidistant positions along a sensing region. Figure 4a presents normalized scattered spectra for ECF SPR sensor collected from different spots on the sensing region of 15 mm length with the same outer dielectric medium. As longer wavelengths are scattered at the beginning of the sensing region, the peak shifts towards the shorter wavelengths. This is also noticeable when light is launched into the support structure (the cladding of the microstructured fiber) rather than the small core (Figure 4b). The 200 µm diameter support structure is sufficiently large that it could be considered as a highly multimode fiber. Sensor spot positions from which the spectra were taken from are depicted in Figure 4c. This effect of shifting the resonant wavelength with a position on the sensor is an artifact of the scattered interrogation method and could be mitigated by collecting signal from a larger area of the sensor or reducing the length of the sensing region. Although we verified that the sensor sensitivity for both coupling conditions does not strongly depend on the position on the sensing region and the observable peak wavelength, the linewidth of the scattered peaks might be affected. In the case of the larger core sensor (support structure coupling), $FWHM$ is larger at the first spot on the sensing region reaching around 180 nm, then reducing down to 150 nm at the further spots (Figure 4b). The broadening of the peak at the beginning of the sensing region for larger core SPR sensors might be attributed to the larger scattering area that introduces more scattered background unrelated to SPR at the boundary of the coated region. This effect is not noticeable for the small core sensor (core coupling condition) where $FWHM$ does not vary with the position on the

sensing region (Figure 4a). In practice, this may signify the importance of ECF SPR sensors for usage in multiplexed sensing architectures where spatially localized specific antibodies along one long sensing region or multiple sensing regions are used for detection.

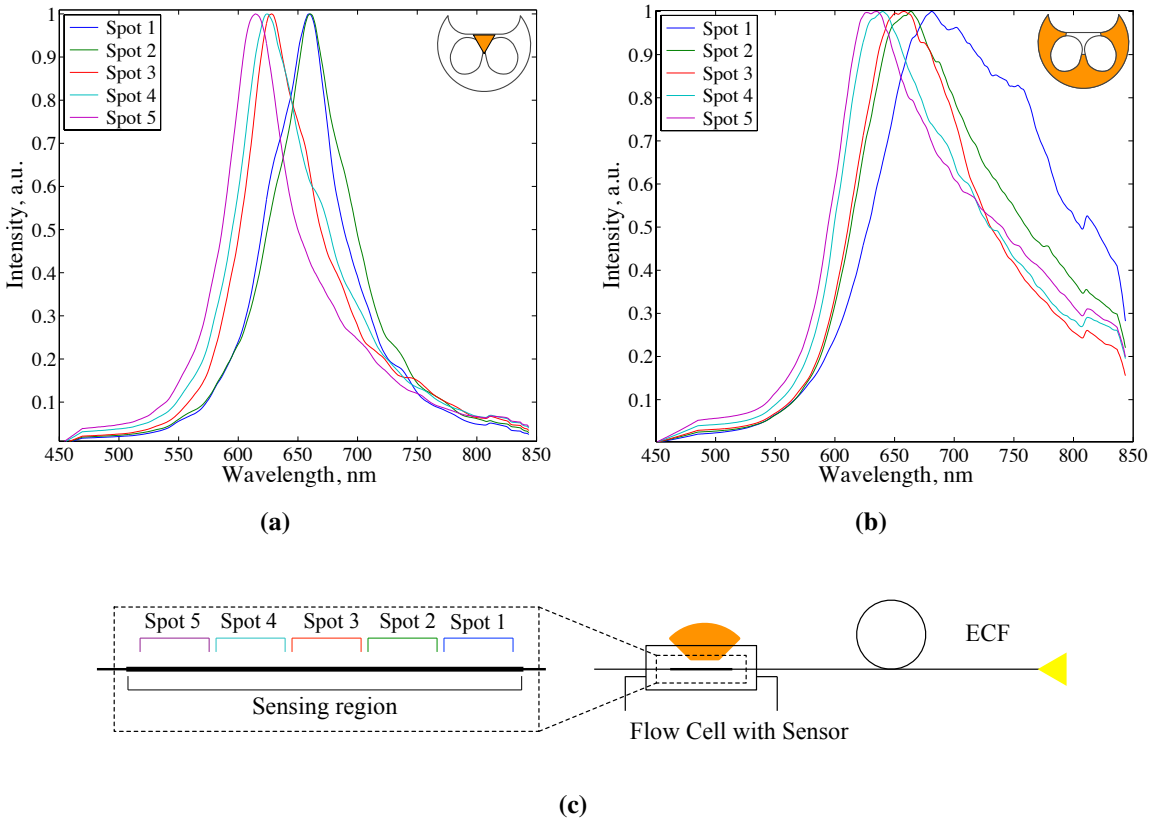


Figure 4. Scattered spectra taken from different spots on a sensing region of the exposed core fibre (ECF) SPR sensor in case of (**a**) core coupling, and (**b**) support structure coupling (as shown on the insets). Refractive index of the outer dielectric medium is 1.33; (**c**) Schematic diagram of five equidistant spots on the sensing region of ECF SPR sensor. Sensing region length is 15 mm.

4. Conclusions

In this work, we have experimentally demonstrated an SPR sensor with a reduced linewidth that is fabricated using ECF with a small core. The refractive index sensitivity of the ECF SPR sensor is 1800 nm/*RIU*, comparable with the sensitivity of a large bare core fiber SPR sensor. The ECF sensor exhibits narrower SPR curves with *FWHM* of 75 nm, a factor of two improvement in comparison to the previously reported large core SPR sensor. Even though the performance of the reported ECF sensor is comparable to the current state of the art fibre optic SPR sensors [38], there is a significant scope for performance improvement, such as further reduction in linewidth, increased durability, enhanced sensitivity, as well as a more sophisticated collection apparatus. A further reduction in the linewidth could potentially be achieved by using even smaller core ECF with a core diameter down to a couple of micron which would support just a few fiber modes. The use of a microstructured fiber allows for easier sensor fabrication and more practical applications in comparison to fragile free standing nanowires or

tapered fibers. The architecture utilizes spectral interrogation of the scattered plasmonic wave mediated by rough metallic coating which provides additional practical advantages such as reduced SNR, lower dependency of the sensor performance on the coating thickness, and possibility of combining SPR with other phenomena, such as fluorescence, in a single device. The proposed SPR configuration is promising for applications such as biological or chemical sensing where improved resolution is required.

Acknowledgments

The authors acknowledge the support of Tanya M. Monro's ARC Georgina Sweet Laureate Fellowship and the ARC Centre for Nanoscale BioPhotonics (CNBP). This work was performed in part at the OptoFab node of the Australian National Fabrication Facility utilizing Commonwealth and SA State Government funding. The authors would like to acknowledge Roman Kostecki for ECF design and fabrication.

Author Contributions

Elizaveta Klantsataya proposed the work, design and performed the experiments and the data analysis; all authors wrote and commented on the paper; Alexandre François, and Tanya M. Monro supervised the project.

Conflicts of Interest

The authors declare no conflict of interest.

References

1. Schasfoort, R.; Tudos, A. *Handbook of Surface Plasmon Resonance*; Royal Society of Chemistry: Cambridge, UK, 2008.
2. Gopinath, S.C.; Tang, T.H.; Chen, Y.; Citartan, M.; Tominaga, J.; Lakshmipriya, T. Sensing strategies for influenza surveillance. *Biosens. Bioelectron.* **2014**, *61*, 357–369.
3. Jahanshahi, P.; Zalnezhad, E.; Sekaran, S.D.; Adikan, F.R.M. Rapid Immunoglobulin M-Based Dengue Diagnostic Test Using Surface Plasmon Resonance Biosensor. *Sci. Rep.* **2014**, doi:10.1038/srep03851.
4. Stahelin, R.V. Surface plasmon resonance: A useful technique for cell biologists to characterize biomolecular interactions. *Mol. Biol. Cell* **2013**, *24*, 883–886.
5. Homola, J. *Surface Plasmon Resonance Based Sensors*; Springer Series on Chemical Sensors and Biosensors; Springer: Berlin, Germany, 2006.
6. Sharma, A.; Jha, R.; Gupta, B. Fiber-Optic Sensors Based on Surface Plasmon Resonance: A Comprehensive Review. *IEEE Sens. J.* **2007**, *7*, 1118–1129.
7. Verma, R.K.; Gupta, B.D. Theoretical modelling of a bi-dimensional U-shaped surface plasmon resonance based fibre optic sensor for sensitivity enhancement. *J. Phys. D Appl. Phys.* **2008**, *41*, 095106.

8. Shevchenko, Y.Y.; Albert, J. Plasmon resonances in gold-coated tilted fiber Bragg gratings. *Opt. Lett.* **2007**, *32*, 211–213.
9. Kim, Y.C.; Peng, W.; Banerji, S.; Booksh, K.S. Tapered fiber optic surface plasmon resonance sensor for analyses of vapor and liquid phases. *Opt. Lett.* **2005**, *30*, 2218–2220.
10. Verma, R.; Sharma, A.; Gupta, B. Modeling of Tapered Fiber-Optic Surface Plasmon Resonance Sensor With Enhanced Sensitivity. *IEEE Photonics Technol. Lett.* **2007**, *19*, 1786–1788.
11. Hassani, A.; Skorobogatiy, M. Design of the microstructured optical fiber-based surface plasmon resonance sensors with enhanced microfluidics. *Opt. Express* **2006**, *14*, 11616–11621.
12. Hautakorpi, M.; Mattinen, M.; Ludvigsen, H. Surface-plasmon-resonance sensor based on three-hole microstructured optical fiber. *Opt. Express* **2008**, *16*, 8427–8432.
13. Nemova, G.; Kashyap, R. Fiber-Bragg-grating-assisted surface plasmon-polariton sensor. *Opt. Lett.* **2006**, *31*, 2118–2120.
14. Jian, A.; Deng, L.; Sang, S.; Duan, Q.; Zhang, X.; Zhang, W. Surface plasmon resonance sensor based on an angled optical fiber. *IEEE Sens. J.* **2014**, *14*, 3229–3235.
15. Maria, L.D.; Martinelli, M.; Vegetti, G. Fiber-optic sensor based on surface plasmon interrogation. *Sens. Actuators B Chem.* **1993**, *12*, 221–223.
16. Fontana, E.; Dulman, H.; Doggett, D.; Pantell, R. Surface plasmon resonance on a single mode optical fiber. *IEEE Trans. Instrum. Meas.* **1998**, *47*, 168–173.
17. Rifat, A.A.; Mahdiraji, G.A.; Chow, D.M.; Shee, Y.G.; Ahmed, R.; Adikan, F.R.M. Photonic Crystal Fiber-Based Surface Plasmon Resonance Sensor with Selective Analyte Channels and Graphene-Silver Deposited Core. *Sensors* **2015**, *15*, 11499–11510.
18. Lu, Y.; Hao, C.J.; Wu, B.Q.; Musideke, M.; Duan, L.C.; Wen, W.Q.; Yao, J.Q. Surface Plasmon Resonance Sensor Based on Polymer Photonic Crystal Fibers with Metal Nanolayers. *Sensors* **2013**, *13*, 956–965.
19. White, I.M.; Fan, X. On the performance quantification of resonant refractive index sensors. *Opt. Express* **2008**, *16*, 1020–1028.
20. Lee, K.S.; Son, J.M.; Jeong, D.Y.; Lee, T.S.; Kim, W.M. Resolution enhancement in surface plasmon resonance sensor based on waveguide coupled mode by combining a bimetallic approach. *Sensors* **2010**, *10*, 11390–11399.
21. Homola, J. On the sensitivity of surface plasmon resonance sensors with spectral interrogation. *Sens. Actuators B Chem.* **1997**, *41*, 207–211.
22. Homola, J.; Yee, S.S.; Gauglitz, G. Surface plasmon resonance sensors: Review. *Sens. Actuators B Chem.* **1999**, *54*, 3–15.
23. Sadowski, J. Method for Carrying out Surface Plasmon Resonance Measurement and Sensor for Use in the Method. EP Patent 0,537,252, 10 January 1996.
24. Piliarik, M.; Homola, J.; Manikova, Z.; Ctyroky, J. Surface plasmon resonance sensor based on a single-mode polarization-maintaining optical fiber. *Sens. Actuators B Chem.* **2003**, *90*, 236–242.
25. Francois, A.; Boehm, J.; Oh, S.; Kok, T.; Monro, T. Collection mode surface plasmon fibre sensors: A new biosensing platform. *Biosens. Bioelectron.* **2011**, *26*, 3154–3159.

26. Sciacca, B.; Francois, A.; Hoffmann, P.; Monro, T.M. Multiplexing of radiative-surface plasmon resonance for the detection of gastric cancer biomarkers in a single optical fiber. *Sens. Actuators B Chem.* **2013**, *183*, 454–458.
27. Sciacca, B.; François, A.; Klingler-Hoffmann, M.; Brazzatti, J.; Penno, M.; Hoffmann, P.; Monro, T. Radiative-surface plasmon resonance for the detection of apolipoprotein E in medical diagnostics applications. *Nanomed. Nanotechnol. Biol. Med.* **2013**, *9*, 550–557.
28. Raether, H. *Surface Plasmons on Smooth and Rough Surfaces and on Gratings*; No. v.111 in Springer Tracts in Modern Physics; Springer: Berlin, Germany, 1988.
29. Kanso, M.; Cuenot, S.; Louarn, G. Roughness effect on the SPR measurements for an optical fibre configuration: Experimental and numerical approaches. *J. Opt. A Pure Appl. Opt.* **2007**, *9*, doi:10.1088/1464-4258/9/7/008.
30. Kostecki, R.; Ebendorff-Heidepriem, H.; Davis, C.; McAdam, G.; Warren-Smith, S.C.; Monro, T.M. Silica exposed-core microstructured optical fibers. *Opt. Mater. Express* **2012**, *2*, 1538–1547.
31. Monro, T.M.; Warren-Smith, S.; Schartner, E.P.; Francois, A.; Heng, S.; Ebendorff-Heidepriem, H.; Afshar, V.S. Sensing with suspended-core optical fibers. *Opt. Fiber Technol.* **2010**, *16*, 343–356.
32. Wei, X.; Roper, D.K. Tin sensitization for electroless plating review. *J. Electrochem. Soc.* **2014**, *161*, D235–D242.
33. Pederson, L.R. Comparison of stannous and stannic chloride as sensitizing agents in electroless deposition of silver on glass using X-Ray photoelectron spectroscopy. *Sol. Energy Mater.* **1982**, *6*, 221–232.
34. Boehm, J.; François, A.; Ebendorff-Heidepriem, H.; Monro, T. Chemical Deposition of Silver for the Fabrication of Surface Plasmon Microstructured Optical Fibre Sensors. *Plasmonics* **2011**, *6*, 133–136.
35. Palik, E. *Handbook of Optical Constants of Solids*; Academic Press Handbook Series; Elsevier Science: Amsterdam, The Netherlands, 1998.
36. Luan, N.; Wang, R.; Lv, W.; Yao, J. Surface plasmon resonance sensor based on exposed-core microstructured optical fibres. *Electron. Lett.* **2015**, *51*, 714–715.
37. Yang, X.; Lu, Y.; Wang, M.; Yao, J. An Exposed-Core Grapefruit Fibers Based Surface Plasmon Resonance Sensor. *Sensors* **2015**, *15*, 17106–17114.
38. Arghir, I.; Delport, F.; Spasic, D.; Lammertyn, J. Smart design of fiber optic surfaces for improved plasmonic biosensing. *New Biotechnol.* **2015**, *32*, 473–484.

© 2015 by the authors; licensee MDPI, Basel, Switzerland. This article is an open access article distributed under the terms and conditions of the Creative Commons Attribution license (http://creativecommons.org/licenses/by/4.0/).

Effect of surface roughness on metal enhanced fluorescence in planar substrates and optical fibers

Elizaveta Klantsataya,[1,*] Alexandre François,[1,2] Heike Ebendorff-Heidepriem,[1] Beniamino Sciacca,[1,3] Agnieszka Zuber,[1] and Tanya M. Monro[1,2]

[1]*Institute for Photonics and Advanced Sensing, The University of Adelaide, Adelaide, SA, 5005, Australia*
[2]*University of South Australia, Adelaide, SA, 5001, Australia*
[3]*Center for Nanophotonics, FOM Institute AMOLF, Science Park Amsterdam 104, 1098 XG Amsterdam, The Netherlands*
[*]*elizaveta.klantsataya@adelaide.edu.au*

Abstract: We investigate the effect of the roughness of thin silver films on the performance of sensors that exploit metal enhanced fluorescence (MEF). Fluorescence enhancement of dye molecules of up to 47 times was observed on planar glass substrates coated with metal films of higher roughness of around 8 nm. We also study the fluorescence enhancement on the rough silver films implemented on a side of an optical fiber and analyze its dependence on the thickness of the metal. A maximum enhancement factor of 15 was demonstrated for thinner coatings where the film could be considered as a layer of particles. The chemical electroless plating technique used here to produce films with desired roughness is a low cost simple alternative to complex procedures that are currently used for fabrication of nanostructured metal coatings on optical fibers for MEF.

©2016 Optical Society of America

OCIS codes: (290.5880) Scattering, rough surfaces; (160.4236) Nanomaterials; (240.0310) Thin films; (240.6680) Surface plasmons; (260.2510) Fluorescence; (060.2370) Fiber optics sensors.

References and links

1. J. R. Lakowicz, *Principles of Fluorescence Spectroscopy* (Springer, 2006).
2. K. Aslan, I. Gryczynski, J. Malicka, E. Matveeva, J. R. Lakowicz, and C. D. Geddes, "Metal-enhanced fluorescence: an emerging tool in biotechnology," Curr. Opin. Biotechnol. **16**(1), 55–62 (2005).
3. C. D. Geddes, *Metal-Enhanced Fluorescence* (John Wiley & Sons, 2010).
4. J. R. Lakowicz, "Radiative decay engineering 5: metal-enhanced fluorescence and plasmon emission," Anal. Biochem. **337**(2), 171–194 (2005).
5. C. D. Geddes and J. R. Lakowicz, "*Topics in Fluorescence Spectroscopy vol. 8: Radiative Decay Engineering* (Springer, 2007)," Phys. Rep. **113**, 195–287 (1984).
6. A. I. Dragan, E. S. Bishop, J. R. Casas-Finet, R. J. Strouse, J. McGivney, M. A. Schenerman, and C. D. Geddes, "Distance dependence of metal-enhanced fluorescence," Plasmonics **7**(4), 739–744 (2012).
7. J. R. Lakowicz, "Radiative decay engineering: biophysical and biomedical applications," Anal. Biochem. **298**(1), 1–24 (2001).
8. J. R. Lakowicz, Y. Shen, S. D'Auria, J. Malicka, J. Fang, Z. Gryczynski, and I. Gryczynski, "Radiative decay engineering. 2. Effects of Silver Island films on fluorescence intensity, lifetimes, and resonance energy transfer," Anal. Biochem. **301**(2), 261–277 (2002).
9. K. Aslan, S. N. Malyn, Y. Zhang, and C. D. Geddes, "Conversion of just-continuous metallic films to large particulate substrates for metal-enhanced fluorescence," J. Appl. Phys. **103**(8), 84307 (2008).
10. A. L. Feng, M. L. You, L. Tian, S. Singamaneni, M. Liu, Z. Duan, T. J. Lu, F. Xu, and M. Lin, "Distance-dependent plasmon-enhanced fluorescence of upconversion nanoparticles using polyelectrolyte multilayers as tunable spacers," Sci. Rep. **5**, 7779 (2015).
11. K. Aslan, Z. Leonenko, J. R. Lakowicz, and C. D. Geddes, "Annealed silver-island films for applications in metal-enhanced fluorescence: interpretation in terms of radiating plasmons," J. Fluoresc. **15**(5), 643–654 (2005).
12. J. Dostálek and W. Knoll, "Biosensors based on surface plasmon-enhanced fluorescence spectroscopy," Biointerphases **3**(3), FD12–FD22 (2008).

#261697 Received 28 Mar 2016; revised 29 Apr 2016; accepted 2 May 2016; published 27 May 2016
© 2016 OSA

13. Y. Jiang, H. Y. Wang, H. Wang, B. R. Gao, Y. Hao, Y. Jin, Q.-D. Chen, and H.-B. Sun, "Y. wei Hao, Y. Jin, Q.-D. Chen, and H.-B. Sun, "Surface plasmon enhanced fluorescence of dye molecules on metal grating films," J. Phys. Chem. C **115**(25), 12636–12642 (2011).
14. M. Bauch, K. Toma, M. Toma, Q. Zhang, and J. Dostàlek, "Plasmon-enhanced fluorescence biosensors: a review," Plasmonics **9**(4), 781–799 (2014).
15. K. Toma, M. Vala, P. Adam, J. Homola, W. Knoll, and J. Dostálek, "Compact surface plasmon-enhanced fluorescence biochip," Opt. Express **21**(8), 10121–10132 (2013).
16. D. Darvill, A. Centeno, and F. Xie, "Plasmonic fluorescence enhancement by metal nanostructures: shaping the future of bionanotechnology," Phys. Chem. Chem. Phys. **15**(38), 15709–15726 (2013).
17. X. Yu, D. Yong, H. Zhang, H. Li, Y. Zhang, C. C. Chan, H.-P. Ho, H. Liu, and D. Liu, "Plasmonic enhanced fluorescence spectroscopy using side-polished microstructured optical fiber," Sens. Actuators B Chem. **160**(1), 196–201 (2011).
18. K. Arya, Z. B. Su, and J. L. Birman, "Localization of the surface plasmon polariton caused by random roughness and its role in surface-enhanced optical phenomena," Phys. Rev. Lett. **54**(14), 1559–1562 (1985).
19. J. Zhang, E. Matveeva, I. Gryczynski, Z. Leonenko, and J. R. Lakowicz, "Metal-enhanced fluoroimmunoassay on a silver film by vapor deposition," J. Phys. Chem. B **109**(16), 7969–7975 (2005).
20. K. Ray, M. H. Chowdhury, and J. R. Lakowicz, "Use of aluminum films as substrates for enhanced fluorescence in the ultraviolet-blue spectral region," Anal. Chem. **79**, 6480–6487 (2007).
21. H. Raether, *Surface Plasmons on Smooth and Rough Surfaces and on Gratings* (Springer 1988).
22. T. Neumann, M. L. Johansson, D. Kambhampati, and W. Knoll, "Surface-plasmon fluorescence spectroscopy," Adv. Funct. Mater. **12**(9), 575–586 (2002).
23. M. Y. Ng and W. C. Liu, "Fluorescence enhancements of fiber-optic biosensor with metallic nanoparticles," Opt. Express **17**(7), 5867–5878 (2009).
24. A. François, J. Boehm, S. Y. Oh, T. Kok, and T. M. Monro, "Collection mode surface plasmon fibre sensors: a new biosensing platform," Biosens. Bioelectron. **26**(7), 3154–3159 (2011).
25. B. Sciacca, A. François, M. Klingler-Hoffmann, J. Brazzatti, M. Penno, P. Hoffmann, and T. M. Monro, "Radiative-surface plasmon resonance for the detection of apolipoprotein E in medical diagnostics applications," Nanomedicine (Lond.) **9**(4), 550–557 (2013).
26. B. Sciacca, A. François, P. Hoffmann, and T. M. Monro, "Multiplexing of radiative-surface plasmon resonance for the detection of gastric cancer biomarkers in a single optical fiber," Sens. Actuators B Chem. **183**, 454–458 (2013).
27. J. Boehm, A. François, H. Ebendorff-Heidepriem, and T. Monro, "Chemical deposition of silver for the fabrication of surface plasmon microstructured optical fibre sensors," Plasmonics **6**(1), 133–136 (2011).
28. R. S. Sennett and G. D. Scott, "The structure of evaporated metal films and their optical properties," J. Opt. Soc. Am. **40**(4), 203–211 (1950).
29. E. Palik, *Handbook of Optical Constants of Solids* (Elsevier 1998).
30. G. Decher, "Fuzzy nanoassemblies: toward layered polymeric multicomposites," Science **277**(5330), 1232–1237 (1997).
31. F. Caruso, K. Niikura, D. N. Furlong, and Y. Okahata, "Ultrathin multilayer polyelectrolyte films on gold: construction and thickness determination," Langmuir **13**(13), 3422–3426 (1997).
32. B. D. Gupta and R. K. Verma, "Surface plasmon resonance-based fiber optic sensors: Principle, probe designs, and some applications," J. Sens. **2009**, 1–12 (2009).
33. A. K. Sharma and B. Gupta, "Theoretical model of a fiber optic remote sensor based on surface plasmon resonance for temperature detection," Opt. Fib. Tech. **12**(1), 87–100 (2006).
34. J. E. Wong, F. Rehfeldt, P. Hanni, M. Tanaka, and R. Klitzing, "Swelling behavior of polyelectrolyte multilayers in saturated water vapor," Macromolecules **37**(19), 7285–7289 (2004).
35. A. D. Rakić, A. B. Djurišić, J. M. Elazar, and M. L. Majewski, "Optical properties of metallic films for vertical-cavity optoelectronic devices," Appl. Opt. **37**(22), 5271–5283 (1998).
36. P. Pavaskar, J. Theiss, and S. B. Cronin, "Plasmonic hot spots: nanogap enhancement vs. focusing effects from surrounding nanoparticles," Opt. Express **20**(13), 14656–14662 (2012).
37. H. Cang, A. Labno, C. Lu, X. Yin, M. Liu, C. Gladden, Y. Liu, and X. Zhang, "Probing the electromagnetic field of a 15-nanometre hotspot by single molecule imaging," Nature **469**(7330), 385–388 (2011).
38. B. J. Messinger, K. U. von Raben, R. K. Chang, and P. W. Barber, "Local fields at the surface of noble-metal microspheres," Phys. Rev. B **24**(2), 649–657 (1981).

1. Introduction

Fluorescence analysis has been a dominant technique in biochemical sensing and medical diagnostics studies due its high sensitivity, simplicity, and availability of fluorophores. However, there is a drive to further improve detection limits as fluorophores detectability is eventually limited by their quantum yield, photostability and autofluorescence [1]. In the last decade Metal Enhanced Fluorescence (MEF) has attracted significant attention as an emerging tool for fluorescence spectroscopy, alleviating the aforementioned issues by

#261697 Received 28 Mar 2016; revised 29 Apr 2016; accepted 2 May 2016; published 27 May 2016
© 2016 OSA

enhancing fluorescence emission and decreasing fluorescence lifetime thereby improving fluorophore detectability [2].

Noble metal particles and planar surfaces exhibit diverse and complex optical properties associated with Surface Plasmons (SPs), which can be described as light-induced collective electron oscillations on metallic thin film surfaces or nanoparticles. The electromagnetic field associated with SPs is at maximum at the interface and decays exponentially in the direction perpendicular to that interface. MEF is attributed to the stronger interactions occurring between fluorophores' excited states and the induced SPs in metal particles or films due to the increased electromagnetic field in the proximity of the metals [3–5]. Therefore, the effect of metal surfaces and particles on fluorophores depends on both the distance separating the fluorophore molecules from the metal and the overlap between the SPs resonance wavelength and the fluorophore absorption [6,7]. Earlier studies have shown that metals can be used to modify the fluorescence intensity (quenching or enhancement), decrease or increase the radiative decay rates, and improve the photostability [2–9].

Nanostructured metal films and nanoparticles have been extensively studied for MEF [10–16]. The enhancement factors depend on the type, shape, size, and separation between nanoparticles, and enhancement values from 10 to 10^6 have been reported for some configurations. However, it remains experimentally challenging to produce large-scale nanostructured surfaces with consistent surface coverage density to achieve reproducible MEF properties [17]. Continuous smooth metal films, while simpler to produce, exhibit dramatically lower enhancement factors, typically on the order of 2 [18]. For this reason, there has been significant interest in studying rough metal surfaces with the intention to bridge the performance gap between metal nanostructures and continuous films, as described below.

The SPs on a rough surface undergo elastic scattering due to the spatial fluctuation in the dielectric function of the metal-dielectric interface. This results in localization of SPs and increased electromagnetic field amplitude near the rough surface in comparison to the field supported by a smooth film [19]. MEF suitable films reported previously have been achieved by annealing of thermally evaporated silver films to produce cracks [12], by using a slow thermal evaporation rate during silver deposition [20], or fabricating very thin particulate metal films [21]. The majority of the MEF experiments are performed on planar substrates with the fluorophore being excited through the SPs. Measurement of such substrates are traditionally performed using attenuated total reflection (ATR) in a prism, also known as Kretschmann configuration, to match the propagation constant of the excitation light with that of the SPs at a given angle of incidence [13,23]. Although this approach offers high resolution and simple experimental realization, it is somewhat cumbersome, expensive, and is not applicable for remote sensing. To overcome those issues, waveguides and fiber based MEF configurations that offer advantages of easy coupling, miniaturization, and potential for multiplexing have been proposed [18,24].

In this paper, we investigate the influence of surface roughness of continuous silver films on fluorescence enhancement in planar glass substrates. Silver films of thicknesses around 50 nm with varying roughness from 2 nm to 8 nm were prepared by two methods, thermal vapor deposition and chemical electroless plating. As the plasmonic enhancement of fluorescence depends on the separation between the fluorophore and the metal [2–4,7,11], the optimal distance that provides maximum enhancement at a given roughness was achieved through layer-by-layer deposition of a polyelectrolyte multilayer spacer. Fluorescence intensity was found to increase for coatings with higher surface roughness. Based on the determined optimal surface roughness and the spacing between the fluorophore and the metal film, we demonstrate the fabrication of MEF based sensor on a side of a multimode optical fiber. It was previously reported that a fiber configuration with a rough silver coating could be used for fabrication of radiative Surface Plasmon Resonance (SPR) sensors that exploit scattering of the plasmonic wave [25–27]. Building on this SPR fiber sensing platform, we study the

#261697 Received 28 Mar 2016; revised 29 Apr 2016; accepted 2 May 2016; published 27 May 2016
© 2016 OSA

dependence of fluorescence intensity on the thickness of the silver films and discuss advantages and limitations of the MEF fiber sensor.

2. Experimental section

2.1. Silver film fabrication

To investigate the dependence of fluorescence intensity on the roughness of the silver coating and determine the optimal distance between the fluorophore and the metal film, we first performed experimental studies in planar geometry. Silver thin films of 50 nm thicknesses, previously determined to be optimal for SPs excitation [28], were deposited on standard microscope glass slides using two methods, electroless plating [28], and thermal evaporation [29]. Different deposition conditions, in particular deposition rates, were used for the thermal evaporation to vary the surface roughness of the deposited silver films [29]. Procedure reported by Boehm *et al.* [28], was followed for fabrication of silver coatings using the electroless plating method. All substrates were thoroughly cleaned by sonication in acetone for 30 min, then rinsed with ethanol and deionized water prior silver thin film deposition. Thermal vacuum evaporation was performed in thermal evaporator (JEOL JEE 420) with a tungsten crucible at a pressure of 2×10^{-4} Pa. The current was varied from 28 to 40 Amps, resulting in deposition rate ranging from 0.32 to 3.52 nm/s to produce coating with a range of surface roughness.

Silver electroless plating was also used to fabricate silver films on a side of a multimode lead silicate optical fiber (F2, refractive index of 1.62 at 633 nm) with a core diameter of 160 μm. To produce MEF fiber sensors, a 1-cm long section of the fiber was stripped off the polymer cladding to allow for silver film deposition onto the fiber core. Fiber samples with different silver film thicknesses of 71, 56, 35 and 22 nm have been produced to analyze the effect of coating thickness on fluorescence enhancement.

2.2. Silver film characterization

The thickness of the deposited silver films on the planar substrates was measured using transmission measurements with a helium neon (HeNe) laser (λ = 633 nm). Calculation of the coating thickness (t) has been carried out using the Beer-Lambert law: $I = I_0 e^{-t\alpha}$, where I_0 and I are the incident and transmitted power respectively, and α = 756310 cm^{-1} is the absorption coefficient of silver at 633 nm [30]. Due to the surface roughness of the metal films, which introduces scattering losses, as well as the reflection from the surfaces, the amount of light detected in transmission is reduced, which might result in overestimates of the film thickness. To evaluate the scale of these effects, the metal film thickness for some samples was also measured using atomic force microscopy (AFM) (NT-MDT) at the edge of the coatings. AFM estimated thicknesses were found to lie within the uncertainty ranges of the values calculated using transmission measurements, which indicates that the transmission method could be used as a simple and fast alternative for measuring the metal film thickness. Topography of the fabricated metal coatings and film roughness were also studied using AFM. Surface roughness values presented in the manuscript are root mean square roughness defined as the average of height deviations measured from the mean line and taken within the evaluation length, and was estimated using scanning probe microscopy data analysis software (Nova NT-MDT and Gwyddion). The results for the metal film thickness, surface roughness and deposition rate for coatings prepared using the two methods are summarized in Table 1.

#261697 Received 28 Mar 2016; revised 29 Apr 2016; accepted 2 May 2016; published 27 May 2016
© 2016 OSA

Table 1. Properties of the different silver films

Deposition method	Thickness (nm)	Deposition rate (nm/s)	Roughness (nm)
Experiment with planar substrates (Kretschmann setup)			
Thermal evaporation, 28 Amps	46.5 ± 1.5	0.32	4.1 ± 0.4
Thermal evaporation, 30 Amps	51.4 ± 3.4	0.73	2.8 ± 0.7
Thermal evaporation, 36 Amps	50.7 ± 0.5	2.29	2.5 ± 0.1
Thermal evaporation, 40 Amps	49.8 ± 0.1	3.52	1.7 ± 0.2
Chemical electroless plating	53.0 ± 5.0	0.12	7.9 ± 0.6
Samples used for fibre coating characterization			
Chemical electroless plating	22.4 ± 2.2	0.08	8.8 ± 0.6
Chemical electroless plating	34.9 ± 2.9	0.15	9.1 ± 0.4
Chemical electroless plating	56.3 ± 3.4	0.13	11.0 ± 0.7
Chemical electroless plating	71.1 ± 2.5	0.15	9.4 ± 0.1

2.3. Surface functionalization

The distance between the silver film and the fluorophore was finely tuned through layer-by-layer adsorption of positively and negatively charged polyelectrolyte (PE) layers, poly(allylamine hydrochloride) (PAH) and (poly(sodium 4-styrenesulfonate) (PSS) respectively [31]. PE solutions of 2 mg/mL were prepared in 1M of aqueous sodium chloride. The samples were immersed in each PE solution for 15 min and rinsed in deionized water between each step. Planar glass substrates with odd number of PE layers ranging from 1 to 21 and starting from PAH layer were prepared to vary the gap between the metal film and the fluorophore with each PE layer adding 1.7 ± 0.1 nm separation, as described in Section 3.1. Fiber samples were prepared using the same protocol. It has previously been reported that PE layer formation follows uniform growth after deposition of four layers, and even a small amount of PAH is sufficient to facilitate subsequent adsorption of PSS [32]. Therefore, it can be assumed that thickness and density of polyelectrolyte for multiple layers is independent on the substrate. A carboxyl functionalized organic fluorescent dye (4-(2-Carboxyphenyl)-7-diethylamino-2-(7-diethylamino-2-oxochroman-3-yl)-chromylium perchlorate) (λ_{ex}~650 nm, λ_{em}~690 nm) was covalently attached to the last PAH layer using amine coupling reagents, 1-Ethyl-3-(3-dimethylaminopropyl)carbodiimide (EDC) and N-Hydroxysuccinimide (NHS). A concentration of 10.9 mg of the organic dye in 10 mL of water and 5 mL of methanol was used.

2.4. Experimental setup

A Kretschmann prism was set up as depicted in Fig. 1(a) with a BK7 prism mounted on a computer controlled rotational stage and a linearly polarized 633 nm HeNe laser as an excitation source. This configuration was used for characterizing surface plasmon fluorescence enhancement on the planar substrates. The minimum in the reflected spectrum as a function of the incidence angle of the excitation light that corresponds to the surface plasmon resonance was monitored with a power meter on the opposite side of the prism. The fluorescent signal was collected from the fluorophore coated glass slide surface with a × 10 microscope objective. After removing the excitation light with a 650 nm long pass filter, the fluorescent signal was analysed with a compact spectrometer (Ocean Optics QE 65000).

Silver coated optical fiber sensors were enclosed in a glass tube to allow liquid to flow around the sensing region as shown in the Fig. 1(b). A short section of the fiber polymer cladding near the silver coating was removed to create an uncoated region for comparison. Having both silver coated and uncoated parts of the sensor inside one flow cell ensured both regions undergo the same surface functionalization procedure. The sensitivity of surface

#261697 Received 28 Mar 2016; revised 29 Apr 2016; accepted 2 May 2016; published 27 May 2016
© 2016 OSA

plasmon resonance (SPR) response has been characterized by flowing aqueous solutions of glycerol with known refractive indices through the flow cell. A white light LED (Thorlabs Inc., MCWHL2) was used for SPR analysis. A presence of significant surface roughness of the metal coating allowed for analysis of light scattered by surface plasmons directly above the sensor surface [25–27] instead of transmission measurements as it is done in conventional SPR fibre sensors [33]. PE layer deposition and dye attachment on the fiber samples were performed inside the flow cell and the SPR response was recorded at each step of the functionalization process. The fluorescence measurement setup shown in Fig. 1(b) is similar to the described SPR configuration with a monochromatic HeNe laser source used for fluorophore and plasmon excitation. The fluorescent signal was collected above the sensing region with a collection apparatus consisting of microscope objective, converging lens, and an optical fibre, and analysed with the Ocean Optics compact spectrometer. A long pass filter (650 nm) was used to block laser background radiation.

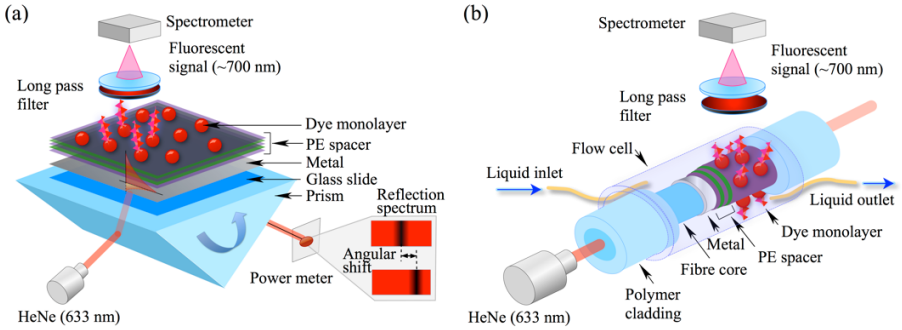


Fig. 1. Schematic of the optical setup for surface plasmon fluorescence enhancement analysis on (a) planar substrates; and (b) optical fibers.

3. Results and discussion

3.1 Surface roughness dependent fluorescence enhancement in planar substrates

A typical SPR response on planar substrates is presented in Fig. 2(a). Upon adsorption of the PE multilayers, the minimum in the reflected light that corresponds to the plasmon resonance is shifted towards higher incidence angles. Figure 2(b) shows the SPR signal and the corresponding fluorescence signal with the maximum fluorescence intensity occurring at the resonance, which is seen as a dip in the reflected light.

The fluorescence enhancement factor (*EF*) is defined as the ratio of maxima of fluorescence intensities of silver (Ag) coated substrate and an uncoated substrate: $EF = I_{coated}/I_{uncoated}$. For all samples coated with silver using thermal evaporation method the maximum fluorescence enhancement occurred after deposition of 7 PE layers. This corresponds to a distance of approximately 12.0 ± 0.8 nm, as shown in the Fig. 3(a) which illustrates the dependence of fluorescence enhancement factor in planar substrates with silver films of different surface roughness as a function of the number of deposited PE layers. The thickness of the PE coating was determined from the SPR response using multilayer model described elsewhere [34], and assuming the refractive indices of glass and PE coating being 1.54 and 1.47 respectively [35], and a complex dielectric function of silver estimated using Lorentz-Drude model [36]. Even though the dielectric function of thin films could differ from that of bulk metal, the Lorentz-Drude model can be used to obtain a rough estimate of the PE layers thickness, which is broadly consistent with previously reported thickness of individual PE layers of ≈1.5 nm [31,32,35]. For the slides with silver coating deposited by chemical method the SPR angular shift was larger than for samples with thermally evaporated coatings.

#261697 Received 28 Mar 2016; revised 29 Apr 2016; accepted 2 May 2016; published 27 May 2016
© 2016 OSA

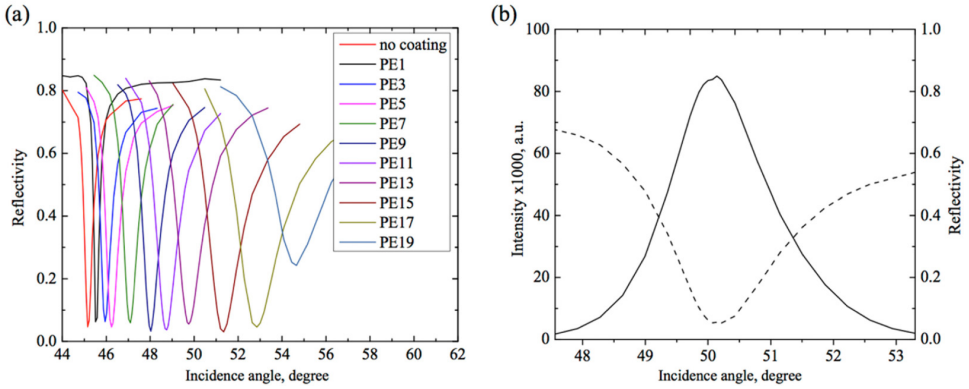


Fig. 2. (a) A typical increase in the angular position of the dip in the reflected spectra corresponding to Surface Plasmon Resonance (SPR) as a function of increasing number of polyelectrolyte layers on a planar substrate; and (b) Fluorescence emission of the dye (solid line) and SPR signal (reflectivity) (dashed line) of a planar substrate. A sample with thermally evaporated coating was used as an example.

This could be attributed to the difference in the dielectric function of silver deposited by chemical technique versus thermally evaporated silver, or could be related to the stronger interaction of the SPs with the environment due to the surface roughness. Nevertheless, the maximum fluorescence enhancement factor for chemically coated glass slides was observed after deposition of 7 PE layers. Figure 3(b) shows the maximum fluorescence enhancement factor as a function of silver coatings' roughness. It demonstrates that fluorescence enhancement increases as the surface roughness of the Ag film increases, ranging from the factor of 3 for low surface roughness of 1.7 nm up to the factor of 47 for the roughness of 8 nm.

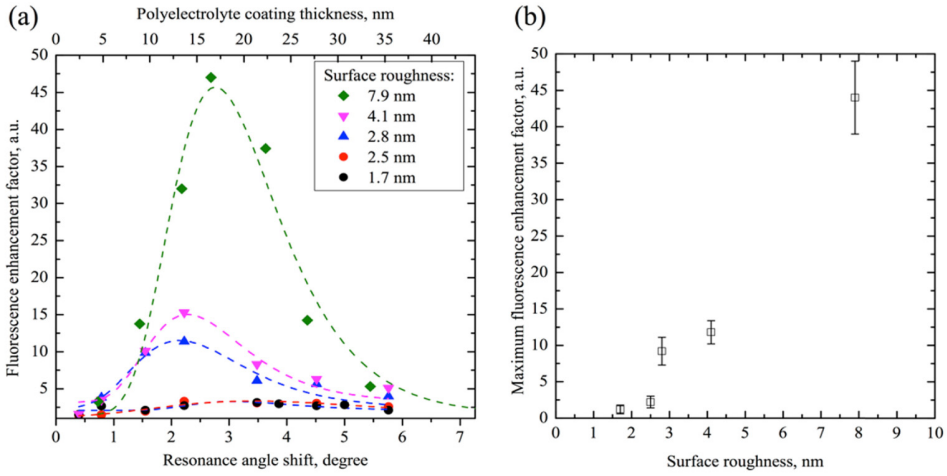


Fig. 3. (a) Dependence of fluorescence enhancement factor of planar substrates coated with silver coating of different surface roughness as a function of PE spacer thickness; and (b) Maximum fluorescence enhancement factor as a function of silver coatings roughness.

The fluorescence enhancement on a rough surface is thought to occur due to the presence of hot spots in the near field due to the larger local density of optical states. When the random surface texture consists of a collection of metal nanoparticles located in a nanoscale distance from each other, SPP field overlaps creating strongly confined electromagnetic modes. This phenomenon is associated with surface enhancement effects such as surface enhanced Raman

#261697 Received 28 Mar 2016; revised 29 Apr 2016; accepted 2 May 2016; published 27 May 2016
© 2016 OSA

scattering and is believed to be responsible for the enhancement of fluorophore excitation [37,38].

3.2 Fluorescence enhancement in an optical fiber

Fluorescence enhancement was also investigated on an optical fiber coated with silver film fabricated using the electroless plating as the rough coating produced with this method showed higher enhancement factor. Typical SPR scattered spectra are depicted in Fig. 4 showing a spectral shift occurring after each step of surface functionalization process. The initial observed fluorescence enhancement factor for the fiber-based configuration was found to be 2.4, which is significantly lower than the factor of 47 achieved on the planar substrates.

This difference can be explained by considering that there is a spectral mismatch between SPR excitation wavelength after the completion of surface functionalization process (around 580 nm, black vertical line in Fig. 4) and the excitation wavelength of the fluorophore (633 nm, red vertical line in Fig. 4). While Kretschmann based systems can easily compensate for this discrepancy by changing the incidence angle ensuring that the propagation constants of both the incident light and the plasmons are always matched, this is not possible for an optical fiber based approach where the range of incidence angles are limited by numerical aperture of the fibre. This suggests that in a fiber based MEF configuration a careful selection of a fluorescent dye is more critical due to the necessity of maximizing the overlap between excitation spectrum of the dye and SPR associated signal. While in practice this introduces a restriction, the thickness of the silver film can be altered to further increase the fluorescence enhancement as shown by Zhang *et al.* [20].

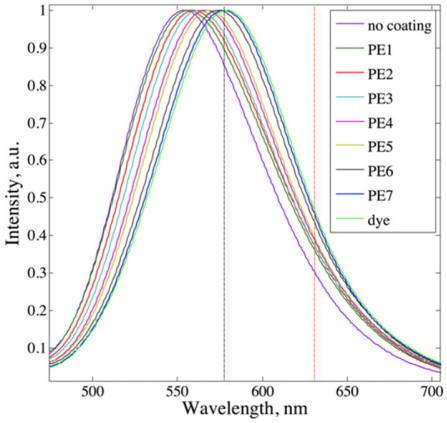


Fig. 4. Normalized scattered SPR signal at each step of the surface functionalization process (PE spacer deposition and dye attachment) on a side of an optical fiber coated with 56 nm silver film. Vertical lines mark the SPR resonant wavelength after dye attachment at around 580 nm (black) and the excitation wavelength of the laser source at 633 nm (red).

To explore this further, we investigated the dependence of fluorescence enhancement on the thickness of the silver coatings fabricated on a side of an optical fiber by chemical deposition, and performed analysis of the topography of the deposited films. We examined the fluorescence enhancement factor for silver films of 71, 56, 35, and 22 nm thicknesses. All films were fabricated using the same chemical electroless plating procedure with varying reaction time keeping the deposition rate constant. This allowed for fabrication of films of different thicknesses without significantly changing the surface structure, in particular, surface roughness. The thickness of the coatings on the fibre samples was estimated by AFM on planar glass substrates that were prepared together with the fibre samples at the same deposition rate. It has been found that fluorescence is quenched on fibres coated with thick films (71 nm) and is enhanced on thinner films (≤ 56 nm) as shown in the Fig. 5(a).

#261697 Received 28 Mar 2016; revised 29 Apr 2016; accepted 2 May 2016; published 27 May 2016
© 2016 OSA

Significantly larger enhancement factors were obtained on thin films reaching up to 15-fold for the thinnest film studied (Fig. 5(b)), while the standard 56 nm-thick silver film exhibited only a 2-fold increase of the fluorescence intensity.

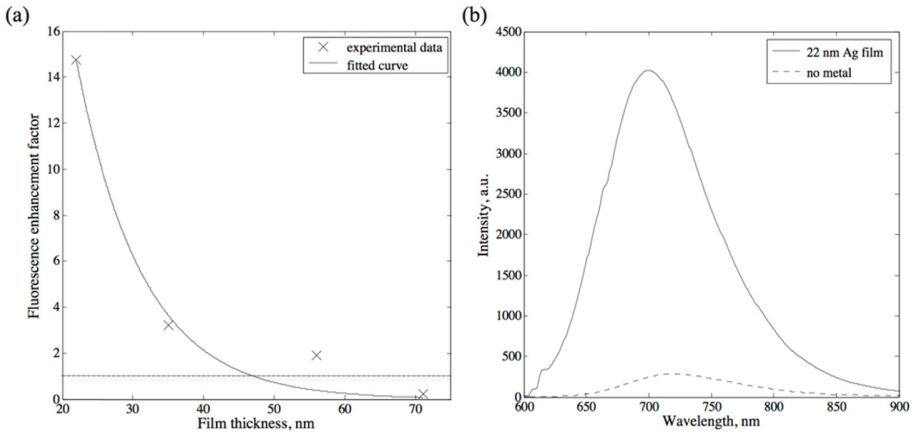


Fig. 5. (a) Fluorescence enhancement factor for varying silver film thickness in fiber samples. Fluorescence enhancement factor above one indicates fluorescence intensity enhancement, below one - reduction of fluorescence intensity; and (b) Fluorescent signal for a fiber coated with 22 nm silver film (solid line), and without metal (dashed line).

The extinction properties of metals depend on both absorption and scattering components [4]. According to Mie theory, the ratio of scattering to total extinction of small metal particles is small, which means that a large fraction of incident light is absorbed, leading to inefficient excitation of fluorophores nearby. On the other hand, in larger metal nanostructures the fraction of light scattered by the particles is increased, which is expected to favor fluorescence enhancement [38]. Surface scattering depends not only on amplitude roughness parameters, such as the root mean square roughness, but also on spatial roughness parameters given by autocorrelation function. The analysis of AFM images was performed to understand the difference in terms of surface features between the 22 and 71 nm silver films. Figures 6(a) and 6(b) show the distribution of equivalent disk radius r_{eq} (radius of a disk with the same projected area as the grain) of thin (22 nm) and thick (71 nm) Ag films on 5 × 5 μm sections with AFM images and statistics of the grain composition presented on the insets. Root mean roughness and autocorrelation lengths for both films were found to be the same within their uncertainty estimates. The analysis suggests that the mean size of the surface features does not change significantly with increasing thickness of the metal films with estimated values of 53.6 ± 2.7 nm to 59.6 ± 4.4 nm for 22 and 71 nm films respectively, confirming that the surface roughness remains unchanged with the range of the thicknesses studied, as long as the deposition rate is kept constant. Composition of particles of different size on the surface is similar for thin and thick coatings with around 35% of the particle populations consisting of small features, around 10 nm radius (large peaks on Figs. 6(a) and 6(b)). However, for the 22 nm film, the relative roughness is around half of the film thickness with the gaps between particles reaching down to a few nanometers depth. This film could be considered as a layer of nanoparticles of various sizes. On the other hand, the thick silver film (71 nm) with the relative surface roughness of around tenth of the film thickness could be visualized as a continuous film. For the thick films the intrinsic absorption in metal is stronger than that in the thinner films which results in less efficient excitation of the fluorophores, and thereby, smaller fluorescence emission intensity.

#261697 Received 28 Mar 2016; revised 29 Apr 2016; accepted 2 May 2016; published 27 May 2016
© 2016 OSA

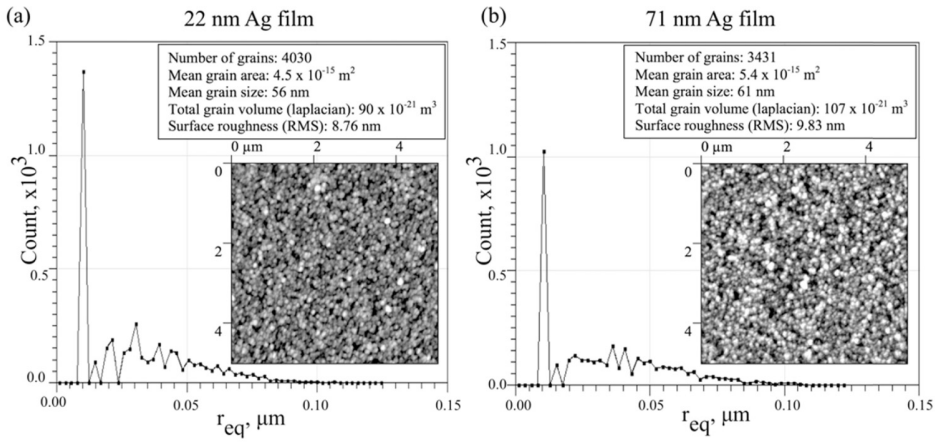


Fig. 6. Particle distribution analysis of thin and thick silver films for 5 × 5 µm sections. Equivalent disk radius (r_{eq}) of the surface features on (a) 22 nm and (b) 71 nm silver films. Statistics of the grain analysis of the coatings as well as AFM images of surface topography are shown on the insets.

In addition to the analysis of the silver film thickness and surface topography, and their influence on enhancement of the fluorescence emission, we performed a simple study of how the fluorescence enhancement depends on the position of the sensing region from where the fluorescent light is collected. Figure 7(a) shows an example of fluorescent signal taken from three different locations on a fiber sensor, a few mm lengths each. As shown schematically in Fig. 7(b), the first fluorescence spectra is collected from a location on the fiber without metal coating, the second from a location at the beginning of the metal coated region, and the third was taken from a location on the metal coated region further away from the fiber end where the light is coupled.

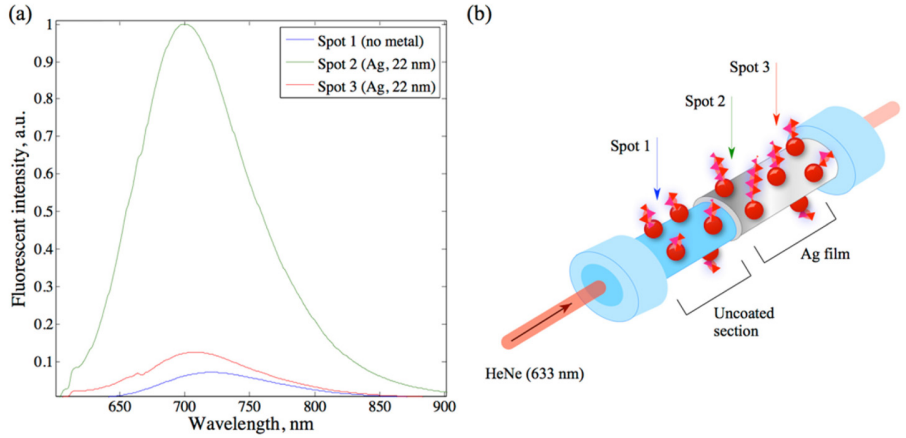


Fig. 7. (a) Comparison of fluorescence intensities from different locations on a fiber coated with 22 nm Ag film and an uncoated section; and (b) Locations of the spots on the fiber sensor.

The results indicate that the fluorescence enhancement strongly depends on the position on the metal-coated region, with higher fluorescence intensities observed at the start of the sensing region where more of the excitation light interacts with the metal. The incident light dissipates quickly through coupling to plasmonic modes and strong scattering enhanced by the roughness of the metal surface. This illustrates that in a fiber-based configuration where

#261697 Received 28 Mar 2016; revised 29 Apr 2016; accepted 2 May 2016; published 27 May 2016
© 2016 OSA

the interaction of propagating light and SPs occurs along the length of the sensing region, intensity of the fluorescent signal is strongly position dependent, and therefore, the detection ideally needs to be integrated over a reasonably large area.

4. Conclusion

In this study, we have investigated the influence of the surface roughness of silver films on the enhancement of emission of fluorophore molecules located at a nanoscale distance from the metal surface. An optimal separation between the fluorophore and the silver film for the maximum enhancement was adjusted by tuning the thickness of a multilayer polyelectrolyte spacer. The maximum fluorescence enhancement factor of up to 47 was achieved on planar glass substrates coated with silver film with significant surface roughness of around 8 nm that was fabricated by a simple electroless plating technique. While this enhancement factor is relatively moderate in comparison to those achieved with nanostructured metal films, it demonstrates that the simple chemical method could be readily used for fabrication of low cost alternative plasmonic coatings suitable for enhancing fluorescence intensity by significant amount when compared with smooth metal films.

We have applied the same silver coating and surface functionalization processes to produce MEF sensors on a side of an optical fiber in order to investigate the prospect of establishing a MEF fibre sensing platform using a straightforward manufacturing technique. The constraints imposed by the fiber geometry significantly reduce the enhancement factor. Indeed, since this configuration removes the ability to tune the incidence angles of the propagating rays onto the metallic coating in optical fibers, the fluorophore has to be carefully chosen to achieve maximum overlap between SPR and fluorophore absorption spectra. Considering this, using fluorescent labels with broad absorption spectrum, such as quantum dots, might be a more suitable option in fibre based MEF sensors. The thickness of the deposited thin film can be reduced to alleviate some of these limitations enabling up to 13-fold increase of the fluorescence emission for a 22 nm thick silver film when compared to an enhancement factor of 2 for a 56 nm film. Finally, we have shown that the length of the metallic coating in optical fibres and the position from where the fluorescence signal is collected, strongly influence the results. It is worth mentioning that this enhancement factor of 15-fold was obtained using a relatively simple fabrication technique and is 7-fold higher than that previously achieved in optical fibre MEF sensors [18]. The MEF fiber sensor could find potential applications in biotechnology, clinical assays and analytical chemistry. The fabrication and analysis procedures are easily adaptable and inexpensive making the fiber MEF sensor a competitive candidate for compact fluorescence spectroscopy.

Acknowledgments

The authors acknowledge the support of Tanya M. Monro's ARC Georgina Sweet Laureate Fellowship and the support of the ARC Centre of Excellence for Nanoscale BioPhotonics. This work was performed in part at the OptoFab node of the Australian National Fabrication Facility utilizing Commonwealth and SA State Government funding.

#261697 Received 28 Mar 2016; revised 29 Apr 2016; accepted 2 May 2016; published 27 May 2016
© 2016 OSA

sensors

MDPI

Review

Plasmonic Fiber Optic Refractometric Sensors: From Conventional Architectures to Recent Design Trends

Elizaveta Klantsataya [1,*], Peipei Jia [1,2], Heike Ebendorff-Heidepriem [1,2], Tanya M. Monro [1,3] and Alexandre François [1,3]

1 Institute for Photonics and Advanced Sensing, The University of Adelaide, Adelaide, SA 5005, Australia; peipei.jia@adelaide.edu.au (P.J.); heike.ebendorff@adelaide.edu.au (H.E.-H.); tanya.monro@unisa.edu.au (T.M.M.); alexandre.francois@unisa.edu.au (A.F.)

2 ARC Centre of Excellence for Nanoscale BioPhotonics (CNBP), The University of Adelaide, Adelaide, SA 5005, Australia

3 The University of South Australia, Adelaide, SA 5001, Australia

* Correspondence: elizaveta.klantsataya@adelaide.edu.au; Tel.: +61-8-8313-0589

Academic Editor: Aydogan Ozcan
Received: 27 October 2016; Accepted: 20 December 2016; Published: 23 December 2016

Abstract: Surface Plasmon Resonance (SPR) fiber sensor research has grown since the first demonstration over 20 year ago into a rich and diverse field with a wide range of optical fiber architectures, plasmonic coatings, and excitation and interrogation methods. Yet, the large diversity of SPR fiber sensor designs has made it difficult to understand the advantages of each approach. Here, we review SPR fiber sensor architectures, covering the latest developments from optical fiber geometries to plasmonic coatings. By developing a systematic approach to fiber-based SPR designs, we identify and discuss future research opportunities based on a performance comparison of the different approaches for sensing applications.

Keywords: fiber sensors; Surface Plasmon Resonance (SPR); plasmonics; optical fiber; Localized Surface Plasmon Resonance (LSPR)

1. Introduction

Plasmonics is a well-established research field which has been extensively studied over the last few decades. Since the pioneering work by Kretschmann et al. [1] and Otto [2] in the late sixties, who demonstrated optical excitation of Surface Plasmons (SPs) by means of attenuated total reflection using a prism, a wide range of sensing architectures has emerged [3]. SPs are collective oscillations of the free electron gas in metals that exist at the interface between two materials with dielectric constants of opposite sign, such as a metal and a dielectric [4]. When the propagation constant of the excitation photons matches that of the electron oscillations, Surface Plasmon Resonance (SPR) occurs, where part of the energy of the incident light is transferred to the SPs. The resonant condition depends on the dielectric constants of the metal and dielectric that support the interface, but also on the refractive index of the medium within the SP evanescent field. The later has been first exploited by Pockrand et al. [5] and Liedberg et al. [6], who both used the change of a resonant condition for monitoring binding events onto a silver thin film, thereby creating the first optical label-free biosensing platform.

Commercial SPR systems are now a reality, with several manufacturers still exploiting the Kretschmann prism configuration in their instruments. However, substituting the prism excitation scheme with optical fibers has rapidly emerged since the early 90s, taking advantage of the cost effectiveness and miniaturization potential associated with optical fibers [7,8]. This early work on SPR fiber sensors paved the way for further development of the fiber geometries, interrogation methods and plasmonic coatings, allowing for improved sensing performance and alternative sensing modalities.

The emergence of fiber-based SPR sensors created unique research and commercial opportunities, such as in vivo medical diagnostic [9], or the development of point-of-care devices using smartphone technologies [10,11].

However, due to the large diversity of SPR fiber sensor designs, it is difficult to understand the pros and cons of each SPR fiber architecture. Although, several reviews on fiber-based SPR sensors have previously been published [12–15], none presented a complete comparison of the different designs encompassing optical fiber and metallic coatings, SPR excitation and interrogation methods, and sensing applications. Therefore, the objective of this review article is to provide a comprehensive comparison of the performance of the state of the art SPR fiber sensors based on the different technological approaches. The following sections describe the different SPR interrogation methods and the resulting operating principles. Various SPR fiber designs from both, the optical fiber architecture and the metallic coating perspectives, are also discussed, along with examples of applications. Finally, a comparison between the different architectures is provided based on their respective performance, followed by a discussion on future research prospects in this field.

2. Operating Principles of Plasmonic Fiber Sensors

SPs can be viewed as an electromagnetic wave that propagates along the interface between metal and dielectric. Electromagnetic field associated with SPs at the resonance reaches maximum at the interface and exponentially decays into both metal and dielectric. The penetration depth and propagation length of the plasmons are determined by the dielectric constant of metal and its thickness, as well as the refractive index of the adjacent dielectric. This enhanced electromagnetic field in the dielectric medium and strong dependency of the resonance condition on the optical properties of the supporting interface make SPR an indispensable tool for refractive index sensing.

The fundamental principle of SP excitation in optical fibers is similar to the prism-based techniques, known as Kretschmann [1] and Otto [2] configurations. Propagating SPs cannot be excited by light incident on the metal film from air, therefore, a dielectric with higher refractive index (such as a prism or a fiber core) is used to enhance the propagation constant of the incident light [4]. For excitation of SPs to occur, the propagation constant of the incident light must match that of the SPs (k_{SP}):

$$k_{SP} = k_0 \left(\frac{\varepsilon_m \varepsilon_s}{\varepsilon_m + \varepsilon_s} \right)^{1/2} \quad (1)$$

where $\varepsilon_m = \mathrm{Re}(\varepsilon_m) + i\mathit{Im}(\varepsilon_m)$ and ε_m and ε_s are the dielectric constants of the metal and dielectric, respectively; and $k_0 = \omega/c$ is the free-space wave number, where ω is the angular frequency of the incident light, and c is the speed of light in vacuum. Equation (1) describes a guided mode (SP wave) only if $\mathrm{Re}(\varepsilon_m) < -\mathrm{Re}(\varepsilon_s)$. This condition is, in general, fulfilled for a metal and dielectric interface [4]. The component of the wave propagation constant parallel to the metal-dielectric interface is given by:

$$k = k_0 \sqrt{\varepsilon_p} \sin(\theta) \quad (2)$$

where ε_p is the dielectric constant of the prism. To satisfy the coupling condition $k = k_{sp}$, the incidence angle (θ) can be adjusted. However, for an optical fiber, the propagation constant of the guides modes is determined by the fiber properties (i.e., core diameter, core and cladding refractive indices), and cannot be changed dynamically. While the fiber-based approach imposes some inherent restrictions compared with the prism coupling scheme, a range of SPR excitation methods have been developed for optical fibers, enabled by the diversity of optical fiber architectures, which is discussed in Section 3.1.

2.1. Interrogation Methods

Most of the SPR interrogation methods in optical fibre are based on the detection of loss in the transmitted light at the resonance, associated with coupling of the guided fibre modes to SP modes. This is achieved through a large variety of methods ranging from the spectral interrogation

of transmitted [7,16–20] or back reflected [21–23] signal using a broadband excitation source, to the measurement of intensity near resonance [10,23–26]. Also, analyses of phase changes due to SPR have been reported [27,28].

2.1.1. Spectral Interrogation

Spectral interrogation is by far the most commonly employed technique for SPR fiber sensors [16–20]. This configuration was first proposed by Jorgenson et al. [7], and is depicted in Figure 1. As the guided white light interacts with a metallic coating deposited onto the fiber core, the transmitted light is being depleted at specific wavelengths, corresponding to the optical modes whose propagation constants match that of the SPs. Spectral interrogation can be achieved either in transmission or in back-reflection measurements, where in the later configuration the light propagating inside the fiber reflects back from a mirror deposited on the fiber tip, allowing for dip sensor architectures [21–23]. The advantage of the back reflection technique is that the analyzed light undergoes interaction with the sensing region twice [21]. However, it increases the complexity of the required optical setup when compared with conventional transmission measurements. A choice between transmission or back reflection measurements is typically dictated by the application.

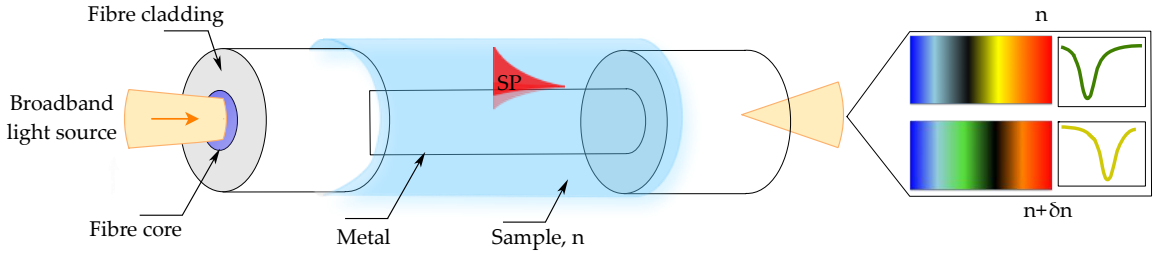


Figure 1. Fiber-based SPR sensor. Change in the refractive index of the sample (δn) causes change in the resonant condition, which is seen as a shift of the resonant wavelength (δλ) (dip in the transmitted spectra).

2.1.2. Intensity Interrogation

A monochromatic light source can be used to excite SPs, providing that the wavelength of excitation is chosen such that the combination of the wavelength and incidence angles satisfies the resonant condition. SPR is observed indirectly through analyzing the intensity of the collected light, either transmitted or back-reflected [10,23–26]. The advantage of this technique is its simplicity and low cost. However, careful selection of the excitation wavelength and SPR resonant wavelength, which is determined by the materials that constitute the sensor, is essential for successful application.

2.1.3. Phase Interrogation

A less common interrogation technique used in SPR fiber sensors is phase interrogation. The method relies on analyzing the phase difference between two light polarizations, p- and s-, at the resonance in the transmitted or back-reflected light [29–31]. This technique offers advantages of lower resolution and higher dynamic range when compared to other methods [31]. However, the requirement for more complex optical instruments and data processing methodologies result in limited applications for this interrogation technique in the context of fiber-based SPR sensors.

2.2. Performance Characteristics of SPR Fiber Sensors

The main characteristics that describe the performance of SPR fiber sensors are the refractive index sensitivity, resolution and detection limit. The refractive index sensitivity (S) is defined as a change in the monitored parameter, such as a resonant wavelength, intensity, or phase difference, with respect to the refractive index change [4]. Higher sensitivity is typically attributed to fibers made of a dielectric with lower refractive index. This fact is mainly due to the material dispersion as described by Homola [32]. Sensitivity analysis of plasmonic probes has shown that the sensitivity is strongly dependent on the optical properties of materials that constitute the sensor, such as the fiber material and metal film, rather than a particular sensor geometry [32,33]. In addition, the spectral sensitivity scales with the resonance wavelength.

While the sensitivity is often perceived as the most important performance parameter, another important characteristic is the sensor's resolution. The resolution (R) is defined as the smallest shift in the monitored parameter, such as a wavelength, detectable by a sensing platform. It depends on the optical setup and parameters of the SPR spectral signature (i.e., Full Width at Half Maximum ($FWHM$) and Signal to Noise Ratio (SNR)) [34,35]. The resolution is also strongly influenced by the properties of the sensor materials (i.e., the metallic coating and fiber glass), interrogation and excitation methods, instrumentation, as well as the system noise [35].

Both, the sensitivity and resolution determine the most crucial performance characteristic—the Detection Limit (DL), which is the smallest change of the refractive index measurable. The detection limit is defined as the ratio between R and S, and, consequently, to improve the sensor's DL, one would have to increase the sensitivity of the sensor, and/or reduce its resolution. The later can be achieved by either minimizing the $FWHM$ of the SPR signature and/or increasing its SNR. However, there is often a trade-off between the sensitivity and spectral linewidth of the SPR response due to the properties of the sensor materials. It is difficult to establish a proper value of the resolution from the information provided in literature. As the resolution is proportional to the $FWHM$, it is more convenient to define a Figure of Merit (FOM), as the ratio between the $FWHM$ and S, for a fair comparison between the different fiber-based SPR architectures.

3. Plasmonic Fiber Sensor Designs

Optical fibers are designed to guide light inside the fiber with as little loss as possible. Therefore, the construction of conventional optical fibers, such as the ones used for telecommunication, prevents guided modes from escaping into the surroundings, typically through the use of fiber claddings. To allow the guided fiber modes to interact with the plasmonic materials, the optical fiber geometry needs to be modified to suit SPR sensing applications. The flow chart in Figure 2 summarizes different fiber-based SPR sensor configurations, encompassing the variety of fiber geometries, plasmonic coatings, excitation and interrogation methods, as well as different applications.

Many fiber sensors are constructed using similar architectural principles as the plasmonic fiber sensors described below. For example, evanescent-field fiber sensors take advantage of the modes that extend beyond the boundary of the optical fiber. Fiber Bragg Grating (FBG) sensors rely on changes in properties of the grating with the change in the measured parameter, such as temperature for example. Fiber dip sensors use specialized coatings that modulate optical or physical properties as a response to a change in the measured parameter. However, plasmonic coatings significantly enhance light-matter interaction due to the strong electromagnetic field near the interface allowing more sensitive probes and enabling surface enhanced spectroscopy.

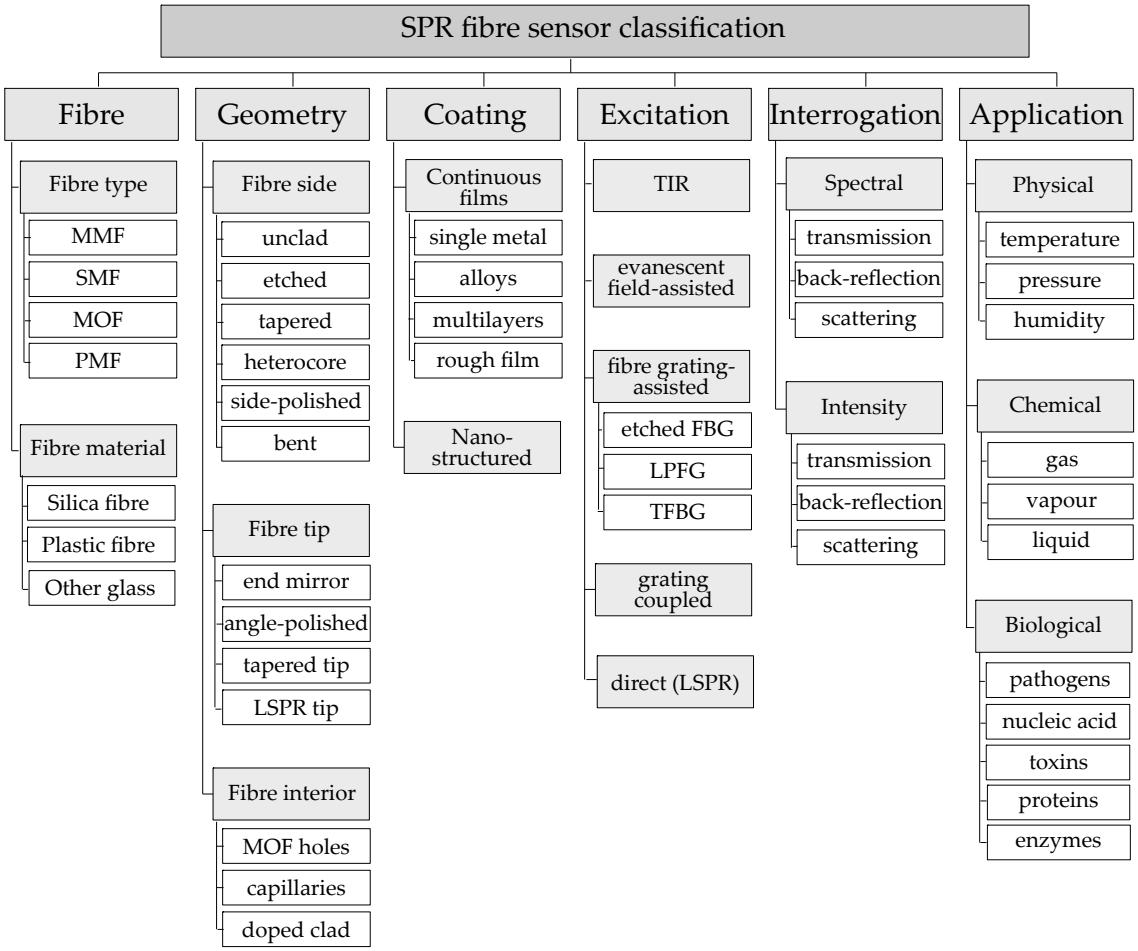


Figure 2. Classification of SPR fiber sensors. MMF: Multi Mode Fiber; SMF: Single Mode Fiber; MOF: Microstructured Optical Fiber; PMF: Polarization Maintaining Fiber; FBG: Fiber Bragg Grating; LPG: Long Period Fiber Gratings; TFBG: Tilted Fiber Bragg Gratings; LSPR: Localized Surface Plasmon Resonance.

3.1. Optical Fiber Architectures

SPR fiber sensors can be categorized according to the type of optical fiber used as: Multimode Fiber (MMF), Single Mode Fiber (SMF), Microstructured Optical Fiber (MOF), Polarization Maintaining Fiber (PMF), or multiple-core fiber SPR sensors. Early fiber optic SPR sensors were mainly constructed from large core MMFs, where a small section of the polymer cladding along the fiber length was removed to expose the core for subsequent metal deposition, as shown in Figure 1. MMFs are among the most common fiber types used in SPR sensing due to their abundance and a relative simplicity of sensor fabrication. However, the large number of modes propagating inside an MMF causes broadening of the SPR spectral linewidth, resulting in decreased sensing performance. One approach to overcome this limitation is the reduction in the number of propagating modes that can satisfy the resonant condition. This could be achieved through the use of fewer mode fibers or SMFs, that typically have step- or graded-refractive index profile, a small core, and a low numerical aperture. SMF-based SPR probes remain the gold standard for the SPR fiber technology due to their low resolution. However, fabricating an SPR sensor from an SMF require additional fiber processing, such as polishing or tapering, as the claddings are typically made of glass. These requirements make the fiber probes extremely fragile, which eventually limits their applicability.

MOFs are becoming increasingly popular as fabrication techniques advance. They offer the convenience of reasonable mechanical strength, together with the ability to achieve desirable guiding

properties through the design of the microstructure. Various MOF-based SPR sensors were explored theoretically [36], but only a handful have been experimentally realized [37]. These include a specialty MOF-based probe with metallized air holes [36], suspended core MOF sensor [38], as well as more recent configurations, such as a D-shaped hollow core MOF [39], a Photonic Crystal Fiber (PCF)-based SPR sensors [40,41], and an exposed core MOF SPR probe [33,37,42]. The major limitation for the use of the MOFs for SPR sensing is the cost of fiber fabrication and the complexity of depositing plasmonic materials on the interior structures of the MOF's core.

3.1.1. Fiber-Side SPR Sensors

Different techniques are used to produce sensing probes on a side of an optical fiber, which depend on the fiber type and fabrication method. These fiber-side SPR configurations range from unclad or etched optical fibers [43,44], to tapered fibers [45], hetero-core structures [19,46], side polished fibers [20,47,48], and bent fiber probes [49]. Figure 3 schematically shows the geometry-modified optical fiber SPR sensors implemented on a side of an optical fiber.

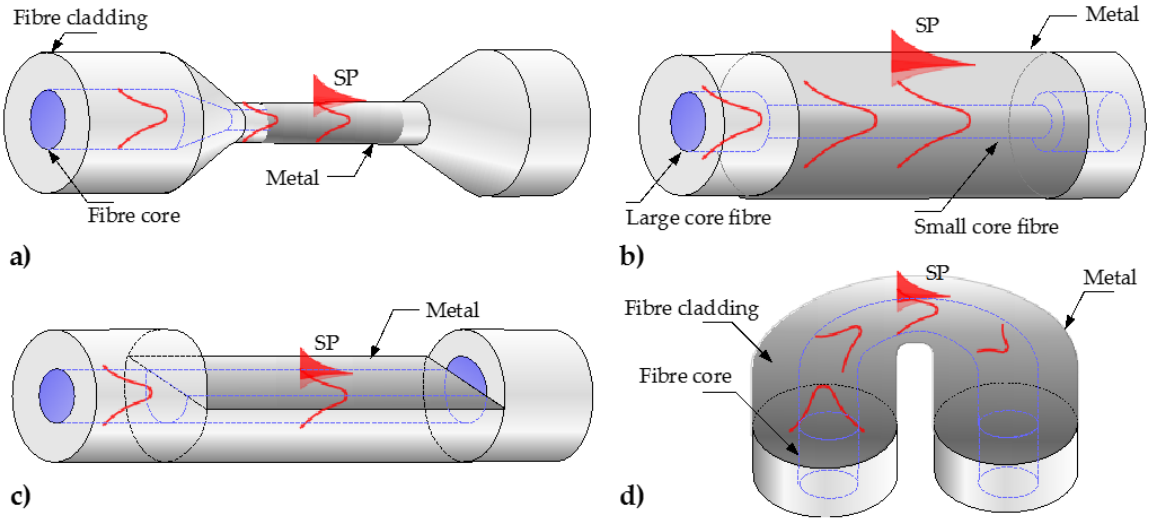


Figure 3. Schematics of geometry-modified optical fiber SPR sensors implemented on a side of an optical fiber: (**a**) Tapered fiber SPR probe; (**b**) Hetero-core structure; (**c**) D-shaped SPR probe; (**d**) U-shaped SPR probe.

For a large core MMF where the cladding typically consists of a soft polymer layer, the core can be easily exposed by removing a section of the polymer layer [43,50,51]. However, if the cladding is made of glass, like in double-clad or graded-index fibers, etching can be performed to access the fiber core for metal deposition [52]. Alternatively, the fiber could be tapered over a short region along its length by heating a section of the fiber with a filament in a controlled manner [45]. In the tapered region of the fiber the evanescent field escapes through the cladding and interacts with the surroundings. The tapered region is then coated with a metal film for SPR sensing, as shown in Figure 3a. These structures predominantly benefit from having small cores, resulting in a narrow SPR feature, and therefore, an increased resolution. The refractive index sensitivity for tapered probes could also be enhanced through the stronger interaction of the propagating modes with the metallic coating, reaching up to 12,000 nm/RIU [45]. However, the fragility of the tapered probes makes them impractical for many applications.

To overcome this issue, other SPR fiber configurations, called hetero-core structures, have been proposed [16,19,46,53]. The configuration consists of two different types of fibers with mismatched core diameters, typically an SMF fiber spliced between two MMF fibers. The SMF region is coated with a metallic thin film for SPR sensing, as shown in Figure 3b. The mismatch between the cores

causes guided modes to couple into the cladding of the SMF fiber where plasmonic interaction can occur. However, the sensitivity of the hetero-core SPR sensors (2000 nm/RIU [46]) is still lower than tapered fibers [45].

As an alternative to etching or tapering, side polishing has also been used to expose a section of the fiber core, resulting in a "D-shape" cross section, as illustrated in Figure 3c. To perform the polishing, a fiber is typically enclosed inside a resin block and polished off [54,55]. Wheel polishing setups have also been used to fabricated D-shaped fibers for SPR sensors [20]. Feasibility of MOFs as D-shaped SPR probes has also been theoretically investigated by many authors [39,47,48,56–58], but has not yielded any experimental demonstrations. Sensitivity of side-polished structures vary depending on fiber core size and material, with up to 4300 nm/RIU reported for an SMF-based side-polished SPR sensor [20]. Recently, an "eccentric core fiber" SPR probe, consisting of two SMFs with angle-polished tips spliced together was proposed and demonstrated by Liu et al. [59] showing the experimental sensitivity of up to 4738 nm/RIU. The ability to adjust the polishing angle allows for realization of sensing probes operating at specific wavelengths. This concept can be expanded for distributed sensing, owing different sensing regions can be produced along a single fiber.

Besides tapering, polishing or splicing different fibers together, bending offers the easiest way of extracting the light propagating inside the fiber core. When a fiber is bent beyond its critical radius, the propagating modes inside the core can couple into the cladding [49,60,61]. If the bent region is coated with a metal, a portion of this radiation can excite SPs. Bent fiber probes, also called "U-shaped" fibers, are usually fabricated from unclad large core MMFs or glass-clad fibers by heating a fiber section and forming a permanent U-shaped bend, as shown on Figure 3d. The sensitivity of bent SPR fiber sensors increases as the bend radius decreases, with theoretical values of up to 70,000 nm/RIU estimated for bend radius of 10 mm [62]. This predicted values are several times higher than for tapered probes, and around 25 times higher than for a straight sensing region implemented on the same fiber [62]. Feasibility of bent MOF SPR sensors have also been theoretically investigated for potential performance improvement, tunable by bending [63]. However, a recent experimental study, comparing bent and straight side-polished SPR probes revealed no significant improvement for the bent SPR fiber (bent radii of 10, 15 and 20 mm) compared with a straight side-polished one [64].

3.1.2. Fiber-Tip SPR Sensors

SPR fiber sensors can be implemented on, or near, a fiber tip, allowing for devices to be used as dip sensors. The simplest fiber tip SPR sensor consists of a plasmonic coating on a side of the fiber near its tip, which is coated with a metallic mirror, as depicted in Figure 4a. The dip SPR sensors are usually fabricated using MMFs and the interrogation is performed through analyzing light back-reflected from the mirrored fiber tip [24,65,66]. As this configuration is essentially the same as the unclad fiber SPR sensors described previously, the sensing performances are comparable to the fiber-side SPR sensors made of the same materials.

Alternatively, a dip sensor can be created by placing a plasmonic coating on the fiber tip. However, the incidence angles of the light propagating inside the fiber onto the straight cleaved end are typically small (near normal incidence), and below the range of SPR excitation angles. As a result, additional preparation of the fiber tip is required to increase the incidence angle. One of the existing techniques involves polishing the fiber end at a specific angle, thereby modifying the incidence onto the coated fiber tip, as shown in Figure 4b. The first fiber optic sensor with angle-polished fiber tip was proposed as early as 1993 [8], followed by further development [24,67–69], including polishing one fiber tip at different angles to acquire sensitivity to both, gas and liquid phases [66].

Recently, an interesting design of an angle-polished fiber tip SPR sensor that utilizes a specialty fiber with a twin core and the sensitivity of 5213 nm/RIU has been demonstrated [22]. An alternative approach to the angled-cleaved fiber tip is the modification of the fiber by tapering its tail until it forms an apex, similar to an Atomic Force Microscope tip. The tapered tip is then coated with a metallic

thin film [52], as shown in Figure 4c. The performance of these SPR fiber sensors is comparable to the analogous side-tapered configurations, however, they are allegedly less fragile.

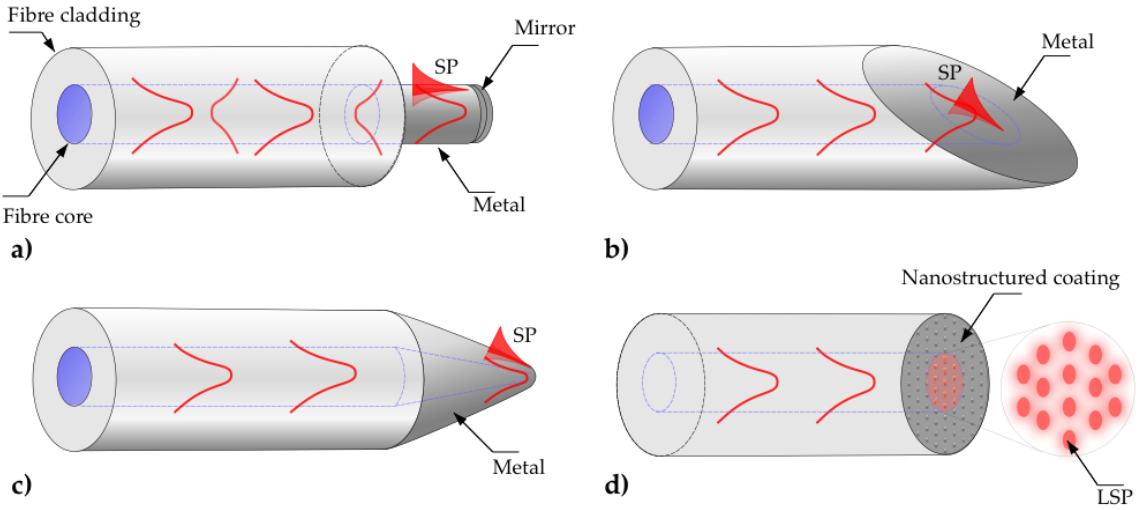


Figure 4. Schematics of geometry-modified optical fiber SPR sensors implemented on a tip of an optical fiber: (**a**) Flat fiber tip SPR probe with end mirror; (**b**) Angle polished flat fiber tip SPR sensor; (**c**) Tapered tip SPR probe; (**d**) LSPR fiber tip probe.

Another important subset of fiber-tip SPR sensors comprise fibers with a metallic pattern, supporting Localized Surface Plasmon Resonance (LSPR), fabricated on the fiber tip, as shown in Figure 4d. LSPR excitation is not restricted by the same constrains as propagating SPs, which require shallow incidence angles from a dielectric with refractive index higher than air, allowing for the excitation of localized SPs at normal incidence. As a result, LSPR sensors can be constructed directly on the straight cleaved fiber tip, which greatly simplifies the sensor architecture. With the recent advances in nanofabrication technologies, a variety of nanostructured surfaces have been used to pattern the fiber tip. These includes coating the fiber end with metal nanoparticle arrays [70,71], two-dimensional nanostructures [72], nano-hole arrays [73,74], as well as using a PCF with holes at the tip [75], or machining the metal coated fiber tip with sub-micron periodicity using Focused Ion Beam [76]. LSPR fiber tip sensors are an attractive platform due to the relative simplicity of the probe fabrication. However, LSPR is known for being less sensitive to refractive index changes when compared with sensors based on propagating plasmons.

3.1.3. Specialty SPR Fiber Sensors

Instead of implementing the sensing region on the exterior of an optical fiber, plasmonic materials can be deposited on the fiber interior. Typically, this requires either MOFs with air holes or micro-capillaries. MOFs allow not only to take advantage of the fundamental guiding properties of these fibers, but also to use them as microfluidic channels for samples at the same time [77].

MOFs with various air cavity shapes coated with metal particles or films have been reported, including circular air holes [78] and crescent-shape holes [36], triangular shaped holes [38], and inner cavities of a PCF [79], as shown in Figure 5. Some specialty MOFs, such as an exposed core fiber, allow the deposition of plasmonic coatings without filling the fiber holes [37]. Nevertheless, practicality of the specialty MOF SPR sensors remains limited by the cost of fabrication of the fiber itself.

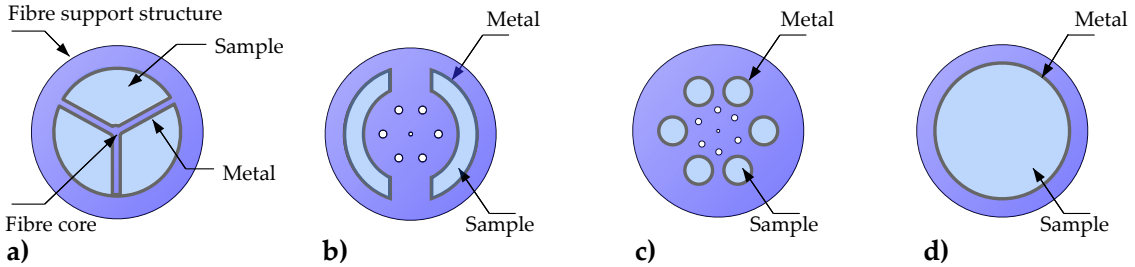


Figure 5. Examples of fiber interior SPR sensors: (**a**) Wagon-wheel fiber SPR sensor with triangular hole geometry [38]; (**b**) MOF fiber SPR sensor with crescent-shaped holes [36]; (**c**) PCF SPR sensor with circular holes [79]; (**d**) Microcapillary fiber SPR sensor geometry [80].

SPR sensor architectures with a silver coating deposited onto the inner microcapillary wall have recently emerged as an alternative to fiber-based SPR sensors [81–83]. Microcapillary-based SPR sensors can be highly advantageous as the capillary itself can be used as a microfluidic channel. However, this particular approach is only applicable for high refractive index liquids (typically $n > 1.5$) due to the requirement for confining the propagating light inside the capillary, which also results in larger sensitivity values of up to 6607 nm/RIU [80]. Despite these few successful experimental demonstrations, this area remains predominantly theoretical due to the practical difficulties of deposition of the plasmonic coatings on the inner cavities of the fiber microstructure, as well as by the cost of fabrication of the MOF itself.

3.1.4. Fiber Grating-Assisted and Grating-Coupled SPR Sensors

The most common method of SPR excitation in optical fibers is Total Internal Reflection (TIR) where a proportion of the evanescent field that penetrates through the interface on ordinary total reflection can excite SPs. An additional increase of the evanescent field can be achieved by introducing inhomogeneity in the fiber core structure, such as tapering, hetero-core, bending, or side-polishing, as described in Section 3.1. A remarkable progress in SPR excitation has been achieved through the use of fiber gratings. A fiber grating is a periodic structure in the refractive index of the fiber core which generates a wavelength-specific dielectric mirror. A review of the fiber grating fabrication techniques can be found elsewhere [84]. Due to their mechanical strength and availability, fiber gratings became popular for construction of SPR sensors in recent years. Instead of modifying the fiber geometry to access the core-guided light, fiber gratings such as FBGs, Long Period Fiber Gratings (LPFGs) or Tilted Fiber Bragg Gratings (TFBGs) can be used to diffract a portion of the guided light from the core into the cladding, where it can interact with the plasmonic coating, as shown in Figure 6a–c, respectively. These fiber gratings, and especially the LPFGs and TFBGs, overcome the major limitation of geometry-modified SPR fiber sensors, enabling the plasmonic coating to be simply deposited onto the cladding. Several configurations of the LPFG-assisted SPR fiber sensors have been reported [23,85,86]. Recently, LPFGs have been proposed to be used in an SPR fiber sensor implemented by bending a fiber in a loop [84,87,88].

The refractive index sensitivity achieved with TFBG SPR sensors is generally moderate (400–1000 nm/RIU) [89] in comparison to TIR and evanescent field-assisted propagating plasmon-based sensors, which typically reaches up to several thousand nm/RIU. Despite that, due to the nature of TFBG SPR excitation, the spectrally well-defined cladding modes allow higher precision in determining the position of the SP resonant feature. This allows much higher detection accuracy and lower resolution, making TFBG SPR probes applicable for real-time biological sensing [90]. In addition, one of the most important features of the TFBG-assisted SPR sensors is the presence of the Bragg resonance which could be used as a reference control for compensation of temperature and optical power fluctuations [12]. It is important to differentiate between grating-assisted and grating-coupled SPR fiber sensors. As described above, in the grating-assisted sensors, the fiber grating inscribed in the

core is used to out-couple the guided light into the cladding, where it interacts with the metal coating, thereby excites SPs. In grating-coupled SPR configurations, the grating is inscribed in the metallic coating and is used as a coupler to adjust the propagation constant of light incident to the metal [91]. As an alternative to the metal grating, periodic corrugations could be fabricated on the fiber surface or fiber tip, where metal is deposited over the dielectric grating [92].

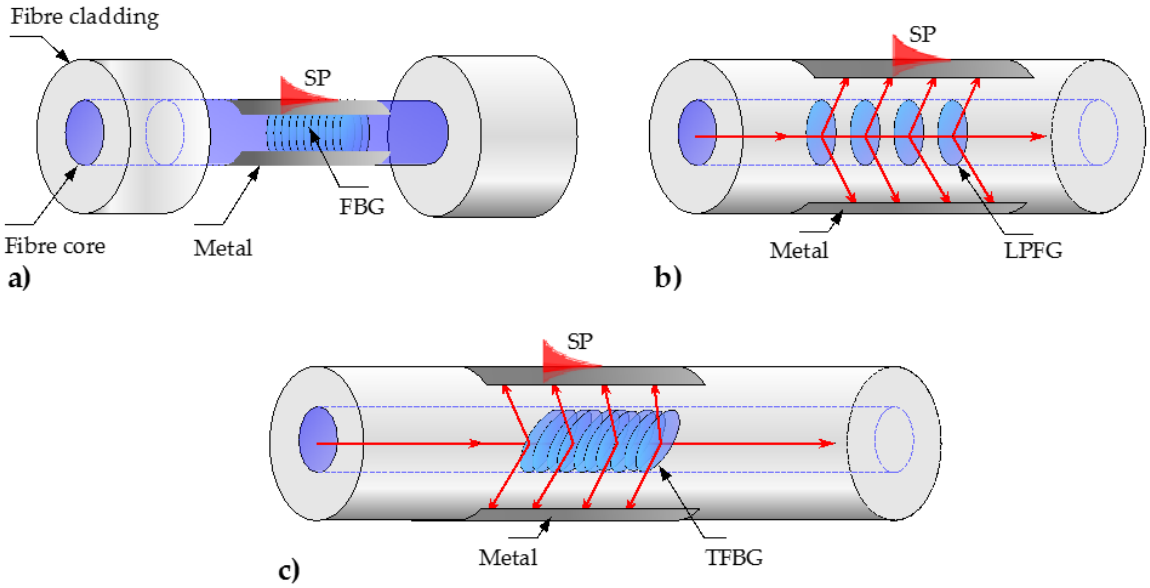


Figure 6. Schematics of the fiber grating-assisted SPR fiber sensors: (**a**) Etched Fiber Bragg Grating (FBG) SPR sensor; (**b**) Long Period Fiber Grating (LPFG) SPR sensor; (**c**) Tilted Fiber Bragg Grating (TFBG) SPR sensor.

3.2. Plasmonic Coatings

As the dielectric function of metals plays a crucial role in the plasmonic interaction, fundamental properties of the surface plasmons, and therefore, their performance parameters, are significantly affected by the metal coating. Typical materials that are used for plasmonic coatings are silver (Ag), gold (Au), aluminum (Al), and copper (Cu) [93]. The sensor performance, such as sensitivity, resolution, and dynamic range, is greatly influenced by the choice of the metal and the metallic coating morphology. Ag generally provides higher sensitivity due to the high magnitude of the real part of its dielectric constant and lower imaginary part [3], but owing to its chemical resilience, Au is more commonly used. Although, more exotic materials, such as indium tin oxide (ITO) [44,94] and graphene [40,95], have recently emerged as alternative plasmonic materials for optical fiber SPR sensors. The metallic thin film thickness is also known to influence the SPR sensor performance, with the optimal thickness of around 40–60 nm [4]. In addition to the metal type and its thickness, the film roughness can significantly affect the SPR signal. Smooth metal films are traditionally used for most SPR configurations due to higher propagation length of the SPs and, therefore, better performance. However, metallic coatings with high surface roughness can be used to induce SPR scattering caused by spatial variation of the dielectric constant of the film [96,97], which allows an alternative approach for SPR spectral interrogation [51]. Surface plasmons can be generated on metal coatings of various structures, such as conventional propagating surface plasmons on a single metal layer, alloys, or double-metal structures, as well as plasmonic nanostructures for LSPR and Long Range Surface Plasmons (LRSPs) on dielectric-metal structures.

3.2.1. Continuous Metal Films: Propagating Plasmons

The most common plasmonic coating is a single-metal smooth continuous thin film deposited using physical deposition methods, such as thermal evaporation or sputtering. However, as physical deposition methods are intrinsically directional, a rotational apparatus is required to fabricate homogeneous coating onto the fiber, especially for fiber-side SPR sensors. Chemical deposition methods, such as chemical vapor deposition [98], or electroless plating [99], can easily achieve symmetric coatings around the fiber circumference [51] or inside MOFs [99]. Metallic coatings with varying thickness, such as single- or double-sided coatings, shown in Figure 7a,b respectively, were reported to result in multiple resonances [100], as well as an increase in the sensor's dynamic range [21,26]. However, these layouts of the plasmonic coatings can influence the sensor performance by broadening the SPR spectral feature. In addition, stronger SPR signals are typically obtained with double-sided (Figure 7b) and cylindrical (Figure 7c) coatings [101].

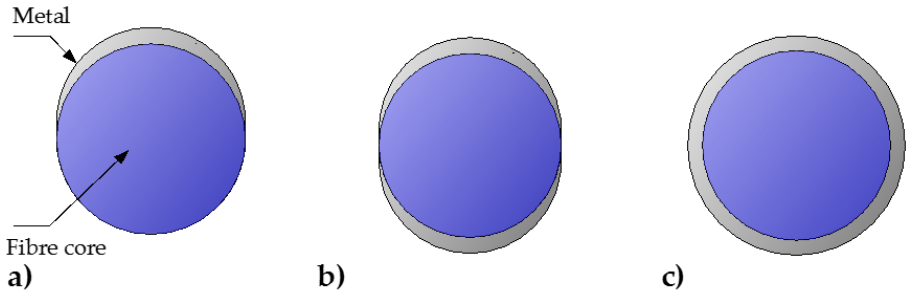


Figure 7. Cross sections of optical fiber core with common metal coating layouts: (**a**) Asymmetric one-sided coating; (**b**) Symmetric double-sided coating; (**c**) Symmetric cylindrical coating, typically produced by chemical deposition.

Using rough metal coatings can provide some advantages despite the lower SPs propagation length. The scattered radiation can be used to infer the SPR signal [43,50,51], instead of performing transmission measurements, as it is done in fiber SPR sensors with smooth plasmonic coatings. In general, the larger spectral linewidth of the SPR response is associated with rough metal surfaces when compared to the smooth metal films [102]. However, amongst advantages of using metal coatings with high roughness are the lower reliance on the film thickness, and the ability to fabricate those coatings using simple wet chemistry techniques, such as electroless plating [51,99].

3.2.2. Layered Coatings: Conventional, Long Range and Waveguide Coupled Plasmons

Instead of using a single metal or alloy as the propagating plasmons' supporting material, coating of multiple metals can be designed to provide the desired performance, as well as to improve binding of the plasmonic coatings to a dielectric substrate. Bimetallic coatings consisting of silver and gold have been used to increase sensor performance, as well as to protect silver from oxidation [103,104]. Plasmonic films can also be stacked with dielectric or metallic layers to produce structures that modify SPR sensor characteristics. Dielectric layers (i.e., silica, magnesium fluoride, fluorinated polymers) deposited on top or between metal films have been used to improve sensing performances [26,105,106], tune the resonant wavelength [107], to generate LRSPR [82,108], or waveguide coupled plasmons [47], and as protective coatings [109].

3.2.3. Nanostructured Coatings and Nanoparticles: Localized Plasmons

Nanostructured periodic and non-periodic plasmonic coatings, including metal particles of various shapes and sizes [110,111], metal nanoshells [112], nanostrips [113], nanorings [114], periodically arranged nanostructures [74], have been used to produce LSPR fiber optic sensors. Various methods to prepare this nano-patterned materials exist today which have been extensively described in literature [115]. The intrinsic refractive index sensitivity of localized SPs is a few orders of magnitude smaller than that of sensors based on SPs propagating on planar surfaces. Nevertheless, LSPR still provides some advantages such as lower cost, smaller sensing elements for high spatial resolution, and better surface sensitivity [116]. The SP field is more tightly concentrated at the vicinity of the sensor surface in the case of LSPR, so the decay length of LSPR is usually significantly smaller than that of SPs. This results in the higher surface sensitivity of localized plasmons, which can be beneficial for small particle detection [117]. In addition, the radiative nature of optical manifestation of localized surface plasmon excitation establishes the dominance of LSPR for surface enhanced optical phenomena in optical fibers [118], such as Surface Enhanced Raman Scattering (SERS), Surface Enhanced Resonant Raman Scattering (SERRS), and Metal Enhanced Fluorescence (MEF).

4. Applications

Intrinsically, an SPR sensor is a refractometer that only produces response to a change in the RI of the sensed medium. SPR fiber sensors have found applications as physical, chemical and biological sensors. However, additional elements, such as surface functionalization or physical modifications to the sensor surface, need to be incorporated in the architecture in order to generate refractive index change in response to the parameter to be determined. Besides, some environment change (e.g., temperature fluctuation) also leads to refractive index change, and thus SPR signal variation, which is especially significant in the case of biosensing. Either monitoring the reference or stabilizing environment could eliminate this effect to some extent from the background.

4.1. Physical SPR Fiber Sensors

SPR sensors have been used for the detection of physical quantities such as temperature, pressure, and humidity. As the SPR resonant condition is, in general, not highly sensitive to those quantities, specially designed functional coatings that translate change in these physical parameters into a change in the refractive index, need to be used. Thermal modulation of the refractive index of a material is described by its thermo-optic coefficient. Refractive index of the fiber core (i.e., typically fused silica) and plasmonic coating materials do not change significantly with temperature [119,120]. Therefore, temperature SPR fiber sensors are typically constructed using dielectric materials with a high-value thermo-optic coefficients deposited onto the sensor surface [121–124]. SPR fiber optic sensors for pressure detection have also been demonstrated. Here, an elastic polymer which refractive index depends on the applied pressure was used [125]. A theoretical design of an SPR fiber probe for pressure sensing has been proposed by Duarte et al. [126], where a U-shaped SPR probe was enclosed in a silicon rubber block. When pressure was applied to the block, the bend radius of the fiber probe changed, resulting in the change of the resonant condition. Similarly, SPR humidity sensors rely on functional materials whose refractive index depends on the number of water molecules adsorbed onto it. Typically, humidity sensitive polymeric over-layers in the proximity of a plasmonic coating are used to construct SPR-based fiber optic humidity sensors [44,127]. Change in humidity near the polymeric layer originates variations of the coating thickness, as well as its refractive index, causing a shift in the SPR condition. SPR dew sensors can detect temperature and humidity gradients in the adjacent environment by detecting changes of thickness of the water layers forming on the sensing surface [128].

4.2. Chemical SPR Fiber Sensors

SPR fiber sensors have also been exploited for chemical sensing in liquid or gas phases. The presence of certain chemicals is detected by either designing a functional coating, capable of specifically interacting with the chemical of interest, or direct change of the refractive index induced by the presence of the sensed target component in the sample. For example, pyrrole/chitosan composite coating was used to bind heavy metal ions onto Ag-ITO coating for detection of water contamination [129]. The detection of hydrogen peroxide using an SPR fiber sensor based on Ag film coated with Ag nanoparticle-doped polyvinyl alcohol nanocomposite has also been reported [130]. Other methods rely on dependence of dielectric's refractive index on concentration of target chemicals, such as a water salinity sensor [131]. Several pH fiber optic LSPR sensors have also been demonstrated [132,133]. Gas sensing with SPR typically relies on metals (palladium, silver) or semiconducting metal oxide over-layers (indium tin oxide, tin dioxide, nickel oxide, zinc oxide, titanium dioxide) that change their electric permittivity when exposed to gaseous environments. Some example of gas SPR chemical fiber optic sensors include ammonia sensor [134], chlorine gas sensor [135], hydrogen SPR sensor [94,107,136], and hydrogen sulfide gas sensor [137].

4.3. Biological SPR Fiber Sensors

By far the largest application domain for SPR fiber sensors is biological sensing. This is due to the important advantages these sensors offer in comparison to other biosensing methods, such as the label free aspect, small volume of samples, quantitative real-time measurements, and possibility of in vivo and in-situ deployment. For an SPR response to occur in a biosensor, the sensing surface is functionalized with bioreceptors, which are designed to interact specifically with the analyte and produce a measurable change in its refractive index. Examples of bioreceptors include antibodies [138], aptamers [139], enzymatic bioreceptors, proteins, and nucleic acids. SPR fiber-based sensors have been applied for detection of pathogens, such as viruses [51,140], bacteria [141], biomarkers of medical conditions [43,50,142,143], study of DNA and DNA-protein interactions [144,145], and detection of bio-hazardous compounds [146–148]. However, even with its high sensitivity, SPR sensors cannot be successfully applied for a single molecule detection, unlike other optical resonance phenomena such as Whispering Gallery Mode [149,150], which typically exhibit much higher resolution. Moreover, the inherent drawback of biosensing with SPR, like any label-free method, lies in the intervening of the outcome of the results by non-specific binding, which can eventually result in false positives. However, due to the nature of the plasmonic coating (i.e., silver or gold), SPR and, therefore SPR fiber sensors, have a decisive advantage compared with other optical methods. Thiols are known to strongly interact with either Au or Ag and form self-assembled monolayers (SAMs), which can subsequently be used for the immobilization of antibodies [138], aptamers [139], or other relevant biomolecules. In addition, thiol-terminated polyethylene glycol SAMs are known for their ability to minimize or completely suppress non-specific binding in complex biological samples, such as serum [151,152].

5. Conclusions and Perspectives

It is often difficult to compare performance of SPR sensing devices due to the large variety of SPR fiber sensor architectures. Table 1 provides a summary of recent experimental demonstrations of SPR fiber sensors with their performance characteristics (S, and $FWHM$) and a description of major aspects of their configurations. In addition, the ratio between the $FWHM$ and sensitivity is presented as a figure of merit to evaluate what would be the best performing platform in terms of an equivalent detection limit.

Table 1. Summary and characteristics of recent experimental demonstrations of SPR fiber optic sensors.

Fiber	Coating	Excitation	Interrogation	S_λ nm/RIU	FWHM nm	FWHM/S_λ RIU	Reference
SMF Fiber tip	Au NPs [4]	direct (LSPR)	spectral, trans.	196	ca. 70	3.6×10^{-1}	[71]
MMF Side etched	Au NPs [3]	TIR (LSPR)	intensity, trans.	ca. 500	ca. 50–150	3×10^{-1}–10^{-1}	[153]
SMF Fiber tip	Au holes [4]	direct (LSPR)	spectral, back-reflect.	755	ca. 200	2.6×10^{-1}	[73]
MMF Fiber tip	Ag NPs [3]	Direct (LSPR)	spectral, back-reflect.	387	ca. 70–100	2.5×10^{-1}–1.6×10^{-1}	[111]
Microcapillary	Ag film	TIR, from sample	spectral, trans.	1000	ca. 200	2×10^{-1}	[81]
MMF Flat & taper. tip	Au holes [4]	direct (LSPR)	spectral, trans.	533	ca. 80	1.5×10^{-1}	[76]
MMF Fiber tip	Au film [1]	TIR	spectral, back-refl.	1433	ca. 150	10^{-1}	[21]
MMF, GI SMF Heterocore	Ag film	ev.-field ass. TIR	spectral, transmission	1500–2100	ca.150–200	10^{-1}–7×10^{-2}	[46]
GI MMF Side-polished	Au film	ev.-field ass. TIR	spectral, trans.	1570	130	8.2×10^{-2}	[48]
MMF Fiber tip	Au film [2]	TIR	spectral, back-reflect.	1557	ca. 80	5.1×10^{-2}	[65]
Plastic MMF Side polish, bent	Au film	ev.-field ass. TIR	spectral, trans.	1654–2978	70	4.2×10^{-2}–2.3×10^{-2}	[64]
Microcapillary	Ag/dielectric	TIR LRSPR	spectral, trans.	2000–6600	50–250	1.2×10^{-1}–7.5×10^{-3}	[82]
MMF Angle-polished tip	Au film	TIR	spectral, back-reflect.	ca. 2650	ca. 100–150	5.6×10^{-2}–3.7×10^{-2}	[66]
SMF Etched tip, side etched	Au film/TiO_2	ev-.field ass. TIR	spectral, back-reflect.	3800–5100	ca. 150–200	5.2×10^{-2}–2.9×10^{-2}	[52]
MMF MOF Fiber side	Ag rough film [2]	TIR	spectral, scatter.	1753	75	4×10^{-2}	[37]
SMF Side-polished	Ag film	TIR	spectral, trans.	1523–4365	40–90	2.6×10^{-2}–9×10^{-3}	[20]
SMF, twin core Angle tip & mirror	Au film	TIR	spectral, back-reflect.	5213	ca. 100	1.9×10^{-2}	[22]
MMF Side-polished	Au/ZnS-SiO_2/Au [1]	ev.-field ass. TIR	spectral, trans. (LSPR)	2200	40	1.8×10^{-2}	[47]
SMF Side-polished	Cr/Au/Ta_2O_5 [1]	TIR	spec.& inten., trans.	3300	ca. 50	1.2×10^{-2}	[54,55]
SMF Side tapered	Au film [1]	ev.-field ass. TIR	spectral, trans.	ca. 25000	ca. 150	6×10^{-3}	[100]
SMF Side tapered	Al/InN bi-layer [1]	ev.-field ass. TIR	spectral, trans	11,800	ca. 50	4.2×10^{-3}	[45]
SMF Fiber side	Ag film [1]	TFBG-assisted	spectral, trans.	550–673	5	7.4×10^{-3}–9×10^{-4}	[154,155]

[1] Asymmetric coating; [2] Symmetric coating; [3] Non periodic structure; [4] Periodic structure.

Looking at Table 1, it becomes obvious that, in general, LSPR-based fiber sensors are vastly outperformed by the standard SPR approach in both, sensitivity and *FWHM*. LSPR is known to have lower refractive index sensitivity compared with SPR and a broader *FWHM*, where both parameters primarily depend on the feature size of either the metallic nanoparticles or patterns. Consequently, the ratio between *FWHM* and sensitivity for LSPR-based fiber sensors is significantly lower than that for SPR-based ones. For SPR fiber sensors, the *FWHM*, and eventually the detection limit, can be improved by reducing the number of propagating modes that satisfy the coupling conditions with the SPs. Therefore, there is a clear trend, where SMF-based SPR sensors tend to exhibit a lower *FWHM* to sensitivity ratio compared with MMFs ones. Yet, even with SMF-based SPR sensors, the *FWHM* is still limited to 40–50 nm [45,47,54,55]. The addition of a TFBG on the SMF core allows for further reduction of the *FWHM* down to 5 nm [154,155], greatly improving the figure of merit. Silver and gold are largely dominant as plasmonic coating materials, although some more exotic ones have been implemented. However, there is no clear trend of what would be the ideal plasmonic coating as either silver or gold exhibit similar refractive index sensitivities when compared with other materials. Similarly, the fiber architecture, whether it is side-coated or tip-coated, does not significantly influence the performance, but allows for different applications (i.e., dip sensing for tip-coated fibers). Among the diverse interrogation methods, transmission or reflectivity measurements yield similar results, although heterodyne interferometry implemented on a D-type SPR fiber sensor looks like a promising approach for improving the refractive index sensitivity [156,157].

With the dozens of commercial SPR instruments based on a prism configuration available today, fiber-optic SPR probes experience a very slow uptake. This is mainly due to the increased complexity of fiber design and plasmonic coating fabrication on an optical fiber, resulting in higher cost of the consumable sensors. Moreover, the necessity of manipulation and optical alignment of small fiber probes by the end-user makes the sensing probes even more expensive. However, SPR fiber sensors provide several important benefits over the standard prism configurations. Although, a considerable range of SPR fiber sensor designs have been proposed and demonstrated, there is significant scope for the development of improved SPR systems suitable for a range of applications.

The aspects of development that need to be addressed for the fiber optic SPR sensors to be commercially feasible include but are not limited to engineering miniature sensing probes, improved microfluidic systems, low cost manufacturing techniques, as well as improved sensing performance, such as sensitivity and detection limit. Yet, some aspects of SPR that can significantly improve the sensing performance have not been demonstrated in fiber platforms. A key example is LRSPR, where only a few demonstrations involving optical waveguides and fibers have been reported [82,158]. LRSPR could be highly beneficial for biosensing applications, especially for large macromolecules, viruses, bacteria and other cells, whose size is beyond the standard penetration depth of SPs. LRSPR with its superior penetration depth compared with SPs would allow probing of entire macromolecules. In addition, it has been reported that the LRSPR refractometric sensing approach can achieve higher refractive index sensitivity [159], and holds the record detection limit of 2×10^{-8} RIU in a prism configuration [160]. Combining the LRSPR method within fiber sensing architectures, and taking advantage of fewer mode fibers for optimizing both, sensitivity and resolution, could lead to the development of new highly performing refractometric sensing approaches.

Acknowledgments: The authors acknowledge the support of Tanya M. Monro's ARC Georgina Sweet Laureate Fellowship and the support of the ARC Centre of Excellence for Nanoscale BioPhotonics. This work was performed in part at the OptoFab node of the Australian National Fabrication Facility utilizing Commonwealth and SA State Government funding.

Author Contributions: All the authors equally contributed to the redaction of this review article.

Conflicts of Interest: The authors declare no conflict of interest.

Abbreviations

The following abbreviations are used in this manuscript:

DL	Detection Limit
FBG	Fiber Bragg Grating
FOM	Figure of Merit
FWHM	Full Width at Half Maximum
GI	Graded Index
ITO	Indium Tin Oxide
LPFG	Long Period Fiber Grating
LRSPR	Long Range Surface Plasmon Resonance
LSPR	Localized Surface Plasmon Resonance
MEF	Metal Enhanced Fluorescence
MMF	Multi-Mode Fiber
MOF	Microstructured Optical Fiber
PCF	Photonic Crystal Fiber
PMF	Polarization Maintaining Fiber
SERRS	Surface-Enhanced Resonance Raman Scattering
SERS	Surface-Enhanced Raman Scattering
SMF	Single Mode Fiber
SNR	Signal to Noise Ratio
SP	Surface Plasmon
SPR	Surface Plasmon Resonance
TIR	Total Internal Reflection

References

1. Kretschmann, E.; Raether, H. Notizen: Radiative decay of non radiative surface plasmons excited by light. *Zeitschrift fur Naturforschung A* **1968**, *23*, 2135–2136. [CrossRef]
2. Otto, A. Excitation of nonradiative surface plasma waves in silver by the method of frustrated total reflection. *Zeitschrift fur Physik* **1968**, *216*, 398–410. [CrossRef]
3. Homola, J.; Yee, S.S.; Gauglitz, G. Surface plasmon resonance sensors: Review. *Sens. Actuators B Chem.* **1999**, *54*, 3–15. [CrossRef]
4. Homola, J. *Surface Plasmon Resonance Based Sensors*; Springer: Berlin, Germany, 2006.
5. Pockrand, I.; Swalen, J.; Gordon, J.; Philpott, M. Surface plasmon spectroscopy of organic monolayer assemblies. *Surf. Sci.* **1978**, *74*, 237–244. [CrossRef]
6. Liedberg, B.; Nylander, C.; Lunström, I. Surface plasmon resonance for gas detection and biosensing. *Sens. Actuators* **1983**, *4*, 299–304. [CrossRef]
7. Jorgenson, R.C.; Yee, S.S. A fiber-optic chemical sensor based on surface plasmon resonance. *Sens. Actuators B Chem.* **1993**, *12*, 213–220. [CrossRef]
8. Maria, L.D.; Martinelli, M.; Vegetti, G. Fiber-optic sensor based on surface plasmon interrogation. *Sens. Actuators B Chem.* **1993**, *12*, 221–223. [CrossRef]
9. Kim, S.A.; Kim, S.J.; Moon, H.; Jun, S.B. In vivo optical neural recording using fiber-based surface plasmon resonance. *Opt. Lett.* **2012**, *37*, 614–616. [CrossRef] [PubMed]
10. Liu, Y.; Liu, Q.; Chen, S.; Cheng, F.; Wang, H.; Peng, W. Surface Plasmon Resonance Biosensor Based on Smart Phone Platforms. *Sci. Rep.* **2015**, *5*, 12864. [CrossRef] [PubMed]
11. Bremer, K.; Roth, B. Fibre optic surface plasmon resonance sensor system designed for smartphones. *Opt. Express* **2015**, *23*, 17179–17184. [CrossRef] [PubMed]
12. Caucheteur, C.; Guo, T.; Albert, J. Review of plasmonic fiber optic biochemical sensors: Improving the limit of detection. *Anal. Bioanal. Chem.* **2015**, *407*, 3883–3897. [CrossRef] [PubMed]
13. Arghir, I.; Delport, F.; Spasic, D.; Lammertyn, J. Smart design of fiber optic surfaces for improved plasmonic biosensing. *New Biotechnol.* **2015**, *32*, 473–484. [CrossRef] [PubMed]
14. Sharma, A.K.; Jha, R.; Gupta, B.D. Fiber-Optic Sensors Based on Surface Plasmon Resonance: A Comprehensive Review. *IEEE Sens. J.* **2007**, *7*, 1118–1129. [CrossRef]
15. Gupta, B.D. Surface Plasmon Resonance Based Fiber Optic Sensors. In *Reviews in Plasmonics 2010*; Geddes, D.C., Ed.; Springer: New York, NY, USA, 2012; pp. 105–137.

16. Hosoki, A.; Nishiyama, M.; Igawa, H.; Seki, A.; Watanabe, K. A hydrogen curing effect on surface plasmon resonance fiber optic hydrogen sensors using an annealed Au/Ta_2O_5/Pd multi-layers film. *Opt. Express* **2014**, *22*, 18556–18563. [CrossRef] [PubMed]
17. Ju, S.; Jeong, S.; Kim, Y.; Lee, S.-H.; Linganna, K.; Kim, C.J.; Han, W.-T. Effect of heat treatment of optical fiber incorporated with Au nano-particles on surface plasmon resonance. *Opt. Mater. Express* **2015**, *5*, 1440–1449. [CrossRef]
18. Lin, H.-Y.; Tsai, W.-H.; Tsao, Y.-C.; Sheu, B.-C. Side-polished multimode fiber biosensor based on surface plasmon resonance with halogen light. *Appl. Opt.* **2007**, *46*, 800–806. [CrossRef] [PubMed]
19. Takagi, K.; Watanabe, K. Near infrared characterization of hetero-core optical fiber SPR sensors coated with Ta_2O_5 film and their applications. *Sensors* **2012**, *12*, 2208–2218. [CrossRef] [PubMed]
20. Zhao, J.; Cao, S.; Liao, C.; Wang, Y.; Wang, G.; Xu, X.; Fu, C.; Xu, G.; Lian, J.; Wang, Y. Surface plasmon resonance refractive sensor based on silver-coated side-polished fiber. *Sens. Actuators B Chem.* **2016**, *230*, 206–211. [CrossRef]
21. Hlubina, P.; Kadulova, M.; Ciprian, D.; Sobota, J. Reflection-based fibre-optic refractive index sensor using surface plasmon resonance. *J. Eur. Opt. Soc. Rapid Publ.* **2014**, *9*. [CrossRef]
22. Liu, Z.; Wei, Y.; Zhang, Y.; Zhang, Y.; Zhao, E.; Yang, J.; Yuan, L. Twin-core fiber SPR sensor. *Opt. Lett.* **2015**, *40*, 2826–2829. [CrossRef] [PubMed]
23. Schuster, T.; Herschel, R.; Neumann, N.; Schäffer, C.G. Miniaturized long-period fiber grating assisted surface plasmon resonance sensor. *J. Lightw. Technol.* **2012**, *30*, 1003–1008. [CrossRef]
24. Suzuki, H.; Sugimoto, M.; Matsui, Y.; Kondoh, J. Fundamental characteristics of a dual-colour fibre optic SPR sensor. *Meas. Sci. Technol.* **2006**, *17*, 1547. [CrossRef]
25. Chiu, M.-H.; Shih, C.-H.; Chi, M.-H. Optimum sensitivity of single-mode D-type optical fiber sensor in the intensity measurement. *Sens. Actuators B Chem.* **2007**, *123*, 1120–1124. [CrossRef]
26. Nguyen, T.T.; Lee, E.-C.; Ju, H. Bimetal coated optical fiber sensors based on surface plasmon resonance induced change in birefringence and intensity. *Opt. Express* **2014**, *22*, 5590–5598. [CrossRef] [PubMed]
27. Kashif, M.; Bakar, A.A.A.; Arsad, N.; Shaari, S. Development of phase detection schemes based on surface plasmon resonance using interferometry. *Sensors* **2014**, *14*, 15914–15938. [CrossRef] [PubMed]
28. Nikitin, P.I.; Beloglazov, A.A.; Kochergin, V.E.; Valeiko, M.V.; Ksenevich, T.I. Surface plasmon resonance interferometry for biological and chemical sensing. *Sens. Actuators B Chem.* **1999**, *54*, 43–50. [CrossRef]
29. Moayyed, H.; Leite, I.; Coelho, L.; Santos, J.; Viegas, D. Analysis of a plasmonic based optical fiber optrode with phase interrogation. *Photon. Sens.* **2016**, *6*, 221–233. [CrossRef]
30. Moayyed, H.; Leite, I.; Coelho, L.; Santos, J.; Viegas, D. Phase interrogated plasmonic optical fiber optrode with bimetallic layers. In Proceedings of the International Conference on Optical Fibre Sensors (OFS24), Curitiba, Brazil, 28 September–2 October 2015; p. 96346B.
31. Moayyed, H.; Leite, I.T.; Coelho, L.; Santos, J.L.; Viegas, D. Analysis of phase interrogated SPR fiber optic sensors with bimetallic layers. *IEEE Sens. J.* **2014**, *14*, 3662–3668. [CrossRef]
32. Homola, J. On the sensitivity of surface plasmon resonance sensors with spectral interrogation. *Sens. Actuators B Chem.* **1997**, *41*, 207–211. [CrossRef]
33. Jia, P.; Yang, J. Universal sensitivity of propagating surface plasmon resonance in nanostructure arrays. *Opt. Express* **2015**, *23*, 18658–18664. [CrossRef] [PubMed]
34. Lee, K.-S.; Son, J.M.; Jeong, D.-Y.; Lee, T.S.; Kim, W.M. Resolution enhancement in surface plasmon resonance sensor based on waveguide coupled mode by combining a bimetallic approach. *Sensors* **2010**, *10*, 11390–11399. [CrossRef] [PubMed]
35. White, I.M.; Fan, X. On the performance quantification of resonant refractive index sensors. *Opt. Express* **2008**, *16*, 1020–1028. [CrossRef] [PubMed]
36. Hassani, A.; Skorobogatiy, M. Design of the microstructured optical fiber-based surface plasmon resonance sensors with enhanced microfluidics. *Opt. Express* **2006**, *14*, 11616–11621. [CrossRef] [PubMed]
37. Klantsataya, E.; François, A.; Ebendorff-Heidepriem, H.; Hoffmann, P.; Monro, T.M. Surface Plasmon Scattering in Exposed Core Optical Fiber for Enhanced Resolution Refractive Index Sensing. *Sensors* **2015**, *15*, 25090–25102. [CrossRef] [PubMed]
38. Hautakorpi, M.; Mattinen, M.; Ludvigsen, H. Surface-plasmon-resonance sensor based on three-hole microstructured optical fiber. *Opt. Express* **2008**, *16*, 8427–8432. [CrossRef] [PubMed]

39. Luan, N.; Wang, R.; Lv, W.; Yao, J. Surface plasmon resonance sensor based on D-shaped microstructured optical fiber with hollow core. *Opt. Express* **2015**, *23*, 8576–8582. [CrossRef] [PubMed]
40. Rifat, A.A.; Mahdiraji, G.A.; Chow, D.M.; Shee, Y.G.; Ahmed, R.; Adikan, F.R.M. Photonic Crystal Fiber-Based Surface Plasmon Resonance Sensor with Selective Analyte Channels and Graphene-Silver Deposited Core. *Sensors* **2015**, *15*, 11499–11510. [CrossRef] [PubMed]
41. Azzam, S.I.; Hameed, M.F.O.; Shehata, R.E.A.; Heikal, A.M.; Obayya, S.S.A. Multichannel photonic crystal fiber surface plasmon resonance based sensor. *Opt. Quantum Electron.* **2016**, *48*, 1–11. [CrossRef]
42. Luan, N.; Wang, R.; Lv, W.; Yao, J. Surface plasmon resonance sensor based on exposed-core microstructured optical fibres. *Electron. Lett.* **2015**, *51*, 714–715. [CrossRef]
43. Sciacca, B.; Francois, A.; Hoffmann, P.; Monro, T.M. Multiplexing of radiative-surface plasmon resonance for the detection of gastric cancer biomarkers in a single optical fiber. *Sens. Actuators B Chem.* **2013**, *183*, 454–458. [CrossRef]
44. Hernaez, M.; Zamarreno, C.R.; Matias, I.R.; Arregui, F.J. Optical fiber humidity sensor based on surface plasmon resonance in the infra-red region. *J. Phys. Conf. Ser.* **2009**, *178*, 012019. [CrossRef]
45. Esteban, Ó.; Naranjo, F.B.; Díaz-Herrera, N.; Valdueza-Felip, S.; Navarrete, M.-C.; González-Cano, A. High-sensitive SPR sensing with Indium Nitride as a dielectric overlay of optical fibers. *Sens. Actuators B Chem.* **2011**, *158*, 372–376. [CrossRef]
46. Iga, M.; Seki, A.; Watanabe, K. Hetero-core structured fiber optic surface plasmon resonance sensor with silver film. *Sens. Actuators B Chem.* **2004**, *101*, 368–372. [CrossRef]
47. Ahn, J.H.; Seong, T.Y.; Kim, W.M.; Lee, T.S.; Kim, I.; Lee, K.-S. Fiber-optic waveguide coupled surface plasmon resonance sensor. *Opt. Express* **2012**, *20*, 21729–21738. [CrossRef] [PubMed]
48. Lin, Y.-C. Characteristics of optical fiber refractive index sensor based on surface plasmon resonance. *Microw. Opt. Technol. Lett.* **2013**, *55*, 574–576. [CrossRef]
49. Kulchin, Y.N.; Vitrik, O.; Dyshlyuk, A. Analysis of surface plasmon resonance in bent single-mode waveguides with metal-coated cladding by eigenmode expansion method. *Opt. Express* **2014**, *22*, 22196–22201. [CrossRef] [PubMed]
50. Sciacca, B.; François, A.; Klingler-Hoffmann, M.; Brazzatti, J.; Penno, M.; Hoffmann, P.; Monro, T.M. Radiative-surface plasmon resonance for the detection of apolipoprotein E in medical diagnostics applications. *Nanomedicine* **2012**, *9*, 550–557. [CrossRef] [PubMed]
51. Francois, A.; Boehm, J.; Oh, S.Y.; Kok, T.; Monro, T.M. Collection mode surface plasmon fibre sensors: A new biosensing platform. *Biosens. Bioelectron.* **2011**, *26*, 3154–3159. [CrossRef] [PubMed]
52. Coelho, L.; de Almeida, J.M.M.M.; Santos, J.L.; Ferreira, R.A.S.; André, P.S.; Viegas, D. Sensing Structure Based on Surface Plasmon Resonance in Chemically Etched Single Mode Optical Fibres. *Plasmonics* **2015**, *10*, 319–327. [CrossRef]
53. Takagi, K.; Sasaki, H.; Seki, A.; Watanabe, K. Surface plasmon resonances of a curved hetero-core optical fiber sensor. *Sens. Actuators A Phys.* **2010**, *161*, 1–5. [CrossRef]
54. Slavık, R.; Homola, J.; Ctyroky, J. Single-mode optical fiber surface plasmon resonance sensor. *Sens. Actuators B Chem.* **1999**, *54*, 74–79. [CrossRef]
55. Slavik, R.; Homola, J.; Ctyroky, J.; Brynda, E. Novel spectral fiber optic sensor based on surface plasmon resonance. *Sens. Actuators B Chem.* **2001**, *74*, 106–111. [CrossRef]
56. Tan, Z.; Li, X.; Chen, Y.; Fan, P. Improving the Sensitivity of Fiber Surface Plasmon Resonance Sensor by Filling Liquid in a Hollow Core Photonic Crystal Fiber. *Plasmonics* **2014**, *9*, 167–173. [CrossRef]
57. Huang, T. Highly Sensitive SPR Sensor Based on D-shaped Photonic Crystal Fiber Coated with Indium Tin Oxide at Near-Infrared Wavelength. *Plasmonics* **2016**. [CrossRef]
58. Dash, J.N.; Jha, R. Highly Sensitive Side-Polished Birefringent PCF-Based SPR Sensor in near IR. *Plasmonics* **2016**, *11*, 1105. [CrossRef]
59. Liu, Z.; Wei, Y.; Zhang, Y.; Liu, C.; Zhang, Y.; Zhao, E.; Yang, J.; Liu, C.; Yuan, L. Distributed fiber surface plasmon resonance sensor based on the incident angle adjusting method. *Opt. Lett.* **2015**, *40*, 4452–4455. [CrossRef] [PubMed]
60. Satija, J.; Punjabi, N.S.; Sai, V.V.R.; Mukherji, S. Optimal Design for U-bent Fiber-optic LSPR Sensor Probes. *Plasmonics* **2014**, *9*, 251–260. [CrossRef]

61. Satija, J.; Tharion, J.; Mukherji, S. Facile synthesis of size and wavelength tunable hollow gold nanostructures for the development of a LSPR based label-free fiber-optic biosensor. *RSC Adv.* **2015**, *5*, 69970–69979. [CrossRef]
62. Verma, R.K.; Gupta, B.D. Theoretical modelling of a bi-dimensional U-shaped surface plasmon resonance based fibre optic sensor for sensitivity enhancement. *J. Phys. D Appl. Phys.* **2008**, *41*, 095106. [CrossRef]
63. Napiorkowski, M.; Urbanczyk, W. Effect of bending on surface plasmon resonance spectrum in microstructured optical fibers. *Opt. Express* **2013**, *21*, 22762–22772. [CrossRef] [PubMed]
64. Gasior, K.; Martynkien, T.; Urbanczyk, W. Effect of constructional parameters on the performance of a surface plasmon resonance sensor based on a multimode polymer optical fiber. *Appl. Opt.* **2014**, *53*, 8167–8174. [CrossRef] [PubMed]
65. Suzuki, H.; Sugimoto, M.; Matsui, Y.; Kondoh, J. Effects of gold film thickness on spectrum profile and sensitivity of a multimode-optical-fiber SPR sensor. *Sens. Actuators B Chem.* **2008**, *132*, 26–33. [CrossRef]
66. Kim, Y.-C.; Peng, W.; Banerji, S.; Booksh, K.S. Tapered fiber optic surface plasmon resonance sensor for analyses of vapor and liquid phases. *Opt. Lett.* **2005**, *30*, 2218–2220. [CrossRef] [PubMed]
67. Fontana, E.; Dulman, H.D.; Doggett, D.E.; Pantell, R.H. Surface plasmon resonance on a single mode optical fiber. *IEEE Trans. Instrum. Meas.* **1998**, *47*, 168–173. [CrossRef]
68. Jian, A.; Deng, L.; Sang, S.; Duan, Q.; Zhang, X.; Zhang, W. Surface plasmon resonance sensor based on an angled optical fiber. **2014**, *14*, 3229–3235. [CrossRef]
69. Kim, Y.-C.; Banerji, S.; Masson, J.-F.; Peng, W.; Booksh, K.S. Fiber-optic surface plasmon resonance for vapor phase analyses. *Analyst* **2005**, *130*, 838–843. [CrossRef] [PubMed]
70. Jeong, H.-H.; Erdene, N.; Lee, S.-K.; Jeong, D.-H.; Park, J.-H. Fabrication of fiber-optic localized surface plasmon resonance sensor and its application to detect antibody-antigen reaction of interferon-gamma. *Opt. Eng.* **2011**, *50*, 124405.
71. Lin, Y.; Zou, Y.; Mo, Y.; Guo, J.; Lindquist, R.G. E-beam patterned gold nanodot arrays on optical fiber tips for localized surface plasmon resonance biochemical sensing. *Sensors* **2010**, *10*, 9397–9406. [CrossRef] [PubMed]
72. Consales, M.; Ricciardi, A.; Crescitelli, A.; Esposito, E.; Cutolo, A.; Cusano, A. Lab-on-fiber technology: Toward multifunctional optical nanoprobes. *ACS Nano* **2012**, *6*, 3163–3170. [CrossRef] [PubMed]
73. Nguyen, H.; Sidiroglou, F.; Collins, S.; Davis, T.; Roberts, A.; Baxter, G. A localized surface plasmon resonance-based optical fiber sensor with sub-wavelength apertures. *Appl. Phys. Lett.* **2013**, *103*, 193116. [CrossRef]
74. Jia, P.; Yang, J. A plasmonic optical fiber patterned by template transfer as a high-performance flexible nanoprobe for real-time biosensing. *Nanoscale* **2014**, *6*, 8836–8843. [CrossRef] [PubMed]
75. Lu, Y.; Hao, C.-J.; Wu, B.-Q.; Musideke, M.; Duan, L.-C.; Wen, W.-Q.; Yao, J.-Q. Surface Plasmon Resonance Sensor Based on Polymer Photonic Crystal Fibers with Metal Nanolayers. *Sensors* **2013**, *13*, 956–965. [CrossRef] [PubMed]
76. Dhawan, A.; Gerhold, M.D.; Muth, J.F. Plasmonic structures based on subwavelength apertures for chemical and biological sensing applications. *IEEE Sens. J.* **2008**, *8*, 942–950. [CrossRef]
77. Schartner, E.P.; Tsiminis, G.; François, A.; Kostecki, R.; Warren-Smith, S.C.; Nguyen, L.V.; Heng, S.; Reynolds, T.; Klantsataya, E.; Rowland, K.J. Taming the light in microstructured optical fibers for sensing. *Int. J. Appl. Glass Sci.* **2015**, *6*, 229–239. [CrossRef]
78. Bing, P.; Yao, J.; Lu, Y.; Li, Z. A surface-plasmon-resonance sensor based on photonic-crystal-fiber with large size microfluidic channels. *Opt. Appl.* **2012**, *42*, 493–501.
79. Gauvreau, B.; Hassani, A.; Fehri, M.F.; Kabashin, A.; Skorobogatiy, M.A. Photonic bandgap fiber-based Surface Plasmon Resonance sensors. *Opt. Express* **2007**, *15*, 11413–11426. [CrossRef] [PubMed]
80. Liu, B.-H.; Jiang, Y.-X.; Zhu, X.-S.; Tang, X.-L.; Shi, Y.-W. Hollow fiber surface plasmon resonance sensor for the detection of liquid with high refractive index. *Opt. Express* **2013**, *21*, 32349–32357. [CrossRef] [PubMed]
81. Chen, P.; He, Y.-J.; Zhu, X.-S.; Shi, Y.-W. Surface Plasmon Resonance Sensor Based on Ethylene Tetra-Fluoro-Ethylene Hollow Fiber. *Sensors* **2015**, *15*, 27917–27929. [CrossRef] [PubMed]
82. Jiang, Y.-X.; Liu, B.-H.; Zhu, X.-S.; Tang, X.-L.; Shi, Y.-W. Long-range surface plasmon resonance sensor based on dielectric/silver coated hollow fiber with enhanced figure of merit. *Opt. Lett.* **2015**, *40*, 744–747. [CrossRef] [PubMed]
83. Jianjun, H.; Xiaoxia, L.; Xiujian, Z.; Chengbin, J. Fabrication silver film inside silica capillary. *J. Wuhan Univ. Technol. Mater. Sci. Ed.* **2005**, *20*, 64–67. [CrossRef]

84. Rego, G. A review of refractometric sensors based on long period fibre gratings. *Sci. World J.* **2013**, *2013*, 913418. [CrossRef] [PubMed]
85. Gu, Z.; Lan, J.; Gao, K. Characteristics of plasmon coupling mode in SPR based LPFG. In Proceedings of the 2015 International Conference on Numerical Simulation of Optoelectronic Devices (NUSOD), Taipei, Taiwan, 7–11 September 2015; pp. 55–56.
86. Schindelin, J.; Arganda-Carreras, I.; Frise, E.; Kaynig, V.; Longair, M.; Pietzsch, T.; Preibisch, S.; Rueden, C.; Saalfeld, S.; Schmid, B.; et al. Fiji: An open-source platform for biological-image analysis. *Nat. Methods* **2012**, *9*, 676–682. [CrossRef] [PubMed]
87. Kulchin, Y.N.; Vitrik, O.B.; Dyshlyuk, A.V.; Zhou, Z. Novel fiber optic refractometric method for liquid and gaseous media. *Pac. Sci. Rev.* **2012**, *14*, 23–27.
88. Kulchin, Y.N.; Vitrik, O.B.; Dyshlyuk, A.V.; Zhou, Z. Conditions for surface plasmon resonance excitation by whispering gallery modes in a bent single mode optical fiber for the development of novel refractometric sensors. *Laser Phys.* **2013**, *23*, 085105. [CrossRef]
89. Shevchenko, Y.; Francis, T.J.; Blair, D.A.; Walsh, R.; DeRosa, M.C.; Albert, J. In situ biosensing with a surface plasmon resonance fiber grating aptasensor. *Anal. Chem.* **2011**, *83*, 7027–7034. [CrossRef] [PubMed]
90. Shevchenko, Y.; Camci-Unal, G.; Cuttica, D.F.; Dokmeci, M.R.; Albert, J.; Khademhosseini, A. Surface plasmon resonance fiber sensor for real-time and label-free monitoring of cellular behavior. *Biosens. Bioelectron.* **2014**, *56*, 359–367. [CrossRef] [PubMed]
91. Jette-Charbonneau, S.; Charbonneau, R.; Lahoud, N.; Mattiussi, G.; Berini, P. Demonstration of Bragg gratings based on long ranging surface plasmon polariton waveguides. *Opt. Express* **2005**, *13*, 4674–4682. [CrossRef] [PubMed]
92. Pi, S.; Zeng, X.; Zhang, N.; Ji, D.; Chen, B.; Song, H.; Cheney, A.; Xu, Y.; Jiang, S.; Sun, D.; et al. Dielectric-Grating-Coupled Surface Plasmon Resonance From the Back Side of the Metal Film for Ultrasensitive Sensing. *IEEE Photonics J.* **2016**, *8*, 1–6.
93. Sharma, N.K. Performances of different metals in optical fibre-based surface plasmon resonance sensor. *Pramana* **2011**, *78*, 417–427. [CrossRef]
94. Mishra, S.K.; Gupta, B.D. Surface Plasmon Resonance-Based Fiber-Optic Hydrogen Gas Sensor Utilizing Indium–Tin Oxide (ITO) Thin Films. *Plasmonics* **2012**, *7*, 627–632. [CrossRef]
95. Kim, J.A.; Hwang, T.; Dugasani, S.R.; Amin, R.; Kulkarni, A.; Park, S.H.; Kim, T. Graphene based fiber optic surface plasmon resonance for bio-chemical sensor applications. *Sens. Actuators B Chem.* **2013**, *187*, 426–433. [CrossRef]
96. Raether, H. *Surface Plasmons on Smooth and Rough Surfaces and on Gratings*; Springer: Berlin, Germany, 1988.
97. Arya, K.; Su, Z.B.; Birman, J.L. Localization of the Surface Plasmon Polariton Caused by Random Roughness and its Role in Surface-Enhanced Optical Phenomena. *Phys. Rev. Lett.* **1985**, *54*, 1559–1562. [CrossRef] [PubMed]
98. Hassani, A.; Skorobogatiy, M. Design criteria for microstructured-optical-fiber-based surface-plasmon-resonance sensors. *JOSA B* **2007**, *24*, 1423–1429. [CrossRef]
99. Boehm, J.; François, A.; Ebendorff-Heidepriem, H.; Monro, T. Chemical Deposition of Silver for the Fabrication of Surface Plasmon Microstructured Optical Fibre Sensors. *Plasmonics* **2011**, *6*, 133–136. [CrossRef]
100. Monzon-Hernandez, D.; Villatoro, J.; Talavera, D.; Luna-Moreno, D. Optical-Fiber Surface-Plasmon Resonance Sensor with Multiple Resonance Peaks. *Appl. Opt.* **2004**, *43*, 1216–1220. [CrossRef] [PubMed]
101. Monzon-Hernandez, D.; Luna-Moreno, D.; Villatoro, J. Multiple-peak surface plasmon resonance optical fiber sensor for high resolution refractive index sensing. In Proceedings of the 17th International Conference on Optical Fibre Sensors, Bruges, Belgium, 23–27 May 2005.
102. Kanso, M.; Cuenot, S.; Louarn, G. Roughness effect on the SPR measurements for an optical fibre configuration: Experimental and numerical approaches. *J. Opt. A Pure Appl. Opt.* **2007**, *9*, 586. [CrossRef]
103. Moayyed, H.; Leite, I.T.; Coelho, L.; Santos, J.L.; Viegas, D. SPR sensing with bimetallic layers in optical fibers and phase interrogation. In Proceedings of the 8th Iberoamerican Optics Meeting and 11th Latin American Meeting on Optics, Lasers, and Applications, Porto, Portugal, 22–26 July 2013.
104. Sharma, A.K.; Mohr, G.J. On the performance of surface plasmon resonance based fibre optic sensor with different bimetallic nanoparticle alloy combinations. *J. Phys. D Appl. Phys.* **2008**, *41*, 055106. [CrossRef]
105. Downes, F.; Taylor, C.M. Optical Fibre Surface Plasmon Resonance Sensor Based on a Palladium-Yttrium Alloy. *Proc. Eng.* **2015**, *120*, 602–605. [CrossRef]

106. Jha, R.; Verma, R.K.; Gupta, B. Surface plasmon resonance-based tapered fiber optic sensor: Sensitivity enhancement by introducing a Teflon layer between core and metal layer. *Plasmonics* **2008**, *3*, 151–156. [CrossRef]
107. Perrotton, C.; Javahiraly, N.; Slaman, M.; Dam, B.; Meyrueis, P. Fiber optic surface plasmon resonance sensor based on wavelength modulation for hydrogen sensing. *Opt. Express* **2011**, *19*, A1175–A1183. [CrossRef] [PubMed]
108. Sharma, A.K.; Gupta, B.D. Fibre optic sensor based on long-range surface plasmon resonance: A theoretical analysis. *J. Opt. A Pure Appl. Opt.* **2007**, *9*, 682. [CrossRef]
109. Chen, Y.; Zheng, R.; Lu, Y.; Wang, P.; Ming, H. Fiber-optic surface plasmon resonant sensor with low-index anti-oxidation coating. *Chin. Opt. Lett.* **2011**, *9*, 100605. [CrossRef]
110. Ortega-Mendoza, J.G.; Padilla-Vivanco, A.; Toxqui-Quitl, C.; Zaca-Morán, P.; Villegas-Hernández, D.; Chávez, F. Optical fiber sensor based on localized surface plasmon resonance using silver nanoparticles photodeposited on the optical fiber end. *Sensors* **2014**, *14*, 18701–18710. [CrossRef] [PubMed]
111. Chen, J.; Shi, S.; Su, R.; Qi, W.; Huang, R.; Wang, M.; Wang, L.; He, Z. Optimization and Application of Reflective LSPR Optical Fiber Biosensors Based on Silver Nanoparticles. *Sensors* **2015**, *15*, 12205–12217. [CrossRef] [PubMed]
112. Tu, M.H.; Sun, T.; Grattan, K.T.V. LSPR optical fibre sensors based on hollow gold nanostructures. *Sens. Actuators B Chem.* **2014**, *191*, 37–44. [CrossRef]
113. He, Y.J. Novel D-shape LSPR fiber sensor based on nano-metal strips. *Opt. Express* **2013**, *21*, 23498–23510. [CrossRef] [PubMed]
114. He, Y.J. High-performance LSPR fiber sensor based on nanometal rings. *IEEE Photonics J.* **2014**, *6*, 1–11. [CrossRef]
115. Fan, M.; Andrade, G.F.; Brolo, A.G. A review on the fabrication of substrates for surface enhanced Raman spectroscopy and their applications in analytical chemistry. *Anal. Chim. Acta* **2011**, *693*, 7–25. [CrossRef] [PubMed]
116. Haes, A.; Duyne, R. A unified view of propagating and localized surface plasmon resonance biosensors. *Anal. Bioanal. Chem.* **2004**, *379*, 920–930. [CrossRef] [PubMed]
117. Otte, M.A.; Sepulveda, B.; Ni, W.; Juste, J.P.; Liz-Marzán, L.M.; Lechuga, L.M. Identification of the optimal spectral region for plasmonic and nanoplasmonic sensing. *ACS Nano* **2009**, *4*, 349–357. [CrossRef] [PubMed]
118. Hutter, E.; Fendler, J.H. Exploitation of Localized Surface Plasmon Resonance. *Adv. Mater.* **2004**, *16*, 1685–1706. [CrossRef]
119. Chiang, H.-P.; Leung, P.; Tse, W. The surface plasmon enhancement effect on adsorbed molecules at elevated temperatures. *J. Chem. Phys.* **1998**, *108*, 2659–2660. [CrossRef]
120. Ghosh, G.; Endo, M.; Iwasaki, T. Temperature-dependent Sellmeier coefficients and chromatic dispersions for some optical fiber glasses. *J. Lightw. Technol.* **1994**, *12*, 1338–1342. [CrossRef]
121. Peng, Y.; Hou, J.; Huang, Z.; Lu, Q. Temperature sensor based on surface plasmon resonance within selectively coated photonic crystal fiber. *Appl. Opt.* **2012**, *51*, 6361–6367. [CrossRef] [PubMed]
122. Sharma, A.K.; Gupta, B.D. Theoretical model of a fiber optic remote sensor based on surface plasmon resonance for temperature detection. *Opt. Fiber Technol.* **2006**, *12*, 87–100. [CrossRef]
123. Sharma, A.K.; Pattanaik, H.S.; Mohr, G.J. On the temperature sensing capability of a fibre optic SPR mechanism based on bimetallic alloy nanoparticles. *J. Phys. D Appl. Phys.* **2009**, *42*, 045104. [CrossRef]
124. Zhao, Y.; Deng, Z.Q.; Hu, H.F. Fiber-Optic SPR Sensor for Temperature Measurement. *IEEE Trans. Instrum. Meas.* **2015**, *64*, 3099–3104. [CrossRef]
125. Mi, H.; Wang, Y.; Jin, P.; Lei, L. Design of a ultrahigh-sensitivity SPR-based optical fiber pressure sensor. *Optik* **2013**, *124*, 5248–5250. [CrossRef]
126. Duarte, D.P.; Alberto, N.; Bilro, L.; Nogueira, R. Theoretical Design of a High Sensitivity SPR-Based Optical Fiber Pressure Sensor. *J. Lightw. Technol.* **2015**, *33*, 4606–4611. [CrossRef]
127. Rivero, P.J.; Urrutia, A.; Goicoechea, J.; Arregui, F. Optical fiber humidity sensors based on Localized Surface Plasmon Resonance (LSPR) and Lossy-mode resonance (LMR) in overlays loaded with silver nanoparticles. *Sens. Actuators B Chem.* **2012**, *173*, 244–249. [CrossRef]
128. Esmaeilzadeh, H.; Rivard, M.; Arzi, E.; Légaré, F.; Hassani, A. Smart textile plasmonic fiber dew sensors. *Opt. Express* **2015**, *23*, 14981–14992. [CrossRef] [PubMed]

129. Verma, R.; Gupta, B.D. Detection of heavy metal ions in contaminated water by surface plasmon resonance based optical fibre sensor using conducting polymer and chitosan. *Food Chem.* **2015**, *166*, 568–575. [CrossRef] [PubMed]
130. Bhatia, P.; Yadav, P.; Gupta, B.D. Surface plasmon resonance based fiber optic hydrogen peroxide sensor using polymer embedded nanoparticles. *Sens. Actuators B Chem.* **2013**, *182*, 330–335. [CrossRef]
131. Díaz-Herrera, N.; Esteban, O.; Navarrete, M.; Le Haitre, M.; González-Cano, A. In situ salinity measurements in seawater with a fibre-optic probe. *Meas. Sci. Technol.* **2006**, *17*, 2227. [CrossRef]
132. Saikia, R.; Buragohain, M.; Datta, P.; Nath, P.; Barua, K. Fiber-Optic pH Sensor Based on SPR of Silver Nanostructured Film. In Proceedings of the International Conference on Transport and Optical Properties of Nanomaterials, Allahabad, India, 5–8 January 2009; Volume 1147, pp. 249–255.
133. Socorro, A.B.; Rivero, P.J.; Hernaez, M.; Goicoechea, J.; Matias, I.R.; Arregui, F.J. Optical fiber pH sensor based on gold nanoparticles into polymeric coatings. In Proceedings of the Smart Sensors, Actuators, and MEMS VII; and Cyber Physical Systems, Barcelona, Spain, 4–6 May 2015.
134. Pathak, A.; Mishra, S.K.; Gupta, B.D. Ag/SnO_2 based SPR fibre optic sensor for the detection of ammonia (NH3) gas. In Proceedings of the International Conference on Fibre Optics and Photonics, Kharagpur, India, 13–16 December 2014.
135. Usha, S.P.; Mishra, S.K.; Gupta, B.D. Fabrication and characterization of a SPR based fiber optic sensor for the detection of chlorine gas using silver and zinc oxide. *Materials* **2015**, *8*, 2204–2216. [CrossRef]
136. Perrotton, C.; Westerwaal, R.J.; Javahiraly, N.; Slaman, M.; Schreuders, H.; Dam, B.; Meyrueis, P. A reliable, sensitive and fast optical fiber hydrogen sensor based on surface plasmon resonance. *Opt. Express* **2013**, *21*, 382–390. [CrossRef] [PubMed]
137. Mishra, S.K.; Rani, S.; Gupta, B.D. Surface plasmon resonance based fiber optic hydrogen sulphide gas sensor utilizing nickel oxide doped ITO thin film. *Sens. Actuators B Chem.* **2014**, *195*, 215–222. [CrossRef]
138. Mauriz, E.; García-Fernández, M.; Lechuga, L. Towards the design of universal immunosurfaces for SPR-based assays: A review. *TrAC Trends Anal. Chem.* **2016**, *79*, 191–198. [CrossRef]
139. Bai, Y.; Zhao, R.; Feng, F.; He, X. Determination of Lysozyme by Thiol-Terminated Aptamer Based Surface Plasmon Resonance. *Anal. Lett.* **2016**. accepted. [CrossRef]
140. Zhao, X.; Tsao, Y.-C.; Lee, F.-J.; Tsai, W.-H.; Wang, C.-H.; Chuang, T.-L.; Wu, M.-S.; Lin, C.-W. Optical fiber sensor based on surface plasmon resonance for rapid detection of avian influenza virus subtype H6: Initial studies. *J. Virol. Methods* **2016**, *233*, 15–22. [CrossRef] [PubMed]
141. Daems, D.; Knez, K.; Delport, F.; Spasic, D.; Lammertyn, J. Real-time PCR melting analysis with fiber optic SPR enables multiplex DNA identification of bacteria. *Analyst* **2016**, *141*, 1906–1911. [CrossRef] [PubMed]
142. Srivastava, S.K.; Verma, R.; Gupta, B.D.; Khalaila, I.; Abdulhalim, I. SPR Based Fiber Optic Sensor for the Detection of Vitellogenin: An Endocrine Disruption Biomarker in Aquatic Environments. *Biosens. J.* **2015**, *4*, 114. [CrossRef]
143. Jang, H.S.; Park, K.N.; Kang, C.D.; Kim, J.P.; Sim, S.J.; Lee, K.S. Optical fiber SPR biosensor with sandwich assay for the detection of prostate specific antigen. *Opt. Commun.* **2009**, *282*, 2827–2830. [CrossRef]
144. Coelho, L.; Queirós, R.; Santos, J.; Martins, M.C.L.; Viegas, D.; Jorge, P. DNA-Aptamer optical biosensors based on a LPG-SPR optical fiber platform for point-of-care diagnostic. In Proceedings of the Plasmonics in Biology and Medicine XI, San Francisco, CA, USA, 1–2 February 2014.
145. Pollet, J.; Delport, F.; Janssen, K.P.F.; Jans, K.; Maes, G.; Pfeiffer, H.; Wevers, M.; Lammertyn, J. Fiber optic SPR biosensing of DNA hybridization and DNA-protein interactions. *Biosens. Bioelectron.* **2009**, *25*, 864–869. [CrossRef] [PubMed]
146. Singh, S.; Mishra, S.K.; Gupta, B.D. SPR based fibre optic biosensor for phenolic compounds using immobilization of tyrosinase in polyacrylamide gel. *Sens. Actuators B Chem.* **2013**, *186*, 388–395. [CrossRef]
147. Slavık, R.; Homola, J.; Brynda, E. A miniature fiber optic surface plasmon resonance sensor for fast detection of staphylococcal enterotoxin B. *Biosens. Bioelectron.* **2002**, *17*, 591–595. [CrossRef]
148. Pollet, J.; Delport, F.; Janssen, K.; Tran, D.; Wouters, J.; Verbiest, T.; Lammertyn, J. Fast and accurate peanut allergen detection with nanobead enhanced optical fiber SPR biosensor. *Talanta* **2011**, *83*, 1436–1441. [CrossRef] [PubMed]
149. Li, M.; Cushing, S.K.; Wu, N. Plasmon-enhanced optical sensors: A review. *Analyst* **2015**, *140*, 386–406. [CrossRef] [PubMed]

150. Baaske, M.D.; Foreman, M.R.; Vollmer, F. Single-molecule nucleic acid interactions monitored on a label-free microcavity biosensor platform. *Nat. Nanotechnol.* **2014**, *9*, 933–939. [CrossRef] [PubMed]
151. Wink, T.; Van Zuilen, S.; Bult, A.; Van Bennekom, W. Self-assembled monolayers for biosensors. *Analyst* **1997**, *122*, 43R–50R. [CrossRef] [PubMed]
152. Benhabbour, S.R.; Sheardown, H.; Adronov, A. Protein resistance of PEG-functionalized dendronized surfaces: Effect of PEG molecular weight and dendron generation. *Macromolecules* **2008**, *41*, 4817–4823. [CrossRef]
153. Shao, Y.; Xu, S.; Zheng, X.; Wang, Y.; Xu, W. Optical fiber LSPR biosensor prepared by gold nanoparticle assembly on polyelectrolyte multilayer. *Sensors* **2010**, *10*, 3585–3596. [CrossRef] [PubMed]
154. Caucheteur, C.; Voisin, V.; Albert, J. Near-infrared grating-assisted SPR optical fiber sensors: Design rules for ultimate refractometric sensitivity. *Opt. Express* **2015**, *23*, 2918–2932. [CrossRef] [PubMed]
155. Caucheteur, C.; Shevchenko, Y.; Shao, L.-Y.; Wuilpart, M.; Albert, J. High resolution interrogation of tilted fiber grating SPR sensors from polarization properties measurement. *Opt. Express* **2011**, *19*, 1656–1664. [CrossRef] [PubMed]
156. Chiu, M.-H.; Wang, S.-F.; Chang, R.-S. D-type fiber biosensor based on surface-plasmon resonance technology and heterodyne interferometry. *Opt. Lett.* **2005**, *30*, 233–235. [CrossRef] [PubMed]
157. Wang, S.-F.; Chiu, M.-H.; Chang, R.-S. Numerical simulation of a D-type optical fiber sensor based on the Kretchmann's configuration and heterodyne interferometry. *Sens. Actuators B Chem.* **2006**, *114*, 120–126. [CrossRef]
158. Leosson, K.; Nikolajsen, T.; Boltasseva, A.; Bozhevolnyi, S.I. Long-range surface plasmon polariton nanowire waveguides for device applications. *Opt. Express* **2006**, *14*, 314–319. [CrossRef] [PubMed]
159. Berini, P. Long-range surface plasmon polaritons. *Adv. Opt. Photonics* **2009**, *1*, 484–588. [CrossRef]
160. Slavík, R.; Homola, J. Ultrahigh resolution long range surface plasmon-based sensor. *Sens. Actuators B Chem.* **2007**, *123*, 10–12. [CrossRef]



© 2016 by the authors; licensee MDPI, Basel, Switzerland. This article is an open access article distributed under the terms and conditions of the Creative Commons Attribution (CC-BY) license (http://creativecommons.org/licenses/by/4.0/).

BIBLIOGRAPHY

[1] Tuan Vo-Dinh. *BioMEMS and Biomedical Nanotechnology, Volume IV: Biomolecular Sensing, Processing and Analysis*, volume 4, chapter Biosensors and Biochips. Springer US, 2007.

[2] F. Scheller and F. Schubert. *Biosensors*. Techniques and Instrumentation in Analytical Chemistry. Elsevier Science, 1991. ISBN 9780080875590. URL http://books.google.com.au/books?id=TF7AW4kSY1gC.

[3] Rakesh Yadav, Sadhana Dwivedi, Sandeep Kumar, and Ashok Chaudhury. Trends and perspectives of biosensors for food and environmental virology. *Food and Environmental Virology*, 2:53–63, 2010. ISSN 1867-0334. doi: 10.1007/s12560-010-9034-5. URL http://dx.doi.org/10.1007/s12560-010-9034-5.

[4] Jiří Homola. *Surface Plasmon Resonance Based Sensors*. Springer series on chemical sensors and biosensors. Springer, 2006. ISBN 9783540339199. URL http://books.google.com.au/books?id=Lhd_JVZW7D0C.

[5] James P Chambers, Bernard P Arulanandam, Leann L Matta, Alex Weis, and James J Valdes. Biosensor recognition elements. Technical report, DTIC Document, 2008.

[6] Rastislav Monošík, Miroslav Streďanskỳ, and Ernest Šturdík. Biosensors-classification, characterization and new trends. *Acta Chimica Slovaca*, 5(1):109–120, 2012.

[7] Bruce Alberts, Alexander Johnson, Julian Lewis, Martin Raff, Keith Roberts, and Peter Walter. *Molecular Biology of the Cell*. Garland Science, New York, 4 edition, 2002.

[8] Rebecca L. Caygill, G. Eric Blair, and Paul A. Millner. A review on viral biosensors to detect human pathogens. *Analytica Chimica Acta*, 681(1-2):8 – 15, 2010. ISSN 0003-2670. doi: 10.1016/j.aca.2010.09.038. URL http://www.sciencedirect.com/science/article/pii/S0003267010012195.

[9] Jose I. Reyes De Corcuera and Ralph P. Cavalieri. Biosensors. Technical report, Washington State University, Pullman, Washington, U.S.A., 2003.

[10] Vijayalakshmi Velusamy, Khalil Arshak, Olga Korostynska, Kamila Oliwa, and Catherine Adley. An overview of foodborne pathogen detection: In the perspective of biosensors. *Biotechnology advances*, 28(2):232–254, 2010.

[11] Adam K Wanekaya, Wilfred Chen, Nosang V Myung, and Ashok Mulchandani. Nanowire-based electrochemical biosensors. *Electroanalysis*, 18 (6):533–550, 2006.

[12] Kerstin Lange, BastianE. Rapp, and Michael Rapp. Surface acoustic wave biosensors: a review. *Analytical and Bioanalytical Chemistry*, 391:1509–1519, 2008. ISSN 1618-2642. doi: 10.1007/s00216-008-1911-5. URL http://dx.doi.org/10.1007/s00216-008-1911-5.

[13] Koutilya R. Buchapudi, Xin Huang, Xin Yang, Hai-Feng Ji, and Thomas Thundat. Microcantilever biosensors for chemicals and bioorganisms. *Analyst*, 136:1539–1556, 2011. doi: 10.1039/C0AN01007C. URL http://dx.doi.org/10.1039/C0AN01007C.

[14] Nardo Ramírez Frómeta. Cantilever biosensors. *Biotecnología Aplicada*, 23(4): 320–323, 2006.

[15] Jonathan Boehm. Surface plasmon resonance fibre sensing. Honors Thesis, Chemistry and Physics, The University of Adeleaide, November 2009.

[16] F. Li, C. Gooneratne, and J. Kosel. Magnetic biosensor system to detect biological targets. In *Electromagnetics in Advanced Applications (ICEAA), 2012 International Conference on*, pages 1238–1241, 2012. doi: 10.1109/ICEAA.2012.6328816.

[17] Pankaj Vadgama and Paul W. Crump. Biosensors: recent trends. a review. *Analyst*, 117:1657–1670, 1992. doi: 10.1039/AN9921701657. URL http://dx.doi.org/10.1039/AN9921701657.

[18] María Espinosa Bosch, Antonio Jesús Ruiz Sánchez, Fuensanta Sánchez Rojas, and Catalina Bosch Ojeda. Recent development in optical fiber biosensors. *Sensors (Peterboroug*, 7(6):797–859, 2007. URL http://www.mdpi.com/1424-8220/7/6/797/.

[19] Jun-Jie Zhu and Jingjing Li. Quantum dot for fluorescent biosensing and bioimaging applications. *Analyst*, pages –, 2013. doi: 10.1039/C3AN36705C. URL http://dx.doi.org/10.1039/C3AN36705C.

[20] Anne-Isabelle Henry, Bhavya Sharma, M. Fernanda Cardinal, Dmitry Kurouski, and Richard P. Van Duyne. Surface-enhanced raman spectroscopy biosensing: In vivo diagnostics and multimodal imaging. *Analytical Chemistry*, 88(13):6638–6647, 2016. doi: 10.1021/acs.analchem.6b01597. URL http://dx.doi.org/10.1021/acs.analchem.6b01597. PMID: 27268724.

[21] Ioan Notingher. Raman spectroscopy cell-based biosensors. *Sensors*, 7(8):1343–1358, 2007. ISSN 1424-8220. doi: 10.3390/s7081343. URL http://www.mdpi.com/1424-8220/7/8/1343.

[22] John R Ferraro. *Introductory raman spectroscopy*. Academic press, 2003.

[23] Jing Neng, Mark H. Harpster, William C. Wilson, and Patrick A. Johnson. Surface-enhanced raman scattering (sers) detection of multiple viral antigens using magnetic capture of sers-active nanoparticles. *Biosensors and Bioelectronics*, 41(0):316 – 321, 2013. ISSN 0956-5663. doi: 10.1016/j.bios.2012.08.048. URL http://www.sciencedirect.com/science/article/pii/S0956566312005726.

[24] Byeong Ha Lee, Young Ho Kim, Kwan Seob Park, Joo Beom Eom, Myoung Jin Kim, Byung Sup Rho, and Hae Young Choi. Interferometric fiber optic sensors. *Sensors*, 12(3):2467–2486, 2012.

[25] Norbert Neumann, Martin Ebermann, Steffen Kurth, and Karla Hiller. Tunable infrared detector with integrated micromachined fabry-perot filter. *Journal of Micro/Nanolithography, MEMS, and MOEMS*, 7(2):021004–021004, 2008.

[26] TM Libish, MC BobbyY, CL Linslal, S Mathew, C Ppadeep, S Indu, Palas Biswas, S Bandyopadhyay, Kamal Dasgupta, VPN Nampoori, et al. Etched and dna coated fiber bragg grating based bio-sensor for protein concentration measurement. *Optoelectronics and Advanced Materials-Rapid Ccommunications*, 9 (11-12):1401–1405, 2015.

[27] Alexandre François and Michael Himmelhaus. Optical biosensor based on whispering gallery mode excitations in clusters of microparticles. *Applied Physics Letters*, 92(14):141107, 2008. doi: 10.1063/1.2907491. URL `http://link.aip.org/link/?APL/92/141107/1`.

[28] Jason M. Gamba. *The role of transport phenomena in whispering gallery mode optical biosensor performance*. PhD thesis, California Institute of Technology, 2011.

[29] VR Dantham, S Holler, V Kolchenko, Z Wan, and S Arnold. Taking whispering gallery-mode single virus detection and sizing to the limit. *Applied Physics Letters*, 101(4):043704–043704, 2012.

[30] SI Shopova, R Rajmangal, S Holler, and S Arnold. Plasmonic enhancement of a whispering-gallery-mode biosensor for single nanoparticle detection. *Applied Physics Letters*, 98(24):243104–243104, 2011.

[31] Xudong Fan, Ian M White, Hongying Zhu, Jonanthan D Suter, and Hesam Oveys. Overview of novel integrated optical ring resonator bio/chemical sensors. In *Lasers and Applications in Science and Engineering*, pages 64520M–64520M. International Society for Optics and Photonics, 2007.

[32] R.B.M. Schasfoort and A.J. Tudos. *Handbook Of Surface Plasmon Resonance*. Royal Society of Chemistry, 2008. ISBN 9780854042678. URL `http://books.google.com.au/books?id=4T7ghXW3HUQC`.

[33] Edy Wijaya, Cedric Lenaerts, Sophie Maricot, Juriy Hastanin, Serge Habraken, Jean-Pierre Vilcot, Rabah Boukherroub, and Sabine Szunerits. Surface plasmon resonance-based biosensors: From the development of different {SPR} structures to novel surface functionalization strategies. *Current Opinion in Solid State and Materials Science*, 15(5):208 – 224, 2011. ISSN 1359-0286. doi: http://dx.doi.org/10.1016/j.cossms.2011.05.001. URL `http://www.sciencedirect.com/science/article/pii/S1359028611000325`.

[34] Stephen Arnold and SI Shopova. Whispering gallery mode biosensor. In *Biophotonics: Spectroscopy, Imaging, Sensing, and Manipulation*, pages 237–259. Springer, 2011.

[35] Paul E Sheehan and Lloyd J Whitman. Detection limits for nanoscale biosensors. *Nano letters*, 5(4):803–807, 2005.

[36] Marta Bally, Moritz Graule, Francisco Parra, Göran Larson, and Fredrik Höök. A virus biosensor with single virus-particle sensitivity based on fluorescent vesicle labels and equilibrium fluctuation analysis. *Biointerphases*, 8(1):4, 2013.

[37] Stephen Christopher Warren-Smith. *Fluorescence-Based Chemical Sensing Using Suspended-Core Microstructured Optical Fibres*. PhD thesis, The University of Adeleaide, Faculty of Science School of Chemistry and Physics, October 2010.

[38] Natalya V. Zaytseva, Richard A. Montagna, and Antje J. Baeumner. Microfluidic biosensor for the serotype-specific detection of dengue virus rna. *Analytical Chemistry*, 77(23):7520–7527, 2005. doi: 10.1021/ac0509206. URL http://pubs.acs.org/doi/abs/10.1021/ac0509206.

[39] Zhengtao Deng, Yun Zhang, Jiachang Yue, Fangqiong Tang, and Qun Wei. Green and orange cdte quantum dots as effective ph-sensitive fluorescent probes for dual simultaneous and independent detection of viruses. *The Journal of Physical Chemistry B*, 111(41):12024–12031, 2007. doi: 10.1021/jp074609z. URL http://pubs.acs.org/doi/abs/10.1021/jp074609z.

[40] Stanley J Goldsmith. Radioimmunoassay: Review of basic principles. In *Seminars in nuclear medicine*, volume 5, pages 125–152. Elsevier, 1975.

[41] Ronghui Wang, Yanbin Li, Xiaole Mao, T. Huang, and Huaguang Lu. Magnetic bio-nanobeads and nanoelectrode based impedance biosensor for detection of avian influenza virus. In *Nano/Molecular Medicine and Engineering (NANOMED), 2010 IEEE 4th International Conference on*, pages 214–217, 2010. doi: 10.1109/NANOMED.2010.5749837.

[42] Matthew Cooper. *Label-free biosensors: techniques and applications*. Cambridge University Press, 2009.

[43] Jiří Homola. Present and future of surface plasmon resonance biosensors. *Analytical and Bioanalytical Chemistry*, 377:528–539, 2003. ISSN 1618-2642. doi: 10.1007/s00216-003-2101-0. URL http://dx.doi.org/10.1007/s00216-003-2101-0.

[44] A. François, J. Boehm, S.Y. Oh, T. Kok, and T.M. Monro. Collection mode surface plasmon fibre sensors: A new biosensing platform. *Biosensors and Bioelectronics*, 26(7):3154 – 3159, 2011. ISSN 0956-5663. doi: 10.1016/j.bios.2010.12.018. URL http://www.sciencedirect.com/science/article/pii/S0956566310008377.

[45] Patrick Englebienne, Anne Van Hoonacker, and Michel Verhas. Surface plasmon resonance: principles, methods and applications in biomedical sciences. *Spectroscopy*, 17(2-3):255–273, 2003.

[46] J. Homola et al. Surface plasmon resonance sensors for detection of chemical and biological species. *Chemical reviews*, 108(2):462, 2008.

[47] Katherine A Willets and Richard P Van Duyne. Localized surface plasmon resonance spectroscopy and sensing. *Annu. Rev. Phys. Chem.*, 58:267–297, 2007.

[48] Z. Hlavenkova and J. Homola. Comparative surface plasmon spectroscopy for characterisation of thin films. *Electronics Letters*, 44(18):1085–1086, 2008. ISSN 0013-5194. doi: 10.1049/el:20081959.

[49] Anthony G. Frutos, Stephen C. Weibel, and Robert M. Corn. Near-infrared surface plasmon resonance measurements of ultrathin films. 2. fourier transform spr spectroscopy. *Analytical Chemistry*, 71(18):3935–3940, 1999. doi: 10.1021/ac9905165. URL http://pubs.acs.org/doi/abs/10.1021/ac9905165.

[50] Stefan Enoch and Nicolas Bonod. *Plasmonics: from basics to advanced topics*, volume 167. Springer, 2012.

[51] H. Raether. *Surface plasmons on smooth and rough surfaces and on gratings*. Number v. 111 in Springer tracts in modern physics. Springer, 1988. ISBN 9783540173632. URL http://books.google.com.au/books?id=ZLwrAAAAYAAJ.

[52] A. Sommerfeld. Ueber die fortpflanzung elektrodynamischer wellen längs eines drahtes. *Annalen der Physik*, 303(2):233–290, 1899. ISSN 1521-3889. doi: 10.1002/andp.18993030202. URL http://dx.doi.org/10.1002/andp.18993030202.

[53] RW Wood. On a remarkable case of uneven distribution of light in a diffraction grating spectrum. *The London, Edinburgh, and Dublin Philosophical Magazine and Journal of Science*, 4(21):396–402, 1902.

[54] RW Wood. Diffraction gratings with controlled groove form and abnormal distribution of intensity. *The London, Edinburgh, and Dublin Philosophical Magazine and Journal of Science*, 23(134):310–317, 1912.

[55] David Pines and David Bohm. A collective description of electron interactions: Ii. collective vs individual particle aspects of the interactions. *Physical Review*, 85(2):338, 1952.

[56] Lewi Tonks and Irving Langmuir. Oscillations in ionized gases. *Physical Review*, 33(2):195, 1929.

[57] Gerhard Ruthemann. Elektronenbremsung an röntgenniveaus. *Annalen der Physik*, 437(3-4):135–146, 1948. ISSN 1521-3889. doi: 10.1002/andp.19484370303. URL http://dx.doi.org/10.1002/andp.19484370303.

[58] RH Ritchie. Plasma losses by fast electrons in thin films. *Physical Review*, 106 (5):874, 1957.

[59] Erwin Kretschmann and Heinz Raether. Radiative decay of non radiative surface plasmons excited by light. *Zeitschrift für Naturforschung A*, 23(12):2135–2136, 1968.

[60] Andreas Otto. Excitation of nonradiative surface plasma waves in silver by the method of frustrated total reflection. *Zeitschrift fur Physik*, 216(4):398–410, 1968.

[61] I Pockrand, JD Swalen, JG Gordon, and MR Philpott. Surface plasmon spectroscopy of organic monolayer assemblies. *Surface Science*, 74(1):237–244, 1978.

[62] KA Peterlinz and R Georgiadis. Two-color approach for determination of thickness and dielectric constant of thin films using surface plasmon resonance spectroscopy. *Optics Communications*, 130(4):260–266, 1996.

[63] L-M Zhang and Deepak Uttamchandani. Optical chemical sensing employing surface plasmon resonance. *Electronics Letters*, 24(23):1469–1470, 1988.

[64] B Liedberg, I Lundström, and E Stenberg. Principles of biosensing with an extended coupling matrix and surface plasmon resonance. *Sensors and Actuators B: Chemical*, 11(1):63–72, 1993.

[65] D.C. Cullen, R.G.W. Brown, and C.R. Lowe. Detection of immuno-complex formation via surface plasmon resonance on gold-coated diffraction gratings. *Biosensors*, 3(4):211–225, 1988.

[66] Ch Striebel, Andreas Brecht, and Günter Gauglitz. Characterization of biomembranes by spectral ellipsometry, surface plasmon resonance and interferometry with regard to biosensor application. *Biosensors and Bioelectronics*, 9(2): 139–146, 1994.

[67] Charles Kittel. *Introduction to solid state physics*. Wiley, 2005.

[68] S.A. Maier. *Plasmonics: Fundamentals and Applications*. Springer, 2007. ISBN 9780387378251. URL http://books.google.com.au/books?id=yT2ux7TmDc8C.

[69] E. Hutter and J.H. Fendler. Exploitation of localized surface plasmon resonance. *Advanced Materials*, 16(19):1685–1706, 2004. ISSN 1521-4095. doi: 10.1002/adma.200400271. URL http://dx.doi.org/10.1002/adma.200400271.

[70] AmandaJ. Haes and RichardP. Duyne. A unified view of propagating and localized surface plasmon resonance biosensors. *Analytical and Bioanalytical Chemistry*, 379:920–930, 2004. ISSN 1618-2642. doi: 10.1007/s00216-004-2708-9. URL http://dx.doi.org/10.1007/s00216-004-2708-9.

[71] N.W. Ashcroft and N.D. Mermin. *Solid State Physics*. HRW international editions. Holt, Rinehart and Winston, 1976. ISBN 9780030839931. URL https://books.google.com.au/books?id=oXIfAQAAMAAJ.

[72] B.E.A. Saleh and M.C. Teich. *Fundamentals of Photonics*. Wiley Series in Pure and Applied Optics. John Wiley & Sons, 2007. ISBN 9780471358329. URL http://books.google.com.au/books?id=Ve8eAQAAIAAJ.

[73] Aleksandar D Rakić, Aleksandra B Djurišić, Jovan M Elazar, and Marian L Majewski. Optical properties of metallic films for vertical-cavity optoelectronic devices. *Applied optics*, 37(22):5271–5283, 1998.

[74] Pierre Berini. Long-range surface plasmon polaritons. *Advances in Optics and Photonics*, 1(3):484–588, 2009.

[75] Pierre Berini and Israel De Leon. Surface plasmon-polariton amplifiers and lasers. *Nat Photon*, 6(1):16–24, 01 2012. URL http://dx.doi.org/10.1038/nphoton.2011.285.

[76] Jae Heon Ahn, Tae Yeon Seong, Won Mok Kim, Taek Sung Lee, Inho Kim, and Kyeong-Seok Lee. Fiber-optic waveguide coupled surface plasmon resonance sensor. *Opt. Express*, 20(19):21729–21738, Sep 2012. doi: 10.1364/OE.20.021729. URL http://www.opticsexpress.org/abstract.cfm?URI=oe-20-19-21729.

[77] Noha H. Anous and Diaa A. Khalil. Performance evaluation of a metal–insulator–metal surface plasmon resonance optical gas sensor under the effect of gaussian beams. *Appl. Opt.*, 53(11):2515–2522, Apr 2014. doi: 10.1364/AO.53.002515. URL http://ao.osa.org/abstract.cfm?URI=ao-53-11-2515.

[78] J. A. Dionne, L. A. Sweatlock, H. A. Atwater, and A. Polman. Plasmon slot waveguides: Towards chip-scale propagation with subwavelength-scale localization. *Phys. Rev. B*, 73:035407, Jan 2006. doi: 10.1103/PhysRevB.73.035407. URL http://link.aps.org/doi/10.1103/PhysRevB.73.035407.

[79] M. Tamura and H. Kagata. Analysis of plasmon excited by metal-insulator-metal structure with insulator thickness of hundreds of nanometers. In *Microwave Symposium Digest (MTT), 2010 IEEE MTT-S International*, pages 356–359, May 2010. doi: 10.1109/MWSYM.2010.5515132.

[80] A. Benabbas, V. Halté, and J.-Y. Bigot. Analytical model of the optical response of periodically structured metallic films. *Opt. Express*, 13(22):8730–8745, Oct 2005. doi: 10.1364/OPEX.13.008730. URL http://www.opticsexpress.org/abstract.cfm?URI=oe-13-22-8730.

[81] Jiří Homola, Ivo Koudela, and Sinclair S. Yee. Surface plasmon resonance sensors based on diffraction gratings and prism couplers: sensitivity comparison. *Sensors and Actuators B: Chemical*, 54(1-2):16 – 24, 1999. ISSN 0925-4005. doi: 10.1016/S0925-4005(98)00322-0. URL http://www.sciencedirect.com/science/article/pii/S0925400598003220.

[82] A. Bouhelier and G. P. Wiederrecht. Excitation of broadband surface plasmon polaritons: Plasmonic continuum spectroscopy. *Phys. Rev. B*, 71:195406, May 2005. doi: 10.1103/PhysRevB.71.195406. URL http://link.aps.org/doi/10.1103/PhysRevB.71.195406.

[83] Alexandre Bouhelier and Lukas Novotny. Near-field optical excitation and detection of surface plasmons. In *Surface Plasmon Nanophotonics*, pages 139–153. Springer, 2007.

[84] Muhammad Kashif, Ahmad Ashrif A Bakar, Norhana Arsad, and Sahbudin Shaari. Development of phase detection schemes based on surface plasmon resonance using interferometry. *Sensors*, 14(9):15914–15938, 2014.

[85] SG Nelson, Kyle S Johnston, and Sinclair S Yee. High sensitivity surface plasmon resonace sensor based on phase detection. *Sensors and Actuators B: Chemical*, 35(1):187–191, 1996.

[86] P.I. Nikitin, A.A. Beloglazov, V.E. Kochergin, M.V. Valeiko, and T.I. Ksenevich. Surface plasmon resonance interferometry for biological and chemical sensing. *Sensors and Actuators B: Chemical*, 54(1-2):43 – 50, 1999. ISSN 0925-4005. doi: http://dx.doi.org/10.1016/S0925-4005(98)00325-6. URL http://www.sciencedirect.com/science/article/pii/S0925400598003256.

[87] AA Kruchinin and Yu G Vlasov. Surface plasmon resonance monitoring by means of polarization state measurement in reflected light as the basis of a dna-probe biosensor. *Sensors and Actuators B: Chemical*, 30(1):77–80, 1996.

[88] Jiri Homola, Sinclair S. Yee, and Gunter Gauglitz. Surface plasmon resonance sensors: review. *Sensors and Actuators B: Chemical*, 54(1 - 2):3 – 15, 1999. ISSN 0925-4005. doi: 10.1016/S0925-4005(98)00321-9. URL http://www.sciencedirect.com/science/article/pii/S0925400598003219.

[89] A Drezet, A Hohenau, D Koller, A Stepanov, H Ditlbacher, B Steinberger, FR Aussenegg, A Leitner, and JR Krenn. Leakage radiation microscopy of surface plasmon polaritons. *Materials science and engineering: B*, 149(3):220–229, 2008.

[90] Ulrich Kubitscheck. *Fluorescence microscopy: from principles to biological applications*. John Wiley & Sons, 2013.

[91] HE Bennett and JL Stanford. Structure-related optical characteristics of thin metallic films in the visible and ultraviolet. In *Standardization in Spectrophotometry and Luminescence Measurements: Proceedings of a Workshop Seminar Held at the National Bureau of Standards, Gaithersburg, Maryland, November, November 19-20, 1975*, volume 466, page 133. US Department of Commerce, National Bureau of Standards, 1976.

[92] GE Healthcare. Biacore concentration analysis handbook, 2007.

[93] Ian M. White and Xudong Fan. On the performance quantification of resonant refractive index sensors. *Opt. Express*, 16(2):1020–1028, Jan 2008. doi: 10.1364/OE.16.001020. URL http://www.opticsexpress.org/abstract.cfm?URI=oe-16-2-1020.

[94] Jiří Homola. On the sensitivity of surface plasmon resonance sensors with spectral interrogation. *Sensors and Actuators B: Chemical*, 41(1-3):207 – 211, 1997. ISSN 0925-4005. doi: 10.1016/S0925-4005(97)80297-3. URL http://www.sciencedirect.com/science/article/pii/S0925400597802973.

[95] Sylvain Herminjard, Lorenzo Sirigu, Hans Peter Herzig, Eric Studemann, Andrea Crottini, Jean-Paul Pellaux, Tobias Gresch, Milan Fischer, and Jérôme Faist. Surface plasmon resonance sensor showing enhanced sensitivity for

co2 detection in the mid-infrared range. *Opt. Express*, 17(1):293–303, January 2009. doi: 10.1364/OE.17.000293. URL http://www.opticsexpress.org/abstract.cfm?URI=oe-17-1-293.

[96] Navneet K Sharma. Performances of different metals in optical fibre-based surface plasmon resonance sensor. *Pramana - Journal of Physics, Indian Academy of Sciences*, 78(3):417–427, March 2011.

[97] Kyeong-Seok Lee, Ju Myeong Son, Dae-Yong Jeong, Taek Sung Lee, and Won Mok Kim. Resolution enhancement in surface plasmon resonance sensor based on waveguide coupled mode by combining a bimetallic approach. *Sensors*, 10(12):11390–11399, 2010.

[98] Shin Ae Kim, Sung June Kim, Hyowon Moon, and Sang Beom Jun. In vivo optical neural recording using fiber-based surface plasmon resonance. *Opt. Lett.*, 37(4):614–616, Feb 2012. doi: 10.1364/OL.37.000614. URL http://ol.osa.org/abstract.cfm?URI=ol-37-4-614.

[99] Iulia Arghir, Filip Delport, Dragana Spasic, and Jeroen Lammertyn. Smart design of fiber optic surfaces for improved plasmonic biosensing. *New Biotechnology*, 32(5):473–484, 2015. ISSN 1871-6784. doi: http://dx.doi.org/10.1016/j.nbt.2015.03.012. URL http://www.sciencedirect.com/science/article/pii/S1871678415000540.

[100] Christophe Caucheteur, Tuan Guo, and Jacques Albert. Review of plasmonic fiber optic biochemical sensors: improving the limit of detection. *Analytical and bioanalytical chemistry*, 407(14):3883–3897, 2015.

[101] Byoungho Lee, Sookyoung Roh, and Junghyun Park. Current status of micro- and nano-structured optical fiber sensors. *Optical Fiber Technology*, 15(3):209 – 221, 2009. ISSN 1068-5200. doi: http://dx.doi.org/10.1016/j.yofte.2009.02.006. URL http://www.sciencedirect.com/science/article/pii/S1068520009000212.

[102] A.K. Sharma, R. Jha, and B.D. Gupta. Fiber-optic sensors based on surface plasmon resonance: A comprehensive review. *Sensors Journal, IEEE*, 7(8):1118 –1129, aug. 2007. ISSN 1530-437X. doi: 10.1109/JSEN.2007.897946.

[103] Yong Chen, Rongsheng Zheng, Yonghua Lu, Pei Wang, and Hai Ming. Fiber-optic surface plasmon resonant sensor with low-index anti-oxidation coating. *Chin. Opt. Lett.*, 9(10):100605, Oct 2011. URL http://col.osa.org/abstract.cfm?URI=col-9-10-100605.

[104] Anuj K Sharma and Gerhard J Mohr. On the performance of surface plasmon resonance based fibre optic sensor with different bimetallic nanoparticle alloy combinations. *Journal of Physics D: Applied Physics*, 41(5):055106, 2008. URL http://stacks.iop.org/0022-3727/41/i=5/a=055106.

[105] A. Hassani and M. Skorobogatiy. Design of the microstructured optical fiber-based surface plasmon resonance sensors with enhanced microfluidics. *Opt.*

Express, 14(24):11616–11621, Nov 2006. doi: 10.1364/OE.14.011616. URL http://www.opticsexpress.org/abstract.cfm?URI=oe-14-24-11616.

[106] Markus Hautakorpi, Maija Mattinen, and Hanne Ludvigsen. Surface-plasmon-resonance sensor based on three-hole microstructured optical fiber. *Opt. Express*, 16(12):8427–8432, 2008.

[107] Nannan Luan, Ran Wang, Wenhua Lv, and Jianquan Yao. Surface plasmon resonance sensor based on d-shaped microstructured optical fiber with hollow core. *Optics express*, 23(7):8576–8582, 2015.

[108] Ahmmed A Rifat, G Amouzad Mahdiraji, Desmond M Chow, Yu Gang Shee, Rajib Ahmed, and Faisal Rafiq Mahamd Adikan. Photonic crystal fiber-based surface plasmon resonance sensor with selective analyte channels and graphene-silver deposited core. *Sensors*, 15(5):11499–11510, 2015.

[109] Elizaveta Klantsataya, Alexandre François, Heike Ebendorff-Heidepriem, Peter Hoffmann, and Tanya M. Monro. Surface plasmon scattering in exposed core optical fiber for enhanced resolution refractive index sensing. *Sensors*, 15(10):25090, 2015. ISSN 1424-8220. doi: 10.3390/s151025090. URL http://www.mdpi.com/1424-8220/15/10/25090.

[110] R.C. Jorgenson and S.S. Yee. A fiber-optic chemical sensor based on surface plasmon resonance. *Sensors and Actuators B: Chemical*, 12(3):213 – 220, 1993. ISSN 0925-4005. doi: 10.1016/0925-4005(93)80021-3. URL http://www.sciencedirect.com/science/article/pii/0925400593800213.

[111] Óscar Esteban, Fernando B Naranjo, Natalia Díaz-Herrera, Sirona Valdueza-Felip, María-Cruz Navarrete, and Agustín González-Cano. High-sensitive spr sensing with indium nitride as a dielectric overlay of optical fibers. *Sensors and Actuators B: Chemical*, 158(1):372–376, 2011.

[112] Ai Hosoki, Michiko Nishiyama, Hirotaka Igawa, Atsushi Seki, and Kazuhiro Watanabe. A hydrogen curing effect on surface plasmon resonance fiber optic hydrogen sensors using an annealed au/ta205/pd multi-layers film. *Opt. Express*, 22(15):18556–18563, Jul 2014. doi: 10.1364/OE.22.018556. URL http://www.opticsexpress.org/abstract.cfm?URI=oe-22-15-18556.

[113] Mitsuhiro Iga, Atsushi Seki, and Kazuhiro Watanabe. Hetero-core structured fiber optic surface plasmon resonance sensor with silver film. *Sensors and Actuators B: Chemical*, 101(3):368–372, 2004.

[114] Keiju Takagi and Kazuhiro Watanabe. Near infrared characterization of hetero-core optical fiber spr sensors coated with ta205 film and their applications. *Sensors*, 12(2):2208–2218, 2012.

[115] Keiju Takagi, Hiroyuki Sasaki, Atsushi Seki, and Kazuhiro Watanabe. Surface plasmon resonances of a curved hetero-core optical fiber sensor. *Sensors and Actuators A: Physical*, 161(1):1–5, 2010.

[116] Radan Slavık, Jiří Homola, and Jiří Čtyrokỳ. Single-mode optical fiber surface plasmon resonance sensor. *Sensors and Actuators B: Chemical*, 54(1):74–79, 1999.

[117] Radan Slavik, Jiri Homola, Jiri Ctiroki, and Eduard Brynda. Novel spectral fiber optic sensor based on surface plasmon resonance. *Sensors and Actuators B: Chemical*, 74:106 – 111, 2001. ISSN 0925-4005. doi: http://dx.doi.org/10.1016/S0925-4005(00)00718-8. URL http://www.sciencedirect.com/science/article/pii/S0925400500007188. <ce:title>Proceedings of the 5th European Conference on Optical Chemical Sensors and Biosensors</ce:title>.

[118] Yu-Cheng Lin. Characteristics of optical fiber refractive index sensor based on surface plasmon resonance. *Microwave and Optical Technology Letters*, 55(3):574–576, 2013. ISSN 1098-2760. doi: 10.1002/mop.27397. URL http://dx.doi.org/10.1002/mop.27397.

[119] R K Verma and B D Gupta. Theoretical modelling of a bi-dimensional u-shaped surface plasmon resonance based fibre optic sensor for sensitivity enhancement. *Journal of Physics D: Applied Physics*, 41(9):095106, 2008. URL http://stacks.iop.org/0022-3727/41/i=9/a=095106.

[120] Hitoshi Suzuki, Mitsunori Sugimoto, Yoshikazu Matsui, and Jun Kondoh. Effects of gold film thickness on spectrum profile and sensitivity of a multimode-optical-fiber {SPR} sensor. *Sensors and Actuators B: Chemical*, 132(1):26 – 33, 2008. ISSN 0925-4005. doi: http://dx.doi.org/10.1016/j.snb.2008.01.003. URL http://www.sciencedirect.com/science/article/pii/S092540050800018X.

[121] Hitoshi Suzuki, Mitsunori Sugimoto, Yoshikazu Matsui, and Jun Kondoh. Fundamental characteristics of a dual-colour fibre optic spr sensor. *Measurement Science and Technology*, 17(6):1547, 2006. URL http://stacks.iop.org/0957-0233/17/i=6/a=036.

[122] Letizia De Maria, Mario Martinelli, and Giorgio Vegetti. Fiber-optic sensor based on surface plasmon interrogation. *Sensors and Actuators B: Chemical*, 12(3):221 – 223, 1993. ISSN 0925-4005. doi: http://dx.doi.org/10.1016/0925-4005(93)80022-4. URL http://www.sciencedirect.com/science/article/pii/0925400593800224.

[123] E. Fontana, H.D. Dulman, D.E. Doggett, and R.H. Pantell. Surface plasmon resonance on a single mode optical fiber. *Instrumentation and Measurement, IEEE Transactions on*, 47(1):168–173, 1998. ISSN 0018-9456. doi: 10.1109/19.728812.

[124] Aoqun Jian, Lili Deng, Shengbo Sang, Qianqian Duan, Xuming Zhang, and Wendong Zhang. Surface plasmon resonance sensor based on an angled optical fiber. 2014.

[125] Yoon-Chang Kim, Soame Banerji, Jean-Francois Masson, Wei Peng, and Karl S Booksh. Fiber-optic surface plasmon resonance for vapor phase analyses. *Analyst*, 130(6):838–843, 2005.

[126] Yoon-Chang Kim, Wei Peng, Soame Banerji, and Karl S. Booksh. Tapered fiber optic surface plasmon resonance sensor for analyses of vapor and liquid phases. *Opt. Lett.*, 30(17):2218–2220, Sep 2005. doi: 10.1364/OL.30.002218. URL http://ol.osa.org/abstract.cfm?URI=ol-30-17-2218.

[127] Zhihai Liu, Yong Wei, Yu Zhang, Yaxun Zhang, Enming Zhao, Jun Yang, and Libo Yuan. Twin-core fiber spr sensor. *Opt. Lett.*, 40(12):2826–2829, Jun 2015. doi: 10.1364/OL.40.002826. URL http://ol.osa.org/abstract.cfm?URI=ol-40-12-2826.

[128] Yinni Yu, Phillip Blake, and D Keith Roper. Tapered optical fibers designed for surface plasmon resonance phase matching. *Langmuir*, 25(1):59–63, 2008.

[129] Hyeon-Ho Jeong, Norov Erdene, Seung-Ki Lee, Dae-Hong Jeong, and Jae-Hyoung Park. Fabrication of fiber-optic localized surface plasmon resonance sensor and its application to detect antibody-antigen reaction of interferon-gamma. *Optical Engineering*, 50(12):124405–124405, 2011.

[130] Yongbin Lin, Yang Zou, Yuanyao Mo, Junpeng Guo, and Robert G Lindquist. E-beam patterned gold nanodot arrays on optical fiber tips for localized surface plasmon resonance biochemical sensing. *Sensors*, 10(10):9397–9406, 2010.

[131] Marco Consales, Armando Ricciardi, Alessio Crescitelli, Emanuela Esposito, Antonello Cutolo, and Andrea Cusano. Lab-on-fiber technology: toward multifunctional optical nanoprobes. *ACS nano*, 6(4):3163–3170, 2012.

[132] H Nguyen, F Sidiroglou, SF Collins, TJ Davis, A Roberts, and GW Baxter. A localized surface plasmon resonance-based optical fiber sensor with sub-wavelength apertures. *Applied Physics Letters*, 103(19):193116, 2013.

[133] Peipei Jia and Jun Yang. A plasmonic optical fiber patterned by template transfer as a high-performance flexible nanoprobe for real-time biosensing. *Nanoscale*, 6(15):8836–8843, 2014.

[134] Ying Lu, Cong-Jing Hao, Bao-Qun Wu, Mayilamu Musideke, Liang-Cheng Duan, Wu-Qi Wen, and Jian-Quan Yao. Surface plasmon resonance sensor based on polymer photonic crystal fibers with metal nanolayers. *Sensors*, 13 (1):956–965, 2013.

[135] Anuj Dhawan, Michael D Gerhold, and John F Muth. Plasmonic structures based on subwavelength apertures for chemical and biological sensing applications. *Sensors Journal, IEEE*, 8(6):942–950, 2008.

[136] Bertrand Gauvreau, Alireza Hassani, M Fassi Fehri, Andrei Kabashin, and Maksim A Skorobogatiy. Photonic bandgap fiber-based surface plasmon resonance sensors. *Opt. Express*, 15(18):11413–11426, 2007.

[137] Pan Chen, Yu-Jing He, Xiao-Song Zhu, and Yi-Wei Shi. Surface plasmon resonance sensor based on ethylene tetra-fluoro-ethylene hollow fiber. *Sensors*, 15(11):27917–27929, 2015.

[138] Yong-Xiang Jiang, Bing-Hong Liu, Xiao-Song Zhu, Xiao-Li Tang, and Yi-Wei Shi. Long-range surface plasmon resonance sensor based on dielectric/silver coated hollow fiber with enhanced figure of merit. *Opt. Lett.*, 40(5):744–747, Mar 2015. doi: 10.1364/OL.40.000744. URL http://ol.osa.org/abstract.cfm?URI=ol-40-5-744.

[139] Han Jianjun, Liu Xiaoxia, Zhao Xiujian, and Jing Chengbin. Fabrication silver film inside silica capillary. *Journal of Wuhan University of Technology-Mater. Sci. Ed.*, 20:64–67, 2005. ISSN 1000-2413. doi: 10.1007/BF02870876. URL http://dx.doi.org/10.1007/BF02870876.

[140] Seongmin Ju, Seongmook Jeong, Youngwoong Kim, Sang-Hyun Lee, Kadathala Linganna, Cheol Jin Kim, and Won-Taek Han. Effect of heat treatment of optical fiber incorporated with au nano-particles on surface plasmon resonance. *Optical Materials Express*, 5(6):1440–1449, 2015.

[141] M Hernaez, C R Zamarreno, I R Matias, and F J Arregui. Optical fiber humidity sensor based on surface plasmon resonance in the infra-red region. *Journal of Physics: Conference Series*, 178(1):012019, 2009. URL http://stacks.iop.org/1742-6596/178/i=1/a=012019.

[142] Satyendra K Mishra and Banshi D Gupta. Surface plasmon resonance-based fiber-optic hydrogen gas sensor utilizing indium–tin oxide (ito) thin films. *Plasmonics*, 7(4):627–632, 2012. ISSN 1557-1955. doi: 10.1007/s11468-012-9351-7. URL http://dx.doi.org/10.1007/s11468-012-9351-7.

[143] David Monzón-Hernández, Joel Villatoro, Dimas Talavera, and Donato Luna-Moreno. Optical-fiber surface-plasmon resonance sensor with multiple resonance peaks. *Appl. Opt.*, 43(6):1216–1220, Feb 2004. doi: 10.1364/AO.43.001216. URL http://ao.osa.org/abstract.cfm?URI=ao-43-6-1216.

[144] Petr Hlubina, Miroslava Kadulova, Dalibor Ciprian, and Jaroslav Sobota. Reflection-based fibre-optic refractive index sensor using surface plasmon resonance. *Journal of the European Optical Society-Rapid publications*, 9, 2014.

[145] Tan Tai Nguyen, Eun-Cheol Lee, and Heongkyu Ju. Bimetal coated optical fiber sensors based on surface plasmon resonance induced change in birefringence and intensity. *Optics express*, 22(5):5590–5598, 2014.

[146] H. Moayyed, I. T. Leite, L. Coelho, J. L. Santos, and D. Viegas. Spr sensing with bimetallic layers in optical fibers and phase interrogation. volume 8785, pages 8785FK–8785FK–7, 2013. doi: 10.1117/12.2027614. URL http://dx.doi.org/10.1117/12.2027614.

[147] F. Downes and C.M. Taylor. Optical fibre surface plasmon resonance sensor based on a palladium-yttrium alloy. *Procedia Engineering*, 120:602 – 605, 2015. ISSN 1877-7058. doi: http://dx.doi.org/10.1016/j.proeng.2015.08.738. URL http://www.sciencedirect.com/science/article/pii/S1877705815024017. Eurosensors 2015.

[148] Rajan Jha, Rajneesh K Verma, and BD Gupta. Surface plasmon resonance-based tapered fiber optic sensor: sensitivity enhancement by introducing a teflon layer between core and metal layer. *Plasmonics*, 3(4):151–156, 2008.

[149] C Perrotton, N Javahiraly, M Slaman, B Dam, and P Meyrueis. Fiber optic surface plasmon resonance sensor based on wavelength modulation for hydrogen sensing. *Optics express*, 19(106):A1175–A1183, 2011.

[150] Anuj K Sharma and B D Gupta. Fibre optic sensor based on long-range surface plasmon resonance: a theoretical analysis. *Journal of Optics A: Pure and Applied Optics*, 9(7):682, 2007. URL `http://stacks.iop.org/1464-4258/9/i=7/a=020`.

[151] Ken-Ming Guo, Shu-Fang Cheng, Lai-Kwan Chau, and Jaw-Luen Tang. Fiber optic biochemical sensing using colloidal gold-modified long period fiber grating. In *Optical Fiber Communication Conference*, page OME18. Optical Society of America, 2005.

[152] Hsing-Ying Lin, Chen-Han Huang, Gia-Ling Cheng, Nan-Kuang Chen, and Hsiang-Chen Chui. Tapered optical fiber sensor based on localized surface plasmon resonance. *Opt. Express*, 20(19):21693–21701, Sep 2012. doi: 10.1364/OE.20.021693. URL `http://www.opticsexpress.org/abstract.cfm?URI=oe-20-19-21693`.

[153] Yunliang Shao, Shuping Xu, Xianliang Zheng, Ye Wang, and Weiqing Xu. Optical fiber lspr biosensor prepared by gold nanoparticle assembly on polyelectrolyte multilayer. *sensors*, 10(4):3585–3596, 2010.

[154] Ye Wang, FQ Pu, Yue-Jiao Gu, Ping Xu, Xiao-Hua Ning, Shu-Ping Xu, Bing Zhao, and Wei-Qing Xu. Preparation of localized surface plasmon resonance sensing film with gold colloid by electrostatic assembly. *Chem. J. Chin. U*, 29: 1539–1543, 2008.

[155] Yongbin Lin, Yang Zou, and Robert G Lindquist. A reflection-based localized surface plasmon resonance fiber-optic probe for biochemical sensing. *Biomedical optics express*, 2(3):478–484, 2011.

[156] Mollye Sanders, Yongbin Lin, Jianjun Wei, Taylor Bono, and Robert G Lindquist. An enhanced lspr fiber-optic nanoprobe for ultrasensitive detection of protein biomarkers. *Biosensors and Bioelectronics*, 61:95–101, 2014.

[157] J Gabriel Ortega-Mendoza, Alfonso Padilla-Vivanco, Carina Toxqui-Quitl, Placido Zaca-Morán, David Villegas-Hernández, and Fernando Chávez. Optical fiber sensor based on localized surface plasmon resonance using silver nanoparticles photodeposited on the optical fiber end. *Sensors*, 14(10):18701–18710, 2014.

[158] Haohua Tu, Tairen Sun, and Kenneth T Grattan. Spr-based optical fiber sensors using gold–silver alloy particles as the active sensing material. *Sensors Journal, IEEE*, 13(6):2192–2199, 2013.

[159] M.H. Tu, T. Sun, and K.T.V. Grattan. Lspr optical fibre sensors based on hollow gold nanostructures. *Sensors and Actuators B: Chemical*, 191:37 – 44, 2014. ISSN 0925-4005. doi: http://dx.doi.org/10.1016/j.snb.2013.09.094. URL http://www.sciencedirect.com/science/article/pii/S0925400513011477.

[160] Haibo Zeng, Xi-Wen Du, Subhash C Singh, Sergei A Kulinich, Shikuan Yang, Jianping He, and Weiping Cai. Nanomaterials via laser ablation/irradiation in liquid: a review. *Advanced Functional Materials*, 22(7):1333–1353, 2012.

[161] K.T.V. Grattan and B.T. Meggitt. *Optical Fiber Sensor Technology: Volume 3: Applications and Systems*. Optical Fiber Sensor Technology. Springer, 1999. ISBN 9780412825705. URL https://books.google.com.au/books?id=1HmAz8L2qnYC.

[162] Jacques Albert, Li-Yang Shao, and Christophe Caucheteur. Tilted fiber bragg grating sensors. *Laser & Photonics Reviews*, 7(1):83–108, 2013. ISSN 1863-8899. doi: 10.1002/lpor.201100039. URL http://dx.doi.org/10.1002/lpor.201100039.

[163] Galina Nemova and Raman Kashyap. Fiber-bragg-grating-assisted surface plasmon-polariton sensor. *Opt. Lett.*, 31(14):2118–2120, Jul 2006. doi: 10.1364/OL.31.002118. URL http://ol.osa.org/abstract.cfm?URI=ol-31-14-2118.

[164] Zhengtian Gu, Jinlong Lan, and Kan Gao. Characteristics of plasmon coupling mode in spr based lpfg. In *Numerical Simulation of Optoelectronic Devices (NUSOD), 2015 International Conference on*, pages 55–56. IEEE, 2015.

[165] Dachao Li, Peng Wu, Rui Zhu, Jia Yang, Haixia Yu, and Kexin Xu. Implantable fiber-optic spr sensor modified with lpfg and paa-ran-paapba for continuous glucose monitoring. In *Sensors, 2012 IEEE*, pages 1–4. IEEE, 2012.

[166] Tobias Schuster, Reinhold Herschel, Niels Neumann, and Christian G Schäffer. Miniaturized long-period fiber grating assisted surface plasmon resonance sensor. *Journal of lightwave Technology*, 30(8):1003–1008, 2012.

[167] Bárbara Rutyna Heidemann, Ismael Chiamenti, Marcela Mohallem Oliveira, Marcia Muller, and José Luís Fabris. Plasmonic optical fiber sensors: enhanced sensitivity in water-based environments. *Applied Optics*, 54(27):8192–8197, 2015.

[168] Yuri N Kulchin, Oleg B Vitrik, Anton V Dyshlyuk, and Zhi Zhou. Novel fiber optic refractometric method for liquid and gaseous media. *Pacific Science Review*, 14:23–27, 2012.

[169] Yu N Kulchin, O B Vitrik, A V Dyshlyuk, and Zh Zhou. Conditions for surface plasmon resonance excitation by whispering gallery modes in a bent single mode optical fiber for the development of novel refractometric sensors. *Laser Physics*, 23(8):085105, 2013. URL http://stacks.iop.org/1555-6611/23/i=8/a=085105.

[170] G Rego. A review of refractometric sensors based on long period fibre gratings. *The Scientific World Journal*, 2013, 2013.

[171] Christophe Caucheteur, Yanina Shevchenko, Li-Yang Shao, Marc Wuilpart, and Jacques Albert. High resolution interrogation of tilted fiber grating spr sensors from polarization properties measurement. *Optics express*, 19(2):1656–1664, 2011.

[172] Christophe Caucheteur, Valérie Voisin, and Jacques Albert. Near-infrared grating-assisted spr optical fiber sensors: design rules for ultimate refractometric sensitivity. *Optics express*, 23(3):2918–2932, 2015.

[173] Changyu Shen, Yang Zhang, Wenjun Zhou, and Jacques Albert. Au-coated tilted fiber bragg grating twist sensor based on surface plasmon resonance. *Applied Physics Letters*, 104(7):071106, 2014.

[174] Yanina Y. Shevchenko and Jacques Albert. Plasmon resonances in gold-coated tilted fiber bragg gratings. *Opt. Lett.*, 32(3):211–213, Feb 2007. doi: 10.1364/OL.32.000211. URL http://ol.osa.org/abstract.cfm?URI=ol-32-3-211.

[175] Valérie Voisin, Christophe Caucheteur, Patrice Mégret, and Jacques Albert. Interrogation technique for tfbg-spr refractometers based on differential orthogonal light states. *Applied optics*, 50(22):4257–4261, 2011.

[176] Stéphanie Jetté-Charbonneau, Robert Charbonneau, Nancy Lahoud, Greg Mattiussi, and Pierre Berini. Demonstration of bragg gratings based on long ranging surface plasmon polariton waveguides. *Opt. Express*, 13(12):4674–4682, Jun 2005. doi: 10.1364/OPEX.13.004674. URL http://www.opticsexpress.org/abstract.cfm?URI=oe-13-12-4674.

[177] S. Pi, X. Zeng, N. Zhang, D. Ji, B. Chen, H. Song, A. Cheney, Y. Xu, S. Jiang, D. Sun, Y. Song, and Q. Gan. Dielectric-grating-coupled surface plasmon resonance from the back side of the metal film for ultrasensitive sensing. *IEEE Photonics Journal*, 8(1):1–6, Feb 2016. ISSN 1943-0655. doi: 10.1109/JPHOT.2015.2509870.

[178] Hong-Yu Lin, Woo-Hu Tsai, Yu-Chia Tsao, and Bor-Chiou Sheu. Side-polished multimode fiber biosensor based on surface plasmon resonance with halogen light. *Appl. Opt.*, 46(5):800–806, Feb 2007. doi: 10.1364/AO.46.000800. URL http://ao.osa.org/abstract.cfm?URI=ao-46-5-800.

[179] Xihong Zhao, Yu-Chia Tsao, Fu-Jung Lee, Woo-Hu Tsai, Ching-Ho Wang, Tsung-Liang Chuang, Mu-Shiang Wu, and Chii-Wann Lin. Optical fiber sensor based on surface plasmon resonance for rapid detection of avian influenza virus subtype h6: Initial studies. *Journal of Virological Methods*, 233:15 – 22, 2016. ISSN 0166-0934. doi: http://dx.doi.org/10.1016/j.jviromet.2016.03.007. URL http://www.sciencedirect.com/science/article/pii/S0166093416000537.

[180] Yun Liu, Qiang Liu, Shimeng Chen, Fang Cheng, Hanqi Wang, and Wei Peng. Surface plasmon resonance biosensor based on smart phone platforms.

Scientific Reports, 5:12864 EP –, 08 2015. URL http://dx.doi.org/10.1038/srep12864.

[181] H-P Chiang, PT Leung, and WS Tse. The surface plasmon enhancement effect on adsorbed molecules at elevated temperatures. *The Journal of chemical physics*, 108(6):2659–2660, 1998.

[182] Gorachand Ghosh, Michiyuki Endo, and Takashi Iwasaki. Temperature-dependent sellmeier coefficients and chromatic dispersions for some optical fiber glasses. *Lightwave Technology, Journal of*, 12(8):1338–1342, 1994.

[183] Yang Peng, Jing Hou, Zhihe Huang, and Qisheng Lu. Temperature sensor based on surface plasmon resonance within selectively coated photonic crystal fiber. *Appl. Opt.*, 51(26):6361–6367, Sep 2012. doi: 10.1364/AO.51.006361. URL http://ao.osa.org/abstract.cfm?URI=ao-51-26-6361.

[184] Anuj K. Sharma and B.D. Gupta. Theoretical model of a fiber optic remote sensor based on surface plasmon resonance for temperature detection. *Optical Fiber Technology*, 12(1):87 – 100, 2006. ISSN 1068-5200. doi: 10.1016/j.yofte.2005.07.001. URL http://www.sciencedirect.com/science/article/pii/S1068520005000374.

[185] Anuj K Sharma, Himansu S Pattanaik, and Gerhard J Mohr. On the temperature sensing capability of a fibre optic spr mechanism based on bimetallic alloy nanoparticles. *Journal of Physics D: Applied Physics*, 42(4):045104, 2009.

[186] Y. Zhao, Z. Q. Deng, and H. F. Hu. Fiber-optic spr sensor for temperature measurement. *IEEE Transactions on Instrumentation and Measurement*, 64(11):3099–3104, Nov 2015. ISSN 0018-9456. doi: 10.1109/TIM.2015.2434094.

[187] Haokun Mi, Yongjiao Wang, Pan Jin, and Liang Lei. Design of a ultrahigh-sensitivity spr-based optical fiber pressure sensor. *Optik - International Journal for Light and Electron Optics*, 124(21):5248 – 5250, 2013. ISSN 0030-4026. doi: http://dx.doi.org/10.1016/j.ijleo.2013.03.097. URL http://www.sciencedirect.com/science/article/pii/S0030402613004221.

[188] Daniel P Duarte, Nélia Alberto, Lúcia Bilro, and Rogério Nogueira. Theoretical design of a high sensitivity spr-based optical fiber pressure sensor. *Journal of Lightwave Technology*, 33(22):4606–4611, 2015.

[189] Pedro J Rivero, A Urrutia, J Goicoechea, and FJ Arregui. Optical fiber humidity sensors based on localized surface plasmon resonance (lspr) and lossy-mode resonance (lmr) in overlays loaded with silver nanoparticles. *Sensors and Actuators B: Chemical*, 173:244–249, 2012.

[190] Hamid Esmaeilzadeh, Maxime Rivard, Ezatollah Arzi, François Légaré, and Alireza Hassani. Smart textile plasmonic fiber dew sensors. *Opt. Express*, 23(11):14981–14992, Jun 2015. doi: 10.1364/OE.23.014981. URL http://www.opticsexpress.org/abstract.cfm?URI=oe-23-11-14981.

[191] Roli Verma and Banshi D. Gupta. Detection of heavy metal ions in contaminated water by surface plasmon resonance based optical fibre sensor using conducting polymer and chitosan. *Food Chemistry*, 166:568 – 575, 2015. ISSN 0308-8146. doi: http://dx.doi.org/10.1016/j.foodchem.2014.06.045. URL http://www.sciencedirect.com/science/article/pii/S0308814614009315.

[192] Priya Bhatia, Parul Yadav, and Banshi D. Gupta. Surface plasmon resonance based fiber optic hydrogen peroxide sensor using polymer embedded nanoparticles. *Sensors and Actuators B: Chemical*, 182:330 – 335, 2013. ISSN 0925-4005. doi: http://dx.doi.org/10.1016/j.snb.2013.03.021. URL http://www.sciencedirect.com/science/article/pii/S092540051300302X.

[193] Natalia Díaz-Herrera, O Esteban, MC Navarrete, Michel Le Haitre, and Agustín González-Cano. In situ salinity measurements in seawater with a fibre-optic probe. *Measurement Science and Technology*, 17(8):2227, 2006.

[194] Rajib Saikia, Mridul Buragohain, Pranayee Datta, Pabitra Nath, and Kishor Barua. Fiber-optic ph sensor based on spr of silver nanostructured film. In *TRANSPORT AND OPTICAL PROPERTIES OF NANOMATERIALS: Proceedings of the International Conference—ICTOPON-2009*, volume 1147, pages 249–255. AIP Publishing, 2009.

[195] A. B. Socorro, Pedro J. Rivero, M. Hernaez, J. Goicoechea, I. R. Matias, and F. J. Arregui. Optical fiber ph sensor based on gold nanoparticles into polymeric coatings. volume 9517, pages 95171W–95171W–6, 2015. doi: 10.1117/12.2179970. URL http://dx.doi.org/10.1117/12.2179970.

[196] Anisha Pathak, Satyendra K Mishra, and Banshi D Gupta. Ag/sno2 based spr fibre optic sensor for the detection of ammonia (nh3) gas. In *International Conference on Fibre Optics and Photonics*, pages S5A–42. Optical Society of America, 2014.

[197] Sruthi P Usha, Satyendra K Mishra, and Banshi D Gupta. Fabrication and characterization of a spr based fiber optic sensor for the detection of chlorine gas using silver and zinc oxide. *Materials*, 8(5):2204–2216, 2015.

[198] Cédric Perrotton, Ruud J Westerwaal, Nicolas Javahiraly, Martin Slaman, Herman Schreuders, Bernard Dam, and Patrick Meyrueis. A reliable, sensitive and fast optical fiber hydrogen sensor based on surface plasmon resonance. *Optics express*, 21(1):382–390, 2013.

[199] Satyendra K. Mishra, Samta Rani, and Banshi D. Gupta. Surface plasmon resonance based fiber optic hydrogen sulphide gas sensor utilizing nickel oxide doped {ITO} thin film. *Sensors and Actuators B: Chemical*, 195:215 – 222, 2014. ISSN 0925-4005. doi: http://dx.doi.org/10.1016/j.snb.2014.01.045. URL http://www.sciencedirect.com/science/article/pii/S0925400514000628.

[200] D. Daems, K. Knez, F. Delport, D. Spasic, and J. Lammertyn. Real-time pcr melting analysis with fiber optic spr enables multiplex dna identification of bacteria. *Analyst*, 141:1906–1911, 2016. doi: 10.1039/C5AN02342D. URL http://dx.doi.org/10.1039/C5AN02342D.

[201] B. Sciacca, A. François, M. Klingler-Hoffmann, J. Brazzatti, M. Penno, P. Hoffmann, and T.M. Monro. Radiative-surface plasmon resonance for the detection of apolipoprotein e in medical diagnostics applications. *Nanomedicine: Nanotechnology, Biology and Medicine*, 2012.

[202] Beniamino Sciacca, Alexandre Francois, Peter Hoffmann, and Tanya M. Monro. Multiplexing of radiative-surface plasmon resonance for the detection of gastric cancer biomarkers in a single optical fiber. *Sensors and Actuators B: Chemical*, 183(0):454 – 458, 2013. ISSN 0925-4005. doi: http://dx.doi.org/10.1016/j.snb.2013.03.131. URL http://www.sciencedirect.com/science/article/pii/S0925400513004243.

[203] Sachin K Srivastava, Roli Verma, Banshi D Gupta, Isam Khalaila, and Ibrahim Abdulhalim. Spr based fiber optic sensor for the detection of vitellogenin: An endocrine disruption biomarker in aquatic environments. *Biosensors Journal*, 2015, 2015.

[204] L Coelho, RB Queirós, JL Santos, M Cristina L Martins, D Viegas, and PAS Jorge. Dna-aptamer optical biosensors based on a lpg-spr optical fiber platform for point-of-care diagnostic. In *SPIE BiOS*, pages 89570K–89570K. International Society for Optics and Photonics, 2014.

[205] Jeroen Pollet, Filip Delport, Kris P.F. Janssen, Karolien Jans, Guido Maes, Helge Pfeiffer, Martine Wevers, and Jeroen Lammertyn. Fiber optic spr biosensing of dna hybridization and dna-protein interactions. *Biosensors and Bioelectronics*, 25(4):864 – 869, 2009. ISSN 0956-5663. doi: http://dx.doi.org/10.1016/j.bios.2009.08.045. URL http://www.sciencedirect.com/science/article/pii/S0956566309004692.

[206] Sarika Singh, Satyendra K. Mishra, and Banshi D. Gupta. Spr based fibre optic biosensor for phenolic compounds using immobilization of tyrosinase in polyacrylamide gel. *Sensors and Actuators B: Chemical*, 186:388 – 395, 2013. ISSN 0925-4005. doi: http://dx.doi.org/10.1016/j.snb.2013.06.034. URL http://www.sciencedirect.com/science/article/pii/S0925400513007156.

[207] Ming Li, Scott K Cushing, and Nianqiang Wu. Plasmon-enhanced optical sensors: a review. *Analyst*, 140(2):386–406, 2015.

[208] Jing Zhao, Shaoqing Cao, Changrui Liao, Ying Wang, Guanjun Wang, Xizhen Xu, Cailing Fu, Guiwen Xu, Jiarong Lian, and Yiping Wang. Surface plasmon resonance refractive sensor based on silver-coated side-polished fiber. *Sensors and Actuators B: Chemical*, 230:206–211, 2016.

[209] F. Abeles. La theorie generale des couches minces. *Le Journal de Physique et le Radium*, (11):307–310, 1950.

[210] Wilford N Hansen. Electric fields produced by the propagation of plane coherent electromagnetic radiation in a stratified medium. *JOSA*, 58(3):380–388, 1968.

[211] Manwen Yao, Ooi-Kiang Tan, Swee-Chuan Tjin, and John C. Wolfe. Effects of intermediate dielectric films on multilayer surface plasmon resonance behavior. *Acta Biomaterialia*, 4(6):2016 – 2027, 2008. ISSN 1742-7061. doi: http://dx.doi.org/10.1016/j.actbio.2008.06.002. URL http://www.sciencedirect.com/science/article/pii/S1742706108001682.

[212] Gorachand Ghosh. Sellmeier coefficients and dispersion of thermo-optic coefficients for some optical glasses. *Applied optics*, 36(7):1540–1546, 1997.

[213] Bora Ung and Yunlong Sheng. Interference of surface waves in a metallic nanoslit. *Opt. Express*, 15(3):1182–1190, 2007.

[214] B.D. Gupta, S.K. Srivastava, and R. Verma. *Fiber Optic Sensors Based on Plasmonics*. World Scientific, 2015. ISBN 9789814619554. URL https://books.google.com.au/books?id=td4BswEACAAJ.

[215] http://www.schott.com/advanced_optics/english/products/optical-materials/optical-glass/index.html.

[216] IH Malitson. Interspecimen comparison of the refractive index of fused silica. *JOSA*, 55(10):1205–1209, 1965.

[217] K. Okamoto. *Fundamentals of Optical Waveguides*. Optics and Photonics. Academic Press, 2006. ISBN 9780125250962. URL http://books.google.com.au/books?id=0SNXgnx6un4C.

[218] Donald M Mattox. *Handbook of physical vapor deposition (PVD) processing*. William Andrew, 2010.

[219] Hugh O Pierson. *Handbook of chemical vapor deposition: principles, technology and applications*. William Andrew, 1999.

[220] G.O. Mallory, J.B. Hajdu, American Electroplaters, and Surface Finishers Society. *Electroless plating: fundamentals and applications*. American Electroplaters and Surface Finishers Society, 1990. ISBN 9780936569079. URL https://books.google.com.au/books?id=tI-Dg_SxU9MC.

[221] F. Endres, D. MacFarlane, and A. Abbott. *Electrodeposition from Ionic Liquids*. Wiley, 2008. ISBN 9783527315659. URL https://books.google.com.au/books?id=0k4XeYrlKdMC.

[222] E. Kretschmann. The angular dependence and the polarisation of light emitted by surface plasmons on metals due to roughness. *Optics Communications*, 5(5):331 – 336, 1972. ISSN 0030-4018. doi: http://dx.doi.org/10.1016/0030-4018(72)90026-0. URL http://www.sciencedirect.com/science/article/pii/0030401872900260.

[223] K. Arya, Z. B. Su, and Joseph L. Birman. Localization of the surface plasmon polariton caused by random roughness and its role in surface-enhanced optical phenomena. *Phys. Rev. Lett.*, 54:1559–1562, Apr 1985. doi: 10.1103/PhysRevLett.54.1559. URL http://link.aps.org/doi/10.1103/PhysRevLett.54.1559.

[224] A.J. Braundmeier and E.T. Arakawa. Effect of surface roughness on surface plasmon resonance absorption. *Journal of Physics and Chemistry of Solids*, 35(4):517 – 520, 1974. ISSN 0022-3697. doi: http://dx.doi.org/10.1016/S0022-3697(74)80005-3. URL http://www.sciencedirect.com/science/article/pii/S0022369774800053.

[225] M Kanso, Stéphane Cuenot, and G Louarn. Roughness effect on the spr measurements for an optical fibre configuration: experimental and numerical approaches. *Journal of Optics A: Pure and Applied Optics*, 9(7):586, 2007.

[226] Y Saito, JJ Wang, DN Batchelder, and DA Smith. Simple chemical method for forming silver surfaces with controlled grain sizes for surface plasmon experiments. *Langmuir*, 19(17):6857–6861, 2003.

[227] Jonathan Boehm, Alexandre François, Heike Ebendorff-Heidepriem, and TanyaM. Monro. Chemical deposition of silver for the fabrication of surface plasmon microstructured optical fibre sensors. *Plasmonics*, 6:133–136, 2011. ISSN 1557-1955. doi: 10.1007/s11468-010-9178-z. URL http://dx.doi.org/10.1007/s11468-010-9178-z.

[228] Johannes Schindelin, Ignacio Arganda-Carreras, Erwin Frise, Verena Kaynig, Mark Longair, Tobias Pietzsch, Stephan Preibisch, Curtis Rueden, Stephan Saalfeld, Benjamin Schmid, et al. Fiji: an open-source platform for biological-image analysis. *Nature methods*, 9(7):676–682, 2012.

[229] David Nečas and Petr Klapetek. Gwyddion: an open-source software for SPM data analysis. *Central European Journal of Physics*, 10:181–188, 2012. ISSN 1895-1082. doi: 10.2478/s11534-011-0096-2.

[230] E.D. Palik. *Handbook of Optical Constants of Solids*. Academic Press handbook series. Elsevier Science, 1998. ISBN 9780080533780. URL https://books.google.com.au/books?id=VpuVttd2cuEC.

[231] URL http://www.luvantix.com/img/PC-373AP_TDS(RevA).pdf.

[232] J. Canning, I. Petermann, and K. Cook. Surface treatment of silicate based glass: base piranha treatment versus 193nm laser processing. pages 83512N–83512N–5, 2012. doi: 10.1117/12.915823. URL +http://dx.doi.org/10.1117/12.915823.

[233] DR Halfpenny, DM Kane, RN Lamb, and B Gong. Surface modification of silica with ultraviolet laser radiation. *Applied Physics A*, 71(2):147–151, 2000.

[234] N. Chitvoranund, S. Jiemsirilers, and D.P. Kashima. Effects of surface treatments on adhesion of silver film on glass substrate fabricated by electroless plating. *Journal of the Australian Ceramic Society*, 49(1):62–69, 2013.

[235] Yinxiang Lu. Improvement of copper plating adhesion on silane modified {PET} film by ultrasonic-assisted electroless deposition. *Applied Surface Science*, 256(11):3554 – 3558, 2010. ISSN 0169-4332. doi: http://dx.doi.org/10.1016/j.apsusc.2009.12.153. URL http://www.sciencedirect.com/science/article/pii/S0169433209018753.

[236] E. Papirer. *Adsorption on Silica Surfaces*. Surfactant Science. Taylor & Francis, 2000. ISBN 9780824700034. URL https://books.google.com.au/books?id=fzEuDBxcg8MC.

[237] Ralph K Iler. *The chemistry of silica: solubility, polymerization, colloid and surface pro perties, and biochemistry*. Wiley, 1979.

[238] Xingfei Wei and Donald K Roper. Tin sensitization for electroless plating review. *Journal of The Electrochemical Society*, 161(5):D235–D242, 2014.

[239] Herbert Tze Cheung Foo. *Optical fibre sensors with surface immobilised fluorophores*. PhD thesis, School of chemisrty and physics, July 2014.

[240] David J. Monk, David S. Soane, and Roger T. Howe. A review of the chemical reaction mechanism and kinetics for hydrofluoric acid etching of silicon dioxide for surface micromachining applications. *Thin Solid Films*, 232(1):1 – 12, 1993. ISSN 0040-6090. doi: http://dx.doi.org/10.1016/0040-6090(93)90752-B. URL http://www.sciencedirect.com/science/article/pii/004060909390752B.

[241] Kalani J. Seu, Anjan P. Pandey, Farzin Haque, Elizabeth A. Proctor, Alexander E. Ribbe, and Jennifer S. Hovis. Effect of surface treatment on diffusion and domain formation in supported lipid bilayers. *Biophysical Journal*, 92(7):2445 – 2450, 2007. ISSN 0006-3495. doi: http://dx.doi.org/10.1529/biophysj.106.099721. URL http://www.sciencedirect.com/science/article/pii/S0006349507710494.

[242] Lorenzo Leandro, Radu Malureanu, Noemi Rozlosnik, and Andrei Lavrinenko. Ultrathin, ultrasmooth gold layer on dielectrics without the use of additional metallic adhesion layers. *ACS applied materials & interfaces*, 7(10): 5797–5802, 2015.

[243] J. Pilipavicius, R. Kaleinikaite, M. Pucetaite, M. Velicka, A. Kareiva, and A. Beganskiene. Controllable formation of high density sers-active silver nanoprism layers on hybrid silica-aptes coatings. *Applied Surface Science*, 377:134 – 140, 2016. ISSN 0169-4332. doi: http://dx.doi.org/10.1016/j.apsusc.2016.03.169. URL http://www.sciencedirect.com/science/article/pii/S0169433216306420.

[244] Xavier Seguí Julià. Attachment of the silver nanoplates on the sio2 surface. 2011.

[245] E.F. Vansant, P. Van Der Voort, and K.C. Vrancken. *Characterization and Chemical Modification of the Silica Surface*. Studies in Surface Science and Catalysis. Elsevier Science, 1995. ISBN 9780080528953. URL http://books.google.com.au/books?id=QL-hZejwyG8C.

[246] J.J Cras, C.A Rowe-Taitt, D.A Nivens, and F.S Ligler. Comparison of chemical cleaning methods of glass in preparation for silanization. *Biosensors and Bioelectronics*, 14(8-9):683 – 688, 1999. ISSN 0956-5663. doi: http://dx.doi.org/10.

1016/S0956-5663(99)00043-3. URL http://www.sciencedirect.com/science/article/pii/S0956566399000433.

[247] Manca Logar, Boštjan Jancar, Danilo Suvorov, and Rok Kostanjšek. In situ synthesis of ag nanoparticles in polyelectrolyte multilayers. *Nanotechnology*, 18(32):325601, 2007. URL http://stacks.iop.org/0957-4484/18/i=32/a=325601.

[248] Pedro Jose Rivero, Javier Goicoechea, Aitor Urrutia, Ignacio Raul Matias, and Francisco Javier Arregui. Multicolor layer-by-layer films using weak polyelectrolyte assisted synthesis of silver nanoparticles. *Nanoscale research letters*, 8(1): 1–10, 2013.

[249] Dmitry G. Shchukin, Igor L. Radtchenko, and Gleb B. Sukhorukov. Photoinduced reduction of silver inside microscale polyelectrolyte capsules. *ChemPhysChem*, 4(10):1101–1103, 2003. ISSN 1439-7641. doi: 10.1002/cphc.200300740. URL http://dx.doi.org/10.1002/cphc.200300740.

[250] L. R. Pederson. Comparison of stannous and stannic chloride as sensitizing agents in electroless deposition of silver on glass using x-ray photoelectron spectroscopy. *Solar Energy Materials*, 1981.

[251] Woldemar Anatol Weyl. *Coloured glasses*. Dawson's of Pall Mall, 1959.

[252] Karim FG Brackenbury, Lynn Jones, Iris Nel, Klaus R Koch, and Jean M Wyrley-Birch. Tin (ii) chloride in the analytical chemistry of the platinum metals: From the "purple of cassius" to polyurethane foams. *Polyhedron*, 6(1): 71–78, 1987.

[253] Howard Nechamkin. *The chemistry of the elements*. McGraw-Hill, 1968.

[254] JF D'Amico, MA De Angelo, JF Henrickson, JT Kenney, and DJ Sharp. Selective electroless metal deposition using patterned photo-oxidation of sn (ii) sensitized substrates. *Journal of The Electrochemical Society*, 118(10):1695–1699, 1971.

[255] DL Mills. Attenuation of surface polaritons by surface roughness. *Physical Review B*, 12(10):4036, 1975.

[256] A Hoffmann, Z Lenkefi, and Z Szentirmay. Effect of roughness on surface plasmon scattering in gold films. *Journal of physics: Condensed matter*, 10(24): 5503, 1998.

[257] Ye Tian, Wenhui Wang, Nan Wu, Xiaotian Zou, and Xingwei Wang. Tapered optical fiber sensor for label-free detection of biomolecules. *Sensors*, 11(4): 3780–3790, 2011.

[258] Maureen A Harrison and Ian F Rae. *General techniques of cell culture*. Cambridge University Press, 1997.

[259] Baoping Chen, Qingqing Hu, Qiang Xiong, Fan Zhang, and Pingang He. An ultrasensitive scanning electrochemical microscopy (secm)-based {DNA} biosensing platform amplified with the long self-assembled {DNA} concatemers. *Electrochimica Acta*, 192:127 – 132, 2016. ISSN 0013-4686. doi: http://dx.doi.org/10.1016/j.electacta.2015.12.102. URL http://www.sciencedirect.com/science/article/pii/S0013468615310288.

[260] Constanze Lamprecht, Peter Hinterdorfer, and Andreas Ebner. Applications of biosensing atomic force microscopy in monitoring drug and nanoparticle delivery. *Expert opinion on drug delivery*, 11(8):1237–1253, 2014.

[261] Karen L Cox, Viswanath Devanarayan, Aidas Kriauciunas, Joseph Manetta, Chahrzad Montrose, and Sitta Sittampalam. Immunoassay methods. 2014.

[262] John M. Walker Ralph Rapley. Molecular biomethods handbook. polymerase chain reaction. 1994.

[263] Michael J Serpe, Youngjong Kang, and Qiang Matthew Zhang. *Photonic Materials for Sensing, Biosensing and Display Devices*. Springer, 2016.

[264] Ganeshram Krishnamoorthy. *Lab-on-a-chip surface plasmon resonance biosensor for multiplex bioassays*. PhD thesis, 2010.

[265] Gero Decher. Fuzzy nanoassemblies: Toward layered polymeric multicomposites. *Science*, 277(5330):1232–1237, 1997. doi: 10.1126/science.277.5330.1232. URL http://www.sciencemag.org/content/277/5330/1232.abstract.

[266] Uri Piran and William J Riordan. Dissociation rate constant of the biotin-streptavidin complex. *Journal of immunological methods*, 133(1):141–143, 1990.

[267] Anke K. Trilling, Jules Beekwilder, and Han Zuilhof. Antibody orientation on biosensor surfaces: a minireview. *Analyst*, 138:1619–1627, 2013. doi: 10.1039/C2AN36787D. URL http://dx.doi.org/10.1039/C2AN36787D.

[268] EF Donaldson, LC Lindesmith, AD Lobue, and RS Baric. Viral shape-shifting: norovirus evasion of the human immune system. *Nature Reviews Microbiology*, 8(3):231–241, March 2010.

[269] Melissa K Jones, Makiko Watanabe, Shu Zhu, Christina L Graves, Lisa R Keyes, Katrina R Grau, Mariam B Gonzalez-Hernandez, Nicole M Iovine, Christiane E Wobus, Jan Vinjé, et al. Enteric bacteria promote human and mouse norovirus infection of b cells. *Science*, 346(6210):755–759, 2014.

[270] A de Rougemont, N Ruvoen-Clouet, B Simon, M Estienney, C Elie-Caille, S Aho, P Pothier, J Le Pendu, W Boireau, and G Belliot. Qualitative and quantitative analysis of the binding of gii.4 norovirus variants onto human blood group antigens. *Journal of virology*, 85(9):4057–4070, 2011.

[271] Haruko Shirato, Satoko Ogawa, Hiromi Ito, Takashi Sato, Akihiko Kameyama, Hisashi Narimatsu, Zheng Xiaofan, Tatsuo Miyamura, Takaji Wakita, Koji Ishii, et al. Noroviruses distinguish between type 1 and type 2 histo-blood group antigens for binding. *Journal of virology*, 82(21):10756–10767, 2008.

[272] Betsy Jean Yakes, Efstathia Papafragkou, Stephen M. Conrad, John D. Neill, Julia F. Ridpath, William Burkhardt III, Michael Kulka, and Stacey L. DeGrasse. Surface plasmon resonance biosensor for detection of feline calicivirus, a surrogate for norovirus. *International Journal of Food Microbiology*, 162(2):152 – 158, 2013. ISSN 0168-1605. doi: 10.1016/j.ijfoodmicro.2013.01.011. URL http://www.sciencedirect.com/science/article/pii/S0168160513000408.

[273] Peng Tian, Anna L Engelbrektson, Xi Jiang, Weiming Zhong, and Robert E Mandrell. Norovirus recognizes histo-blood group antigens on gastrointestinal cells of clams, mussels, and oysters: a possible mechanism of bioaccumulation. *Journal of Food Protection*, 70(9):2140–2147, 2007.

[274] R Barer and S Tkaczyk. Refractive index of concentrated protein solutions. *Nature*, 1954.

[275] Nor Aliya Hamizi and Mohd Rafie Johan. Optical properties of cdse quantum dots via non-top based route. *International Journal of Electrochemical Science*, 7: 8458–8467, 2012.

[276] Erik P. Schartner, Georgios Tsiminis, Alexandre François, Roman Kostecki, Stephen C. Warren-Smith, Linh Viet Nguyen, Sabrina Heng, Tess Reynolds, Elizaveta Klantsataya, Kris J. Rowland, Andrew D. Abell, Heike Ebendorff-Heidepriem, and Tanya M. Monro. Taming the light in microstructured optical fibers for sensing. *International Journal of Applied Glass Science*, pages n/a–n/a, 2015. ISSN 2041-1294. doi: 10.1111/ijag.12128. URL http://dx.doi.org/10.1111/ijag.12128.

[277] Adrian Amezcua Correa. *Deposition of electronic and plasmonic materials inside microstructured optical fibres*. PhD thesis, University of Southampton, November 2007.

[278] Roman Kostecki, Heike Ebendorff-Heidepriem, Claire Davis, Grant McAdam, Stephen C. Warren-Smith, and Tanya M. Monro. Silica exposed-core microstructured optical fibers. *Opt. Mater. Express*, 2(11):1538–1547, Nov 2012. doi: 10.1364/OME.2.001538. URL http://www.opticsinfobase.org/ome/abstract.cfm?URI=ome-2-11-1538.

[279] Stephen C. Warren-Smith, Heike Ebendorff-Heidepriem, Tze Cheung Foo, Roger Moore, Claire Davis, and Tanya M. Monro. Exposed-core microstructured optical fibers for real-time fluorescence sensing. *Opt. Express*, 17(21):18533–18542, Oct 2009. doi: 10.1364/OE.17.018533. URL http://www.opticsexpress.org/abstract.cfm?URI=oe-17-21-18533.

[280] Yeuk L Hoo, Wei Jin, Chunzheng Shi, Hoi L Ho, Dong N Wang, and Shuang C Ruan. Design and modeling of a photonic crystal fiber gas sensor. *Applied Optics*, 42(18):3509–3515, 2003.

[281] Felicity M Cox, Richard Lwin, Maryanne CJ Large, and Cristiano MB Cordeiro. Opening up optical fibres. *Optics Express*, 15(19):11843–11848, 2007.

[282] Elizaveta Klantsataya, Alexandre Francois, Agnieszka Zuber, Valeria Torok, Roman Kostecki, and Tanya M. Monro. Exposed core microstructured optical fiber surface plasmon resonance biosensor. In *Proc. SPIE*. SPIE, 2014.

[283] Nannan Luan, Ran Wang, Wenhua Lv, and Jianquan Yao. Surface plasmon resonance sensor based on exposed-core microstructured optical fibres. *Electronics Letters*, 51(9):714–715, 2015.

[284] Xianchao Yang, Ying Lu, Mintuo Wang, and Jianquan Yao. An exposed-core grapefruit fibers based surface plasmon resonance sensor. *Sensors*, 15 (7):17106–17114, 2015.

[285] Matthew Ryan Henderson. *Nanodiamond in optical fibre*. PhD thesis, School of Chemistry and Physics, 2013.

[286] URL `http://www.tpub.com/neets/tm/108-3.htm`.

[287] Stephen C. Warren-Smith, Jingxuan Wie, Mario Chemnitz, Roman Kostecki, Heike Ebendorff-Heidepriem, Tanya M. Monro, and Markus A. Schmidt. Third harmonic generation in exposed-core microstructured optical fibers. *Opt. Express*, 24(16):17860–17867, Aug 2016. doi: 10.1364/OE.24.017860. URL `http://www.opticsexpress.org/abstract.cfm?URI=oe-24-16-17860`.

[288] Joseph R Lakowicz. *Principles of fluorescence spectroscopy*. Springer Science & Business Media, 2013.

[289] Chris D Geddes, Ignacy Gryczynski, Joanna Malicka, Zygmunt Gryczynski, and Joseph R Lakowicz. Metal-enhanced fluorescence: potential applications in hts. *Combinatorial chemistry & high throughput screening*, 6(2):109–117, 2003.

[290] Kadir Aslan, Ignacy Gryczynski, Joanna Malicka, Evgenia Matveeva, Joseph R Lakowicz, and Chris D Geddes. Metal-enhanced fluorescence: an emerging tool in biotechnology. *Current Opinion in Biotechnology*, 16(1):55 – 62, 2005. ISSN 0958-1669. doi: http://dx.doi.org/10.1016/j.copbio.2005.01.001. URL `http://www.sciencedirect.com/science/article/pii/S0958166905000029`. Analytical biotechnology.

[291] Kadir Aslan, Stuart N. Malyn, Yongxia Zhang, and Chris D. Geddes. Conversion of just-continuous metallic films to large particulate substrates for metal-enhanced fluorescence. *Journal of Applied Physics*, 103(8):084307, 2008. doi: http://dx.doi.org/10.1063/1.2905319. URL `http://scitation.aip.org/content/aip/journal/jap/103/8/10.1063/1.2905319`.

[292] Ai Ling Feng, Min Li You, Limei Tian, Srikanth Singamaneni, Ming Liu, Zhenfeng Duan, Tian Jian Lu, Feng Xu, and Min Lin. Distance-dependent plasmon-enhanced fluorescence of upconversion nanoparticles using polyelectrolyte multilayers as tunable spacers. *Scientific Reports*, 5:7779 EP –, 01 2015. URL `http://dx.doi.org/10.1038/srep07779`.

[293] Kadir Aslan, Zoya Leonenko, JosephR. Lakowicz, and ChrisD. Geddes. Annealed silver-island films for applications in metal-enhanced fluorescence:

Interpretation in terms of radiating plasmons. *Journal of Fluorescence*, 15 (5):643–654, 2005. ISSN 1053-0509. doi: 10.1007/s10895-005-2970-z. URL http://dx.doi.org/10.1007/s10895-005-2970-z.

[294] Jakub Dostalek and Wolfgang Knoll. Biosensors based on surface plasmon-enhanced fluorescence spectroscopy (review). *Biointerphases*, 3(3):FD12–FD22, 2008. doi: http://dx.doi.org/10.1116/1.2994688. URL http://scitation.aip.org/content/avs/journal/bip/3/3/10.1116/1.2994688.

[295] Ying Jiang, Hai-Yu Wang, Hai Wang, Bing-Rong Gao, Ya wei Hao, Yu Jin, Qi-Dai Chen, and Hong-Bo Sun. Surface plasmon enhanced fluorescence of dye molecules on metal grating films. *The Journal of Physical Chemistry C*, 115 (25):12636–12642, 2011. doi: 10.1021/jp203530e. URL http://dx.doi.org/10.1021/jp203530e.

[296] Martin Bauch, Koji Toma, Mana Toma, Qingwen Zhang, and Jakub Dostalek. Plasmon-enhanced fluorescence biosensors: a review. *Plasmonics*, 9(4):781–799, 2014.

[297] Koji Toma, Milan Vala, Pavel Adam, Jiří Homola, Wolfgang Knoll, and Jakub Dostálek. Compact surface plasmon-enhanced fluorescence biochip. *Opt. Express*, 21(8):10121–10132, Apr 2013. doi: 10.1364/OE.21.010121. URL http://www.opticsexpress.org/abstract.cfm?URI=oe-21-8-10121.

[298] Daniel Darvill, Anthony Centeno, and Fang Xie. Plasmonic fluorescence enhancement by metal nanostructures: shaping the future of bionanotechnology. *Physical Chemistry Chemical Physics*, 15(38):15709–15726, 2013.

[299] Jian Zhang and Joseph R Lakowicz. Metal-enhanced fluorescence of an organic fluorophore using gold particles. *Optics express*, 15(5):2598–2606, 2007.

[300] Rafal Luchowski, Tanya Shtoyko, Evgenia Matveeva, Pabak Sarkar, Julian Borejdo, Zygmunt Gryczynski, and Ignacy Gryczynski. Molecular fluorescence enhancement on fractal-like structures. *Applied spectroscopy*, 64(6):578–583, 2010.

[301] Thomas J Sørensen, Bo W Laursen, Rafal Luchowski, Tanya Shtoyko, Irina Akopova, Zygmunt Gryczynski, and Ignacy Gryczynski. Enhanced fluorescence emission of me-adota+ by self-assembled silver nanoparticles on a gold film. *Chemical physics letters*, 476(1):46–50, 2009.

[302] GP Acuna, FM Möller, P Holzmeister, S Beater, B Lalkens, and P Tinnefeld. Fluorescence enhancement at docking sites of dna-directed self-assembled nanoantennas. *Science*, 338(6106):506–510, 2012.

[303] Anika Kinkhabwala, Zongfu Yu, Shanhui Fan, Yuri Avlasevich, Klaus Müllen, and WE Moerner. Large single-molecule fluorescence enhancements produced by a bowtie nanoantenna. *Nature Photonics*, 3(11):654–657, 2009.

[304] Anatoliy I Dragan, Eric S Bishop, Jose R Casas-Finet, Robert J Strouse, James McGivney, Mark A Schenerman, and Chris D Geddes. Distance dependence of metal-enhanced fluorescence. *Plasmonics*, 7(4):739–744, 2012.

[305] Joseph R. Lakowicz. Radiative decay engineering 5: metal-enhanced fluorescence and plasmon emission. *Analytical Biochemistry*, 337(2):171 – 194, 2005. ISSN 0003-2697. doi: http://dx.doi.org/10.1016/j.ab.2004.11.026. URL http://www.sciencedirect.com/science/article/pii/S0003269704009303.

[306] Weihua Zhang, Fei Ding, Wen-Di Li, Yuxuan Wang, Jonathan Hu, and Stephen Y Chou. Giant and uniform fluorescence enhancement over large areas using plasmonic nanodots in 3d resonant cavity nanoantenna by nanoimprinting. *Nanotechnology*, 23(22):225301, 2012.

[307] Xia Yu, Derrick Yong, Huiyu Zhang, Hao Li, Ying Zhang, Chi Chiu Chan, Ho-Pui Ho, Hairong Liu, and Deming Liu. Plasmonic enhanced fluorescence spectroscopy using side-polished microstructured optical fiber. *Sensors and Actuators B: Chemical*, 160(1):196 – 201, 2011. ISSN 0925-4005. doi: http://dx.doi.org/10.1016/j.snb.2011.07.033. URL http://www.sciencedirect.com/science/article/pii/S0925400511006757.

[308] Jian Zhang, Evgenia Matveeva, Ignacy Gryczynski, Zoya Leonenko, and Joseph R Lakowicz. Metal-enhanced fluoroimmunoassay on a silver film by vapor deposition. *The Journal of Physical Chemistry B*, 109(16):7969–7975, 2005.

[309] Mustafa H Chowdhury, Krishanu Ray, and Joseph R Lakowicz. Use of aluminum films as substrates for enhanced fluorescence in the ultraviolet-blue spectral region. In *Biomedical Optics (BiOS) 2008*, pages 68690E–68690E. International Society for Optics and Photonics, 2008.

[310] Thomas Neumann, M-L Johansson, Dev Kambhampati, and Wolfgang Knoll. Surface-plasmon fluorescence spectroscopy. *Advanced Functional Materials*, 12 (9):575–586, 2002.

[311] Ming-Yaw Ng and Wei-Chih Liu. Fluorescence enhancements of fiber-optic biosensor with metallic nanoparticles. *Opt. Express*, 17(7):5867–5878, Mar 2009. doi: 10.1364/OE.17.005867. URL http://www.opticsexpress.org/abstract.cfm?URI=oe-17-7-5867.

[312] Alexandre François, Beniamino Sciacca, Agnieszka Zuber, Elizaveta Klantsataya, and Tanya M Monro. Dependence of metal-enhanced fluorescence on surface roughness. In *SPIE BiOS*, pages 89570O–89570O. International Society for Optics and Photonics, 2014.

[313] Elizaveta Klantsataya, Alexandre François, Heike Ebendorff-Heidepriem, Beniamino Sciacca, Agnieszka Zuber, and Tanya M. Monro. Effect of surface roughness on metal enhanced fluorescence in planar substrates and optical fibers. *Opt. Mater. Express*, 6(6):2128–2138, Jun 2016. doi: 10.1364/OME.6.002128. URL http://www.osapublishing.org/ome/abstract.cfm?URI=ome-6-6-2128.

[314] R. S. Sennett and G. D. Scott. The structure of evaporated metal films and their optical properties. *J. Opt. Soc. Am.*, 40(4):203–211, Apr 1950. doi: 10.1364/JOSA.40.000203. URL http://www.osapublishing.org/abstract.cfm?URI=josa-40-4-203.

[315] Krishanu Ray, Ramachandram Badugu, and Joseph R Lakowicz. Polyelectrolyte layer-by-layer assembly to control the distance between fluorophores and plasmonic nanostructures. *Chemistry of Materials*, 19(24):5902–5909, 2007.

[316] Frank Caruso, Kenichi Niikura, D Neil Furlong, and Yoshio Okahata. Ultrathin multilayer polyelectrolyte films on gold: construction and thickness determination. *Langmuir*, 13(13):3422–3426, 1997.

[317] George W Ford and Willes H Weber. Electromagnetic interactions of molecules with metal surfaces. *Physics Reports*, 113(4):195–287, 1984.

[318] Barbara J. Messinger, K. Ulrich von Raben, Richard K. Chang, and Peter W. Barber. Local fields at the surface of noble-metal microspheres. *Phys. Rev. B*, 24:649–657, Jul 1981. doi: 10.1103/PhysRevB.24.649. URL `http://link.aps.org/doi/10.1103/PhysRevB.24.649`.

[319] A. François, J. Boehm, S. Y. Oh, T. Kok, and T. M. Monro. Surface scattering plasmon resonance fibre sensors: demonstration of rapid influenza a virus detection. pages 80280J–80280J–11. Proceedings of SPIE, 2011. doi: 10.1117/12.883825. URL `+http://dx.doi.org/10.1117/12.883825`.

[320] Prathamesh Pavaskar, Jesse Theiss, and Stephen B. Cronin. Plasmonic hot spots: nanogap enhancement vs. focusing effects from surrounding nanoparticles. *Opt. Express*, 20(13):14656–14662, Jun 2012. doi: 10.1364/OE.20.014656. URL `http://www.opticsexpress.org/abstract.cfm?URI=oe-20-13-14656`.

[321] Masahiko Daimon and Akira Masumura. Measurement of the refractive index of distilled water from the near-infrared region to the ultraviolet region. *Applied optics*, 46(18):3811–3820, 2007.

[322] Jörg Rheims, T Wriedt, et al. Refractive-index measurements in the near-ir using an abbe refractometer. *Measurement Science and Technology*, 8(6):601, 1997.

[323] Eric Le Ru and Pablo Etchegoin. *Principles of Surface-Enhanced Raman Spectroscopy: and related plasmonic effects*. Elsevier, 2008.